

Dissertation zur Erlangung des Doktorgrades  
der Fakultät für Chemie und Pharmazie  
der  
Ludwig-Maximilians-Universität München

Expanding the toolbox of DNA-PAINT  
microscopy: from method development  
to cellular applications

Thomas Schlichthärle

aus

Ulm, Deutschland

2020



# Erklärung

Diese Dissertation wurde im Sinne von § 7 der Promotionsordnung vom 28. November von Herrn Prof. Dr. Ralf Jungmann betreut und von Herrn Prof. Dr. Karl-Peter Hopfner von der Fakultät für Chemie und Pharmazie vertreten.

# Eidesstattliche Versicherung

Diese Dissertation wurde eigenständig und ohne unerlaubte Hilfe erarbeitet.

München, 28.02.2020

Thomas Schlichthärle

Dissertation eingereicht am: 28.02.2020

1. Gutachter: Prof. Dr. Karl-Peter Hopfner
2. Gutachter: Prof. Dr. Ralf Jungmann

Mündliche Prüfung am: 20.04.2020



# Contents

List of Figures.....	iv
Summary.....	v
Abbreviations.....	vi
Publications.....	vii
1 Introduction.....	1
1.1 Microscopy.....	1
1.2 Microscopy Methods and Setup Types.....	3
1.3 Super-Resolution Microscopy.....	5
1.4 Single-Molecule Localization Microscopy.....	7
1.5 DNA Nanotechnology as standard for microscopy.....	10
1.6 DNA-PAINT.....	11
1.7 Labeling probes for super-resolution microscopy.....	15
1.8 Labeling Chemistries.....	20
1.9 Focal Adhesion Biology.....	23
1.10 Clustering.....	25
2 Aim of Thesis.....	29
3 Brief summary of manuscripts.....	30
3.1 Paper I : DNA nanotechnology and fluorescence applications.....	30
3.2 Paper II : Super-Resolution Microscopy with DNA-PAINT.....	31
3.3 Paper III: Site-specific labeling of Affimers for DNA-PAINT microscopy.....	32
3.4 Paper IV: Bacterial-derived antibody binders as small adapters for DNA-PAINT microscopy.....	33
3.5 Paper V : Direct visualization of single nuclear pore complex proteins using genetically-encoded probes for DNA-PAINT.....	35
3.6 Paper VI: Spatial association of integrin-talin-kindlin during cell matrix adhesion.....	37
4 Further developments.....	38
4.1 DNA origami as a universal platform to analyze probes and cluster formation.....	38
4.2 Quantitative cluster analysis and detection.....	40
5 Discussion and Outlook.....	44
6 Bibliography.....	48
7 Acknowledgements.....	59
8 Appendix.....	60
8.1 Methods.....	60
8.2 Publications.....	75

# List of Figures

Figure 1: Jablonski diagram.....	2
Figure 2: Basic microscopy setup design and total internal reflection fluorescence .....	4
Figure 3: Basic super-resolution microscopy strategies .....	6
Figure 4: Single Molecule Localization Microscopy.....	7
Figure 5: 3D single molecule localization microscopy with astigmatism.....	9
Figure 6: DNA Nanotechnology and its applications .....	11
Figure 7: DNA-PAINT overview .....	14
Figure 8: Phage Display schematics.....	17
Figure 9: Labeling probes.....	19
Figure 10: Chemical labeling strategies .....	21
Figure 11: Super-resolution microscopy of cellular components .....	22
Figure 12: Focal adhesion architecture.....	24
Figure 13: Clustering methods in SMLM.....	28
Figure 14: Labeling platform .....	39
Figure 15: Cluster detection.....	41
Figure 16: Simulated complex formation.....	43

# Summary

Light microscopy has enabled biologists to visualize life with unprecedented resolution, however, super-resolution microscopy was not able to reach a resolution at the single-protein level until recently. Due to the relatively new technology developments in the field and especially to the emergence and implementation of DNA-PAINT, localization precisions in the size range of single fluorophore molecules have been reported<sup>1</sup>. Additionally, the programmable nature of DNA probes, which encode the molecular identity of a target, has enabled to perform multiplexing without being limited by the properties of fluorophores<sup>2</sup>. The third major advance using this technology is to count single biomolecules<sup>3</sup>.

However, in order to apply this impressive technological development within a cellular context, it is of utmost importance to attach the DNA docking site to the target under investigation via labeling probes<sup>4</sup>. Different labeling strategies were explored during the course of the thesis, ranging from NHS ester and maleimide chemistry to attach DNA strands to antibodies, nanobodies and Affimers, to genetically encoded tags, including SNAP- or HaloTags. To evaluate the performance of the binders and their capability to resolve artificially templated nanopatterns, a DNA origami based labeling platform was developed.

The high affinity reagents were then applied in a vast variety of different internal and collaborative research projects which harnessed different properties and advantages of DNA-PAINT super-resolution microscopy, with the goal to advance the technique to single protein imaging. For example, we were able to measure the 12 nm distance separation of two structural NUP96 proteins within the nuclear pore complex. Additionally, we demonstrated the existence of a triple molecular complex within the densely packed focal adhesion structure consisting of activated  $\beta$ 1 integrin, talin-1 and kindlin-2.

Data analysis plays an important role in super-resolution microscopy to dissect protein organization and colocalization. In the last part of this thesis, an analysis pipeline was developed to detect single sites and simulations were performed to analyze complex formation under reduced labeling efficiency conditions.

# Abbreviations

BG	benzylguanine
BSA	bovine serum albumin
CRISPR	clustered regularly interspaced short palindromic repeats
DBCO	dibenzocyclooctyne
DBSCAN	density-based spatial clustering of applications with noise
DNA	deoxyribonucleic acid
dSTORM	direct stochastic optical reconstruction microscopy
EM	electron microscopy
EPI	epifluorescence
GFP	green fluorescent protein
HILO	highly inclined and laminated optical sheet
kDa	kilo dalton
NeNA	nearest neighbor based analysis
NHS	N-Hydroxysuccinimid
NPC	nuclear pore complex
MINFLUX	minimal photon fluxes
PAINT	point accumulation for imaging in nanoscale topography
PALM	photo-activated localization microscopy
RNA	ribonucleic acid
SMLM	single-molecule localization microscopy
SNR	signal-to-noise ratio
STED	stimulated emission depletion
STORM	stochastic optical reconstruction microscopy
TCO	trans-cyclooctene
TIRFM	total internal reflection fluorescence microscopy
tris-NTA	tris-nitrilotriacetic acid
TZ	tetrazine

# Publications

This thesis is based on following publications:

Paper I: **T. Schlichthaerle**, M.T. Strauss, F. Schueder, J.B. Woehrstein, R. Jungmann  
*DNA nanotechnology and fluorescence applications*  
Current Opinion in Biotechnology (2016). 39: 41-47

Paper II: J. Schnitzbauer\*, M.T. Strauss\*, **T. Schlichthaerle**, F. Schueder, R. Jungmann  
*Super-Resolution Microscopy with DNA-PAINT*  
Nature Protocols (2017). 12: 1198-1228

Paper III: **T. Schlichthaerle**, A.S. Eklund, F. Schueder, M.T. Strauss, C. Tiede, A. Curd, J. Ries, M. Peckham, D.C. Tomlinson, R. Jungmann  
*Site-specific labeling of Affimers for DNA-PAINT microscopy*  
Angewandte Chemie Int. Ed. (2018). 57: 11060-11063

Paper IV: **T. Schlichthaerle**\*, M. Ganji\*, A. Auer, O.K. Wade, R. Jungmann  
*Bacterially derived antibody binders as small adapters for DNA-PAINT microscopy*  
ChemBioChem (2019). 20(8): 1032-1038.

Paper V: **T. Schlichthaerle**\*, M.T. Strauss\*, F. Schueder\*, A. Auer, B. Nijmeijer, M. Kueblbeck, V.J. Sabinina, J.V. Thevathasan, J. Ries, J. Ellenberg, R. Jungmann  
*Direct visualization of single nuclear pore complex proteins using genetically-encoded probes for DNA-PAINT*  
Angewandte Chemie Int. Ed. (2019). 58: 13004-13008

Paper VI: L. Fischer\*, C. Klingner\*, **T. Schlichthaerle**\*, M. T. Strauss, R. Böttcher, C. Schreiber, J. O. Rädler, R. Fässler, C. Grashoff°, R. Jungmann°  
*Spatial association of integrin-talin-kindlin during cell matrix adhesions (to be submitted)*

\*Co-first authors

°Co-corresponding authors



# 1 Introduction

## 1.1 Microscopy

With the invention and application of highly precise lenses for microscopy apparatus, Antoni van Leeuwenhoek had a close look on the microworld already in the 17th century and was able to discover bacteria, analyzed sperm cells and observed the typical banded architecture of muscle fibers<sup>5</sup>. Since the significant advances in lens production and microscopy designs later advanced by Fraunhofer and Carl Zeiss, microscopes became a standard tool for biologists to dissect biological specimen<sup>6,7</sup>. In particular, they helped to understand the distribution of biomolecules, their trafficking<sup>8</sup> as well as their molecular mechanisms of action. Many different mechanisms have been elucidated so far using microscopy approaches, ranging from isolated protein systems and in vitro reconstitution assays<sup>9</sup> to animal studies<sup>10</sup>.

However, in order to visualize those biomolecules and determine their molecular identity, fluorescent markers are necessary. In fluorescence microscopy, electrons of a fluorophore molecule can absorb photon energy from a laser light source and are excited from the ground state  $S_0$ , to a higher energy state  $S_1$ . Once the electrons return back into their energetic ground state, a photon with lower energy and higher wavelength is emitted. The shift in wavelength is called Stokes shift<sup>11</sup>. However, the electrons can also lose energy via vibrational relaxation and would not emit any photons during this process. The different processes occurring when electrons absorb light to reach a higher energy level can be depicted in a Jablonski diagram (Figure 1)<sup>12</sup>. Electrons can also converse into a triplet or a dark state  $T_1$  from their higher energy level, where they can reside longer and do not emit any photons upon returning back to the ground state  $S_0$ . The requirement that a molecule can emit fluorescence depends on the electrons in the outer orbitals. In double bonds, the energy difference between the excited state and the ground state is lower, which enables electrons to change from the ground state to the excited state by absorbing light energy. Heterocyclic compound molecules harbor a multitude of double bonds and are therefore particularly suited as fluorophore agents<sup>13</sup>. These agents can be derived from small molecule scaffolds, for example from the cyanine family<sup>14,15</sup>. One major parameter important for the quality of a fluorophore is the quantum yield, which describes the percentage of absorbed photons necessary to yield in a fluorescent event.

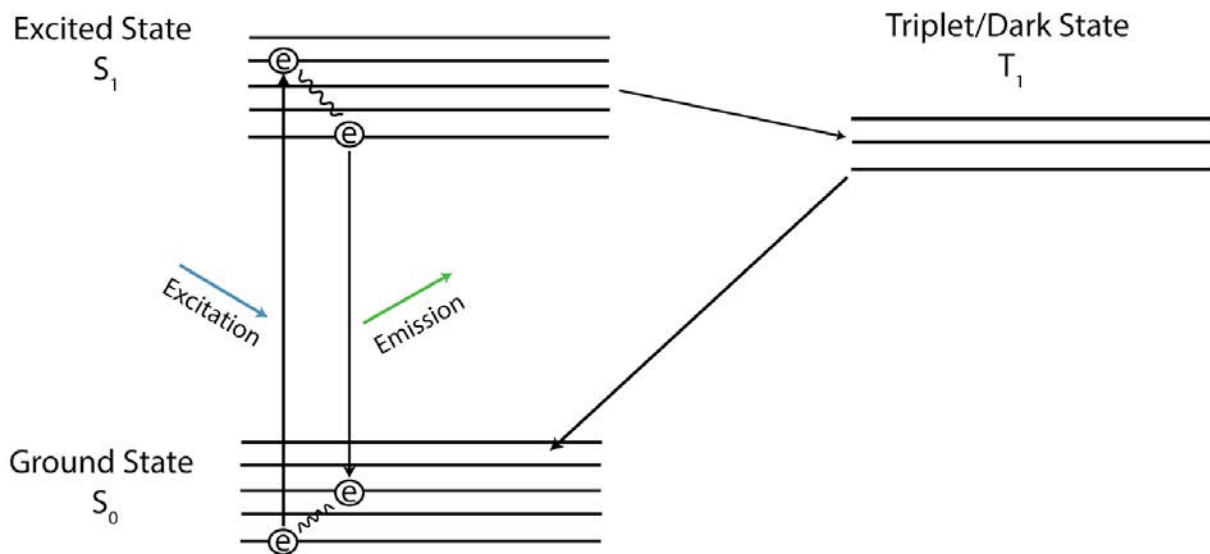


Figure 1: Jablonski diagram. Electrons reside in a ground state  $S_0$  from which they can be excited to an activated energy state  $S_1$  by absorbing the energy of photons. Within the different levels of the excited state, they are able to undergo vibrational coupling and can return into a lower energy state in  $S_1$  or converse into a triplet or dark state  $T_1$ . From there, electrons can return back into the ground state  $S_0$  without emitting a photon. They can also return back from the excited state into the ground state and emit a photon with higher wavelength then previously absorbed. This shift in wavelength is called the Stokes shift and the process is called fluorescence.

In order to dissect cell biological systems, these fluorescent molecules need to be brought to their target under investigation. There are two basic strategies of how this can be achieved. First, the biomolecule of interest can be tagged via a genetically encoded protein, which directly has or can be modified with a small molecule ligand to have fluorescent properties. Second, a high-affinity reagent against the protein of interest can be labeled with a fluorophore and added to the cell after fixation. The green fluorescent protein (GFP), as an example for the first case, was discovered by Osamu Shimomura in the jellyfish *aequorea victoria*<sup>16</sup> and later engineered and applied to cell biological research by Roger Tsien<sup>17</sup>. GFP is a protein, which is 27 kDa in size and consists of a cylindrical beta barrel fold, harboring a chromophoric region in the center<sup>18</sup>. The basic discovery of the green fluorescent protein has led to countless variants with a variety of fluorescent properties within the visible light spectrum, for example mCherry<sup>19</sup> or mNeonGreen<sup>20</sup>. Additionally, fluorescence encoded in those protein structures has proven particularly useful and led to a large variety of different applications, ranging from the analysis of protein trafficking<sup>21</sup> to the tracing of neurons in whole brains<sup>22</sup>. For their groundbreaking work on the discovery and development of GFP, Tsien, Shimomura and Chalfie received the nobel prize in chemistry in 2008.

Antibody-based reagents, which are an example for the second category, exploit the unique capability of the immune system of animals including donkeys, rabbits, goats or mice, to

produce high-affinity binders after several rounds of vaccination with the target protein of interest<sup>23</sup>.

These high affinity reagents, can be extracted from the serum of the animals via affinity purification<sup>24</sup>. The antibodies are then labeled covalently with small organic fluorophores via available chemical residues for use in fluorescence microscopy. Labeling probes and covalent attachment strategies will be described in more detail in the chapters 1.7 and 1.8. In the next chapters we will first discuss the basics of microscopy and super-resolution.

## 1.2 Microscopy Methods and Setup Types

Different microscopy setup types exist and are suitable for different applications. The basic design consists of an epi-fluorescence setup, detailed in Figure 2a<sup>25</sup>. In this specific setup, a laser beam is coupled into the objective via a dichroic-mirror. Upon excitation of the sample, the emission light harboring a longer wavelength is collected via the objective and guided through the dichroic mirror to reach an array detector, e.g. a camera. However, for single molecule applications, where it is most important to achieve a high signal-to-noise ratio and which are therefore sensitive to background light, total internal reflection fluorescence microscopy (TIRF) was implemented to only excite fluorophores close to the surface<sup>26</sup>. In TIRF microscopy, the laser excitation beam creates an exponentially decaying evanescent electromagnetic field in the sample after being totally reflected at the coverglass-water interface<sup>27</sup>, which is depicted in Figure 2b. The total reflection usually takes place if the laser reaches the glass at an angle larger than the critical angle, which depends on the refractive index of the glass  $n_1$  as well as the refractive index of the water/cell side  $n_2$  and can be calculated with following formula:

$$\arcsin(\theta_{critical}) = \frac{n_2}{n_1}$$

For a typically used borosilicate glass in microscopy with a refractive index  $n_1$  of 1.52 and  $n_2$  of 1.33 for water, the critical angle can be calculated to 61.04°.

The evanescent wave along the glass-water interface can only penetrate ~100-200 nm into the sample. Therefore, only fluorophore molecules at the bottom of the glass coverslip are excited, which reduces the background from undesired excitation taking place deeper in the sample and ultimately increases the signal to noise ratio. The decay of the evanescent wave follows an exponential distribution and the depth can be described as:

## 1.2 Microscopy Methods and Setup Types

$$d = \frac{\lambda}{4\pi\sqrt{n_1^2 \sin^2(\theta) - n_2^2}}$$

Deducing from this formula, the depth of the evanescent field depends on the incident angle of the laser beam, the refractive indices as well as the used wavelength  $\lambda$ <sup>27</sup>. For wavelengths at 640 nm, 561 nm or 488 nm under an incident angle of 66°, the calculated penetration depths would be 127.6 nm, 111.9 nm and 97.3 nm respectively. One disadvantage of using this method is that structures located deeper within the cell are difficult to investigate. In order to image deeper, the TIRF principle can be modified to a highly inclined and laminated optical sheet (HILO), where the laser beam is highly inclined, creating an optical sheet through the sample<sup>28</sup>.

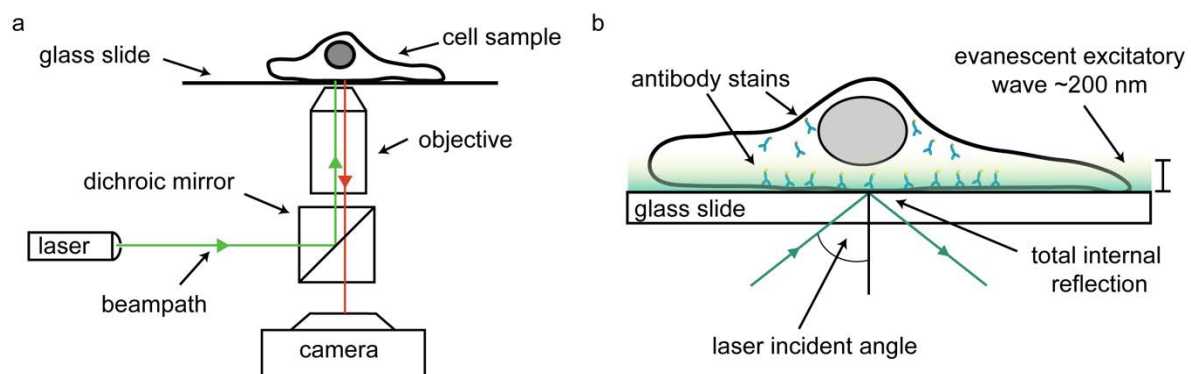


Figure 2: Basic microscopy setup design and total internal reflection fluorescence. a) A basic microscope uses a laser to excite the fluorophores. This laser beam is guided via a dichroic mirror into the objective, where it excites the fluorophores in the sample. The fluorescence emission, which carries a longer wavelength, travels through the dichroic mirror and is detected on the camera where the image is displayed. b) In TIRF microscopy, the laser beam is totally reflected on the glass slide and creates an evanescent excitatory wave, which travels only ~100-200 nm into the sample for excitation. Fluorophores located deeper in the sample are not excited and therefore cannot be detected anymore.

Ernst Abbe, a German Mathematician, developed in the 19th century a theory for the resolution limit of microscopy setups. Resolution of an imaging system can be defined as the distance at which two lines can be visualized as two separate entities<sup>29</sup>. According to Abbe, this can be described using following formula:

$$d = \frac{\lambda}{2 * NA}$$

In contrast, Rayleigh defined a microscopy image as consisting of point like emitters<sup>30</sup>, due to the wave nature of light and the process of diffraction and interference at interfaces. The resolution was described as the distance at which two spots can still be resolved following:

$$d = \frac{1.22 * \lambda}{2 * NA}$$

The resolution therefore depends on the emitted wavelength  $\lambda$  and the numerical aperture of the used objective. Assuming a short wavelength of 488 nm and a high-numerical aperture objective of 1.49, a maximal resolution of approximately 200 nm can be achieved. Unfortunately, biomolecules are on the order of several nanometers, which is 1-2 orders of magnitude below this resolution limit. Therefore, there was a need to develop super-resolution microscopy methods to circumvent this fundamental resolution limit, which is detailed in the next chapter.

### 1.3 Super-Resolution Microscopy

Several super-resolution microscopy methods have been developed to circumvent the fundamental resolution limit proposed by Abbe. The initial concepts were proposed in the 1990s, with experimental proofs in the late 90s and 2000s<sup>31,32</sup>. They all engineer the states of fluorophores within a diffraction limited spot using different technical implementations. Stimulated emission depletion microscopy (STED) depletes the ground state of the fluorophores in the periphery of the excitation<sup>32-34</sup>. This depletion is performed using a ring-shaped laser beam aligned around a central excitation beam. The molecules in the periphery of the excitation are switched off, whereas in the center, where a minimum of the depletion laser resides, the fluorescence of the molecules can be read out. Identically to a confocal microscope setup, the two aligned beams scan the whole sample area to acquire a full image. The achievable resolution of this super-resolution microscopy technique can be described using the following formula:

$$\Delta x = \frac{\lambda}{2 * NA * \sqrt{1 + \frac{I_{STED}}{I_{SAT}}}}$$

In this respect, the achievable localization precision in STED inversely scales with the intensity of the STED laser ( $I_{STED}$ ).

In contrast to that, single molecule localization microscopy (SMLM) uses the stochastic switching of fluorescent molecules from a fluorescence emitting state into a dark state, so that in a diffraction limited spot only a single emitter is detected at a timepoint  $t^{31}$ . In comparison to the previously mentioned STED example, where the beams scan the field of view and only

### 1.3 Super-Resolution Microscopy

excite/deplete molecules at their current position, a full field of view is excited and multiple emitters are detected on the camera at the same time. The detected spots are fitted with a centroid estimation to find the center position of the molecule with high precision. The localization precision and therefore the resolution is inversely proportional to the square root of the detected photons<sup>35</sup>:

$$\Delta x \approx \frac{1}{\sqrt{N}}$$

The key to perform SMLM is to switch fluorophores from an off-state into an on-state and vice-versa. Up to this point, different strategies were implemented to achieve this switching of states, which are detailed in chapter 1.4.

Recently, a new super-resolution technique was proposed, combining targeted readout of the fluorophore position, like in STED, with the stochastic switching of fluorophores as implemented in SMLM. This new technique was termed MINFLUX<sup>36,37</sup>, and uses a ring-shaped excitation pattern to find the local minimum of excitation by only probing four different positions with fast optical positioning components. This enables high resolution on microsecond timescales, with the use of only a minimal of photons. The three described methods for super-resolution microscopy are depicted in Figure 3.

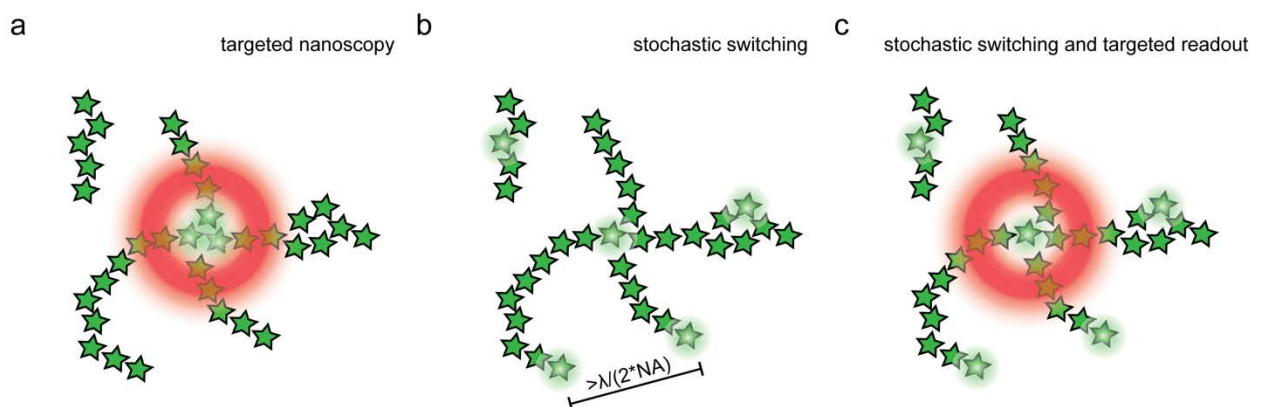


Figure 3: Basic super-resolution microscopy strategies. a) In STED microscopy, the ring-shaped depletion laser depletes the fluorescence from the surrounding molecules. Fluorophores within the inner circle are still excited and can be read-out. b) Single-Molecule Localization Microscopy: Fluorophores are stochastically switched on and off, so that fluorophores in the on-state can be separately detected on the camera. c) MINFLUX concept: combination of stochastic switching and targeted nanoscopy. The readout only takes place in the targeted spot. Adapted from [38].

## 1.4 Single-Molecule Localization Microscopy

The concept of single-molecule localization microscopy was first proposed by Eric Betzig in 1995<sup>31</sup>. The basic principle of SMLM is, that at a timepoint  $t$ , only one fluorophore is detected on the camera within a diffraction limited spot. The center positions of these spots are determined using a fitting procedure<sup>35,39</sup>, for example, using least-square estimations. Over the time course of the acquisition, all available fluorophores are sampled and a list of  $x$ ,  $y$  and  $z$ -coordinates of the positions is generated from which the final super-resolution image can be reconstructed. The workflow of SMLM imaging is depicted in Figure 4. The main challenge for implementing SMLM is making the fluorophores switch from an on- to an off- state and vice versa<sup>40</sup>.

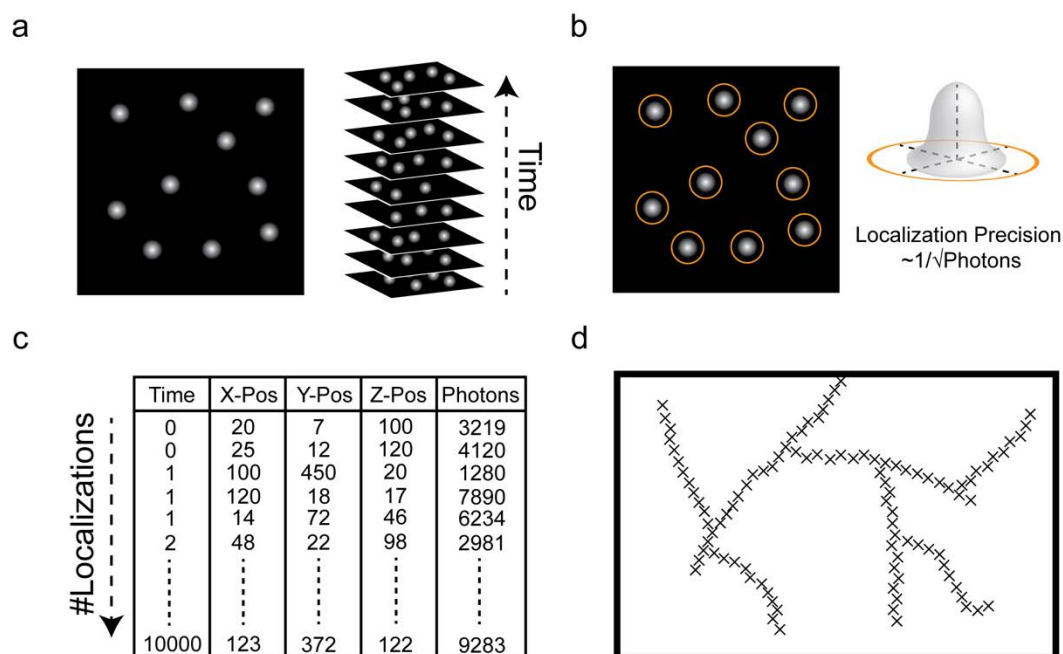


Figure 4: Single Molecule Localization Microscopy. a) In single molecule localization microscopy, spots from single fluorophores are detected on a camera over a time course and a stack of images is generated. b) During the analysis, the spots are detected and fitted with a least square estimation. The quality of the fit, the localization precision, is inversely proportional to the square root of the detected photons. c) All important parameters of the fit for each spot/localization are noted in a table, e.g. when the spot was detected (Time), the exact position and the number of photons. d) From the list of spots, the final super-resolution image can be reconstructed.

Different implementations of single-molecule localization microscopy have been introduced. The first one to mention is PALM (Photo-activated localization microscopy)<sup>41</sup>, which uses fluorescent proteins that are first switched off, then activated by a brief 405 nm laser pulse. After activation they emit photons and their position can be determined on the camera until they are bleached. Repeated activations using the 405 nm laser will switch a subset of fluorescent proteins into a fluorescence emitting state. These cycles are repeated until all

## 1.4 Single-Molecule Localization Microscopy

---

fluorescent proteins are bleached or until enough sampling of the positions was achieved. The second approach is STORM<sup>42</sup> or dSTORM<sup>43</sup>, which uses organic dyes, that can also be brought into a dark state and re-activated by UV laser (405 nm) excitation. However, optimized buffer conditions, allowing the fluorophore to be switched off and reactivated need to be established<sup>44</sup>. PAINT (Point-Accumulation in Nanoscale Topography)<sup>45</sup>, as a final class of SMLM, induces the stochastic switching of the fluorophores in an entirely different fashion. Freely diffusing probes from solution interact with their target and upon immobilization at the target site, their residence time becomes larger than the frame length of the acquisition and the fluorophore can be detected as a spot on the camera. In contrast, when the molecules diffuse in solution, their residence time in one pixel of the camera is smaller than the frame length and therefore the signal to noise ratio is too low in order to detect the molecule. In its original implementation, the molecules were immobilized in a membrane upon interaction and bleached after a certain time. This was extended by the concept of universal PAINT, in which a fluorophore labeled ligand of a receptor was used as a PAINT probe, that interacts with its corresponding receptor and is bleached after the fluorophore's photon budget is exhausted<sup>46</sup>. However, there are also more novel approaches which use the concept of transient interactions, such as in DNA-PAINT<sup>47,48</sup> or with IRIS probes<sup>49</sup>. DNA-PAINT uses short DNA-labeled oligonucleotides (~7-10 bp) which transiently interact with their complementary target sequence to create the necessary stochastic on- and off-states. DNA-PAINT, which is the major method used in this thesis, will be explained in more detail in chapter 1.6. In contrast, IRIS probes take advantage of naturally occurring transient interactions of proteins. Investigating protein interaction networks carefully allows to deduct protein fragments which can be used as fluorophore labeled transient binders to perform the stochastic switching between an on- and an off- state.

3D single molecule localization microscopy can be achieved by introducing an astigmatism in the beam path<sup>50</sup>. By placing a cylindrical lens just before the camera, the point spread function detected on the camera changes its shape according to the position of the fluorophore emitter with respect to the focal plane of the objective. If the emitter is in the focal plane, the detected signal of a spot on the camera is circular. Whereas if the emitter resides above or below the focal plane of the objective, the detected spot becomes elliptical, with the minor half-axis pointing towards the horizontal or in the vertical direction. Measuring the ellipticity of the point spread function at defined distances from the objectives focal plane, e.g. by using fluorescence beads and positioning them accurately via a piezo stage, enables the acquisition of a calibration curve which can be used as reference for the final sample acquisition. Figure 5 describes the concept of introducing the astigmatism for point spread function shaping and 3D imaging in more detail.

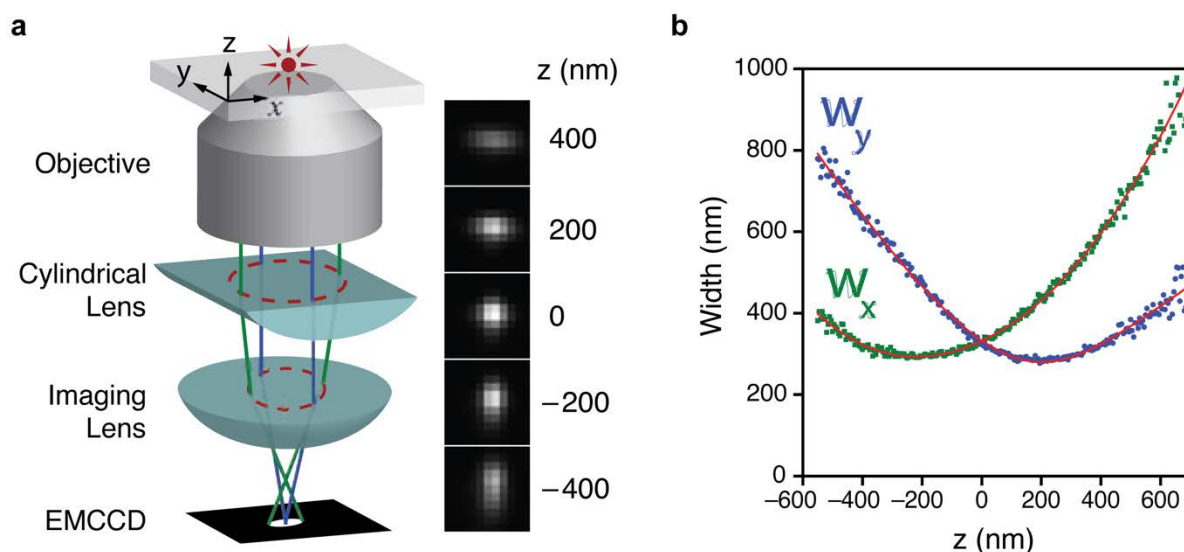


Figure 5: 3D single molecule localization microscopy with astigmatism. a) A cylindrical lens is inserted into the beam path and depending on the position of the fluorescence emitter with respect to the focal plane of the objective, the detected point spread function on the camera turns the minor semi-axis of the ellipse to the vertical direction (above the focal plane) or in the horizontal direction (below the focal plane). b) Fitting the width of the ellipse for the distinct distance from the objectives focal plane, a calibration curve can be generated and subsequently compared to the final sample acquisitions. From [50]. Reprinted with permission from AAAS.

Beyond this easy to implement astigmatism lens approach, several efforts have been made to advance the 3D resolution capabilities of super-resolution implementations, such as 4Pi microscopy<sup>51,52</sup> or super-critical angle 3D imaging<sup>53</sup>.

The main challenges in the field, besides achieving high resolution, is also to detect multiple single species of proteins and map their interaction pattern in space. This requires not only a method that can achieve resolutions on the order of single proteins ( $\leq 5\text{-}10\text{ nm}$ ) but also the detection of multiple protein species and counting of the involved biomolecules. However, in order to assay if the super-resolution microscopy method can deliver on the above-mentioned requirements, it is essential to have a reliable reference standard for imaging. Known biological standards in the super-resolution community have mainly included the measurement of microtubule filament size<sup>54</sup> or the symmetric arrangement of nuclear pore proteins<sup>55</sup>. Besides these biological reference structures, it is important to have a flexible tool that can be used as a universal reference standard and that can adapt to meet the resolution demands. DNA nanostructures provide excellent properties as a universal tool for super-resolution imaging, which will be discussed in the next chapter<sup>56,57</sup>.

## 1.5 DNA Nanotechnology as standard for microscopy

DNA is the building material of the genetic code. It consists of 4 different bases, adenine (A), guanine (G), thymine (T) and cytosine (C) which can form base pairs through two hydrogen bonds between A and T and three hydrogen bonds between G and C. Additionally, one base molecule consists of two different modules, the sugar phosphate backbone and the base. Due to the Watson-Crick base pairing, DNA forms a double-helical arrangement, which turns every 10.5 base pairs<sup>58</sup>. The double helical structure is connected by the hydrogen bonding network between the bases and the base stacking interaction contributes additionally to its stability<sup>59</sup>. The basic structural units of DNA are depicted in Figure 6a. Due to its unique structural features, DNA can be used as a building material for nanoscale arrangement of elements. Ned Seemann first proposed to use crossover junctions and the base pairing of DNA to build nanoscale patterns of proteins to improve crystallization<sup>60</sup>. After initial proof of concepts with different structures<sup>61</sup>, for example cages<sup>62</sup>, this concept was expanded to the scaffolded DNA origami technique by Paul Rothemund in 2006<sup>63</sup>.

To assemble DNA origami structures, a single stranded scaffold strand, derived from M13mp18 phage (~7k bases long), is pooled together with short DNA oligonucleotides in the size range of 32-60 bases. The short DNA oligonucleotides, also called staple strands, are designed using freely available software packages, such as cadnano<sup>33</sup> or Daedalus<sup>34</sup> to form base pairs with the scaffold to mediate the folding process. With the addition of magnesium in the buffer, the oligonucleotides together with the DNA scaffold self-assemble into the preprogrammed two- or three-dimensional shape of interest during the course of a thermal annealing protocol, typically ranging from 80 °C to 4 °C. Since 2006, structural DNA nanotechnology was extended to different lattices<sup>64-66</sup>, to 3D curved and bended shapes<sup>67</sup> and even to larger structural assemblies in the gigadalton range<sup>68</sup>.

The ability to be able to fold structures in the size-range of viruses with 5 nm addressability opens up exciting new avenues for applications, where nanoscale spacing plays an important role, which is depicted in Figure 6b. Different applications were developed, using DNA nanostructures as tools to study biophysics, such as motor proteins<sup>69</sup>, to engineer more efficient enzyme cascades by spatial proximity<sup>70</sup> or to template biomolecules for signaling studies<sup>71</sup>. However, one of the most promising applications is its use as a universal reference standard for microscopy, where fluorophores can be attached to any position. In this way the microscopy method can be evaluated on a standardized sample, templated with different fluorophore distances<sup>56,72</sup>.

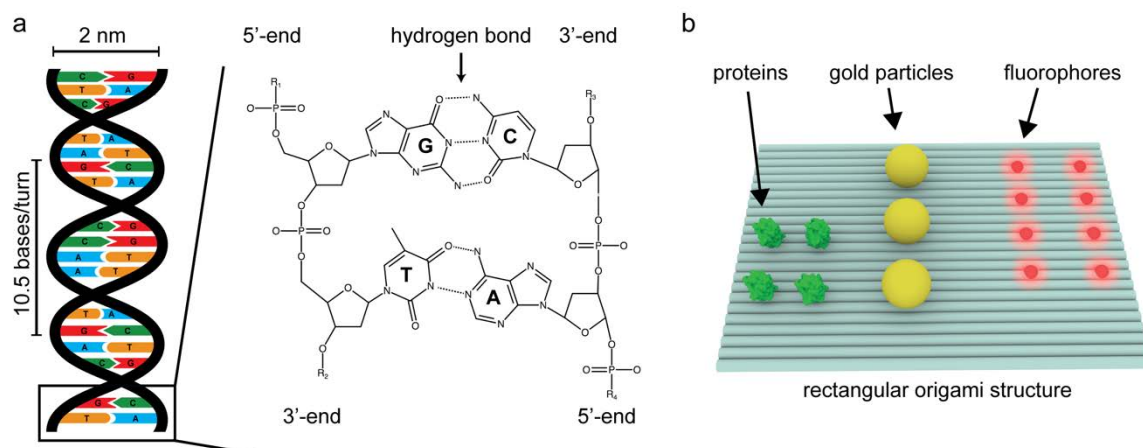


Figure 6: DNA Nanotechnology and its applications. a) The basic building block of DNA are its bases, guanine and cytosine, which form three hydrogen bonds and thymine and adenine, which form two hydrogen bonds. The DNA is connected through a sugar-phosphate backbone via the 5' and the 3' carbon atoms of the deoxyribose. The overall structure of the DNA consists of a double helical arrangement which is  $\sim 2$  nm in diameter and rises  $\sim 0.335$  nm per base with approximately 10.5 bases/turn. b) Due to the programmability of the bases, DNA can be used as a building material to form nanostructures. These structures can be functionalized with any guest molecule of interest, such as fluorophores (red dots), gold particles (yellow) or proteins (green) with 5 nm addressability. Adapted from [73].

## 1.6 DNA-PAINT

In DNA-PAINT, a modification of the single molecule localization-based microscopy variant of PAINT<sup>45</sup>, fluorophore-labeled short oligonucleotides are used, which transiently hybridize to their complementary DNA strands on the target of interest to create the typically observed blinking behavior in SMLM<sup>47</sup>. The programmable DNA sequence (adenine base-pairs with thymine and cytosine base-pairs with guanine) with the hydrogen bonding network between the base-pairs stabilizes the interaction for an extended period of time so that the residence time of the fluorophore-labeled DNA strand at one position is larger than the camera readout frame rate. These binding events are detected as a spot on the camera during the course of acquisition.

Since the transient and repetitive interaction of the fluorophore labeled oligonucleotide with its immobilized complementary strand is only encoded in the DNA sequence and does not need the complex engineering of fluorophores, the brightest obtainable dye can be chosen in order to extract all the photons from a single binding event. Additionally, the repetitive and reversible interaction enables to obtain in principle unlimited photons per single site. This enables super-resolution imaging with resolutions down to 5 nm as was demonstrated on DNA nanostructures<sup>1,74</sup>.

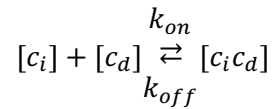
The programmable nature of DNA encodes the molecular identity of the target which allows to DNA-barcode biomolecules. One major challenge in fluorescence microscopy is that most

## 1.6 DNA-PAINT

---

multiplexing relies on the microscopy setup in terms of available laser lines and optical filter sets. In DNA-PAINT this can be completely circumvented by only using the DNA sequence as a barcode, without the need to change the fluorophore. This is advantageous for multiplexing applications as it avoids any chromatic aberrations or performance differences from using different fluorophores. Since the whole DNA interaction process is of transient nature, the fluorophore labeled DNA strands can be washed away in a flow channel and substituted with new imager solution harboring a different DNA sequence for a new target. Exploring the whole sequence space of DNA base-pairing of 8-10 nucleotides<sup>2,4</sup> enables for almost unlimited multiplexing. DNA encoded multiplexing was shown to be a powerful tool, not only for DNA-PAINT super-resolution microscopy but also as a universal approach for different imaging modalities, such as STED<sup>75</sup>, STORM<sup>76</sup> or even diffraction limited confocal microscopy<sup>77</sup>.

The last challenge that DNA-PAINT tackles is how to accurately predict protein copy numbers. Different approaches were previously reported, such as intensity calibrations<sup>78</sup>, PALM counting<sup>79</sup> or counting of blinking events<sup>80</sup>. However, due to the replenishment of fluorophores from solution in DNA-PAINT, the process is highly predictable and molecular numbers can be extracted from the frequency of binding<sup>3</sup>. The association process of the imager strand can be described as a second order kinetic model:



$C_i$  and  $c_d$  describe the concentration of the imager strand and the docking site respectively. The bright time  $\tau_b$ , in which the imager strand is bound to its complementary docking site, as well as the dark time  $\tau_d$ , in which the docking strand is not occupied, can be explained by following formulae:

$$\tau_b = \frac{1}{k_{off}}$$

$$\tau_d = \frac{1}{k_{on} * c_i}$$

The mean dark time  $\tau_d$  and the mean bright time  $\tau_b$  can be extracted directly from the experiment by analyzing the repetitive visits (length of interaction as well as event free time) of the imager strand to its complementary single docking site:  $k_{off}$  as the inverse of the bright time and  $k_{on}$  from a linear fit of the inverse mean dark time at different known imager

oligonucleotide concentrations can be inferred from these values. Typical values for a 9 nt interaction at 20 °C and 600 mM NaCl are for  $k_{\text{on}} = 2.3 * 10^6 \frac{1}{M*s}$  and for  $k_{\text{off}} = 1.6 \frac{1}{s}$ .<sup>47</sup>

For an imager concentration of 1 nM, a single docking site would be visited every ~435 seconds, for an imager concentration of 10 nM, the single docking site would be visited every ~43 seconds. As single visits of docking sites are assumed to be independent events, two docking sites would be visited every ~218 seconds at a concentration of 1 nM. This relationship can be used to count the absolute number of molecules in an area of interest<sup>3</sup>.

The three major advantages of DNA-PAINT are all derived from the programmable nature of the DNA, which decouples the blinking properties from the fluorophore, enabling highest resolution, decouples the molecular identity from the dye molecule, enabling highly multiplexed target detection and the predictable repetitive nature of the interaction, enabling quantitative counting of target sites. These advantages and the basic principle of DNA-PAINT are summarized in Figure 7.

## 1.6 DNA-PAINT

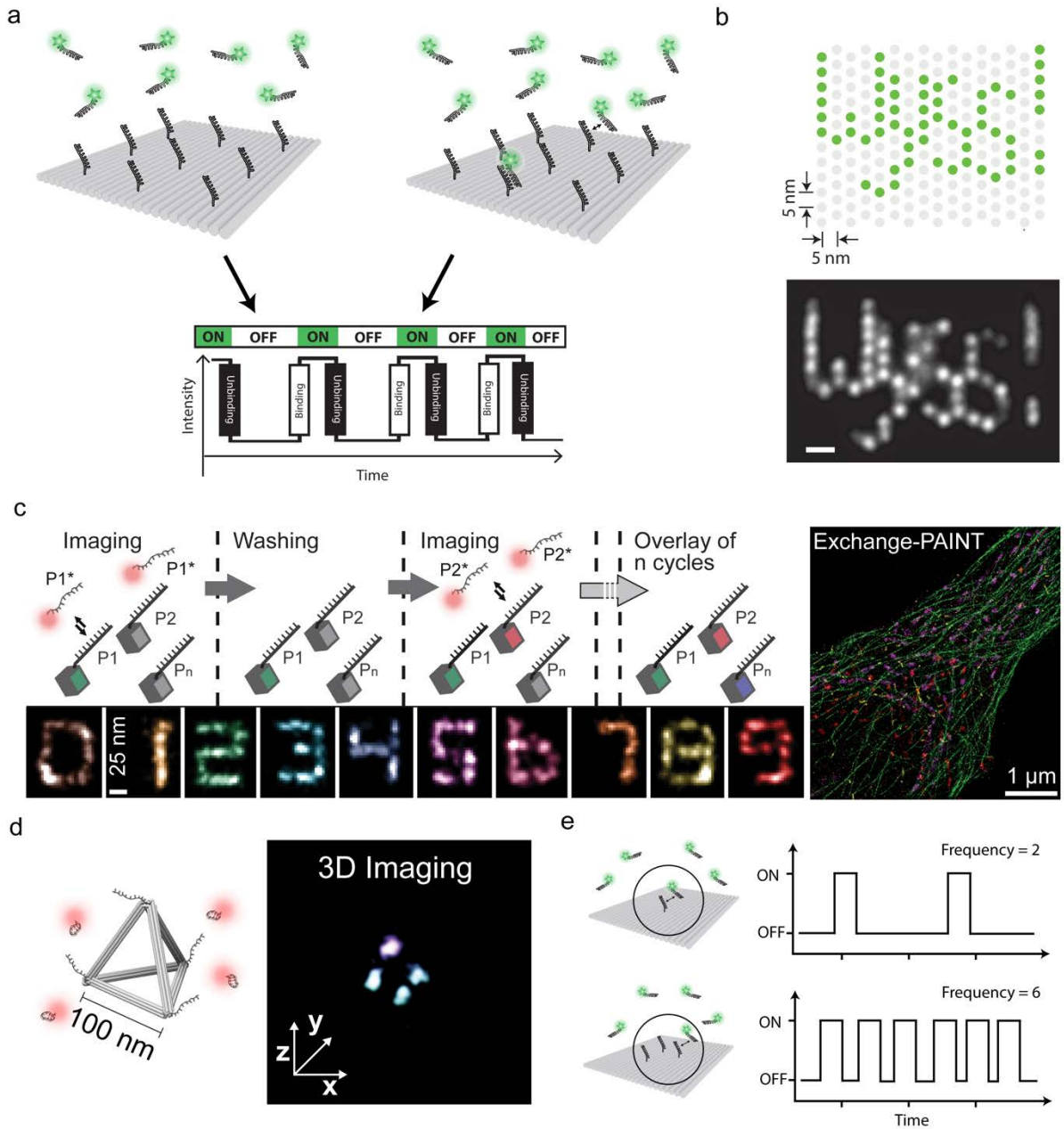


Figure 7: DNA-PAINT overview. a) DNA-PAINT uses the transient hybridization of fluorophore labeled DNA-strands to create the typical blinking pattern observed in SMLM. If the imager strands are diffusing in solution, no signal on the camera is detected, however once they bind to the docking strand a signal is detected. As the binding and unbinding is a very dynamic process, this process is completely reversible. b) The blinking behavior is only engineered by the DNA sequence, therefore the brightest fluorophores can be chosen and very high resolutions on the order of 5 nm can be achieved. Here exemplary displayed as a DNA origami structure depicted with a Wyss logo. Scale bar: 10 nm. Reprinted by permission from Springer Nature, Nature Nanotechnology [1], 2016. c) Multiple rounds of imaging and washing cycles, introducing fluorophore labeled DNA strands with different sequences can be employed to image many different targets in the field of view. Here depicted as 10 different numbers on DNA origami and a 3-color cell sample. Reprinted by permission from Springer Nature, Nature Methods [2], 2014. d) Introducing a cylindrical lens into the beam path allows to acquire 3D images, here depicted as a 3D DNA origami tetrahedron with 100 nm side-lengths. From [81]. Reprinted with permission from AAAS. e) The predictable interaction of single docking strands to their complementary imager strands enables to count docking sites. As an example, three docking sites in one spot are visited three times more often than a single docking site<sup>3</sup>.

In order to apply the advantages of DNA-PAINT microscopy in cell biological research, labeling probes against the targets of interest need to be established. The following two chapters will briefly describe common labeling probes and strategies of how to equip them with DNA strands for use in DNA-PAINT super-resolution microscopy.

## 1.7 Labeling probes for super-resolution microscopy

Highly efficient small binders are essential for a super-resolution technique which enables to acquire images with a resolution below 5 nm<sup>48</sup>. The adaptive immune system developed strategies to produce highly efficient binders to fight foreign pathogens. Antibodies, which are produced from B cells can recognize epitopes on bacteria or viruses and direct them to destruction. Vaccinations, which use virally derived antigens in combination with immune activators stimulate the immune system to produce antibodies against the respective pathogen and therefore establish a protection from infections<sup>82</sup>. Custom antibodies can be produced by immunizing animals, such as donkeys, mice, rabbits, rats as typical animal species, using the immunogen derived from the target of interest<sup>83</sup>. Polyclonal antibodies are directly purified from the blood serum via affinity chromatography techniques, e.g. the antigen of interest is bound at a column and binds the available high affinity antibodies. Low pH washes elute the antibody from the column<sup>24</sup>, which can be subsequently fluorophore labeled and used for imaging studies. However, one major limitation with polyclonal antibodies is, that there is a multitude of reagents in solution with different properties, exhibiting higher or lower affinity or different epitope binding specificities. This is undesired in applications where absolute protein copy number counting is indispensable. To circumvent these issues, monoclonal antibodies can be used, which are produced from B-cell clones isolated from the circulating B-cell population and produce one specific type of antibody<sup>84</sup>.

The perfect binder for a target of interest for super-resolution microscopy should be small, smaller than the size of the protein under investigation, should have high affinity, specificity and labeling efficiency to the target of interest, and it should be possible to label it with a single chemical component, such as a fluorophore or a DNA strand for quantitative super-resolution microscopy. To unravel the full potential of DNA-PAINT multiplexing, it should also be commonly available for multiple targets of interest. Unfortunately, antibodies lack a few before mentioned traits: they are not small and it is not straightforward to label them site-specifically with a single DNA strand or fluorophore.

As an alternative to antibodies, sharks and camelids, like alpacas, developed a different toolbox for antibody-based binders. Their antibodies only consist of 2x heavy chains with a 15

## 1.7 Labeling probes for super-resolution microscopy

---

kDa large epitope-binding domain. This binding domain can be isolated to have small, highly efficient affinity reagents and they are called nanobodies<sup>85,86</sup>. Nanobodies are easily produced in bacterial cell culture and can be modified with a single fluorophore or DNA moiety via cysteines<sup>87</sup>. It was shown that nanobodies can outperform antibodies in terms of label size, by measuring the microtubule diameter, which was closer to the ground truth known from electron microscopy studies, in comparison to an antibody-based measurement<sup>88</sup>. However, there is still a limited repertoire of nanobodies available for different targets.

Many small protein binding scaffolds have emerged during recent years, such as darpins<sup>89</sup>, Affimers (formerly adhirons)<sup>90</sup> or anticalines<sup>91</sup>. They have in common, that the binders can be selected via phage-display libraries and do not rely on immunization of animals. A great advantage is, that they can be easily modified for attachment of single or double chemical moieties of interest, as they can be expressed in E.coli or cell-free expression systems. These binders have all their specific strengths and disadvantages, one of the main points being their current relatively low availability for any protein target of interest. How these binders are evolved and characterized is detailed in the next two paragraphs.

### **Phage-display libraries for selection of high affinity reagents**

Phage-display libraries are an important tool to find novel small binders for any target of interest and was awarded the nobel prize in chemistry in 2018. In phage-display, the binder of interest is directly attached to a coat protein on the surface of a bacteriophage. The phages usually encode a large library of binders and interact with the antigen of interest on a support. Unbound phages can be washed away and only tightly bound phages are left leading to an enrichment of high affinity reagents. Over several cycles of washing and adapting the phage display library, high affinity binders for the target of interest are enriched and can be genetically identified and isolated from the bacteriophages. Once these binders are identified, they need to be thoroughly tested for their performance<sup>92</sup>. The general schematics of phage display is depicted in Figure 8.

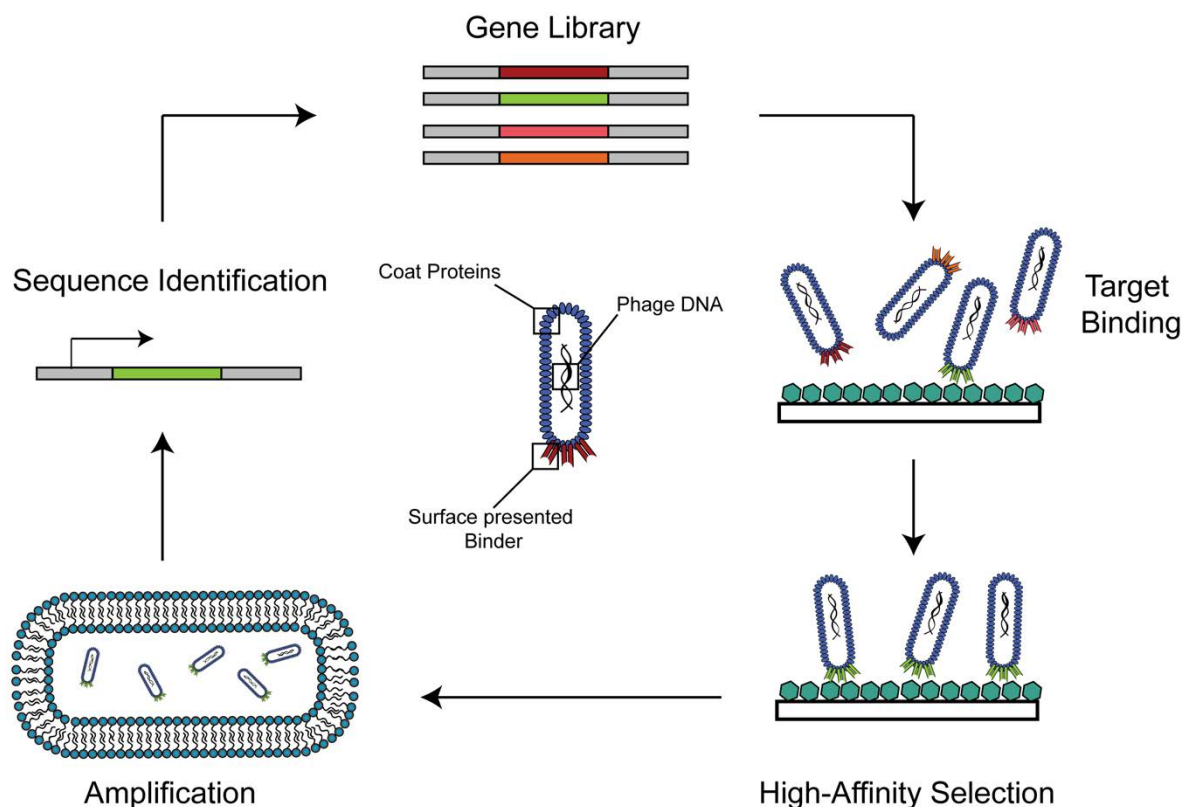


Figure 8: Phage Display schematics. Phages are able to present protein-based binders on their surface. Starting with a gene library, phages expressing binders on their surface interact with the antigen of interest on a solid support. Low affinity binders are washed away, whereas high affinity binders are enriched. The high-affinity binders are washed away under stringent (low pH, high salt) conditions and can be expanded in bacteria. The high-affinity binder sequence can then be identified. After several cycles of selection, mutation, gene library adaptation and selection, high-affinity reagents are enriched and selected for further use.

### Evaluating reagent performance

An important parameter for the quality of the binder is its affinity to the target of interest. The  $k_D$  value describes the concentration at which half of the molecules are bound to each other.  $K_D$  values can be measured with surface plasmon resonance, where the antigen of interest is immobilized on the surface, and a surface plasmon is created via laser excitation, which is very sensitive to changes at the interface. Different concentrations of the binder of interest are flown over the surface and from the changes in the interaction, the  $k_D$  values including the specific on- and off- rates of the binder can be inferred<sup>93</sup>. In contrast to that, microscale thermophoresis is an immobilization free technique. A fluorophore-labeled protein interacts with its potential ligand in a capillary and upon a temperature gradient diffuses different distances. The diffusion is highly dependent on the size of the protein and upon interaction and complex formation of the proteins decreases. Testing different ligand concentrations enables to deduct the  $k_D$  values of two proteins<sup>94</sup>.

## 1.7 Labeling probes for super-resolution microscopy

---

All these binders have in common, that they are modified with a chemical moiety for detection (fluorophore, DNA strand) and are added to the cell system under investigation after fixation. Besides externally applied affinity reagents, protein tags are commonly used. Protein tags are directly fused to the protein of interest on a genetic level and are expressed as part of the protein under investigation. Some of the most common representatives are fluorescent proteins, such as GFP<sup>18</sup> or mCherry<sup>19</sup>. However, although fluorescent proteins showed exquisite performance and allowed to visualize many different processes in nature, their fluorophore properties are not always the most desired one for super-resolution applications in terms of blinking behavior or quantum yield and extinction coefficient. For this reason, some of these tags can be additionally targeted with nanobodies attached with the chemical moiety of desire. Besides the fluorescent protein tags, small self-labeling tags have been developed, with the well-known representatives of SNAP-<sup>95</sup> or HaloTag<sup>96</sup> fused to the target protein of interest. These protein tags, which are 20 kDa and 33 kDa in size, react with a small-molecule ligand (benzylguanine or chloroalkane respectively) to attach any chemical moiety of interest. There are also smaller peptide tags to intervene as little as possible with the function of the protein of interest. These small peptide tags mostly interact with an enzyme to catalyze a reaction in order to attach a chemical moiety of interest, most prominent are the sortase tag<sup>97</sup>, which uses a triple-glycine motif or the yBBR-tag<sup>98</sup> which uses a co-enzyme A catalyzed reaction. Some newer development showed, that small peptide-based tags can also be used to bind nanobodies with high affinity. The ALFA-tag<sup>99</sup> and the bivBC2-tag<sup>100,101</sup> are examples of such systems, which provide high affinity nanobody-reagents to small peptide tags (<20 aa). The smallest site possible however is to stain a single amino acid in a target protein under investigation. This can be achieved with modifying the genetic code in combination with a clickable unnatural amino acid. This was shown for DNA-PAINT with nuclear pores by the Lemke Lab<sup>102</sup>. To label proteins with unnatural amino acids the amber (TAG) stop codon is repurposed to bind to an additional tRNA. The additional tRNA combined with an additional tRNA synthetase need to be expressed in the cell together with the protein of interest with the repurposed stop-codon. The incorporated unnatural amino acid usually harbors a cyclooctyne derivative and can attach covalently to a tetrazine harboring chemical moiety of interest via strain-promoted inverse-electron-demand Diels-Alder cycloaddition<sup>103,104</sup>.

An overview over available labeling strategies for immunolabeling is shown in Figure 9. All these methods require to add an externally applied binder, engineered to bind the target of interest, or an engineered cell-line harboring a tag at the protein under investigation to attach the chemical moiety of interest.

Protein networks in cells are highly dynamic and highly specific transient interactions occur between many different proteins. One particularly elegant way, which was published in 2015 was to harness the transient binding of protein domains to their complementary interaction

partners and perform super-resolution microscopy with it. These protein domains or peptides, modified with a fluorescent moiety can be directly used to visualize the protein in the cell with super-resolution microscopy<sup>49</sup>.

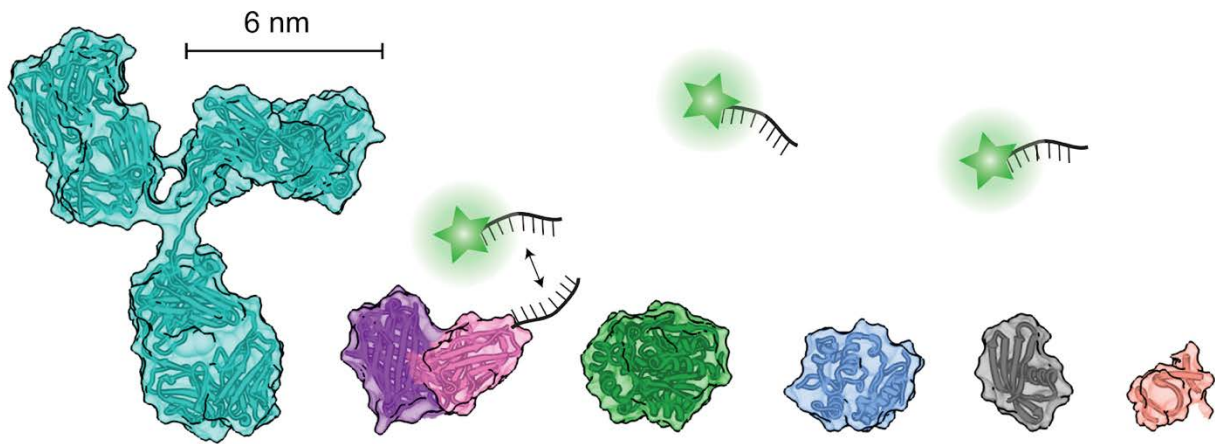


Figure 9: Labeling probes. Labeling probes are used to stain cell samples. From left to right: Antibodies, GFP in complex with a GFP nanobody, HaloTag, SNAP-Tag, Affimer and Somamer. For DNA-PAINT microscopy, probes have to be labeled with a DNA docking strand as depicted with the GFP nanobody construct. Cartoons were made in Chimera<sup>105</sup> using following pdb IDs. Antibody: 1IGT, GFP and GFP Nanobody: 3K1K, HaloTag: 4KAF, SNAPTAG: 3KZZ, Affimer: 4N6T, Somamer: 4HQU.

Once the binders are characterized to have high affinity and specificity to the target protein under investigation, the desired chemical moiety, such as a fluorophore or, in case of DNA-PAINT, a DNA strand need to be covalently attached in order to use them for the desired microscopy application.

The next chapter will discuss how to attach a DNA strand to the binder of interest.

## 1.8 Labeling Chemistries

There are different methods available to attach a chemical moiety, such as a fluorophore or a DNA strand covalently to the binder of interest. The presented methods mainly attach to a single amino acid residue. Amine-based labeling, which can attach to available primary amines, available for example at surface lysine residues or at the N-terminus of a protein, attaches via NHS-chemistry, which yields in a covalent amide bond formation and the release of the NHS molecule<sup>106</sup>. Usually bi-functional crosslinkers are used, which attach to the primary amines at the protein binder of interest and brings along a second reactive moiety in order to attach to the DNA strand. For example, in the case of NHS-chemistry, the crosslinker harbors an additional dibenzocyclooctyne, which can react via a strain promoted azide-alkyne cycloaddition (SPAAC) with an azide-modified DNA strand<sup>107</sup>. As an alternative for SPAAC, the trans-cyclooctene tetrazine ligation which is an inverse-electron-demand Diels-Alder reaction (IEDDA)<sup>108</sup> can be used.

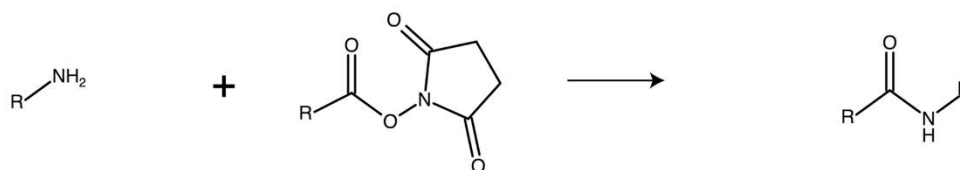
One disadvantage of the first step in the reaction chain is that it is relatively unspecific as primary amines are relatively common on proteins and multiple sites can be targeted without control of exact stoichiometry. On small proteins, this can be tuned via the excess of reactant and buffer conditions to only attach the moiety to the N-terminus of the protein. Another elegant way to improve the site-selectivity for this chemistry was proposed by Rosen and colleagues, where they used conserved histidine clusters on an antibody, targeted via Tris-NTA and a guide DNA strand to attach an oligonucleotide via NHS chemistry to a nearby primary amine<sup>109</sup>.

Nevertheless, NHS chemistry is usually not an option for large proteins, if absolute protein copy number counting is desired for which absolute control over stoichiometry of attached DNA strands is necessary. For more specific attachments, engineered cysteines can be used which harbor a sulfhydryl/thiol group and can be labeled via maleimide groups<sup>110</sup>. This enables a highly site-specific attachment of single DNA strands to the binder of interest. Staying with the single amino-acid targeting chemistry, DNA strands can also be attached to methionine via redox reactivity, which is also highly specific as methionine's are usually the start codons and not very prevalent in proteins. For the reaction to proceed, an oxaziridine group is used which forms a sulfimide bond upon oxidation<sup>111</sup>. All of the above methods are performed in a two-step reaction, first the amino-acid residues (Lysines, Cysteines, Methionines) are attacked on the protein of interest with a chemical crosslinker and afterwards the DNA strand is clicked to the crosslinker. In addition to the direct amino-acid targeting and attachment of the DNA strand, the tools mentioned in chapter 1.7, such as implementing an unnatural amino acid in the expression system<sup>112</sup> or adding a small peptide- ( $\gamma$ BBR)<sup>98</sup>, or protein tag (SNAP/HALO)

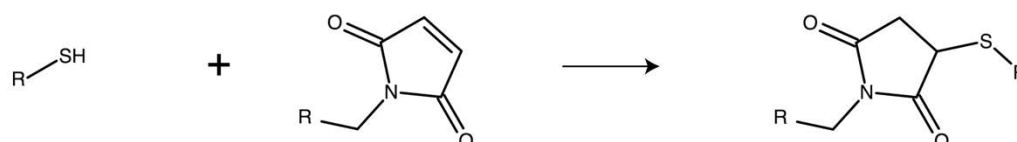
for site-specific attachment of the DNA strand can be used. However, these increase the size of the reagent, which should be avoided. Three major chemical labeling strategies used in this thesis are shown in Figure 10.

One problem which remains after successful attachment of the DNA strand is to purify the successfully conjugated high-affinity reagent from unconjugated reagents. There are different methods available to purify oligonucleotides from proteins from oligonucleotide-protein constructs. The major methods used are size-exclusion chromatography or ion-exchange chromatography, in which for the first one, the molecules are separated by size and for the latter one by charge<sup>113</sup>. Depending on the protein, usually the DNA strand adds a significant amount of charge to the binder of interest and anion exchange chromatography is a method of choice, where a positively charged resin retains the negatively charged DNA tail, which can be eluted under high salt conditions. Via a gradient based elution, the free DNA, the protein and the protein-DNA conjugate can be eluted in separate fractions.

a NHS-Ester Conjugation



b Maleimide-Cysteine Coupling



c Azide-DBCO Cycloaddition

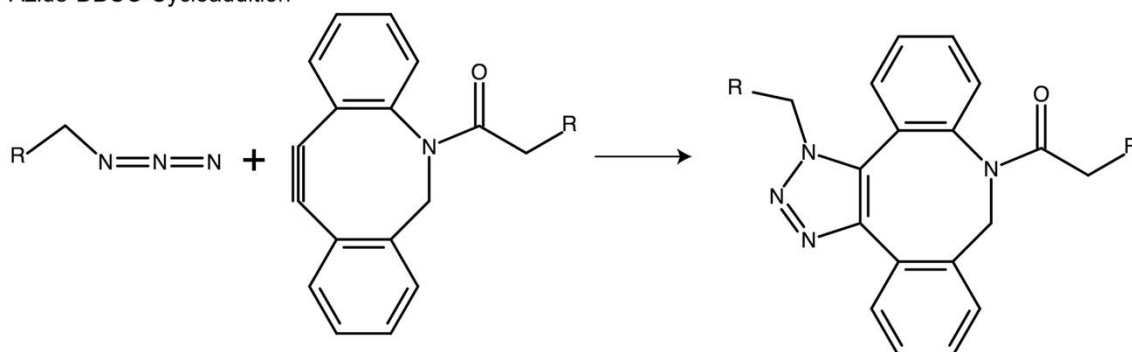


Figure 10: Chemical labeling strategies. a) NHS-ester reaction uses primary amines to couple a linker to it. b) In maleimide chemistry, cysteines or free-thiols are coupled. c) Click chemistry, especially a strain promoted azide-alkyne cycloaddition (SPAAC) works under physiological conditions and is used to attach DNA strands.

## 1.8 Labeling Chemistries

Once the binders of interest are produced with an attached DNA strand, biological phenomena can be investigated. Figure 11 shows a brief overview over typical super-resolution microscopy data of a diverse array of targets in cell biological research. One particular macromolecular complex of interest are focal adhesions, which mediate the interaction of cells with their extracellular environment and will be discussed in more detail in chapter 1.9.

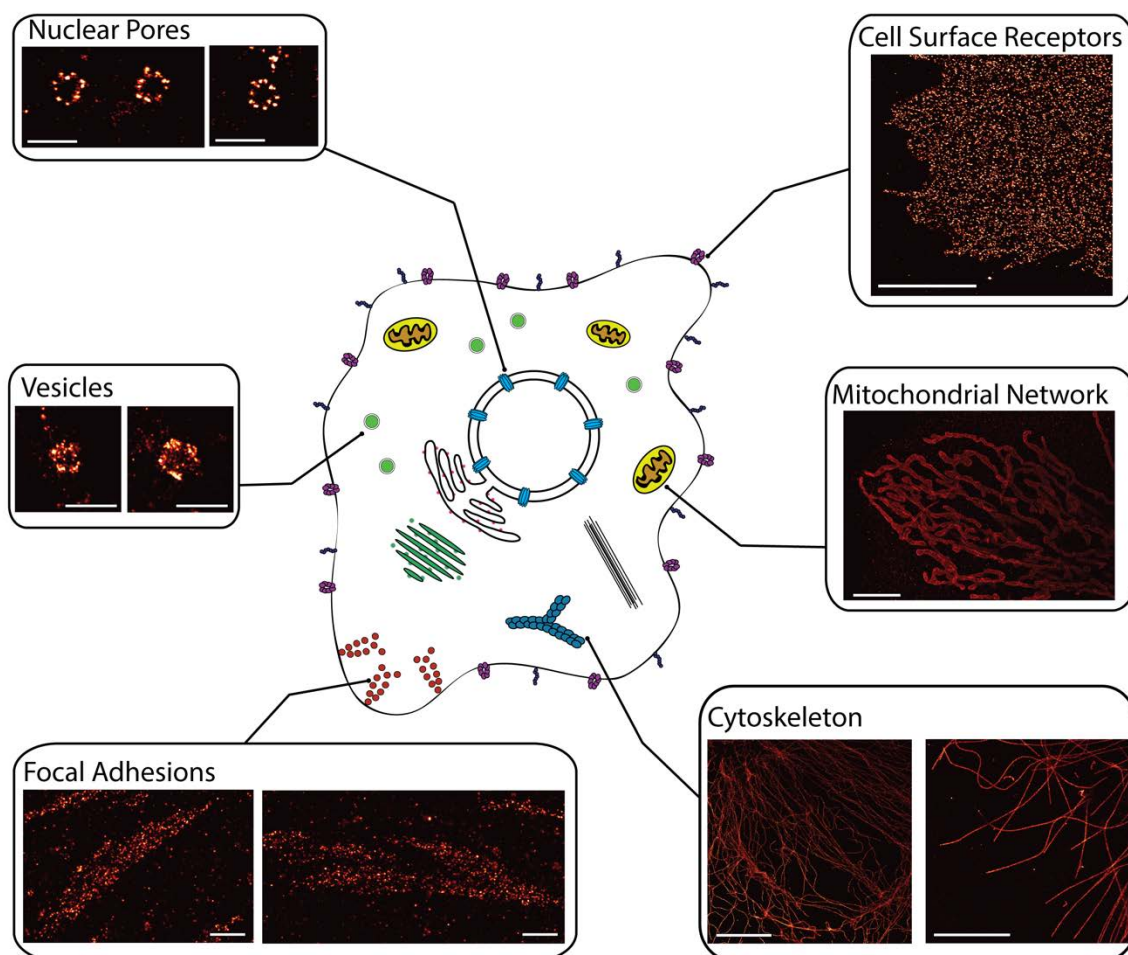


Figure 11: Super-resolution microscopy of cellular components. Different organelles and higher-order molecular structures in cells can now be investigated with unprecedented resolution. Cell surface receptors, here EGF-receptors appear under non-stimulated conditions as homogenously distributed spots on the cell surface. Organelles like the mitochondrial network are studied for their internal organization. With super-resolution microscopy, details of the cytoskeletal architecture can be visualized, which were previously unseen, here vimentin (left) and microtubules (right) as two examples. Focal adhesions, here stained for talin-1 are a macromolecular complex which regulates cell homeostasis, migration and proliferation. Clathrin-coated vesicles are here depicted as vesicles. Nuclear pores are the gate keeper of the nucleus, which harbors the genetic information. NUP107, one of the structural proteins which build the nuclear pore architecture is depicted here. For further information and acquisition parameters see supplementary table 6. Scale bars: Nuclear Pores: 200 nm, Vesicles: 300 nm, Focal Adhesions: 500 nm, Cell Surface Receptors: 5  $\mu$ m, Mitochondrial Network: 5  $\mu$ m, Cytoskeleton: 5  $\mu$ m

It is now possible to acquire images with molecular scale resolution using DNA-PAINT. The final processed data consists of single spots, which can include single or multiple proteins. To analyze, if there are underlying patterns or if the organization of the proteins follow random distributions, thorough investigation of the resulting localization clouds and clustering plays an important role, especially considering the low labeling efficiencies, on the order of 30-50 %<sup>55</sup>. In chapter 1.10 clustering algorithms will be discussed in more detail.

## 1.9 Focal Adhesion Biology

Focal adhesions play a crucial part for the cell in sensing the extracellular matrix. The mechanical properties of the extracellular environment influence heavily cell homeostasis, migration or differentiation<sup>114</sup>. Focal adhesions are a multimolecular complex involving hundreds of proteins which are responsible to transduce the extracellular environment sensing to intracellular mechanical and chemical signalling<sup>115</sup>. It was shown that adhesions are organized in three main horizontal layers spreading over around 50 nm: the integrin signaling layer, the force transduction layer and the actin regulatory layer<sup>116</sup> (Figure 12). Integrins, which are heterodimeric proteins consisting of an  $\alpha$ - and a  $\beta$ -unit engage directly with extracellular matrix proteins<sup>117,118</sup>. 24 different heterodimeric combinations of  $\alpha$ - and  $\beta$ -units exist build from 18  $\alpha$  and 8  $\beta$  proteins exposing different ligand specificities and harbor characteristic tissue distributions. Ligands for integrin engagement are derived from extracellular matrix proteins and are fibronectin, collagen or laminin as examples. Both subunits contribute to the tuning of the binding affinity to the extracellular ligand. Upon binding to its ligand, integrins can reinforce the binding by forming a catch bond, which leads to the opening of additional binding interfaces that strengthen the interaction between the receptor and the ligand<sup>119</sup>. Integrin clustering at the cell surface by ligand engagement plays an important role for focal adhesion formation. The cytoplasmic tails of both subunits are short peptide tails harboring motifs that interact with intracellular force transducing or signaling molecules. Two major adaptor proteins, which are crucial for integrin activation and focal adhesion formation are talin and kindlin<sup>120</sup>. Talin, which is a 270 kDa large protein, binds via its FERM domain to the NPxY peptide motif at the  $\beta$  integrin tail. There are two different talin isoforms reported, talin-1 which is expressed in all tissues and talin-2, which is predominantly expressed in muscle and neuronal tissue<sup>120</sup>. Talin harbors various actin and vinculin binding sites, which are force sensitive and get exposed upon tensile stress. It was shown, that talin as well as vinculin transduce mechanical load within focal adhesions<sup>121,122</sup> and are coupling the focal adhesome directly to the force-loading actomyosin network.

In contrast to that, kindlin is ~75 kDa in size and binds to the NxxY motif at the  $\beta$  integrin tail. Kindlin consists of 3 family members, Kindlin 1 is predominantly found in epithelial cells,

## 1.9 Focal Adhesion Biology

whereas kindlin 2 and 3 are expressed outside or inside the hematopoietic system<sup>123</sup>. Kindlin functions as a signaling hub, by activating paxillin, focal adhesion kinase and recruiting the Arp 2/3 complex to the integrin tail<sup>124</sup>. In focal adhesions, no tension was detected over kindlin, suggesting that it regulates the focal adhesion formation mainly by regulating the actin network. It is still unknown if talin and kindlin interact with the peptide motifs at the  $\beta$  integrin tail at the same time in the cell.

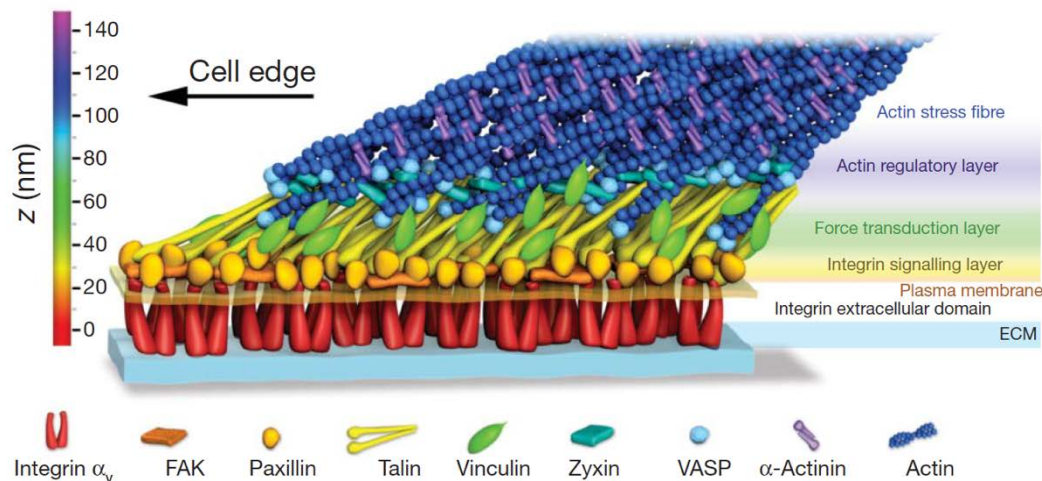


Figure 12: Focal adhesion architecture. The focal adhesion macromolecular complex is built up on several layers, the integrin signaling layer is followed by the force transduction layer, including one of its main players talin (yellow rod), followed by the actin regulatory layer as well as actin stress fibers (dark blue). Reprinted by permission from Springer Nature, Nature [116], 2010.

## 1.10 Clustering

Analyzing the clustering properties of proteins in cells is inherently different in a fixed system compared to life dynamics. Some of the proteins might be *en route* to their interaction partner of interest, whereas others are shuttled to their destruction and only a portion of the proteins might engage with their dedicated interaction partners and from those, due to the low labeling efficiencies only 30-50% can be detected<sup>55</sup>. Due to the high-resolution capabilities of SMLM, where high density clouds of localizations can originate from single sites, traditional co-organization or colocalization definitions, which analyze the degree of overlap like for example the Manders coefficient does, are outdated<sup>125</sup>. With these new high-resolution capabilities, co-organization can be defined as distance measure to the next protein.

However, this problem is multi-faceted, the first problem is how to detect the organization of the proteins under investigation in an automated fashion. In order to achieve this different methods have been proposed, like Density-Based Spatial Clustering of Applications with Noise (DBSCAN)<sup>126</sup>. The main problem in SMLM is that there is an ocean of noise, interrupted by high density islands, which are the spots of interest. Noise can be multifold, noise or undesired detection can occur by sticking of a fluorophore labeled oligonucleotide to an undesired site in the cell, it can be an accidental double blinking event, which leads to a track of localizations in between two true sites or it can be an unspecific attachment of an affinity reagent to the cell, which shows the same signature as true repetitive visits. The first challenge in this respect is to detect true sites: high density localization clouds in an ocean of noise and the second part of the clustering is to detect patterns of the detected high-density localization clouds.

Different clustering algorithms have been proposed to find the localization islands, one prominent example is k-means clustering<sup>127</sup>. K-means divides the image into a predefined number of clusters and optimizes for minimal quadratic distance deviation from the cluster centers and selects for clusters with similar sizes. K-means cluster optimization can be described with following formula:

$$A = \sum_{i=1}^k \sum_{x_j \in S_i} \|x_j - \mu_i\|^2$$

$S_i$  are the clusters,  $x_j$  the localizations and  $\mu_i$  the cluster centers. The biggest disadvantage of k-means clustering is, that it requires a predefined number of expected clusters as input parameter. For single-molecule localization microscopy of arbitrary patterns, it is not very straightforward to estimate the number of clusters as input parameter.

## 1.10 Clustering

---

As an alternative, the DBSCAN clustering method considers high-density areas with noise, which fit the description requirement for SMLM data above. To find clusters, DBSCAN has two input parameters, one parameter is density as a number of points, the second parameter defines a search radius. DBSCAN defines core points of the clusters as points which have at least the density number of points within the local search radius. Border points of the cluster are points, which can be reached by the search radius, but do not have more neighbors than the defined number of points and are therefore at the edge of the cluster. Via connectivity through the distance search radius parameter as well as the local density definition of core and border points, DBSCAN defines the clusters. Advantageous of DBSCAN is, that it does not require any preknowledge of how many clusters it should detect, like k-means does, additionally it can detect any kind of shapes and patterns as a cluster and it does consider noise, which is usually less dense than the high-density islands. A disadvantage is, that depending on the density of the separate clusters, subclustering or undesired merging of individual clusters can occur<sup>126</sup>.

Specific for single molecule localization data, Tesseler has been proposed, which uses Voronoi based tessellation to find high density areas and apply this to multicolor and 3D imaging<sup>128</sup>. Voronoi diagrams subdivide an area defined by points or so-called seeds, by drawing polygons, in which the edges are equidistantly apart from the neighboring points. Each position within a polygon is closer to its defining point than to any other point of the whole area. In this respect, the polygon surrounding a point can be defined as its direct area of influence. The full image is subdivided into these polygons. From the created polygons, different parameters can be computed which give an impression of the clustering, such as the area or the smallest distance to the next point, a polygon shape index or a density value. As an example, for large polygons, above the localization precision, the local density of points is low, whereas high-density areas are marked by small polygon areas. By thresholding the parameters and merging neighboring polygons, objects and clusters can be identified, for which downstream further parameters, like localizations, center of mass or area size can be computed. Choosing different density parameters enables to segment out areas of interest. While the tessellation-based approach showed to detect organizations on multiple length scales, it is still prone for noise in densely packed areas and merges clusters<sup>128,129</sup>.

Localizations in SMLM data consist of highest density areas, originating in a circular fashion from single sites, in which the true center position has the highest density of localizations. Ripley's K function analyzes the local density, by calculating the number of neighbors within a certain distance and compares the occurring density to randomly dispersed particles to detect clustering. Different distances are usually evaluated to detect cluster formation over different length scales<sup>130,131</sup>. Figure 13 shows an overview over clustering algorithms which have been developed and applied to SMLM data.

Once these single sites/single clusters have been determined, potential patterns can be investigated. One measure is the nearest neighbor distance, which should yield a different distance distribution at the same molecular density in comparison to a random distribution, if an underlying organization of the proteins is present. The same holds true for colocalization with a second or third protein species, however with protein-based probes the labeling efficiency needs to be considered.

Once these clusters and patterns have been determined, machine learning approaches can be used to automatically detect them and perform statistical analysis, which was previously reported with ASAP<sup>132</sup>.

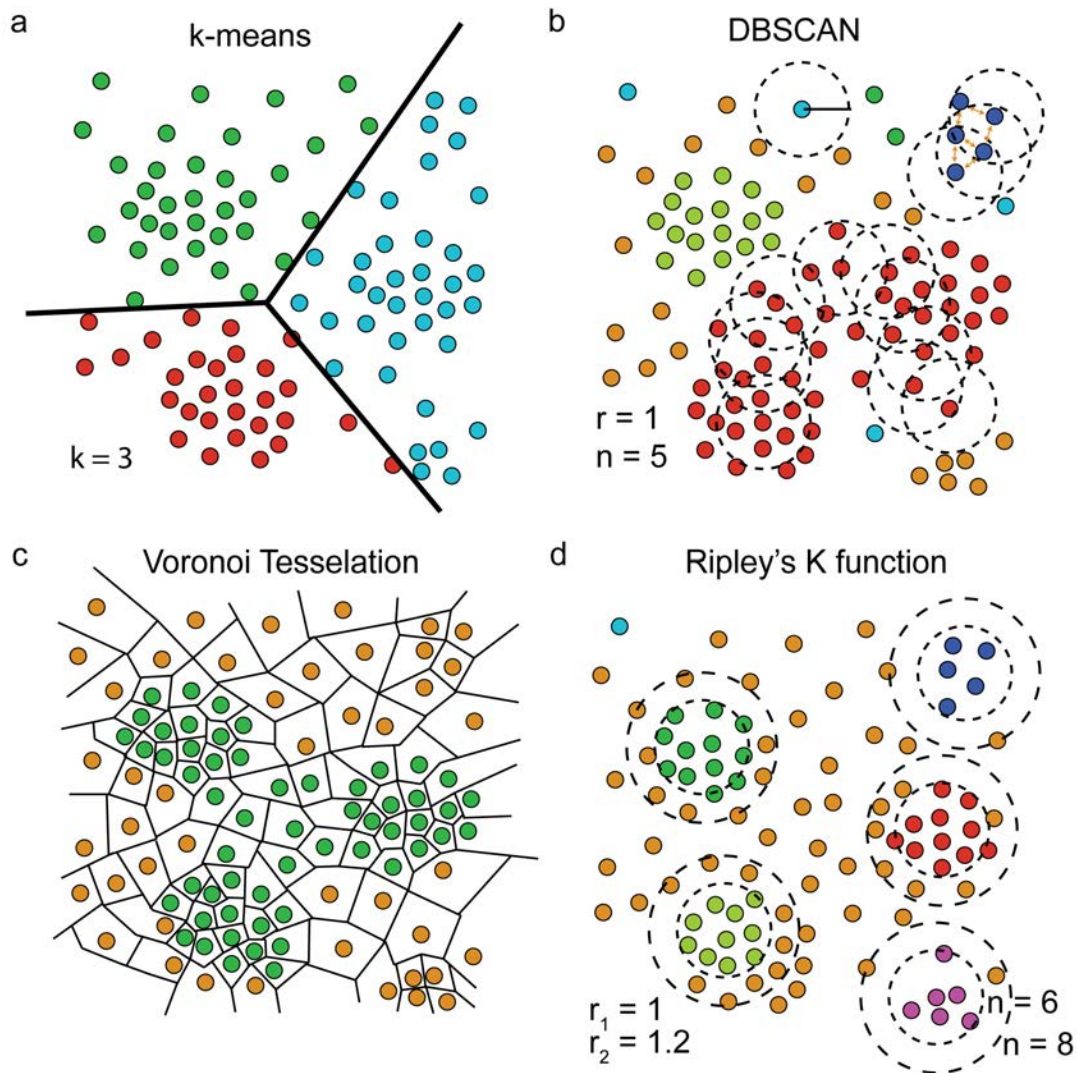


Figure 13: Clustering methods in SMLM. a) Explanation of k means clustering, where an expected value of clusters is given and the algorithm tries to find the clusters via minimal distances to their center points. b) DBSCAN. DBSCAN is a density-based method, which checks for neighbors in a certain radius and defines a cluster if the threshold of minimal elements in the defined radius is reached. c) Voronoi tessellation d) Ripley's K function analyzes the local density over different distances and compares it to randomly dispersed particles.

## 2 Aim of Thesis

In this PhD thesis I aimed to develop a toolbox for DNA-PAINT microscopy for the dissection of molecular complexes in cells. The major advantages of DNA-PAINT are that the molecular identity of the proteins under investigation is encoded in the attached DNA sequence, which enables to perform super-resolution imaging, almost unlimited multiplexing in subsequent rounds of imaging and counting of biomolecules.

However, to harness its full potential, small and efficient high affinity reagents are necessary. Therefore, **aim 1** of the thesis was to develop strategies to attach DNA strands to any binder of interest using a diverse array of covalent biochemical linking strategies. NHS chemistry was used to attach DNA strands to antibodies or small secondary binders, maleimide chemistry was used for site-specific attachment of DNA strands via engineered cysteine residues to nanobodies and Affimers. Additionally, small genetically encoded tags, such as SNAP and Halo were used to attach DNA strands via small molecule ligands. These binders were applied to a diverse array of applications in cell biology. Specifically, I was able to show for the first time, the 12 nm distance of the Y-complex in the nuclear pore architecture.

In **aim 2**, the influence of the reagent probe size on the true achievable resolution was investigated. In order to achieve a controlled analysis, a DNA origami nanoplatfrom, which can harbor several antigens of interest at distinct nanopatterns, was developed and applied to two different probe sets, a nanobody against the ALFA-tag and an antibody against a phosphorylated peptide CTD motif.

**Aim 3** was to dissect cluster formation and complex detection computationally. In order to accomplish this, a modified Ripley's K function was implemented to detect single, repetitively visited sites in DNA-PAINT data and was used for downstream clustering analysis to detect underlying patterns. For complex detection, simulations were implemented to analyze the influence of labeling efficiency.

In **aim 4**, I wanted to investigate if DNA-PAINT based super-resolution microscopy can be used to prove the existence of molecular complexes on a single protein level. For this we chose to investigate the co-organization of talin, kindlin and integrin as important players in focal adhesion formation and regulation, combining all the previously established tools.

---

## 3 Brief summary of manuscripts

### 3.1 Paper I: DNA nanotechnology and fluorescence applications

**T. Schlichthaerle**, M.T. Strauss, F. Schueder, J.B. Woehrstein, R. Jungmann

DNA nanotechnology has enabled great advances in fluorescence applications in recent years. In this review we analyzed the current state-of-the-art of DNA as a biotechnological tool for fluorescence applications. The programmable nature of DNA enables to build nanostructures with molecular addressability and use them as breadboards to template a large variety of molecules<sup>63</sup>. One particularly interesting aspect is to harness the molecular addressability of DNA to template fluorophores and subsequently use DNA origamis as size-standards in two and three dimensions for super-resolution fluorescence microscopy<sup>56</sup>. Dynamic DNA hybridization with short fluorophore-labeled oligonucleotides was also recently developed to be used as a transiently interacting probe for single-molecule localization based super-resolution microscopy<sup>47</sup>. These probes were used to characterize a diverse array of DNA nanostructures or molecules templated on DNA origamis. In addition, another advantage of the DNA programmability enables it to encode the molecular identity of the target within the DNA sequence and use it for multiplexed imaging in cell biology<sup>2</sup>. The third pillar, where DNA nanotechnology plays an important role in fluorescence applications, is again linked to its programmable nature as a building material. There is a large research direction in which gold nanoparticles of different shapes and sizes are templated on DNA origami structures, particularly to build plasmonic devices with local field enhancements for sensitive detection of biomolecules<sup>133</sup>. In this review, we emphasized three main research directions in which DNA nanotechnology helped to advance fluorescence applications.

## 3.2 Paper II: Super-Resolution Microscopy with DNA-PAINT

J. Schnitzbauer\*, M.T. Strauss\*, **T. Schlichthaerle**, F. Schueder, R. Jungmann

DNA-PAINT as single molecule localization microscopy method has major advantages over previously established SMLM techniques. Since the repetitive blinking behavior and the molecular identity is encoded in the programmable DNA probes, super-resolution can be achieved with almost unlimited photons for localization per single site<sup>1</sup>. Additionally, from exchanging the buffer and imager solutions, an almost unlimited number of targets can be visualized within the same cell. In fact, multiplexing is only truly limited by the available labeling probes and the orthogonal DNA sequence space<sup>4</sup>. Although different software packages for SMLM are already available, they are not adapted to the variety of experiments and analysis that can be achieved with DNA-PAINT. Therefore, Picasso was developed and included in this paper as a software tool to be specifically applied for DNA-PAINT. My part in this project was to devise a strategy to make DNA conjugation to antibodies more easily adaptable and scalable. For this the original protocol using NHS-maleimide chemistry (which has a laborious reduction step of the DNA via DTT) was redesigned to a protocol using a strain-promoted alkyne-azide cycloaddition, thereby reducing the time to produce antibody DNA-conjugates down to four hours and can be easily parallelized. These conjugates were tested in cellular applications in imaging microtubule networks and mitochondria.

In summary, this paper was published as a universal reference to make DNA-PAINT highly available to the super-resolution community, covering a range of methods from labeling chemistry of antibodies, to DNA origami design, to cellular investigations and provide the software tool Picasso for downstream data analysis.

---

### 3.3 Paper III: Site-specific labeling of Affimers for DNA-PAINT microscopy

T. Schlichthaerle, A.S. Eklund, F. Schueder, M.T. Strauss, C. Tiede, A. Curd, J. Ries, M. Peckham, D.C. Tomlinson, R. Jungmann

One of the main challenges in DNA-PAINT microscopy is to attach a DNA strand via an affinity reagent to the target molecule under investigation. There is a large repertoire of labeling chemistries available to attach a DNA strand to a specific binder, however having stoichiometric control over the number of docking strands is more challenging. Stoichiometric labeling of binders with a specific amount of DNA strands is important in order to count biomolecules in clusters. In this publication, we used a site-specific attachment chemistry via engineered cysteine residues. A second challenge in the field of super-resolution microscopy is to apply the technique to any biological target of desire. However, this is still limited by the available affinity reagents. Therefore, it is of great importance to expand the spectrum of usable binders. In this paper, small scaffolds called Affimers were site-specifically labeled with a DNA strand via cysteine-maleimide chemistry. Affimers are a 12 kDa large protein scaffold, derived from cystatins, which are cysteine protease inhibitors and consist of a beta-sheet and an alpha-helix<sup>90</sup>. Two loops can be engineered with various amounts of amino acid insertions to engineer affinity for any target of interest. As exemplary Affimer, an actin binder was chosen to make it available for DNA-PAINT<sup>134</sup>. Since the blinking behavior in DNA-PAINT is usually controlled by the imager sequence, concentration and buffer conditions, it is challenging to find the phenotype under investigation in cells. Therefore, a strategy was devised for diffraction-limited screening of cellular phenotypes. To achieve this, the DNA docking strand was equipped at its 3'-end with a fixed Atto488 fluorophore. Beyond the demonstration of the Affimers' general applicability for site-specific labeling for DNA-PAINT microscopy, we also investigated the actin network in Cos-7 cells in three-dimensions. We were able to show a layer-to-layer distance of the dorsal and ventral side of the actin fiber network of ~130 nm. In the future our devised strategy could pave the way for molecular counting applications with site-specifically labeled small protein scaffolds in a highly multiplexed fashion.

### 3.4 Paper IV: Bacterially derived antibody binders as small adapters for DNA-PAINT microscopy

T. Schlichthaerle\*, M. Ganji\*, A. Auer, O.K. Wade, R. Jungmann (\* equal contribution)

Labeling probes are essential to visualize cellular targets with fluorescence microscopy. However as current super-resolution microscopy techniques approach molecular resolution, it becomes increasingly important to have small and efficient binders for the target of interest. In order to perform DNA-PAINT imaging, a DNA strand needs to be attached to the target, usually via a protein-based binder. Unfortunately, there are only limited amount of small protein ligands available against any target of interest. In contrast, there is a large repertoire of antibody-based binders which can be applied at the cost of compromising the size of the probe. However, labeling primary antibodies with DNA strands can be tedious, if they are not commercially available in the correct buffer conditions (e.g. if they are supplemented with protein stabilizers like BSA or gelatin). In these cases, before the actual labeling procedure can take place, a pre-purification step might be necessary. Additionally, even with careful optimization of labeling conditions, the antibody might lose the ability to bind to the antigen of interest. Usually polyclonal secondary antibodies are used to visualize the binding of primary antibodies but they are relatively large in size (150 kDa) and therefore do not display the true target positions. In this publication, we implemented small bacterially derived antibody binders, which were previously already extensively used in antibody purification strategies<sup>135</sup>, namely protein A and protein G, to show their universal applicability as adapters for different primary antibodies.

Protein A and protein G are bacterially derived FC binders (*staphylococcus aureus* and *streptococcus*), which help the bacteria to evade detection by the immune system. These two proteins have nanomolar affinity to different antibody species and are only a fraction of the size of full antibodies (42 kDa and 58 kDa in comparison to 150 kDa)<sup>136,137</sup>. Their capability to bind site-specifically to antibodies makes them an excellent probe to reduce probe sizes. My part in this project was to devise a conjugation strategy to attach DNA strands to the small probes and apply them to biological targets. First, protein A and protein G were conjugated to DNA strands by targeting primary amines via NHS-chemistry and attaching the DNA strand in a second step via an inverse-electron-demand Diels-Alder cycloaddition between a TCO group and a TZ-modified DNA. Protein A was shown to bind to rabbit antibodies staining the mitochondrial marker Tom20 and protein G was shown to bind to rat antibodies staining for microtubule filaments. After the initial proof of concept, the capability of the small secondary binder to decrease resolution and avoid labeling probe size artefacts was evaluated. As an

---

ideal test case for single spots, EGF receptors were investigated. EGF receptors in A549 cells were labeled with primary/secondary antibodies as well as with the primary antibody in combination with protein A as secondary adapter. At the same technical resolution, the detected cluster sizes, defined by the full width half maximum, was increased by a factor of two in the case of the double antibody staining in comparison to the small secondary probe. As a last experiment, the resolution enhancement was tested with microtubule staining as a three-dimensional test system. According to EM data, the microtubule diameter is around 25 nm, however, when imaged with three-dimensional DNA-PAINT microscopy and primary-secondary antibody staining, the diameter of microtubules was measured to be 57 nm. Applying the newly developed secondary adapters for DNA-PAINT decreased the measured diameter by 9 nm to 48 nm which demonstrates the impact of the probe size. Taken together we showed that commonly applied primary - secondary antibody stainings lead to artificially increased cluster sizes and we provide a small universal and cheap labeling probe, which can be used for multiple primary antibodies of different species and can display the true molecular identity more accurately.

## 3.5 Paper V: Direct visualization of single nuclear pore complex proteins using genetically-encoded probes for DNA-PAINT

T. Schlichthaerle\*, M.T. Strauss\*, F. Schueder\*, A. Auer, B. Nijmeijer, M. Kueblbeck, V.J. Sabinina, J.V. Thevathasan, J. Ries, J. Ellenberg, R. Jungmann (\* equal contribution)

DNA-PAINT relies on the labeling of proteins with high-affinity reagents. One route to target the proteins is by using genetically-encoded tags, such as SNAP<sup>95</sup>, Halo<sup>96</sup> or GFP-tags<sup>87</sup>. These tags provide well established ligands, such as benzylguanine (BG), chloroalkane or GFP nanobodies, which can be easily modified with DNA strands and allow for stoichiometric labeling of the target under investigation. The cell lines were tagged via zinc-finger nucleases and CRISPR Cas9 technology to ensure endogenous expression levels. In this paper the position of nuclear pore scaffolding proteins, namely NUP107 and NUP96 in the nuclear pore architecture was investigated. The nuclear pore consists of a cytoplasmic and a nuclear ring, harboring an 8-fold symmetry with two protein copies in one symmetry center predicting 32 copies of each individual protein forming the two rings<sup>138</sup>. This knowledge, previously acquired through cryo-EM, enables the use of the nuclear pore architecture as a reference standard for counting proteins and estimating absolute labeling efficiencies. SNAP- and HaloTag are self-labeling enzymatic tags, which use small molecule ligands for covalent attachment of respective DNA strands to the target protein. As an additional tool, a DNA-modified GFP nanobody, which was site-specifically labeled via a single cysteine residue, as previously established in the Affimer paper (Paper III), was used to evaluate the NUP107 protein distribution and directly compared to a GFP antibody-based staining. We found that the antibody increased the measured diameter. For NUP96 and NUP107 we found an average diameter of 55.9 nm and 53.7 nm respectively and a z-separation of NUP96 of 61 nm between the nuclear and the cytoplasmic ring, which agrees with previously published EM data. The diameter for the different tags, GFP, SNAP & Halo did not vary, meaning that they can be equally applied. Using the nuclear pores as an estimate for labeling efficiency, we were able to show that from the expected 32 copies, only ~8-14 were labeled on average for all the different targets, which lead to a labeling efficiency of around ~30%. According to EM data, the two copies of NUP96 are ~12 nm apart in one symmetry center. I tried to optimize the imaging conditions with respect to number of visits of a single DNA docking site as well as optimized the resolution in 2D and 3D carefully in order to resolve these two sites in the nuclear pore. Using super-resolution fluorescence microscopy in 3D, I was able to show for the first time the arrangement of two NUP96 protein copies that are only 12 nm apart exist in cells.

---

Taken together, we showed in this manuscript, that SNAP/Halo and GFP tags perform equally well at around ~30% labeling efficiency and that it is possible to resolve closely spaced proteins (~12 nm) in a dense macromolecular complex. This technology can now be applied to study any kind of biological complexes in cells.

## 3.6 Paper VI: Spatial association of integrin-talin-kindlin during cell matrix adhesion

L. Fischer<sup>\*</sup>, C. Klingner<sup>\*</sup>, T. Schlichthaerle<sup>\*</sup>, M. T. Strauss, R. Böttcher, C. Schreiber, J. O. Rädler, R. Fässler, C. Grashoff<sup>°</sup>, R. Jungmann<sup>°</sup> (\* equal contribution, ° co-corresponding)

Mechanosensing of the extracellular environment plays an essential role for cell homeostasis and differentiation. Focal adhesions, which are a macromolecular complex at the cell surface, mediate the extracellular rigidity sensing. Upon integrin engagement and cell adhesion, a macromolecular complex assembles which ultimately connects the extracellular matrix to the cellular cytoskeleton. However, until now it is still unclear how the molecular clustering of the involved protein species occurs in such a dense structure. In this publication, we analyzed the co-organization of talin-1, kindlin-2 and  $\beta 1$  integrins during cell adhesion on fibronectin. For this, we used genetically-encoded tags such as SNAP-tag and HaloTag in combination with a 9EG7 antibody, which binds to an epitope available upon  $\beta 1$  integrin engagement and extension and measured the nanoscale distribution of the three proteins in and out of focal adhesions. We determined, that their distribution within focal adhesions peaks at protein to protein distances between 40 nm – 70 nm in fibroblasts. To estimate, whether we were analyzing truly single proteins within this densely packed structure, I used DNA nanostructures for calibrating the DNA-PAINT kinetics and was able to conclude that they were single binding sites. Additionally, we were not able to find any unimodal monomolecular complex formation of talin-1 within the focal adhesion, but its distribution followed an extracellular matrix fibronectin micropatterned surface and therefore the clustering of integrin. Furthermore, we determined the degree of spatial association within the focal adhesion by calculating a threshold interprotein distance of 25 nm. Kindlin-2, Talin-1 as well as extended  $\beta 1$  integrins seem to associate together, which was not only driven by the high density of the proteins as demonstrated with simulations of randomly distributed particles. Our data shows the existence of a basic functional unit between three proteins which mediate cell-matrix adhesion. We showed for the first time that a triple molecular complex formation can be imaged using super-resolution microscopy even in high density environments such as focal adhesions.

## 4 Further developments

### 4.1 DNA origami as a universal platform to analyze probes and cluster formation

Super-resolution microscopy enabled the biological community to shed light on different biological phenomena. However up to this point, mainly findings concerning structural proteins, such as microtubule filaments, nuclear pore structures<sup>139</sup> or actin-spectrin rings<sup>140</sup> were reported. Additionally, different studies presented the analysis of surface receptor nanoclusters, such as EGFR<sup>141</sup> or ryanodine receptors in heart tissue<sup>142</sup>. However, since novel super-resolution microscopy techniques, such as DNA-PAINT or MINFLUX can obtain resolutions down to the level of single proteins, the size of the labeling probe on the target becomes increasingly important<sup>1,37</sup>. Novel tools including DNA origami structures can be used to assay the performance of microscopy techniques with the highest resolution<sup>56</sup>, but so far, there are only limited tools<sup>55</sup> available to assay the labeling probe performance at the highest resolution level. These labeling probes should not only be small, label quantitatively to extract true molecular numbers, easily available for multiple targets but also have a high efficiency of binding. Common artefacts arising from imaging with large probes were recently reported in different applications, such as analyzing the nuclear pore architecture, investigating microtubules or looking at surface receptor nanoclusters<sup>141,143,144</sup>. However, a comparison of the true molecular position of the antigen within the same sample is so far elusive.

Here we aimed to evaluate binders on a DNA origami platform to truly determine the influence of the probe size on nanopattern recognition. To achieve this, we built synthetic antigen nanoclusters on DNA origami structures to show that large labeling probes can mask underlying antigen spacings, which can be circumvented by using novel small labeling probes. We demonstrated that combining novel super-resolution methods, such as DNA-PAINT, with the availability of small labeling probes should enable to dissect true molecular spacings and absolute compositions of molecular complexes within the next decade.

In cell signaling events, proteins come together and form nanoclusters for efficient triggering of the signaling pathway. To mimic such behavior, we nanotemplated antigens on a DNA origami platform and compared their resolvability with different binders (Figure 14a,b). The antigens were anchored via complementary DNA strands to the DNA origami structure harboring an additional site for DNA-PAINT microscopy to assay its presence and the true antigen position. The antigens in question were short peptides either derived from the ALFA-tag<sup>99</sup> regarding the nanobody analysis, or phosphorylated CTD (derived from RNA Polymerase 2) in case of the antibody and were conjugated via a strain-promoted azide-alkyne

cycloaddition reaction to the DNA oligonucleotide of interest. The DNA-conjugated peptides were directly added in the folding reaction with the DNA origami structures, which were designed to arrange the antigens in a 20 nm grid pattern. The DNA-conjugated binders of interest were added after the origami structures were surface immobilized on a PEG-passivated glass coverslip via biotin-streptavidin linkages. In an Exchange-PAINT experiment, the binder position was first assayed and compared to the true antigen position on the origami. We demonstrated, that nanobody staining clearly resolves the underlying nanocluster at a spacing of 20 nm, whereas antibody staining masks the underlying complex formation (Figure 14c,d). Therefore, we proved that the ultimate goal of SMLM to dissect single complex formation on a single protein scale, is only achievable with small labeling probes.

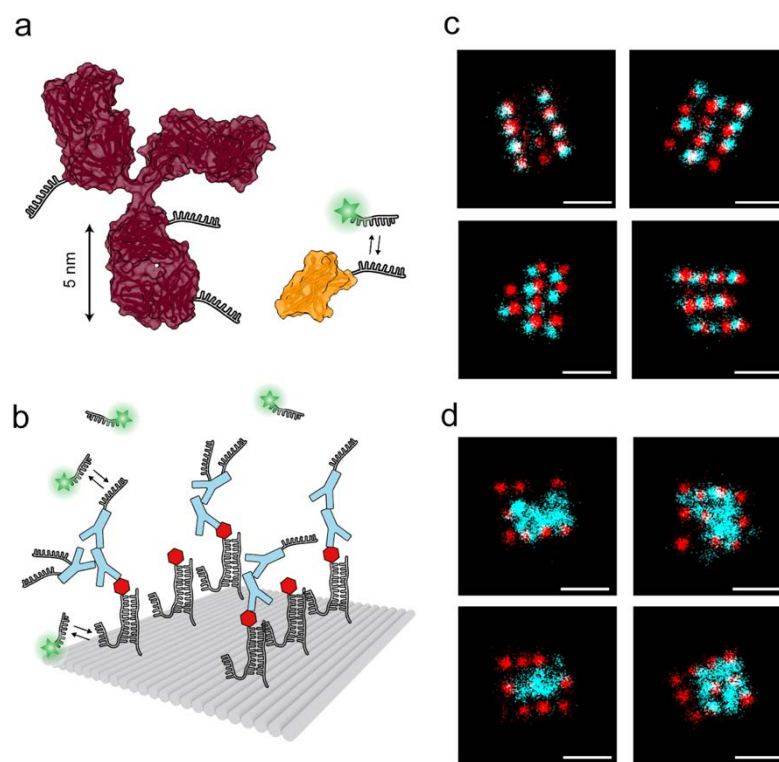


Figure 14: Labeling platform. a) Antibodies and nanobodies were assayed to resolve artificially templated nanoclusters on DNA origami. Both were labeled with DNA strands. b) Artificially templated antigen clusters (red) on DNA origami, in which the position of the antigen can be visualized in order to readout the underlying true position. Labeling probes (cyan) can be assayed for their performance with DNA-PAINT microscopy. c) Nanobody imaging (cyan) of the ALFA-tag antigen demonstrates, that the single antigen sites (red) spaced 20 nm apart can be clearly separated. d) Antibody imaging (cyan) of pCTD does not show single antigen sites (red) spaced 20 nm apart. Scale bar: 50 nm (c,d). PDB IDs: Antibody: 1IGT, ALFA-tag nanobody: 6I2G.

### 4.2 Quantitative cluster analysis and detection

Novel approaches in super-resolution microscopy, such as MINFLUX<sup>36</sup>, DNA-PAINT<sup>1</sup> or expansion microscopy<sup>145</sup> can achieve resolutions down to the size of single proteins. This was not possible with previous techniques. Therefore, novel discoveries were mainly made for structural proteins or higher order clusters. However, dissecting the protein composition within high density nanoclusters is only possible to a limited extent, as the cluster sizes are highly biased depending on the size of the labeling probe<sup>146</sup>.

However with the established tools, it should now be possible to use super-resolution microscopy to quantitatively assess cluster distributions as well as their heterogeneity and utilize this to reconstruct single-molecular complexes. This should enable to truly map distances between proteins interacting in transient signaling events. However, to detect single sites, the single molecule localization data needs to be analyzed via clustering algorithms as previously emphasized in section 1.10. DNA-PAINT data achieves high-resolution so that single-binding sites even within 10 nm distance can be detected<sup>1</sup>. The profile of a single site in DNA-PAINT resembles a gaussian distribution of localizations around the true position of a single docking site. A modified Ripley's K function was implemented for cluster detection as a possible method to find the centers of the gaussian distribution of localizations. Ripley's K function analyses the local density of the localizations by calculating the number of neighbors within a certain radius<sup>130</sup>. To find the local cluster centers, the algorithm was modified, so that within a distance  $r$  to one localization, no other localization harbors a larger number of neighbors within the same distance  $r$ . This creates a gradient ascent towards the point of highest density. The clusters are then defined as the localizations within the defined radius from the cluster center and can be filtered for a threshold number of localizations or repetitive visits over the whole course of imaging (Figure 15a). For performance evaluation we tested the implemented novel clusterer against the DBSCAN algorithm in simulations. First, the algorithms were tested at an exemplary simulated dataset of 50 pairs of two single clusters, spaced 10 nm apart and at a NeNa<sup>147</sup> localization precision of 2.5 nm. The optimal distance parameter for the novel clusterer was a window (2-4 nm) around the localization precision to detect all clusters. Smaller values led to subclustering, whereas larger values merged the paired clusters. For the DBSCAN algorithm, no parameter was found which could successfully detect the single clusters (Figure 15b,c). In a second simulation, the resolvable distance was determined by simulating again 50 pairs at various distances (2 nm – 20 nm) at a fixed localization precision of 2.5 nm. The optimal parameter of 3 nm derived from the previous experiment was chosen as distance input parameter for the algorithm. The novel clusterer was already able to successfully detect the pair separations at 6 nm, whereas DBSCAN only started to detect single clusters at separations of 12 nm (Figure 15d).

Additionally, the novel clustering algorithm was assayed on two different DNA origami samples, which were previously published<sup>48</sup>. One dataset with 20 nm distances on DNA origami and one Exchange-PAINT dataset, where sites were as close as ~6 nm apart. The 20 nm grid distances, its underlying pattern of 29 nm in the diagonal direction to the nearest neighbor and 40 nm to the second nearest neighbor in the horizontal direction could be automatically detected. Additionally it was possible to find the distances between the different docking sites in the exchange experiment (Figure 15e,f,g).

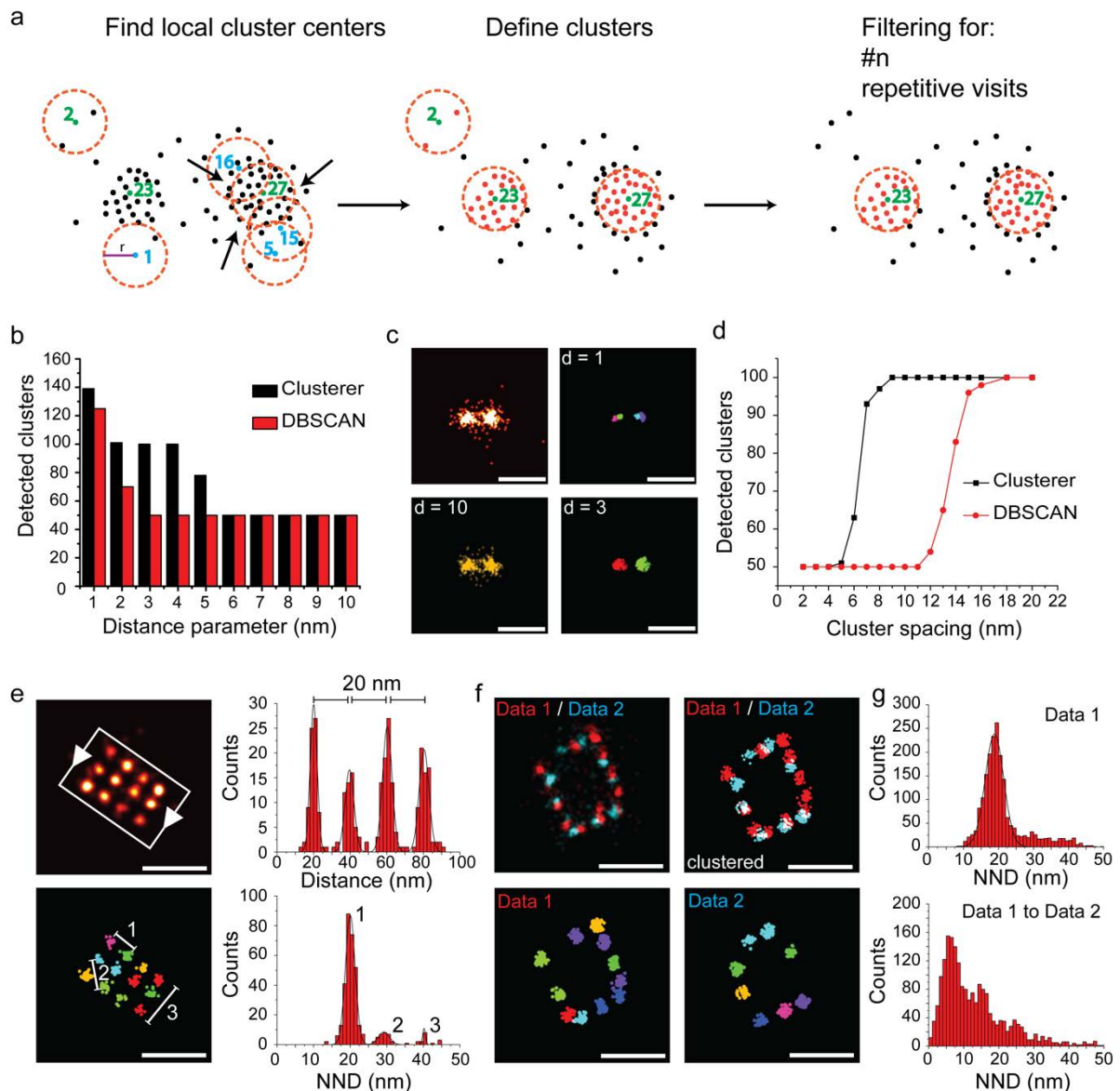


Figure 15: Cluster detection. a) Depiction of implemented clustering algorithm, which counts the number of neighbors within a certain radius and performs a gradient ascent to detect the cluster center (left). The detected cluster centers are then defined as clusters with their appropriate neighbors (middle), these clusters can afterwards be filtered for repetitive visits or the number of elements in them (right). b) Successful detection of clusters depends on the distance parameter plugged into the used clustering algorithm. Values smaller than the localization precision lead to subclustering, whereas larger values lead to combined clusters. For the novel clustering algorithm (Clusterer), the optimal distance parameter

## 4.2 Quantitative cluster analysis and detection

---

is a window around the localization precision, for the DBSCAN algorithm, no distance parameter was found to optimally detect all clusters. Data from 50 simulated pairs with two clusters at 10 nm distance at a NeNa localization precision of 2.5 nm. c) Images from datasets from b. Top left: localized data, top right: subclustering induced by a small distance parameter, bottom left: Merging of clusters due to large distance parameter, bottom right: successful detection of clusters with the optimal distance parameter of 3 nm. d) Comparison of detected clusters through the two different clustering methods (Clusterer and DBSCAN) in comparison to the cluster pair spacing at a fixed distance parameter of 3 nm. The clusterer detects the clusters at a distance difference of 6 nm, whereas DBSCAN only detects the clusters properly at a distance separation of 12 nm. Data from 50 simulated pairs at increasing distances and fixed NeNa localization precision of 2.5 nm. e) 20 nm DNA origami image (top left) and corresponding distance analysis (top right). Automated detection of clusters with the clustering algorithm (bottom left) and distance measurements for a large sample area (bottom right). The major peak corresponds to a distance of 20 nm and peaks corresponding to distances of 29 nm and 40 nm can also be observed. The later distances are a result of low incorporation efficiencies, e.g. if staples are missing. f) Exchange experiment on DNA origami structure and the cluster detection. g) Nearest neighbor distance analysis of one dataset yields a peak at 20 nm (top). Nearest neighbor distance analysis of one dataset to the other, yields a major peak at 6 nm, which corresponds to the designed pattern (bottom). Scale bars: 20 nm (c), 50 nm (e,f).

After successful detection of the single sites in DNA-PAINT data, it is important to determine whether distances in the histogram occur randomly or if complex formation occurs. In order to extract the degree of complex formation, simulations of the data were performed. As previously reported, the labeling efficiency for different binders can be in the order of ~30% in cell biological applications<sup>55,144</sup>. How do these low percentages influence the analysis of complex formation? To investigate a relatively high-density environment in a cell, 867 particles per  $\mu\text{m}^2$  were assumed for two species and different degrees of complex formation (0-100%) were simulated (Figure 16). Complex formation was defined as percentage of colocalization within 25 nm. Particles were otherwise randomly distributed at x and y positions, complexes were set to be between 12-16 nm and labeling efficiency was assumed to be 30%. The simulated point pattern was not subjected to an additional SMLM process or cluster detection pipeline, to prevent biased interpretation of the system. At 0% complex formation, the analysis showed that already ~40% of proteins appear colocalized just by proximity. At 100% complex formation only ~58% of colocalization was detected. Extracting molecular densities from real data enables now to apply simulations to assume the percentage of complex formation between different protein species in cells.

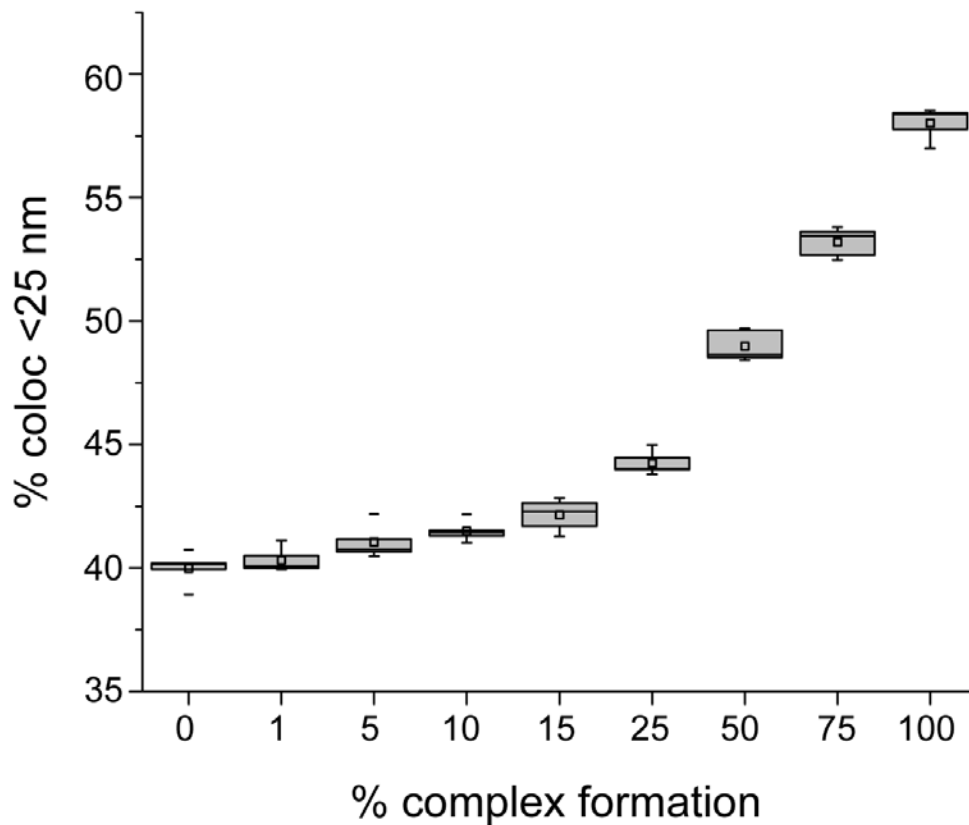


Figure 16: Simulated complex formation. In cells, labeling efficiency is a major issue and was reported to be in the order of  $\sim 30\%$  for genetically encoded tags. Here colocalization was defined as the distance to the nearest neighbor within 25 nm and 0-100% of the molecules were simulated to reside in a complex. Assuming a protein copy number density of 867 particles per  $\mu\text{m}^2$  at 0% complex formation, already  $\sim 40\%$  of colocalized molecules were detected. At 100% complex formation only  $\sim 58\%$  of colocalization was detected.

---

# 5 Discussion and Outlook

## General

In this thesis, DNA-PAINT was further developed to unravel its true potential in cellular systems. Different labeling chemistries were developed to attach DNA strands to biomolecules. Additionally, DNA nanoplatfoms were generated to test the capability of labeling probes to resolve nanotemplated antigens. The probes were in the end applied to cellular super-resolution imaging to dissect molecular complexes. Finally, a cluster detection method to detect single DNA docking sites was implemented and simulations were performed for a more comprehensive interpretation of the DNA-PAINT data.

Some important topics and challenges for the future of super-resolution microscopy are discussed in the following paragraphs.

## Resolution

The field of super-resolution microscopy enabled the imaging and analysis of cellular processes beyond the diffraction limit of light. However, until recently it was not possible to analyze the distribution of single proteins. With the resolution revolution of the newly emerging technologies such as DNA-PAINT<sup>47</sup>, MINFLUX<sup>36</sup> and expansion microscopy<sup>145</sup>, the resolution capabilities from a technical perspective are now on the order of single fluorophores. With this strong technical development, other aspects in super-resolution microscopy including labeling probes and data analysis pipelines have become the limiting factors.

## Labeling Probes

Antibodies are a powerful tool for cell imaging, since they are widely available and have high specificity and high affinity to their targets. However, as depicted with the nanotemplating of antigens in chapter 4.1, antibodies are relatively large in size in comparison to the technical resolution capabilities of DNA-PAINT. Additionally, it is not straightforward to label them site-specifically with a single DNA docking site for quantitative imaging approaches. To obtain site-specifically modified DNA-Antibody constructs, site-click<sup>148</sup> chemistry has been developed, which uses sugar side-chains of the antibody to modify them with a single chemical moiety. An alternative approach uses conserved histidine clusters that can mediate the local attachment of a chemical moiety to the antibody via tris-NTA guidance<sup>109</sup>. However, these methods are still tedious to implement. Small genetically-encoded tags such as SNAP<sup>95</sup>, Halo<sup>96</sup>, GFP<sup>87</sup> or the ALFA tag<sup>99</sup> can alternatively be used with small-molecule ligands or site-specifically labeled nanobodies for the detection of single proteins in cells. Unfortunately, their

labeling efficiency has been recently reported to be only on the order of 30-60%<sup>55</sup>. Furthermore, these tags are not universally applicable since certain cell lines are difficult to engineer and an additional level of complexity arises if three or more targets are to be investigated in the same cell.

In general, the remaining challenge in the field of labeling probes is that a perfect reagent needs to fulfill four main requirements: they need to be small (ideally the size of a fluorophore or a single amino acid), provide high labeling efficiency (~90-100%), have the possibility to be labeled site-specifically with a single DNA strand (for quantitative analysis and single-protein counting) and be universally applicable. This implies that a probe should be available for any target of interest, without the requirement of genetic engineering and tagging, which is not always possible. One universally applicable tool could be the use of FAB fragments, where screening libraries such as HUCAL<sup>149</sup> are already available. FAB fragments can be site-specifically labeled via the available disulfide-bridge between the heavy and light chain<sup>150</sup>. Beyond that, there are emerging scaffold libraries, including previously mentioned Affimers<sup>151</sup>, anticalines<sup>152</sup>, nanobodies<sup>87</sup> or darpins<sup>89</sup> which can be used as small alternative probes. Taken together, validated binders for super-resolution imaging are still limited.

As an alternative to available scaffold libraries, the previously mentioned IRIS probes<sup>49</sup> could be a solution as universally applicable binders with high labeling efficiency. IRIS probes utilize fragments of transiently and highly specific interacting proteins extracted from protein interaction networks and can be directly applied for PAINT imaging. However, one disadvantage of using IRIS probes is that the kinetics of each probe would have to be characterized in a cell-free system to truly quantify the molecular density. In this respect, DNA-PAINT is much more universally applicable. Another attractive route would be to rationally design binders against targets of interest<sup>153</sup>.

Nevertheless, in order to move DNA-PAINT based super-resolution microscopy to massive multiplexing applications, well characterized probes for 100s or 1000s of targets would be necessary.

### **Massive high-throughput multiplexing**

So far, multiplexing was mainly limited to the microscopy setup specifics including available laser lines in combination with appropriate filter sets, thereby limiting the readout to three to four colors. More advanced strategies were able to decode up to 5-8 colors<sup>154</sup>. However, using programmable DNA sequences to encode different pseudo-colors has given a new perspective on multiplexing where up to 10 colors in one sample have been imaged with DNA-PAINT<sup>2</sup>. Unfortunately, at some point the manual exchange of probes by buffer exchange is experimentally difficult, meaning that it needs to be highly automated. Regardless, the process is highly time consuming as it scales linearly with the number of targets. DNA as a

---

programmable building material harnesses the unique opportunity to encode the target with binary-encoding schemes as proposed by the Zhuang lab. Their approach enabled imaging of >1000 targets in only 12-16 exchange rounds with a method called MERFISH<sup>155</sup>. One pitfall of their method is that the sites need to be clearly discernible, for example using single mRNA species hybridized to tens of fluorophores. However, with DNA-PAINT and its associated high-resolution, unlimited imaging and high sensitivity capabilities, this approach could in principle be translated to single protein imaging.

### **Data analysis**

Once the data has been acquired with the highest resolution, using small labeling probes and with the largest number of targets possible, the data needs to be analyzed adequately and the main question remains: what can a list of spots tell us about the organization of proteins, which cannot be derived by other means? For example, protein interactions can be identified using mass spectrometry pull down assays. It is mainly the context in the cellular environment and the interplay with other proteins, which cannot be easily retrieved by other means. The first step is to really define the single protein sites, which can be determined by a variety of methods, including k-means<sup>127</sup> clustering, DBSCAN<sup>126</sup>, a modification of Ripley's  $K$ <sup>130</sup> or the newly developed bagol<sup>156</sup>. All of these methods have their shortcomings and advantages, therefore, they need to be thoroughly evaluated against each other and against an underlying truth. To a certain extent, this can only be done accurately using DNA nanostructures. However, in a cellular environment, different factors come into play, such as the sticking of DNA labeled fluorophores to random sites. Once these single sites are determined, the second challenge of data analysis begins. Protein networks inside cells are highly dynamic systems. For instance, there are proteins that engage in the desired complex formation, proteins that are shuttled towards their site of action or towards degradation and more importantly, only a fraction of the molecules will be labeled and detected. In order to correctly interpret the data, simulations can be an extremely helpful tool to consider the labeling efficiency and extract the true molecular densities of the proteins. Such simulations can help to understand the distribution pattern of proteins. Additionally, machine learning approaches were developed<sup>132</sup> to automatically detect patterns and assay their heterogeneity or their complex formation. With those tools at hand it should now become possible to dissect single protein distributions.

### **Molecular Timers**

Another major challenge in single-molecule localization microscopy, and especially in DNA-PAINT is that it is currently not applicable for live-cell microscopy due to several technical limitations, hence why it is mostly performed in fixed cell systems. Therefore, if a molecular

mechanism needs to be dissected (such as a receptor activation), the timing of signaling events play an important role. For this, a molecular timer could be extremely useful, which could be envisioned using micropatterns, where cells repetitively perform the same action. For example, it would be possible to infer the timing of focal adhesion formation through progression of the cell within the micropatterned environment<sup>157</sup>. Such a molecular timer could alternatively be envisioned as a reference protein which is known to progress in a certain way and was demonstrated in Mund et al's work for clathrin mediated endocytosis<sup>158</sup>.

### **Structural context**

Single-molecule localization data consists of a list of spots or clustered spots. However, cells are usually organized in organelles, such as mitochondria, vesicles, ER or Golgi. One remaining challenge is that there is barely any structural context associated with the localization data, unless structural proteins are investigated. To achieve this, it could be of interest to combine SMLM with electron microscopy to provide organellar and structural context, as was previously reported by Hoffman et al.<sup>159</sup>.

With the now available tools, super-resolution microscopy techniques should aim to unravel the function of single bio-functional units on the single-protein level in the future.

---

## 6 Bibliography

- 1 Dai, M., Jungmann, R. & Yin, P. Optical imaging of individual biomolecules in densely packed clusters. *Nat Nanotechnol* **11**, 798-807, doi:10.1038/nnano.2016.95 (2016).
- 2 Jungmann, R. *et al.* Multiplexed 3D cellular super-resolution imaging with DNA-PAINT and Exchange-PAINT. *Nat Methods* **11**, 313-318, doi:10.1038/nmeth.2835 (2014).
- 3 Jungmann, R. *et al.* Quantitative super-resolution imaging with qPAINT. *Nat Methods* **13**, 439-442, doi:10.1038/nmeth.3804 (2016).
- 4 Agasti, S. S. *et al.* DNA-barcoded labeling probes for highly multiplexed Exchange-PAINT imaging. *Chem Sci* **8**, 3080-3091, doi:10.1039/c6sc05420j (2017).
- 5 Britannica, T. E. o. E. Antonie van Leeuwenhoek. *Encyclopaedia Britannica* (2019).
- 6 Britannica, T. E. o. E. Joseph von Fraunhofer. *Encyclopaedia Britannica* (2019).
- 7 Britannica, T. E. o. E. Carl Zeiss. *Encyclopaedia Britannica* (2019).
- 8 von Blume, J. *et al.* Cab45 is required for Ca<sup>2+</sup>-dependent secretory cargo sorting at the trans-Golgi network. *Journal of Cell Biology* **199**, 1057-1066, doi:10.1083/jcb.201207180 (2012).
- 9 Yildiz, A. *et al.* Myosin V walks hand-over-hand: single fluorophore imaging with 1.5-nm localization. *Science* **300**, 2061-2065, doi:10.1126/science.1084398 (2003).
- 10 Stosiek, C., Garaschuk, O., Holthoff, K. & Konnerth, A. In vivo two-photon calcium imaging of neuronal networks. *Proc Natl Acad Sci U S A* **100**, 7319-7324, doi:10.1073/pnas.1232232100 (2003).
- 11 Kirk, W. Solvent Stokes' shifts revisited: application and comparison of Thompson-Schweizer-Chandler-Song-Marcus theories with Ooshika-Bakshiev-Lippert theories. *J Phys Chem A* **112**, 13609-13621, doi:10.1021/jp806208w (2008).
- 12 Jablonski, A. Efficiency of anti-stokes fluorescence in dyes. *Nature* **131**, 839-840, doi:DOI 10.1038/131839b0 (1933).
- 13 Lichtman, J. W. & Conchello, J. A. Fluorescence microscopy. *Nat Methods* **2**, 910-919, doi:10.1038/nmeth817 (2005).
- 14 Ernst, L. A., Gupta, R. K., Mujumdar, R. B. & Waggoner, A. S. Cyanine Dye Labeling Reagents for Sulfhydryl-Groups. *Cytometry* **10**, 3-10, doi:DOI 10.1002/cyto.990100103 (1989).
- 15 Mujumdar, R. B., Ernst, L. A., Mujumdar, S. R., Lewis, C. J. & Waggoner, A. S. Cyanine Dye Labeling Reagents - Sulfoindocyanine Succinimidyl Esters. *Bioconjugate Chem* **4**, 105-111, doi:DOI 10.1021/bc00020a001 (1993).
- 16 Shimomura, O. Structure of the Chromophore of Aequorea Green Fluorescent Protein. *Febs Letters* **104**, 220-222, doi:Doi 10.1016/0014-5793(79)80818-2 (1979).
- 17 Heim, R., Prasher, D. C. & Tsien, R. Y. Wavelength Mutations and Posttranslational Autoxidation of Green Fluorescent Protein. *P Natl Acad Sci USA* **91**, 12501-12504, doi:DOI 10.1073/pnas.91.26.12501 (1994).
- 18 Yang, F., Moss, L. G. & Phillips, G. N. The molecular structure of green fluorescent protein. *Nature Biotechnology* **14**, 1246-1251, doi:DOI 10.1038/nbt1096-1246 (1996).
- 19 Shu, X. K., Shaner, N. C., Yarbrough, C. A., Tsien, R. Y. & Remington, S. J. Novel chromophores and buried charges control color in mFruits. *Biochemistry* **45**, 9639-9647, doi:10.1021/bi060773l (2006).

- 
- 20 Shaner, N. C. *et al.* A bright monomeric green fluorescent protein derived from *Branchiostoma lanceolatum*. *Nature Methods* **10**, 407-+, doi:10.1038/Nmeth.2413 (2013).
- 21 Li, D. *et al.* ADVANCED IMAGING. Extended-resolution structured illumination imaging of endocytic and cytoskeletal dynamics. *Science* **349**, aab3500, doi:10.1126/science.aab3500 (2015).
- 22 Livet, J. *et al.* Transgenic strategies for combinatorial expression of fluorescent proteins in the nervous system. *Nature* **450**, 56-+, doi:10.1038/nature06293 (2007).
- 23 Goto, H. & Inagaki, M. Production of a site- and phosphorylation state-specific antibody. *Nature Protocols* **2**, 2574-2581, doi:10.1038/nprot.2007.374 (2007).
- 24 Huse, K., Bohme, H. J. & Scholz, G. H. Purification of antibodies by affinity chromatography. *J Biochem Biophys Methods* **51**, 217-231, doi:10.1016/s0165-022x(02)00017-9 (2002).
- 25 Webb, D. J. & Brown, C. M. Epi-fluorescence microscopy. *Methods Mol Biol* **931**, 29-59, doi:10.1007/978-1-62703-056-4\_2 (2013).
- 26 Thompson, N. L., Burghardt, T. P. & Axelrod, D. Measuring surface dynamics of biomolecules by total internal reflection fluorescence with photobleaching recovery or correlation spectroscopy. *Biophys J* **33**, 435-454, doi:10.1016/S0006-3495(81)84905-3 (1981).
- 27 Fish, K. N. Total internal reflection fluorescence (TIRF) microscopy. *Curr Protoc Cytom Chapter 12*, Unit12 18, doi:10.1002/0471142956.cy1218s50 (2009).
- 28 Tokunaga, M., Imamoto, N. & Sakata-Sogawa, K. Highly inclined thin illumination enables clear single-molecule imaging in cells. *Nat Methods* **5**, 159-161, doi:10.1038/nmeth1171 (2008).
- 29 Abbe, E. Beiträge zur Theorie des Mikroskops und der mikroskopischen Wahrnehmung. *Archiv für mikroskopische Anatomie*. **9**, 413-468 (1873).
- 30 John William Strutt, B. R. On the theory of optical images, with special reference to the microscope. *Philosophical Magazine Series 5* **42**, 167-195 (1896).
- 31 Betzig, E. Proposed method for molecular optical imaging. *Opt Lett* **20**, 237-239, doi:10.1364/ol.20.000237 (1995).
- 32 Hell, S. W. & Wichmann, J. Breaking the Diffraction Resolution Limit by Stimulated-Emission - Stimulated-Emission-Depletion Fluorescence Microscopy. *Optics Letters* **19**, 780-782, doi:Doi 10.1364/Ol.19.000780 (1994).
- 33 Hell, S. W. & Kroug, M. Ground-State-Depletion Fluorescence Microscopy - a Concept for Breaking the Diffraction Resolution Limit. *Appl Phys B-Lasers O* **60**, 495-497, doi:Doi 10.1007/Bf01081333 (1995).
- 34 Klar, T. A., Jakobs, S., Dyba, M., Egner, A. & Hell, S. W. Fluorescence microscopy with diffraction resolution barrier broken by stimulated emission. *Proc Natl Acad Sci U S A* **97**, 8206-8210, doi:10.1073/pnas.97.15.8206 (2000).
- 35 Thompson, R. E., Larson, D. R. & Webb, W. W. Precise nanometer localization analysis for individual fluorescent probes. *Biophys J* **82**, 2775-2783, doi:10.1016/S0006-3495(02)75618-X (2002).
- 36 Balzarotti, F. *et al.* Nanometer resolution imaging and tracking of fluorescent molecules with minimal photon fluxes. *Science* **355**, 606-612, doi:10.1126/science.aak9913 (2017).
- 37 Gwosch, K. C. *et al.* MINFLUX nanoscopy delivers 3D multicolor nanometer resolution in cells. *Nat Methods*, doi:10.1038/s41592-019-0688-0 (2020).

- 
- 38 Sahl, S. J., Hell, S. W. & Jakobs, S. Fluorescence nanoscopy in cell biology. *Nat Rev Mol Cell Biol* **18**, 685-701, doi:10.1038/nrm.2017.71 (2017).
- 39 Smith, C. S., Joseph, N., Rieger, B. & Lidke, K. A. Fast, single-molecule localization that achieves theoretically minimum uncertainty. *Nature Methods* **7**, 373-U352, doi:10.1038/Nmeth.1449 (2010).
- 40 van de Linde, S. & Sauer, M. How to switch a fluorophore: from undesired blinking to controlled photoswitching. *Chem Soc Rev* **43**, 1076-1087, doi:10.1039/c3cs60195a (2014).
- 41 Betzig, E. *et al.* Imaging intracellular fluorescent proteins at nanometer resolution. *Science* **313**, 1642-1645, doi:10.1126/science.1127344 (2006).
- 42 Rust, M. J., Bates, M. & Zhuang, X. Sub-diffraction-limit imaging by stochastic optical reconstruction microscopy (STORM). *Nat Methods* **3**, 793-795, doi:10.1038/nmeth929 (2006).
- 43 Heilemann, M. *et al.* Subdiffraction-resolution fluorescence imaging with conventional fluorescent probes. *Angew Chem Int Ed Engl* **47**, 6172-6176, doi:10.1002/anie.200802376 (2008).
- 44 Vogelsang, J. *et al.* Make them Blink: Probes for Super-Resolution Microscopy. *Chemphyschem* **11**, 2475-2490, doi:10.1002/cphc.201000189 (2010).
- 45 Sharonov, A. & Hochstrasser, R. M. Wide-field subdiffraction imaging by accumulated binding of diffusing probes. *Proc Natl Acad Sci U S A* **103**, 18911-18916, doi:10.1073/pnas.0609643104 (2006).
- 46 Giannone, G. *et al.* Dynamic superresolution imaging of endogenous proteins on living cells at ultra-high density. *Biophys J* **99**, 1303-1310, doi:10.1016/j.bpj.2010.06.005 (2010).
- 47 Jungmann, R. *et al.* Single-molecule kinetics and super-resolution microscopy by fluorescence imaging of transient binding on DNA origami. *Nano Lett* **10**, 4756-4761, doi:10.1021/nl103427w (2010).
- 48 Schnitzbauer, J., Strauss, M. T., Schlichthaerle, T., Schueder, F. & Jungmann, R. Super-resolution microscopy with DNA-PAINT. *Nat Protoc* **12**, 1198-1228, doi:10.1038/nprot.2017.024 (2017).
- 49 Kiuchi, T., Higuchi, M., Takamura, A., Maruoka, M. & Watanabe, N. Multitarget super-resolution microscopy with high-density labeling by exchangeable probes. *Nat Methods* **12**, 743-746, doi:10.1038/nmeth.3466 (2015).
- 50 Huang, B., Wang, W., Bates, M. & Zhuang, X. Three-dimensional super-resolution imaging by stochastic optical reconstruction microscopy. *Science* **319**, 810-813, doi:10.1126/science.1153529 (2008).
- 51 Hell, S. W., Stelzer, E. H., Lindek, S. & Cremer, C. Confocal microscopy with an increased detection aperture: type-B 4Pi confocal microscopy. *Opt Lett* **19**, 222, doi:10.1364/ol.19.000222 (1994).
- 52 Huang, F. *et al.* Ultra-High Resolution 3D Imaging of Whole Cells. *Cell* **166**, 1028-1040, doi:10.1016/j.cell.2016.06.016 (2016).
- 53 Deschamps, J., Mund, M. & Ries, J. 3D superresolution microscopy by supercritical angle detection. *Opt Express* **22**, 29081-29091, doi:10.1364/OE.22.029081 (2014).
- 54 Dempsey, G. T., Vaughan, J. C., Chen, K. H., Bates, M. & Zhuang, X. Evaluation of fluorophores for optimal performance in localization-based super-resolution imaging. *Nat Methods* **8**, 1027-1036, doi:10.1038/nmeth.1768 (2011).

- 55 Thevathasan, J. V. *et al.* Nuclear pores as versatile reference standards for quantitative superresolution microscopy. *Nat Methods* **16**, 1045-1053, doi:10.1038/s41592-019-0574-9 (2019).
- 56 Schmied, J. J. *et al.* Fluorescence and super-resolution standards based on DNA origami. *Nat Methods* **9**, 1133-1134, doi:10.1038/nmeth.2254 (2012).
- 57 Schmied, J. J. *et al.* DNA origami-based standards for quantitative fluorescence microscopy. *Nat Protoc* **9**, 1367-1391, doi:10.1038/nprot.2014.079 (2014).
- 58 Watson, J. D. & Crick, F. H. C. Molecular Structure of Nucleic Acids - a Structure for Deoxyribose Nucleic Acid. *Nature* **171**, 737-738, doi:DOI 10.1038/171737a0 (1953).
- 59 Yakovchuk, P., Protozanova, E. & Frank-Kamenetskii, M. D. Base-stacking and base-pairing contributions into thermal stability of the DNA double helix (vol 34, pg 564, 2006). *Nucleic Acids Research* **34**, 1082-+, doi:10.1093/nar/gkj523 (2006).
- 60 Seeman, N. C. Nucleic acid junctions and lattices. *J Theor Biol* **99**, 237-247 (1982).
- 61 Chen, J. H. & Seeman, N. C. Synthesis from DNA of a molecule with the connectivity of a cube. *Nature* **350**, 631-633, doi:10.1038/350631a0 (1991).
- 62 Du, S. M. & Seeman, N. C. The construction of a trefoil knot from a DNA branched junction motif. *Biopolymers* **34**, 31-37, doi:10.1002/bip.360340105 (1994).
- 63 Rothmund, P. W. Folding DNA to create nanoscale shapes and patterns. *Nature* **440**, 297-302, doi:10.1038/nature04586 (2006).
- 64 Douglas, S. M. *et al.* Self-assembly of DNA into nanoscale three-dimensional shapes. *Nature* **459**, 414-418, doi:10.1038/nature08016 (2009).
- 65 Ke, Y. *et al.* Multilayer DNA origami packed on a square lattice. *J Am Chem Soc* **131**, 15903-15908, doi:10.1021/ja906381y (2009).
- 66 Ke, Y., Voigt, N. V., Gothelf, K. V. & Shih, W. M. Multilayer DNA origami packed on hexagonal and hybrid lattices. *J Am Chem Soc* **134**, 1770-1774, doi:10.1021/ja209719k (2012).
- 67 Dietz, H., Douglas, S. M. & Shih, W. M. Folding DNA into twisted and curved nanoscale shapes. *Science* **325**, 725-730, doi:10.1126/science.1174251 (2009).
- 68 Wagenbauer, K. F., Sigl, C. & Dietz, H. Gigadalton-scale shape-programmable DNA assemblies. *Nature* **552**, 78-83, doi:10.1038/nature24651 (2017).
- 69 Derr, N. D. *et al.* Tug-of-war in motor protein ensembles revealed with a programmable DNA origami scaffold. *Science* **338**, 662-665, doi:10.1126/science.1226734 (2012).
- 70 Linko, V., Eerikainen, M. & Kostianen, M. A. A modular DNA origami-based enzyme cascade nanoreactor. *Chem Commun (Camb)* **51**, 5351-5354, doi:10.1039/c4cc08472a (2015).
- 71 Shaw, A. *et al.* Spatial control of membrane receptor function using ligand nanocalipers. *Nat Methods* **11**, 841-846, doi:10.1038/nmeth.3025 (2014).
- 72 Schmied, J. J. *et al.* DNA origami nanopillars as standards for three-dimensional superresolution microscopy. *Nano Lett* **13**, 781-785, doi:10.1021/nl304492y (2013).
- 73 Schlichthaerle, T., Strauss, M. T., Schueder, F., Woehrstein, J. B. & Jungmann, R. DNA nanotechnology and fluorescence applications. *Curr Opin Biotechnol* **39**, 41-47, doi:10.1016/j.copbio.2015.12.014 (2016).
- 74 Raab, M., Schmied, J. J., Jusuk, I., Forthmann, C. & Tinnefeld, P. Fluorescence microscopy with 6 nm resolution on DNA origami. *Chemphyschem* **15**, 2431-2435, doi:10.1002/cphc.201402179 (2014).

- 
- 75 Beater, S., Holzmeister, P., Lalkens, B. & Tinnefeld, P. Simple and aberration-free 4color-STED--multiplexing by transient binding. *Opt Express* **23**, 8630-8638, doi:10.1364/OE.23.008630 (2015).
- 76 Schueder, F. *et al.* Universal Super-Resolution Multiplexing by DNA Exchange. *Angew Chem Int Ed Engl* **56**, 4052-4055, doi:10.1002/anie.201611729 (2017).
- 77 Schweller, R. M. *et al.* Multiplexed in situ immunofluorescence using dynamic DNA complexes. *Angew Chem Int Ed Engl* **51**, 9292-9296, doi:10.1002/anie.201204304 (2012).
- 78 Gordon, M. P., Ha, T. & Selvin, P. R. Single-molecule high-resolution imaging with photobleaching. *Proc Natl Acad Sci U S A* **101**, 6462-6465, doi:10.1073/pnas.0401638101 (2004).
- 79 Lee, S. H., Shin, J. Y., Lee, A. & Bustamante, C. Counting single photoactivatable fluorescent molecules by photoactivated localization microscopy (PALM). *Proc Natl Acad Sci U S A* **109**, 17436-17441, doi:10.1073/pnas.1215175109 (2012).
- 80 Hummer, G., Fricke, F. & Heilemann, M. Model-independent counting of molecules in single-molecule localization microscopy. *Mol Biol Cell* **27**, 3637-3644, doi:10.1091/mbc.E16-07-0525 (2016).
- 81 Inuma, R. *et al.* Polyhedra self-assembled from DNA tripods and characterized with 3D DNA-PAINT. *Science* **344**, 65-69, doi:10.1126/science.1250944 (2014).
- 82 Clem, A. S. Fundamentals of vaccine immunology. *J Glob Infect Dis* **3**, 73-78, doi:10.4103/0974-777X.77299 (2011).
- 83 Leenaars, M. & Hendriksen, C. F. Critical steps in the production of polyclonal and monoclonal antibodies: evaluation and recommendations. *ILAR J* **46**, 269-279, doi:10.1093/ilar.46.3.269 (2005).
- 84 Seeber, S. *et al.* A Robust High Throughput Platform to Generate Functional Recombinant Monoclonal Antibodies Using Rabbit B Cells from Peripheral Blood. *PLoS One* **9**, doi:ARTN e86184 10.1371/journal.pone.0086184 (2014).
- 85 Hamers-Casterman, C. *et al.* Naturally occurring antibodies devoid of light chains. *Nature* **363**, 446-448, doi:10.1038/363446a0 (1993).
- 86 Greenberg, A. S. *et al.* A new antigen receptor gene family that undergoes rearrangement and extensive somatic diversification in sharks. *Nature* **374**, 168-173, doi:10.1038/374168a0 (1995).
- 87 Ries, J., Kaplan, C., Platonova, E., Eghlidi, H. & Ewers, H. A simple, versatile method for GFP-based super-resolution microscopy via nanobodies. *Nat Methods* **9**, 582-584, doi:10.1038/nmeth.1991 (2012).
- 88 Mikhaylova, M. *et al.* Resolving bundled microtubules using anti-tubulin nanobodies. *Nat Commun* **6**, 7933, doi:10.1038/ncomms8933 (2015).
- 89 Binz, H. K. *et al.* High-affinity binders selected from designed ankyrin repeat protein libraries. *Nat Biotechnol* **22**, 575-582, doi:10.1038/nbt962 (2004).
- 90 Tiede, C. *et al.* Adhiron: a stable and versatile peptide display scaffold for molecular recognition applications. *Protein Eng Des Sel* **27**, 145-155, doi:10.1093/protein/gzu007 (2014).
- 91 Beste, G., Schmidt, F. S., Stibora, T. & Skerra, A. Small antibody-like proteins with prescribed ligand specificities derived from the lipocalin fold. *Proc Natl Acad Sci U S A* **96**, 1898-1903, doi:10.1073/pnas.96.5.1898 (1999).

- 92 Smith, G. P. Filamentous Fusion Phage - Novel Expression Vectors That Display Cloned Antigens on the Virion Surface. *Science* **228**, 1315-1317, doi:DOI 10.1126/science.4001944 (1985).
- 93 Nguyen, H. H., Park, J., Kang, S. & Kim, M. Surface Plasmon Resonance: A Versatile Technique for Biosensor Applications. *Sensors-Basel* **15**, 10481-10510, doi:10.3390/s150510481 (2015).
- 94 Wienken, C. J., Baaske, P., Rothbauer, U., Braun, D. & Duhr, S. Protein-binding assays in biological liquids using microscale thermophoresis. *Nature Communications* **1**, doi:ARTN 100 10.1038/ncomms1093 (2010).
- 95 Keppler, A. *et al.* A general method for the covalent labeling of fusion proteins with small molecules in vivo. *Nat Biotechnol* **21**, 86-89, doi:10.1038/nbt765 (2003).
- 96 Los, G. V. *et al.* HaloTag: a novel protein labeling technology for cell imaging and protein analysis. *ACS Chem Biol* **3**, 373-382, doi:10.1021/cb800025k (2008).
- 97 Mazmanian, S. K., Liu, G., Ton-That, H. & Schneewind, O. Staphylococcus aureus sortase, an enzyme that anchors surface proteins to the cell wall. *Science* **285**, 760-763, doi:10.1126/science.285.5428.760 (1999).
- 98 Yin, J. *et al.* Genetically encoded short peptide tag for versatile protein labeling by Sfp phosphopantetheinyl transferase. *Proc Natl Acad Sci U S A* **102**, 15815-15820, doi:10.1073/pnas.0507705102 (2005).
- 99 Gotzke, H. *et al.* The ALFA-tag is a highly versatile tool for nanobody-based bioscience applications. *Nat Commun* **10**, 4403, doi:10.1038/s41467-019-12301-7 (2019).
- 100 Braun, M. B. *et al.* Peptides in headlock--a novel high-affinity and versatile peptide-binding nanobody for proteomics and microscopy. *Sci Rep* **6**, 19211, doi:10.1038/srep19211 (2016).
- 101 Virant, D. *et al.* A peptide tag-specific nanobody enables high-quality labeling for dSTORM imaging. *Nat Commun* **9**, 930, doi:10.1038/s41467-018-03191-2 (2018).
- 102 Nikic, I. *et al.* Debugging Eukaryotic Genetic Code Expansion for Site-Specific Click-PAINT Super-Resolution Microscopy. *Angew Chem Int Ed Engl* **55**, 16172-16176, doi:10.1002/anie.201608284 (2016).
- 103 Blackman, M. L., Royzen, M. & Fox, J. M. Tetrazine ligation: fast bioconjugation based on inverse-electron-demand Diels-Alder reactivity. *J Am Chem Soc* **130**, 13518-13519, doi:10.1021/ja8053805 (2008).
- 104 Seitchik, J. L. *et al.* Genetically encoded tetrazine amino acid directs rapid site-specific in vivo bioorthogonal ligation with trans-cyclooctenes. *J Am Chem Soc* **134**, 2898-2901, doi:10.1021/ja2109745 (2012).
- 105 Pettersen, E. F. *et al.* UCSF Chimera--a visualization system for exploratory research and analysis. *J Comput Chem* **25**, 1605-1612, doi:10.1002/jcc.20084 (2004).
- 106 Kalkhof, S. & Sinz, A. Chances and pitfalls of chemical cross-linking with amine-reactive N-hydroxysuccinimide esters. *Anal Bioanal Chem* **392**, 305-312, doi:10.1007/s00216-008-2231-5 (2008).
- 107 Agard, N. J., Prescher, J. A. & Bertozzi, C. R. A strain-promoted [3+2] azide-alkyne cycloaddition for covalent modification of biomolecules in living systems (vol 126, pg 15046, 2004). *Journal of the American Chemical Society* **127**, 11196-11196, doi:10.1021/ja059912x (2005).

- 
- 108 Oliveira, B. L., Guo, Z. & Bernardes, G. J. L. Inverse electron demand Diels-Alder reactions in chemical biology. *Chem Soc Rev* **46**, 4895-4950, doi:10.1039/c7cs00184c (2017).
- 109 Rosen, C. B. *et al.* Template-directed covalent conjugation of DNA to native antibodies, transferrin and other metal-binding proteins. *Nat Chem* **6**, 804-809, doi:10.1038/nchem.2003 (2014).
- 110 Mukhortava, A. & Schlierf, M. Efficient Formation of Site-Specific Protein-DNA Hybrids Using Copper-Free Click Chemistry. *Bioconj Chem* **27**, 1559-1563, doi:10.1021/acs.bioconjchem.6b00120 (2016).
- 111 Lin, S. *et al.* Redox-based reagents for chemoselective methionine bioconjugation. *Science* **355**, 597-602, doi:10.1126/science.aal3316 (2017).
- 112 Lee, K. J., Kang, D. & Park, H. S. Site-Specific Labeling of Proteins Using Unnatural Amino Acids. *Mol Cells* **42**, 386-396, doi:10.14348/molcells.2019.0078 (2019).
- 113 Fu, J. *et al.* Assembly of multienzyme complexes on DNA nanostructures. *Nat Protoc* **11**, 2243-2273, doi:10.1038/nprot.2016.139 (2016).
- 114 Engler, A. J., Sen, S., Sweeney, H. L. & Discher, D. E. Matrix elasticity directs stem cell lineage specification. *Cell* **126**, 677-689, doi:10.1016/j.cell.2006.06.044 (2006).
- 115 Kuo, J. C., Han, X., Hsiao, C. T., Yates, J. R., 3rd & Waterman, C. M. Analysis of the myosin-II-responsive focal adhesion proteome reveals a role for beta-Pix in negative regulation of focal adhesion maturation. *Nat Cell Biol* **13**, 383-393, doi:10.1038/ncb2216 (2011).
- 116 Kanchanawong, P. *et al.* Nanoscale architecture of integrin-based cell adhesions. *Nature* **468**, 580-584, doi:10.1038/nature09621 (2010).
- 117 Hynes, R. O. Integrins: bidirectional, allosteric signaling machines. *Cell* **110**, 673-687, doi:10.1016/s0092-8674(02)00971-6 (2002).
- 118 Campbell, I. D. & Humphries, M. J. Integrin structure, activation, and interactions. *Cold Spring Harb Perspect Biol* **3**, doi:10.1101/cshperspect.a004994 (2011).
- 119 Kong, F., Garcia, A. J., Mould, A. P., Humphries, M. J. & Zhu, C. Demonstration of catch bonds between an integrin and its ligand. *J Cell Biol* **185**, 1275-1284, doi:10.1083/jcb.200810002 (2009).
- 120 Calderwood, D. A., Campbell, I. D. & Critchley, D. R. Talins and kindlins: partners in integrin-mediated adhesion. *Nat Rev Mol Cell Biol* **14**, 503-517, doi:10.1038/nrm3624 (2013).
- 121 Grashoff, C. *et al.* Measuring mechanical tension across vinculin reveals regulation of focal adhesion dynamics. *Nature* **466**, 263-266, doi:10.1038/nature09198 (2010).
- 122 Austen, K. *et al.* Extracellular rigidity sensing by talin isoform-specific mechanical linkages. *Nat Cell Biol* **17**, 1597-1606, doi:10.1038/ncb3268 (2015).
- 123 Rognoni, E., Ruppert, R. & Fassler, R. The kindlin family: functions, signaling properties and implications for human disease. *J Cell Sci* **129**, 17-27, doi:10.1242/jcs.161190 (2016).
- 124 Bottcher, R. T. *et al.* Kindlin-2 recruits paxillin and Arp2/3 to promote membrane protrusions during initial cell spreading. *J Cell Biol* **216**, 3785-3798, doi:10.1083/jcb.201701176 (2017).
- 125 Dunn, K. W., Kamocka, M. M. & McDonald, J. H. A practical guide to evaluating colocalization in biological microscopy. *Am J Physiol-Cell Ph* **300**, C723-C742, doi:10.1152/ajpcell.00462.2010 (2011).

- 126 Martin Ester, H.-P. K., Jörg Sander, Xiaowei Xu. A Density-Based Algorithm for Discovering Clusters in Large Spatial Databases with Noise. *KDD 1996* (1996).
- 127 J.A. Hartigan, M. A. W. A K-Means Clustering Algorithm. *Journal of Royal Statistical Society. Series C (Applied Statistics)* **28, No. 1**, 100-108 (1979).
- 128 Levet, F. *et al.* SR-Tesseler: a method to segment and quantify localization-based super-resolution microscopy data. *Nat Methods* **12**, 1065-1071, doi:10.1038/nmeth.3579 (2015).
- 129 Andronov, L., Orlov, I., Lutz, Y., Vonesch, J. L. & Klaholz, B. P. ClusterViSu, a method for clustering of protein complexes by Voronoi tessellation in super-resolution microscopy. *Sci Rep* **6**, 24084, doi:10.1038/srep24084 (2016).
- 130 Rubin-Delanchy, P. *et al.* Bayesian cluster identification in single-molecule localization microscopy data. *Nat Methods* **12**, 1072-1076, doi:10.1038/nmeth.3612 (2015).
- 131 Ripley, B. D. Modelling Spatial Patterns. *Journal of Royal Statistical Society. Series B (Methodological)* **39**, 172-212 (1977).
- 132 Danial, J. S. H. & Garcia-Saez, A. J. Quantitative analysis of super-resolved structures using ASAP. *Nat Methods* **16**, 711-714, doi:10.1038/s41592-019-0472-1 (2019).
- 133 Acuna, G. P. *et al.* Fluorescence enhancement at docking sites of DNA-directed self-assembled nanoantennas. *Science* **338**, 506-510, doi:10.1126/science.1228638 (2012).
- 134 Lopata, A. *et al.* Affimer proteins for F-actin: novel affinity reagents that label F-actin in live and fixed cells. *Sci Rep* **8**, 6572, doi:10.1038/s41598-018-24953-4 (2018).
- 135 Ey, P. L., Prowse, S. J. & Jenkin, C. R. Isolation of Pure IgG1, IgG2a and IgG2b Immunoglobulins from Mouse Serum Using Protein a-Sepharose. *Immunochemistry* **15**, 429-436, doi:Doi 10.1016/0161-5890(78)90070-6 (1978).
- 136 Gouda, H. *et al.* Three-dimensional solution structure of the B domain of staphylococcal protein A: comparisons of the solution and crystal structures. *Biochemistry* **31**, 9665-9672, doi:10.1021/bi00155a020 (1992).
- 137 Achari, A. *et al.* 1.67-Å X-ray structure of the B2 immunoglobulin-binding domain of streptococcal protein G and comparison to the NMR structure of the B1 domain. *Biochemistry* **31**, 10449-10457, doi:10.1021/bi00158a006 (1992).
- 138 von Appen, A. *et al.* In situ structural analysis of the human nuclear pore complex. *Nature* **526**, 140-143, doi:10.1038/nature15381 (2015).
- 139 Szymborska, A. *et al.* Nuclear pore scaffold structure analyzed by super-resolution microscopy and particle averaging. *Science* **341**, 655-658, doi:10.1126/science.1240672 (2013).
- 140 Xu, K., Zhong, G. & Zhuang, X. Actin, spectrin, and associated proteins form a periodic cytoskeletal structure in axons. *Science* **339**, 452-456, doi:10.1126/science.1232251 (2013).
- 141 Strauss, S. *et al.* Modified aptamers enable quantitative sub-10-nm cellular DNA-PAINT imaging. *Nat Methods* **15**, 685-688, doi:10.1038/s41592-018-0105-0 (2018).
- 142 Jayasinghe, I. *et al.* True Molecular Scale Visualization of Variable Clustering Properties of Ryanodine Receptors. *Cell Rep* **22**, 557-567, doi:10.1016/j.celrep.2017.12.045 (2018).
- 143 Schlichthaerle, T., Ganji, M., Auer, A., Kimbu Wade, O. & Jungmann, R. Bacterially Derived Antibody Binders as Small Adapters for DNA-PAINT Microscopy. *ChemBiochem* **20**, 1032-1038, doi:10.1002/cbic.201800743 (2019).

- 
- 144 Schlichthaerle, T. *et al.* Direct Visualization of Single Nuclear Pore Complex Proteins Using Genetically-Encoded Probes for DNA-PAINT. *Angew Chem Int Ed Engl* **58**, 13004-13008, doi:10.1002/anie.201905685 (2019).
- 145 Chen, F., Tillberg, P. W. & Boyden, E. S. Optical imaging. Expansion microscopy. *Science* **347**, 543-548, doi:10.1126/science.1260088 (2015).
- 146 Spiess, M. *et al.* Active and inactive beta1 integrins segregate into distinct nanoclusters in focal adhesions. *J Cell Biol* **217**, 1929-1940, doi:10.1083/jcb.201707075 (2018).
- 147 Endesfelder, U., Malkusch, S., Fricke, F. & Heilemann, M. A simple method to estimate the average localization precision of a single-molecule localization microscopy experiment. *Histochem Cell Biol* **141**, 629-638, doi:10.1007/s00418-014-1192-3 (2014).
- 148 Zeglis, B. M. *et al.* Enzyme-Mediated Methodology for the Site-Specific Radiolabeling of Antibodies Based on Catalyst-Free Click Chemistry. *Bioconjugate Chem* **24**, 1057-1067, doi:10.1021/bc400122c (2013).
- 149 Rothe, C. *et al.* The human combinatorial antibody library HuCAL GOLD combines diversification of all six CDRs according to the natural immune system with a novel display method for efficient selection of high-affinity antibodies. *Journal of Molecular Biology* **376**, 1182-1200, doi:10.1016/j.jmb.2007.12.018 (2008).
- 150 Maruani, A. *et al.* A plug-and-play approach to antibody-based therapeutics via a chemoselective dual click strategy. *Nat Commun* **6**, 6645, doi:10.1038/ncomms7645 (2015).
- 151 Tiede, C. *et al.* Affimer proteins are versatile and renewable affinity reagents. *Elife* **6**, doi:10.7554/eLife.24903 (2017).
- 152 Skerra, A. Alternative binding proteins: Anticalins - harnessing the structural plasticity of the lipocalin ligand pocket to engineer novel binding activities. *Febs J* **275**, 2677-2683, doi:10.1111/j.1742-4658.2008.06439.x (2008).
- 153 Chevalier, A. *et al.* Massively parallel de novo protein design for targeted therapeutics. *Nature* **550**, 74-79, doi:10.1038/nature23912 (2017).
- 154 Valm, A. M. *et al.* Applying systems-level spectral imaging and analysis to reveal the organelle interactome. *Nature* **546**, 162-167, doi:10.1038/nature22369 (2017).
- 155 Chen, K. H., Boettiger, A. N., Moffitt, J. R., Wang, S. Y. & Zhuang, X. W. Spatially resolved, highly multiplexed RNA profiling in single cells. *Science* **348**, doi:ARTN aaa6090  
10.1126/science.aaa6090 (2015).
- 156 Mohamadreza Fazel, M. J. W., Bernd Rieger, Ralf Jungmann, Leith A. Lidke. Sub-Nanometer Precision using Bayesian Grouping of Localizations. *bioRxiv* (2019).
- 157 Bruckner, D. B. *et al.* Stochastic nonlinear dynamics of confined cell migration in two-state systems (vol 15, pg 595, 2019). *Nat Phys* **15**, 617-617, doi:10.1038/s41567-019-0493-9 (2019).
- 158 Mund, M. *et al.* Systematic Nanoscale Analysis of Endocytosis Links Efficient Vesicle Formation to Patterned Actin Nucleation. *Cell* **174**, 884-896 e817, doi:10.1016/j.cell.2018.06.032 (2018).
- 159 Hoffman, D. P. *et al.* Correlative three-dimensional super-resolution and block-face electron microscopy of whole vitreously frozen cells. *Science* **367**, doi:10.1126/science.aaz5357 (2020).

- 160 Schlichthaerle, T. *et al.* Site-Specific Labeling of Affimers for DNA-PAINT Microscopy. *Angew Chem Int Ed Engl* **57**, 11060-11063, doi:10.1002/anie.201804020 (2018).
- 161 Wagenbauer, K. F. *et al.* How We Make DNA Origami. *ChemBiochem* **18**, 1873-1885, doi:10.1002/cbic.201700377 (2017).
- 162 Jain, A., Liu, R., Xiang, Y. K. & Ha, T. Single-molecule pull-down for studying protein interactions. *Nat Protoc* **7**, 445-452, doi:10.1038/nprot.2011.452 (2012).



## 7 Acknowledgements

First of all, I would like to thank my parents and my brother for guiding my path and supporting me in pursuing my passion.

Thank you, Ralf, for accepting me in your lab as one of the first PhD students and for supporting me always in presenting our work at conferences or pursuing self-conceived projects.

A big thank you goes to the Focal Adhesion Crew, Lisa and Christoph for working hard two years for defining colocalization-coorganization on a new level and especially Lisa for always having super inspirational discussions about crazy scientific ideas.

Thanks a lot to the friends crew: Alexandra, Susi & Linh, you're great in helping to get distracted from the hard lab work.

A big thank you goes to the cool room crew: Sebastian & Alexandra, for great discussions & (unlimited) double chocolate cookie supply.

Thank you very much to the whole Jungmann Lab first generation, I had lots of fun discussing with you about fun science projects! Especially I want to mention Mahipal, I'm happy we pushed through our ideas which emerged during lunch walks! :)

And not to forget thank you to the Physics Crew: Maximilian, Alexander, Florian who always kept the microscopes running and especially to Maximilian and Jörg who set up the amazing Picasso pipeline - without it, we wouldn't be able to do the projects we are doing.

I want to thank Karl-Peter Hopfner for accepting me as PhD student and as internal supervisor at the faculty of chemistry and pharmacy of the LMU.

At last, I am truly thankful of having been able to work in the excellent Munich science environment, with inspirational collaborations at the MPI of Biochemistry, the QBM Graduate School as well as the truly amazing SFB1032.

## 8 Appendix

The first part of the Appendix includes the methods applied in chapter 4 of the thesis followed by the publications which were written during the course of the PhD.

### 8.1 Methods

#### **Microscopy Setup**

Fluorescence imaging was carried out on an inverted Nikon Eclipse Ti microscope (Nikon Instruments) equipped with the Perfect Focus System, using an objective-type TIRF configuration with an oil-immersion objective (Apo SR TIRF 100×, NA 1.49, Oil) as previously reported<sup>160</sup>. In brief, TIRF/Hilo angle was adjusted for highest signal to noise ratio when imaging. A 561 nm (200 mW, Coherent Sapphire) laser was used for excitation. The laser beam was passed through cleanup filters (ZET561/10, Chroma Technology) and coupled into the objective using a beam splitter (ZT561rdc, Chroma Technology). Fluorescence light was spectrally filtered with an emission filter (ET600/50m and ET575lp, Chroma Technology) and imaged on a sCMOS camera (Andor Zyla 4.2) without further magnification, resulting in an effective pixel size of 130 nm (sCMOS after 2×2 binning).

#### **Nanobody conjugation**

ALFA-tag nanobody conjugation to DNA strands was performed at cysteine residues as reported previously<sup>144,160</sup>. In brief, ALFA-tag nanobodies (NanoTag Biotechnologies, cat. no. N1502) were first concentrated for 5 min via Amicon 10 kDa spin filters (Merck, cat. no. UFC501096) and buffer was changed to 5 mM TCEP (ThermoFisher Scientific, cat. no. 20490) in 1xPBS (ThermoFisher Scientific, cat. no. 20012-019) supplemented with 3 mM EDTA (Ambion, cat. no. AM9261). 5 mM TCEP was additionally added to 100 µl of nanobody solution and incubated in the dark at 4°C. Afterwards, nanobody was buffer exchanged with 10 kDa Amicon Spin filters at 14.000xg for 5 min for 5 rounds and subsequently DBCO-Maleimide crosslinker (Sigma-Aldrich, cat. no. 760668) was added to 100 µl of nanobody solution at 20x molar excess of linker over nanobody in 5 µl and reacted at 4°C overnight. Free crosslinker was removed via 10 kDa Amicon spin filters at 14.000xg for 5 min for 5 rounds. Azide-modified DNA was then added to the nanobody at 10x molar excess over nanobody. Removal of free DNA from nanobody was performed using a GE Aekta purifier system and a 1 ml RESOURCE Q (GE Healthcare, cat. no. 17-1177-01) anion-exchange chromatography column. Salt

gradient from 1xPBS to 1xPBS+1M NaCl was performed at a flow rate of 1 ml/min over 30 min. Peak fractions were concentrated and buffer exchanged into 1xPBS via 10 kDa Amicon spin filters. DNA conjugated nanobody was stored at 4 °C until further use.

### **Antibody Conjugation**

Antibody conjugation was performed as reported previously<sup>48</sup> using SPAAC. In brief, 300 µl of secondary donkey anti-rabbit antibody (Jackson ImmunoResearch, cat. no. 711-005-152) was concentrated using 100 kDa Amicon ultra spin filters (Merck, cat. no. UFC510096) at 14.000xg for 5 min and adjusted to 100 µl in 1xPBS. NHS-DBCO heterobifunctional crosslinker (Jena Bioscience, cat. no. CLK-A124-10) was added in 10x molar excess over antibody in 5 µl to 100 µl of antibody solution and incubated at 4 °C in the dark for 2 h. Free crosslinker was removed after 2 h using 7 kDa zeba spin columns (ThermoFisher Scientific, cat. no. 89882) according to the manual and commercially available azide-modified DNA (Biomers.net) was added at 10x molar excess to the antibody for 1 h at room temperature. Final purification was performed via 100 kDa amicon spin filters for three rounds at 14.000xg for 5 min each and antibody was adjusted to 100 µl and stored at 4 °C until further use.

### **Peptide-DNA conjugation**

Peptides were ordered and produced at the Max-Planck Institute of Biochemistry Peptide facility, harboring an azide-modified amino acid at their N-terminus (Iris Biotech, cat. no. FAA1793). Peptide was reacted at 20x molar excess over commercially available DBCO-DNA (Biomers.net) at 4°C overnight in 1xPBS. Purification of DNA-peptide conjugates was performed via a RESOURCE Q anion-exchange chromatography column using a 30 min gradient from 1xPBS to 1xPBS+1M NaCl. Peak fractions were concentrated via 3 kDa Amicon ultra spin filters (Merck, cat. no. UFC500396). DNA-Peptide conjugates were aliquoted and stored at -20°C.

Peptides were attached to following strand:

5'-DBCO-TTC CTC TAC CAC CTA CAT CAC TTT CTT CAT TA – 3'

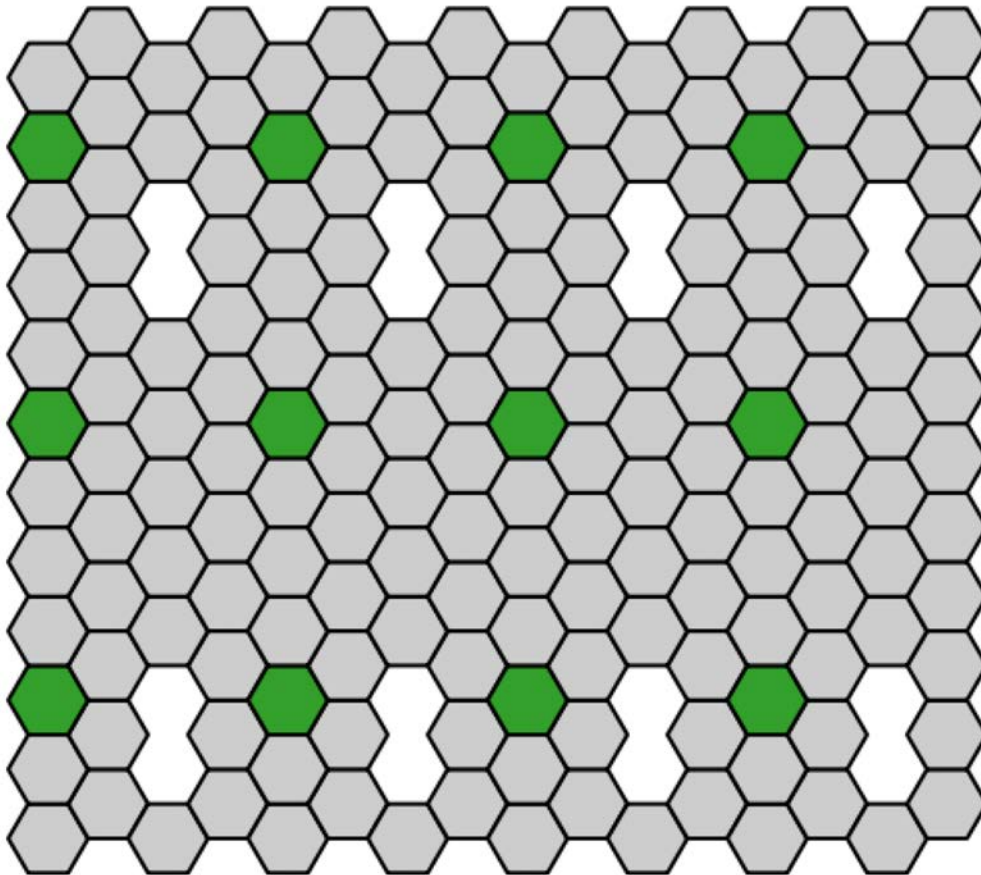
Peptides:

ALFA: Azide-Lysine-SRLEEELRRRLTE

pCTD: Azide-Lysine-YSPTSpPS

**DNA Origami Design**

20 nm grid DNA origami structure was designed with the Picasso software suite as reported previously<sup>48</sup>. Following design was chosen:



Supplementary Figure 1: 20 nm grid DNA origami design. Green hexagons mark the staple extension positions, grey hexagons are core staples without extension.

Supplementray Table 1: Staple list for DNA origami assembly:

Plate	Staple	Staple Name	Sequence
1	A1	21[32]23[31]BLK	TTTTCACTCAAAGGGCGAAAAACCATCACC
1	A2	19[32]21[31]BLK	GTCGACTTCGGCCAACGCGCGGGGTTTTTC
1	A3	17[32]19[31]S1	TGCATCTTTCCCAGTCACGACGGCCTGCAG TTGTGATGTAGGTGGTAGAGGAA
1	A4	15[32]17[31]BLK	TAATCAGCGGATTGACCGTAATCGTAACCG
1	A5	13[32]15[31]BLK	AACGCAAAATCGATGAACGGTACCGGTTGA
1	A6	11[32]13[31]BLK	AACAGTTTTGTACCAAAAACATTTTATTTTC
1	A7	9[32]11[31]S1	TTTACCCCAACATGTTTTAAATTTCCATAT TTGTGATGTAGGTGGTAGAGGAA
1	A8	7[32]9[31]BLK	TTTAGGACAAATGCTTTAAACAATCAGGTC
1	A9	5[32]7[31]BLK	CATCAAGTAAACGAACTAACGAGTTGAGA
1	A10	3[32]5[31]BLK	AATACGTTTGAAAGAGGACAGACTGACCTT
1	A11	1[32]3[31]S1	AGGCTCCAGAGGCTTTGAGGACACGGGTAA TTGTGATGTAGGTGGTAGAGGAA
1	A12	0[47]1[31]BLK	AGAAAGGAACAACCTAAAGGAATTCAAAAAAA
1	B1	23[32]22[48]BLK	CAAATCAAGTTTTTTGGGGTTCGAAACGTGGA
1	B2	22[47]20[48]BLK	CTCCAACGCAGTGAGACGGGCAACCAGCTGCA
1	B3	20[47]18[48]BLK	TTAATGAACTAGAGGATCCCCGGGGGTAACG
1	B4	18[47]16[48]BLK	CCAGGGTTGCCAGTTTGAGGGGACCCGTGGGA
1	B5	16[47]14[48]BLK	ACAAACGGAAAAGCCCCAAAAACACTGGAGCA
1	B6	14[47]12[48]BLK	AACAAGAGGGATAAAAATTTTTAGCATAAAGC
1	B7	12[47]10[48]BLK	TAAATCGGGATTCCCAATTCTGCGATATAATG
1	B8	10[47]8[48]BLK	CTGTAGCTTGACTATTATAGTCAGTTCATTGA
1	B9	8[47]6[48]BLK	ATCCCCCTATACCACATTCAACTAGAAAAATC
1	B10	6[47]4[48]BLK	TACGTTAAAGTAATCTTGACAAGAACCGAACT
1	B11	4[47]2[48]BLK	GACCAACTAATGCCACTACGAAGGGGGTAGCA
1	B12	2[47]0[48]BLK	ACGGCTACAAAAGGAGCCTTTAATGTGAGAAT
1	C1	21[56]23[63]BLK	AGCTGATTGCCCTTCAGAGTCCACTATTAAGGGTGCCGT
1	C2		
1	C3		
1	C4	15[64]18[64]BLK	GTATAAGCCAACCCGTCGGATTCTGACGACAGTATCGGCCGCAAGGCG
1	C5	13[64]15[63]BLK	TATATTTTGTCAATTGCCTGAGAGTGGAAGATT
1	C6	11[64]13[63]BLK	GATTTAGTCAATAAAGCCTCAGAGAACCCTCA
1	C7	9[64]11[63]BLK	CGGATTGCAGAGCTTAATTGCTGAAACGAGTA
1	C8	7[56]9[63]BLK	ATGCAGATACATAACGGGAATCGTCATAAATAAAGCAAAG
1	C9		
1	C10		
1	C11	1[64]4[64]BLK	TTTATCAGGACAGCATCGGAACGACACCAACCTAAAACGAGGTCAATC
1	C12	0[79]1[63]BLK	ACAACCTTCAACAGTTTCAGCGGATGTATCGG

## 8.1 Methods

1	D1	23[64]22[80]BLK	AAAGCACTAAATCGGAACCCTAATCCAGTT
1	D2	22[79]20[80]BLK	TGGAACAACCGCCTGGCCCTGAGGCCCGCT
1	D3	20[79]18[80]BLK	TTCCAGTCGTAATCATGGTCATAAAAGGGG
1	D4	18[79]16[80]BLK	GATGTGCTTCAGGAAGATCGCACAAATGTGA
1	D5	16[79]14[80]BLK	GCGAGTAAAAATATTTAAATTGTTACAAAG
1	D6	14[79]12[80]BLK	GCTATCAGAAATGCAATGCCTGAATTAGCA
1	D7	12[79]10[80]BLK	AAATTAAGTTGACCATTAGATACTTTTGCG
1	D8	10[79]8[80]BLK	GATGGCTTATCAAAAAGATTAAGAGCGTCC
1	D9	8[79]6[80]BLK	AATACTGCCAAAAGGAATTACGTGGCTCA
1	D10	6[79]4[80]BLK	TTATACCACCAAATCAACGTAACGAACGAG
1	D11	4[79]2[80]BLK	GCGCAGACAAGAGGCCAAAAGAATCCCTCAG
1	D12	2[79]0[80]BLK	CAGCGAACTTGCTTTTCGAGGTGTTGCTAA
1	E1	21[96]23[95]BLK	AGCAAGCGTAGGGTTGAGTGTGTTAGGGAGCC
1	E2	19[96]21[95]BLK	CTGTGTGATTGCGTTGCGCTCACTAGAGTTGC
1	E3	17[96]19[95]S1	GCTTTCCGATTACGCCAGCTGGCGGCTGTTTC TTGTGATGTAGGTGGTAGAGGAA
1	E4	15[96]17[95]BLK	ATATTTTGGCTTTCATCAACATTATCCAGCCA
1	E5	13[96]15[95]BLK	TAGGTAACTATTTTTGAGAGATCAAACGTTA
1	E6	11[96]13[95]BLK	AATGGTCAACAGGCAAGGCCAAAGAGTAATGTG
1	E7	9[96]11[95]S1	CGAAAGACTTTTGATAAGAGGTCATATTTTCGCA TTGTGATGTAGGTGGTAGAGGAA
1	E8	7[96]9[95]BLK	TAAGAGCAAATGTTTAGACTGGATAGGAAGCC
1	E9	5[96]7[95]BLK	TCATTCAGATGCGATTTTAAGAACAGGCATAG
1	E10	3[96]5[95]BLK	ACACTCATCCATGTTACTTAGCCGAAAGCTGC
1	E11	1[96]3[95]S1	AAACAGCTTTTTGCGGGATCGTCAACACTAAA TTGTGATGTAGGTGGTAGAGGAA
1	E12	0[111]1[95]BLK	TAAATGAATTTTCTGTATGGGATTAATTTCTT
1	F1	23[96]22[112]BLK	CCCGATTTAGAGCTTGACGGGGAAAAAGAATA
1	F2	22[111]20[112]BLK	GCCCGAGAGTCCACGCTGGTTTGCAGCTAACT
1	F3	20[111]18[112]BLK	CACATTAATAATTGTTATCCGCTCATGCGGGCC
1	F4	18[111]16[112]BLK	TCTTCGCTGCACCGCTTCTGGTGCGGCCTTCC
1	F5	16[111]14[112]BLK	TGTAGCCATTAATAATTCGCATTAATGCCGGA
1	F6	14[111]12[112]BLK	GAGGGTAGGATTCAAAAGGGTGAGACATCCAA
1	F7	12[111]10[112]BLK	TAAATCATATAACCTGTTTAGCTAACCTTTAA
1	F8	10[111]8[112]BLK	TTGCTCCTTTCAAATATCGCGTTTGAGGGGGT
1	F9	8[111]6[112]BLK	AATAGTAAACACTATCATAACCCTCATTGTGA
1	F10	6[111]4[112]BLK	ATTACCTTTGAATAAGGCTTGCCCAAATCCGC
1	F11	4[111]2[112]BLK	GACCTGCTCTTTGACCCCAGCGAGGGAGTTA
1	F12	2[111]0[112]BLK	AAGGCCGCTGATACCGATAGTTGCGACGTTAG
1	G1	21[120]23[127]BLK	CCCAGCAGGCGAAAAATCCCTTATAAATCAAGCCGGCG
1	G2		

1	G3		
1	G4	15[128]18[128]BLK	TAAATCAAATAATTCGCGTCTCGGAAACCAGGCAAAGGGAAGG
1	G5	13[128]15[127]BLK	GAGACAGCTAGCTGATAAATTAATTTTTGT
1	G6	11[128]13[127]BLK	TTTGGGGATAGTAGTAGCATTAAAAGGCCG
1	G7	9[128]11[127]BLK	GCTTCAATCAGGATTAGAGAGTTATTTTCA
1	G8	7[120]9[127]BLK	CGTTTACCAGACGACAAAGAAGTTTTGCCATAATTCGA
1	G9		
1	G10		
1	G11	1[128]4[128]BLK	TGACAACTCGCTGAGGCTTGCATTATACCAAGCGCGATGATAAA
1	G12	0[143]1[127]BLK	TCTAAAGTTTTGTGCTCTTTCCAGCCGACAA
1	H1	21[160]22[144]BLK	TCAATATCGAACCTCAAATATCAATTCCGAAA
1	H2	19[160]20[144]BLK	GCAATTCACATATTCTGATTATCAAAGTGTA
1	H3	17[160]18[144]BLK	AGAAAACAAAGAAGATGATGAAACAGGCTGCG
1	H4	15[160]16[144]BLK	ATCGCAAGTATGTAAATGCTGATGATAGGAAC
1	H5	13[160]14[144]BLK	GTAATAAGTTAGGCAGAGGCATTTATGATATT
1	H6	11[160]12[144]BLK	CCAATAGCTCATCGTAGGAATCATGGCATCAA
1	H7	9[160]10[144]BLK	AGAGAGAAAAAATGAAAATAGCAAGCAAAC
1	H8	7[160]8[144]BLK	TTATTACGAAGAACTGGCATGATTGCGAGAGG
1	H9	5[160]6[144]BLK	GCAAGGCCTCACCAGTAGCACCATGGGCTTGA
1	H10	3[160]4[144]BLK	TTGACAGGCCACCACCAGAGCCGCGATTTGTA
1	H11	1[160]2[144]BLK	TTAGGATTGGCTGAGACTCCTCAATAACCGAT
1	H12	0[175]0[144]BLK	TCCACAGACAGCCCTCATAGTTAGCGTAACGA
2	A1	23[128]23[159]BLK	AACGTGGCGAGAAAGGAAGGGAAACCAGTAA
2	A2	22[143]21[159]BLK	TCGGCAAATCCTGTTTGATGGTGGACCCTCAA
2	A3	20[143]19[159]S1	AAGCCTGGTACGAGCCGGAAGCATAGATGATG TTGTGATGTAGGTGGTAGAGGAA
2	A4	18[143]17[159]BLK	CAACTGTTGCGCCATTTCGCCATTCAAACATCA
2	A5	16[143]15[159]BLK	GCCATCAAGCTCATTTTTTAACCACAAATCCA
2	A6	14[143]13[159]BLK	CAACCGTTTCAAATCACCATCAATTCGAGCCA
2	A7	12[143]11[159]S1	TTCTACTACGCGAGCTGAAAAGGTTACCGCGC TTGTGATGTAGGTGGTAGAGGAA
2	A8	10[143]9[159]BLK	CCAACAGGAGCGAACCCAGACCGGAGCCTTTAC
2	A9	8[143]7[159]BLK	CTTTTGCAGATAAAAAACCAAATAAAGACTCC
2	A10	6[143]5[159]BLK	GATGGTTTGAACGAGTAGTAAATTTACCATTA
2	A11	4[143]3[159]S1	TCATCGCCAACAAAGTACAACGGACGCCAGCA TTGTGATGTAGGTGGTAGAGGAA
2	A12	2[143]1[159]BLK	ATATTCGGAACCATCGCCCACGCAGAGAAGGA
2	B1	23[160]22[176]BLK	TAAAAGGGACATTCTGGCCAACAAAGCATC
2	B2	22[175]20[176]BLK	ACCTTGCTTGGTCAGTTGGCAAAGAGCGGA
2	B3	20[175]18[176]BLK	ATTATCATTCAATATAATCCTGACAATTAC
2	B4	18[175]16[176]BLK	CTGAGCAAAAATTAATTACATTTTGGGTTA

## 8.1 Methods

2	B5	16[175]14[176]BLK	TATAACTAACAAAGAACGCGAGAACGCCAA
2	B6	14[175]12[176]BLK	CATGTAATAGAATATAAAGTACCAAGCCGT
2	B7	12[175]10[176]BLK	TTTTATTTAAGCAAATCAGATATTTTTTGT
2	B8	10[175]8[176]BLK	TTAACGTCTAACATAAAAAACAGGTAACGGA
2	B9	8[175]6[176]BLK	ATACCCAACAGTATGTTAGCAAATTAGAGC
2	B10	6[175]4[176]BLK	CAGCAAAAGGAAACGTCACCAATGAGCCGC
2	B11	4[175]2[176]BLK	CACCAGAAAGGTTGAGGCAGGTCATGAAAG
2	B12	2[175]0[176]BLK	TATTAAGAAGCGGGGTTTTGCTCGTAGCAT
2	C1	21[184]23[191]BLK	TCAACAGTTGAAAGGAGCAAATGAAAAATCTAGAGATAGA
2	C2		
2	C3		
2	C4	15[192]18[192]BLK	TCAAATATAACCTCCGGCTTAGGTAACAATTTTCATTTGAAGGCGAATT
2	C5	13[192]15[191]BLK	GTAAAGTAATCGCCATATTTAACAAAACTTTT
2	C6	11[192]13[191]BLK	TATCCGGTCTCATCGAGAACAAGCGACAAAAG
2	C7	9[192]11[191]BLK	TTAGACGGCCAAATAAGAAACGATAGAAGGCT
2	C8	7[184]9[191]BLK	CGTAGAAAATACATACCGAGGAAACGCAATAAGAAGCGCA
2	C9		
2	C10		
2	C11	1[192]4[192]BLK	GCGGATAACCTATTATTCTGAAACAGACGATTGGCCTTGAAGAGCCAC
2	C12	0[207]1[191]BLK	TCACCAGTACAACTACAACGCCTAGTACCAG
2	D1	23[192]22[208]BLK	ACCCTTCTGACCTGAAAGCGTAAGACGCTGAG
2	D2	22[207]20[208]BLK	AGCCAGCAATTGAGGAAGGTTATCATCATTTTT
2	D3	20[207]18[208]BLK	GCGGAACATCTGAATAATGGAAGGTACAAAAT
2	D4	18[207]16[208]BLK	CGCGCAGATTACCTTTTTTAATGGGAGAGACT
2	D5	16[207]14[208]BLK	ACCTTTTTATTTTAGTTAATTTTCATAGGGCTT
2	D6	14[207]12[208]BLK	AATTGAGAATTCTGTCCAGACGACTAAACCAA
2	D7	12[207]10[208]BLK	GTACCGCAATTCTAAGAACGCGAGTATTATTT
2	D8	10[207]8[208]BLK	ATCCCAATGAGAATTAACGAACAGTTACCAG
2	D9	8[207]6[208]BLK	AAGGAAACATAAAGGTGGCAACATTATCACCG
2	D10	6[207]4[208]BLK	TCACCGACGCACCGTAATCAGTAGCAGAACCG
2	D11	4[207]2[208]BLK	CCACCCTCTATTCACAAACAAATACCTGCCTA
2	D12	2[207]0[208]BLK	TTTCGGAAGTGCCGTCGAGAGGGTGAGTTTCG
2	E1	21[224]23[223]BLK	CTTTAGGGCCTGCAACAGTGCCAATACGTG
2	E2	19[224]21[223]BLK	CTACCATAGTTTGAGTAACATTTAAAATAT
2	E3	17[224]19[223]S1	CATAAATCTTTGAATACCAAGTGTTAGAAC TTGTGATGTAGGTGGTAGAGGAA
2	E4	15[224]17[223]BLK	CCTAAATCAAATCATAGGTCTAAACAGTA
2	E5	13[224]15[223]BLK	ACAACATGCCAACGCTCAACAGTCTTCTGA
2	E6	11[224]13[223]BLK	GCGAACCTCCAAGAACGGGTATGACAATAA
2	E7	9[224]11[223]S1	AAAGTCACAAAATAAACAGCCAGCGTTTTA TTGTGATGTAGGTGGTAGAGGAA

2	E8	7[224]9[223]BLK	AACGCAAAGATAGCCGAACAAACCCTGAAC
2	E9	5[224]7[223]BLK	TCAAGTTTCATTAAAGGTGAATATAAAAGA
2	E10	3[224]5[223]BLK	TTAAAGCCAGAGCCGCCACCCTCGACAGAA
2	E11	1[224]3[223]S1	GTATAGCAAACAGTTAATGCCCAATCCTCA TTGTGATGTAGGTGGTAGAGGAA
2	E12	0[239]1[223]BLK	AGGAACCCATGTACCGTAACACTTGATATAA
2	F1	23[224]22[240]BLK	GCACAGACAATATTTTTGAATGGGGTCAGTA
2	F2	22[239]20[240]BLK	TTAACACCAGCACTAACAATAATCGTTATTA
2	F3	20[239]18[240]BLK	ATTTTAAAATCAAATTATTTGCACGGATTCCG
2	F4	18[239]16[240]BLK	CCTGATTGCAATATATGTGAGTGATCAATAGT
2	F5	16[239]14[240]BLK	GAATTTATTTAATGGTTTGAAATATTCTTACC
2	F6	14[239]12[240]BLK	AGTATAAAGTTCAGCTAATGCAGATGTCTTTC
2	F7	12[239]10[240]BLK	CTTATCATTCCCGACTTGCGGGAGCCTAATTT
2	F8	10[239]8[240]BLK	GCCAGTTAGAGGGTAATTGAGCGCTTTAAGAA
2	F9	8[239]6[240]BLK	AAGTAAGCAGACACCACGGAATAATATTGACG
2	F10	6[239]4[240]BLK	GAAATTATTGCCTTTAGCGTCAGACCGGAACC
2	F11	4[239]2[240]BLK	GCCTCCCTCAGAATGGAAAGCGCAGTAACAGT
2	F12	2[239]0[240]BLK	GCCCGTATCCGGAATAGGTGTATCAGCCCAAT
2	G1	21[248]23[255]BLK	AGATTAGAGCCGTCAAAAAACAGAGGTGAGGCCTATTAGT
2	G2		
2	G3		
2	G4	15[256]18[256]BLK	GTGATAAAAAGACGCTGAGAAGAGATAACCTTGCTTCTGTTCCGGGAGA
2	G5	13[256]15[255]BLK	GTTTATCAATATGCGTTATACAAACCGACCGT
2	G6	11[256]13[255]BLK	GCCTTAAACCAATCAATAATCGGCACGCGCCT
2	G7	9[256]11[255]BLK	GAGAGATAGAGCGTCTTCCAGAGGTTTTGAA
2	G8	7[248]9[255]BLK	GTTTATTTTGTCACAATCTTACCGAAGCCCTTTAATATCA
2	G9		
2	G10		
2	G11	1[256]4[256]BLK	CAGGAGGTGGGGTCAGTGCCTTGAGTCTCTGAATTTACCGGGAACCAG
2	G12	0[271]1[255]BLK	CCACCCTCATTTTCAGGGATAGCAACCGTACT
2	H1	23[256]22[272]BLK	CTTTAATGCGCGAACTGATAGCCCCACCAG
2	H2	22[271]20[272]BLK	CAGAAGATTAGATAATACATTTGTGACAA
2	H3	20[271]18[272]BLK	CTCGTATTAGAAATTGCGTAGATACAGTAC
2	H4	18[271]16[272]BLK	CTTTTACAAAATCGTCTGCTATTAGCGATAG
2	H5	16[271]14[272]BLK	CTTAGATTTAAGGCGTTAAATAAAGCCTGT
2	H6	14[271]12[272]BLK	TTAGTATCACAATAGATAAGTCCACGAGCA
2	H7	12[271]10[272]BLK	TGTAGAAATCAAGATTAGTTGCTCTTACCA
2	H8	10[271]8[272]BLK	ACGCTAACACCCACAAGAATTGAAAATAGC
2	H9	8[271]6[272]BLK	AATAGCTATCAATAGAAAATTCAACATTCA
2	H10	6[271]4[272]BLK	ACCGATTGTGCGCATTTCGGTCATAATCA
2	H11	4[271]2[272]BLK	AAATCACCTTCCAGTAAGCGTCAGTAATAA

## 8.1 Methods

2	H12	2[271]0[272]BLK	GTTTAACTTAGTACCGCCACCCAGAGCCA
---	-----	-----------------	-------------------------------

Supplementary Table 2: Sequences of biotinylated staples:

No	Position	Name	Sequence	Mod.
1	C02	18[63]20[56]BIOTIN	ATTAAGTTTACCGAGCTCGAATTCGGGA AACCTGTCGTGC	5'-BT
2	C09	4[63]6[56]BIOTIN	ATAAGGGAACCGGATATTCATTACGTCA GGACGTTGGGAA	5'-BT
3	G02	18[127]20[120]BIOTIN	GCGATCGGCAATTCCACACAACAGGTG CCTAATGAGTG	5'-BT
4	G09	4[127]6[120]BIOTIN	TTGTGTCGTGACGAGAAACACCAAATTT CAACTTTAAT	5'-BT
5	K02	18[191]20[184]BIOTIN	ATTCATTTTTGTTTGGATTATACTAAGAA ACCACCAGAAG	5'-BT
6	K09	4[191]6[184]BIOTIN	CACCCTCAGAAACCATCGATAGCATTGA GCCATTTGGGAA	5'-BT
7	O02	18[255]20[248]BIOTIN	AACAATAACGTAACAGAAATAAAAAAT CCTTTGCCCGAA	5'-BT
8	O09	4[255]6[248]BIOTIN	AGCCACCACTGTAGCGCGTTTTCAAGG GAGGGAAGGTTAA	5'-BT

Staple strands for peptide attachment were extended with following sequence:

Staple – TTGTGATGTAGGTGGTAGAGGAA-3'

### DNA Origami Folding

DNA origami structures were folded with 10 nM M13mp18 scaffold strand (tilibit nanosystems), 100 nM core staple strands (Eurofins Genomics, see supplementary table), 300 nM biotinylated strands (Eurofins Genomics, see supplementary table) for surface attachment, 300 nM of extension strands (Eurofins Genomics, see supplementary table) and 4  $\mu$ M of Peptide-DNA in a total of 50  $\mu$ l. Buffer conditions were 5 mM Tris (Ambion, cat. no. AM9856) and 1 mM EDTA (Ambion, cat. no. AM9261) supplemented with 12.5 mM MgCl<sub>2</sub> (Ambion, cat. no. AM9530G) Folding reaction was carried out in a thermocycler with following program: 5 min at 80 °C followed by a fast cool down to 60 °C and a slow cooling from 60-4 °C over the course of 3 h in 1 °C steps.

### DNA Origami Purification

DNA nanostructures were purified via PEG purification as previously reported<sup>161</sup>. In brief, folded DNA origami was mixed 1:1 with 15 % of PEG-buffer (consisting of: 7.5 g PEG-8k, 1xTAE, 12.5 mM MgCl<sub>2</sub> and 500 mM NaCl). Mixed solution was centrifuged at 20.000xg at 4 °C for 30 min after which supernatant was removed and the DNA was resuspended with 50  $\mu$ l of folding buffer and 50  $\mu$ l of 15 % PEG-buffer was added. Centrifugation and supernatant

removal were repeated three additional times, at the last step, DNA origami was resuspended in 50  $\mu$ l folding buffer only. DNA origami structures were stored at -20 °C.

### **Microscopy Slide Preparation**

PEG surfaces were prepared as previously reported<sup>162</sup>. Microscopy slides (Marienfeld, cat. no. 0107032) were rinsed twice with Milli-Q water and bath-sonicated for 10 min to remove any organic residue from the surface. Rinsing and sonication steps were repeated with methanol (Sigma Aldrich, cat. no. 34860-2.5l-M) and acetone (ThermoFisher Scientific, cat. no. A060017). To activate the surface for silane functionalization, the slides were sonicated in 1 M KOH (Carl Roth, cat. no. K017.1) for 20 min and then rinsed with Milli-Q water. Afterwards, the slides were blow dried and aminosilane solution mix (86 ml of methanol, 5 ml acetic acid (Honeywell, cat. no. 607-002-00-6) and 10 ml aminosilane (Sigma Aldrich, cat. no. 104884-100ML)) were poured over the slides and incubated in the dark for 20 min. The slides were then washed with methanol and water for 1-2 min per wash, blow dried and stored under argon atmosphere until use. For PEG passivation, slides were attached to a home build channel system on a microscopy slide. 16 mg of NHS-mPEG 5000 (Rapp Polymere, cat. no. 125000-35) were mixed with 0.3 mg of NHS-biotin-PEG (Rapp Polymere, cat. no. 135000-25-35) in sodium bicarbonate buffer (Sigma Aldrich, cat. no. S5761-1kg) at pH 8.5 for 2 h. The channel was then washed with milli-Q water and buffer A (10 mM Tris-HCL supplemented with 100 mM NaCl at pH 8.0) and incubated with 0.5 mg/ml neutravidin (ThermoFisher Scientific, cat. no. 31000) in buffer A for 10 min. Afterwards, the slide was washed with buffer A, buffer C (1xPBS supplemented with 500 mM NaCl) and DNA nanostructures harboring the antigenic peptide were added to the surface for 10 min at a concentration of 500 pM in buffer C. After washing the channel with buffer C, DNA-labeled binders were added and incubated with the origami structures for 20 min. In case of the pCTD antigen, the primary probe was washed away and the secondary DNA labeled antibody was added in an additional round for 20 min. After an additional washing step, gold nanoparticles (Cytodiagnosics, cat. no. CG-90-100) in a 1:3 ratio in buffer C were incubated for 5 min on the slide. After washing the slide with buffer C, the prepared channels were used directly for imaging.

### **Super-Resolution Microscopy with DNA-PAINT**

The prepared microchannels on the microscopy slide with the DNA origami structures were imaged in imaging buffer (1xPBS supplemented with 500 mM NaCl and 1xPCA/1xPCD/1xTrolox) with P1 first and an exchange was performed to the true target position P3. Imaging was performed for P1 (6 nM imager concentration) and P3 (7 nM imager concentration) for 20.000 frames at a frame rate of 100 ms and a readout rate of 540 MHz on a 2x2 binned sCMOS camera with a power density of 0.8 kW/cm<sup>2</sup>.

## 8.1 Methods

---

Supplementary Table 3: DNA-PAINT imager strands

<b>Imager Name</b>	<b>Sequence</b>	<b>5'mod</b>	<b>3'mod</b>	<b>Company</b>
P1	AGA TGT AT	None	Cy3b	Eurofins
P3	AAT GAA GA	None	Cy3b	Eurofins
X61	AATTGAGGA	None	Cy3b	Eurofins
P7	GTAACAATT	None	Cy3b	Eurofins

Supplementary Table 4: DNA-PAINT docking site strands

<b>Docking Site</b>	<b>Sequence</b>	<b>5'mod</b>	<b>3'mod</b>	<b>Company</b>
P1	TTATACATCTA	Azide	None	Biomers
P3	TTTCTTCATTA	Azide/Halo Ligand	None	Biomers
X61	TTTCCTCAATT	Snap Ligand		Biomers
P7	TTAATTGAGTA	Azide		Biomers

## **Image Reconstruction**

Image reconstruction was performed via the Picasso software suite<sup>48</sup>. First, single localizations were detected and fitted with Picasso localize. Localized lists were then drift corrected and aligned in Picasso Render using gold nanoparticles.

## **Description of modified Ripley's K Function implementation (Clusterer)**

The function was implemented to find cluster centers and only uses a distance parameter as input variable. The number of neighboring localizations within the distance parameter is calculated for each localization. The first step of the algorithm is to make it fast and generate overlapping 30nmx30nm quadrants of the dataset. Afterwards from every localization in a quadrant all localizations within a distance  $r$  are counted. In the next step, the cluster centers are determined via a gradient ascent to the localization at the point of highest density. A cluster center is defined if within the distance  $r$ , no localization is found, which harbors a larger number of neighbors. Once the cluster centers are determined, the localizations within distance  $r$  are assigned to the cluster. In the next step, the clusters are filtered for the number of localizations and for the mean frame of all localizations to be within 20 and 80 percent of the total acquisition. As a last filtering step, if in one localization window (5% of total acquisition) more than 70% of the localizations occur, the cluster is removed. This step is performed to remove clusters which were detected only due to imager sticking events. The algorithm yields a list of localizations assigned to a certain cluster, which can be displayed with Picasso Render. Additionally, it provides the center of mass for every detected cluster, which was further used to calculate the nearest neighbor distances between the individual clusters. The code works with any Picasso generated hdf5 localization file.

## **Performance evaluation of clustering algorithm**

50 pairs of DNA-PAINT clusters were simulated with the parameters depicted in supplementary table 5. For the 10 nm separated clusters, various distances as input parameter (1-10 nm) were assayed for the clustering algorithms (Clusterer and DBSCAN) using a fixed threshold value of 10 localizations to be a specific cluster. The detected clusters were counted and compared to the simulated input number of clusters. To assay the performance to resolve pairs at various distances (2 – 20 nm), 3 nm was chosen as input distance parameter for the different clustering algorithms. Detected sites were compared to the simulated number of clusters (100) and analyzed with OriginPro 9.1.

## **Simulation of complex formation**

Particles were positioned with a random  $x$  and  $y$  coordinate. Depending on the degree of complex formation (0-100%), molecules of dataset two were reassigned within a distance of

## 8.1 Methods

---

12-16 nm in a random direction of a molecule from dataset one. After repositioning of the molecules, 70% of the simulated particles were randomly removed in both datasets to account for the labeling efficiency. The percentage of colocalization below 25 nm between the remaining molecules of the two datasets was afterwards calculated and analyzed with OriginPro 9.1. Five replicates of the simulation were performed and a total of 25000 molecules per dataset and replicate were simulated.

Supplementary Table 5: Simulations for performance evaluation of clustering algorithms

<b>Parameter</b>	<b>Value</b>
Number of Structures	50
Columns:	2
Rows:	1
Structure X	0.0, variable distance (2-20 nm)
Structure Y	0.0, 0.0
$k_{on}$	$2300000 \text{ M}^{-1}\text{s}^{-1}$
Imager concentration	7 nM
Bright time	500 ms
Incorporation	100 %
PSF	0.82
Power density	$1 \text{ kW}/\text{cm}^2$
Photonbudget	1500000
Photon detection rate	$35 \text{ cm}^2\text{kW}^{-1} \text{ ms}^{-1}$
Image size	32 Px
Integration time	200 ms
Frames	15000
Pixelsize	130

Supplementary Table 6: Imaging parameters for Figure 11

Target & Cells	Fixation Condition	Staining	Acquisition Parameters
Nuclear Pores: Cells: SNAP-UO2S	2.4 % PFA for 30 min	SNAP-X61	[c] = 100 pM, 68143 Frames, 200 ms/frame, Power: 0.3 kW/cm <sup>2</sup>
Vesicles: Cells: U2OS	Prefixation: 0.4% Glutaraldehyde + 0.25% Triton X-100 for 90 sec Fixation: 3% Glutaraldehyde for 15 min	Clathrin: SantaCruz, cat. no. sc-11415 Secondary antibody: Dianova, cat. no. DKxGt-003-F (P7- conjugated)	[c] = 1 nM, 30000 Frames, 100 ms/frame, Power: 1.5 kW/cm <sup>2</sup>
Focal Adhesions: Cells: Fibroblasts (Tln1 <sup>-/-</sup> Tln2 <sup>-/-</sup> ) resubstituted with Tln-HaloTag <sup>447</sup>	Fixation: 4 % PFA for 20 min	Halo-P3	[c] = 2.5 nM, 140000 Frames, 100 ms/frame, Power: 0.8 kW/cm <sup>2</sup>
Cytoskeleton: Microtubules Vimentin Cells: Cos-7	Prefixation: 0.4% Glutaraldehyde + 0.25% Triton X-100 for 90 sec Fixation: 3% Glutaraldehyde for 15 min	$\alpha$ -Tubulin: ThermoFisher Scientific, cat. no. MA1-80017 Secondary: Jackson ImmunoResearch, cat. no. 712-005-150 (P1- conjugated) Vimentin: Abcam, cat. no. ab24525 Secondary: Jackson ImmunoResearch, cat. no. 703-005-155 (P3- conjugated)	Tubulin: [c] = 200 pM, 20000 Frames, 250 ms/frame, Power: 3.3 kW/cm <sup>2</sup>  Vimentin: [c] = 1.5 nM, 20000 Frames, 100 ms/frame, Power: 1.4 kW/cm <sup>2</sup>
Surface Receptors Cells: A549	4 % PFA for 20 min	EGFR: Cell Signalling, cat. no. 4267 Secondary: Dianova, cat. no. 711-005-152 (P3-conjugated)	[c] = 200 pM, 80000 Frames, 100 ms/frame, Power: 2.5 kW/cm <sup>2</sup>
Mitochondrial Network Cells: HeLa	3 % PFA + 0.1 % Glutaraldehyde for 20 min	Tom20: SantaCruz, cat. no. sc-11415 Secondary: Dianova, cat. no. 711- 005-152 (P3- conjugated)	[c] = 200 pM, 20000 Frames, 200 ms/frame, Power: 1.2 kW/cm <sup>2</sup>



## **8.2 Publications**

# **DNA nanotechnology and fluorescence applications**

**T. Schlichthaerle**, M.T. Strauss, F. Schueder, J.B. Woehrstein, R. Jungmann

published in

*Current Opinion in Biotechnology (2016)*

Reprinted from [73]

Available online at [www.sciencedirect.com](http://www.sciencedirect.com)

ScienceDirect

Current Opinion in  
Biotechnology

## DNA nanotechnology and fluorescence applications

Thomas Schlichthaerle<sup>1,2</sup>, Maximilian T Strauss<sup>1,2</sup>,  
Florian Schueder<sup>1,2</sup>, Johannes B Woehrstein<sup>1,2</sup> and  
Ralf Jungmann<sup>1,2</sup>

Structural DNA nanotechnology allow researchers to use the unique molecular recognition properties of DNA strands to construct nanoscale objects with almost arbitrary complexity in two and three dimensions. Abstracted as molecular breadboards, DNA nanostructures enable nanometer-precise placement of guest molecules such as proteins, fluorophores, or nanoparticles. These assemblies can be used to study biological phenomena with unprecedented control over number, spacing, and molecular identity. Here, we give a general introduction to structural DNA nanotechnology and more specifically discuss applications of DNA nanostructures in the field of fluorescence and plasmonics.

### Addresses

<sup>1</sup> Department of Physics and Center for Nanoscience, Ludwig Maximilian University, 80539 Munich, Germany

<sup>2</sup> Max Planck Institute of Biochemistry, 82152 Martinsried near Munich, Germany

Corresponding author: Jungmann, Ralf ([jungmann@biochem.mpg.de](mailto:jungmann@biochem.mpg.de))

Current Opinion in Biotechnology 2016, 39:41–47

This review comes from a themed issue on **Nanobiotechnology**

Edited by **Michael A Nash** and **Oded Shoseyov**

For a complete overview see the [Issue](#) and the [Editorial](#)

Available online 13th January 2016

<http://dx.doi.org/10.1016/j.copbio.2015.12.014>

0958-1669/© 2016 Elsevier Ltd. All rights reserved.

### Introduction

In 1982, Nadrian Seeman proposed that DNA molecules, beyond their purpose as carriers of genetic information, could be used to build two and three-dimensional rationally designed objects with prescribed size, shape, and function on the nanoscale [1]. Using the unique programmability and molecular recognition properties of DNA, objects ranging from junctions [1] to more complex structures such as a 3D cube [2] and extended lattices [3] could be constructed. In 2004, Shih and co-workers created a DNA octahedron (~22 nm in diameter) by ‘folding’ a ~1600 nucleotides (nt) long single-stranded synthetic DNA molecule using five complementary ~40 nt long oligonucleotides [4].

2006 marked a major breakthrough in structural DNA nanotechnology, when Paul Rothemund developed DNA

origami [5<sup>\*\*</sup>]. Here, a long single-stranded DNA molecule (called the ‘scaffold’, usually derived from M13mp18 phage, ~7000 nt long) is folded into programmable shapes by ~200 short, single-stranded DNA oligonucleotides (called ‘staples’). Every staple has a defined sequence and specifically binds to defined parts of the scaffold, thus folding it into the desired shape. Structures are usually assembled in a one-pot reaction using thermal annealing. DNA origami sparked a true revolution in the field, for the first time enabling researchers to use relatively simple design rules to create self-assembled nanostructures with thus far unprecedented complexity and yield. In 2009, Douglas *et al.* extended DNA origami to three dimensions [6<sup>\*</sup>], now even allowing the construction of a larger variety of structures, which could be based on different underlying lattice types [7,8], exhibit curvature and twist [9,10] or use principles of tensegrity [11]. In 2012, Wei *et al.* demonstrated, that structures could be formed without the use of a scaffold strand using single-stranded tiles (SST) [12]. Recently, Benson *et al.* introduced structures, which construction is based on arbitrary polygonal meshes, allowing the creation of shapes that would be currently difficult to realize with incumbent approaches [13].

Part of the still developing success story of using DNA to construct shapes and patterns on the nanoscale is the ease of construction of these structures. The design process is considerably facilitated by the availability of free, computer-aided design and analysis tools such as caDNAo [6<sup>\*</sup>], vHelix [13], or CanDo [14]. With these tools at their disposal, even ‘non-experts’ from outside the DNA nanotechnology community can now design and construct structures *de novo* within only a few days.

In this review we will discuss recent developments in structural and dynamic DNA nanotechnology for applications in fluorescence microscopy and plasmonics.

### DNA nanostructures as molecular breadboards

The creation of DNA nanostructures with ever increasing complexity and shape diversity demonstrates the generality and modularity of their construction approaches. However, the true utility of the structures lies in their unique addressability. This makes them useful for applications where exact positioning of distinct molecular species may be required. Abstracted as molecular breadboards, DNA origami enable nanometer-precise placement of guest molecules such as proteins, fluorophores, or

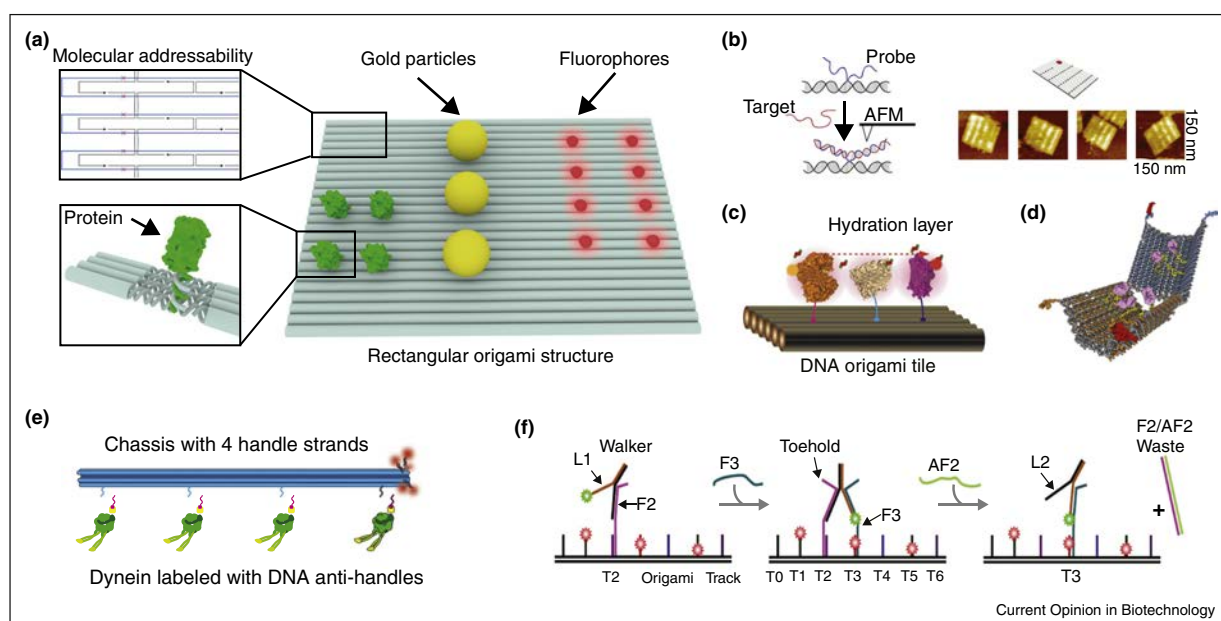
nanoparticles and can thus be used to study molecular interactions of these molecules on the nanoscale. A schematic representation demonstrating the unique addressability of DNA origami structures is depicted in Figure 1a. A large variety of, for example DNA-labeled guest molecules (carrying an 'anti-handle' strand) can be easily placed on DNA origami structures by hybridization to their complementary staple strand extensions (handle strands).

In one of the first applications for DNA origami as sensory entities, Ke *et al.* employed the unique addressability of rectangular sheets for multiplexed, label-free detection of RNA by using atomic force microscopy to study position-dependent hybridization to handle strands on the structure [15] (Figure 1b). In a different application, Fu *et al.* assayed and enhanced enzymatic activity in protein cascades by placing enzymes in close proximity on DNA origami structures [16] (Figure 1c). Shaw and co-workers used DNA origami to unravel distance-dependent effects in receptor–ligand interactions on cell membranes. The

authors used ephrin-A5 ligands attached to DNA nanostructures with different distances and applied them to breast cancer cell lines [17]. They could show that the activation of EphA2 receptors was enhanced when ligands were spaced 40 nm apart in comparison to a spacing of 100 nm. Recently, Douglas *et al.* reported on one of the first 'active' DNA origami-based devices [18]. These structures were able to undergo a conformational change upon detection of a cellular input signal: Two aptamer locks 'opened' upon recognition of tumor antigens on the cell surface and activated the 'device'. Molecular payload placed in the interior of the structure could then interact with cell surface receptors and induce programmed cell death (Figure 1d). Recently, this device was applied *in vivo* in a cockroach model, where a population of these structures performed logical operations [19].

DNA nanostructures were also used to study molecular motor protein assemblies. In 2012, Derr *et al.* analyzed the behavior of these motors walking in different directions on microtubule filaments. Coupled to the same cargo, a

Figure 1



DNA origami as molecular breadboards. **(a)** Synthetic DNA nanostructures can be used to position different molecular species, such as fluorophores (red), gold particles (yellow) or proteins (green) with nanometer precision. Top left: Staple and scaffold strand routing details. Bottom left: Staple strands can be extended with a specific sequence (handle strands). DNA-conjugated proteins can be attached to the structure via complementary sequences (anti-handle strands). **(b)** Staple strands can be extended to detect RNA via hybridization. Molecular binding events are visualized using atomic force microscopy. Adapted from [15]. Reprinted with permission from AAAS. **(c)** Nanoscale artificial assembly lines can be constructed to study enzyme cascades. Horseradish peroxidase (HRP) as well as glucose oxidase (GOx) are positioned on a DNA origami. A bridging molecule mediates transfer of intermediate products. Reprinted with permission from [16]. Copyright (2012) American Chemical Society. **(d)** Decision making DNA 'devices' can be constructed using DNA origami. Two aptamer locks open upon recognition of target molecules, that is on cancer cells. The inside of the device can be functionalized with proteins to specifically trigger cell death. From [18]. Reprinted with permission from AAAS. **(e)** Dynein motors are attached to a 12 helix-bundle chassis nanostructure via DNA handles. From [20], reprinted with permission from AAAS. **(f)** DNA 'nanomotors' can walk over a synthetic track on DNA origami structures. Adding fuel and anti-fuel strands powers the DNA walker and leads to binding and unbinding from the structure by strand displacement reactions. 'Walking' is visualized using single-molecule Förster Resonance Energy Transfer (FRET). Reprinted with permission from [21]. Copyright 2013 American Chemical Society.

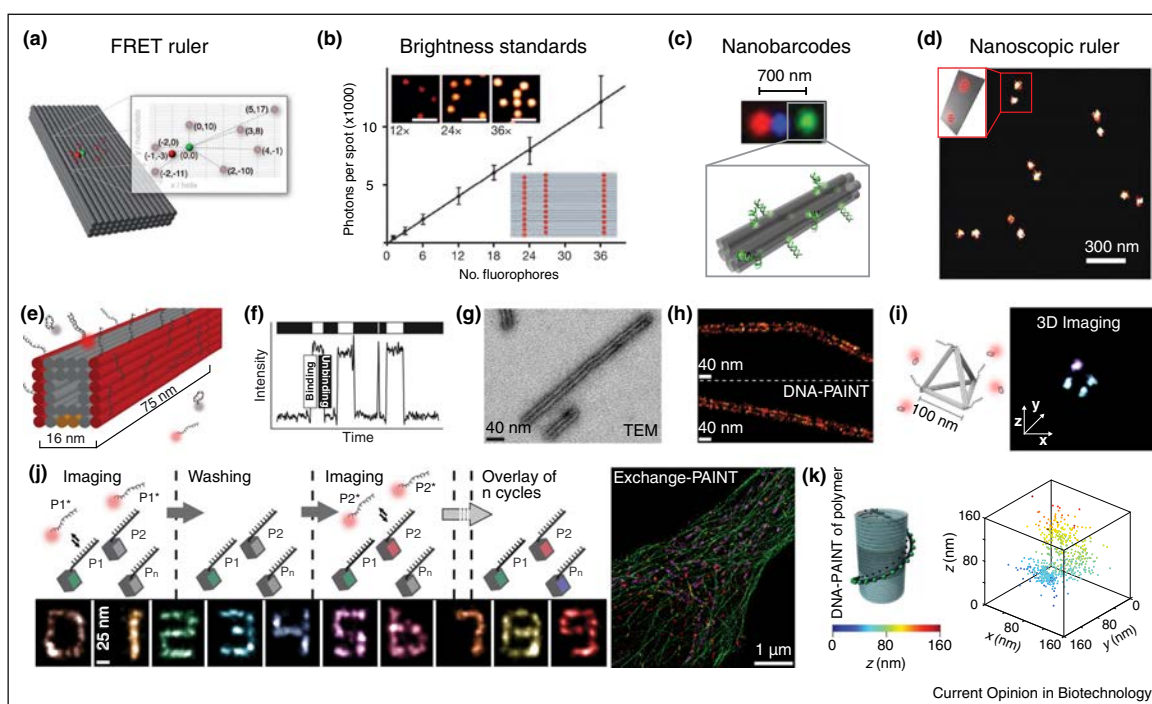
synthetic 12 helix-bundle DNA nanostructure, kinesin-1 and dynein engaged in a tug-of-war. By specifically disengaging one motor species using photocleavable linkers, this tug-of-war could be resolved [20\*] (Figure 1e). Similarly, DNA nanostructures can also be used as molecular tracks for synthetic walkers. In 2013, Tomov *et al.* used toehold-mediated strand displacement cascades and single-molecule fluorescence techniques to design and characterize DNA-based walkers along origami tracks [21] (Figure 1f).

### Fluorescence and super-resolution applications

Using the addressability of DNA nanostructures, it is also possible to arrange fluorescent molecules at defined

positions and distances, thus providing a unique tool to study a multitude of properties of single and multiple fluorophores in defined geometries. Stein *et al.* used DNA origami to investigate Förster resonance energy transfer (FRET) between donor and acceptor dyes placed at specific distances on DNA origami [22] (Figure 2a). By comparing their results to single dsDNA molecules (traditionally used in FRET studies), they found that the FRET data obtained on the DNA origami structures directly yielded the theoretical distance dependence of the energy transfer. The authors contributed this to the fact that the influence of fluorophore-linker distances is significantly reduced in the more rigid and geometrically defined DNA origami structures. Schmied *et al.* used DNA origami to position defined numbers of fluorophores

Figure 2



Fluorescence and super-resolution applications. **(a)** Single-molecule FRET ruler based on rigid DNA origami blocks. Green dots indicate donor, red dots acceptor positions. FRET distance dependency can be studied with high precision. Reprinted by permission from Wiley [22], copyright 2011. **(b)** Fluorescence brightness standards constructed from DNA origami. Bottom right inset: DNA origami with 36 dye molecules. Top insets: fluorescence images of 12x, 24x, 36x ATTO647N dyes attached to origami. Intensity increased linearly with the number of dyes. Reprinted by permission from Macmillan Publishers Ltd: Nature Methods [23], copyright 2012. **(c)** Geometrically encoded DNA nanobarcodes constructed from DNA origami. By dimerizing two six-helix bundle structures (each consisting of 28 segments of 42 bp) a structure with a total length of ~700 nm is constructed, allowing for diffraction-limited readout of fluorescent zones. Top: three-color fluorescence micrograph of DNA nanobarcode. Bottom: detailed view of structure and dye attachment of one fluorescently labeled zone (green). Reprinted by permission from Macmillan Publishers Ltd: Nature Chemistry [24], copyright 2012. **(d)** Calibration structures for super-resolution microscopy: Dyes can be placed at designed distances using DNA origami structures. Reprinted by permission from Macmillan Publishers Ltd: Nature Protocols [28\*], copyright 2014. **(e)** DNA-PAINT super-resolution microscopy: DNA nanostructure 'labeled' with single-stranded 'docking' strands on two faces (red, 16 nm distance). **(f)** Transient binding of 'imager' strands creates 'blinking' and allows super-resolution imaging. **(g)** Transmission Electron Micrograph (TEM) of DNA structure. **(h)** Optical DNA-PAINT super-resolution image reveals two lines spaced ~16 nm apart. **(i)** 3D DNA-PAINT image of a DNA tetrahedron. **(j)** Exchange-PAINT allows sequential multiplexing with a single color dye on origami structures (digits 0-9) and inside a cell. **(k)** 3D DNA-PAINT super-resolution imaging of a conducting polymer immobilized on a 3D DNA nanostructure in a helical shape. Reprinted by permission from Macmillan Publishers Ltd: Nature Nanotechnology [34], copyright 2015.

at distances as small as  $\sim 5$  nm from each other [23] (Figure 2b). Placing up to 36 fluorophores per DNA origami interestingly resulted in a linear dependency of fluorescence intensity versus number of fluorophores. This underlines the unique capability of DNA nanostructures to precisely define molecular spacing, making them ideal ‘standards’ for fluorescence intensity calibration [23].

While exact spatial control not only allows the placement of fluorophores at defined positions and to study their interactions, it does also create the possibility to use fluorescently-labeled DNA origami structures as unique identifiers — or barcodes — based on their programmable fluorescent properties. In 2012, Lin *et al.* developed geometric barcodes by arranging spectrally distinct fluorophores in defined spots spaced beyond the optical diffraction limit on six-helix-bundle DNA origami [24] (Figure 2c). This allowed them to create 216 unique barcoded DNA origami using three spots and up to two spectrally distinct colors per spot. These barcoded structures could, for example be used for multiplexed *in vitro* quantification of RNA molecules from cell lysates [25].

Beyond their use as brightness standards, origami’s ability to place fluorescent molecules at precise distances below the optical diffraction limit renders them ideal as molecular rulers for emerging super-resolution techniques. In 2009, Steinhauer *et al.* reported on the creation of the first super-resolution rulers based on DNA origami [26\*\*] (Figure 2d). In their study, they found that the inaccuracy of the measured distance could be almost completely attributed to the localization precision of their employed super-resolution technique, thus indicating that DNA origami are robust and reproducible ‘nanoscopic rulers’ for super-resolution microscopes. The same group also used three-dimensional DNA origami structures as rulers for 3D super-resolution techniques [27]. Detailed experimental protocols for the preparation of DNA structures in fluorescence microscopy are also available [28\*].

As discussed in the paragraphs above, DNA nanostructures possess unique features that make them ideally suited for fluorescence studies and calibration standards. However, dynamic DNA nanotechnology was used to enable a novel super-resolution technique, based on points accumulation imaging in nanoscale topography (PAINT). In 2010, Jungmann *et al.* developed DNA-PAINT, which uses the molecular recognition capability and programmability of DNA molecules (Figure 2e) to create the necessary blinking for stochastic super-resolution microscopy. In DNA-PAINT, stochastic switching between fluorescence on-states and off-states is facilitated by repetitive, transient binding of short fluorescently labeled oligonucleotides (‘imager’ strands) to complementary ‘docking’ strands. Upon binding of an imager strand, its fluorescence emission is detected and subsequently localized for super-resolution

reconstruction. DNA-PAINT is able to overcome some of the limitations of current super-resolution approaches such as photo-activated localization microscopy (PALM) [29] or stochastic optical reconstruction microscopy (STORM) [30], by allowing researchers to decouple the blinking of fluorophores from their complex photophysical properties using programmable DNA-based imaging probes. DNA-PAINT can also be used for 3D super-resolution imaging of 3D DNA origami structures (Figure 2f). Additionally, as the imager strands only transiently bind to the docking strand, orthogonal imager strands can be sequentially applied to the same biological sample. In this technique, called Exchange-PAINT, a single fluorophore and a single laser source is used to achieve 10-color super-resolution imaging of DNA origami targets and a 4-color image of cellular proteins in fixed cells (Figure 2g). In addition to imaging, Johnson-Buck and co-workers used DNA-PAINT to analyze binding and dissociation kinetics of imager strands to docking strands on DNA origami structures. Their studies elucidated apparent differences in association and dissociation kinetics dependent on the length of docking strands, their positions and spacing on the DNA nanostructures [31,32]. Additionally, using the predictable binding kinetics of transient nucleic acid hybridization, Johnson-Buck *et al.* were able to ‘count’ miRNA molecules from solution and distinguish between single nucleotide polymorphisms with high accuracy [33].

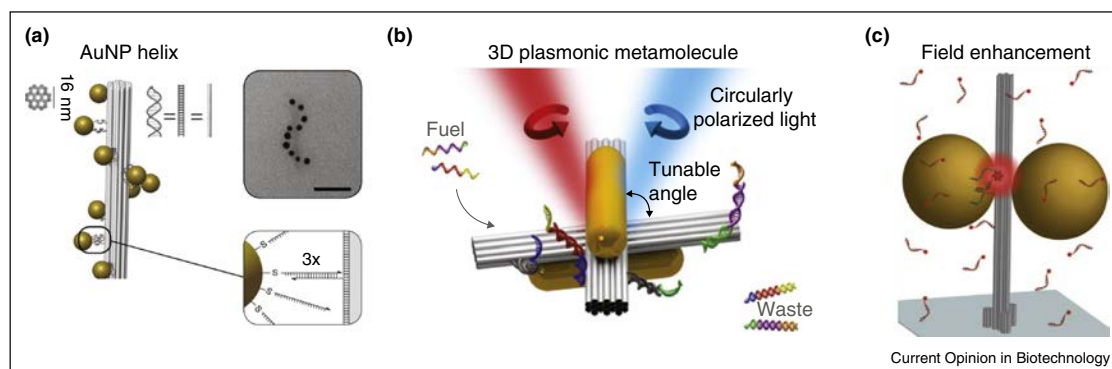
Combining DNA nanostructures to arrange molecules in three dimensions and DNA-based super-resolution imaging, Knudsen *et al.* used a novel DNA barrel structure to route a conducting polymer in a ‘nano-helical’ shape [34]. The polymer was modified with anti-handle sequences to attach to handle sequences on the barrel. Subsequently, 3D DNA-PAINT imaging was used to confirm the correct routing of the polymer in its designated 3D helical shape (Figure 2h).

### Plasmonic applications

Besides placing fluorescent molecules, DNA origami can also be used to arrange inorganic nanoparticles to study plasmonic effects. Plasmonic interactions strongly depend on the spatial arrangement, stoichiometry, distance, and orientation of nanoparticles with respect to each other. Recent studies demonstrated the ability to place a multitude of inorganic molecules such as gold nanoparticles [35], silver nanoparticles [36], quantum dots [37], and fluorescent nanodiamonds [38] on DNA origami structures.

In 2012, Kuzyk *et al.* arranged gold particles with a defined size into a prescribed nano-helical shape using 24 helix-bundle DNA origami (Figure 3a). The authors found, that inline with their theoretical predictions, the structures exhibited a defined circular dichroism (CD) emerging from nanoparticle plasmon–plasmon interactions. DNA origami structures allowed them to precisely design and

Figure 3



Plasmonic applications. **(a)** DNA origami bundle composed of 24 parallel double helices. Gold nanoparticles are arranged in a 'secondary' left-handed helix on the DNA origami structure. Zoom in: 10 nm gold nanoparticle functionalized with thiolated ssDNA hybridized to the DNA origami 24HB. Upper right: TEM image of a gold-labeled DNA nanohelix. Scale bar: 50 nm. Reprinted by permission from Macmillan Publishers Ltd: Nature [39\*\*], copyright 2012. **(b)** Reconfigurable 3D plasmonic metamolecule: two gold nanorods (AuNRs) are attached to a 'switchable' DNA origami structure consisting of two connected bundles with a tunable angle in-between. The relative angle between the AuNRs and therefore the handedness of the 3D chiral nanostructure can be actively controlled by two DNA locks, which are extended from the sides of the DNA origami template. Reprinted by permission from Macmillan Publishers Ltd: Nature Materials [41], copyright 2014. **(c)** DNA origami nanopillar with two Au NPs forming a dimer. Using transient DNA hybridization as in DNA-PAINT, dye-labeled strands (red sphere) are temporarily immobilized between the NPs within the central bundle of the pillar, and thus placed in a plasmonic hotspot, leading to a ~117-fold increase in fluorescence emission. From [43\*\*]. Reprinted with permission from AAAS.

tune the plasmonic properties of the assemblies, such as their handedness. Experimentally, after excitation with electromagnetic radiation, a plasmonic response was observed by measuring the CD absorption spectra of the nanoscale gold assembly in the visible range [39\*\*,40]. Furthermore, the authors demonstrated that DNA origami gold nanoparticle arrangements can also be reconfigured by either a toehold-mediated strand displacement reaction [41] (Figure 3b) or by attaching them to a glass substrate and switching the orientation by a change in the surrounding environment from PBS buffer solution (structures perpendicular to the glass surface) to a 'dry' environment (structures parallel to the glass) [42].

In 2012, Acuna *et al.* used DNA origami structures to create fluorescent field enhancement at plasmonic hotspots. In their study, they placed a pair of 100 nm gold nanoparticles 23 nm apart. A DNA origami structure placed 'upright' on a glass surface allowed them to achieve the precise placement of the nanoparticles away from the surface at a designed height (Figure 3c). Using transient hybridization of fluorescently-labeled strands to their targets (as in DNA-PAINT) within this reaction volume showed that the fluorescence of a dye molecule can be enhanced 117-fold at the plasmonic hotspot [43\*\*]. In a study by Kuhler *et al.* plasmonic hotspots were used for signal enhancement in Raman spectroscopy [44].

### Summary and outlook

In summary, structural DNA nanotechnology provides a unique way to position molecules in a programmable and

self-assembled fashion on the nanoscale. Very recently, Funke *et al.* [45] increased the positioning accuracy of DNA origami from ~5 nm down to ~0.04 nm. In the future, this might allow researcher to, for example engineer rationally designed catalytic functionalities into DNA nanostructures similar to enzymes. Extending the toolkit of barcoded, fluorescent DNA origami structures, one could envision the creation of barcodes based on fluorescence intensities in addition to geometrically encoded structures. In combination with recently developed compact DNA cubes [46], these barcodes could see applications as multiplexed labeling probes for the detection of dynamic processes such as membrane-bound molecules on cell surfaces. Furthermore, ultra-compact DNA-based barcodes could enable the identification of, for example, a multitude of RNA molecules *in situ* in single cells.

Combining recently developed fast and sensitive light sheet microscopes [47] with novel cargo-carrying fluorescently-barcoded DNA structures, it will be possible to study their cellular uptake mechanisms with high spatial and temporal resolution, thus paving the way to engineer smarter DNA nanostructure-based drugs. So far different delivery devices made of DNA were reported which for example stimulated the immune system by CpG oligonucleotide presentation [48,49].

Finally, DNA nanostructures as plasmonic hotspots are promising tools to characterize a multitude of biomolecular reactions. The local field enhancement provides an

ideal environment to study these reactions in physiologically relevant concentration regimes [50].

## Acknowledgements

TS acknowledges support from the DFG through the Graduate School of Quantitative Biosciences Munich (QBM). MTS acknowledges support from the International Max Planck Research School for Molecular and Cellular Life Sciences (IMPRS-LS). FS acknowledges support from the DFG through the SFB 1032 (Nanoagents for the spatiotemporal control of molecular and cellular reactions). All authors acknowledge supports from the DFG through an Emmy Noether Fellowship to RJ (DFG JU 2957/1-1) and the Max Planck Society.

## References and recommended reading

Papers of particular interest, published within the period of review, have been highlighted as:

- of special interest
  - of outstanding interest
1. Seeman NC: **Nucleic acid junctions and lattices.** *J Theor Biol* 1982, **99**:237-247.
  2. Chen JH, Seeman NC: **Synthesis from DNA of a molecule with the connectivity of a cube.** *Nature* 1991, **350**:631-633.
  3. Winfree E, Liu F, Wenzler LA, Seeman NC: **Design and self-assembly of two-dimensional DNA crystals.** *Nature* 1998, **394**:539-544.
  4. Shih WM, Quispe JD, Joyce GF: **A 1.7-kilobase single-stranded DNA that folds into a nanoscale octahedron.** *Nature* 2004, **427**:618-621.
  5. Rothemund PW: **Folding DNA to create nanoscale shapes and patterns.** *Nature* 2006, **440**:297-302.
  - Introduction of the DNA origami technique for creating self-assembled DNA nanostructures with thus far unprecedented yield and complexity.
  6. Douglas SM, Marblestone AH, Teerapittayanon S, Vazquez A, Church GM, Shih WM: **Rapid prototyping of 3D DNA-origami shapes with caDNAo.** *Nucleic Acids Res* 2009, **37**:5001-5006.
  - Freely available computer-aided design tool to facilitate the design of DNA origami structures.
  7. Ke Y, Voigt NV, Gothelf KV, Shih WM: **Multilayer DNA origami packed on hexagonal and hybrid lattices.** *J Am Chem Soc* 2012, **134**:1770-1774.
  8. Ke Y, Douglas SM, Liu M, Sharma J, Cheng A, Leung A, Liu Y, Shih WM, Yan H: **Multilayer DNA origami packed on a square lattice.** *J Am Chem Soc* 2009, **131**:15903-15908.
  9. Dietz H, Douglas SM, Shih WM: **Folding DNA into twisted and curved nanoscale shapes.** *Science* 2009, **325**:725-730.
  10. Han D, Pal S, Nangreave J, Deng Z, Liu Y, Yan H: **DNA origami with complex curvatures in three-dimensional space.** *Science* 2011, **332**:342-346.
  11. Liedl T, Hogberg B, Tytell J, Ingber DE, Shih WM: **Self-assembly of three-dimensional prestressed tensegrity structures from DNA.** *Nat Nanotechnol* 2010, **5**:520-524.
  12. Wei B, Dai M, Yin P: **Complex shapes self-assembled from single-stranded DNA tiles.** *Nature* 2012, **485**:623-626.
  13. Benson E, Mohammed A, Gardell J, Masich S, Czeizler E, Orponen P, Hogberg B: **DNA rendering of polyhedral meshes at the nanoscale.** *Nature* 2015, **523**:441-444.
  14. Kim DN, Kilchherr F, Dietz H, Bathe M: **Quantitative prediction of 3D solution shape and flexibility of nucleic acid nanostructures.** *Nucleic Acids Res* 2012, **40**:2862-2868.
  15. Ke Y, Lindsay S, Chang Y, Liu Y, Yan H: **Self-assembled water-soluble nucleic acid probe tiles for label-free RNA hybridization assays.** *Science* 2008, **319**:180-183.
  16. Fu J, Liu M, Liu Y, Woodbury NW, Yan H: **Interenzyme substrate diffusion for an enzyme cascade organized on spatially addressable DNA nanostructures.** *J Am Chem Soc* 2012, **134**:5516-5519.
  17. Shaw A, Lundin V, Petrova E, Fordos F, Benson E, Al-Amin A, Herland A, Blokzijl A, Hogberg B, Teixeira AI: **Spatial control of membrane receptor function using ligand nanocalipers.** *Nat Methods* 2014, **11**:841-846.
  - First demonstration of distance-dependent stimulation of membrane receptors in a controllable fashion using DNA origami 'nanocalipers' functionalized with ligands.
  18. Douglas SM, Bachelet I, Church GM: **A logic-gated nanorobot for targeted transport of molecular payloads.** *Science* 2012, **335**:831-834.
  - Demonstration of the first autonomous DNA nanodevice able to deliver molecular cargo in a programmed fashion in a live cell environment.
  19. Amir Y, Ben-Ishay E, Levner D, Ittah S, Abu-Horowitz A, Bachelet I: **Universal computing by DNA origami robots in a living animal.** *Nat Nanotechnol* 2014, **9**:353-357.
  20. Derr ND, Goodman BS, Jungmann R, Leschziner AE, Shih WM, Reck-Peterson SL: **Tug-of-war in motor protein ensembles revealed with a programmable DNA origami scaffold.** *Science* 2012, **338**:662-665.
  - First demonstration of using DNA origami's unique programmability to enable biophysical studies of motor protein complexes in a very defined setting.
  21. Tomov TE, Tsukanov R, Liber M, Masoud R, Plavner N, Nir E: **Rational design of DNA motors: fuel optimization through single-molecule fluorescence.** *J Am Chem Soc* 2013, **135**:11935-11941.
  22. Stein IH, Schuller V, Bohm P, Tinnefeld P, Liedl T: **Single-molecule FRET ruler based on rigid DNA origami blocks.** *Chemphyschem* 2011, **12**:689-695.
  23. Schmied JJ, Gietl A, Holzmeister P, Forthmann C, Steinhauer C, Dammeyer T, Tinnefeld P: **Fluorescence and super-resolution standards based on DNA origami.** *Nat Methods* 2012, **9**:1133-1134.
  24. Lin C, Jungmann R, Leifer AM, Li C, Levner D, Church GM, Shih WM, Yin P: **Submicrometre geometrically encoded fluorescent barcodes self-assembled from DNA.** *Nat Chem* 2012, **4**:832-839.
  25. Geiss GK, Bumgarner RE, Birditt B, Dahl T, Dowidar N, Dunaway DL, Fell HP, Ferree S, George RD, Grogan T et al.: **Direct multiplexed measurement of gene expression with color-coded probe pairs.** *Nat Biotechnol* 2008, **26**:317-325.
  26. Steinhauer C, Jungmann R, Sobey TL, Simmel FC, Tinnefeld P: **DNA origami as a nanoscopic ruler for super-resolution microscopy.** *Angew Chem Int Ed Engl* 2009, **48**:8870-8873.
  - First combination of DNA origami structures with single-molecule fluorescence readout techniques. Creation of the first 'ruler' made of DNA origami.
  27. Schmied JJ, Forthmann C, Pibiri E, Lalkens B, Nickels P, Liedl T, Tinnefeld P: **DNA origami nanopillars as standards for three-dimensional superresolution microscopy.** *Nano Lett* 2013, **13**:781-785.
  28. Schmied JJ, Raab M, Forthmann C, Pibiri E, Wunsch B, Dammeyer T, Tinnefeld P: **DNA origami-based standards for quantitative fluorescence microscopy.** *Nat Protoc* 2014, **9**:1367-1391.
  - Comprehensive toolkit describing the design and assembly of fluorescently-labeled DNA origami structures for calibration purposes.
  29. Betzig E, Patterson GH, Sougrat R, Lindwasser OW, Olenych S, Bonifacino JS, Davidson MW, Lippincott-Schwartz J, Hess HF: **Imaging intracellular fluorescent proteins at nanometer resolution.** *Science* 2006, **313**:1642-1645.
  30. Rust MJ, Bates M, Zhuang X: **Sub-diffraction-limit imaging by stochastic optical reconstruction microscopy (STORM).** *Nat Methods* 2006, **3**:793-795.
  31. Johnson-Buck A, Nangreave J, Jiang S, Yan H, Walter NG: **Multifactorial modulation of binding and dissociation kinetics on two-dimensional DNA nanostructures.** *Nano Lett* 2013, **13**:2754-2759.

32. Johnson-Buck A, Nangreave J, Kim DN, Bathe M, Yan H, Walter NG: **Super-resolution fingerprinting detects chemical reactions and idiosyncrasies of single DNA pegboards.** *Nano Lett* 2013, **13**:728-733.
33. Johnson-Buck A, Su X, Giraldez MD, Zhao M, Tewari M, Walter NG: **Kinetic fingerprinting to identify and count single nucleic acids.** *Nat Biotechnol* 2015, **33**:730-732.
34. Knudsen JB, Liu L, Bank Kodal AL, Madsen M, Li Q, Song J, Woehrstein JB, Wickham SF, Strauss MT, Schueder F *et al.*: **Routing of individual polymers in designed patterns.** *Nat Nanotechnol* 2015, **10**:892-898.
35. Aldaye FA, Sleiman HF: **Dynamic DNA templates for discrete gold nanoparticle assemblies: control of geometry, modularity, write/erase and structural switching.** *J Am Chem Soc* 2007, **129**:4130-4131.
36. Pal S, Deng Z, Ding B, Yan H, Liu Y: **DNA-origami-directed self-assembly of discrete silver-nanoparticle architectures.** *Angew Chem Int Ed Engl* 2010, **49**:2700-2704.
37. Sharma J, Ke Y, Lin C, Chhabra R, Wang Q, Nangreave J, Liu Y, Yan H: **DNA-tile-directed self-assembly of quantum dots into two-dimensional nanopatterns.** *Angew Chem Int Ed Engl* 2008, **47**:5157-5159.
38. Zhang T, Neumann A, Lindlau J, Wu Y, Pramanik G, Naydenov B, Jelezko F, Schuder F, Huber S, Huber M *et al.*: **DNA-based self-assembly of fluorescent nanodiamonds.** *J Am Chem Soc* 2015, **137**:9776-9779.
39. Kuzyk A, Schreiber R, Fan Z, Pardatscher G, Roller EM, Hogele A, Simmel FC, Govorov AO, Liedl T: **DNA-based self-assembly of chiral plasmonic nanostructures with tailored optical response.** *Nature* 2012, **483**:311-314.  
First demonstration of using DNA origami structures to precisely design and tune plasmonic properties.
40. Shen X, Song C, Wang J, Shi D, Wang Z, Liu N, Ding B: **Rolling up gold nanoparticle-dressed DNA origami into three-dimensional plasmonic chiral nanostructures.** *J Am Chem Soc* 2012, **134**:146-149.
41. Kuzyk A, Schreiber R, Zhang H, Govorov AO, Liedl T, Liu N: **Reconfigurable 3D plasmonic metamolecules.** *Nat Mater* 2014, **13**:862-866.
42. Schreiber R, Luong N, Fan Z, Kuzyk A, Nickels PC, Zhang T, Smith DM, Yurke B, Kuang W, Govorov AO *et al.*: **Chiral plasmonic DNA nanostructures with switchable circular dichroism.** *Nat Commun* 2013, **4**:2948.
43. Acuna GP, Moller FM, Holzmeister P, Beater S, Lalkens B, Tinnefeld P: **Fluorescence enhancement at docking sites of DNA-directed self-assembled nanoantennas.** *Science* 2012, **338**:506-510.  
First comprehensive characterization study demonstrating fluorescence enhancement in plasmonic hotspots created by placing gold particles in prescribed distances from each other and away from a surface.
44. Kuhler P, Roller EM, Schreiber R, Liedl T, Lohmuller T, Feldmann J: **Plasmonic DNA-origami nanoantennas for surface-enhanced Raman spectroscopy.** *Nano Lett* 2014, **14**:2914-2919.
45. Funke JJ, Dietz H: **Placing molecules with Bohr radius resolution using DNA origami.** *Nat Nanotechnol* 2015.
46. Scheible MB, Ong LL, Woehrstein JB, Jungmann R, Yin P, Simmel FC: **A compact DNA cube with side length 10 nm.** *Small* 2015, **11**:5200-5210.
47. Chen BC, Legant WR, Wang K, Shao L, Milkie DE, Davidson MW, Janetopoulos C, Wu XS, Hammer JA III, Liu Z *et al.*: **Lattice light-sheet microscopy: imaging molecules to embryos at high spatiotemporal resolution.** *Science* 2014, **346**:1257-998.
48. Schuller VJ, Heidegger S, Sandholzer N, Nickels PC, Suhartha NA, Endres S, Bourquin C, Liedl T: **Cellular immunostimulation by CpG-sequence-coated DNA origami structures.** *ACS Nano* 2011, **5**:9696-9702.
49. Liu X, Xu Y, Yu T, Clifford C, Liu Y, Yan H, Chang Y: **A DNA nanostructure platform for directed assembly of synthetic vaccines.** *Nano Lett* 2012, **12**:4254-4259.
50. Puchkova A, Vietz C, Pibiri E, Wuensch B, Sanz Paz M, Acuna GP, Tinnefeld P: **DNA origami nanoantennas with over 5000-fold fluorescence enhancement and single-molecule detection at 25  $\mu$ M.** *Nano Lett* 2015.

# Super-Resolution Microscopy with DNA-PAINT

**J. Schnitzbauer\***, **M.T. Strauss\***, T. Schlichthaerle, F. Schueder, R. Jungmann

published in

*Nature Protocols (2017)*

Reprinted with permission from [48]  
Copyright 2017, Springer Nature

## PROTOCOL

# Super-resolution microscopy with DNA-PAINT

Joerg Schnitzbauer<sup>1–3</sup>, Maximilian T Strauss<sup>1–3</sup>, Thomas Schlichthaerle<sup>1,2</sup>, Florian Schueder<sup>1,2</sup> & Ralf Jungmann<sup>1,2</sup>

<sup>1</sup>Department of Physics and Center for Nanoscience, Ludwig Maximilian University, Munich, Germany. <sup>2</sup>Max Planck Institute of Biochemistry, Martinsried, Germany.

<sup>3</sup>These authors contributed equally to this work. Correspondence should be addressed to R.J. (jungmann@biochem.mpg.de).

Published online 18 May 2017; doi:10.1038/nprot.2017.024

Super-resolution techniques have begun to transform biological and biomedical research by allowing researchers to observe structures well below the classic diffraction limit of light. DNA points accumulation for imaging in nanoscale topography (DNA-PAINT) offers an easy-to-implement approach to localization-based super-resolution microscopy, owing to the use of DNA probes. In DNA-PAINT, transient binding of short dye-labeled ('imager') oligonucleotides to their complementary target ('docking') strands creates the necessary 'blinking' to enable stochastic super-resolution microscopy. Using the programmability and specificity of DNA molecules as imaging and labeling probes allows researchers to decouple blinking from dye photophysics, alleviating limitations of current super-resolution techniques, making them compatible with virtually any single-molecule-compatible dye. Recent developments in DNA-PAINT have enabled spectrally unlimited multiplexing, precise molecule counting and ultra-high, molecular-scale (sub-5-nm) spatial resolution, reaching ~1-nm localization precision. DNA-PAINT can be applied to a multitude of *in vitro* and cellular applications by linking docking strands to antibodies. Here, we present a protocol for the key aspects of the DNA-PAINT framework for both novice and expert users. This protocol describes the creation of DNA origami test samples, *in situ* sample preparation, multiplexed data acquisition, data simulation, super-resolution image reconstruction and post-processing such as drift correction, molecule counting (qPAINT) and particle averaging. Moreover, we provide an integrated software package, named Picasso, for the computational steps involved. The protocol is designed to be modular, so that individual components can be chosen and implemented per requirements of a specific application. The procedure can be completed in 1–2 d.

## INTRODUCTION

For biomedical research, super-resolution microscopy is a promising tool developed in recent years, allowing optical imaging beyond the diffraction limit of light, for up to molecular-scale resolution inside cells. The significance of this group of imaging modalities is underlined by the Nobel Prize in Chemistry in 2014 'for the development of super-resolved fluorescence microscopy'. Super-resolution has been achieved by a variety of imaging modalities, most notably nonlinear structured illumination microscopy (SIM)<sup>1</sup>, stimulated emission depletion (STED) microscopy<sup>2</sup>, (fluorescent) photo-activated localization microscopy ((f)PALM)<sup>3,4</sup> and (direct) stochastic optical reconstruction microscopy ((d)STORM)<sup>5,6</sup>. All these techniques achieve image resolution beyond the diffraction limit by controlling the state of fluorophores such that only a small subset of them are detectable at any given time. However, super-resolution approaches can be generally divided into the following two groups according to the specific mechanism for controlling the fluorophore state<sup>7</sup>: (i) illumination-pattern-based (SIM and STED) and (ii) single-molecule-localization-based (PALM and STORM) methods. All these super-resolution methods have been successfully used to reveal biological insights<sup>8–12</sup>, but each has its own advantages and difficulties. A practical advantage of both illumination-based methods is that they do not require specific fluorophores, which makes these techniques straightforward to use for biologists with conventional samples. However, instrumental implementations are typically more complex and intricate. By contrast, the branch of localization-based techniques uses stochastic blinking of specific fluorescent probes. This blinking permits them to be observed one at a time so that their spatial coordinates can be localized with subdiffraction precision<sup>13</sup>. Typically, this blinking is an intrinsic property of fluorescent proteins (PALM) or specific organic dyes (STORM), which can be provoked by specific excitation schemes and buffer conditions<sup>14,15</sup>. Although instrumentation is typically

simpler for localization-based as compared with illumination-based modalities, the complexity lies in achieving suitable blinking behavior of the dyes. Troubleshooting often means testing a number of parameters such as the choice of dye, labeling density, buffer conditions and excitation illumination, making the blinking a hard-to-control phenomenon. In fact, the choice of 'well-behaving' probes is limited, and further development of substantially improved probes is complex and time-consuming. Moreover, because of the limited choice of probes with appropriate blinking kinetics, photon rates and excitation conditions, multiplexing is still difficult to implement. Furthermore, the complex photophysics of the probes impedes the predictability of blinking events so that quantitative image interpretation is error-prone. Last, owing to limited photon rates and bleaching, optimal localization precision and spatial sampling are still not achieved—the two major factors in resolution<sup>16</sup>. Although many biological questions could be addressed with the aforementioned techniques<sup>8–12</sup>, researchers are still struggling with these complications to truly exploit the power of super-resolution microscopy.

A different route to single-molecule localization microscopy is PAINT<sup>17</sup>. Here, instead of labeling target molecules with fixed fluorophores, freely diffusing dyes<sup>17</sup> or dye-labeled ligands (as in uPAINT)<sup>18</sup> target molecules of interest by permanent or transient binding. PAINT is straightforward to implement and does not require special experimental conditions to obtain photoswitching, as long as probes are able to diffuse and reach their target molecules. However, PAINT's original implementation makes it difficult to specifically label a larger variety of biomolecules, as interactions are mainly limited to hydrophobic interactions or electrostatic coupling and are thus difficult to program.

DNA nanotechnology represents a promising tool for utilizing the advantages of the PAINT concept and establishing a programmable target–probe interaction system at the same time.

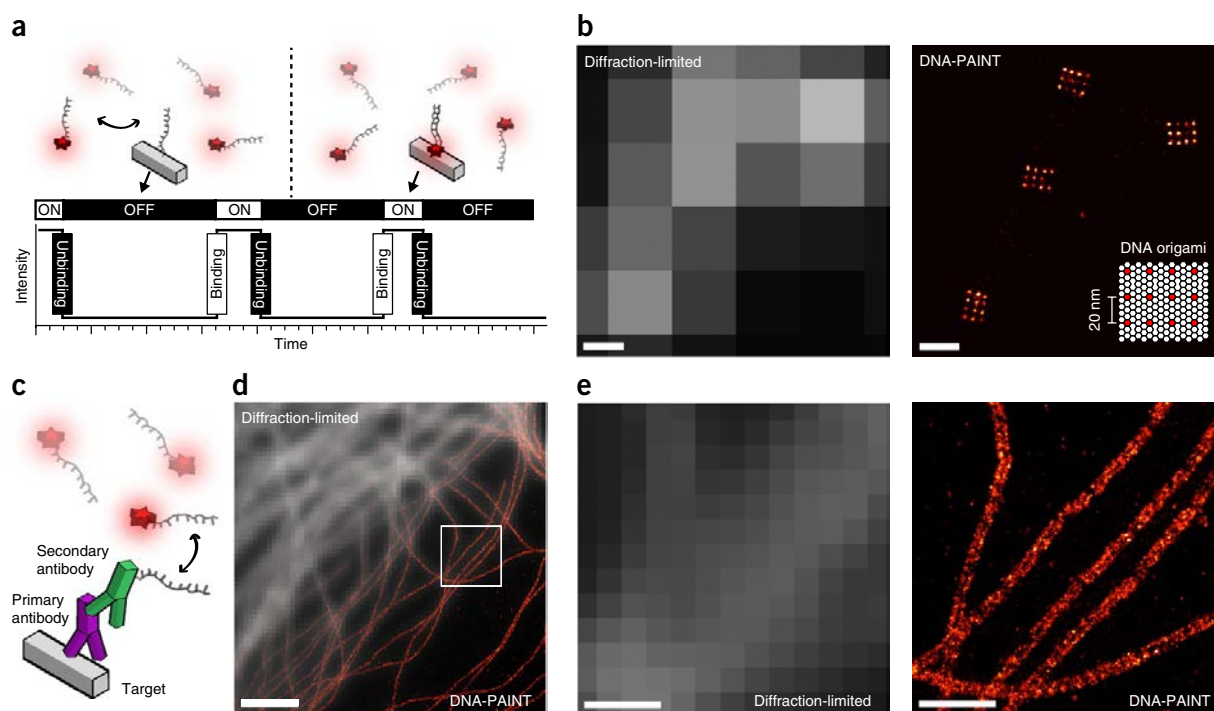


**Figure 1** | DNA-PAINT. (a) DNA-PAINT concept. Transient binding of dye-labeled DNA strands (imagers) to their complementary target sequence (docking site) attached to a molecule of interest. The transient binding of imager strands is detected as 'blinking', illustrated by the intensity versus time trace. (b) Diffraction-limited (left) and super-resolved DNA-PAINT images (right) of DNA origami nanostructures. Each structure consists of 12 docking strands that are arranged in a 20-nm grid (scheme in lower right corner). (c) *In situ* protein-labeling strategy for DNA-PAINT using primary and DNA-conjugated secondary antibodies. (d) Overlay of a diffraction-limited  $\alpha$ -tubulin image (top left) with a super-resolved DNA-PAINT image (bottom right). (e) Close-ups of the highlighted area in d, comparing diffraction-limited image (left) with DNA-PAINT super-resolved image (right). Scale bars, 100 nm (b), 2  $\mu$ m (d), 500 nm (e).

Specifically, DNA-based PAINT (DNA-PAINT) has been developed as a straightforward approach to overcome some limitations of current localization-based super-resolution techniques<sup>19–24</sup>. Similar to the original PAINT concept, DNA-PAINT decouples blinking from dye photophysics, but it also adds the programmability and specificity of using DNA molecules as imaging and labeling probes. A DNA-PAINT system, illustrated in **Figure 1a**, consists of the following two components: a docking strand and an imager strand. These are short, complementary single-stranded DNA oligomers, usually 8–10 nucleotides long. Although the docking strand is fixed to a biological target of interest (e.g., using standard immunolabeling approaches with DNA-conjugated antibodies targeting proteins of interest<sup>25</sup> or direct hybridization of docking strands to DNA or RNA molecules), the imager strand is conjugated to an organic dye and diffuses freely in the imaging buffer. Generally, imager strands appear undetectable in the camera because they diffuse over numerous camera pixels during the duration of a single frame. However, owing to their complementary sequence, imager strands can transiently bind to docking strands. During the bound state, imager strands are fixed at the same place for an extended amount of time, allowing the camera to accumulate enough photons from the dye to be detected. The binding duration depends solely on the stability of the formed DNA duplex, and can hence be programmed at will (e.g., by modulating strand length, GC content, temperature or salinity of the imaging buffer). On the other hand, the frequency of binding events is tunable by the influx rate of imager strands

(e.g., by modulating either the concentration of imager strands in the buffer or the association constant). As a result, the user has fine control over the blinking kinetics, which is independent of dye properties or illumination specifics. To date, DNA-PAINT has been used to resolve nanometer-scale structures of DNA origami (**Fig. 1b**), as well as those of cellular proteins, by conjugating docking strands to antibodies (**Fig. 1c–e**).

#### Advantages and limitations of the method

The properties of DNA-PAINT result in several improvements over more traditional super-resolution approaches. First, the use of DNA-based imaging probes enables high multiplexing by Exchange-PAINT<sup>20</sup> that is restricted only by the number of orthogonal DNA sequences, as compared with the spectrally distinct dyes used in classic multiplexing experiments. **Figure 2** illustrates the concept, procedure and results of Exchange-PAINT experiments *in vitro* and *in situ*. When tagging biological targets with orthogonal docking strand sequences, they can be probed sequentially by the respective complementary imager strands (**Fig. 2a**). Specifically, after one DNA-PAINT image has been acquired, the buffer can be exchanged to introduce a different imager strand species. Repeated imaging, washing and reintroduction of new imager strand species then allows researchers to create a multiplexed image of many biological targets. Although we have thus far demonstrated nine-target super-resolution imaging<sup>25</sup>, multiplexing could reach thousands of species, as the only limitation is the orthogonality of DNA-PAINT sequences.

## PROTOCOL

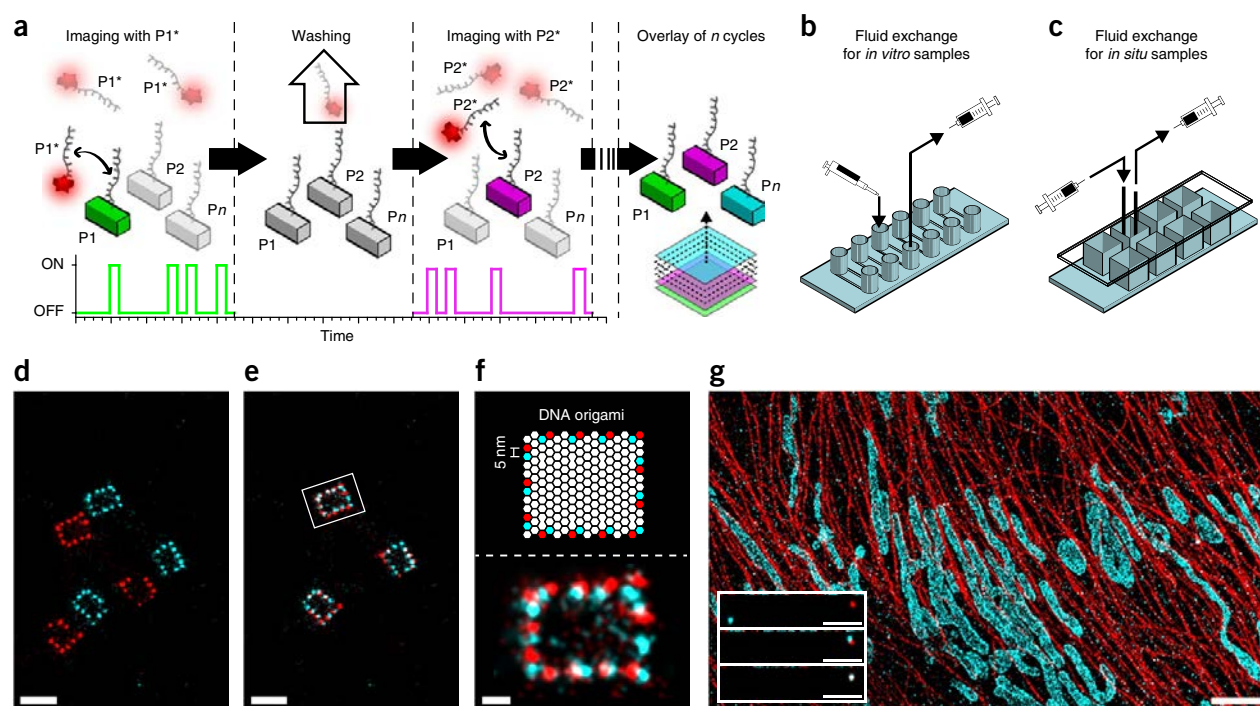


**Figure 2** | Exchange-PAINT. (a) Schematic representation of sequential Exchange-PAINT imaging of multiple targets with orthogonal sequences using the same fluorophore. Left to right: P1\* imager strands are in solution and interact with their complementary target sequence, P1. After the first acquisition round, the P1\* imager strands are washed away and P2\* imagers are introduced to image the next target. This is then repeated for the remaining target cycles, and pseudocolors are assigned for each respective imaging round. Last, all rounds are aligned and overlaid to form the final multiplexed Exchange-PAINT image of  $n$  targets. (b) Fluid exchange chamber for *in vitro* samples (e.g., for DNA origami imaging). Liquid is introduced by pipetting into the inlet. The outlet is attached to a syringe with a flexible tube to remove the liquid. (c) Fluid exchange chamber for *in situ* samples (i.e., used for *in situ* cellular imaging). Two tubes with syringes are connected to an 8-well chambered cover glass to facilitate fluid exchange. (d) Two rounds ('colors') Exchange-PAINT image of a frame-like DNA origami structure carrying two orthogonal docking strand species (red and cyan; see also f, for design schematics). (e) Pseudocolor image after alignment of the imaging rounds using Picasso's automated align function. (f) Top: DNA origami design. Bottom: Close-up (white box from e) of one frame-like structure. The distance between red and blue handles is  $\sim 5$  nm. (g) *In situ* Exchange-PAINT image of protein targets  $\alpha$ -tubulin (red) and Tom20 (cyan) with two primary and DNA-conjugated secondary antibody sandwiches. Inset: Images of one alignment marker (gold nanoparticle) in each Exchange-PAINT round without channel alignment (top), after Picasso's automated cross-correlation analysis (middle) and after manually selecting the particle as an alignment fiducial (bottom). Scale bars, 100 nm (d, e), 20 nm (f), 2  $\mu$ m (g), 300 nm (g, insets).

Second, the predictability and tunability of DNA binding and unbinding events, combined with effectively nonexistent bleaching, allow for accurate quantitative image interpretation (i.e., counting of single molecules in an integer manner), implemented in quantitative PAINT (qPAINT)<sup>22</sup>. **Figure 3** depicts the qPAINT concept, procedure and results. A more detailed description of the method will be given below.

Third, DNA-PAINT simplifies the selection of suitable dyes for imaging, as the parameter space is reduced from rather complex photophysical properties (e.g., switching behavior) to basically a single parameter—the photon budget. This also means that DNA-PAINT can use a large pool of existing fluorophores that were previously not applicable to localization-based super-resolution microscopy.

Finally, by programming the binding duration, an extremely high number of photons can be detected from a single binding (or blink) event, enabling optimal localization precision. The only limitations regarding the achievable photon budget are experimental time and photobleaching during a single binding event. However, the latter can be greatly reduced by specific imaging buffer compositions, such as oxygen-scavenging systems

and triplet-state quenchers<sup>26–28</sup>. Even if bleaching of individual dyes does occur, it has only a minimal detrimental effect overall, because of the practically infinite supply of replenishable 'fresh' imager strands from solution. All things considered, photobleaching—which is a considerable complication for all other super-resolution techniques—is eliminated as a restriction on achieving optimal sampling of the biological structure under investigation. Such optimized experimental conditions for high localization precision, combined with intricate drift correction methods, enable imaging at thus far unprecedented resolution in optical microscopy, for the first time enabling true molecular-scale resolution<sup>23</sup>, which, to our knowledge, has not been achieved using any other super-resolution method. Example results of images with localization precisions of  $\sim 1$  nm, yielding resolution better than 5 nm, and intermediate results of the applied drift correction are shown in **Figure 4**. To achieve these results, a large number of DNA origami structures were used as drift markers, considering first the whole structure, followed by the use of individual DNA-PAINT binding sites as fiducials. To eventually translate the *in vitro* ultra-resolution achievements to *in situ* samples such as fixed cells, a key challenge is the labeling

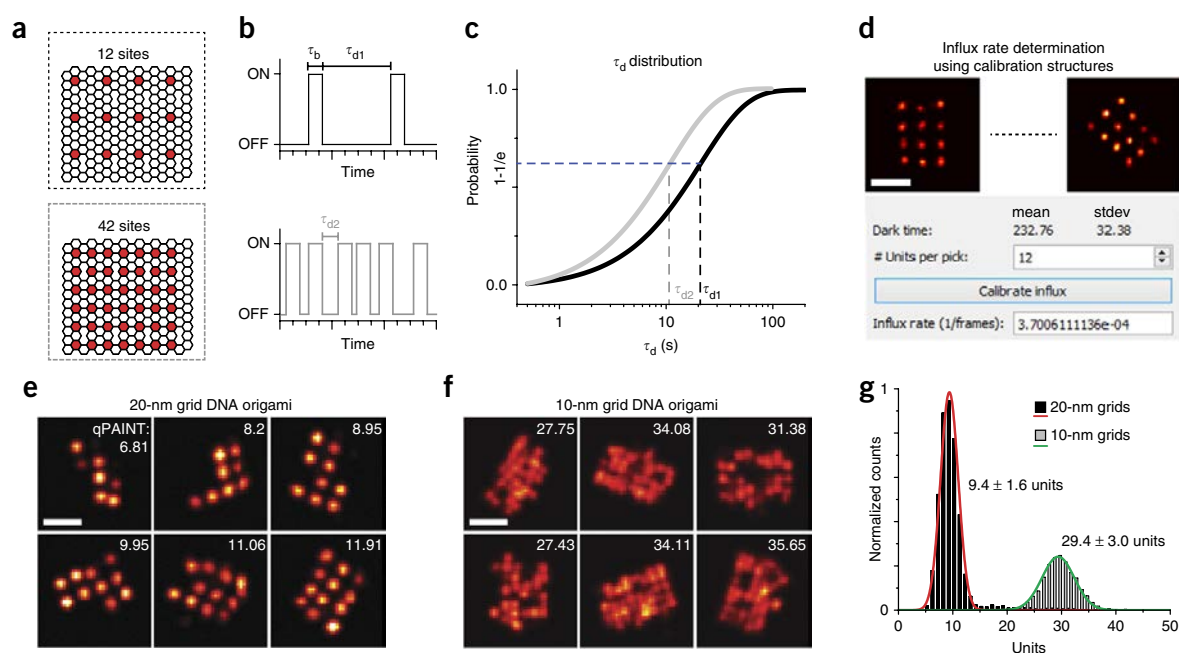


**Figure 3** | qPAINT. (a) Design schematics for two DNA origami structures with 12 target sites spaced 20 nm apart (top, black-dotted box) and 42 binding sites spaced 10 nm apart (bottom, gray-dotted box), respectively. (b) DNA origami structures with 12 binding sites (top) exhibit fewer binding (blinking) events as compared with structures with 42 binding sites (bottom), resulting in longer dark times ( $\tau_{d1}$ ) and shorter dark times ( $\tau_{d2}$ ) for the 20-nm grids and 10-nm grids, respectively. (c) Mean dark times  $\tau_{d1}$  and  $\tau_{d2}$  are obtained by fitting the cumulative distribution function of the dark times. (d) To measure binding sites for a structure of interest, DNA origami nanostructures are used to calibrate the influx rate (here displayed as the number of blinks per frame). Visual inspection of the DNA origami defines the units (or binding sites) per pick (here only origami displaying 12 binding sites are picked for calibration, top) and can be used to calculate the influx rate (Picasso software dialog, bottom). (e) Visual inspection of 20-nm-grid DNA origami structures in comparison with qPAINT-predicted binding sites after calibration shows good agreement. (f) Visual comparison of 10-nm-grid DNA origami with predicted binding sites via qPAINT. (g) Histogram distribution of binding sites for 20-nm-grid structure (black and red,  $n = 4,210$ ) in comparison with 10-nm-grid structure (gray and green,  $n = 1,818$ ). Scale bars, 50 nm.

probe size. The size of the labeling probes introduces a linkage error and effectively limits the labeling density (because of sterical hindrance). Both these effects finally limit the achievable resolution. One way to address these issues in cells could be the use of smaller labeling agents such as nanobodies<sup>29</sup> or aptamers<sup>30</sup>, rather than antibodies.

Although DNA-PAINT offers several advantages over traditional super-resolution techniques, as discussed above, we also note that there are currently limitations. One disadvantage is the fact that ‘imager’ strands are nonfluorogenic, with the following two implications: first, DNA-PAINT is limited to optical sectioning techniques such as total internal reflection (TIR), oblique<sup>31</sup> or light-sheet<sup>32</sup> illumination because of elevated background fluorescence originating from unbound imager strands. Second, the nonfluorogenic nature of imager strands furthermore sets an upper limit to the achievable image acquisition speed as compared with those of STED, PALM, STORM or SIM. Furthermore, DNA-PAINT applications are currently limited to fixed specimens. Live-cell imaging could be more difficult to achieve as compared with the aforementioned techniques, because of the complexity of infusing dye-labeled nucleic acid strands into living cells and the unforeseen consequences of introducing nucleic acids in general. However, we note that DNA-PAINT applications to molecules on cell surfaces such as membrane-bound receptors should be feasible even for living cells.

All in all, the DNA-PAINT imaging framework greatly reduces many technical difficulties of localization-based super-resolution microscopy and opens up possibilities for new technical development and biological applications. It will therefore allow many research groups to address their biological question with much greater efficiency. To ease the adoption of DNA-PAINT for novice and expert researchers in the super-resolution field, this protocol details the involved procedures and provides an integrated software package, named Picasso, which is specifically designed for DNA-PAINT applications. Except for data acquisition, Picasso can handle all computational efforts required in this protocol, including *in silico* data simulation, DNA origami design, and basic and advanced functionality for localization-based super-resolution microscopy.

#### Overview of the main procedures

The overarching goal of this protocol is to enable both novices and expert users to quickly obtain high-quality DNA-, Exchange-PAINT and qPAINT imaging data *in silico*, *in vitro* and *in situ*, without prior expertise in super-resolution microscopy. Here, we are using the term *in vitro* for DNA-PAINT studies with DNA origami structures on BSA/biotin/streptavidin-coated glass slides. By contrast, *in situ* is used to describe experiments involving fixed-cell samples. The protocol is based on several studies<sup>19,20,22,23,25</sup> and is arranged into four major sections, as illustrated in **Figure 5**: sample

## PROTOCOL

preparation (*in vitro* and *in situ*), data acquisition, image reconstruction and image post-processing. For sample preparation, we describe the following two procedures: *in vitro* imaging (i.e., of DNA origami nanostructures) (Steps 1–18; **Box 1**) and *in situ*

imaging (i.e., of cell samples) (Steps 19–33). Although not covered in this protocol, the procedures could be adjusted for DNA-PAINT imaging in tissue or whole organisms. Subsequently, we explain data acquisition (Steps 34–49), including a detailed procedure

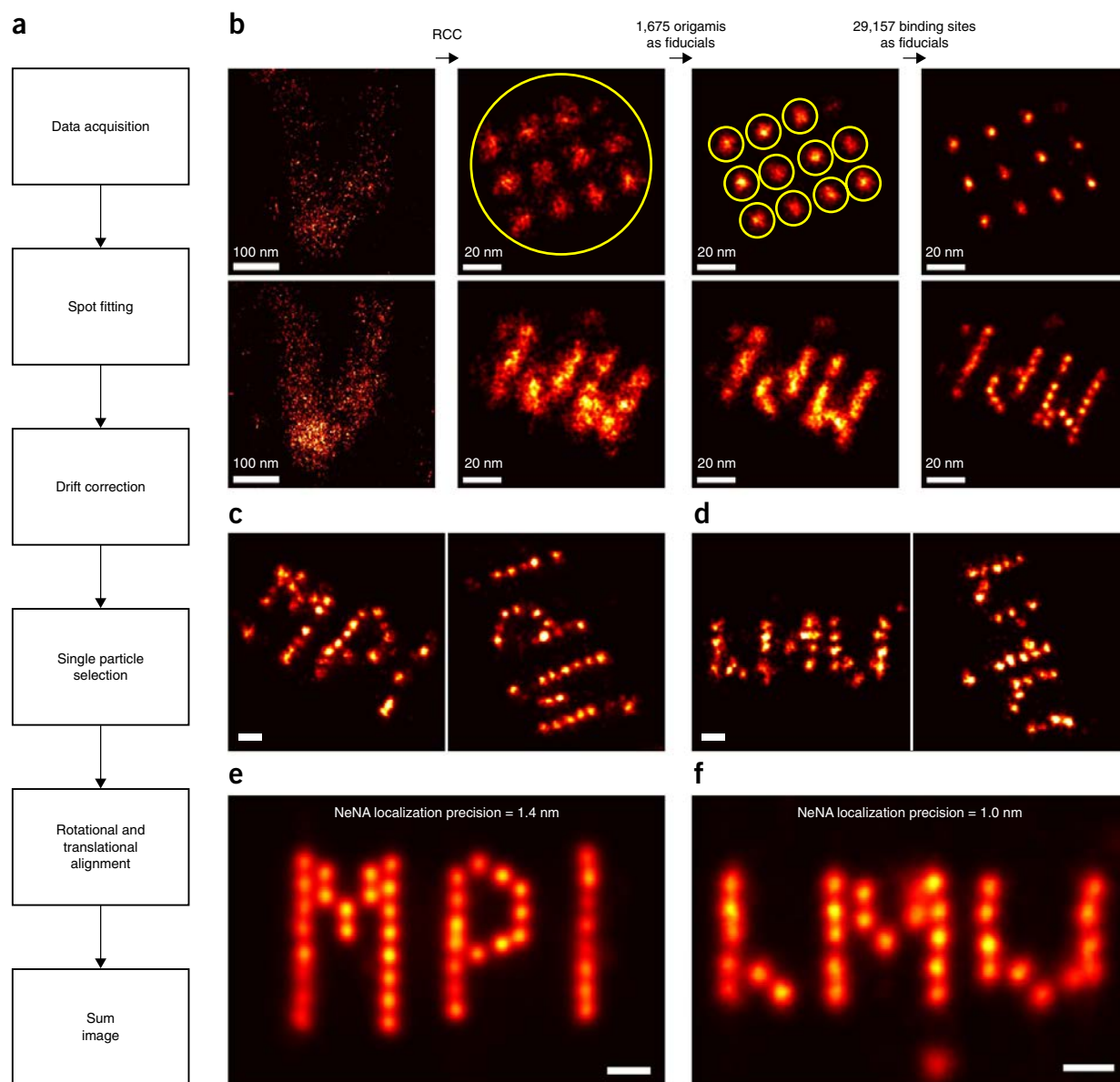


**Figure 4** | ‘Ultra-resolution’ with DNA-PAINT. **(a)** Workflow for ultra-resolution imaging with advanced drift correction and particle averaging. **(b)** Multistage drift correction with Picasso. Top: 20-nm-grid DNA origami structures used as reference structures and drift markers. Bottom: DNA origami target structure (designed to display the letters ‘MPI’ upside down) with 5-nm ‘docking strand resolution’ present in the same sample as the 20-nm origami. In the first drift correction stage, an RCC procedure is applied to the whole field of view (image column after RCC arrow shows results). The second step uses Picasso’s semiautomated particle pick function (picked structure visualized by yellow circle) to select 1,675 DNA origami structures as fiducials for drift correction (drift for all structures is globally averaged and subtracted from the localization data). The result for this step is depicted in the third column. The third and last iteration uses the individual binding sites of the 20-nm grid for drift correction. Here, 29,157 binding sites were used as fiducial markers. The resulting image for the MPI target structures shows clearly resolved single binding sites spaced 5 nm apart. **(c)** Selection of two MPI origami after drift correction. Localization clusters of individual DNA-PAINT binding sites with a distance of ~5 nm are well resolved and circular, indicating that the residual drift is minimal and rotationally invariant. **(d)** Selection of two DNA origami, designed to show the letters ‘LMU’, from a different sample than in **b, c, e**, but after an analogous drift correction as shown in **b**. The images demonstrate minimal residual drift similar to that of the MPI structures shown in **c**. **(e)** Average image of 295 DNA origami with the letters ‘MPI’. The mean number of localizations in individual images is  $3,485 \pm 1,197$ . All DNA-PAINT binding sites are visible, even though individual images miss binding sites because of incomplete strand incorporation, as seen in **c**. **(f)** Average image of 215 DNA origami with the letters ‘LMU’. The mean number of localizations in the individual images is  $2,323 \pm 436$ . Scale bars, 10 nm (**c–f**).

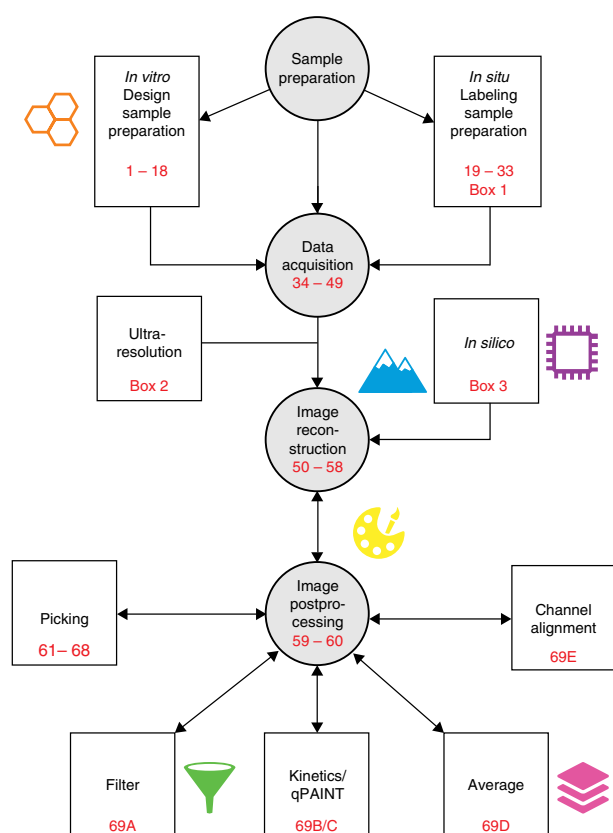


**Figure 5** | DNA-PAINT protocol workflow. Starting with sample preparation, the user can perform either *in vitro* or *in situ* experiments. Next, data acquisition is performed (parameters for ‘Ultra-resolution’ are described in **Box 2**). The user may additionally generate DNA-PAINT data by *in silico* simulations. During image reconstruction, single-molecule fluorescence spots are localized, and resulting super-resolution images are visualized with ‘Picasso: Render’. Image post-processing focuses first on drift-correction procedures. Then, special emphasis is given to analyzing the localization-based DNA-PAINT data through picking regions of interest, performing kinetic and qPAINT analysis, averaging images for ultra-resolution analysis and channel alignment for Exchange-PAINT or filtering of the localization list. Program icons indicate in which Picasso component the respective step is performed—hexagons: ‘Design’; microchip: ‘Simulate’; mountain peaks: ‘Localize’; paint palette: ‘Render’; funnel: ‘Filter’; stacked layers: ‘Average’. The Picasso program icons are based on contributions from the Noun Project (<https://thenounproject.com>)—‘Design’: hexagon by Creative Stall; ‘Simulate’: microchip by Futishia; ‘Localize’: mountains by Montana Rucobo; ‘Filter’: funnel by José Campos; ‘Render’: paint palette by Vectors Market; ‘Average’: layers by Creative Stall.

to achieve very high spatial resolution (<5 nm) with DNA-PAINT, which requires particular care in sample preparation and data acquisition (**Box 2**). Furthermore, we lay out the procedure to simulate typical DNA-PAINT data *in silico* for test and optimization purposes (**Box 3**). Then, image reconstruction is explained in two steps: fitting of single-molecule spots and subsequent rendering of the super-resolution image (Steps 50–58). Finally, we describe multiple procedures for post-processing such as drift correction (Steps 59 and 60), selection of regions of interest (Steps 61–68), filtering of localizations (Step 69A), quantitative imaging with qPAINT (Step 69B and C), particle averaging (Step 69D) and channel alignment for multiplexed images (Step 69E). Additional

steps required for multiplexed imaging with Exchange-PAINT are described as optional steps in the respective sections.

One of the defining components of this protocol for DNA-PAINT is an integrated software package called Picasso, which enables researchers to quickly obtain meaningful reconstructed image results without the need of additional third-party software tools.

### The Picasso software package

Like similar localization-based super-resolution methods, DNA-PAINT requires intricate data analysis. For that matter, we provide an integrated software package named ‘Picasso’ (free to download from <http://www.jungmannlab.org>). Although Picasso is suitable for any localization microscopy technique, it provides specific support for DNA-PAINT applications, e.g., qPAINT. All computational steps described in this protocol can be performed with Picasso. This includes designing of DNA origami structures and simulating typical DNA-PAINT data. After installation, Picasso is available as several stand-alone (but interlinked) modular components with graphical user interfaces. The components are named ‘Design’, ‘Simulate’, ‘Localize’, ‘Filter’, ‘Render’ and ‘Average’. The ‘Design’ component allows the user to visually design rectangular 2D DNA origami structures, which we call Rothmund’s rectangular origami (RRO)<sup>33</sup>, with DNA-PAINT handles. For that matter, ‘Design’ autogenerates order lists and pipetting instructions. With ‘Simulate’, the user may generate typical DNA-PAINT raw data from *in silico* simulations. After data have been acquired or simulated, the ‘Localize’ component allows the user to identify and fit the coordinates of single-molecule spots. ‘Picasso: Filter’ offers a convenient tool to inspect the localization list, plot histograms of localization properties and filter localizations with undesired properties. Super-resolution images can be rendered and inspected with the Picasso component ‘Render’. ‘Picasso: Render’ also offers various post-processing functions such as advanced drift correction and quantitative image evaluation by qPAINT. Last, the ‘Average’ module provides the functionality to perform particle averaging (i.e., rotational and translational alignment) of multiple images of the same structure. Analogous to single-particle reconstruction in the electron microscopy field, this procedure helps to improve the signal-to-noise ratio of images. Overviews of the graphical user interfaces for the ‘Design’, ‘Simulate’, ‘Localize’, ‘Render’ and ‘Filter’ components are shown in **Supplementary Figures 1–5**.

Although in principle a cross-platform development, we currently supply a one-click installer of Picasso for Microsoft Windows 64-bit operating systems. This single executable setup file can be downloaded from our website at <http://www.jungmannlab.org>. Picasso is developed in Python, and the source code is available at <https://github.com/jungmannlab/picasso>.

### Design and preparation of DNA origami structures

As DNA-PAINT makes use of the programmability of (transient) DNA strand hybridization to enable super-resolution imaging, DNA-based objects are convenient *in vitro* test targets for imaging. Nucleic acids can serve as powerful building blocks for nanometer-scale structures based on sequence-guided self-assembly, which is the foundation of structural DNA nanotechnology<sup>34,35</sup>. DNA origami are complex, self-assembled, 2D or 3D structures created by annealing DNA strands of specifically designed sequences<sup>33</sup>. In DNA origami, a long single-stranded DNA

## PROTOCOL

### Box 1 | Construction of a fluid exchange chamber for *in situ* imaging

#### ● TIMING 30 min

##### Procedure

For *in situ* Exchange-PAINT experiments, we recommend a simple, custom-built fluid exchange system. The lid of an 8-well chambered cover glass can be modified with one inlet and one outlet, which can be connected to imaging and washing buffer reservoirs by silicone tubing. The modified lid can be used for multiple imaging experiments, although the connected tubing should be thoroughly cleaned before reuse. Using a syringe, flush at least 3 ml (as reference for 1-m tubing with a 1.5-mm diameter; adjust accordingly) of H<sub>2</sub>O, followed by 3 ml of 80% EtOH and finally 3 ml of H<sub>2</sub>O, through the tubing. Follow these instructions to prepare such a lid:

1. Drill two holes with a diameter of 1.5 mm into the lid of an 8-well chambered cover glass, so that two needles can penetrate it.
2. Use a rotary tool with cutting disc or equivalent to remove the syringe connectors from two 1.2 × 40-mm needles. Alternatively, use a side cutter (although this could potentially lead to a 'less clean cut') and squeeze the channel shut. To reopen, carefully apply pressure with the side cutter at the side of the cut. Make sure that the needle is at least 2.5 cm long to be able to reach the bottom of the chambered cover glass.

! **CAUTION** Handle the needles with care and do not puncture yourself.

3. Cut away the sharp end of one of the needles, so the channel can reach the bottom of the wells. Carefully apply pressure to open the metallic channel of the needle at the cut side with the side cutter.

! **CAUTION** Handle the needles with care and do not puncture yourself.

4. Connect the cut needles to ~50 cm of tubing. Make sure that the tubing is long enough that there is enough space to handle the liquids and syringes at the microscope. To connect the tubing to the syringes, use 1.1 × 40-mm needles on the other end of the tubing.

▲ **CRITICAL STEP** The length of the tubing depends heavily on the accessibility of the microscope; adjust the tubing length for proper handling.

5. For imaging, fix the tubing to the microscope body via tape.

▲ **CRITICAL STEP** Leakage could lead to damage of the microscope. Check all tubing and connections before use.

molecule (called the 'scaffold', derived from M13mp18 single-stranded phage DNA) is folded into a desired shape by ~200 short, single-stranded DNA strands (called 'staples'). Each staple has a defined sequence and specifically binds certain parts of the scaffold together. Structures are usually assembled in a one-pot reaction using thermal annealing. After the self-assembly is completed, the scaffold is 'folded' into the desired shape with the staple strands at prescribed positions in the final origami.

The rather complex and time-consuming procedure of manually designing DNA origami structures has been markedly simplified by computer-aided design tools, such as the freely available caDNA<sup>36</sup> and vHelix<sup>37</sup> packages, as well as by simulation programs such as CanDo<sup>38</sup>. Furthermore, folding protocols for structure formation are now optimized for structure yield and folding speed<sup>39–41</sup>. In addition, several methods for subsequent purification of DNA nanostructures from unwanted excess of staple strands are described in the literature, such as agarose gel purification<sup>42</sup>, rate-zonal centrifugation<sup>43</sup> or PEG purification<sup>44</sup>.

One of the early applications of DNA origami was its use as a microscopy standard in the form of a self-assembled nanoruler<sup>45</sup>. Owing to the unique positioning accuracy of DNA origami and its excellent structural integrity, the structures present an ideal platform to directly validate imaging methods and compare instrumentation. Specifically, they are a valuable tool in calibrating fluorescence and super-resolution microscopes<sup>46</sup>.

Although it is possible to create a wide range of structures with the DNA origami technique, some are more suitable for use as a reference structure with DNA-PAINT than others. In this protocol, we use a flat, rectangular 2D DNA origami structure, adapted from the one originally described<sup>33</sup>, here referred to as RRO. With dimensions of 90 × 70 nm and, in our case, 176 freely addressable staples arranged in a hexagonal lattice with 5-nm spacing,

it is an ideal structure for DNA-PAINT imaging (see **Fig. 1b** as an example). For surface immobilization, the structure is modified with eight biotinylated staple strands that can bind to a BSA-biotin-streptavidin-coated glass surface.

'Picasso: Design' is an essential tool in this protocol that reduces all design steps to a minimum. **Figure 6** shows screenshots and outlines the procedure for creating DNA origami, from design to purification. For a detailed overview of the graphical user interface, refer to **Supplementary Figure 1**. The program displays a hexagonal lattice that serves as a canvas representing all possible staple positions available for modification in the RRO structure. It features a 'point-and-click' approach, so that the desired pattern can be made by simply 'painting' on the canvas. Clicking a hexagon will fill it with a previously selected color; each color corresponds to a built-in staple extension on the 3'-end. As all modifications are just staple extensions of the RRO structure, the core sequences are not altered, and time-consuming tasks such as altering the routing of staples or modifying their base sequence are not necessary. In addition, 'Picasso: Design' automatically calculates folding recipes for a given design based on optimized excess rates for the RRO and creates visual pipetting aids for 96-well plates so that pipetting of staple mixes is greatly facilitated. In consequence, the creation of DNA origami reference structures for DNA-PAINT can be achieved in the most straightforward way.

##### *In situ* sample preparation

A unique advantage of fluorescence microscopy, making it one of the preferred characterization tools in biological research, is its ability to interrogate biomolecules of interest, such as proteins or nucleic acids, with high efficiency and specificity. Generally, fluorescent labeling of target molecules is achieved either by

**Box 2 | Ultra-resolution imaging ● TIMING ~7 h****Procedure**

To achieve ultra-resolution (<5 nm), imaging conditions must be carefully adjusted. The key to higher spatial resolution is to extract more photons per frame from a blinking event while simultaneously keeping the background low. This can be achieved by optimizing the laser excitation power, as well as the fluorescence ON time (and adjusting the integration time accordingly). The background can be reduced, for example, by decreasing the imager concentration. In this case, the acquisition time should be increased to ensure proper sampling of the target structure. However, with an imager concentration that is too low, drift correction might become less accurate owing to the smaller number of localizations per frame. We also want to note that the number of drift markers in a field of view should be as high as possible, to ensure precise drift correction. One way to achieve this is to make use of the larger field of view obtainable with today's sCMOS cameras. For advanced drift correction, a 20-nm and a 10-nm grid DNA origami should be used as fiducials. Furthermore, oxygen-scavenging systems, such as the PCA/PCD/Trolox (PPT) system, allow the harvesting of more photons as they increase fluorophore stability<sup>27</sup>. The following steps describe in detail how to achieve ultra-resolution for imaging DNA origami structures.

1. Design and fold DNA origami structures for ultra-resolution imaging—e.g., the LMU or MPI logo. In addition, fold 20-nm and 10-nm grid DNA origami for use as drift markers (see Steps 1–17).
2. Prepare the oxygen-scavenging system PPT at least 1 h before imaging.
3. Prepare a sample with the target structure and DNA origami drift markers (see Step 18) using the following parameters:
  - Origami solution ratio: 1/4 target structure (i.e. LMU or MPI logo), 1/4 20-nm drift marker, 1/4 10-nm drift marker and 1/4 Buffer B+
  - Imager concentration (with PPT): 0.5 nM–1 nM.
4. Follow steps 34–48 with the following adjustments: 350 ms exposure time, 80,000 total number of frames. Set the excitation power density to ~4.5 kW/cm<sup>2</sup> at the sample plane.

genetically fusing a protein tag to the target<sup>47</sup> or by attaching an external binder molecule during a staining procedure—e.g., dye-labeled antibodies<sup>48</sup>. For DNA-PAINT, the labeling requirement is that a DNA docking strand is attached to the target. Although a variety of strategies could be feasible for that<sup>29,30,49–52</sup>, this protocol focuses on immunostaining with DNA-conjugated antibodies<sup>25</sup>. Specifically, we describe how antibodies can be chemically modified and used for *in situ* DNA-PAINT imaging of fixed cells (Steps 19–33).

The concept of *in situ* DNA-PAINT with primary and secondary antibody labeling is shown in **Figure 1c**: imager strands from solution transiently bind to handle sites on the secondary antibody. Imaging results for *in situ* samples prepared with antibody labeling are shown in **Figure 1d,e**, displaying a gradient overlay of diffraction-limited microtubules in comparison with the reconstructed super-resolved image. Furthermore, **Figure 2g** shows DNA DBCO-labeled antibody staining of Tom20, located mainly at the outer mitochondrial membrane, and DNA thiol-labeled antibody staining of microtubules.

Various avenues are possible for attaching DNA strands to antibodies, including biotin–streptavidin linkage<sup>20</sup> or covalent attachment of the DNA to the antibody<sup>22,53,54</sup>. Although biotin–streptavidin linkage was used in the initial *in situ* DNA-PAINT demonstration<sup>20</sup>, we here discuss a covalent attachment strategy, which was used in subsequent work<sup>22</sup> similar to previously reported strategies for DNA–protein conjugation<sup>53,54</sup>. Here, an NHS ester linker is covalently attached to amino groups on the antibody and to certain functional groups on the DNA, such as reduced thiols<sup>22</sup>, azides<sup>53,55</sup>, alkynes<sup>53</sup> or DBCO<sup>55</sup>, for click chemistry. This results in cross-talk-free attachment, as well as smaller linker sizes between antibody and DNA strand, as compared with the biotin–streptavidin linkage<sup>20</sup>.

Depending on the target molecules under investigation, it is furthermore important to evaluate different fixation strategies.

For example, structural proteins, such as actin filaments or microtubules, can be fixed with pre-extraction and glutaraldehyde to decrease background and preserve structural integrity<sup>56</sup>. However, structural artifacts can arise from the various fixation strategies. For an in-depth discussion of fixation artifacts, we refer to a recent article by Whelan *et al.*<sup>57</sup>. DNA-PAINT was also applied to tissue samples, as was recently shown in *Drosophila* embryos<sup>22</sup>, generally following the same procedures as described here. However, we do note that potential changes to the herein described protocol for more complex tissue samples might become necessary.

**Data acquisition**

A multitude of acquisition software packages are available for performing localization-based super-resolution microscopy, in particular for commercial microscope setups. In this protocol, we describe our procedures based on the freely available open-source acquisition software  $\mu$ Manager<sup>58</sup>.  $\mu$ Manager is used in a wide range of microscopy areas and offers broad device support for microscope bodies, cameras and peripherals. The Picasso software suite is specifically designed to be compatible with  $\mu$ Manager.

Currently, two types of cameras are typically used in the field of single-molecule localization-based imaging—scientific complementary metal oxide semiconductor (sCMOS)- and electron-multiplying charge coupled device (EMCCD)-based cameras. sCMOS cameras provide better temporal resolution because of their faster readout electronics, resulting in a larger optical field of view as compared with EMCCDs under similar conditions. EMCCD cameras, in comparison, provide better quantum yields in low-light applications and thus higher signal-to-noise ratios<sup>59</sup>. As DNA-PAINT provides comparably higher signal-to-noise ratios (SNRs), both camera types are suitable in this context.

It has been shown that a pixel-dependent noise calibration for sCMOS cameras can improve localization precision in STORM<sup>60</sup>. However, for DNA-PAINT experiments—including the

## PROTOCOL

### Box 3 | *In silico* simulation of DNA-PAINT data ● TIMING 10–60 min

Picasso's simulation module ('Picasso: Simulate') is a tool for evaluating experimental conditions for DNA-PAINT and generating ground-truth data for test purposes. This allows systematic analysis of how different experimental parameters such as imager concentration, target density or integration time influence the imaging quality and whether the target structure can be resolved with DNA-PAINT. By default, 'Picasso: Simulate' starts with preset parameters that are typical for a DNA-PAINT experiment. Thus, meaningful raw DNA-PAINT data can be readily simulated for a given input structure without the need of a super-resolution microscope. The simulation output is a movie file in .raw format, as it would be generated during an *in vitro* DNA-PAINT experiment on a microscope.

#### Procedure

1. Start 'Picasso: Simulate'.
2. Define the number and type of structures that should be simulated in the group 'Structure'. Predefined grid- and circle-like structures can be readily defined by their number of columns and rows, or their diameter and the number of handles, respectively. Alternatively, a custom structure can be defined in an arbitrary coordinate system. To do so, enter comma-separated coordinates into 'Structure X' and 'Structure Y'. The unit of length of the respective axes can be changed by setting the spacing in 'Spacing X,Y'. For each coordinate point, an identifier for the docking site sequence needs to be set in 'Exchange labels' as a comma-separated list. Correctly defined points will be updated live in the 'Structure [nm]' window. Note that entries with missing *x* coordinate, *y* coordinate or exchange label will be disregarded. When a structure has been previously designed with 'Picasso: Design', it can be imported with 'Import structure from design'. A probability for the presence of a handle can be set with 'Incorporation'. By default, all structures are arranged on a grid with boundaries defined by 'Image size' in 'Camera parameters' and the 'Frame' parameter in the 'Structure' group. 'Random arrangement' distributes the structures randomly within that area, whereas 'Random orientation' rotates the structures randomly. Selecting the button 'Generate positions' will generate a list of positions with the current settings and update the preview panels. A preview of the arrangement of all structures is shown in 'Positions [Px]', whereas an individual structure is shown in 'Structure [nm]'.
  3. The group 'PAINT Parameters' allows adjustment of the duty cycle of the DNA-PAINT imaging system. The mean dark time is calculated by  $\tau_d = (k_{on} \cdot c)^{-1}$ . The mean ON time in a DNA-PAINT system is dependent on the DNA duplex properties. For typical 9-bp imager/docking interactions, the ON time is ~500 ms. ON times can be experimentally estimated with Picasso as described in Step 69B.
  4. In 'Imager Parameters', fluorophore characteristics such as PSF width and photon budget can be set. Adjusting the 'Power density' field affects the simulation analogously to changing the laser power in an experiment.
  5. The 'Camera parameters' group allows the user to set the number of acquisition frames and integration time. The default image size is set to 32 pixels. As the computation time increases considerably with image size, it is recommended to simulate only a subset of the actual camera field of view.
  6. Select 'Simulate data' to start the simulation. The simulation will begin by calculating the photons for each handle site of every structure and then converting it to a movie that will be saved as a .raw file, ready for subsequent localization. All simulation settings are saved and can be loaded at a later time with 'Load from previous simulation'.

#### ? TROUBLESHOOTING

7. (Optional step for multiplexing) Multiplexed Exchange-PAINT data can be simulated by adjusting the 'Exchange Labels' setting. For each handle in the custom coordinate system ('Structure X', 'Structure Y'), an Exchange round can be specified. The different imaging rounds can be visually identified by color in the 'Structure [nm]' figure. For each round, a new movie file will be generated. By default, the simulation software detects the number of exchange rounds based on the structure definition and will simulate all multiplexing rounds with the same imaging parameters. It is possible to have different imaging parameters for each round, e.g., when using images with different ON-times. To do so, one can simulate multiplexing rounds individually. In the 'Exchange rounds to be simulated' field, enter only the rounds that should be simulated with the current set of parameters. Change the set parameters and the multiplexing round and simulate the next data sets. Repeat until all multiplexing rounds are simulated.

ultra-resolution measurements in this protocol—we did not account for the pixel-dependent noise of our sCMOS camera. Although such calibration might also improve DNA-PAINT image quality, it was not required to achieve the ~1-nm localization precision that allowed us to resolve 5-nm spaced binding sites on DNA origami structures (Fig. 4).

In this protocol, we generally suggest rather long camera integration times (a few hundred milliseconds) as compared with other localization-based microscopy methods such as PALM or STORM. Typically, for localization-based super-resolution techniques, the integration time is roughly matched to the ON-time of blink events to maximize the signal-to-noise ratio of the fluorescence image. Analogously, the integration times suggested here are roughly matched to the binding kinetics of the recommended nine-base-pair DNA duplex. This allows the collection of far more

photons in a single frame as compared with typical PALM or STORM experiments, thus enabling better localization precision. However, it is worth noting that the combination of slower blinking and longer integration time comes at the expense of extended total data acquisition time to detect the same number of events. Nonetheless, it is certainly possible to shorten the binding duration, integration time and thus the total acquisition time by using DNA duplexes with fewer base pairs. For example, the recommended integration time for 8-mers is only tens of milliseconds and that for 7-mers is even less. With such faster kinetics, the integration time and achievable localization precision would then be similar to those in PALM or STORM experiments. An advantage of DNA-PAINT is therefore that it gives the researcher intricate control over the desired localization precision as a trade-off for total acquisition time.

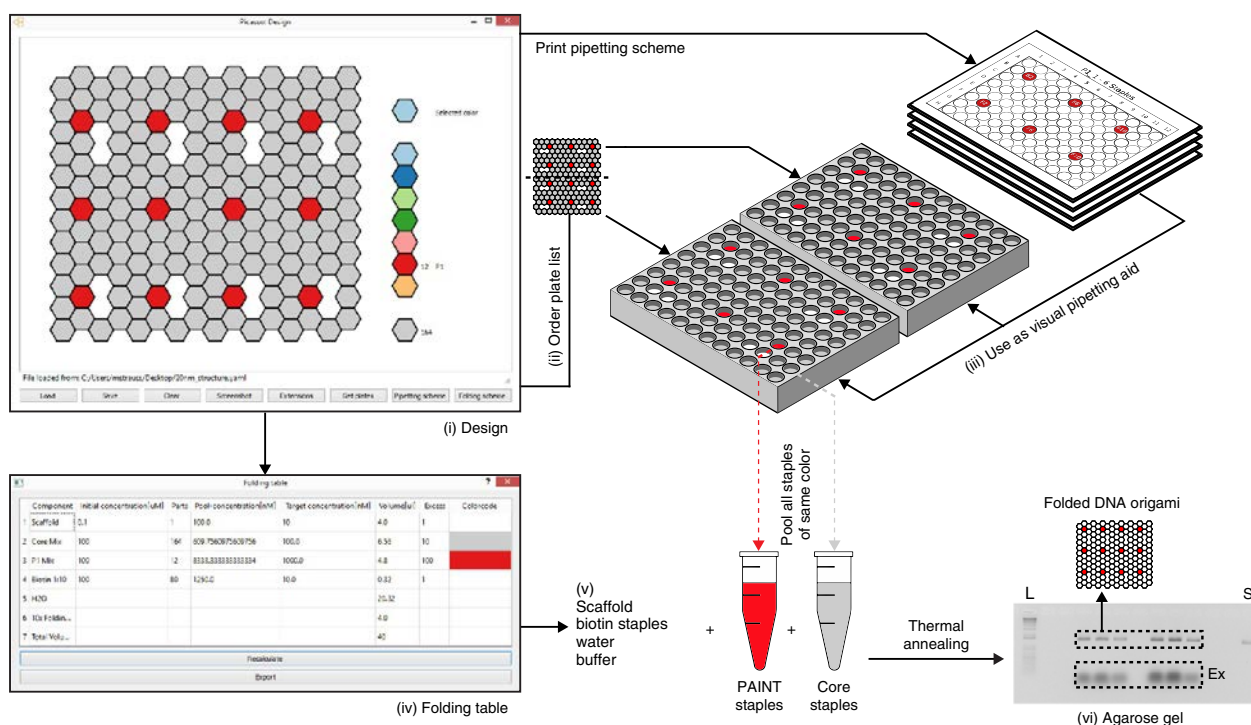


**Figure 6** | Designing DNA origami structures for DNA-PAINT with ‘Picasso: Design’. (i) Screenshot of the design interface displaying a 20-nm grid structure with 12 docking sites (red) selected to carry the extension P1. After design is completed, a list of plates is generated as a .csv file ready for ordering (ii). ‘Picasso: Design’ also creates PDF sheets that can be placed underneath the ordered 96-well plates to facilitate pipetting of staple strands (iii). The folding table (iv) gives detailed instructions for preparing components to assemble the DNA nanostructure through thermal annealing. Staple master mixes are pipetted from the plates according to the pipetting scheme. For a successful assembly process, single-stranded DNA scaffold, biotinylated staples, staple master mixes (unmodified core (gray) and docking-strand-extended (red) staples), water and folding buffer need to be mixed (v). After structures are formed (usually through thermal annealing), an agarose gel can be run for analysis or subsequent structure purification (vi). Here, a DNA ladder (L) and the scaffold strand (S) are seen as clear bands together with bands for the correctly folded DNA structures and excess staple strands (Ex). Extracted origami structures are now ready for DNA-PAINT imaging.

The number of localizations and thus the total experiment time strongly influence the resolution of a localization-based super-resolution image. Ideally, to resolve a target structure, it should be spatially probed at least at its Nyquist frequency<sup>61</sup>. More precisely, it has been shown that the overall image resolution for localization-based super-resolution microscopy is governed by two main factors: sampling density and localization precision<sup>16</sup>. In the same work, it was demonstrated that longer acquisition times increase spatial resolution of the reconstructed image because of increased spatial sampling up to the point at which image resolution is solely limited by localization precision. As the molecule density of a target structure might be unknown, it is often necessary to evaluate a range of acquisition times to determine how many frames are sufficient to represent the structure with the desired resolution. *In silico* simulations of localization-based super-resolution imaging can be a practical method of assaying a large number of data acquisition parameters such as the total acquisition time<sup>62</sup>, reducing the need for time-consuming experiments. The Picasso software package comes with a module for simulating DNA-PAINT data, thus providing the tools for this approach. A more detailed discussion of the ‘Picasso: Simulate’ module follows below. Finally, we want to provide an exemplary thought-experiment as a guide to estimating appropriate acquisition lengths  $t$ . Consider an imager concentration

$c$  of 10 nM and a probe association rate  $k_{on}$  of  $10^6$  (Ms)<sup>-1</sup>. This leads to a mean time in between binding events (or dark time  $\tau_d$ ) for a single site of 100 s according to  $\tau_d = (k_{on} \times c)^{-1}$ . For an ~98% probability ( $P$ ) of any single binding site being visited at least once, a total imaging time of  $t = 4 \times \tau_d = 400$  s is required, according to  $P = 1 - e^{-t/\tau_d}$ . To achieve multiple binding events per site resulting in a decent image quality, we recommend a total imaging time of ~33 min.

#### *In silico* simulation of DNA-PAINT data

A fundamental challenge in single-molecule localization microscopy is to systematically design, optimize and validate super-resolution experiments. *In silico* simulations provide a convenient way to address this challenge. Software packages such as SuReSim generate a ground truth model and simulate localization microscopy data using parameters matching an experimental microscope setup<sup>62</sup>. Similar to this approach, the Picasso software suite can simulate localization data with its ‘Simulate’ component, which is specifically tailored to DNA-PAINT. In a graphical user interface, shown in **Figure 7** and **Supplementary Figure 2**, simulation parameters can be set for the type of target structure, DNA-PAINT kinetics, dye properties and hypothetical data acquisition settings such as integration time and total number of acquisition frames.

## PROTOCOL

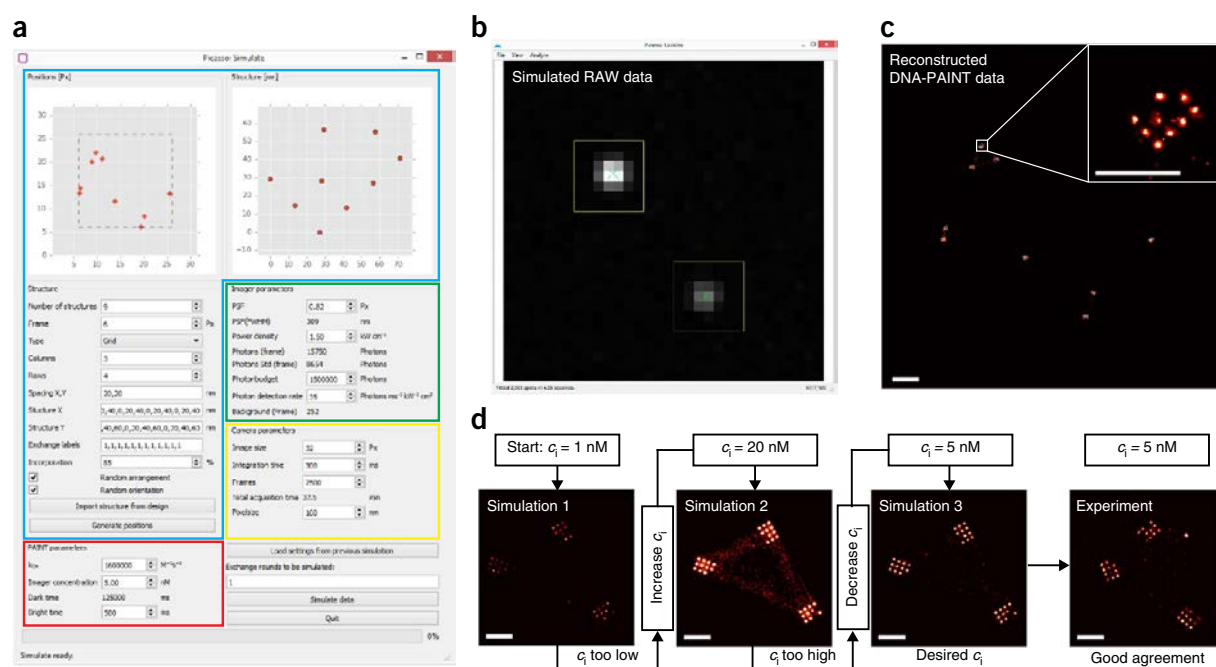


**Figure 7** | Simulating DNA-PAINT raw data from DNA origami-like structures. **(a)** Overview of the graphical user interface for ‘Picasso: Simulate’. A DNA-PAINT simulation can be defined by parameters in four categories, indicated by colored frames: ‘Structure’ (blue), ‘PAINT parameters’ (red), ‘Imager parameters’ (green) and ‘Camera parameters’ (yellow). Two overview plots are shown in the upper row. ‘Positions [Px]’ shows the arrangement of individual structures within the field of view and ‘Structure [nm]’ shows the positions of DNA-PAINT binding sites in an individual structure. The positions of binding sites in individual structures can be defined in the ‘Structure’ section by (i) importing RRO structures designed with ‘Picasso: Design’, (ii) using predefined geometric shapes (circles, grids), or (iii) manually entering coordinates. In the ‘PAINT parameters’ section, kinetic parameters for DNA-duplex formation can be set. Imager-related properties (PSF width, laser power, photon budget, photon detection rate and background) are defined in the ‘Imager parameters’ section. Last, acquisition settings, such as image size, integration time, number of frames and pixel size can be set in the ‘Camera parameters’ section. **(b)** Example of simulated raw DNA-PAINT data in ‘Picasso: Localize’ after spot identification and fitting. The simulation program simulates blinking events as if they were acquired with a microscope. **(c)** Reconstructed DNA-PAINT image from data generated with ‘Picasso: Simulate’. The overview of all structures corresponds to the ‘Positions [Px]’ window shown in **a**. A close-up shows the structure that is presented in the ‘Structure [nm]’ window in **a**. **(d)** Example of an iterative process for optimizing DNA-PAINT experiments with simulations. A DNA origami structure is simulated with an imager concentration of 1 nM (Simulation 1). The simulation shows that the concentration is too low, because features of the structure are not clearly visible. Consequently, in a next iteration, data are simulated with a higher concentration, here 20 nM (Simulation 2). Now the simulation reveals that the imager concentration chosen is too high, resulting in ‘cross-talk’ localizations between the structures. Such cross-talk arises when two imagers bind simultaneously to nearby structure sites. Their diffraction-limited images spatially overlap and are falsely identified as a single event with a fitted center coordinate in between the two true positions. For the next iteration, the imager concentration is decreased to 5 nM. The resulting simulation shows structures with clear features and no inter-structure cross-talk. Hence, the 5 nM imager concentration was chosen to perform a DNA-PAINT experiment (Experiment), which in turn is in good agreement with the simulation. Scale bars, 500 nm (**c**), 100 nm (**c** inset, **d**).

The simulated imaging targets are nanometer-sized 2D structures (similar to RROs) on which the positions of DNA-PAINT handles can be defined. These handles serve as a ground truth model for localization events. On the basis of the values set for DNA-PAINT kinetics, the simulation algorithm will calculate a kinetic series of ON- and OFF-events over the total acquisition time for each handle.

The duration of an ON-event is calculated by random selection from an exponential distribution defined by a mean ON-time. This time can be either determined experimentally (i.e., using Picasso’s kinetic analysis tool; see Step 69B) or estimated by the number of base pairs in the imager/docking strand duplex<sup>19</sup>. The length of an OFF-event is generated accordingly. Here, the mean OFF-time is calculated from the user-defined binding rate constant and the imager concentration<sup>19</sup>.

The user-defined integration time of the simulated camera is used as a sampling window to calculate how long an imager was

bound during each frame. To emulate experimental results, the simulation randomly selects a photon detection rate for each binding event from a normal distribution. The mean and standard deviation of this normal distribution increase linearly with the user-definable laser power density according to experimentally determined coefficients. For each frame (or fraction of a frame) in which the binding event occurs, the detected number of photons is then selected randomly from a Poisson distribution. The mean of this Poisson distribution is equal to the mean expected photon number for the binding event duration within this frame (photon detection rate × duration). In addition, the simulation considers an upper-limit for detected photons from a single binding event, based on a user-defined photon budget per fluorophore.

After the number of photons for all binding events in each frame is calculated, photons are distributed around the center position of their handle by a user-adjustable 2D normal distribution, representing the microscope’s point spread function (PSF).

This results in a list of all photon positions for each frame, which is converted to an image by calculating a 2D histogram. Poissonian noise is added to each frame specified by the background level. Finally, the frames are exported as a raw movie file. The default values for all parameters were estimated from calibration experiments on our TIR fluorescence (TIRF) setup described in the EQUIPMENT section. The imager sequence for calibration experiments was CTAGATGTAT (P1), which was labeled with a Cy3B dye that was excited by a 561-nm laser.

### Super-resolution image reconstruction

After a movie of DNA-PAINT data has been acquired (either *in silico*, *in vitro* or *in situ*), single-molecule spots must be identified and fitted to find their center position with subpixel accuracy. These routines are performed with Picasso's 'Localize' component. An overview of the graphical user interface with identified and fitted localizations is shown in **Supplementary Figure 3**, as well as screenshots of parameter dialogs.

A multitude of spot identification algorithms have been developed and applied to localization-based super-resolution microscopy<sup>63</sup>. In 'Picasso: Localize', spot identification makes use of the image gradient to minimize the impact of nonhomogeneous background. First, local maxima are detected by identifying pixels with highest count in their local neighborhood. This local neighborhood is defined by a square box around the pixel with a user-defined side length. Then, the net gradient ( $G_{net}$ ) is calculated for each box around a local maximum pixel by

$$G_{net} = \sum_{box} g_i \cdot \mathbf{u}_i$$

where the sum is taken over all pixels of the box,  $g_i$  is the central difference gradient at pixel  $i$  and  $\mathbf{u}_i$  is a unit vector originating at pixel  $i$  and pointing toward the center pixel of the box. Hence, the net gradient of a spot is the sum of intensity flowing toward the spot center, which is roughly proportional to the number of signal photons. A user-defined minimum threshold for the net gradient defines whether a spot will be further considered for fitting or disregarded.

After spots have been identified by the net gradient method, their box serves as input for a maximum likelihood fitting procedure<sup>64</sup>. Although a plethora of spot-fitting algorithms have been published and used for localization microscopy<sup>63</sup>, we chose to implement the maximum likelihood algorithm because it achieves theoretically minimum uncertainty at the Cramer-Rao lower bound with good computational performance. However, it is critical to this fitting algorithm that the camera images be converted correctly to photons, because the algorithm incorporates the Poisson noise statistics inherent to light detection. In 'Picasso: Localize', the user can set the required parameters for converting camera counts to photons. One result of the maximum likelihood fitting is the Cramer-Rao lower bound (CRLB) for each spot. The localization precision is then obtained by calculating the square root of the CRLB.

Finally, super-resolution images are rendered with the 'Picasso: Render' component based on a list of subpixel spot center coordinates (see **Supplementary Fig. 4** for an interface overview). The super-resolution image is a pixel image with arbitrary pixel size, although super-resolution pixels that are too large result in insufficient spatial sampling and a potential loss in resolution. We define the ratio

of super-resolution image pixels to camera pixels as the 'oversampling' parameter. In Picasso, the oversampling can be set either manually or automatically according to how far the user zooms into the image. In the dynamic case, each computer display pixel corresponds to one pixel of the super-resolution image.

Picasso offers several rendering modes for the super-resolution image. The basic option is to use no 'Blur', in which case the super-resolution image is merely a 2D histogram of localization coordinates<sup>65</sup>. The second option is 'One-Pixel-Blur', in which the 2D histogram is convolved with a Gaussian probability density function of volume and standard deviation equal to one. The third option, 'Global Localization Precision', is similar to the 'One-Pixel-Blur'. However, the standard deviation of the Gaussian kernel is set to the median localization precision of all localization coordinates. In the fourth option, 'Individual Localization Precision', each localization is added to the super-resolution image as a Gaussian probability density with volume equal to one and standard deviation equal to the individual coordinate localization precision<sup>3</sup>. For the localization-precision-based representation methods ('Global' and 'Individual Localization Precision'), a minimum blur width can be defined by the user, so that the blur width is equal to the localization precision, unless the precision is smaller than the set minimum blur width.

Picasso furthermore allows for contrast adjustment of the super-resolution image based on the density of localizations in one super-resolution image—i.e., the number of localizations per pixel (or in the case of 'blurred' images, the sum of probability densities from localizations at each pixel).

### Drift correction

A critical post-processing step for localization-based super-resolution imaging is to compensate for stage drift that occurred during data acquisition. In fact, with intricate drift correction methods, extremely high resolution (well below 5 nm) can be achieved<sup>23</sup>. After such post-processing steps, drift is almost completely removed as a factor for resolution degradation. Consequently, localization precision and structure sampling are the only remaining factors that determine image quality. Even so, localization precision can be greatly optimized, because DNA-PAINT decouples dye photophysics from blinking, and particle averaging (described below) allows reducing of the effects of undersampling the structure of interest.

Picasso offers two major routes for drift correction: (i) using the localization events themselves and (ii) using specific fiducials in the sample. The localization-events-based drift correction is an implementation of a redundant cross-correlation (RCC) algorithm<sup>66</sup> in which localizations are split and rendered into multiple super-resolution images according to their temporal appearance in the movie. Image cross-correlation of all resulting super-resolution images then yields the spatial shift between temporal movie segments from which the drift is interpolated. Another conventional way for compensating drift in localization-based super-resolution microscopy is by using fiducial markers<sup>3</sup>. Such fiducial markers are luminescent and typically observed in the same emission channel as the fluorescent signal. Commonly used fiducials are gold nanoparticles, quantum dots and fluorescently dyed microspheres. With Picasso, localizations from such fiducial markers can be selected and used for drift correction, as the localizations can be assumed to originate from a single

## PROTOCOL

point-like source. Recent developments in extremely high resolution in DNA-PAINT applications have used a large number of DNA origami as fiducial markers<sup>23</sup>. When using hundreds of DNA origami structures as markers, their intrinsic size does not affect the drift estimation because of their random rotational orientation. In the same work, an additional drift correction step was applied by selecting single DNA-PAINT binding sites as drift markers. Similar to the case of whole DNA origami, a large number of binding sites (usually several thousands) are required, as each individual site does not comprise sufficient localizations to interpolate the drift for each movie frame accurately. Although DNA origami and their DNA-PAINT binding sites are excellent choices, this type of fiducial-based drift estimation is not limited to these structures. It is feasible to use any distinctly visible landmarks in the image as fiducial markers—for example, protein clusters such as the nuclear pore complex.

In this protocol, we recommend subsequent applications of drift correction by RCC and, if available, fiducial-based correction with DNA origami markers followed by fiducial-based correction with single DNA-PAINT binding sites as markers. Example results after each drift correction step of such a process are shown in **Figure 4b**. In the final images, drift is almost completely eliminated as a factor in image resolution. This is corroborated by the fact that the spread of imaged DNA-PAINT binding sites is similar to the estimated localization precision by nearest neighbor analysis (NeNA)<sup>67</sup>.

### Multiplexing

One major benefit of DNA-PAINT is its straightforward extension to multiplexed imaging. Here, the simplest implementation is to use spectrally distinct dyes coupled to orthogonal imager sequences<sup>68</sup>. Unlike other multiplexed localization-based super-resolution techniques<sup>69</sup>, no photo-switching of dyes is necessary, and thus it is rather simple to find compatible spectrally distinct fluorophores<sup>68</sup> (i.e., Atto488, Cy3B and Atto655).

However, one major drawback of spectral multiplexing is the limited number of distinguishable dyes in the visible spectrum. This limitation can be overcome with Exchange-PAINT<sup>20</sup>. Here, the unique programmability of DNA-PAINT docking and imager strands is used to enable spectrally unlimited multiplexing by sequentially applying orthogonal imager strands (carrying the same dye) to targets of interest.

In each imaging round, only one imager species is present in solution for one target. After acquisition, the imager is washed out and the imager for the next round is introduced. This is then repeated for the total number of targets. A multicolor image is achieved by assigning a pseudocolor to each imaging round and stacking the acquisitions on top of each other, which is depicted in **Figure 2a**.

Preparation of samples for Exchange-PAINT is similar to that for singleplex experiments, only that an open chamber allowing for fluid exchange is used as displayed in **Figure 2b,c**.

To create multicolor images, Picasso automatically assigns pseudocolors when several data sets are loaded. Different imaging rounds potentially comprise an offset with respect to each other because of instrumentation drift during data acquisition. However, alignment procedures can detect and correct for such image offsets.

Picasso offers cross-correlation or fiducial-based alignment algorithms. When images share features as reference points, such as DNA origami or the general cell shape, the cross-correlation can align images with high precision—e.g., sub-5-nm channel

alignment, as demonstrated in **Figure 2d–f**. When few reference points are available, e.g., for *in situ* imaging of different cell targets, alignment markers or drift fiducials can be added to the sample and used in Picasso's alignment procedure.

A distinct advantage of Exchange-PAINT over spectral multiplexing is that for each imaging round the same dye is used, and thus misalignment and inhomogeneous image warping due to chromatic aberrations are avoided. This allows for very precise channel alignment and makes Exchange-PAINT ideal for colocalization studies to assess spatial proximity and possible molecular interactions. Such results are illustrated in the *in situ* example in **Figure 2g**, in which the morphology of the mitochondrial network and the spatial relationship to microtubules is studied. It shows how mitochondria are embedded in the microtubule network, as described in previous work<sup>70</sup>.

### Quantitative imaging with qPAINT

Most super-resolution studies to date harness their exquisite sub-diffraction spatial resolution to address challenges in the biological sciences by structural imaging. However, although still challenging, counting integer numbers of biomolecules when localization precision is insufficient to spatially resolve them can bring further insight into biological systems<sup>8,71,72</sup>. To achieve this, researchers began using the spatiotemporal information of single-molecule localization microscopy data sets beyond just binning localization events for visualization. The basic concept involves extracting molecule numbers by evaluating the kinetics of the blinking behavior of photoswitchable molecules<sup>73–75</sup>. Most of these counting techniques use rather complex modeling of the dye photophysics, in some cases combined with spatiotemporal clustering<sup>72–76</sup>. However, incumbent techniques have certain limitations that prevent them from achieving the highest accuracy and precision over a wide range of molecular densities in resolution-limited areas. These limitations generally lead to overcounting or undercounting artifacts, because the dyes typically have environmentally sensitive photophysics that are hard to predict and model. Furthermore, distinct dyes behave differently even under similar experimental conditions, which severely complicates multiplexed quantitative imaging. In addition, inhomogeneous excitation and photoactivation intensities due to uneven illumination across a sample can lead to inaccurate quantification as well. Last, dyes typically bleach over the course of an experiment, which deteriorates quantification accuracy and precision.

Recently, DNA-PAINT has been used to achieve precise and accurate counting—because of its independence from dye photophysics and immunity to photobleaching—in an implementation called qPAINT<sup>22</sup>. In contrast to the traditional approach of fixing blinking dyes to the target molecule, DNA-PAINT creates target 'blinking' by transient binding of dye-labeled imager strands to complementary docking strands on the target. As opposed to dye photoswitching, DNA hybridization kinetics is more predictable. Hence, combined with the effective absence of photobleaching, qPAINT can extract molecule numbers with high precision and accuracy.

**Figure 3** illustrates the procedure and results of a typical qPAINT experiment. Using Picasso's quantification capabilities, we now provide users with an integrated software solution for calibrating and quantifying molecule numbers in DNA-PAINT data sets. qPAINT relies on the fact that mean dark times for a given influx rate of imager strands ( $\xi = k_{\text{on}} \times c$ ) are dependent

only on the number of docking strands (and thus biomolecules) in an area of interest. To illustrate this, we compare two DNA origami structures, carrying 12 or 42 binding sites in 20-nm and 10-nm grid arrangements, respectively (Fig. 3a). A schematic representation of their respective intensity vs. time traces is shown in Figure 3b. By plotting the cumulative distribution function of both dark time distributions, we can obtain mean dark times for the two structures (Fig. 3c). To translate these dark times to actual numbers of binding sites (or units), the influx rate per unit needs to be calibrated. This can be achieved with DNA origami structures in which binding sites can be visually identified (see Fig. 3d, 20-nm grid structures displaying 12 binding sites). In Picasso, users can now select these calibration structures displaying a known number of units (or binding sites in this case) and calibrate the probe influx rate for subsequent quantification of target molecules of interest in the same data set (Fig. 3d).

The results for a typical qPAINT experiment post calibration are illustrated in Figure 3e–g. 20-nm DNA origami grid structures can be used to compare visually counted numbers of spots with qPAINT results, which are in good agreement (Fig. 3e). Note that not all DNA origami carry all binding sites, because typical staple incorporation efficiencies are <100%. qPAINT allows binding-site identification on 10-nm DNA origami grid structures, in which single sites are not clearly identifiable (Fig. 3f).

Finally, Picasso allows users to quickly obtain statistics from qPAINT data sets using its integrated ‘Pick’ and ‘Pick similar’ tools. Figure 3g illustrates the resulting number of binding-site distributions for 20-nm and 10-nm DNA origami grid structures in a single sample. The average number of binding sites is in excellent agreement with expectations. For 20-nm structures, the incorporation efficiency is ~78%, whereas it is slightly lower for 10-nm grid structures at 70%. This, however, is to be expected, as staple incorporation efficiency should be lower for larger numbers of modified staple strands in DNA origami structures.

### Filtering localizations

After identification and fitting of single-molecule spots, filtering the list of localizations might improve super-resolution image quality<sup>3,5,6,69,70,77</sup>. Only after fitting a single-molecule spot, are properties such as spot width or an accurate estimation of the number of photons available. Hence, spot identification itself may not reliably rule out false-spot detections. A typical filtering procedure is to remove localizations with spot widths that are too small or too large. Ideally the spot width matches that of the microscope’s PSF. Therefore, if the spot width is, for example, too big, it is likely that the spot originates from two close-by and overlapping events. The resulting fit coordinate will be between the two correct center positions and should therefore be disregarded. Another example of filtering is to remove localizations with a number of photons or a localization precision that is too low. After such filtering, the super-resolution image quality can improve, because only high-precision localizations remain. Picasso’s ‘Filter’ component provides a convenient, visually guided way to filter localizations based on histograms of their properties. An overview of its graphical user interface, as well as screenshots of filtering procedures in progress, is shown in Supplementary Figure 5. We recommend studying histograms of localization properties and joint histogram maps of two localization properties with the goal of identifying the true signal

population and removing false populations or outliers. An overview of localization properties saved by Picasso is shown in the Supplementary Manual.

### Particle averaging

When imaging a structure that appears multiple times in the field of view, aligning the individual images on top of each other and ‘summing them up’ can generate an ‘average’ image with improved image quality<sup>23,78</sup>. Such a procedure is analogous to the particle averaging often applied for structural biology in single-particle electron microscopy<sup>79</sup> and has already been successfully applied to localization-based super-resolution microscopy<sup>80,81</sup>. Although, strictly speaking, we do not create an ‘averaged’ but rather a ‘sum image’ from all localizations, we here will continue to use the notion of averaging as a historical term from the electron microscopy field. ‘Averaging’ primarily increases the image signal-to-noise ratio, which translates for localization microscopy to the proportion of true, high-precision localizations (signal) to false or imprecise localizations (noise). Hence, structure sampling, a major factor for image resolution<sup>16</sup>, can be improved by the averaging procedure. This is exemplified by the individual and average images of two RRO DNA origami structures in Figure 4c–f, showing the letters ‘MPI’ and ‘LMU’. The average image comprises a greatly enhanced signal-to-noise ratio as compared with images of individual structures. Moreover, even though some binding sites are missing in individual structures, averaging could reconstruct all binding sites and resolve their ~5-nm distances well.

Picasso offers a graphical user interface for averaging multiple images of the same structure with the ‘Average’ component. The underlying algorithm does not require a reference and is based on a traditional procedure borrowed from single-particle electron microscopy<sup>82</sup>. Briefly, the individual images are first translationally aligned on top of each other by overlaying the center of mass of localizations. Then, several iterations of rotational and refined translational alignment are applied. In each iteration, an average image is constructed by pooling all localizations and rendering them on a super-resolution pixel grid. Then, localizations from each individual structure are rotated over 360 degrees in small steps and rendered as a super-resolution image for each rotational step. The angular step size is dynamically chosen so that the rotation distance at twice the root mean square (RMS) deviation of all localizations from their center of mass matches the size of a super-resolution pixel. Each rotated image is cross-correlated with the average image of the current iteration, and the maximum value and position of the cross-correlation are recorded. Finally, the localizations of an individual structure are rotated and translated according to the rotation and translation with the highest cross-correlation value. In the next iteration, a new improved average image can be generated from the now updated localization coordinates. After a certain number of iterations, the average image will converge—i.e., the pixel values will not change after an iteration. At this point, the algorithm can be stopped, and the new localization list is saved.

Averaging results, as shown in Figure 4e,f, rely on experimental conditions and post-processing steps that are specifically aimed at ultra-resolution. In particular, intricate drift correction as described above is a key contribution. Experimental conditions for ultra-resolution are described in Box 2; refer to Supplementary Figures 6–9 for structure design.

## PROTOCOL

### MATERIALS

#### REAGENTS

**! CAUTION** All reagents can be potentially hazardous and should be handled only by trained personnel.

#### DNA labeling

- PBS, pH 7.2 (Life Technologies, cat. no. 20012-019)
- 0.5 M EDTA, pH 8.0 (Ambion, cat. no. AM9261) **! CAUTION** EDTA may cause eye and skin irritation; avoid breathing the dust or fumes.
- DMF (Thermo Fisher Scientific, cat. no. 20673) **! CAUTION** DMF is a toxic and flammable liquid; protect your eyes and skin, and avoid breathing the dust or fumes. It may also damage fertility and cause harm to the unborn child. Handle it under a chemical hood.
- AffiniPure Donkey Anti-Rat IgG (Jackson ImmunoResearch, cat. no. 712-005-150)
- AffiniPure Donkey Anti-Rabbit IgG (Jackson ImmunoResearch, cat. no. 711-005-152)
- AffiniPure Goat Anti-Mouse IgG (Jackson ImmunoResearch, cat. no. 115-005-003)

#### Antibody labeling via maleimide-PEG2-succinimidyl ester

- Maleimide-PEG2-succinimidyl ester (Sigma-Aldrich, cat. no. 746223)
- No-Weigh Format DTT (Thermo Fisher Scientific, cat. no. 20291) **! CAUTION** This compound causes skin and respiratory pathway irritation, as well as serious eye irritation. It is toxic if swallowed and causes long-term damage to aquatic life.
- Micro BCA Protein Assay Kit (Thermo Fisher Scientific, cat. no. 23235)
- Thiol-DNA (P1 handle: Thiol-TTATACATCTA; MWG Eurofins)
- Thiol-DNA (P3 handle: Thiol-TTCTTCATTA; MWG Eurofins)

#### Antibody labeling via DBCO-sulfo-NHS ester

- DBCO-sulfo-NHS ester (Jena Bioscience, cat. no. CLK-A124-10)
- Azide-DNA (Biomers.net) P1 Handle: Azide-TTATACATCTA
- Azide-DNA (Biomers.net) P3 Handle: Azide-TTCTTCATTA

#### Immunofixation and cell imaging

- 8-well chambered cover glasses (Eppendorf, cat. no. 0030742036 or Thermo Fisher Scientific, cat. no. 155409)
- BSA (Sigma-Aldrich, cat. no. A4503-10g)
- Triton X-100 (Carl Roth, cat. no. 6683.1) **! CAUTION** This compound is toxic if swallowed, and it can cause serious eye damage.
- 0.22- $\mu$ m sterile filters (Merck/EMD Millipore, cat. no. SLGS033SS)
- Sodium chloride (Ambion, cat. no. AM9759) **! CAUTION** Sodium chloride may cause skin and eye irritation, and it may be harmful if inhaled or swallowed.
- Sodium borohydride (Carl Roth, cat. no. 4051.1) **! CAUTION** This compound reacts in a volatile manner with H<sub>2</sub>O, is toxic if swallowed and can cause serious skin damage. Handle it under a chemical hood.
- 16% (vol/vol) Paraformaldehyde (Electron Microscopy Sciences, cat. no. 15710) **! CAUTION** This compound is flammable, a carcinogen and toxic if swallowed; avoid breathing the fumes or dust. It can cause serious eye, skin or respiratory pathway irritation. Handle it under a chemical hood.
- 25% (vol/vol) Glutaraldehyde (SERVA, cat. no. 23115.01) **! CAUTION** Glutaraldehyde is toxic if swallowed; it causes serious skin damage, and acute and chronic toxicity in aquatic life. Avoid breathing the fumes or dust. Wear protective equipment and handle the compound under a chemical hood.
- $\alpha$ -Tubulin (YL1/2) antibody (Thermo Fisher Scientific, cat. no. MA1-80017)
- $\alpha$ -Tubulin (DM1A) mouse antibody (Cell Signaling, cat. no. 3873S)
- Tom20 (FL-145) rabbit antibody (Santa Cruz, cat. no. sc-11415)
- DNA-labeled secondary antibodies and imager kit (Ultivue, cat. no. U10001)
- Imager strand (P1-Cy3B: CTAGATGTAT-Cy3B; Eurofins Genomics)
- Imager strand (P3-Atto655: GTAATGAAGA-Atto655; Eurofins Genomics)
- Imager strand (P3-Cy3B: GTAATGAAGA-Cy3B; Eurofins Genomics)

#### Cell culture

- PBS, pH 7.2 (Thermo Fisher Scientific, cat. no. 20012-019)
- MEM (Thermo Fisher Scientific, cat. no. 31095-052)
- Eagle's Minimum Essential Medium (EMEM; ATCC, cat. no. 30-2003)
- L-Glutamine (Thermo Fisher Scientific, cat. no. 25030-149)
- Non-essential amino acids (Thermo Fisher Scientific, cat. no. 11140-035)
- FBS (Thermo Fisher Scientific, cat. no. 10500-064)
- Penicillin-streptomycin (P/S; Thermo Fisher Scientific, cat. no. 15140-122) **! CAUTION** It may damage fertility and cause harm to the unborn child. Avoid breathing fumes or dust.
- Trypsin-EDTA (Thermo Fisher Scientific, cat. no. 25300-054)

- HELA cell line (Leibniz Institute DSMZ: Catalogue of Human and Animal Cell Lines (<http://www.dsmz.de>), cat. no. ACC-57) **! CAUTION** The cell lines used in your research should be regularly checked to ensure that they are authentic and they are not infected with mycoplasma.
- BS-C-1 cell line (ATCC, cat. no. CCL-26) **! CAUTION** The cell lines used in your research should be regularly checked to ensure that they are authentic and they are not infected with mycoplasma.

#### DNA origami folding

- Staple strands, modified and unmodified (Eurofins Genomics)
- M13 bacteriophage ssDNA scaffold p7249 (New England BioLabs, cat. no. N4040S)
- Tris, pH 8.0, 1 M (Ambion, cat. no. AM9856) **! CAUTION** Tris can cause skin and serious eye irritation.
- EDTA, pH 8.0, 0.5 M (Ambion, cat. no. AM9261) **! CAUTION** EDTA may cause eye and skin irritation; avoid breathing the dust or fumes.
- Water (Gibco, cat. no. 10977-035)
- Magnesium, 1 M (Ambion, cat. no. AM9530G)
- Agarose (Biomol, cat. no. 01280.100)
- 50 $\times$  TAE Buffer (Fluka Analytical, cat. no. 67996-10L-F)
- SYBR safe DNA gel stain (Invitrogen, cat. no. S33102) **! CAUTION** Protect your eyes and avoid breathing the dust, fumes or mist; it causes eye, skin and respiratory irritation.
- DNA gel loading dye (Thermo Fisher Scientific, cat. no. R0611)
- DNA ladder (Invitrogen, cat. no. 10787-018)

#### In vitro sample preparation

- Protocatechuic acid (PCA; Sigma-Aldrich, cat. no. 37580-25G-F) **! CAUTION** PCA causes skin, respiratory pathway and serious eye irritation. Avoid breathing the dust, fumes or mist.
- Protocatechuate 3,4-dioxygenase (PCD; Sigma-Aldrich, cat. no. P8279-25UN)
- Trolox (Sigma-Aldrich, cat. no. 238813-1G) **! CAUTION** Trolox causes skin, respiratory pathway and serious eye irritation. Avoid breathing the dust, fumes or mist.
- NaOH (VWR, cat. no. 31627.290) **! CAUTION** NaOH causes serious skin and eye damage; avoid breathing the dust, fumes or mist. Wear protective equipment.
- Methanol (Sigma-Aldrich, cat. no. 32213-2.5L) **! CAUTION** Methanol is a flammable liquid, and it is toxic upon ingestion and skin contact; avoid breathing the dust, fumes or mist.
- Potassium chloride (Carl Roth, cat. no. 6781.1)
- Glycerol (Sigma-Aldrich, cat. no. 65516-500ml)
- Isopropanol (Carl Roth, cat. no. 33539-2.5L-R) **! CAUTION** Vapor and liquid phases are easily flammable, and the compound causes heavy eye irritation.
- Epoxy Glue (Toolcraft, cat. no. TC-EPO5-24)
- Albumin, biotin-labeled bovine (Sigma-Aldrich, cat. no. A8549-10MG)
- Streptavidin (Thermo Fisher Scientific, cat. no. S888)
- Tween 20 (Sigma-Aldrich, cat. no. p2287)

#### EQUIPMENT

- Thermocycler (Mastercycler Nexus Gradient; Eppendorf, cat. no. 6331000017)
- 10-liter Tank (Carl Roth, cat. no. K653.1)
- Sub-cell GT system gel chamber (Bio-Rad, cat. nos. 170 4401-4406 and 170 4481-4486)
- PowerPac basic power supply (Bio-Rad, cat. no. 1645050)
- Microwave (Severin, cat. no. 7891)
- Erlenmeyer flask, 250 ml (Carl Roth, cat. no. NY87.1)
- Razor blade (Carl Roth, cat. no. CK07.1)
- Visi-blue light transilluminator (UVP, cat. no. 95-0461-02)
- Centrifuge 5430R (Eppendorf, cat. no. 5428000414)
- NanoDrop 2000c (Thermo Fisher Scientific, cat. no. ND-2000c)
- Shaker (GFL, cat. no. 3015)
- Biological safety cabinet (HeraSafe; Thermo Electron Corporation, cat. no. 51022482)
- Water purification system (PURELAB classic; ELGA LabWater, cat. no. CLXXUVFM2)
- Incubator (Heracell 240; Thermo Fisher Scientific, cat. no. 51026333)
- Pipetboy acu 2 (Integra, cat. no. 155017)
- Eppendorf Research plus 0.1–2.5  $\mu$ l pipette (Eppendorf, cat. no. 3120000011)
- Eppendorf Research plus 0.5–10  $\mu$ l pipette (Eppendorf, cat. no. 3120000020)
- Eppendorf Research plus 2–20  $\mu$ l pipette (Eppendorf, cat. no. 3120000038)
- Eppendorf Research plus 10–100  $\mu$ l pipette (Eppendorf, cat. no. 3120000046)

- Eppendorf Research plus 20–200  $\mu$ l pipette (Eppendorf, cat. no. 312000054)
- Eppendorf Research plus 100–1000  $\mu$ l pipette (Eppendorf, cat. no. 312000062)
- Multipette M4 pipette (Eppendorf, cat. no. 4982000314)
- Eppendorf Research plus, 8-channel, 0.5–10  $\mu$ l pipette (Eppendorf, cat. no. 3122000019)
- Gel imager (Typhoon FLA 9500; GE, cat. no. 28996943)
- Side cutter (Hoffmann Group, cat. no. 725310)
- Amicon spin filters, 3 kDa (Merck/EMD Millipore, cat. no. UFC500396)
- Amicon spin filters, 100 kDa (Merck/EMD Millipore, cat. no. UFC510096)
- Nap5 columns (GE Healthcare, cat. no. 17-0853-02)
- Zeba desalting spin columns (Thermo Fisher Scientific, cat. no. 89882)
- Amicon spin filters, 100 kDa (Merck/EMD Millipore, cat. no. UFC510096)
- NORM-JECT 2-ml syringe (Henke Sass Wolf, cat. no. 4020-000V0)
- NORM-JECT 10-ml syringe (Henke Sass Wolf, cat. no. 4100-000V0)
- NORM-JECT 20-ml syringe (Henke Sass Wolf, cat. no. 4200-000V0)
- FINE-JECT Needle, 1.2  $\times$  40 mm (Henke Sass Wolf, cat. no. 4710012040)
- FINE-JECT Needle, 1.1  $\times$  40 mm (Henke Sass Wolf, cat. no. 4710011040)
- Silicon tubing, inner diameter = 0.5 mm, outer diameter = 1 mm (GM GmbH, cat. no. 35605)
- T75 Flasks (Falcon, cat. no. 353136)
- 10-ml Serological pipettes (Greiner Bio-One, cat. no. 607180)
- 5-ml Serological pipettes (Greiner Bio-One, cat. no. 606180)
- 2-ml Serological pipettes (Falcon, cat. no. 357507)
- Glass Pasteur pipettes (Brand, cat. no. 747720)
- 90-nm Gold particles (prepared in house<sup>83</sup>)
- DNA LoBind Tube, 0.5 ml (Eppendorf, cat. no. 0030 108.035)
- PCR tubes (Trefflab, cat. no. 96.09852.9.01)
- Freeze 'N Squeeze columns (Bio-Rad, cat. no. 732-6165)
- Aluminum foil (VWR, cat. no. 391-1257)
- 1.5-ml Eppendorf tubes (Eppendorf, cat. no. 0030 120.086)
- 15-ml Falcon tubes (Falcon, cat. no. 352096)
- 50-ml Falcon tubes (Falcon, cat. no. 352070)
- ibidi sticky-Slide VI 0.4 (ibidi, cat. no. 80608)
- High-precision cover glasses 18  $\times$  18 mm, no. 1.5H (Marienfeld, cat. no. 0107032)
- High-precision cover glasses 24  $\times$  60 mm, no. 1.5H (Marienfeld, cat. no. 0107242)
- Microscopy slide (Thermo Fisher Scientific, cat. no. 10756991)
- Double-sided adhesive tape (Scotch, cat. no. 665D)
- Weighing paper (VWR International, cat. no. 12578-121)

#### TIRF super-resolution setup

- Optical air table (Newport, cat. no. RS4000-46-12)
- Inverted fluorescence microscope (Nikon, Ti Eclipse with Perfect Focus System)
- XY Stage (Physik Instrumente, cat. no. M-545.2MN)
- Lenses and mirrors (Thorlabs)
- Filter cubes (Chroma Technology, cat. nos. TRF49904-NK, TRF49909-NK, TRF49914-NK)
- Oil-immersion objective, 100 $\times$  Apo SR TIRF objective, numerical aperture (NA) = 1.49, working distance (WD) = 0.12 (Nikon)
- Immersion oil, refractive index ( $n$ ) = 1.515 (23  $^{\circ}$ C), (Nikon, Type A)
- sCMOS camera (Hamamatsu Orca Flash 4.0 V2)
- EMCCD camera (Andor, iXon Ultra, model no. DU-897)
- Excitation laser, 488 nm, 200 mW (Toptica iBeam smart, model no. 488-S-HP)
- Excitation laser, 561 nm, 200 mW (Coherent Sapphire, model no. 561-200 CW CDRH)
- Excitation laser, 640 nm, 150 mW (Toptica, iBeam smart, model no. 640-S)
- Microscopy slide thermal power sensor (Thorlabs, model no. S170C)
- Digital power meter (Thorlabs, model no. PM100D)
- Acquisition computer: a computer used to acquire microscope data with the  $\mu$ Manager software package<sup>58</sup>. See EQUIPMENT SETUP for hardware requirements.
- Analysis computer: a computer with a Microsoft Windows 64-bit operating system. See EQUIPMENT SETUP for hardware requirements.
- Analysis software: our analysis software package 'Picasso' can be downloaded from our website at <http://www.jungmannlab.org>.

#### REAGENT SETUP

**Pre-extraction buffer** The pre-extraction buffer consists of 0.4% (vol/vol) glutaraldehyde and 0.25% (vol/vol) Triton X-100 in 1 $\times$  PBS at pH 7.2. It can be stored at  $-20^{\circ}$  C for 12 months.

**Enhanced microtubule fixative** The enhanced microtubule fixative consists

of 3% (vol/vol) glutaraldehyde in 1 $\times$  PBS at pH 7.2, and it can be stored at  $-20^{\circ}$  C for 12 months.

**Standard fixative** The standard fixative consists of 3% (vol/vol) paraformaldehyde and 0.1% (vol/vol) glutaraldehyde in 1 $\times$  PBS at pH 7.2. It can be stored at  $-20^{\circ}$  C for 12 months.

**Blocking solution** The blocking solution contains 3% (wt/vol) BSA and 0.2% (vol/vol) Triton X-100 in 1 $\times$  PBS at pH 7.2, and it must be filter-sterilized. It can be stored at 4  $^{\circ}$ C for up to 6 weeks.

**Antibody dilution solution** The antibody dilution solution contains 3% (wt/vol) BSA in 1 $\times$  PBS at pH 7.2, and it must be filter-sterilized. It can be stored at 4  $^{\circ}$ C for up to 6 weeks.

**DTT solution** The DTT solution consists of 250 mM DTT, 1.5 mM EDTA and 0.5 $\times$  PBS, pH 7.2. It must be freshly prepared for the reduction of the thiolated DNA.

**BCA mix** The BCA mix includes 500  $\mu$ l of reagent A, 500  $\mu$ l of reagent B and 25  $\mu$ l of reagent C (from the Micro BCA Protein Assay Kit), and it must be freshly prepared.

**HeLa cell medium** The HeLa cell medium consists of MEM, 10% (vol/vol) FCS, 1% (vol/vol) P/S, 2 mM L-glutamine and 1 $\times$  non-essential amino acids. HeLa cell medium can be stored at 4  $^{\circ}$ C for up to 4 months.

**BSC1 cell medium** The BSC1 cell medium consists of EMEM, 10% (vol/vol) FCS and 1% (vol/vol) P/S.

**Cross-linker aliquots** Cross-linkers should be divided into aliquots at a concentration of 10 mg/ml in DME, and they can be stored at  $-80^{\circ}$  C for up to 12 months.

**Buffer A** Buffer A consists of 10 mM Tris-HCl and 100 mM NaCl at pH 8.0, and it can be stored at room temperature (RT; 21  $^{\circ}$ C) for 6 months.

**Buffer A+** Buffer A+ consists of 10 mM Tris-HCl, 100 mM NaCl and 0.05% (vol/vol) Tween 20 at pH 8.0, and it can be stored at RT for 6 months.

**Buffer B** Buffer B consists of 5 mM Tris-HCl, 10 mM MgCl<sub>2</sub> and 1 mM EDTA at pH 8.0, and it can be stored at RT for 6 months.

**Buffer B+** Buffer B+ consists of 5 mM Tris-HCl, 10 mM MgCl<sub>2</sub>, 1 mM EDTA and 0.05% (vol/vol) Tween 20 at pH 8.0, and it can be stored at RT for 6 months.

**Buffer C** Buffer C consists of 1 $\times$  PBS at pH 7.2 supplemented with additional 500 mM NaCl, and it can be stored at RT for up to 6 months.

**Exchange washing buffer** Exchange washing buffer consists of Buffer B+ for *in vitro* samples and of 1 $\times$  PBS, pH 7.2, for *in situ* samples; it can be stored at RT for 6 months.

**100 $\times$  Trolox solution** 100 $\times$  Trolox solution consists of 100 mg of Trolox, 430  $\mu$ l of methanol and 345  $\mu$ l of NaOH (1 M) in 3.2 ml of H<sub>2</sub>O. It should be divided into 20- $\mu$ l portions in PCR tubes and can be stored at  $-20^{\circ}$  C for up to 6 months.

**40 $\times$  PCA solution** 40 $\times$  PCA solution consists of 154 mg of PCA in 10 ml of water, adjusted to pH 9.0 with NaOH. The solution should be divided into 20- $\mu$ l aliquots in PCR tubes and can be stored at  $-20^{\circ}$  C for up to 6 months.

**100 $\times$  PCD solution** 100 $\times$  PCD solution consists of 9.3 mg of PCD and 13.3 ml of buffer (50% glycerol stock in 50 mM KCl, 1 mM EDTA and 100 mM Tris-HCl, pH 8.0). It should be divided into 20- $\mu$ l aliquots in PCR tubes and can be stored at  $-20^{\circ}$  C for up to 6 months.

**Oxygen-scavenging system PPT solution** PPT solution consists of a 1:1:1 ratio of 1 $\times$  PCA/1 $\times$  PCD/1 $\times$  Trolox. Mix with imaging buffer at least 1 h before imaging.

**Imager solution** For *in vitro* samples, the imager solution consists of 1 $\times$  Buffer B+, optional scavenger system PPT solution (1 $\times$  Buffer B+, 1 $\times$  PCA, 1 $\times$  PCD, 1 $\times$  Trolox) and a fluorophore-labeled DNA strand. For *in situ* samples, the imager solution consists of 1 $\times$  Buffer C, optional scavenger system PPT solution (1 $\times$  Buffer C, 1 $\times$  PCA, 1 $\times$  PCD, 1 $\times$  Trolox) and a fluorophore-labeled DNA strand. The concentration range for the fluorophore-labeled DNA strand is highly target dependent, but it ranges between 100 pM and 10 nM. The solution should always be freshly prepared.

**10 $\times$  Folding buffer** 10 $\times$  folding buffer consists of 125 mM MgCl<sub>2</sub>, 100 mM Tris and 10 mM EDTA at pH 8.0, and it can be stored at RT for up to 6 months.

**Gel buffer** Gel buffer consists of 1 $\times$  TAE buffer, and it can be stored at RT for 1 year.

**Gel running buffer** Gel running buffer consists of 1 $\times$  TAE buffer and 12.5 mM MgCl<sub>2</sub>, and it can be stored at RT for up to 1 year.

**BSA-biotin stock** BSA-biotin stock contains 10 mg/ml BSA-biotin in Buffer A, and it should be divided into 20- $\mu$ l aliquots. It can be stored at  $-20^{\circ}$  C for up to 6 months.

## PROTOCOL

**BSA–biotin solution** BSA–biotin solution contains 1 mg/ml BSA–biotin in Buffer A+ and should be freshly prepared. It can be stored for up to 3 d at 4 °C.

**Streptavidin stock** Streptavidin stock contains 10 mg/ml streptavidin in Buffer A and should be divided into 10- $\mu$ l aliquots. It can be stored at –20 °C for up to 6 months.

**Streptavidin solution** Streptavidin solution contains 0.5 mg/ml streptavidin in Buffer A+ and should be freshly prepared. It can be stored for up to 3 d at 4 °C.

**Staple strands** Staple strands can be ordered in different purity grades.

High-purity salt-free purification is sufficient for standard staples; however, we recommended ordering modified staples, such as those with fluorophores or biotins, HPLC or PAGE purified. Staple strands for nanostructures should be ordered in 96-well plates (0.2 ml) to facilitate the handling and creation of master mixes with the help of multipipettes. To keep the manual handling to a minimum, the staples should be ordered prediluted at a concentration of 100  $\mu$ M in H<sub>2</sub>O. The plates can be stored at –20 °C for at least 12 months.

### EQUIPMENT SETUP

**Acquisition computer** The following computer system was used for all data acquisition in this protocol: Dell Precision T7910, Dual Intel Xeon Processor E5-2620 v3 at 2.4 GHz (12 cores), 32 GB RAM, four 2 TB HDD configured in a Hardware RAID 0, Windows 7 Professional 64-bit operating system.

▲ **CRITICAL** A RAID 0 setup is optimized for fast input/output. For long-term data storage, users are advised to use data storage facilities with daily backup available to research groups at universities or research institutes.

**Acquisition software** As image acquisition software, install  $\mu$ Manager, an open-source software<sup>38</sup> that can be downloaded from <https://micro-manager.org>. Follow the installation instructions and set up the software to control the microscope equipment.

**Analysis computer** We do recommend performing all postacquisition steps with Picasso on a separate analysis workstation. The hardware requirements depend on the specific file size of the data set to be analyzed. Generally, the most important factors are the number of available CPU cores and RAM. The following system was used for all analyses in this protocol: Dell Precision T7910, Dual Intel Xeon CPU E5-2680 v3 at 2.5 GHz (24 cores), 256 GB RAM and four 2 TB HDD configured in a Hardware RAID 0, Windows Server 2012 R2 64-bit operating system. ▲ **CRITICAL** A RAID 0 setup is optimized for fast input/output. For long-term data storage, users are advised to use data storage facilities with daily backup available to research groups at universities or research institutes.

**Analysis software** Download the ‘Picasso’ installer available at our website (<http://www.jungmannlab.org>). Follow the installation instructions. Multiple Picasso components will appear as shortcuts in a start menu subfolder named ‘Picasso’.

**Power density calibration** Determine the laser power at the sample by placing the microscopy slide thermal power sensor with immersion oil on the sample holder. The power density is then calculated as an average density over the illuminated area. See **Supplementary Table 1** for an exemplary calibration on our microscope.

**Fluid exchange chamber** To prepare a fluid exchange chamber for *in situ* imaging, see **Box 1**.

## PROCEDURE

### Design of DNA nanostructures ● TIMING 1 h

1| Start ‘Picasso: Design’, which displays a canvas of a hexagonal lattice, representing the staple strand positions (**Fig. 6**) in a 2D RRO<sup>33</sup>.

2| Design a pattern of DNA-PAINT binding sites by clicking on the canvas hexagons. Clicking on a hexagon will change its color and marks the respective staple to be extended with an external sequence. Each color corresponds to a specific extension that may be defined later. The default state without an external extension is indicated by a gray hexagon. The center-to-center distance between two hexagons is ~5 nm on the DNA origami. To change the ‘current color’, click on a colored hexagon in the color palette to the right. Clicking on a hexagon with a currently selected color will reset the ‘current color’ to the unmarked state (gray). Click ‘Clear’ to reset all hexagons in the lattice. The eight white double-hexagons within the structure are placeholders for biotinylated staples for surface attachment and are not intended for modification. In total, the structure consists of 176 staples available for modification.

3| Click ‘Save’ to save the design. Progress can be saved at any time and loaded at a later point by selecting ‘Load’. A screenshot of the design can be saved by clicking on ‘Screenshot’.

4| Click on ‘Extensions’ to specify the extensions corresponding to each color. A table with all the colors present in the design will open. A selection of commonly used DNA-PAINT handles can be obtained via the dropdown menu in the ‘Preselection’ column. This list can be extended by modifying ‘paint\_sequences.csv’ in the subfolder ‘picasso’ of the Picasso install directory. See **Supplementary Table 2** for a table of the default sequences. Alternatively, define a custom ‘Shortname’ and ‘Extension’ by entering them in the table. After defining all colors used in the canvas, select ‘OK’ to confirm the extensions. The display will update with the ‘Shortname’. The sequence specified will be added to the 3’-end of the staple and will point out of the structure (away from the cover glass). For a full list of all unmodified core staples, refer to **Supplementary Table 3**.

5| Once the design step is complete, the sequences for the corresponding structure need to be obtained. Click on ‘Get plates’ to generate a staple list for ordering. As an RRO origami structure consists of 184 staples, the staples in the list are arranged in two 96-well plates, so that each well corresponds to a position on the hexagonal lattice. It is possible to export only the sequences of a particular structure (in total, two plates) or to get a list of plates for which all possible positions are extended with all extensions used in the design. This is particularly useful in the case in which different origami designs with different extensions and patterns will be tested, so all staples are ready to be mixed and matched for subsequent design iterations. The software will export the list in .csv format, so that the file can be used for direct ordering at your favorite oligo synthesis company. Choose high-purity salt-free purification and order oligonucleotides in solution with a

concentration of 100  $\mu\text{M}$  in  $\text{H}_2\text{O}$  (see also Reagent Setup). Store the .csv file in a folder so that the program can later create pipetting schemes based on your plate stock. In addition, order the biotinylated staples (for cover glass attachment of the DNA origami) that can be found in **Supplementary Table 4**.

■ **PAUSE POINT** Typically, synthesis of unmodified oligonucleotides at a commercial vendor will take between 2 and 10 working days.

### Folding of DNA structures ● TIMING 6–7 h

6| Once all sequences are obtained, staples with the same extension are pooled together from plates and placed in microcentrifuge tubes as stock mixes. Picasso will generate a visual pipetting aid to help identify which staples need to be pooled together in a separate microcentrifuge tube. To so initiate this, select 'Pipetting scheme' and select the folder with all previously generated plates. 'Picasso: Design' will search in all .csv files in that folder for sequences that are needed for the design. Note that only .csv files that contain staple lists (that were generated with 'Get plates' in 'Picasso: Design') should be present in that folder. A list will be generated with all necessary sequences and the visual pipetting aid in .pdf format for the origami stock mixes. The dimensions of the printed pipetting scheme match those of typical 96-well plates, so that wells that need to be pipetted can be easily identified.

▲ **CRITICAL STEP** If the software does not find all sequences that are needed in the plate list, it will display an error message but still compile the pipetting aid and the staple list. Missing staples are indicated by 'NOT FOUND' in the list.

7| Print out the pipetting aid and place a transparent 96-well plate above it. Pool staples according to their color and the pipetting aid for stock mixes in microcentrifuge tubes. The volume of each staple that is needed when pooling can be estimated considering the final amount of structures. When folding, i.e., 40  $\mu\text{l}$  of DNA origami with a 10-nM final scaffold concentration (enough for ~80 DNA-PAINT experiments), the amount of staples needed is ~0.04  $\mu\text{l}$  for each core staple and ~0.4  $\mu\text{l}$  for each extended staple. As pipetting precision decreases with small volumes, pipette at least 1  $\mu\text{l}$  per staple when pooling for mixes. Avoid contamination of the plates, do not talk while pipetting and cover the plates whenever possible. Seal the plates immediately after use. Store mixes at  $-20\text{ }^\circ\text{C}$  in tubes for up to 12 months.

8| Select 'Folding Scheme' to generate a table with a folding protocol. Adjust the initial concentrations in the table according to the ordered stocks and click 'Recalculate', if applicable. The software will automatically calculate the concentration of a strand in a staple mix depending on the number of staples in the mix. Adjust 'Excess' or 'Total Volume' to your needs and mix all items on the folding scheme list in the calculated quantities. Refer to **Supplementary Table 5** for an exemplar folding table.

9| Use a thermocycler and fold the origami mix using the following thermal gradient:

Cycle number	Parameters
1	80 $^\circ\text{C}$
2–57	60 $^\circ\text{C}$ –4 $^\circ\text{C}$ , 3 min 12 s per $^\circ\text{C}$
58	Hold at 4 $^\circ\text{C}$

■ **PAUSE POINT** The structures can be stored at 4  $^\circ\text{C}$  for up to 1 week or at  $-20\text{ }^\circ\text{C}$  in DNA LoBind Tubes for long-term storage (at least several months).

### Purification of DNA nanostructures ● TIMING ~3.5 h

10| Purify the DNA nanostructures using your favorite method. Several methods for purification of DNA nanostructures, such as Gel<sup>42</sup>, rate-zonal centrifugation<sup>43</sup> and PEG<sup>44</sup>, are described in the literature. For DNA-PAINT, it is possible in most cases to use the structures without purification, as excess staple strands will be washed out of the flow chamber.

▲ **CRITICAL STEP** When folding DNA origami for the first time, it is recommended to run an agarose gel to confirm the folding (**Fig. 6**). Typically, well-folded monomeric structures will appear as a single sharp gel band (upper highlighted area in the gel in **Fig. 6**) together with a faster migrating band consisting of excess staple strands (lower highlighted area in the gel in **Fig. 6**).

■ **PAUSE POINT** The structures can be stored at 4  $^\circ\text{C}$  for up to 1 week or at  $-20\text{ }^\circ\text{C}$  in DNA LoBind Tubes for at least 1 year.

11| Prepare a solution of 1.8 g of agarose in 120 ml of gel buffer in an Erlenmeyer flask (1.5% (wt/vol)).

**PROTOCOL**

12| Use a microwave to heat up and completely solubilize the agarose solution by stirring the flask in between the heating phases.  
**! CAUTION** Use heat-resistant gloves when handling the hot flask to avoid burns.

13| If no agarose particle traces are visible anymore, let the solution cool for 1 min, and add 1.5 ml of 1M MgCl<sub>2</sub> and 14 µl of Sybr Safe.  
**! CAUTION** Avoid inhaling solutions with Sybr Safe.

14| Pour the solution into a gel chamber, add an appropriate comb and let it solidify for 45 min.

15| Load the gel with the DNA origami structures. Prepare two lanes for a DNA ladder and scaffold (same concentration as origami) as reference. Mix the origami solution with loading dye (20 µl of folded DNA Origami + 5 µl of loading dye) and run the gel in running buffer at 90 V for 90 min at 4 °C or on ice.

16| Acquire an image using a gel imager for documentation.

17| Cut out the origami band with a razor blade on a blue-light transilluminator table. The origami band should appear as a distinct band with a slight shift as compared with the scaffold. Excess staples will have created a broader band that traveled further. Crush the gel piece with a pestle, transfer it to a Freeze 'N Squeeze column, and spin it for 6 min at 1,000g at 4 °C. Keep the flow-through and discard the filter.

**? TROUBLESHOOTING**

**■ PAUSE POINT** The origami can be stored at 4 °C for 1 week or at –20 °C in LoBind tubes for long-term storage.

**Preparation of DNA origami for DNA-PAINT imaging ● TIMING ~45 min**

18| There are two options for preparing microscopy slides. See option A for the preparation in a custom-built flow chamber that will be sealed after immobilization of structures and addition of imager solution. For Exchange-PAINT experiments that require fluid exchange, see option B for preparation in an open chamber. The process of making custom-built chambers is also depicted in **Supplementary Figure 10**.

**(A) Immobilization in a custom-built chamber**

- (i) Clean the microscopy slide and the cover glass with isopropanol and dry it with lab wipes.
- (ii) Prepare a flow chamber by taping two stripes of double-sided adhesive tape ~8 mm apart on the microscopy slide and form a flow chamber by placing a cover glass on top. The resulting channel will have a volume of ~20–30 µl. Use a pipette tip and press the cover glass firmly against the sticky tape. The sticky tape will appear darker when the cover glass is in good contact.  
**▲ CRITICAL STEP** Do not use excessive force, as the glass may break.
- (iii) Remove excess adhesive tape by pulling the tape over the edges of the cover glass.
- (iv) Fill the chamber with 20 µl of BSA–Biotin solution (1 mg/ml) and incubate it for 2 min.
- (v) Wash the channel with 40 µl of Buffer A+ by holding the tip of a folded lab wipe on one end of the channel and simultaneously pipetting in washing buffer on the other side. The capillary forces of the tissue will suck the liquid out of the chamber, whereas the pipetting will introduce additional volume. Control the flow by variation of pipetting speed and tissue pressure.  
**▲ CRITICAL STEP** Avoid bubbles by keeping an even flow. Do not let the chamber dry out. Practice with an empty slide and water if necessary.
- (vi) Add 20 µl of streptavidin solution (0.5 mg/ml) to the channel and incubate it for 2 min.
- (vii) Wash the channel with 40 µl of Buffer A+.
- (viii) Wash the channel with 40 µl of Buffer B+.
- (ix) Add 20 µl of (5 µl of gel-purified DNA origami and 15 µl of Buffer B+) origami solution and incubate for 2 min.  
**? TROUBLESHOOTING**
- (x) Wash the channel with 40 µl of Buffer B+.
- (xi) Add 20 µl of imager solution to the channel.  
**▲ CRITICAL STEP** Imager concentration has a critical role in proper acquisition of DNA-PAINT data. For *in vitro* samples, consider an ~5 nM imager concentration for a DNA nanostructure with 12 binding sites as a start value.
- (xii) (Optional) For spectral multiplexing, use 2 different DNA sequences with spectrally distinct fluorophores, such as Cy3B and Atto655.
- (xiii) Use epoxy glue to seal the chamber. Pour the glue on a piece of weighing paper, mix with a pipette tip and distribute the glue evenly on the edges of the cover glass. Once the chamber is sealed, place the pipette tip standing up in the remaining epoxy to later evaluate the glue dryness.

- (xiv) Wait for ~15 min for the epoxy to dry. The drying process can be evaluated by checking the pipette tip in the epoxy. Once the epoxy is completely dry, the pipette tip should stick. The sample is now ready for imaging.

▲ **CRITICAL STEP** Wait until the epoxy is completely dry to avoid glue contamination of the microscope objective.

#### (B) Immobilization in a 6-channel ibidi sticky-Slide

- (i) Clean the cover glass (24 × 60 mm) with isopropanol and dry it with lab wipe.
- (ii) Attach the cover glass upside down to the sticky-Slide and press it with the help of a pipette tip against the cover glass.
- (iii) Add 80 μl of BSA–biotin solution to the channel. Tilt the slide slightly to ensure that the chamber is completely filled and incubate it for 5 min.
- (iv) Wash the channel with 180 μl of Buffer A+ by pipetting the solution into one opening and pipetting out 180 μl from the opposing opening.
- (v) Incubate 40 μl of streptavidin solution twice for 5 min.
- (vi) Wash the channel with 180 μl of Buffer A+.
- (vii) Wash the channel with 180 μl of Buffer B+.
- (viii) Incubate the DNA origami solution (20 μl of gel-purified DNA origami + 60 μl of Buffer B+) for 20 min.

#### ? TROUBLESHOOTING

- (ix) Wash the channel two times with 100 μl of Buffer B+.
- (x) Add Imager strand solution to the sample for imaging.
 

▲ **CRITICAL STEP** Imager concentration has a critical role in proper acquisition of DNA-PAINT data. For *in vitro* samples, consider ~5 nM for DNA nanostructures with 12 binding sites as a start value. (Optional) For spectral multiplexing, use two different DNA sequences with spectrally distinct fluorophores, such as Cy3B and Atto655.
- (xi) Put the lid back on the chamber. The sample is now ready for imaging.

#### Sample preparation for *in situ* samples

**19|** Generate DNA-conjugated secondary antibodies. Here, two methods are presented: option A describes the use of a maleimide-PEG2-succinimidyl ester cross-linker, which links free amino groups on the protein to reduced thiolated DNA<sup>22</sup>, and option B describes the use of a DBCO-sulfo-NHS ester, which binds to amino groups on the protein and via copper-free click chemistry to an azide-modified DNA strand<sup>55</sup>. The copper-free click chemistry allows for conjugation of multiple antibody species in parallel, whereas the attachment via Maleimide chemistry is more cost-effective, considering the DNA components. The reduction of the thiol group and the subsequent purification of the DNA from DTT using the Nap-5 column is time-consuming and time-critical. Long waiting times will lead to disulfide bridging of the DNA strands. The copper-free click chemistry in comparison does not have such a time-consuming and time-critical step in regard to the reagent stability, and therefore allows for parallel labeling of the antibodies. Alternatively, DNA-labeled antibodies can also be obtained from Ultivue (<http://www.ultivue.com>).

#### (A) DNA labeling of antibodies via maleimide-PEG2-succinimidyl ester for cellular labeling ● TIMING 1 d 1 h

- (i) To reduce the thiolated DNA for the Maleimide reaction, mix 30 μl of 1-mM thiolated DNA with 70 μl of freshly prepared DTT solution and incubate the mixture on a shaker for 2 h at RT covered with aluminum foil.
- (ii) Concentrate the antibody using Amicon spin filters (100 kDa). Wash the filters with 1× PBS for 10 min at 14,000g at 4 °C. Discard the flow-through, add 300 μl of antibody solution and spin at 14,000g for 5 min at 4 °C. Discard the flow-through and invert the spin filter in an empty tube. Spin for 6 min at 1,000g at 4 °C. Adjust the volume to 100 μl with 1× PBS, and measure the concentration with the NanoDrop spectrophotometer. Keep the antibody on ice. The final concentration should be >1.5 mg/ml.
- (iii) Prepare the cross-linker solution in 1× PBS and add it to the antibody in a 10:1 molar ratio. Incubate the solution for 90 min at 4 °C on a shaker covered in aluminum foil. Start the reaction 1 h after the DNA reduction step was started.
 

▲ **CRITICAL STEP** The desired amount of cross-linker must be no more than 5 μl in volume in order to avoid adding too much of DMF or diluting the antibody further.
- (iv) 20 min before the DNA reduction step is completed, start to equilibrate a Nap-5 column with ddH<sub>2</sub>O filled to the top three times. Add DNA–DTT solution to the column and immediately add 400 μl of ddH<sub>2</sub>O. After 400 μl has passed through, add 1 ml of ddH<sub>2</sub>O and start collecting fractions immediately. Collect three drops in the first four tubes, two drops in the following four and one drop in the last eight tubes. Starting from the last collected tube, add 25 μl of BCA mix to the tubes. If DTT is still present, the solution turns purple. Discard those tubes. If no color change is visible anymore, discard the next tube as well and measure the concentration of the remaining fractions via the NanoDrop spectrophotometer. Pool the fractions with the highest concentrations. The highest fractions will have a DNA concentration between 200 and 800 ng/μl.
 

▲ **CRITICAL STEP** If DTT is still present in the DNA solution, it will interfere with the Maleimide reaction.

**PROTOCOL**

- (v) Concentrate the reduced DNA using Amicon spin filters (3 kDa). Wash the filter with 1× PBS for 30 min at 14,000g at 4 °C. Discard the flow-through and add the pooled fractions of reduced DNA to the filter. Centrifuge for 30 min at 14,000g at 4 °C and discard the flow-through. Invert the spin filter in an empty new tube and spin for 6 min at 1,000g at 4 °C. Measure the concentration with the NanoDrop spectrophotometer; the DNA should have a concentration >700 ng/μl.
- (vi) After the antibody–cross-linker reaction has completed, use a Zeba desalting column to remove the linker. Remove the storage solution by centrifugation at 1,500g for 1 min at 4 °C. Mark the side where the resin slid up, and perform the subsequent centrifugation steps in the same orientation. Wash the Zeba column with 300 μl of PBS and centrifuge it at 1,500g for 1 min at 4 °C. Dry the bottom of the column and use a fresh 1.5-ml tube. Add the antibody–cross-linker solution to the Zeba column, and spin at 1,500g for 2 min at 4 °C. Discard the Zeba column, retain the flow-through and measure the concentration with the NanoDrop spectrophotometer. The antibody concentration should be > 1.5 mg/ml.
- (vii) Incubate a 10:1 molar ratio of thiolated DNA to antibody overnight on a shaker covered in aluminum foil in a cold room.
- (viii) Remove excess DNA by Amicon spin filtration (100 kDa). For this, wash the filters with 1× PBS for 10 min at 14,000g at 4 °C. Discard the flow-through, add antibody–DNA solution, add 300 μl PBS and spin at 14,000g for 5 min at 4 °C. Discard the flow-through and invert the spin filter into an empty tube. Spin the solution for 6 min at 1,000g at 4 °C. Adjust the volume to 100 μl with 1× PBS, and measure the concentration with the NanoDrop spectrophotometer. The peak signal should be shifted toward 260 nm from 280 nm, and the concentration should be >5 mg/ml because of the stronger absorbance of DNA. Keep the antibody on ice and store it at 4 °C for a maximum of 6 months.

**? TROUBLESHOOTING****(B) Labeling via DBCO-sulfo-NHS ester ● TIMING 4 h**

- (i) Concentrate the antibody using Amicon spin filters (100 kDa). For this, wash the filters with 1× PBS for 10 min at 14,000g at 4 °C. Discard the flow-through, add 300 μl of antibody solution and spin at 14,000g for 5 min at 4 °C. Discard the flow-through and invert the spin filter in an empty tube. Spin for 6 min at 1,000g at 4 °C. Adjust the volume to 100 μl with 1× PBS, and measure the concentration with the NanoDrop spectrophotometer. Keep the antibody on ice. The final concentration should be >1.5 mg/ml.
- (ii) Prepare 5 μl of cross-linker solution in 1× PBS so that the final solution after addition of 100 μl of the antibody contains a 10:1 molar ratio of cross-linker to antibody. Incubate the solution for 90 min at 4 °C on a shaker covered in aluminum foil.
- (iii) After the antibody–cross-linker reaction is completed, use a Zeba desalting column to remove the linker. Remove the storage solution by centrifugation at 1,500g for 1 min at 4 °C. Mark the side where the resin slid up, and perform the subsequent centrifugation steps in the same orientation. Wash the Zeba column with 300 μl of 1× PBS at 1,500g for 1 min at 4 °C. Dry the bottom of the column and use a fresh 1.5-ml tube. Add antibody–cross-linker solution to the Zeba column and spin it at 1,500g for 2 min at 4 °C. Discard the Zeba column, retain the flow-through and measure the concentration on the NanoDrop spectrophotometer. The antibody concentration should be >1.5 mg/ml.
- (iv) Create a 15:1 molar ratio of DNA to antibody and incubate the solution for 1 h at RT on a shaker covered in aluminum foil.
- (v) Remove the excess DNA by Amicon spin filtration (100 kDa). For this, wash the filters with 1× PBS for 10 min at 14,000g at 4 °C. Discard the flow-through, add antibody–DNA solution, add 300 μl of 1× PBS and spin at 14,000g for 5 min at 4 °C. Discard the flow-through and invert the spin filter in an empty tube. Spin for 6 min at 1,000g at 4 °C. Adjust the volume to 100 μl with 1× PBS, and measure the concentration with the NanoDrop spectrophotometer. The peak signal should be shifted toward 260 nm from 280 nm, and the concentration should be >5 mg/ml because of the stronger absorbance of DNA.

**? TROUBLESHOOTING**

■ **PAUSE POINT** Keep the antibody on ice and store it at 4 °C for a maximum of 6 months.

**Immunofixation of cells ● TIMING 2.5 h**

▲ **CRITICAL** In Steps 20–33, we describe procedures for immunofixation optimized for DNA-PAINT super-resolution microscopy. Fixation strategies depend on the target of interest, as well as on the antibody-recognition motifs<sup>57</sup>.

20| Seed 30,000 cells in 8-well chambered cover glasses, and let them grow overnight at 37 °C and 5% CO<sub>2</sub> in an incubator.

21| After 24 h, the cells are ready to be fixed.

22| In this step, fixative is added to the cells; this can be performed in two ways: option A, an optimized protocol for maximum preservation of cellular cytoskeletal structures (recommended for imaging microtubules) and option B, a standard protocol.

**(A) Optimized microtubule fixation**

- (i) Pre-extract the cells with prewarmed (37 °C for 10 min) pre-extraction buffer for 90 s.
- (ii) Remove the extraction buffer and fix the cells for 15 min in prewarmed enhanced microtubule fixative.

**(B) Standard fixation**

- (i) Fix the cells in standard fixative for 15 min.

23| Aspirate the fixative solution and reduce the sample with 1 mg/ml sodium borohydride for 7 min.

▲ **CRITICAL STEP** Sodium borohydride must be prepared just before application to the sample and is very volatile.

24| Wash the chamber four times (1 × 20 s, 3 × 5 min) with 1× PBS at pH 7.2.

25| Block and permeabilize the cell sample in blocking buffer for 90 min at RT.

26| Dilute the primary antibody according to supplier instructions in antibody dilution buffer, and incubate the sample at 4 °C overnight on a rocking platform.

27| Wash the sample three times for 5 min in 1× PBS.

28| Dilute DNA-labeled secondary antibody (5–50 µg/ml) in antibody dilution buffer, and apply it to the sample for 60 min. (Optional) For multiplexing experiments, use different secondary antibodies with orthogonal DNA handles; see **Supplementary Table 2** for recommended sequences.

29| Wash the sample three times for 5 min in 1× PBS.

30| Dilute 90-nm gold particles at a 1:10 ratio in PBS as fiducial markers and incubate for 5 min on the cell sample.

31| Wash the sample three times for 5 min in 1× PBS.

32| Add a target-specific imager solution to the sample.

▲ **CRITICAL STEP** Imager concentration has a critical role in proper acquisition of DNA-PAINT data. The concentration should be adjusted for the target (hence docking strand) density. For microtubules, we recommend starting with a 500 pM imager strand concentration and adjusting as necessary.

33| (Optional) For multiplexed Exchange-PAINT experiments, place the exchange lid with the connected tubing on the chambered cover glass.

**Data acquisition ● TIMING 10 min to 10 hours**

▲ **CRITICAL** The following section describes the procedure for performing DNA-PAINT experiments using imager sequences labeled with Cy3B fluorophores. As the SNR for DNA-PAINT is rather high, both CCD or sCMOS cameras are suitable for imaging. The procedure is written for use of an iXon Ultra DU-897 EMCCD camera, although electron-multiplying is not necessary. Considerations in regard to acquisition of images with ultra-high resolution are described in **Box 2**. For test purposes, raw DNA-PAINT data can also be simulated *in silico* with 'Picasso: Simulate' (see **Box 3** for procedure details).

34| Place the sample on the microscope stage, and move the objective up until the immersion oil touches the sample.

35| (Optional) For multiplexing with Exchange-PAINT, attach tubing with syringes to the exchange chamber. Consider using an ~15-ml syringe volume of exchange buffer per exchange round for *in situ* exchange experiments, and ~1 ml of exchange buffer per exchange round for *in vitro* experiments. For *in situ* experiments, additionally attach tubing to the chamber inlet. Put the connected syringes into plastic trays to avoid accidental fluid spills. The syringes should be at the same level as the chamber to avoid liquid exchange, as they are communicating vessels.

▲ **CRITICAL STEP** Handle liquids extremely carefully if they are close to the microscope. Improper handling and leakage can lead to damage of delicate microscope components.

36| Start µManager, select the configuration file for the camera and select 'OK'. The main window of µManager will open.

37| Set 'Exposure [ms]' with regard to the following considerations: exposure times for DNA-PAINT experiments are dependent on the imager length and concentration, the imaging buffer and the docking strand density of the target structure. Typical

## PROTOCOL

exposure times for 9-bp DNA duplexes are hundreds of milliseconds, and those for 8-bp DNA duplexes are tens of milliseconds, as they have a shorter ON-time. For the samples used in **Figure 1**, an exposure time of 300 ms for *in vitro* (Buffer B+) and 200 ms for *in situ* (Buffer C) samples was used. 'Picasso: Simulate' can be used to determine ideal exposure times for given sample parameters. As a general rule of thumb, camera integration times should be matched to mean ON-times of DNA-PAINT imager/docking duplexes for best performance; these can be experimentally determined using Picasso (see Step 69B). Refer to **Supplementary Table 6** for the acquisition settings used for the images in this protocol.

38| Open 'Tools' > 'Device Property Browser'.

39| Set the camera parameters: set 'Output\_Amplifier' to 'Conventional', set 'Region of Interest' to 'Full Image', set 'Frame Transfer' to 'On', set 'PixelFormat' to '16bit', set 'ReadMode' to 'Image' and set 'Camera shutters' to 'Open'.

40| Click on 'Live' in the main window, and the 'Snap/Live' window will appear. Select 'Autostretch' in the contrast settings. The 'Snap/Live' window should show background noise.

41| Set the laser to a low power density of 0.25 kW/cm<sup>2</sup> at the sample plane (refer to the calibration as performed in the Equipment Setup), and open the laser shutter.

### ? TROUBLESHOOTING

42| Focus the image.

▲ **CRITICAL STEP** A focused image should show blinking diffraction-limited spots, each representing the binding and unbinding of an imager strand to its target. Adjust the contrast by dragging the black and white triangles in the 'Contrast' window if needed. For prefocusing, preferably use a focus-lock system such as the Nikon Perfect Focus System or, in case of *in situ* samples, prefocus with the bright-field image.

### ? TROUBLESHOOTING

43| Increase the laser power to a power density of ~ 2.5 kW/cm<sup>2</sup> at the sample plane.

44| Adjust the laser incident angle. When starting in an epifluorescence configuration, increase the angle until total internal reflection occurs. Continue until no more light is reflected and the signal decreases. Then, go back by decreasing the angle and optimize the SNR. When imaging structures beyond the TIRF illumination range, decrease the incident angle—potentially moving to oblique (HILO) illumination<sup>31</sup>—just until the structure of interest is properly illuminated. Keeping the incident angle as high as possible limits out-of-focus excitation above the target structure, which is particularly critical for DNA-PAINT, as free imager strands in solution increase background and therefore affect imaging quality adversely.

45| In the device manager, adjust the 'Readout Mode' to the frequency with the lowest readout noise possible for the currently selected integration time. This is usually the lowest frequency at which the readout time does not exceed the exposure time. The readout time will be displayed in 'ReadoutTime' and should be shorter than the 'Exposure' time. Please double-check that the field 'ActualInterval-ms', which denotes the true duration between two frames, does not exceed the exposure time.

46| Click on 'Multi-D-Acq.' in the main window to open the 'Multi-Dimensional Acquisition' window. Activate 'Time points' and set the 'Number' to the number of frames to be acquired—e.g., 7,500 for *in vitro* samples and 15,000 for *in situ* samples. These exemplar numbers for total acquisition frames are suggestions for initial experiments and may have to be adjusted according to the specific experiment. For a detailed discussion of optimal acquisition time, refer to Nieuwenhuizen *et al.*<sup>16</sup> and respective sections in the introduction of this protocol.

47| Set the interval to '0' and 'ms'. Set 'Acquisition Order' to 'Time'. Activate 'Save images' and set a destination filename and folder.

48| Select 'Acquire!' to start the acquisition. A live image will pop up. The progress of the acquisition can be followed on the upper left corner.

### ? TROUBLESHOOTING

49| (Optional) *Multiplexed image acquisition.* There are two methods for performing multiplexed target acquisition with DNA-PAINT. Spectral multiplexing (option A) uses spectrally distinct fluorophores, whereas Exchange-PAINT multiplexing

(option B) uses (typically) the same fluorophore attached to orthogonal DNA species that are sequentially supplied to the sample. With Exchange-PAINT, only one species is present in the imager buffer in each multiplexing round, and it will be washed out afterward. Option A provides a relatively fast workflow for imaging multiple targets by imaging in multiple emission channels. Option B has almost no limitation in multiplexing but requires a fluid exchange system. In addition, option B provides the capability of using the most favorable fluorophore for all targets. Refer to **Supplementary Table 7** for a list of dye recommendations for DNA-PAINT.

#### (A) Spectral multiplexing

- (i) Perform Steps 34–48 for the first fluorophore.
  - ▲ **CRITICAL STEP** To reduce photodamage, start acquisition with the dye that has the longest excitation wavelength, and then proceed to those with shorter wavelengths.
- (ii) After acquisition of the first imager species, change the laser line and the filter set on the microscope to match the next wavelength.
- (iii) Click on 'Live' in the main window of  $\mu$ Manager and adjust the TIRF angle if necessary.
- (iv) Adjust the file name in the 'Multi-Dimensional Acquisition' window.
- (v) Select 'Acquire!' to start a new acquisition.
- (iv) (Optional) Repeat the procedure for any other spectrally distinct imager species in solution.

#### (B) Exchange multiplexing

- (i) Perform Steps 34–48 to acquire a movie for the first imager species.
- (ii) Click on 'Live' in the main window and adjust the contrast so that individual blinking events are visible. Deselect 'Autostretch'. It is important to keep the contrast to determine when all imagers are washed out.
- (iii) Apply several washing steps while observing the 'Live/Snap' window until no more blinking events are visible. One washing step consists of filling the chamber by adding exchange buffer (for *in vitro* imaging use  $\sim 180 \mu\text{l}$ , and for *in situ* imaging use 1 ml) to the inlet and then removing the same volume from the outlet. For *in situ* imaging a total of  $\sim 15$  ml and for *in vitro* imaging a total of  $\sim 1$  ml of exchange buffer will be needed per exchange round.
  - ▲ **CRITICAL STEP** Do not remove all liquid from the chamber; it should never dry out. Perform liquid exchange slowly to avoid introducing air bubbles into the chamber or disturbing the sample.
  - ? **TROUBLESHOOTING**
- (iv) After washing, introduce a new imager solution into the chamber. For *in vitro* samples, simply pipette the required amount into the chamber and remove the same amount from the outlet. For *in situ* samples, empty the inlet tubing by disconnecting the empty syringe and pumping air through it. Connect a new 2-ml syringe with a new imager solution and fill the chamber.
- (v) While introducing the new imager, the 'Live/Snap' window should show reappearing blinking events.
- (vi) Adjust the filename in the 'Multi-Dimensional Acquisition' window.
- (vii) Select 'Acquire!' to start a new acquisition.
- (viii) (Optional) Repeat the procedure for subsequent imaging rounds.

#### Image reconstruction ● **TIMING** 5–30 min

**50| Identification and fitting of single-molecule spots.** In 'Picasso: Localize', open a movie file by dragging the file into the window or by selecting 'File' > 'Open'. If the movie is split into multiple  $\mu$ Manager .tif files, open only the first file. Picasso will automatically detect the remaining files according to their file names.

**51|** Adjust the image contrast (select 'View' > 'Contrast') so that the single-molecule spots are clearly visible.

**52|** To adjust spot identification and fit parameters, open the 'Parameters' dialog (select 'Analyze' > 'Parameters').

**53|** In the 'Identification' group, set the 'Box side length' to the rounded integer value of  $6 \times \sigma + 1$ , where  $\sigma$  is the standard deviation of the PSF. In an optimized microscope setup,  $\sigma$  is one pixel, and the respective 'Box side length' should be set to 7. The value of 'Min. net gradient' specifies a minimum threshold above which spots should be considered for fitting. The net gradient value of a spot is roughly proportional to its intensity, independent of its local background. By checking 'Preview', the spots identified with the current settings will be marked in the displayed frame. Adjust 'Min. net gradient' to a value at which only spots are detected (no background).

**54|** In the 'Photon conversion' group, adjust 'EM Gain', 'Baseline', 'Sensitivity' and 'Quantum Efficiency' according to your camera specifications and the experimental conditions. Set 'EM Gain' to 1 for conventional output amplification. 'Baseline' is

## PROTOCOL

the average dark camera count. ‘Sensitivity’ is the conversion factor (electrons per analog-to-digital (A/D) count) and ‘Quantum Efficiency’ should be set according to the average emission wavelength.

▲ **CRITICAL STEP** These parameters are critical to converting camera counts to photons correctly. The quality of the upcoming maximum likelihood fit strongly depends on a Poisson photon noise model, and thus on the absolute photon count.

For simulated data, generated with ‘Picasso: Simulate’ as described in **Box 3** and **Figure 7**, set the parameters as follows: ‘EM Gain’ = 1, ‘Baseline’ = 0, ‘Sensitivity’ = 1, ‘Quantum Efficiency’ = 1.

**55** | From the menu bar, select ‘Analyze’ > ‘Localize (Identify & Fit)’ to start spot identification and fitting in all movie frames. The status of this computation is displayed in the window’s status bar. After completion, the fit results will be saved in a new file in the same folder as the movie, in which the filename is the base name of the movie file with the extension ‘\_locs.hdf5’. Furthermore, information about the movie and analysis procedure will be saved in an accompanying file with the extension ‘\_locs.yaml’; this file can be inspected using a text editor.

**56** | *Rendering of the super-resolution image:* In ‘Picasso: Render’, open a movie file by dragging a localization file (ending with ‘.hdf5’) into the window or by selecting ‘File’ > ‘Open’. The super-resolution image will be rendered automatically. A region of choice can be zoomed into by a rectangular selection using the left mouse button. The ‘View’ menu contains more options for zooming and panning.

**57** | (Optional) Adjust rendering options by selecting ‘View’ > ‘Display Settings’. The field ‘Oversampling’ defines the number of super-resolution pixels per camera pixel. The contrast settings ‘Min. Density’ and ‘Max. Density’ define at which number of localizations per super-resolution pixel the minimum and maximum color of the colormap should be applied.

**58** | (Optional) For multiplexed image acquisition, open HDF5 localization files from other channels subsequently. Alternatively, drag and drop all HDF5 files to be displayed simultaneously.

### Image post-processing: drift correction ● **TIMING** seconds to minutes

**59** | Picasso offers two procedures to correct for drift: an RCC algorithm<sup>66</sup> (option A), and use of specific structures in the image as drift markers<sup>23</sup> (option B). Although option A does not require any additional sample preparation, option B depends on the presence of either fiducial markers or inherently clustered structures in the image. On the other hand, option B often supports more precise drift estimation and thus allows for higher image resolution. To achieve the highest possible resolution (ultra-resolution), we recommend consecutive applications of option A and multiple rounds of option B. The drift markers for option B can be features of the image itself (e.g., protein complexes or DNA origami) or intentionally included markers (e.g., DNA origami or gold nanoparticles). When using DNA origami as drift markers, the correction is typically applied in two rounds: first, with whole DNA origami structures as markers, and, second, using single DNA-PAINT binding sites as markers. In both cases, the precision of drift correction strongly depends on the number of selected drift markers.

#### (A) Redundant cross-correlation drift correction

- (i) In ‘Picasso: Render’, select ‘Postprocess’ > ‘Undrift by RCC’.
- (ii) A dialog will appear asking for the segmentation parameter. Although the default value, 1,000 frames, is a sensible choice for most movies, it might be necessary to adjust the segmentation parameter of the algorithm, depending on the total number of frames in the movie and the number of localizations per frame<sup>66</sup>. A smaller segment size results in better temporal drift resolution but requires a movie with more localizations per frame.
- (iii) After the algorithm finishes, the estimated drift will be displayed in a pop-up window and the display will show the drift-corrected image.

#### (B) Marker-based drift correction

- (i) In ‘Picasso: Render’, pick drift markers as described in Steps 61–64. Use the ‘Pick similar’ option (Step 65) to automatically detect a large number of drift markers similar to a few manually selected ones.
 

▲ **CRITICAL STEP** If the structures used as drift markers have an intrinsic size larger than the precision of individual localizations (e.g., DNA origami, large protein complexes), it is critical to select a large number of structures. Otherwise, the statistic for calculating the drift in each frame (the mean displacement of localization to the structure’s center of mass) is not valid.
- (ii) Select ‘Postprocess; > ‘Undrift from picked’ to compute and apply the drift correction.

**60** | (Optional) Save the drift-corrected localizations by selecting ‘File’ > ‘Save localizations’.

**Picking of regions of interest** ● **TIMING 5–30 min**

- 61| *Manual selection.* Open 'Picasso: Render' and load the localization HDF5 file to be processed.
- 62| Switch the active tool by selecting 'Tools' > 'Pick'. The mouse cursor will now change to a circle.
- 63| Set the size of the pick circle by adjusting the 'Diameter' field in the tool settings dialog ('Tools' > 'Tools Settings').
- 64| Pick regions of interest using the circular mouse cursor by clicking the left mouse button. All localizations within the circle will be selected for further processing.
- 65| *(Optional) Automated region of interest selection.* Select 'Tools' > 'Pick similar' to automatically detect and pick structures that have similar numbers of localizations and RMS deviation (RMSD) from their center of mass than already-picked structures. The upper and lower thresholds for these similarity measures are the respective standard deviations of already-picked regions, scaled by a tunable factor. This factor can be adjusted using the field 'Tools' > 'Tools Settings' > 'Pick similar  $\pm$  range'. To display the mean and standard deviation of localization number and RMSD for currently picked regions, select 'View' > 'Show info' and click 'Calculate info below'.
- 66| *(Optional) Exporting of pick information.* All localizations in picked regions can be saved by selecting 'File' > 'Save picked localizations'. The resulting HDF5 file will contain a new integer column 'group' indicating to which pick each localization is assigned.
- 67| *(Optional) Statistics about each pick region can be saved by selecting 'File' > 'Save pick properties'. The resulting HDF5 file is not a localization file. Instead, it holds a data set called 'groups' in which the rows show statistical values for each pick region.*
- 68| *(Optional) The picked positions and diameter itself can be saved by selecting 'File' > 'Save pick regions'. Such saved pick information can also be loaded into 'Picasso: Render' by selecting 'File' > 'Load pick regions'.*

**Additional post-processing steps**

69| Depending on the experimental goals, a variety of post-processing steps may be used. To filter localizations based on their properties, for example to remove localizations below a certain photon threshold, use option A. For investigating the statistics of DNA-PAINT binding kinetics and how to count DNA-PAINT binding sites with qPAINT<sup>22</sup>, use options B and C, respectively. Option D describes the procedure to generate an average image of multiple structures. Finally, option E describes the procedure to align images from multiplexed experiments.

**(A) Filtering of localizations** ● **TIMING 5–10 min**

- (i) Open a localization HDF5 file in 'Picasso: Filter' by dragging it into the main window or by selecting 'File' > 'Open'. The displayed table shows the properties of each localization in rows. Each column represents one property (e.g., coordinates, number of photons); see the **Supplementary Manual** for details.
- (ii) To display a histogram from values of one property, select the respective column in the header and select 'Plot' > 'Histogram' (Ctrl + h). 2D histograms can be displayed by selecting two columns (press Ctrl to select multiple columns) and then selecting 'Plot' > '2D Histogram' (Ctrl + d).
- (iii) Left-click and hold the mouse button down to drag a selection area in a 1D or 2D histogram. The selected area will be shaded in green, as shown in **Supplementary Figure 5b,c**. Each localization event with histogram properties outside the selected area is immediately removed from the localization list.
- (iv) Save the filtered localization table by selecting 'File' > 'Save'.

**(B) Analysis of blinking kinetics** ● **TIMING 5–60 min**

- (i) In 'Picasso: Render', pick regions of interest as described in Steps 61–65.
- (ii) Select 'View' > 'Show info'.
- (iii) In the opened dialog, click 'Calculate info below'. The mean and standard deviation per pick of several values will be calculated and displayed. The 'Length' row describes the blinking 'ON' time ( $\tau_b$ ) and the 'Dark time' row describes the blinking 'OFF' time ( $\tau_d$ ).
- (iv) Click 'Histograms' to open a new window showing histograms for the picked region's kinetics.
- (v) *(Optional) Individual values for each picked region can be obtained by exporting the data. Select 'File' > 'Save pick properties'. The saved HDF5 file will contain a data set called 'groups', in which each row corresponds to one pick region.*

**PROTOCOL****(C) Counting of molecule numbers with qPAINT ● TIMING 5–60 min**

- (i) In 'Picasso: Render', pick calibration regions as described in Steps 61–64. Typically, calibration regions are regions with a known number of binding sites. Do not use the option 'Pick similar' (Step 65), as this may bias the calibration.
- (ii) Select 'View' > 'Show info' and click 'Calculate info below'.
- (iii) Set '# Units per pick' to the number of units to which the counting should be calibrated. Typically, one unit is equal to one DNA-PAINT binding site, but other user-defined units might be suitable too. This could, i.e., be useful in the case in which calibration is performed on single antibodies, which can carry multiple docking strands for protein quantification using qPAINT. The final counting result will be reported in number of units. For example, if the calibration regions contain 12 binding sites and the counting result should be reported in 'number of binding sites', then '# Units per pick' should be set to 12.
- (iv) Click 'Calibrate influx' for an estimation of the influx rate from the calibration regions kinetics. The influx rate will be displayed in the respective field. As an alternative to the experimental calibration, the influx rate ( $\xi$ ) can be theoretically calculated via  $\xi = k_{\text{on}} \times c$  if the ON rate ( $k_{\text{on}}$ ) and imager concentration ( $c$ ) are known. In that case, enter the influx rate manually into the respective field.
- (v) Select 'Tools' > 'Clear picks' to remove the calibration pick selections.
- (vi) Pick structures of interest (Steps 61–65) from which the unknown number of units should be determined.
- (vii) In the 'Info' dialog, click 'Calculate info below'. The mean number of units per picked region will be displayed in the '# Units' row, as calculated from the currently displayed influx rate.
- (viii) (Optional) The individual number of units for each picked region can be obtained by exporting pick property data. Select 'File' > 'Save pick properties'. The saved HDF5 file will contain a data set called 'groups', which holds statistics about each pick region as rows, including a column for the unit number ('n\_units').

**(D) Particle averaging ● TIMING 10–30 min**

- (i) In 'Picasso: Render', pick structures to be averaged as in Steps 61–65.
- (ii) Save the picked localizations by selecting 'File' > 'Save picked localizations'.
- (iii) Load the resulting file with picked localizations into 'Picasso: Average' by selecting 'File' > 'Open' or dragging and dropping it into the window.
- (iv) 'Picasso: Average' will immediately perform a translational alignment of the picked structures and display an average image. Rotational and refined translational alignment will follow in the next steps.
- (v) Select 'Process' > 'Parameters' and adjust the 'Oversampling' parameter. We recommend choosing the highest number at which the average image still appears smooth. High oversampling values result in substantial computational time. Hence, it might be useful to first use low oversampling to generate a less-refined average image and perform a second averaging step with higher oversampling for optimized resolution.
- (vi) Adjust the number of average iterations in the 'Iterations' field. In most cases, a value of 10 is more than sufficient. If you are unsure about the computational time of the process, choose one iteration as a starting point. More iterations can be added later by repeating the processing steps. After a certain number of iterations, the average image will converge, meaning that it will not change with more iterations.
- (vii) Select 'Process' > 'Average' to perform particle averaging with the current oversampling for the set number of iterations. This step can be repeated with different settings. The program will use the current average image as a starting point.
- (viii) Once the average image has converged, save the transformed localizations by selecting 'File' > 'Save'. The resulting HDF5 localization file contains the aligned localizations in the center of the movie dimensions. It can be loaded like any other HDF5 localization file into 'Picasso: Render'.

**(E) Aligning of channels from multiplexed experiments ● TIMING 5–10 min**

- (i) To align images from multiplexed data acquisition, the images need to share some features as reference points. Such reference features can be the cell shape for *in situ* images (typically, background is higher inside the cell) or overlapping clusters (for example, on the same DNA origami). If alignment results are ambiguous or not satisfying because of the lack of inherent reference features, drift or alignment markers should be included and imaged in all channels.
- (ii) In 'Picasso: Render' display all HDF5 localization files to be aligned.
- (iii) (Optional) If the reference features are too weak to create proper alignment, they can be selected manually, as described in Steps 61–65. Ensure that within a picked region the reference structures of all channels are included.
- (iv) Select 'Postprocess' > 'Align'.
- (v) (Optional) Export the aligned localizations by selection 'File' > 'Save localizations'.

**? TROUBLESHOOTING**

Troubleshooting advice can be found in **Table 1**.

TABLE 1 | Troubleshooting table.

Steps	Problem	Possible reason	Solution
<b>Sample preparation</b>			
Step 17	There is no band visible on the gel	Depending on the used final scaffold concentration, the bands can appear very faint on the blue-light transilluminator table and seem difficult to excise	To improve brightness of the sample band, use a more sensitive DNA stain such as SYBR Gold, or increase scaffold concentration
	The structure does not fold	Thermal gradients have an important role during the assembly process of DNA nanostructures. However, the rectangle 2D origami design shows extremely robust folding behavior and forms with high yield within ~75 min	Different temperature gradients between 15 and 72 h can be used to improve folding performance. Prepare fresh staple stocks for the origami structure with particular focus on correct magnesium concentration and staple excess
Step 18A(ix), 18B(viii)	There are not enough DNA origami structures on the surface	Depending on the purification method, different origami concentrations are obtained—e.g., the size of the excised gel band will influence the concentration after the Freeze 'N Squeeze column purification step	Compensate for this by incubating with a higher origami concentration and/or increased incubation time. Concentration adjustment can be estimated by counting the number of targets on the surface and interpolating to the desired density. A good sample density can be achieved by incubation with 125–500 pM of origami. Typical concentrations after gel purification are between 1 and 2 nM, and those after PEG purification are approximately 8–10 nM. Alternatively, the DNA origami solution can be incubated longer (up to 45 min)
Step 19A(viii), 19B(v)	After purification, there still seem to be free DNA strands in solution	The DNA strands might not be completely filtered out by the spin columns, which are optimized for protein concentration	For further purification of DNA-labeled antibodies, use size-exclusion column chromatography to remove the free DNA (with a Superdex 75/200)
	Not enough DNA strands are attached to the antibodies	Not enough cross-linker or DNA was used	For more DNA handles attached to the antibodies, use larger excess of cross-linker (40×) and DNA (30×). However, please note that an increased DNA-to-antibody ratio might lead to reduced binding affinity of antibodies or increased off-target binding
<b>Data acquisition</b>			
Step 41	Poor data quality	Laser power not adjusted to sample	To achieve the best possible data quality, it is important to extract the largest possible number of photons from a single binding (blinking) event of the fluorophores. A good indicator of a suitable laser power setting can be estimated by measuring the bright time versus laser power. Increase laser power until the bright time decreases. What happens is that imager strands start to bleach while they are still bound to docking strands. This should be the upper limit of your laser power setting. When a laser power meter is available, a good reference value for power densities in DNA-PAINT experiments using, i.e., Cy3B as dye and 561-nm laser excitation is 1–6 kW/cm <sup>2</sup>
Step 42	The focal plane is difficult to find	Focusing was not performed in bright-field mode, or the immersion oil was not in contact with the cover glass.	For cellular samples, focusing should be performed in bright-field. For DNA nanostructures, the immersion oil on the objective should touch the cover glass; use oblique illumination and then slowly raise the objective until the surface of the cover glass is reached. Monitor the approach in 'Live' mode. Reaching the cover glass will be visible via an increase in fluorescence and appearance of diffraction-limited blinking spots. Add fluorescent beads that have increased brightness to find the focal plane, if necessary

(continued)

## PROTOCOL

**TABLE 1** | Troubleshooting table (continued).

Steps	Problem	Possible reason	Solution
Step 48	The sample drifts in xy and/or focus is lost during image acquisition	Setup not equilibrated	Before image acquisition, allow the sample to 'equilibrate' on the microscope for 5–15 min. Adjust room temperature to maintain a constant ambient temperature to avoid additional thermal drift of microscope and stage components
Step 49B(iii)	The imager strands are difficult to wash away	Cellular samples are highly cross-linked through the fixation process. Imager strands might be trapped in the cross-linked network	We recommend incubating with the washing solution for 3 min so that the imager strands can diffuse into the large reservoir. In addition, washing with gentle flow can be effective
<b>Box 3</b> , step 6	The simulation of a DNA-PAINT data set takes a long time	The time required to simulate data sets is dependent on the number of structures, imager concentration, frames and image size	As computation time increases with image size, it is recommended to avoid exceeding an image size of 64 × 64 pixels. A simulation with the standard settings should take <1 min on the described analysis computer

### ● TIMING

Steps 1–5, design of DNA nanostructures: 1 h

Steps 6–9, folding of DNA nanostructures: 6–7 h

Steps 10–17, purification of DNA nanostructures: ~3.5 h

Step 18, preparation of DNA origami for DNA-PAINT imaging: 45 min

Step 19A, preparation of DNA-labeled antibodies using maleimide-PEG2-succinimidyl ester: 1 d and 1 h

Step 19B, labeling via DBCO-sulfo-NHS ester: 4 h

Steps 20–33, immunofixation of cells: 2.5 d

Steps 34–49, data acquisition: 10 min to 10 h; for each multiplexing round ~20 min–2 h

Steps 50–58, image reconstruction: 5–30 min

Steps 59 and 60, drift correction: seconds to minutes

Steps 61–68, picking of regions of interest: 5–30 min

Step 69A, filtering of localizations: 5–10 min

Step 69B, analysis of blinking kinetics with qPAINT: 5–60 min

Step 69C, counting of molecule numbers with qPAINT: 5–60 min

Step 69D, particle averaging: 10–30 min

Step 69E, aligning of channels for multiplexed experiments: 5–10 min

**Box 1**, construction of a fluid exchange chamber for *in situ* imaging: 30 min

**Box 2**, ultra-resolution imaging: ~7 h

**Box 3**, *in silico* simulation of DNA-PAINT: 10–60 min

### ANTICIPATED RESULTS

Examples of single-color DNA-PAINT super-resolution images can be found in **Figure 1**. Panel **b** presents an image of a DNA origami with a three-by-four grid of binding sites, as designed with 'Picasso: Design'. Measured distances between individual binding sites are in good agreement with the designed origami. Panels **d** and **e** show a DNA-PAINT image of microtubules *in situ*, immunolabeled with primary and secondary antibodies. Hollow microtubule structures, observed here as two parallel lines because of the 2D projection, are characteristic for a high labeling density and localization precision.

Expected results for multiplexed DNA-PAINT experiments by Exchange-PAINT are shown in **Figure 2**. Panels **d**, **e** and **f** show *in vitro* DNA origami imaged with multiple 'Exchange' rounds before (**d**) and after (**e, f**) alignment. The image after alignment shows that the DNA nanostructure is in good agreement with the designed pattern of binding sites. *In situ* Exchange-PAINT images of microtubules and Tom20, which localizes to mitochondria, are shown in panel **g**. The inset in panel **g** shows gold particles imaged in both rounds and demonstrates the alignment steps for the two images. The gold particles colocalize after the alignment procedure, and the different channels do not comprise any cross talk between them.

Results for counting DNA-PAINT binding sites via quantitative PAINT (qPAINT) can be found in **Figure 3**. Visual inspection of individual origami structures shows they match the predicted binding sites from the qPAINT analysis.

Expected results for ultra-resolution imaging, including the intermediate steps for drift correction and a final image from averaging multiple structures, can be seen in **Figure 4**. Key features of a successful ultra-resolution experiment are very high NeNA localization precision (~1 to 1.5 nm) and the ability to visually separate individual binding sites spaced 5 nm apart on the origami structures.

Note: Any Supplementary Information and Source Data files are available in the online version of the paper.

**ACKNOWLEDGMENTS** We thank B. Rieger, S.S. Agasti, S. Strauss, D. Haas, J.B. Woehrstein and E. Woehrstein for helpful discussions. This work was supported by the German Research Foundation (DFG) through an Emmy Noether Fellowship (DFG JU 2957/1-1), the European Research Council (ERC) through an ERC Starting Grant (MolMap, grant agreement no. 680241), the Max Planck Society, the Max Planck Foundation and the Center for Nanoscience (CeNS). M.T.S. acknowledges support from the International Max Planck Research School for Molecular and Cellular Life Sciences (IMPRS-LS). T.S. acknowledges support from the DFG through the Graduate School of Quantitative Biosciences Munich (QBM). F.S. acknowledges support from the DFG through the SFB 1032 (Nanagents for the spatiotemporal control of molecular and cellular reactions).

**AUTHOR CONTRIBUTIONS** J.S. and M.T.S. contributed equally to this work. J.S. designed and developed the Picasso software suite. M.T.S. developed 'Picasso: Design' and 'Simulate' and performed *in vitro* experiments. T.S. developed antibody labeling strategies and performed *in situ* experiments. F.S. performed ultra-resolution experiments. R.J. conceived the study and supervised the project. All authors contributed to the writing of the manuscript.

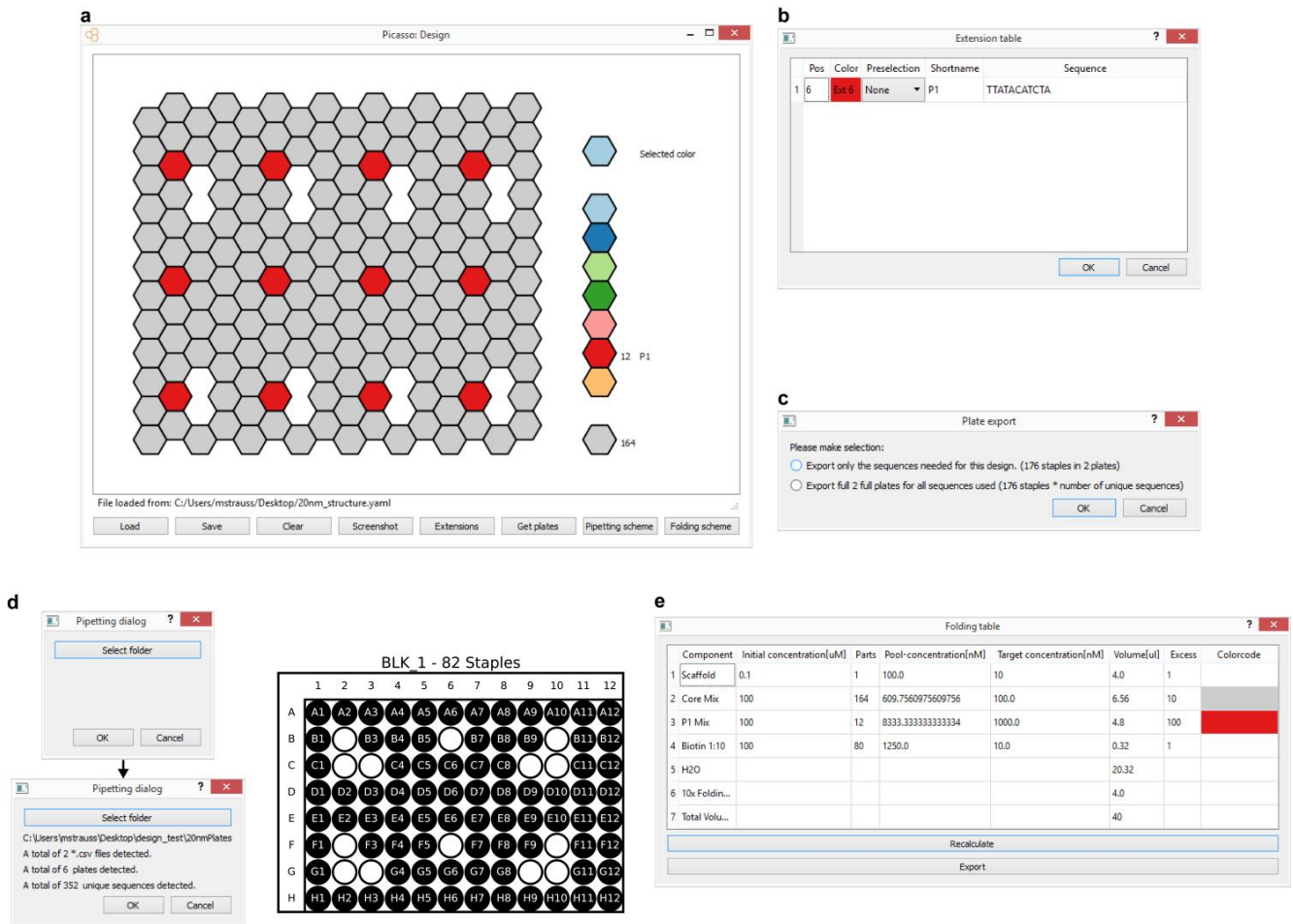
**COMPETING FINANCIAL INTERESTS** The authors declare competing financial interests: details are available in the online version of the paper.

Reprints and permissions information is available online at <http://www.nature.com/reprints/index.html>. Publisher's note: Springer Nature remains neutral with regard to jurisdictional claims in published maps and institutional affiliations.

- Gustafsson, M.G.L. Nonlinear structured-illumination microscopy: wide-field fluorescence imaging with theoretically unlimited resolution. *Proc. Natl. Acad. Sci. USA* **102**, 13081–13086 (2005).
- Hell, S.W. & Wichmann, J. Breaking the diffraction resolution limit by stimulated emission: stimulated-emission-depletion fluorescence microscopy. *Opt. Lett.* **19**, 780–782 (1994).
- Betzig, E. *et al.* Imaging intracellular fluorescent proteins at nanometer resolution. *Science* **313**, 1642–1645 (2006).
- Hess, S.T., Girirajan, T.P.K. & Mason, M.D. Ultra-high resolution imaging by fluorescence photoactivation localization microscopy. *Biophys. J.* **91**, 4258–4272 (2006).
- Rust, M.J., Bates, M. & Zhuang, X. Sub-diffraction-limit imaging by stochastic optical reconstruction microscopy (STORM). *Nat. Methods* **3**, 793–795 (2006).
- Heilemann, M. *et al.* Subdiffraction-resolution fluorescence imaging with conventional fluorescent probes. *Angew. Chem. Int. Ed. Engl.* **47**, 6172–6176 (2008).
- Hell, S.W. Far-field optical nanoscopy. *Science* **316**, 1153–1158 (2007).
- Sengupta, P. *et al.* Probing protein heterogeneity in the plasma membrane using PALM and pair correlation analysis. *Nat. Methods* **8**, 969–975 (2011).
- Xu, K., Zhong, G. & Zhuang, X. Actin, spectrin, and associated proteins form a periodic cytoskeletal structure in axons. *Science* **339**, 452–456 (2012).
- Honigsmann, A. *et al.* Phosphatidylinositol 4,5-bisphosphate clusters act as molecular beacons for vesicle recruitment. *Nat. Struct. Mol. Biol.* **20**, 679–686 (2013).
- Li, D. *et al.* ADVANCED IMAGING. Extended-resolution structured illumination imaging of endocytic and cytoskeletal dynamics. *Science* **349**, aab3500 (2015).
- Galiani, S. *et al.* Super-resolution microscopy reveals compartmentalization of peroxisomal membrane proteins. *J. Biol. Chem.* **291**, 16948–16962 (2016).
- Hell, S.W. *et al.* The 2015 super-resolution microscopy roadmap. *J. Phys. D Appl. Phys.* **48**, 443001 (2015).
- Huang, B., Bates, M. & Zhuang, X. Super-resolution fluorescence microscopy. *Annu. Rev. Biochem.* **78**, 993–1016 (2009).
- Lippincott-Schwartz, J., Jennifer, L.-S. & Patterson, G.H. Photoactivatable fluorescent proteins for diffraction-limited and super-resolution imaging. *Trends Cell Biol.* **19**, 555–565 (2009).
- Nieuwenhuizen, R.P.J. *et al.* Measuring image resolution in optical nanoscopy. *Nat. Methods* **10**, 557–562 (2013).
- Sharonov, A. & Hochstrasser, R.M. Wide-field subdiffraction imaging by accumulated binding of diffusing probes. *Proc. Natl. Acad. Sci. USA* **103**, 18911–18916 (2006).
- Giannone, G. *et al.* Dynamic superresolution imaging of endogenous proteins on living cells at ultra-high density. *Biophys. J.* **99**, 1303–1310 (2010).
- Jungmann, R. *et al.* Single-molecule kinetics and super-resolution microscopy by fluorescence imaging of transient binding on DNA origami. *Nano Lett.* **10**, 4756–4761 (2010).
- Jungmann, R. *et al.* Multiplexed 3D cellular super-resolution imaging with DNA-PAINT and Exchange-PAINT. *Nat. Methods* **11**, 313–318 (2014).
- Iinuma, R. *et al.* Polyhedra self-assembled from DNA tripods and characterized with 3D DNA-PAINT. *Science* **344**, 65–69 (2014).
- Jungmann, R. *et al.* Quantitative super-resolution imaging with qPAINT. *Nat. Methods* **13**, 439–442 (2016).
- Dai, M., Jungmann, R. & Yin, P. Optical imaging of individual biomolecules in densely packed clusters. *Nat. Nanotechnol.* **11**, 798–807 (2016).
- Schlichthaerle, T., Strauss, M.T., Schueder, F., Woehrstein, J.B. & Jungmann, R. DNA nanotechnology and fluorescence applications. *Curr. Opin. Biotechnol.* **39**, 41–47 (2016).
- Agasti, S. *et al.* DNA-barcoded labeling probes for highly multiplexed Exchange-PAINT imaging. *Chem. Sci.* (2017) <http://dx.doi.org/10.1039/c6sc05420j>.
- Rasnik, I., McKinney, S.A. & Ha, T. Nonblinking and long-lasting single-molecule fluorescence imaging. *Nat. Methods* **3**, 891–893 (2006).
- Aitken, C.E., Marshall, R.A. & Puglisi, J.D. An oxygen scavenging system for improvement of dye stability in single-molecule fluorescence experiments. *Biophys. J.* **94**, 1826–1835 (2008).
- Ha, T. & Tinnefeld, P. Photophysics of fluorescent probes for single-molecule biophysics and super-resolution imaging. *Annu. Rev. Phys. Chem.* **63**, 595–617 (2012).
- Ries, J., Kaplan, C., Platonova, E., Eghlidi, H. & Ewers, H. A simple, versatile method for GFP-based super-resolution microscopy via nanobodies. *Nat. Methods* **9**, 582–584 (2012).
- Opazo, F. *et al.* Aptamers as potential tools for super-resolution microscopy. *Nat. Methods* **9**, 938–939 (2012).
- Tokunaga, M., Imamoto, N. & Sakata-Sogawa, K. Highly inclined thin illumination enables clear single-molecule imaging in cells. *Nat. Methods* **5**, 159–161 (2008).
- Legant, W.R. *et al.* High-density three-dimensional localization microscopy across large volumes. *Nat. Methods* **13**, 359–365 (2016).
- Rothemund, P.W.K. Folding DNA to create nanoscale shapes and patterns. *Nature* **440**, 297–302 (2006).
- Seeman, N.C. Nucleic acid junctions and lattices. *J. Theor. Biol.* **99**, 237–247 (1982).
- Seeman, N.C. An overview of structural DNA nanotechnology. *Mol. Biotechnol.* **37**, 246–257 (2007).
- Douglas, S.M. *et al.* Rapid prototyping of 3D DNA-origami shapes with caDNAo. *Nucleic Acids Res.* **37**, 5001–5006 (2009).
- Benson, E. *et al.* DNA rendering of polyhedral meshes at the nanoscale. *Nature* **523**, 441–444 (2015).
- Kim, D.-N., Kilchherr, F., Dietz, H. & Bathe, M. Quantitative prediction of 3D solution shape and flexibility of nucleic acid nanostructures. *Nucleic Acids Res.* **40**, 2862–2868 (2012).
- Douglas, S.M. *et al.* Self-assembly of DNA into nanoscale three-dimensional shapes. *Nature* **459**, 414–418 (2009).
- Martin, T.G. & Dietz, H. Magnesium-free self-assembly of multi-layer DNA objects. *Nat. Commun.* **3**, 1103 (2012).
- Sobczak, J.-P.J., Martin, T.G., Gerling, T. & Dietz, H. Rapid folding of DNA into nanoscale shapes at constant temperature. *Science* **338**, 1458–1461 (2012).
- Bellot, G., Gaëtan, B., McClintock, M.A., Chenxiang, L. & Shih, W.M. Recovery of intact DNA nanostructures after agarose gel-based separation. *Nat. Methods* **8**, 192–194 (2011).
- Lin, C., Perrault, S.D., Kwak, M., Graf, F. & Shih, W.M. Purification of DNA-origami nanostructures by rate-zonal centrifugation. *Nucleic Acids Res.* **41**, e40 (2013).
- Stahl, E., Martin, T.G., Praetorius, F. & Dietz, H. Facile and scalable preparation of pure and dense DNA origami solutions. *Angew. Chem. Int. Ed. Engl.* **53**, 12735–12740 (2014).
- Steinhauer, C., Jungmann, R., Sobey, T.L., Simmel, F.C. & Tinnefeld, P. DNA origami as a nanoscopic ruler for super-resolution microscopy. *Angew. Chem. Int. Ed. Engl.* **48**, 8870–8873 (2009).
- Schmied, J.J. *et al.* DNA origami-based standards for quantitative fluorescence microscopy. *Nat. Protoc.* **9**, 1367–1391 (2014).
- Dean, K.M. & Palmer, A.E. Advances in fluorescence labeling strategies for dynamic cellular imaging. *Nat. Chem. Biol.* **10**, 512–523 (2014).

## PROTOCOL

48. Dempsey, G.T., Vaughan, J.C., Chen, K.H., Bates, M. & Zhuang, X. Evaluation of fluorophores for optimal performance in localization-based super-resolution imaging. *Nat. Methods* **8**, 1027–1036 (2011).
49. Mikhaylova, M. *et al.* Resolving bundled microtubules using anti-tubulin nanobodies. *Nat. Commun.* **6**, 7933 (2015).
50. Los, G.V. *et al.* HaloTag: a novel protein labeling technology for cell imaging and protein analysis. *ACS Chem. Biol.* **3**, 373–382 (2008).
51. Keppler, A., Pick, H., Arrivoli, C., Vogel, H. & Johnsson, K. Labeling of fusion proteins with synthetic fluorophores in live cells. *Proc. Natl. Acad. Sci. USA* **101**, 9955–9959 (2004).
52. Wang, L., Xie, J. & Schultz, P.G. Expanding the genetic code. *Annu. Rev. Biophys. Biomol. Struct.* **35**, 225–249 (2006).
53. Schweller, R.M. *et al.* Multiplexed *in situ* immunofluorescence using dynamic DNA complexes. *Angew. Chem. Int. Ed. Engl.* **51**, 9292–9296 (2012).
54. Ullal, A.V. *et al.* Cancer cell profiling by barcoding allows multiplexed protein analysis in fine-needle aspirates. *Sci. Transl. Med.* **6**, 219ra9 (2014).
55. Gong, H. *et al.* Simple method to prepare oligonucleotide-conjugated antibodies and its application in multiplex protein detection in single cells. *Bioconjug. Chem.* **27**, 217–225 (2016).
56. Xu, K., Babcock, H.P. & Zhuang, X. Dual-objective STORM reveals three-dimensional filament organization in the actin cytoskeleton. *Nat. Methods* **9**, 185–188 (2012).
57. Whelan, D.R. & Bell, T.D.M. Image artifacts in single molecule localization microscopy: why optimization of sample preparation protocols matters. *Sci. Rep.* **5**, 7924 (2015).
58. Edelstein, A.D. *et al.* *J. Biol. Methods* **1**, 10 (2014).
59. Beier, H.T. & Ibey, B.L. Experimental comparison of the high-speed imaging performance of an EM-CCD and sCMOS camera in a dynamic live-cell imaging test case. *PLoS One* **9**, e84614 (2014).
60. Huang, F. *et al.* Video-rate nanoscopy using sCMOS camera-specific single-molecule localization algorithms. *Nat. Methods* **10**, 653–658 (2013).
61. Shroff, H., Galbraith, C.G., Galbraith, J.A. & Betzig, E. Live-cell photoactivated localization microscopy of nanoscale adhesion dynamics. *Nat. Methods* **5**, 417–423 (2008).
62. Venkataramani, V., Herrmannsdörfer, F., Heilemann, M. & Kuner, T. SuReSim: simulating localization microscopy experiments from ground truth models. *Nat. Methods* **13**, 319–321 (2016).
63. Sage, D. *et al.* Quantitative evaluation of software packages for single-molecule localization microscopy. *Nat. Methods* **12**, 717–724 (2015).
64. Smith, C.S., Joseph, N., Rieger, B. & Lidke, K.A. Fast, single-molecule localization that achieves theoretically minimum uncertainty. *Nat. Methods* **7**, 373–375 (2010).
65. Egner, A. *et al.* Fluorescence nanoscopy in whole cells by asynchronous localization of photoswitching emitters. *Biophys. J.* **93**, 3285–3290 (2007).
66. Wang, Y. *et al.* Localization events-based sample drift correction for localization microscopy with redundant cross-correlation algorithm. *Opt. Express* **22**, 15982–15991 (2014).
67. Endesfelder, U., Malkusch, S., Fricke, F. & Heilemann, M. A simple method to estimate the average localization precision of a single-molecule localization microscopy experiment. *Histochem. Cell Biol.* **141**, 629–638 (2014).
68. Lin, C. *et al.* Submicrometre geometrically encoded fluorescent barcodes self-assembled from DNA. *Nat. Chem.* **4**, 832–839 (2012).
69. Bates, M., Huang, B., Dempsey, G.T. & Zhuang, X. Multicolor super-resolution imaging with photo-switchable fluorescent probes. *Science* **317**, 1749–1753 (2007).
70. Huang, B., Jones, S.A., Brandenburg, B. & Zhuang, X. Whole-cell 3D STORM reveals interactions between cellular structures with nanometer-scale resolution. *Nat. Methods* **5**, 1047–1052 (2008).
71. Shin, J.Y. *et al.* Visualization and functional dissection of coaxial paired SpoIIIE channels across the sporulation septum. *Elife* **4** (2015).
72. Puchner, E.M., Walter, J.M., Kasper, R., Huang, B. & Lim, W.A. Counting molecules in single organelles with superresolution microscopy allows tracking of the endosome maturation trajectory. *Proc. Natl. Acad. Sci. USA* **110**, 16015–16020 (2013).
73. Lee, S.-H., Shin, J.Y., Lee, A. & Bustamante, C. Counting single photoactivatable fluorescent molecules by photoactivated localization microscopy (PALM). *Proc. Natl. Acad. Sci. USA* **109**, 17436–17441 (2012).
74. Rollins, G.C., Shin, J.Y., Bustamante, C. & Pressé, S. Stochastic approach to the molecular counting problem in superresolution microscopy. *Proc. Natl. Acad. Sci. USA* **112**, E110–8 (2015).
75. Nieuwenhuizen, R.P.J. *et al.* Quantitative localization microscopy: effects of photophysics and labeling stoichiometry. *PLoS One* **10**, e0127989 (2015).
76. Sengupta, P., Jovanovic-Talman, T. & Lippincott-Schwartz, J. Quantifying spatial organization in point-localization superresolution images using pair correlation analysis. *Nat. Protoc.* **8**, 345–354 (2013).
77. Juette, M.F. *et al.* Three-dimensional sub-100 nm resolution fluorescence microscopy of thick samples. *Nat. Methods* **5**, 527–529 (2008).
78. Broeken, J. *et al.* Resolution improvement by 3D particle averaging in localization microscopy. *Methods Appl. Fluoresc.* **3**, 014003 (2015).
79. Cheng, Y., Yifan, C., Nikolaus, G., Penczek, P.A. & Thomas, W. A primer to single-particle cryo-electron microscopy. *Cell* **161**, 438–449 (2015).
80. Szymborska, A. *et al.* Nuclear pore scaffold structure analyzed by super-resolution microscopy and particle averaging. *Science* **341**, 655–658 (2013).
81. Loschberger, A. *et al.* Super-resolution imaging visualizes the eightfold symmetry of gp210 proteins around the nuclear pore complex and resolves the central channel with nanometer resolution. *J. Cell Sci.* **125**, 570–575 (2012).
82. Penczek, P., Radermacher, M. & Frank, J. Three-dimensional reconstruction of single particles embedded in ice. *Ultramicroscopy* **40**, 33–53 (1992).
83. Perrault, S.D. & Chan, W.C.W. Synthesis and surface modification of highly monodispersed, spherical gold nanoparticles of 50–200 nm. *J. Am. Chem. Soc.* **131**, 17042–17043 (2009).



**Supplementary Figure 1**

Overview of "Picasso: Design"

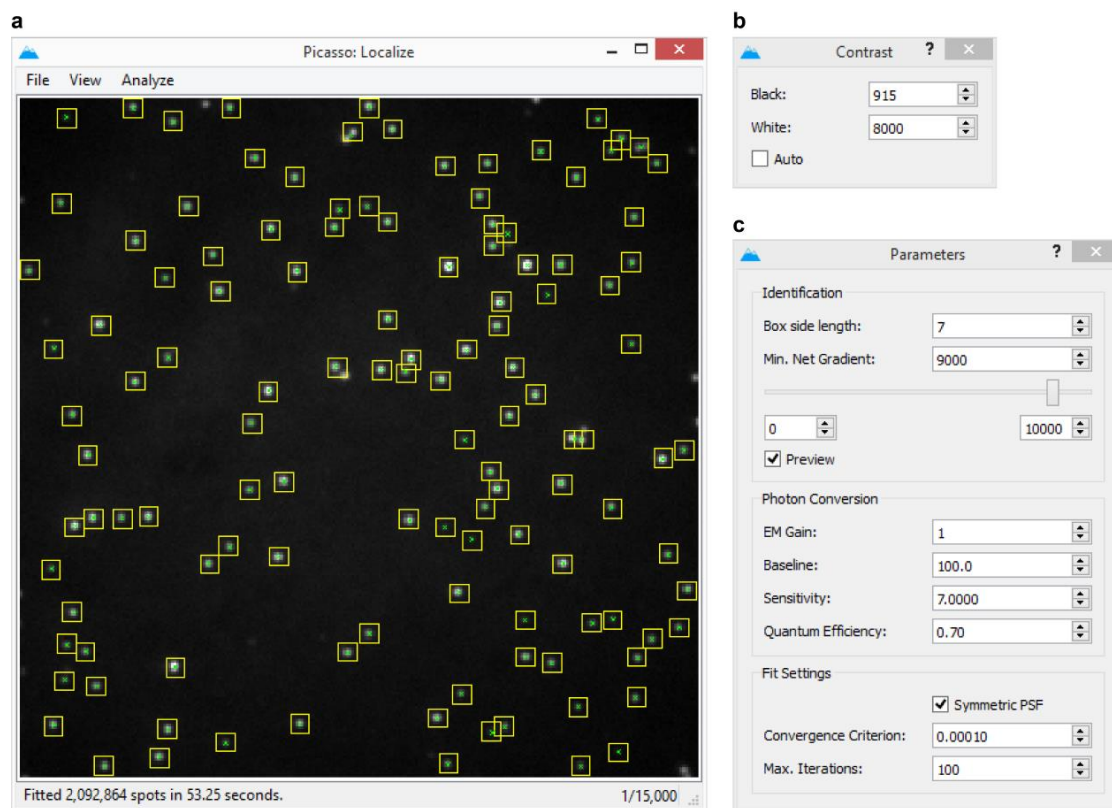
(a) The main window showing the origami canvas with the hexagonal tiles. (b) Extensions dialog to set extensions corresponding to each selected color. (c) Plate export dialog to specify the export format of the plates. (d) Pipetting dialog to select a folder with \*.csv files to generate a list of sequences that need to be pipetted and to create a visual pipetting aid. (e) Folding table to calculate volumes that are needed for pipetting.



Supplementary Figure 2

Overview of “Picasso: Simulate”

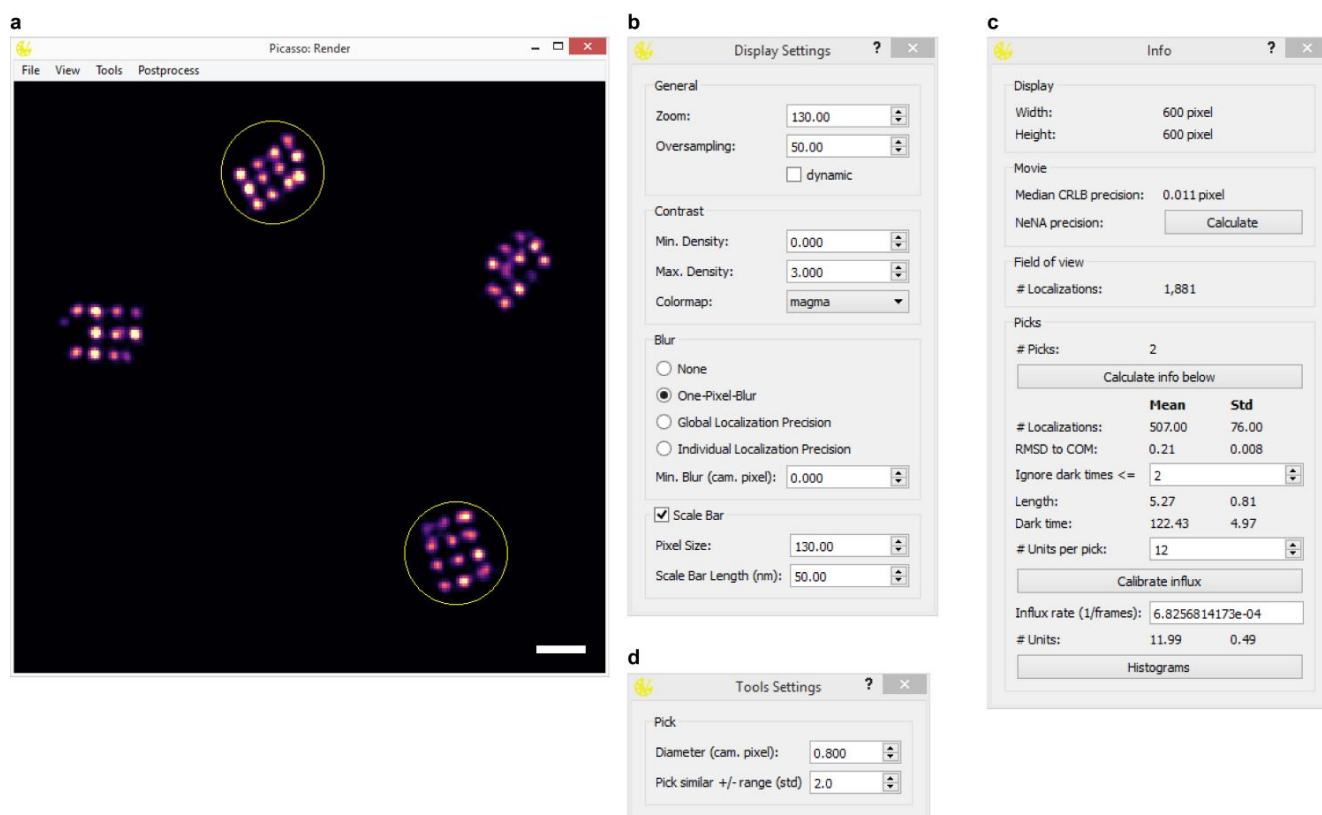
The main window has two preview windows, the left one to display the positions of structures in the full frame, the right one to display an individual structure. Structural parameters such as number and structure definition can be set in the group box “Structure”. All PAINT-related parameters, *i.e.* mean dark and bright times are set with the “PAINT parameters” group box. The group box “Imager parameters” is used to define properties of the simulated imaging probe.



**Supplementary Figure 3**

Overview of "Picasso: Localize"

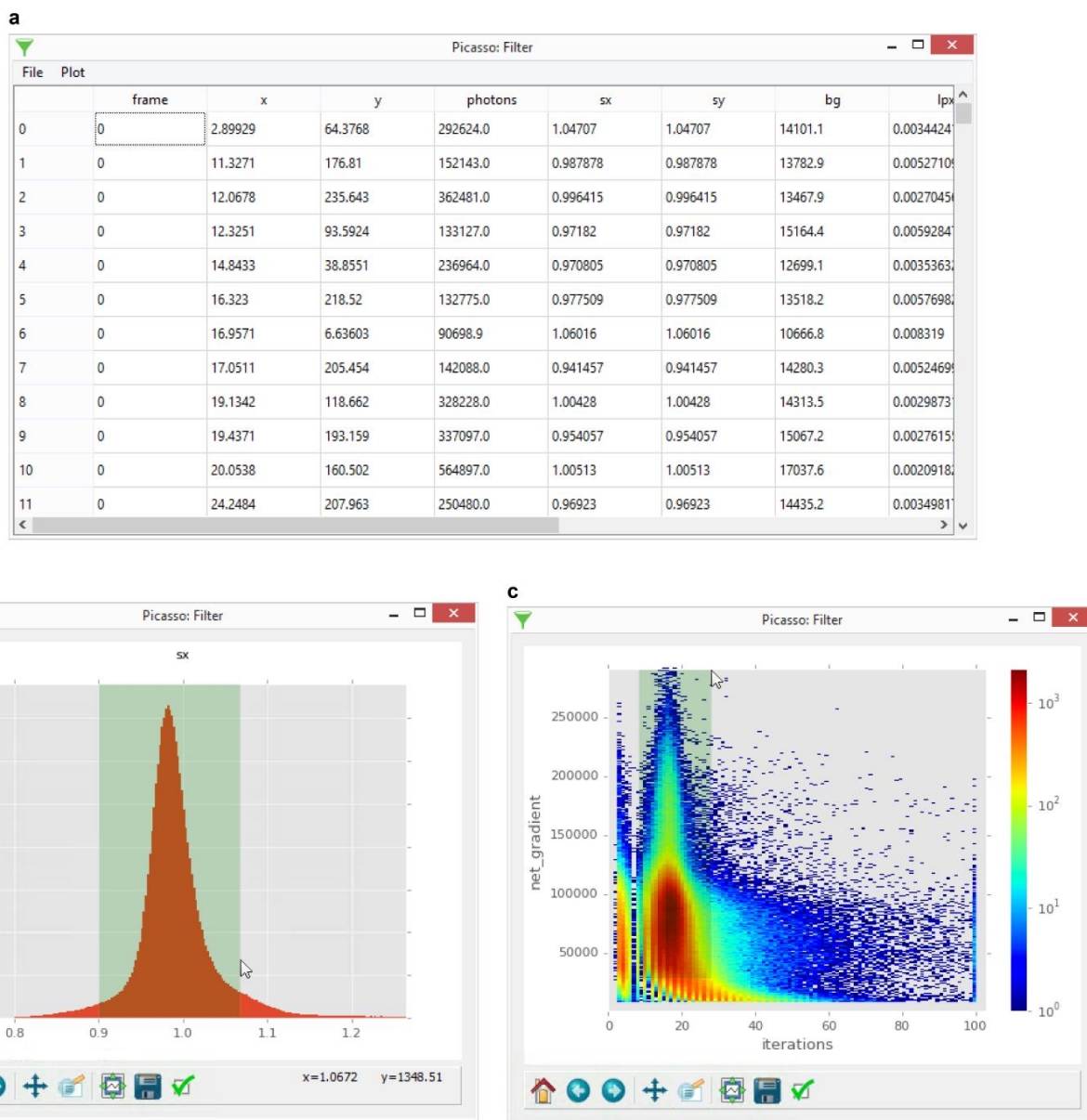
(a) The main window after the analysis of a movie file. Yellow boxes indicate the identification of a spot, green crosses show the fitted subpixel coordinate. (b) The contrast setting dialog. (c) The parameters setting dialog.



#### Supplementary Figure 4

Overview of "Picasso: Render"

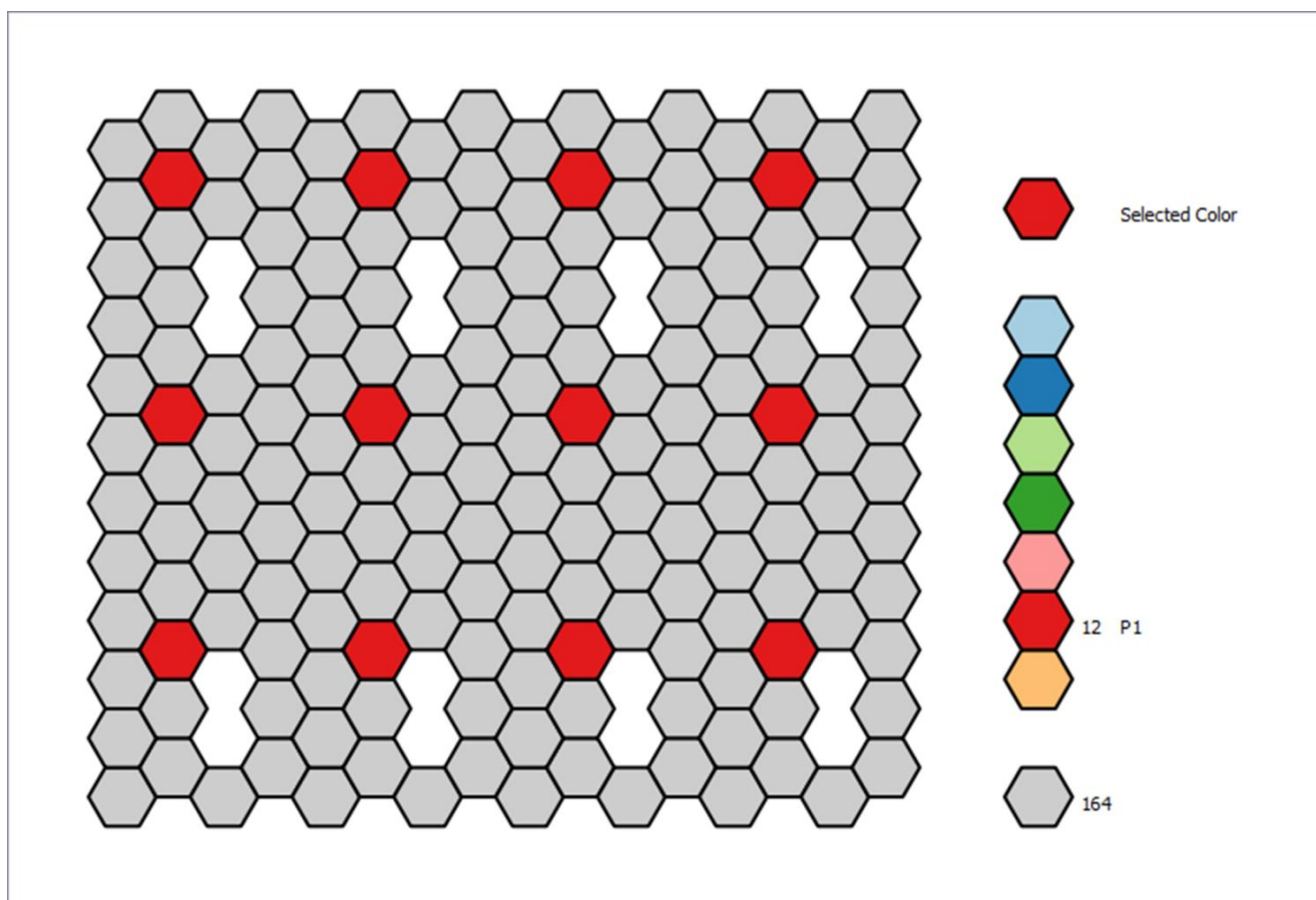
**(a)** The main window with two picked regions of interest (yellow circles). **(b)** The display settings dialog for the render scene in **(a)**. **(c)** The info dialog for the picked regions in **(a)**. **(d)** The tools settings dialog.



**Supplementary Figure 5**

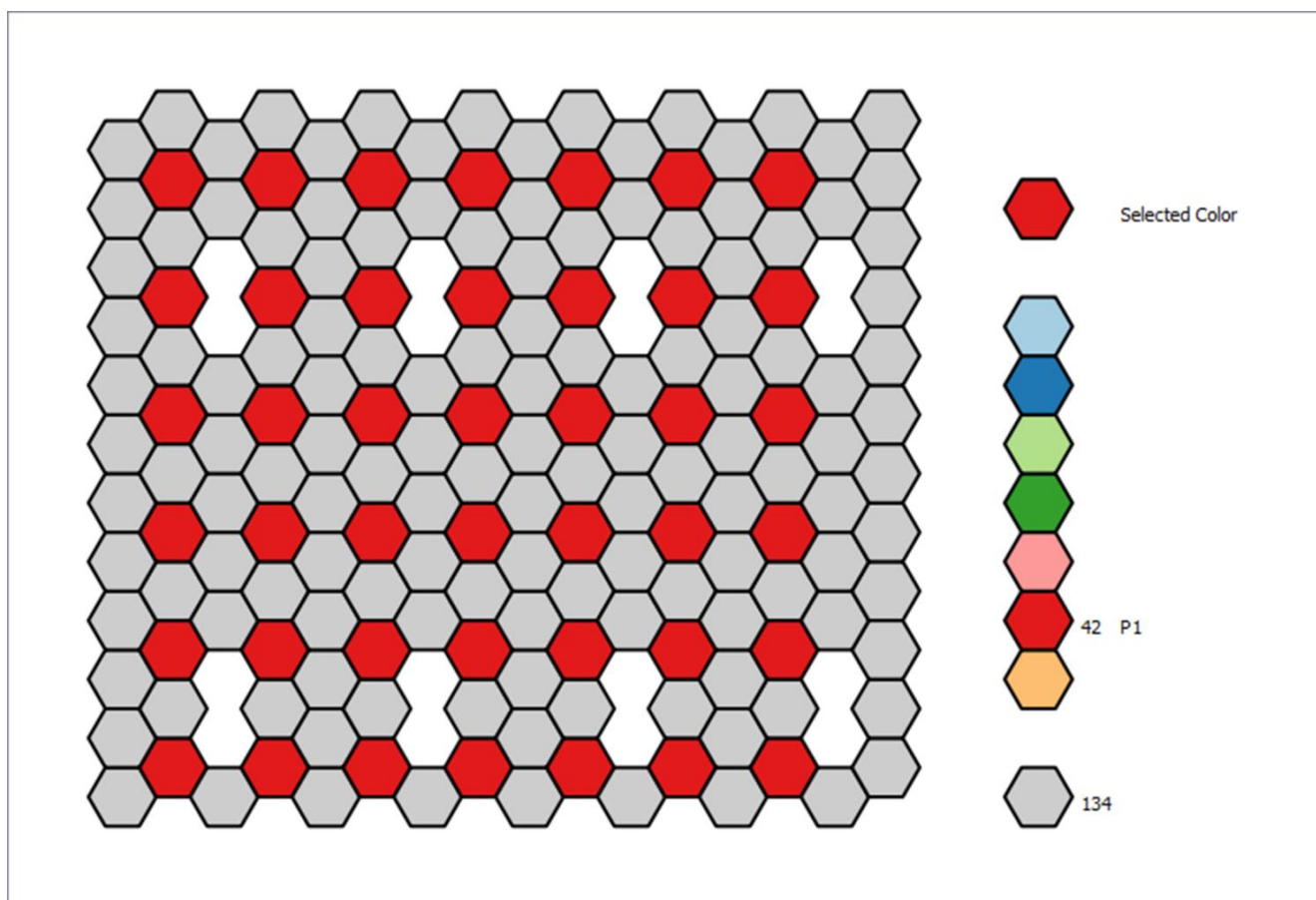
Overview of “Picasso: Filter”

**(a)** The main window showing properties (columns) of localizations (rows). **(b)** Filtering in a histogram of a property column. **(c)** Filtering in a two-dimensional histogram of two property columns. The green areas in **(b)** and **(c)** have been selected with a pressed left mouse button. After releasing the mouse button, any localization with property values outside the green range will be removed.



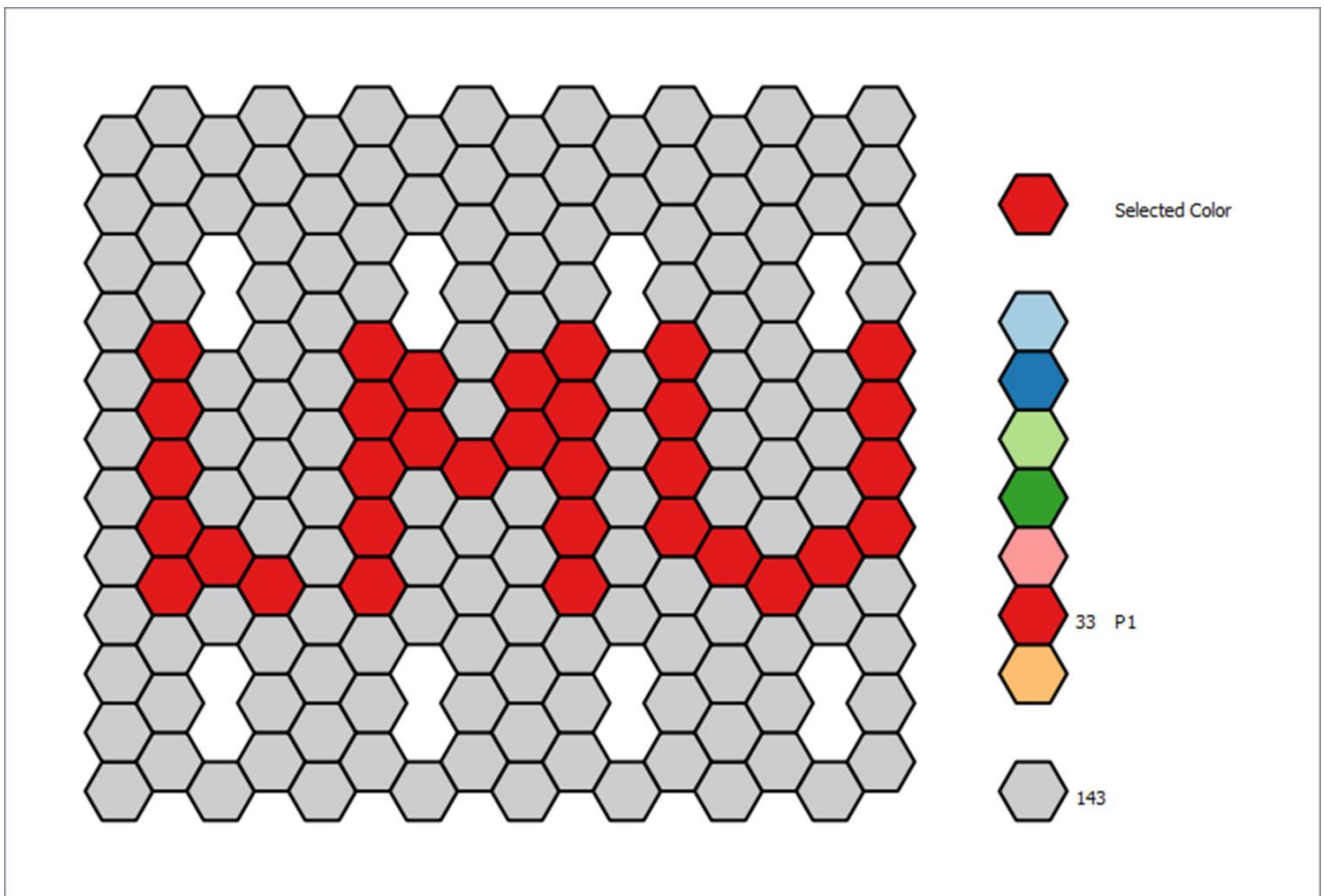
**Supplementary Figure 6**

20 nm DNA origami grid



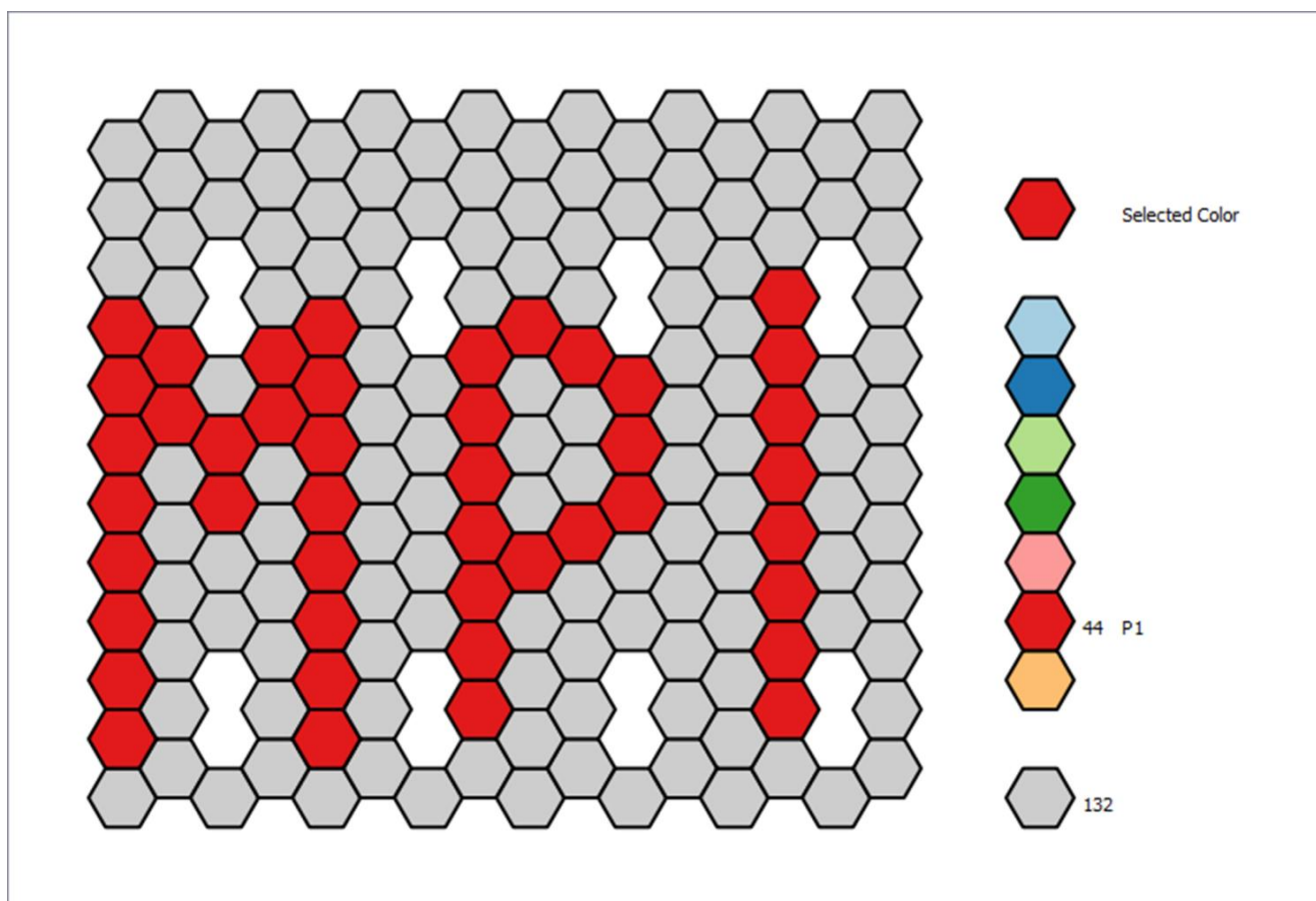
**Supplementary Figure 7**

10 nm DNA origami grid



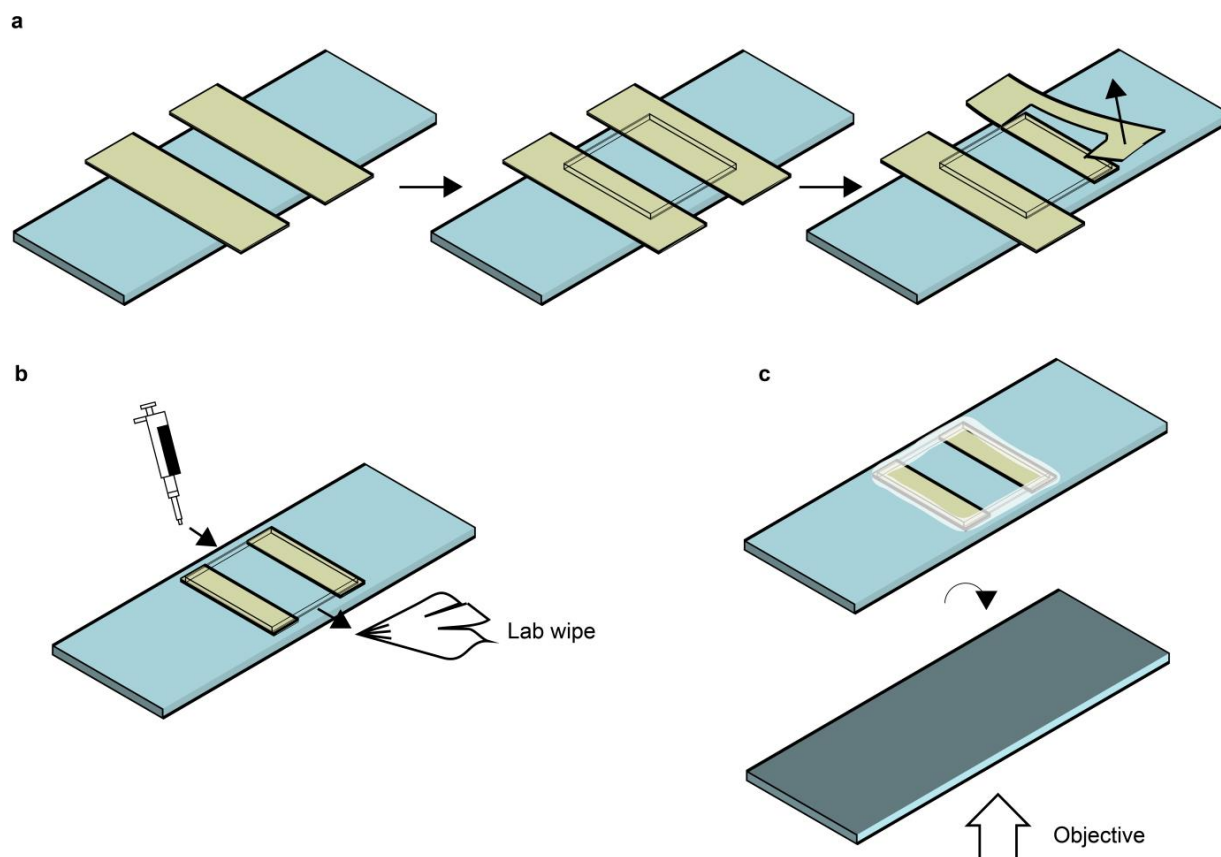
Supplementary Figure 8

LMU Logo



Supplementary Figure 9

MPI Logo



Supplementary Figure 10

## Custom-made flow chamber

(a) Two stripes of double-sided sticky tape are placed on a 76x26 mm microscopy slide with a distance of  $\sim 8$ mm. A coverglass is placed on top of the sticky tape stripes. After pressing the coverglass thoroughly against the sticky tape, overlapping tape can be removed. (b) To immobilize DNA nanostructures, fluids are pipetted from one side while simultaneously being sucked out with a lab wiper from the other side. (c) The coverglass is sealed with epoxy glue and can be used with the coverglass facing towards the objective in a microscope stage once the glue is hardened.

## Supplementary Manual

This manual describes details about the Picasso program.

### File Format and Name Conventions

#### *Movie Files*

Picasso accepts two type of raw movie files: TIFF (preferably from  $\mu$ Manager, <https://www.micro-manager.org>) and raw binary data (file extension “.raw”).

When loading raw binary files, the user will be prompted for movie metadata such as the number of frames, number of pixels, etc. Alternatively, this metadata can be supplied by an accompanying metadata file with the same filename as the raw binary file, but with the extension “.yaml”. See “YAML Metadata Files” for more details.

#### *HDF5 Files*

HDF5 is a generic and efficient binary file format for storing data (<https://support.hdfgroup.org/HDF5/>). In Picasso, HDF5 files are used for storing tabular data of localization properties with the file extension “.hdf5”. Furthermore, Picasso saves statistical properties of groups of localizations in an HDF5 file.

Generally, several datasets can be stored within an HDF5 file. These datasets are accessible by specifying a path within the HDF5 file, similar to a path of an operating system. When saving localizations, Picasso stores tabular data under the path “/locs”. When saving statistical properties of groups of localizations, Picasso saves the table under the path “/groups”.

#### *Importing HDF5 files in MATLAB and Origin*

In MATLAB, execute the command “locs = h5read(filename, dataset)”. Replace dataset with ‘locs’ for localization files and with ‘groups’ for pick property files.

In Origin, select “File > Import > HDF5” or drag and drop the file into the main window.

#### *Localization HDF5 Files*

Localization HDF5 files must always be accompanied by a YAML metadata file with the same filename, but with the extension ‘.yaml’. See “YAML Metadata File” for more details. The localization table is stored as a dataset of the HDF5 file in the path “/locs”. This table can be visualized by opening the HDF5 file with “Picasso: Filter”. The localization table can have an unlimited number of columns. **Table 1** describes the meaning of Picasso’s main column names.

Column Name	Description	C Data Type
frame	The frame in which the localization occurred, starting with zero for the first frame.	unsigned long
x	The subpixel x coordinate in camera pixels	float
y	The subpixel y coordinate in camera pixels	float
photons	The total number of detected photons from this event, not including background or camera offset	float
sx	The Point Spread Function width in camera pixels	float
sy	The Point Spread Function height in camera pixels	float
bg	The number of background photons per pixel, not including the camera offset	float
lpx	The localization precision in x direction, in camera pixels, as estimated by the Cramer-Rao Lower Bound of the Maximum Likelihood fit.	float
lpy	The localization precision in y direction, in camera pixels, as estimated by the Cramer-Rao Lower Bound of the Maximum Likelihood fit.	float
net_gradient	The net gradient of this spot which is defined by the sum of gradient vector magnitudes within the fix box, projected to the spot center.	float
likelihood	The log-likelihood of the fit	float
iterations	The number of iterations of the fit procedure	long
group	(Optional) An identifier to assign multiple localizations to groups, for example by picking regions of interest	long
len	(Optional) The length of the event, if localizations from consecutive frames have been linked	long
n	(Optional) The number of localizations in this event, if localizations from consecutive frames have been linked, potentially diverging from the “len” column due to a transient dark time tolerance	long
photon_rate	(Optional) The mean number of photons per frame, if localizations from consecutive frames have been linked. The total number of photons is set in the “photons” column.	float

**Table 1** | Name, description and data type for the main columns used in Picasso.

#### *HDF5 Pick Property Files*

When selecting “File > Save pick properties” in “Picasso: Render”, the properties of picked regions are stored in an HDF5 file. Within the HDF5 file, the data table is stored in the path “/groups”.

Each row in the “groups” table corresponds to one picked region. For each localization property (see **Table 1**), two columns are generated in the “groups” table: the mean and standard deviation of the respective column

over the localizations in a pick region. For example, if the localization table contains a column “len”, the “groups” table will contain a column “len\_mean” and “len\_std”.

Furthermore, the following columns are included: “group” (the group identifier), “n\_events” (the number of localizations in the region) and “n\_units” (the number of units from a qPAINT measurement).

## YAML Metadata Files

YAML files are document-oriented text files that can be opened and changed with any text editor (<http://www.yaml.org>). In Picasso, YAML files are used to store metadata of movie or localization files.

Each localization HDF5 file must always be accompanied with a YAML file of the same filename, except for the extension, which is “.yaml”. Deleting this YAML metadata file will result in failure of the Picasso software!

Raw binary files may be accompanied by a YAML metadata file to store data about the movie dimensions, etc. While the metadata file in this case is not required, it reduces the effort of typing in this metadata each time the movie is loaded with “Picasso: Localize”. To generate such a YAML metadata file, load the raw movie into “Picasso: Localize”, then enter all required information in the appearing dialog. Check the checkbox “Save info to yaml file” and click ok. The movie will be loaded and the metadata saved in a YAML file. This file will be detected the next time this raw movie is loaded and the metadata does not need to be entered again.

## Supplementary Table 1: Laser power conversion table

Set Power (mW)	Power at sample (mW)	Power density at sample (kW/cm <sup>2</sup> )
20	13.7	0.82
30	20.8	1.24
40	28	1.67
50	34.8	2.07
60	42.2	2.52
70	48.5	2.89

Power was set at the driver unit of the Coherent Sapphire Laser, 200 mW nominal power, 561 nm. Laser power was measured with a digital power meter (THORLABS, PM100D) by placing a microscopy slide thermal power sensor (THORLABS, S170C) with immersion oil in the sample holder. The power density was calculated as an average of the the gaussian illumination with an area of 256 px<sup>2</sup> with pixel size of 160 nm.

## Supplementary Table 2: DNA-PAINT sequences

Shortname	Docking sequence	Imager sequence
P1	TTATACATCTA	CTAGATGTAT-Dye
P2	TTATCTACATA	TATGTAGATC-Dye
P3	TTTCTTCATTA	GTAATGAAGA-Dye
P4	TTATGAATCTA	GTAGATTCAT-Dye
P5	TTTCAATGTAT	CATACATTGA-Dye
P6	TTTTAGGTAAA	CTTTACCTAA-Dye
P7	TTAATTGAGTA	GTAACAATT-Dye
P8	TTATGTTAATG	CCATTAACAT-Dye
P9	TTAATTAGGAT	CATCCTAATT-Dye
P10	TTATAATGGAT	GATCCATTAT-Dye

## Supplementary Table 3: List of core staples

Position	Name	Sequence
A1	21 [32] 23 [31] BLK	TTTCACTCAAAGGGCGAAAACCATCACC
B1	23 [32] 22 [48] BLK	CAAATCAAGTTTTTTGGGGTCGAAACGTGGA
C1	21 [56] 23 [63] BLK	AGCTGATTGCCCTTCAGAGTCCACTATTAAGGGTGCCGT
D1	23 [64] 22 [80] BLK	AAAGCACTAAATCGGAACCTAATCCAGTT
E1	21 [96] 23 [95] BLK	AGCAAGCGTAGGGTTGAGTGTGTAGGGAGCC
F1	23 [96] 22 [112] BLK	CCCGATTTAGAGCTTGACGGGGAAAAGAATA
G1	21 [120] 23 [127] BLK	CCCAGCAGCGGAAAATCCCTTATAAATCAAGCCGGCG
H1	21 [160] 22 [144] BLK	TCAATATCGAACCTCAAATATCAATTCGAAA
I1	23 [128] 23 [159] BLK	AACGTGGCGAGAAAGGAAGGAAACCAGTAA
J1	23 [160] 22 [176] BLK	TAAAAGGGACATTTCTGGCCAACAAAGCATC
K1	21 [184] 23 [191] BLK	TCAACAGTTGAAAGGAGCAAATGAAAATCTAGAGATAGA
L1	23 [192] 22 [208] BLK	ACCCTTCTGACCTGAAAGCGTAAGACGCTGAG
M1	21 [224] 23 [223] BLK	CTTTAGGGCCTGCAACAGTGCCAATACGTG
N1	23 [224] 22 [240] BLK	GCACAGACAATATTTTTGAATGGGGTCAGTA
O1	21 [248] 23 [255] BLK	AGATTAGAGCCGTCAAAAAACAGAGGTGAGGCCTATTAGT
P1	23 [256] 22 [272] BLK	CTTTAATGCGGCACTGATAGCCCCACCAG
A2	19 [32] 21 [31] BLK	GTCGACTTCGGCCAACGCGGGGGTTTTTC
B2	22 [47] 20 [48] BLK	CTCCAACGCAGTGAGACGGGCAACCAGCTGCA

## Super-Resolution Microscopy with DNA-PAINT

D2	22[79]20[80]BLK	TGGAACAACCGCCTGGCCCTGAGGCCCGCT
E2	19[96]21[95]BLK	CTGTGTGATTGCGTTGCGCTCACTAGAGTTGC
F2	22[111]20[112]BLK	GCCCGAGAGTCCACGCTGGTTTGCAGCTAACT
H2	19[160]20[144]BLK	GCAATTCACATATTCCTGATTATCAAAGTGTA
I2	22[143]21[159]BLK	TCGGCAAATCCTGTTTGTGATGGTGGACCCCTCAA
J2	22[175]20[176]BLK	ACCTTGCTTGGTGAGTTGGCAAAGAGCGGA
L2	22[207]20[208]BLK	AGCCAGCAATTGAGGAAGGTATCATCATTTT
M2	19[224]21[223]BLK	CTACCATAGTTTGAGTAACATTTAAAATAT
N2	22[239]20[240]BLK	TTAACACCAGCACTAACAACTAATCGTTATTA
P2	22[271]20[272]BLK	CAGAAGATTAGATAATACATTTGTGCGACAA
A3	17[32]19[31]BLK	TGCATCTTTCCAGTCACGACGGCCTGCAG
B3	20[47]18[48]BLK	TTAATGAACTAGAGGATCCCGGGGGTAACG
D3	20[79]18[80]BLK	TTCCAGTCGTAATCATGGTCATAAAAGGGG
E3	17[96]19[95]BLK	GCTTTCCGATTACGCCAGCTGGCGGCTGTTTC
F3	20[111]18[112]BLK	CACATTAATAATTGTTATCCGCTCATGCGGGCC
H3	17[160]18[144]BLK	AGAAAACAAAGAAGATGATGAAACAGGCTGCG
I3	20[143]19[159]BLK	AAGCCTGGTACGAGCCGGAAGCATAGATGATG
J3	20[175]18[176]BLK	ATTATCATTCAATATAATCCTGACAATTAC
L3	20[207]18[208]BLK	GCGGAACATCTGAATAATGGAAGGTACAAAAT
M3	17[224]19[223]BLK	CATAAATCTTTGAATACCAAGTGTAGAAC
N3	20[239]18[240]BLK	ATTTTAAAATCAAAATTATTTGCACGGATTTCG
P3	20[271]18[272]BLK	CTCGTATTAGAAATGCGTAGATACAGTAC
A4	15[32]17[31]BLK	TAATCAGCGGATTGACCGTAATCGTAACCG
B4	18[47]16[48]BLK	CCAGGGTTGCCAGTTTGGAGGGACCCGTGGGA
C4	15[64]18[64]BLK	GTATAAGCCAACCCGTCGGATTCTGACGACAGTATCGGCCGCAAGGCG
D4	18[79]16[80]BLK	GATGTGCTTCAGGAAGATCGCACAATGTGA
E4	15[96]17[95]BLK	ATATTTTGGCTTTCATCAACATTATCCAGCCA
F4	18[111]16[112]BLK	TCTTCGCTGCACCGCTTCTGGTGGCGCCTTCC
G4	15[128]18[128]BLK	TAAATCAAAATAATTCGCGTCTCGGAAACCAGGCAAAGGGAAGG
H4	15[160]16[144]BLK	ATCGCAAGTATGTAATGCTGATGATAGGAAC
I4	18[143]17[159]BLK	CAACTGTTGCGCCATTGCCATTCAAACATCA
J4	18[175]16[176]BLK	CTGAGCAAAAATTAATTACATTTTGGGTTA
K4	15[192]18[192]BLK	TCAAATATAACCTCCGGCTTAGGTAACAATTTCAATTTGAAGGCGAATT

L4	18[207]16[208]BLK	CGCGCAGATTACCTTTTTTAATGGGAGAGACT
M4	15[224]17[223]BLK	CCTAAATCAAATCATAGGTCTAAACAGTA
N4	18[239]16[240]BLK	CCTGATTGCAATATATGTGAGTGATCAATAGT
O4	15[256]18[256]BLK	GTGATAAAAAGACGCTGAGAAGAGATAACCTTGCTTCTGTTCGGGAGA
P4	18[271]16[272]BLK	CTTTTACAAAATCGTCGCTATTAGCGATAG
A5	13[32]15[31]BLK	AACGCAAAATCGATGAACGGTACCGGTTGA
B5	16[47]14[48]BLK	ACAAACGGAAAAGCCCCAAAACACTGGAGCA
C5	13[64]15[63]BLK	TATATTTTGTCAATTGCCTGAGAGTGGAAAGATT
D5	16[79]14[80]BLK	GCGAGTAAAAATATTTAAATGTTCACAAAG
E5	13[96]15[95]BLK	TAGGTAACTATTTTTGAGAGATCAAACGTTA
F5	16[111]14[112]BLK	TGTAGCCATTAAAATTCGCATTAAATGCCGGA
G5	13[128]15[127]BLK	GAGACAGCTAGCTGATAAATTAATTTTTGT
H5	13[160]14[144]BLK	GTAATAAGTTAGGCAGAGGCATTTATGATATT
I5	16[143]15[159]BLK	GCCATCAAGCTCATTTTTTAACCACAAATCCA
J5	16[175]14[176]BLK	TATAACTAACAAAGAACGCGAGAACGCCAA
K5	13[192]15[191]BLK	GTAAAGTAATCGCCATATTTAACAAAACCTTTT
L5	16[207]14[208]BLK	ACCTTTTTATTTTAGTTAATTCATAGGGCTT
M5	13[224]15[223]BLK	ACAACATGCCAACGCTCAACAGTCTTCTGA
N5	16[239]14[240]BLK	GAATTTATTTAATGGTTTGAATATTTCTTACC
O5	13[256]15[255]BLK	GTTTATCAATATGCGTTATACAAACCGACCGT
P5	16[271]14[272]BLK	CTTAGATTTAAGGCGTTAAATAAAGCCTGT
A6	11[32]13[31]BLK	AACAGTTTTGTACCAAAAACATTTTATTTT
B6	14[47]12[48]BLK	AACAAGAGGGATAAAAATTTTAGCATAAAGC
C6	11[64]13[63]BLK	GATTTAGTCAATAAAGCCTCAGAGAACCCTCA
D6	14[79]12[80]BLK	GCTATCAGAAATGCAATGCCTGAATTAGCA
E6	11[96]13[95]BLK	AATGGTCAACAGGCAAGGCAAGAGTAATGTG
F6	14[111]12[112]BLK	GAGGGTAGGATTCAAAAGGGTGAGACATCCAA
G6	11[128]13[127]BLK	TTTGGGGATAGTAGTAGCATTAAAAGGCCG
H6	11[160]12[144]BLK	CCAATAGCTCATCGTAGGAATCATGGCATCAA
I6	14[143]13[159]BLK	CAACCGTTCAAATCACCATCAATTCGAGCCA
J6	14[175]12[176]BLK	CATGTAATAGAATATAAAGTACCAAGCCGT
K6	11[192]13[191]BLK	TATCCGGTCTCATCGAGAACAAGCGACAAAAG
L6	14[207]12[208]BLK	AATTGAGAATTCTGTCCAGACGACTAAACCAA

## Super-Resolution Microscopy with DNA-PAINT

M6	11[224]13[223]BLK	GCGAACCTCCAAGAACGGGTATGACAATAA
N6	14[239]12[240]BLK	AGTATAAAGTTCAGCTAATGCAGATGTCTTTC
O6	11[256]13[255]BLK	GCCTTAAACCAATCAATAATCGGCACGCGCCT
P6	14[271]12[272]BLK	TTAGTATCACAATAGATAAGTCCACGAGCA
A7	9[32]11[31]BLK	TTTACCCCAACATGTTTTAAATTTCCATAT
B7	12[47]10[48]BLK	TAAATCGGGATTCCCAATTCGCGATATAATG
C7	9[64]11[63]BLK	CGGATTGCAGAGCTTAATGCTGAAACGAGTA
D7	12[79]10[80]BLK	AAATTAAGTTGACCATTAGATACTTTTGCG
E7	9[96]11[95]BLK	CGAAAGACTTTGATAAGAGGTCATATTTGCA
F7	12[111]10[112]BLK	TAAATCATATAACCTGTTTAGCTAACCTTTAA
G7	9[128]11[127]BLK	GCTTCAATCAGGATTAGAGAGTTATTTTCA
H7	9[160]10[144]BLK	AGAGAGAAAAAATGAAAATAGCAAGCAAATC
I7	12[143]11[159]BLK	TTCTACTACGCGAGCTGAAAAGGTTACCGCGC
J7	12[175]10[176]BLK	TTTTATTTAAGCAAATCAGATATTTTTTGT
K7	9[192]11[191]BLK	TTAGACGGCCAAATAAGAAACGATAGAAGGCT
L7	12[207]10[208]BLK	GTACCGCAATTC TAAGAACGCGAGTATTATTT
M7	9[224]11[223]BLK	AAAGTCACAAAATAAACAGCCAGCGTTTTA
N7	12[239]10[240]BLK	CTTATCATTCCCGACTTGCGGGAGCCTAATTT
O7	9[256]11[255]BLK	GAGAGATAGAGCGTCTTTCCAGAGGTTTGAA
P7	12[271]10[272]BLK	TGTAGAAATCAAGATTAGTTGCTCTTACCA
A8	7[32]9[31]BLK	TTTAGGACAAATGCTTTAAACAATCAGGTC
B8	10[47]8[48]BLK	CTGTAGCTTGACTATTATAGTCAGTTCATTGA
C8	7[56]9[63]BLK	ATGCAGATACATAACGGGAATCGTCATAAATAAGCAAAG
D8	10[79]8[80]BLK	GATGGCTTATCAAAAAGATTAAGAGCGTCC
E8	7[96]9[95]BLK	TAAGAGCAAATGTTTAGACTGGATAGGAAGCC
F8	10[111]8[112]BLK	TTGCTCCTTTCAAATATCGCGTTTGAGGGGGT
G8	7[120]9[127]BLK	CGTTTACCAGACGACAAAGAAGTTTTGCCATAATTCGA
H8	7[160]8[144]BLK	TTATTACGAAGAACTGGCATGATTGCGAGAGG
I8	10[143]9[159]BLK	CCAACAGGAGCGAACCAGACCGGAGCCTTTAC
J8	10[175]8[176]BLK	TTAACGTCTAACATAAAAACAGGTAACGGA
K8	7[184]9[191]BLK	CGTAGAAAATACATACCGAGGAAACGCAATAAGAAGCGCA
L8	10[207]8[208]BLK	ATCCCAATGAGAATTAACGAACAGTTACCAG
M8	7[224]9[223]BLK	AACGCAAAGATAGCCGAACAAACCCTGAAC

N8	10[239]8[240]BLK	GCCAGTTAGAGGGTAATTGAGCGCTTTAAGAA
O8	7[248]9[255]BLK	GTTTATTTTGTGCACAATCTTACCGAAGCCCTTAAATATCA
P8	10[271]8[272]BLK	ACGCTAACACCCACAAGAATTGAAAATAGC
A9	5[32]7[31]BLK	CATCAAGTAAAACGAACTAACGAGTTGAGA
B9	8[47]6[48]BLK	ATCCCCCTATACCACATTCAACTAGAAAAATC
D9	8[79]6[80]BLK	AATACTGCCCAAAGGAATTACGTGGCTCA
E9	5[96]7[95]BLK	TCATTTCAGATGCGATTTTAAAGAACAGGCATAG
F9	8[111]6[112]BLK	AATAGTAAACACTATCATAACCCTCATTGTGA
H9	5[160]6[144]BLK	GCAAGGCCTCACCAGTAGACCATGGGCTTGA
I9	8[143]7[159]BLK	CTTTTGCAGATAAAAACCAAAATAAAGACTCC
J9	8[175]6[176]BLK	ATACCCAACAGTATGTTAGCAAATTAGAGC
L9	8[207]6[208]BLK	AAGGAAACATAAAGGTGGCAACATTATCACCG
M9	5[224]7[223]BLK	TCAAGTTTCATTAAAGGTGAATATAAAAGA
N9	8[239]6[240]BLK	AAGTAAGCAGACACCACGGAATAATATTGACC
P9	8[271]6[272]BLK	AATAGCTATCAATAGAAAATTCAACATTCA
A10	3[32]5[31]BLK	AATACGTTTGAAAGAGGACAGACTGACCTT
B10	6[47]4[48]BLK	TACGTTAAAGTAATCTTGACAAGAACCGAACT
D10	6[79]4[80]BLK	TTATACCACCAAATCAACGTAACGAACGAG
E10	3[96]5[95]BLK	ACACTCATCCATGTTACTTAGCCGAAAGCTGC
F10	6[111]4[112]BLK	ATTACCTTTGAATAAGGCTTGCCCAAATCCGC
H10	3[160]4[144]BLK	TTGACAGGCCACCACCAGAGCCGCGATTTGTA
I10	6[143]5[159]BLK	GATGGTTTGAACGAGTAGTAAATTTACCATTA
J10	6[175]4[176]BLK	CAGCAAAGGAAACGTCACCAATGAGCCGC
L10	6[207]4[208]BLK	TCACCGACGCACCGTAATCAGTAGCAGAACCG
M10	3[224]5[223]BLK	TTAAAGCCAGAGCCGCCACCTCGACAGAA
N10	6[239]4[240]BLK	GAAATTATGCTTTAGCGTCAGACCGGAACC
P10	6[271]4[272]BLK	ACCGATTGTCGGCATTTTCGGTCATAATCA
A11	1[32]3[31]BLK	AGGCTCCAGAGGCTTTGAGGACACGGGTAA
B11	4[47]2[48]BLK	GACCAACTAATGCCACTACGAAGGGGGTAGCA
C11	1[64]4[64]BLK	TTTATCAGGACAGCATCGGAACGACACCAACCTAAAACGAGGTCAATC
D11	4[79]2[80]BLK	GCGCAGACAAGAGGCAAAGAATCCCTCAG
E11	1[96]3[95]BLK	AAACAGCTTTTTCGGGGATCGTCAACACTAAA
F11	4[111]2[112]BLK	GACCTGCTCTTTGACCCCCAGCGAGGGAGTTA

G11	1[128]4[128]BLK	TGACAACCTCGCTGAGGCTTGCATTATACCAAGCGCGATGATAAA
H11	1[160]2[144]BLK	TTAGGATTGGCTGAGACTCCTCAATAACCGAT
I11	4[143]3[159]BLK	TCATCGCCAACAAAGTACAACGGACGCCAGCA
J11	4[175]2[176]BLK	CACCAGAAAGGTTGAGGCAGGTCATGAAAG
K11	1[192]4[192]BLK	GCGGATAACCTATATTCTGAAACAGACGATTGGCCTTGAAGAGCCAC
L11	4[207]2[208]BLK	CCACCCTCTATTCCAAAACAAATACCTGCCTA
M11	1[224]3[223]BLK	GTATAGCAAACAGTTAATGCCCAATCCTCA
N11	4[239]2[240]BLK	GCCTCCCTCAGAATGGAAAGCGCAGTAACAGT
O11	1[256]4[256]BLK	CAGGAGGTGGGGTCAGTGCCTTGAGTCTCTGAATTTACCGGGAACCAG
P11	4[271]2[272]BLK	AAATCACCTTCCAGTAAGCGTCAGTAATAA
A12	0[47]1[31]BLK	AGAAAGGAACAACATAAGGAATTCAAAAAAA
B12	2[47]0[48]BLK	ACGGCTACAAAAGGAGCCTTTAATGTGAGAAT
C12	0[79]1[63]BLK	ACAACCTTCAACAGTTTCAGCGGATGTATCGG
D12	2[79]0[80]BLK	CAGCGAAACTTGCTTTCGAGGTGTTGCTAA
E12	0[111]1[95]BLK	TAAATGAATTTTCTGTATGGGATTAATTTCTT
F12	2[111]0[112]BLK	AAGCCGCTGATACCGATAGTTGCGACGTTAG
G12	0[143]1[127]BLK	TCTAAAGTTTTGTGCTCTTTCAGCCGACAA
H12	0[175]0[144]BLK	TCCACAGACAGCCCTCATAGTTAGCGTAACGA
I12	2[143]1[159]BLK	ATATTCGGAACCATCGCCCCACGCAGAGAAGGA
J12	2[175]0[176]BLK	TATTAAGAAGCGGGTTTTGCTCGTAGCAT
K12	0[207]1[191]BLK	TCACCAGTACAAACTACAACGCCTAGTACCAG
L12	2[207]0[208]BLK	TTTCGGAAGTGCCGTCGAGAGGGTGAGTTTCG
M12	0[239]1[223]BLK	AGGAACCCATGTACCCTAACACTTGATATAA
N12	2[239]0[240]BLK	GCCCGTATCCGGAATAGGTGTATCAGCCCAAT
O12	0[271]1[255]BLK	CCACCCTCATTTTCAGGGATAGCAACCGTACT
P12	2[271]0[272]BLK	GTTTTAACTTAGTACCGCCACCCAGAGCCA

### Supplementary Table 4: List of biotinylated staples

No	Position	Name	Sequence	Mod
1	C02	18[63]20[56]BIOTIN	ATTAAGTTTACCGAGCTCGAATTCGGGAAACCTGTCGTGC	5'-BT
2	C09	4[63]6[56]BIOTIN	ATAAGGGAACCGGATATTCATTACGTCAGGACGTTGGGAA	5'-BT
3	G02	18[127]20[120]BIOTIN	GCGATCGGCAATTCACACAACAGGTGCCTAATGAGTG	5'-BT
4	G09	4[127]6[120]BIOTIN	TTGTGTCGTGACGAGAAACACCAATTTCAACTTAAAT	5'-BT

5	K02	18[191]20[184]BIOTIN	ATTCATTTTTGTTTGGATTATACTAAGAAACCACCAGAAG	5'-BT
6	K09	4[191]6[184]BIOTIN	CACCCTCAGAAACCATCGATAGCATTGAGCCATTTGGGAA	5'-BT
7	O02	18[255]20[248]BIOTIN	AACAATAACGTAAACAGAAATAAAAAATCCTTTGCCCGAA	5'-BT
8	O09	4[255]6[248]BIOTIN	AGCCACCACTGTAGCGCGTTTTCAAGGGAGGGAAGGTAAA	5'-BT

## Supplementary Table 5: Exemplary folding table

Component	Initial conc. ( $\mu\text{M}$ )	Parts	Pool conc. (nM)	Target conc. (nM)	Volume ( $\mu\text{l}$ )	Excess
Scaffold	0.1	1	100	10	4	1
Core Mix	100	164	609.7560976	100	6.56	10
P1 Mix	100	12	8333.333333	1000	4.8	100
Biotin 1:10	100	80	1250	10	0.32	1
H <sub>2</sub> O					20.32	
10x Folding Buffer					4	
Total Volume					40	

## Supplementary Table 6: Experimental conditions

Figure	Type	Sample	Imager	Buffer	Frames	$t_{int}$	$c_i$	Power	PPT	Camera
1b, 7c	in vitro	20 nm grids	P1	B+	7500	300 ms	5 nM	1.5 kW/cm <sup>2</sup>	Yes	EMCCD
1d, e	in situ	Microtubules	P3	C	50000	100 ms	2 nM	2.5 kW/cm <sup>2</sup>	No	EMCCD
2d-f	in vitro	Exchange rectangle	P1,P3	B+	7500	300 ms	10 nM	6 kW/cm <sup>2</sup>	Yes	EMCCD
2g	in situ	Microtubules / Mitochondria	P1,P3	C	20000	150 ms	0.8 nM	2 kW/cm <sup>2</sup>	No	EMCCD
3d-f 4d, f	in vitro	10 and 20 nm grids, LMU logo	P1	B+	80000	350 ms	0.7 nM	4.5 kW/cm <sup>2</sup>	Yes	sCMOS
4b, c, e	in vitro	10 and 20 nm grids, MPI logo	P1	B+	80000	350 ms	1 nM	4.5 kW/cm <sup>2</sup>	Yes	sCMOS

For full details on acquisition settings see corresponding YAML files.

## Supplementary Table 7: Dye recommendations

Excitation	Rank	Excitation wavelength (nm)	Dye	Compatible with PCA/PCD/Trolox System
Red	1	640	Atto647N	Yes
	2	640	Cy5	Yes
	3	640	Atto655	No
Green	1	561	Cy3b	Yes
	2	561	Atto565	Yes
	3	561	Cy3	Yes
Blue	1	488	Atto488	Yes
	2	488	Alexa488	Yes

## **Site-specific labeling of Affimers for DNA- PAINT microscopy**

**T. Schlichthaerle**, A.S. Eklund, F. Schueder, M.T. Strauss, C. Tiede, A. Curd, J. Ries, M. Peckham, D.C. Tomlinson, R. Jungmann

published in

*Angewandte Chemie (2018)*

Reprinted with Permission from [160]  
Copyright 2018 WILEY

## VIP Super-resolution Microscopy Very Important Paper

International Edition: DOI: 10.1002/anie.201804020  
German Edition: DOI: 10.1002/ange.201804020

## Site-Specific Labeling of Affimers for DNA-PAINT Microscopy

Thomas Schlichthaerle, Alexandra S. Eklund, Florian Schueder, Maximilian T. Strauss, Christian Tiede, Alistair Curd, Jonas Ries, Michelle Peckham, Darren C. Tomlinson, and Ralf Jungmann\*

**Abstract:** Optical super-resolution techniques allow fluorescence imaging below the classical diffraction limit of light. From a technology standpoint, recent methods are approaching molecular-scale spatial resolution. However, this remarkable achievement is not easily translated to imaging of cellular components, since current labeling approaches are limited by either large label sizes (antibodies) or the sparse availability of small and efficient binders (nanobodies, aptamers, genetically-encoded tags). In this work, we combined recently developed Affimer reagents with site-specific DNA modification for high-efficiency labeling and imaging using DNA-PAINT. We assayed our approach using an actin Affimer. The small DNA-conjugated affinity binders could provide a solution for efficient multitarget super-resolution imaging in the future.

Super-resolution (SR) microscopy techniques<sup>[1]</sup> are evolving to become standard characterization tools in the life sciences. Due to the use of target-specific fluorescent labels, super-resolution—in contrast to electron microscopy (EM)—enables high-contrast imaging in complex 3D cellular architectures,<sup>[2]</sup> and thus combines the advantages of increased spatial resolution with molecular affinity probes. While the use of labels with high target specificity such as antibodies is one of the biggest advantages of fluorescence microscopy over, for example, EM, it is at the same time also one of the most severe limitations for SR approaches to date. As current SR methods reach localization precisions on the order of only a few nanometers,<sup>[3]</sup> this achievement does not translate to achievable image resolution in biological specimens due to the relatively large size of commonly used labeling probes. In

the case of primary and secondary antibodies, the size of the probes easily adds an additional linkage error of around 10–15 nm to the actual position of the molecule of interest.<sup>[1]</sup> This results in the fact that high-performance super-resolution techniques actually report the location of the probe rather than the one of the biomolecules under investigation.

The ideal labeling probe would need to be small and target-specific to reduce the linkage error and allow high labeling densities due to minimal steric hindrance. Furthermore, quantitative imaging approaches<sup>[4]</sup> demand stoichiometric labeling, that is, ideally one reporter molecule should be bound to exactly one copy of the target molecule.

The issue of efficient labeling using small probes has recently been advanced by the development of novel affinity reagents including nanobodies,<sup>[5]</sup> aptamers,<sup>[6]</sup> and genetically encoded self-labeling tags such as SNAP or HALO.<sup>[7]</sup> Besides the size of the labeling probe, it is equally important to be able to engineer these binders against a large library of target molecules in a rapid and straightforward fashion. This has traditionally been difficult for, nanobodies, for example, since the selection process of novel binders usually relies on immunization of animals,<sup>[8]</sup> which makes it both time-consuming and expensive. While aptamers are promising candidates for the rapid development of small and efficient labeling probes, only a few candidates have been shown to work for extracellular target molecules. Self-labeling tags such as SNAP (19.4 kDa) or HALO (33 kDa) allow efficient target labeling, however, they require genetic engineering of cell lines, for example, using CRISPR/Cas,<sup>[9]</sup> Zinc finger,<sup>[10]</sup> or TALEN technology.<sup>[11]</sup> The same argument holds true for the large amount of GFP-tagged cell lines which can be targeted using GFP nanobodies.<sup>[5a,12]</sup> In addition, GFP fusion (25 kDa) adds an additional linkage error to the one from the nanobody (15 kDa).

Affimers<sup>[13]</sup> are a recently developed class of labeling probes (ca. 10–12 kDa, ca. 2 nm) that are isolated from large phage-display libraries (approx. 10<sup>10</sup> members). The ability to quickly isolate Affimers<sup>[14]</sup> with high specificity and affinity that can be used in a range of applications<sup>[15]</sup> highlights their potential as alternatives to traditional antibodies. In SR microscopy, Affimer reagents have been used to image tubulin and a receptor tyrosine kinase by site-specific labeling with a fluorophore.<sup>[13b]</sup> Interestingly, the anti-tubulin Affimer labels interphase microtubules in a similar way to a widely used antibody, but it also labels the central region of the cytokinetic furrow, from which antibodies are usually excluded. This highlights a further advantage of using smaller probes, namely, that their small size allows them to penetrate dense structures that exclude antibodies.

[\*] T. Schlichthaerle, A. S. Eklund, F. Schueder, M. T. Strauss, R. Jungmann  
Faculty of Physics and Center for Nanoscience, LMU Munich Munich (Germany)

and  
Max Planck Institute of Biochemistry, Martinsried (Germany)  
E-mail: jungmann@biochem.mpg.de

C. Tiede, A. Curd, M. Peckham, D. C. Tomlinson  
Astbury Centre for Structural and Molecular Biology  
University of Leeds, Leeds (UK)

and  
School of Molecular and Cellular Biology  
University of Leeds, Leeds (UK)

J. Ries  
European Molecular Biology Laboratory  
Cell Biology and Biophysics Unit, Heidelberg (Germany)

Supporting information and the ORCID identification number(s) for the author(s) of this article can be found under:  
<https://doi.org/10.1002/anie.201804020>.

In this work, we combined site-specific DNA labeling of Affimers with the recently developed DNA-PAINT super-resolution technique.<sup>[16]</sup> In DNA-PAINT, the apparent “switching” between bright and dark states of dye molecules used for super-resolution reconstruction is achieved through the transient interaction of a dye-labeled imager strand with its complementary docking strand linked to a target molecule of interest. In order to perform DNA-PAINT on proteins in a cellular context, the docking strand needs to be attached to an affinity reagent (e.g., antibodies). To achieve quantitative, site-specific one-to-one labeling of Affimers with DNA-PAINT docking strands, we made use of a C-terminal cysteine modification of the Affimer to site-specifically attach a single DNA strand using cysteine-maleimide chemistry.<sup>[17]</sup> We assayed the achievable imaging resolution of an actin Affimer in comparison to phalloidin, a small molecule commonly used for actin labeling and super-resolution imaging, and achieved comparable results.<sup>[18]</sup>

To site-specifically modify Affimers, we first labeled a reduced C-terminal cysteine residue with maleimide-DBCO which was then linked to azide-functionalized DNA using a strain-promoted azide-alkyne cycloaddition (SPAAC) reaction (Figure 1, see also Material and Methods in the Supporting Information for details). Subsequently, the Affimer was purified using a HisTrap column to remove the free unreacted DNA (Figure S1 in the Supporting Information). The successful conjugation was evaluated using SDS-PAGE gel analysis. In comparison to the unconjugated Affimer, the molecular weight increased by around 5 kDa, which suggests a stoichiometric 1:1 labeling of DNA to Affimers (Figure S2).

The DNA-PAINT docking strand was additionally labeled with a fixed Atto488 dye (Figure 1), which allowed us to rapidly identify a specific cellular phenotype using diffraction-limited widefield microscopy before subsequent DNA-PAINT image acquisition was performed. We then labeled actin filaments in fixed Cos7 cells with our purified DNA-Affimer conjugate and performed 3D DNA-PAINT microscopy (Figure 2a). Comparison of the diffraction-limited image acquired using the fixed Atto488 dye shows a clear improvement in resolution and highlights the high labeling specificity and efficiency of our DNA-conjugated actin Affimer (Figure 2b,c, see also Figure S3 for comparison

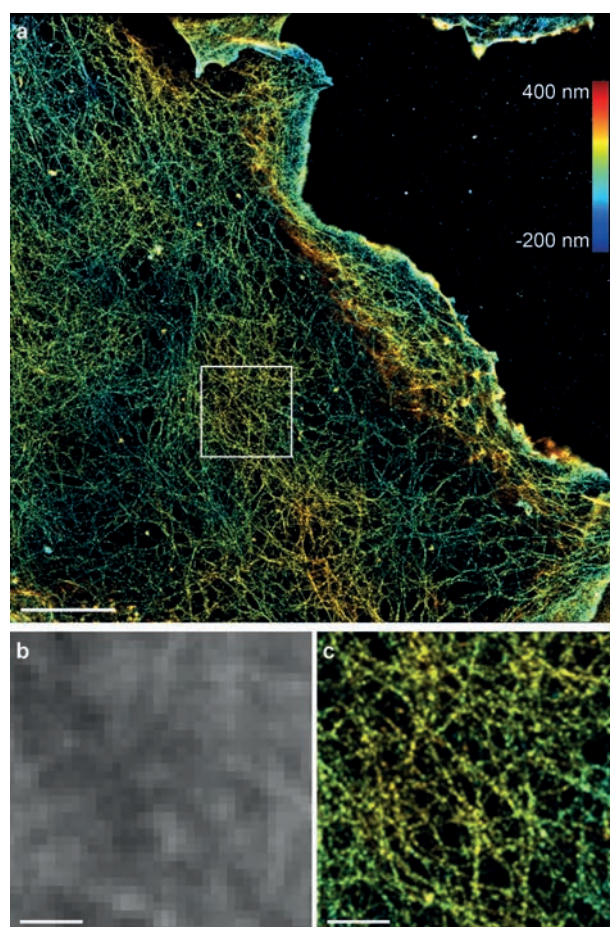


**Figure 2.** a) DNA-PAINT imaging of Affimer-labeled actin network in fixed Cos7 cells (color indicates height). b) Diffraction-limited zoom-in of the highlighted area in (a). c) Super-resolved zoom-in of the highlighted area in (a) shows increased spatial resolution and dense actin labeling. Scale bars: 5  $\mu\text{m}$  (a), 1  $\mu\text{m}$  (b, c).

with phalloidin labeling). To quantify the achievable resolution, we overlaid thirteen single actin fibers by the center of each filament and measured a line width of approximately 18 nm (FWHM). In comparison, we also performed the same

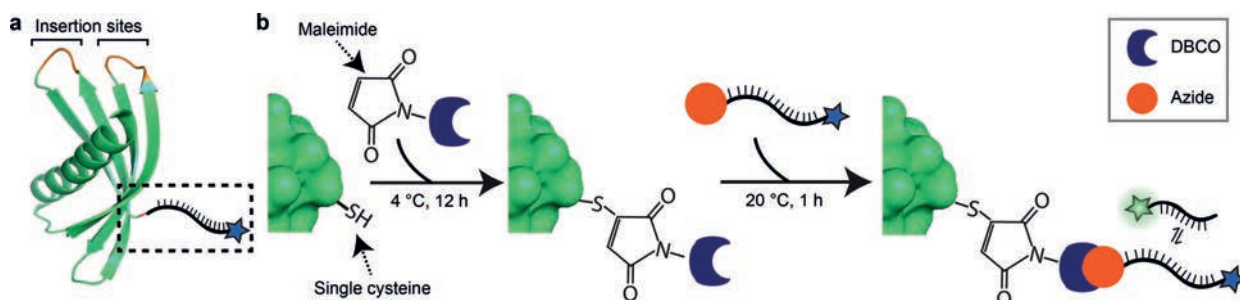


**Figure 1.** a) Site-specific DNA labeling of Affimer reagents. Insertion sites for binder evolution against target proteins are highlighted in orange. The site-specifically attached DNA strand (dotted box) contains an additional Atto488 fluorophore for fast diffraction-limited imaging. b) Labeling of single cysteines using maleimide-DBCO (left). Subsequently, azide-labeled DNA is added and binds covalently to the DBCO (center). Finally, DNA-labeled Affimers can be used for DNA-PAINT imaging (right). Affimer cartoons modified from PDB ID: 4N6T.

analysis on a phalloidin dataset and measured a line width of approximately 13 nm. Both values are in good agreement with earlier studies<sup>[18,19]</sup> (Figure S4), taking the different binder size of phalloidin versus Affimers into account.

Additionally, we performed a copper-catalyzed cycloaddition reaction (CuAAC) as alternative labeling strategy (Figure S5), achieving similar labeling and imaging performance (Figure S6). While labeling efficiency and image quality is similar, we recommend the use of SPAAC because it is less time consuming and involves fewer reagents. In addition, we also performed direct stochastic optical reconstruction microscopy (dSTORM) imaging using an Alexa647-labeled Affimer (Figure S7) to further demonstrate the wide applicability of Affimers as labeling reagents for super-resolution methods.

Next, we assayed the achievable 3D resolution of our DNA-conjugated Affimers and DNA-PAINT by evaluating the actin network in Cos7 cells in three dimensions (Figure 3 a,b). We were able to confirm two distinct layers of actin in 3D (Figure 3d) with an apparent thickness of approximately 40 nm and a distance of around 130 nm (Figure 3e), as previously reported using dual-objective STORM imaging<sup>[18]</sup> (See Figure S8 for additional 3D data). The combination of the efficient labeling of the actin Affimers with the high-resolution capability of DNA-PAINT allowed us to achieve similar imaging performance (localization precision  $\approx 5$  nm) using a standard inverted fluorescence microscope without the need for dual-objective detection. In the DNA-PAINT case, the higher resolution in 2D, as well as in 3D, is due to the high photon numbers available from the repetitive and transient binding of probes, rather than improved instrumentation.

In conclusion, site-specific conjugation of single DNA strands to Affimer reagents provides an attractive route for DNA-based super-resolution techniques due to their small label size and quantitative labeling capability. We envision

applications in absolute quantitative microscopy approaches such as qPAINT and multiplexed target detection using orthogonal Affimer binders coupled to distinct DNA sequences, for example, for Exchange-PAINT microscopy. In general, cysteine-based DNA labeling of affinity reagents could be an efficient way to obtain quantitative DNA-PAINT reagents and it should also be possible to apply it for other probes such as nanobodies,<sup>[5a]</sup> FAB fragments,<sup>[20]</sup> or Darpins.<sup>[21]</sup>

### Acknowledgements

We thank Sebastian Strauss for useful discussions and the optimization of the fixation protocol. We thank Jae Shin for fruitful discussions and the initial CuAAC labeling protocol. We thank Orsolya Kimbu Wade and Philipp Nickels for useful discussions. We thank Alexander Auer for microscopy and analysis support. We thank Bianca Sperl for help with cell culture. We thank Ruth Hughes for help with cell culture and imaging. We thank Bernd Haas from the Core Facility of the Max Planck Institute of Biochemistry for the synthesis of the phalloidin-DNA conjugate. We thank Amy Turner for work on optimization of protocols for dSTORM. This work was supported by the DFG through the Emmy No-ether Program (DFG JU 2957/1-1), the SFB 1032 (Nanoagents for spatio-temporal control of molecular and cellular reactions, Project A11), the ERC through an ERC Starting Grant (MolMap, Grant agreement number 680241), the Max Planck Society, the Max Planck Foundation and the Center for Nano-science (CeNS) to R.J. M.P. acknowledges funding from the UK MRC (grant MR/K015613/1). M.T.S. and A.S.E. acknowledges support from the International Max Planck Research School for Molecular and Cellular Life Sciences (IMPRS-LS). T.S. acknowledges support from the DFG through the Graduate School of Quantitative Biosciences Munich

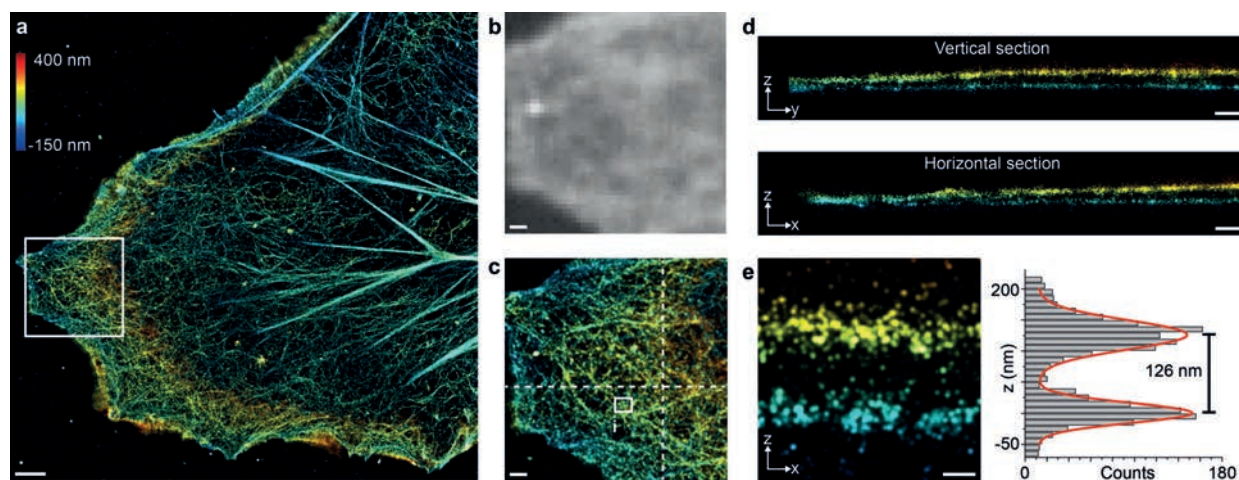


**Figure 3.** Actin Affimer imaging of a Cos7 cell in 3D reveals the dual-layer organization of actin. a) Overview DNA-PAINT image of actin filaments in a Cos7 cell (color indicates height). b) Diffraction-limited zoom-in of the highlighted area (a). c) Zoom-in of the super-resolved image of the highlighted area in (a). d) Vertical and horizontal Z-sections indicated as dashed lines in (c). e) Z-section of the highlighted area (i) in (c), indicating the two-layer organization of the actin filaments. Cross-sectional histogram analysis shows a layer-to-layer distance of 126 nm in a single cell. Scale bars: 2  $\mu$ m (a), 500 nm (b, c), 300 nm (d), 50 nm (e).

(QBM). The dSTORM system was generously funded by alumnus M. Beverley, in support of the University of Leeds “making a world of difference” campaign.

### Conflict of interest

The authors declare no conflict of interest.

**Keywords:** Affimers · DNA-PAINT · quantitative microscopy · small binders · super-resolution microscopy

**How to cite:** *Angew. Chem. Int. Ed.* **2018**, *57*, 11060–11063  
*Angew. Chem.* **2018**, *130*, 11226–11230

- [1] S. J. Sahl, S. W. Hell, S. Jakobs, *Nat. Rev. Mol. Cell Biol.* **2017**, *18*, 685–701.
- [2] F. Huang, G. Sirinakakis, E. S. Allgeyer, L. K. Schroeder, W. C. Duim, E. B. Kromann, T. Phan, F. E. Rivera-Molina, J. R. Myers, I. Irnov, M. Lessard, Y. Zhang, M. A. Handel, C. Jacobs-Wagner, C. P. Lusk, J. E. Rothman, D. Toomre, M. J. Booth, J. Bewersdorf, *Cell* **2016**, *166*, 1028–1040.
- [3] a) F. Balzarotti, Y. Eilers, K. C. Gwosch, A. H. Gynna, V. Westphal, F. D. Stefani, J. Elf, S. W. Hell, *Science* **2017**, *355*, 606–612; b) M. Dai, R. Jungmann, P. Yin, *Nat. Nanotechnol.* **2016**, *11*, 798–807.
- [4] a) R. Jungmann, M. S. Avendano, M. Dai, J. B. Woehrstein, S. S. Agasti, Z. Feiger, A. Rodal, P. Yin, *Nat. Methods* **2016**, *13*, 439–442; b) C. Karathanasis, F. Fricke, G. Hummer, M. Heilemann, *ChemPhysChem* **2017**, *18*, 942–948.
- [5] a) J. Ries, C. Kaplan, E. Platonova, H. Eghlidi, H. Ewers, *Nat. Methods* **2012**, *9*, 582–584; b) M. Mikhaylova, B. M. Cloin, K. Finan, R. van den Berg, J. Teeuw, M. M. Kijanka, M. Sokolowski, E. A. Katrukha, M. Maidorn, F. Opazo, S. Moutel, M. Vantard, F. Perez, P. M. van Bergen en Henegouwen, C. C. Hoogenraad, H. Ewers, L. C. Kapitein, *Nat. Commun.* **2015**, *6*, 7933.
- [6] F. Opazo, M. Levy, M. Byrom, C. Schafer, C. Geisler, T. W. Groemer, A. D. Ellington, S. O. Rizzoli, *Nat. Methods* **2012**, *9*, 938–939.
- [7] a) A. Keppler, S. Gendreizig, T. Gronemeyer, H. Pick, H. Vogel, K. Johnsson, *Nat. Biotechnol.* **2003**, *21*, 86–89; b) G. V. Los, L. P. Encell, M. G. McDougall, D. D. Hartzell, N. Karassina, C. Zimprich, M. G. Wood, R. Learish, R. F. Ohana, M. Urh, D. Simpson, J. Mendez, K. Zimmerman, P. Otto, G. Vidugiris, J. Zhu, A. Darzins, D. H. Klaubert, R. F. Bulleit, K. V. Wood, *ACS Chem. Biol.* **2008**, *3*, 373–382.
- [8] a) E. Pardon, T. Laeremans, S. Triest, S. G. Rasmussen, A. Wohlkonig, A. Ruf, S. Muyltermans, W. G. Hol, B. K. Kobilka, J. Steyaert, *Nat. Protoc.* **2014**, *9*, 674–693; b) T. Pleiner, M. Bates, S. Trakhanov, C. T. Lee, J. E. Schliep, H. Chug, M. Bohning, H. Stark, H. Urlaub, D. Gorlich, *Elife* **2015**, *4*, e11349.
- [9] M. Ratz, I. Testa, S. W. Hell, S. Jakobs, *Sci. Rep.* **2015**, *5*, 9592.
- [10] D. Carroll, J. J. Morton, K. J. Beumer, D. J. Segal, *Nat. Protoc.* **2006**, *1*, 1329–1341.
- [11] N. E. Sanjana, L. Cong, Y. Zhou, M. M. Cuniff, G. Feng, F. Zhang, *Nat. Protoc.* **2012**, *7*, 171–192.
- [12] I. Poser, M. Sarov, J. R. Hutchins, J. K. Heriche, Y. Toyoda, A. Pozniakovsky, D. Weigl, A. Nitzsche, B. Hegemann, A. W. Bird, L. Pelletier, R. Kittler, S. Hua, R. Naumann, M. Augsburg, M. M. Sykora, H. Hofmeister, Y. Zhang, K. Nasmyth, K. P. White, S. Dietzel, K. Mechtler, R. Durbin, A. F. Stewart, J. M. Peters, F. Buchholz, A. A. Hyman, *Nat. Methods* **2008**, *5*, 409–415.
- [13] a) C. Tiede, A. A. Tang, S. E. Deacon, U. Mandal, J. E. Nettleship, R. L. Owen, S. E. George, D. J. Harrison, R. J. Owens, D. C. Tomlinson, M. J. McPherson, *Protein Eng. Des. Sel.* **2014**, *27*, 145–155; b) C. Tiede, R. Bedford, S. J. Heseltine, G. Smith, I. Wijetunga, R. Ross, D. AlQallaf, A. P. Roberts, A. Balls, A. Curd, R. E. Hughes, H. Martin, S. R. Needham, L. C. Zanetti-Domingues, Y. Sadigh, T. P. Peacock, A. A. Tang, N. Gibson, H. Kyle, G. W. Platt, N. Ingram, T. Taylor, L. P. Coletta, I. Manfield, M. Knowles, S. Bell, F. Esteves, A. Maqbool, R. K. Prasad, M. Drinkhill, R. S. Bon, V. Patel, S. A. Goodchild, M. Martin-Fernandez, R. J. Owens, J. E. Nettleship, M. E. Webb, M. Harrison, J. D. Lippiat, S. Ponnambalam, M. Peckham, A. Smith, P. K. Ferrigno, M. Johnson, M. J. McPherson, D. C. Tomlinson, *Elife* **2017**, *6*, e24903.
- [14] A. A. Tang, C. Tiede, D. J. Hughes, M. J. McPherson, D. C. Tomlinson, *Sci. Signaling* **2017**, *10*, eaan0868.
- [15] a) D. J. Hughes, C. Tiede, N. Penswick, A. A. Tang, C. H. Trinh, U. Mandal, K. Z. Zajac, T. Gaule, G. Howell, T. A. Edwards, J. Duan, E. Feyfant, M. J. McPherson, D. C. Tomlinson, A. Whitehouse, *Sci. Signaling* **2017**, *10*, eaaj2005; b) M. A. Michel, K. N. Swatek, M. K. Hospenthal, D. Komander, *Mol. Cell* **2017**, *68*, 233; c) J. I. Robinson, E. W. Baxter, R. L. Owen, M. Thomsen, D. C. Tomlinson, M. P. Waterhouse, S. J. Win, J. E. Nettleship, C. Tiede, R. J. Foster, R. J. Owens, C. W. G. Fishwick, S. A. Harris, A. Goldman, M. J. McPherson, A. W. Morgan, *Proc. Natl. Acad. Sci. USA* **2018**, *115*, E72–E81; d) P. Zhuravski, S. K. Arya, P. Jolly, C. Tiede, D. C. Tomlinson, P. Ko Ferrigno, P. Estrela, *Biosens. Bioelectron.* **2018**, *108*, 1–8.
- [16] a) R. Jungmann, C. Steinhauer, M. Scheible, A. Kuzyk, P. Tinnefeld, F. C. Simmel, *Nano Lett.* **2010**, *10*, 4756–4761; b) R. Jungmann, M. S. Avendano, J. B. Woehrstein, M. Dai, W. M. Shih, P. Yin, *Nat. Methods* **2014**, *11*, 313–318; c) J. Schnitzbauer, M. T. Strauss, T. Schlichthaerle, F. Schueder, R. Jungmann, *Nat. Protoc.* **2017**, *12*, 1198–1228.
- [17] a) A. Mukhortava, M. Schlierf, *Bioconjugate Chem.* **2016**, *27*, 1559–1563; b) T. Nojima, H. Konno, N. Kodera, K. Seio, H. Taguchi, M. Yoshida, *PLoS One* **2012**, *7*, e52534.
- [18] K. Xu, H. P. Babcock, X. Zhuang, *Nat. Methods* **2012**, *9*, 185–188.
- [19] S. S. Agasti, Y. Wang, F. Schueder, A. Sukumar, R. Jungmann, P. Yin, *Chem. Sci.* **2017**, *8*, 3080–3091.
- [20] C. T. Mender, L. Friedrich, I. Laitinen, M. Schlapschy, M. Schwaiger, H. J. Wester, A. Skerra, *MAbs* **2015**, *7*, 96–109.
- [21] H. K. Binz, P. Amstutz, A. Pluckthun, *Nat. Biotechnol.* **2005**, *23*, 1257–1268.

Manuscript received: April 4, 2018

Revised manuscript received: May 11, 2018

Accepted manuscript online: June 6, 2018

Version of record online: July 15, 2018



## Supporting Information

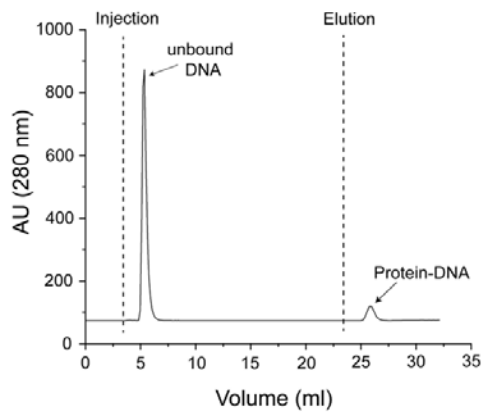
### **Site-Specific Labeling of Affimers for DNA-PAINT Microscopy**

*Thomas Schlichthaerle, Alexandra S. Eklund, Florian Schueder, Maximilian T. Strauss, Christian Tiede, Alistair Curd, Jonas Ries, Michelle Peckham, Darren C. Tomlinson, and Ralf Jungmann\**

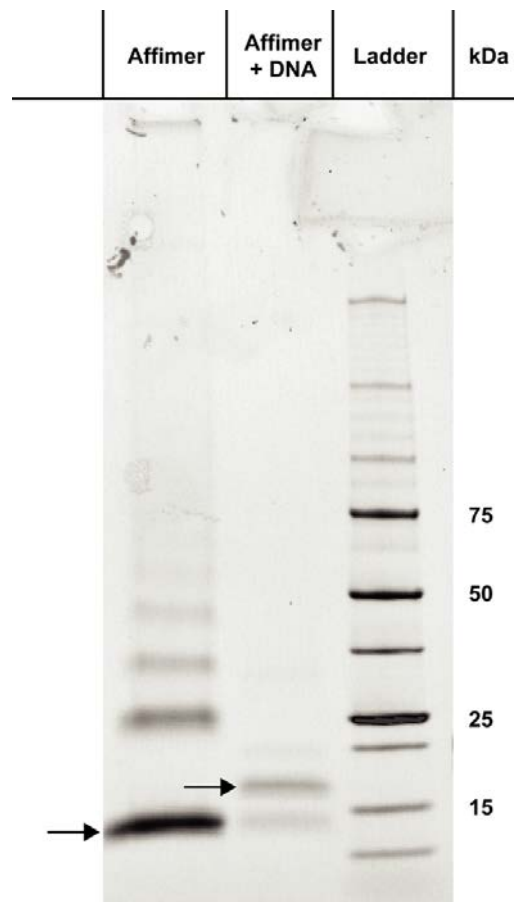
anie\_201804020\_sm\_miscellaneous\_information.pdf

## Supplementary Information

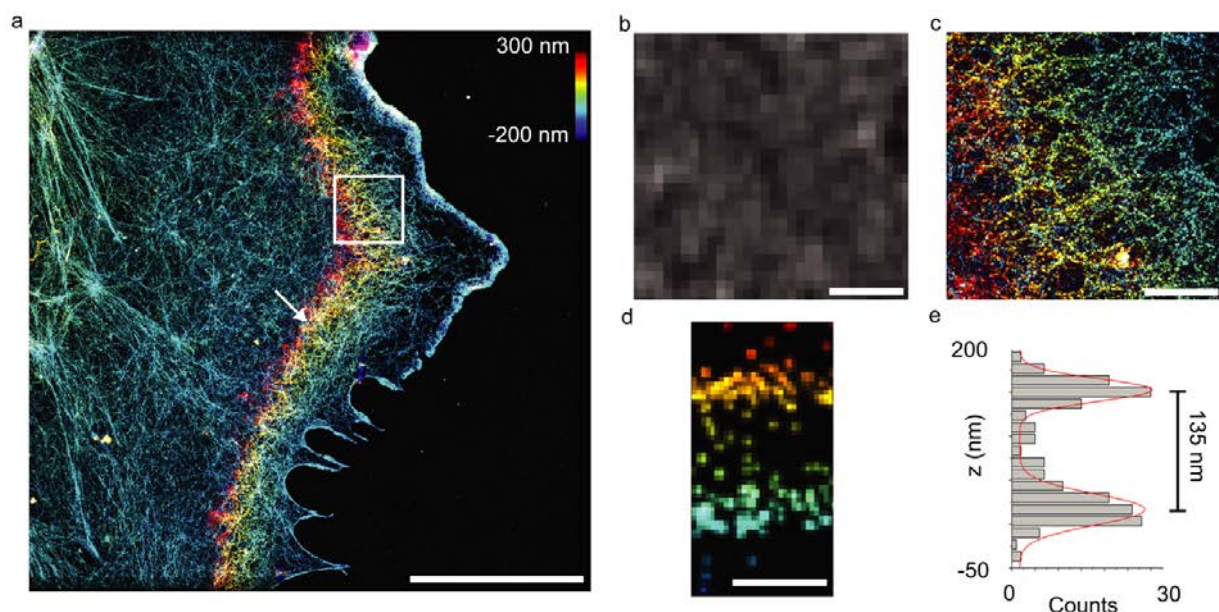
<b>Supplementary Figure 1</b>	HisTrap purification scheme
<b>Supplementary Figure 2</b>	SDS-PAGE gel of Affimer
<b>Supplementary Figure 3</b>	Phalloidin imaging
<b>Supplementary Figure 4</b>	Apparent actin filament width from Affimer and Phalloidin imaging
<b>Supplementary Figure 5</b>	CuAAC labeling scheme
<b>Supplementary Figure 6</b>	2D actin imaging with DNA-labeled Affimer using CuAAC
<b>Supplementary Figure 7</b>	dSTORM with Actin Affimer
<b>Supplementary Figure 8</b>	3D actin imaging of Cos7 cells with Affimer
<b>Supplementary Table 1</b>	Affimer preparation
<b>Supplementary Table 2</b>	Crosslinker dilution calculation
<b>Supplementary Table 3</b>	Addition of Azide-modified DNA via SPAAC
<b>Supplementary Table 4</b>	Addition of Azide-modified DNA via CuAAC
<b>Supplementary Table 5</b>	Handle sequences
<b>Supplementary Table 6</b>	Imager sequences
<b>Supplementary Table 7</b>	Imaging parameters



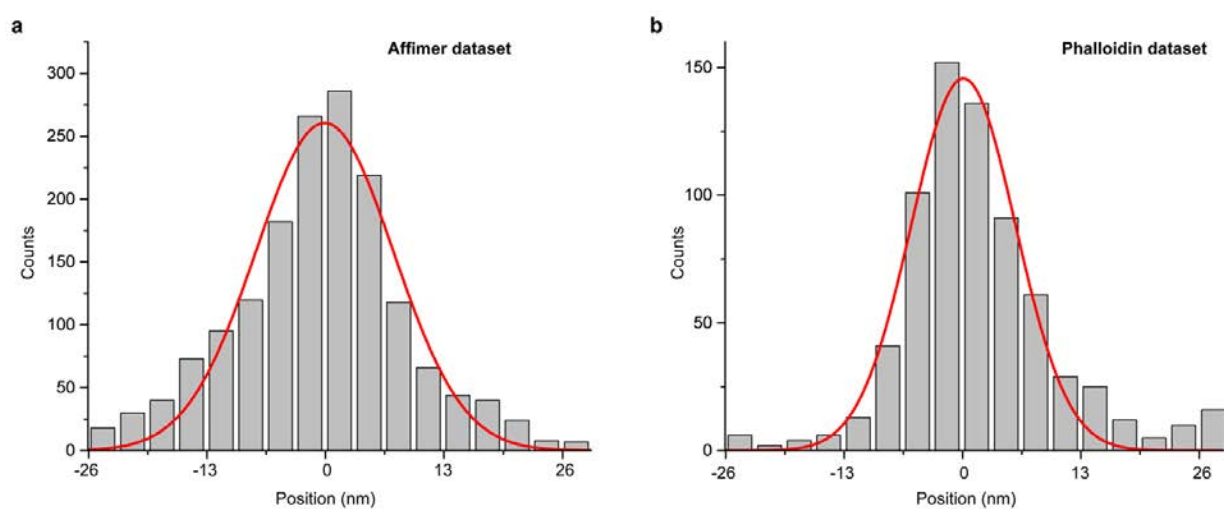
**Supplementary Figure 1 | Histag purification to remove unbound DNA.** The Affimer binds via its Histag to the HisTrap column and the unbound DNA can be removed from the solution. Washing the column with 500 mM Imidazole elutes the Protein and Protein-DNA conjugates.



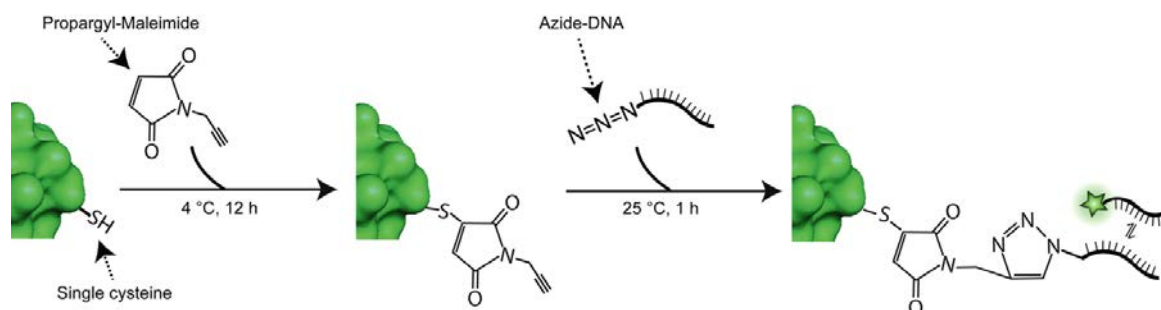
**Supplementary Figure 2 | SDS-PAGE gel of actin 14c Affimer.** Arrows indicate the shift of unlabeled Affimer (left lane) towards the higher molecular weight of the DNA labeled Affimer (second to left lane).



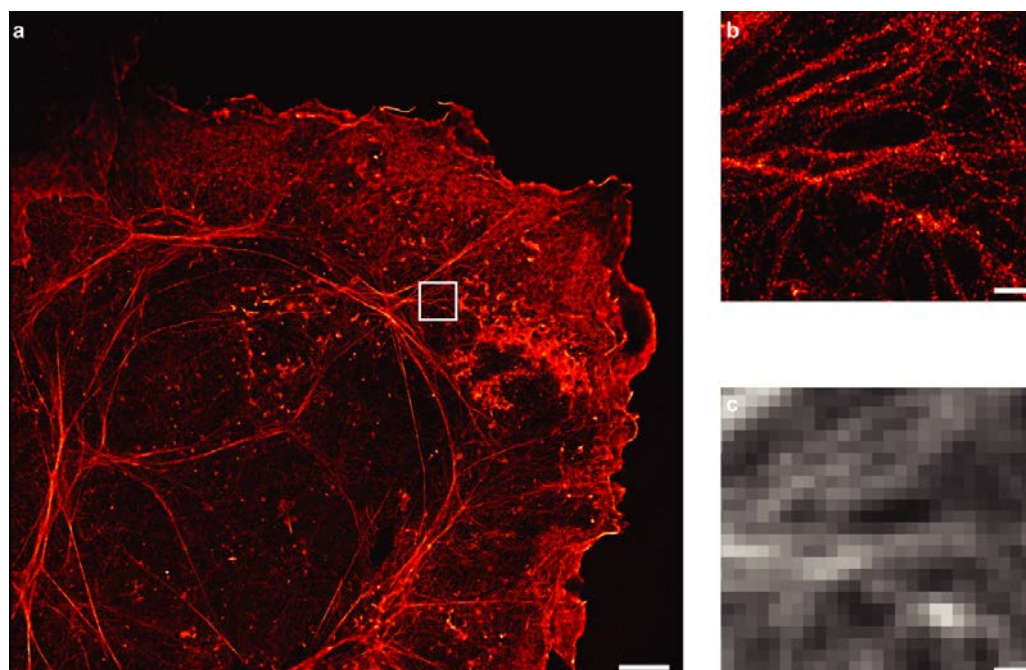
**Supplementary Figure 3 | Actin imaging with phalloidin-DNA in Cos7 cells.** (a) Overview image of super-resolved actin filaments imaged with phalloidin-DNA conjugate. (b) Diffraction-limited (standard deviation of first 10000 frames) zoom-in of highlighted area (white box) in a. (c) Super-resolved zoom-in of the same area showing the actin filaments. (d) Z-section of the highlighted area (white arrow) indicating the two-layer organization of the actin filaments. (e) Cross-sectional histogram analysis shows a layer-to-layer distance of 135 nm. Scale bars: 10  $\mu\text{m}$  (a), 5  $\mu\text{m}$  (b), 1  $\mu\text{m}$  (c), 100 nm (d).



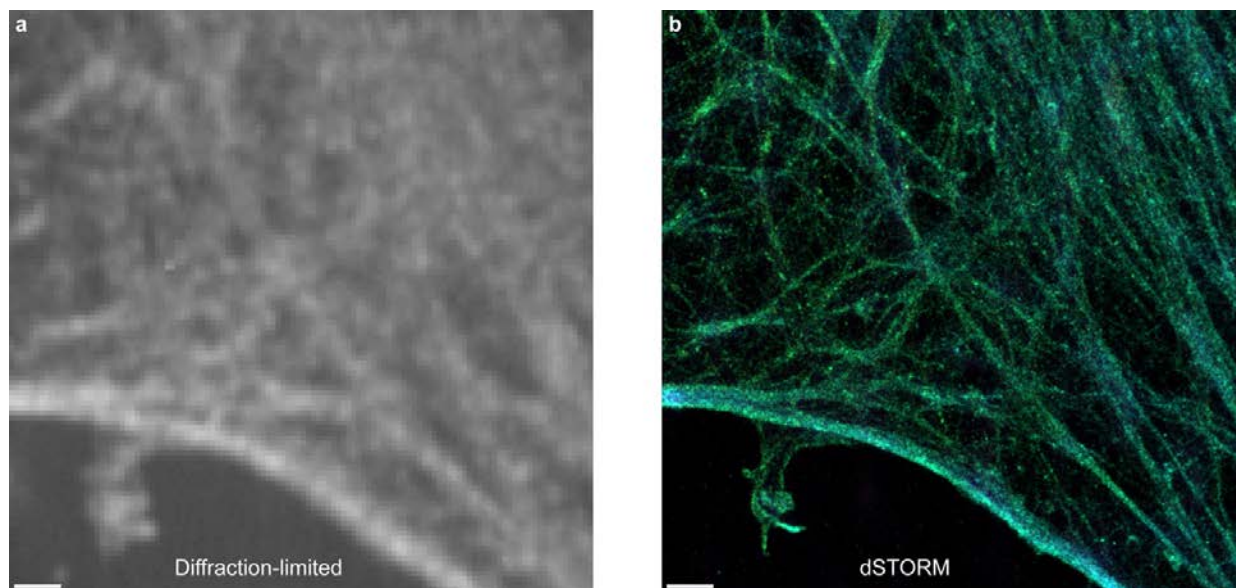
**Supplementary Figure 4 | Apparent actin filament width from Affimer and Phalloidin imaging.** (a) Cross-sectional profile of 13 filaments aligned by the center of each filament (Dataset from the Affimer binder, Figure 2). Red: Gaussian fit with FWHM of  $\sim 18$  nm. (b) Cross-sectional profile of 24 filaments aligned by the center of each filament (Dataset from the Phalloidin binder, Supplementary Figure 3). Red: Gaussian fit with FWHM of  $\sim 13$  nm.



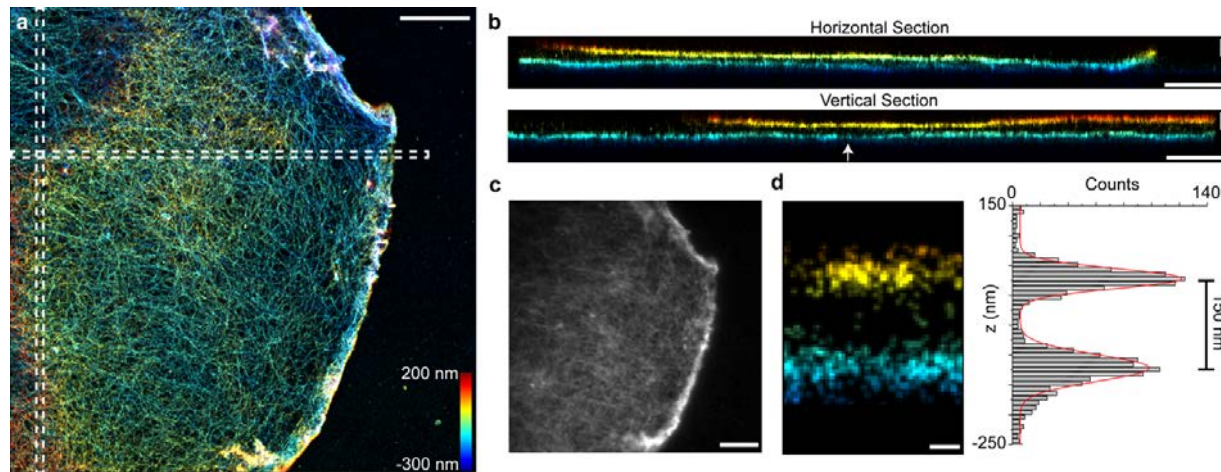
**Supplementary Figure 5 | Alternative labeling strategy using copper-catalysed azide alkyne cycloaddition (CuAAC).** First reaction of Propargyl-Maleimide to the reduced cysteine residue takes place at 4 °C for 12 h. After buffer exchange via Amicon 10 kDa Spin Filters, the second reaction takes place at 25 °C for 1 h, which links the alkyne group to the Azide-labeled DNA. The final conjugate can be used for DNA-PAINT imaging, where the fluorophore-labeled DNA strand binds transiently to the handle strand on the Affimer.



**Supplementary Figure 6 | 2D imaging with actin Affimer labeled via copper-catalysed azide alkyne cycloaddition.** (a) Overview image of Cos7 cell, imaged without fixed Atto 488 fluorophore on the P3 handle sequence. (b) Zoom in image from white box in a. (c) Standard deviation (diffraction-limited) image of first 75000 frames. Scale bars: 5 μm (a), 2 μm (b, c).



**Supplementary Figure 7 | dSTORM using actin Affimer.** (a) Diffraction-limited actin image using Alexa647-labeled Affimers. (b) 3D-dSTORM super-resolution image (color indicates height). Localization precision (NeNA metric): 23 nm. Scale bar: 1 µm.



**Supplementary Figure 8 | 3D Actin imaging in Cos7 cells with Affimers.** (a) Overview image of actin Affimer stained Cos7 cell with colormap representing the z-height. (b) 1 µm wide horizontal and vertical sections from dashed boxes in (a). Colormap indicates the z-height. Dual layer organization of the actin network can be visualized. (c) Diffraction-limited image of the same cell visualized with the fixed Atto488 fluorophore on the DNA handle strand. (d) Zoom into the area in the vertical section indicated by the white arrow showing the dual-layer organization in greater detail. A histogram analysis shows that the two layers of the actin network are ~150 nm apart in z. Scale bars: 5 µm (a, c), 2.5 µm (b, lateral) and 200 nm (b, vertical), 50 nm (d).

## Materials & Methods

### Buffer reagents

Buffer C consists of 1xPBS (ThermoFisher Scientific, Cat.No. 20012-019) mixed with 500 mM Sodium Chloride at pH 7.2.

#### *Oxygen Scavenger System – PCD/PCA/Trolox*

100xPCD (Sigma-Aldrich, Cat. No. P8279-25UN) includes 9.3 mg PCD solved in 13.3 ml of buffer (50% glycerol stock in 50 mM KCL, 1 mM EDTA and 100 mM Tris-HCL at pH 8.0). It is usually stored as 20 µl aliquots at -20 °C.

40xPCA (Sigma-Aldrich, Cat. No. 37580-25G-F) solution includes 154 mg PCA in 10 ml H<sub>2</sub>O and is adjusted to pH 9.0 with NaOH. It is stored as 20 µl aliquots at -20 °C.

100xTrolox (Sigma-Aldrich, Cat. No. 238813-1G) solution includes 100 mg Trolox, 430 µl methanol and 345 µl NaOH (1M) in 3.2 ml of H<sub>2</sub>O and is aliquoted in 20 µl batches and stored at -20 °C.

10x SDS-PAGE Gel Buffer Running Buffer consists of 250 mM Tris, 1.92 M Glycine and 0.1% (w/v) SDS at pH 8.3.

4x Gel Loading Buffer includes 250 mM Tris-HCL pH 6.8, 40 % (v/v) Glycerol, 5 % (w/v) SDS, 0.005 % (w/v) Bromophenol Blue and 400 mM DTT.

dSTORM buffer: 10 mM Tris-HCl (pH 8.0), 50 mM NaCl, 5 mg/ml glucose, 114 mM β-mercaptoethanol, 0.5 mg/ml glucose oxidase and 40 µg/ml catalase, used fresh and kept on ice.

### Actin Affimer (14c) Production

Affimer reagents were produced as described before<sup>1</sup>.

### Actin Affimer14c Protein Sequence

MASNSLEIEELARFAVDEHNKKNALLEFVRVVKAKEQSDTPHWWWTTMYYLTLEAKDGGKKKLYEA  
KVWVKESPVHPKRLNFKDLQEFKPVGDACAAAHHHHHHHH

**Strain-promoted Azid-Alkyne Cycloaddition (SPAAC)**

Affimers are concentrated via Amicon 10kDa spin filters (Merck/EMD Millipore, Cat. No. UFC501096) and buffer exchanged into 5 mM TCEP (Pierce, Cat. No.: 20490) in 1×PBS (ThermoFisher Scientific, Cat.No. 20012-019) + 3 mM EDTA (Ambion, Cat. No. AM9261) at pH 7. 5 mM TCEP in 1×PBS + 3 mM EDTA is then added to the Affimer and is incubated for 2 h at 4 °C on a shaker. Subsequently, Amicon 10 kDa Spin Filters are prewashed with 1×PBS, and Affimers are buffer exchanged into 1×PBS for 5×5min at 14 000×g and the volume is adjusted to 100 µl. DBCO-Maleimide Crosslinker (Sigma-Aldrich, Cat. No. 760668) is added in 20× molar excess in 5 µl to the Affimer and incubated overnight at 4 °C on a shaker. Crosslinker aliquots are stored at 40 mg/ml concentration in DMF (Thermo Fisher Scientific, Cat. No. 20673).

DBCO crosslinker is removed via 10 kDa Amicon Spin Filters for 5×5min at 14 000×g. Azide-DNA is added to the Affimer crosslinker at 10× excess for 1 h at 20 °C. The final product is buffer exchanged into HisTrap binding buffer (20 mM Sodium Phosphate, 500 mM NaCl, 20 mM Imidazole) via Amicon 10 kDa Spin Filters. Purification from free DNA was performed using a GE Aekta purifier system and a HisTrap 1 ml column (GE, Cat. No. 29-0510-21) via a one-step purification scheme with 500 mM Imidazole (Carl Roth, Cat. No. X998.4) and 500 mM NaCl. Peak fractions are afterwards concentrated and buffer-exchanged via Amicon 10 kDa spin filters. The conjugated product does not necessarily have to be purified from the unreacted DNA, however it is highly recommended, to avoid unspecific staining from the free DNA. Note: The reaction was performed with and without fixed Atto 488 fluorophore on the azide-modified DNA.

*Example Calculations***Supplementary Table 1 | Affimer preparation (after reduction/buffer exchange)**

Affimer	
MW (g/mol)	12577
measured concentration (mg/ml)	1.34
desired amount in nmol	10
volume of Affimer to use (µl)	93.86
add volume of 1xPBS (µl)	6.14

**Supplementary Table 2 | Crosslinker dilution calculation.** Take 20x in 5  $\mu$ l

DBCO-Mal	
MW (g/mol)	427.45
c (mg/ml)	40
c (nmol/ $\mu$ l)	93.58
desired amount (nmole)	200
desired c (nmol/ $\mu$ l)	40
dilution factor	2.34
crosslinker ( $\mu$ l)	4.27
add volume of PBS to crosslinker ( $\mu$ l)	5.73

→ Add 5  $\mu$ l of diluted crosslinker to 100  $\mu$ l of reduced Affimer

Affimer after crosslinker reaction: 1.229 mg/ml – 97.7 pmol/ $\mu$ l (take 40  $\mu$ l – 3.909 nmole)

**Supplementary Table 3 | Addition of azide-modified DNA via SPAAC.** Adding 10x molar excess of DNA to Affimer+Crosslinker

DNA-P1-Atto488	
MW (g/mol)	5885
c (mmol/l)	5
desired amount (nmole)	39.09
Volume of DNA to add to Affimer ( $\mu$ l)	7.82

This is an example calculation. More Affimer can be used; the limiting factor is more often the amount of DNA available.

### **Copper-catalysed azide alkyne cycloaddition reaction (CuAAC)**

Affimers are concentrated via Amicon 10kDa spin filters and buffer exchanged into 5 mM TCEP (Pierce, Cat. No.: 20490) in 1×PBS (ThermoFisher Scientific, Cat.No. 20012-019) + 3 mM EDTA (Ambion, Cat. No. AM9261) at pH 7. 5 mM TCEP in 1×PBS + 3 mM EDTA is then added to the Affimer and is incubated for 2 h at 4 °C on a shaker. Subsequently, Amicon 10 kDa Spin Filters (Merck/EMD Millipore, Cat. No. UFC501096) are prewashed with 1×PBS, and Affimers are buffer exchanged into 1×PBS for 5×5min at 14 000×g and the volume is adjusted to 100 µl. Propargyl-Maleimide Crosslinker (Jena Bioscience, Cat. No. CLK-TA113-25) is added in 20× molar excess in 5 µl to the Affimer and incubated overnight at 4 °C on a shaker. Crosslinker aliquots are stored at 400 mM concentration in DMF (Thermo Fisher Scientific, Cat. No. 20673).

Propargyl-Maleimide crosslinker is removed via 10 kDa Amicon Spin Filters at 5×5min for 14 000×g. Azide-DNA is added including 0.1 mM CuSO<sub>4</sub> (Sigma-Aldrich, Cat. No. C1297-100g), 0.5 mM THPTA (Sigma-Aldrich, Cat. No. 762342-100mg), 5 mM Sodium L-Ascorbate (Sigma-Aldrich, Cat. No. A7631-25mg) and 5 mM Aminoguanidine hydrochloride (Sigma-Aldrich, Cat. No. 396494-25g) to the Affimer with the alkyne group at 10× excess for 1 h at 25 °C. The final product is buffer exchanged into 1×PBS using Amicon 10kDa spin filters. The conjugated product was not purified from non-reacted DNA. The conjugated product does not necessarily have to be purified from the unreacted DNA, however it is highly recommended, to avoid unspecific staining from the free DNA. Note: The reaction was performed only with DNA handles without the fixed fluorophore on the 3'-end, however should be translatable to use also with an additional fixed dye.

*Example Calculations*

Steps 1 & 2 are the same as previously written.

**Supplementary Table 4 | Addition of azide-modified DNA via CuAAC.**

Name	Stock	Target concentration	Dilution factor	Volume (μl)
PBS (pH 7.2, 1×)				41.36
Alkyne-Affimer (mM)	0.21	0.07	3.02	33.14
Azide-DNA (mM)	5	0.7	7.14	14
CuSO <sub>4</sub> (mM)	20	0.1	200	0.5
THPTA (mM)	50	0.5	100	1
Aminoguanidine hydrochloride (mM)	100	5	20	5
Sodium ascorbate (mM)	100	5	20	5
<b>Final volume (μl)</b>				<b>100</b>

**Labeling efficiencies**

Labeling efficiencies of the DNA-conjugated Affimers were determined via absorption spectroscopy after HisTag purification. Typical labeling efficiencies were on the order of 0.65 DNA/fluorophore molecules per Affimer.

### SDS-PAGE Gel

Samples were diluted in Gel Loading buffer and heated to 95 °C for 5 min. The samples were then loaded onto a Mini-PROTEAN TGX Stain-Free Gel (Biorad, Cat. No. 456-8083). 7.5 µl of Ladder (Biorad, Cat. No. 1610363) was loaded next to the Affimers. The gel was run at 180 Volt for 35 min. Gel imaging was performed with 2 min activation of the stain-free technology and imaged with autoexposure on a Biorad gel imaging system (Biorad, Gel Doc XR+).

### Synthesis of phalloidin-DNA construct

*1<sup>st</sup> step, disulfide reduction:* 97.1 nmol (11.9 OD<sub>260</sub>) of the synthetic 5'-thiol (C<sub>6</sub>)pTTATACATCTA DNA oligonucleotide (Eurofins Genomics) present in its homo-dimeric disulfide form was reduced at 37 °C for one hour with a 10× excess of TCEP-HCl (Tris(2-carboxyethyl)phosphine hydrochloride), from a solution of 100 mM in water, brought to pH 8.5 with 1 N NaOH, in a buffer containing 100 mM HEPES-NaOH, 2 mM EDTA at pH 7.4. The oligonucleotide was ethanol-precipitated, centrifuged and the pellet was dried using a SpeedVac concentrator (Savant, Thermo Scientific).

*2<sup>nd</sup> step, synthesis of the phalloidin-DNA construct:* the reaction mixture contained 75 µl of 100 mM HEPES-NaOH, 2 mM EDTA at pH 7.8 as buffer, plus 50 µl of the reduced 5'-modified oligonucleotide, 40 µl (200 nmol) of the amino modified phalloidin tosylate derivative (from Enzo Life Sciences, CASRN 17466-45-4, Cat. No. ALX-350-266-M001), both substances dissolved in water, respectively, and 41 µl (96 nmol) of maleimide-PEG2-succinimidyl ester (Sigma-Aldrich, CASRN 955094-26-5, Cat. No. 746223), dissolved in DMF. The mixture was incubated at room temperature and the progress of the reaction was followed by analytical RP-HPLC on an XBridge™ C18 column, 5 µm, 3.0×150 mm (Waters).

After 4 hours of total incubation time the reaction mixture was separated on a semi-preparative column (Gemini-NX C18, 5 µm, 110A, 250 x 10.0 mm, Phenomenex). RP-HPLC was performed using an increasing gradient of acetonitrile (7 to 40 % v/v) in 100 mM Et<sub>3</sub>NHOAc at pH 7.8.

The corresponding fractions of several peaks were pooled, lyophilized, and the separated compounds were dissolved in water and analyzed by their UV-spectrum as well as by mass spectrometry. 35.17 nmol (4.93 OD<sub>260</sub>) of the desired construct (calculated monoisotopic MW: 4582.079 g/mol, measured: 4582.057 g/mol) were finally obtained and used downstream for cell staining experiments.

### Cell culture

Cos7 cells (ATCC, Cat. No. CRL-1651) were passaged every other day and used between passage number 5 and 20. The cells were maintained in DMEM (ThermoFisher Scientific, Cat. No. 10566016) supplemented with 10 % Fetal Bovine Serum (ThermoFisher Scientific, Cat. No. 10500-064) and 1 % Pencillin/Streptomycin (ThermoFisher Scientific, Cat. No. 15140-122). Passaging was performed using 1×PBS and Trypsin-EDTA 0.05 % (ThermoFisher Scientific, Cat.No. 25300-054). 24 h before immunostaining, cells were seeded on IBIDI 8-well glass coverslips (ibidi, Cat. No. 80827) at 30,000 cells/well. Prefixation was performed with prewarmed 0.4% Glutaraldehyde (SERVA, Cat. No. 23115.01) and 0.25% Triton X-100 (Carl Roth, Cat. No. 6683.1) for 90 seconds followed by the main fixation at 3 % glutaraldehyde for 15 min. Reduction was done using 1 mg/ml Sodium Borohydride (Carl Roth, Cat. No. 4051.1) in 1×PBS followed by one brief 1×PBS rinse and 3×5 min washing with 1×PBS. Blocking and permeabilization was done for 90 min with sterile filtered 3% (w/v) BSA (Sigma-Aldrich, Cat. No. A4503-10g) and 0.25% (v/v) Triton X-100 in PBS at room temperature. Cells were stained overnight with Affimer in sterile filtered 3% (w/v) BSA in 1×PBS on a shaker at 4 °C. Cells were washed 3× for 5 min in 1×PBS, incubated with 1:10 dilution of 90 nm gold particles (cytodiagnosics, Cat. No. G-90-100) in 1×PBS as drift markers, washed 3×5 min and immediately imaged.

### Microscopy setup

Fluorescence imaging was carried out on an inverted Nikon Eclipse Ti microscope (Nikon Instruments) with the Perfect Focus System, applying an objective-type TIRF configuration with an oil-immersion objective (Apo SR TIRF 100×, NA 1.49, Oil). Two lasers were used for excitation: 561 nm (200 mW, Coherent Sapphire) or 488 nm (200 mW, Toptica iBeam smart). The laser beam was passed through a cleanup filter (ZET488/10x or ZET561/10x, Chroma Technology) and coupled into the microscope objective using a beam splitter (ZT488rdc or ZT561rdc, Chroma Technology). Fluorescence light was spectrally filtered with two emission filters (ET525/50m and ET500lp for 488 nm excitation and ET600/50 and ET575lp for 561 nm excitation, Chroma Technology) and imaged on a sCMOS camera (Andor Zyla 4.2) without further magnification, resulting in an effective pixel size of 130 nm after 2×2 binning.

### **DNA-PAINT super-resolution image acquisition**

Cells were screened for a certain phenotype with 488 nm laser excitation at 0.01 kW/cm<sup>2</sup>. After acquisition of the 488 channel, the excitation was switched to 561 nm, focal plane and TIRF angle were readjusted and imaging was subsequently performed using ~3 kW/cm<sup>2</sup> 561 laser excitation. Imager strand concentration varied dependent on the measurement from 200 pM – 800 pM Cy3b-P1 and was adjusted to minimize double-binding events. Imaging was performed in 1×PCA (Sigma-Aldrich, Cat. No. 37580-25G-F)/1×PCD (Sigma-Aldrich, Cat. No. P8279-25UN)/1×Trolox (Sigma-Aldrich, Cat. No. 238813-1G) in Buffer C (1×PBS + 500mM NaCl) and imaged for 300,000-500,000 frames at 15 ms / 50 ms exposure time (see also **Supplementary Table 7**). 3D imaging was performed using an astigmatism lens in the detection path.

### **3D direct stochastic optical reconstruction microscopy (3D dSTORM)**

For dSTORM imaging, the C-terminal cysteine of actin Affimer 14c was directly labelled with the maleimide derivative of Alexa Fluor 647 (Thermo Fisher Scientific), as described previously<sup>1</sup>. The labelled Affimer was stored at -20°C at a final concentration of 0.25 mg/ml in an equal volume of 80% glycerol. Coverslips (#1.5, 25-mm diameter; Scientific Laboratory Supplies, MIC3350) were cleaned as described previously<sup>2</sup>. VOT-E36 cells (a kind gift from Mathew Holley, University of Sheffield) were cultured as described<sup>3</sup>. Cells were differentiated in culture medium supplemented with 10 µM retinoic acid at 37°C, 5% CO<sub>2</sub> for 7 days. Cells were fixed in 2% paraformaldehyde (PFA) dissolved in PEM buffer (80 mM PIPES pH 6.8, 5 mM EGTA, 2 mM MgCl<sub>2</sub>). Cells were permeabilised with 0.5% Triton X-100 for 5 min and washed three times with PBS, before blocking with 5% BSA in PBS for 1 hr. Cells were incubated with labelled actin Affimer (1:1000) prepared in PBS supplemented with 0.25% BSA for 1 hr at room temperature. Coverslips were washed three times with PBS prior to imaging.

dSTORM data acquisition and reconstruction were carried out as described previously<sup>1</sup>. Data was acquired over 143,000 frames, with 200 µl of dSTORM buffer initially present and further 200 µl volume added when the blinking rate of the labels was noticeably reduced.

### **Image data analysis**

Images were reconstructed with the Picasso and SMAP Software Suite. Drift correction was performed with a redundant cross-correlation and/or gold particles as fiducials.

**Supplementary Table 5 | Handle sequences**

Handle Name	Sequence	5'-mod	3'-mod	Vendor
P1-Atto488	TTA TAC ATC TA TTTT	Azide	Atto 488	Biomers.net
P1	TTATACATCTA	Azide	None	Biomers.net
P3	TTTCTTCATTA	Azide	None	Biomers.net

**Supplementary Table 6 | Imager sequences**

Imager name	Sequence	5'-mod	3'-mod	Vendor
P1*	CTAGATGTAT	None	Cy3b	Eurofins Genomics
P3*	GTAATGAAGA	none	Cy3b	Eurofins Genomics

**Supplementary Table 7 | Imaging parameters**

Dataset	Parameters	Laser power @561 nm	Localization precision (NeNA)
Figure 2	50 ms, 3D, 300k Frames, 800 pM P1*	3.3 kW/cm <sup>2</sup>	4.9 nm
Figure 3	50 ms, 3D, 479285 Frames, 800 pM P1*	3.3 kW/cm <sup>2</sup>	4.7 nm
Supplementary Figure 3	50 ms, 3D, 171229 Frames, 800 pM P1*	3.3 kW/cm <sup>2</sup>	5.6 nm
Supplementary Figure 5	15 ms, 2D, 300k Frames, 1 nM P3*	1.78 kW/cm <sup>2</sup>	8.0 nm
Supplementary Figure 6	50 ms, 3D, 300k Frames, 800 pM P1*	3.3 kW/cm <sup>2</sup>	5.0 nm

**Supplementary References**

1. Tiede, C.; Bedford, R.; Heseltine, S. J.; Smith, G.; Wijetunga, I.; Ross, R.; AlQallaf, D.; Roberts, A. P.; Balls, A.; Curd, A.; Hughes, R. E.; Martin, H.; Needham, S. R.; Zanetti-Domingues, L. C.; Sadigh, Y.; Peacock, T. P.; Tang, A. A.; Gibson, N.; Kyle, H.; Platt, G. W.; Ingram, N.; Taylor, T.; Coletta, L. P.; Manfield, I.; Knowles, M.; Bell, S.; Esteves, F.; Maqbool, A.; Prasad, R. K.; Drinkhill, M.; Bon, R. S.; Patel, V.; Goodchild, S. A.; Martin-Fernandez, M.; Owens, R. J.; Nettleship, J. E.; Webb, M. E.; Harrison, M.; Lippiat, J. D.; Ponnambalam, S.; Peckham, M.; Smith, A.; Ferrigno, P. K.; Johnson, M.; McPherson, M. J.; Tomlinson, D. C., Affimer proteins are versatile and renewable affinity reagents. *Elife* **2017**, *6*.

2. Shroff, H.; Galbraith, C. G.; Galbraith, J. A.; White, H.; Gillette, J.; Olenych, S.; Davidson, M. W.; Betzig, E., Dual-color superresolution imaging of genetically expressed probes within individual adhesion complexes. *P Natl Acad Sci USA* **2007**, *104* (51), 20308-20313.
3. Helyer, R.; Cacciabue-Rivolta, D.; Davies, D.; Rivolta, M. N.; Kros, C. J.; Holley, M. C., A model for mammalian cochlear hair cell differentiation in vitro: effects of retinoic acid on cytoskeletal proteins and potassium conductances. *Eur J Neurosci* **2007**, *25* (4), 957-973.

## **Bacterially derived antibody binders as small adapters for DNA-PAINT microscopy**

**T. Schlichthaerle\***, M. Ganji\*, A. Auer, O.K. Wade, R. Jungmann  
*\*authors contributed equally*

published in

*ChemBioChem* (2019)

Reprinted with permission from [143]  
Copyright 2019 WILEY



# Bacterially Derived Antibody Binders as Small Adapters for DNA-PAINT Microscopy

Thomas Schlichthaerle<sup>+</sup>,<sup>[a, b]</sup> Mahipal Ganji<sup>+</sup>,<sup>[a, b]</sup> Alexander Auer,<sup>[a, b]</sup> Orsolya Kimbu Wade,<sup>[a, b]</sup> and Ralf Jungmann<sup>\*[a, b]</sup>

Current optical super-resolution implementations are capable of resolving features spaced just a few nanometers apart. However, translating this spatial resolution to cellular targets is limited by the large size of traditionally employed primary and secondary antibody reagents. Recent advancements in small and efficient protein binders for super-resolution microscopy, such as nanobodies or aptamers, provide an exciting avenue for the future; however, their widespread availability is still limited. To address this issue, here we report the combination of bacterial-derived binders commonly used in antibody purification with DNA-based point accumulation for imaging in nanoscale topography (DNA-PAINT) microscopy. The small sizes of these protein binders, relative to secondary antibodies, make them an attractive labeling alternative for emerging super-resolution techniques. We present here a labeling protocol for DNA conjugation of bacterially derived proteins A and G for DNA-PAINT, having assayed their intracellular performance by targeting primary antibodies against tubulin, TOM20, and the epidermal growth factor receptor (EGFR) and quantified the increases in obtainable resolution.

Super-resolution microscopy is starting to become a standard tool for cell biology research.<sup>[1]</sup> Several seminal discoveries that were only feasible by surpassing the classical diffraction limit of light have been made.<sup>[2]</sup> Recent technical advances in super-resolution are providing sub-5 nm spatial resolution capabilities,<sup>[3]</sup> so the size of the labeling probes is becoming increasingly more important.

A popular branch of super-resolution techniques consists of approaches based on the localization of single molecules.<sup>[4]</sup> DNA-based point accumulation for imaging in nanoscale topography (DNA-PAINT) is a variation of these single-molecule localization microscopy (SMLM) methods, in which the necessary blinking behavior used for downstream super-resolution recon-

struction is mediated by the transient hybridization of short dye-labeled oligonucleotides ("imager" strands), which interact transiently with their complementary docking strands on the target of interest.<sup>[5]</sup> DNA-PAINT possesses several advantages over more traditional SMLM methods such as photoactivated localization microscopy (PALM)<sup>[6]</sup> or stochastic optical reconstruction microscopy (STORM).<sup>[7]</sup> These advantages are mainly based on the fact that blinking in DNA-PAINT is decoupled from the photophysical properties of dye molecules, thus allowing for the use of bright and photostable dyes rather than ones that efficiently photoswitch. Additionally, the target identity is encoded in the DNA sequence (a programmable probe), similar to a molecular barcode. The binding interaction between imager and docking strands occurs only transiently, so separate imaging rounds can be performed sequentially by using different DNA species harboring the same fluorophore, allowing for technically unlimited multiplexing.<sup>[5b]</sup>

However, for application of DNA-PAINT to a question in cell biology, the docking strands need to be "linked" to the target of interest through DNA-conjugated affinity reagents.<sup>[5b, 8]</sup> The optimal labeling probe should ideally be smaller than the target protein under investigation, allow for quantitative labeling (1:1 stoichiometry), be available for a large variety of targets, and ultimately be cost-effective. A multitude of small binders for super-resolution microscopy have recently been introduced, with nanobodies,<sup>[9]</sup> aptamer probes,<sup>[10]</sup> or other small protein scaffolds<sup>[11]</sup> among them. Although these binders offer great future promise, antibody-based affinity reagents are—for many applications—still the preferred labels for many targets of interest. This is mainly due to the fact that the available probe library vastly exceeds those of any other available binders. However, monoclonal antibodies can be costly and sometimes unavailable in sufficient quantities to perform direct DNA labeling. Immunostaining with secondary antibodies, on the other hand, adds a large linkage error to the already rather large size of a primary antibody. There is thus a need for small secondary adapter binders.

Previously, nanobodies were reported to bind primary antibodies from mouse and rabbit as host species for super-resolution microscopy.<sup>[12]</sup> Inspired by this, we introduce here the use of DNA-conjugated bacterially derived protein A (molecular weight 46 kDa) and protein G (molecular weight 22 kDa) molecules as small binders for primary antibodies in combination with DNA-PAINT super-resolution microscopy (Figure 1). Protein A, derived from *Staphylococcus aureus*, has a high affinity towards various mammalian immunoglobulin G (IgG) molecules (e.g., to IgG1 with  $\approx 10$  nM) and binds to the Fc domain; how-

[a] T. Schlichthaerle,<sup>+</sup> Dr. M. Ganji,<sup>+</sup> A. Auer, O. Kimbu Wade, Prof. R. Jungmann  
Faculty of Physics and Center for Nanoscience, LMU Munich  
Geschwister-Scholl-Platz 1, 80539 Munich (Germany)

[b] T. Schlichthaerle,<sup>+</sup> Dr. M. Ganji,<sup>+</sup> A. Auer, O. Kimbu Wade, Prof. R. Jungmann  
Max Planck Institute of Biochemistry  
Am Klopferspitz 18, 82152 Martinsried (Germany)  
E-mail: jungmann@biochem.mpg.de

[<sup>+</sup>] These authors contributed equally to this work.

 Supporting information and the ORCID identification numbers for the authors of this article can be found under <https://doi.org/10.1002/cbic.201800743>.

 This article is part of the young researchers' issue ChemBioTalents. To view the complete issue, visit <http://chembiochem.org/chembiotalents>

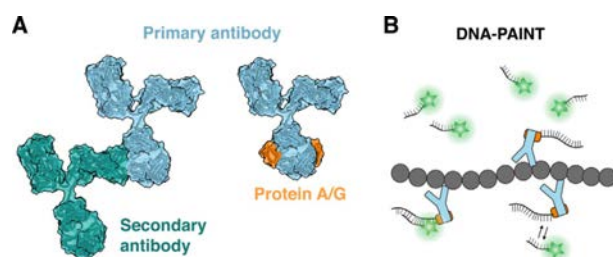


**Figure 1.** Small bacterially derived protein adapters for DNA-PAINT. A) Schematic representation of primary-/secondary-antibody-based labeling (left) and small bacterially derived protein adapter labeling (right), highlighting a decrease in overall label size (Modified from PDB IDs: 1FCC and 1IGT). B) Schematic representation of the DNA-PAINT concept. Transient hybridization of fluorophore-labeled single-stranded oligonucleotides to their complementary target strands, conjugated to target binders, enables programable super-resolution imaging.

ever, the binding varies for different species and IgG subclasses.<sup>[13]</sup> Protein G, derived from *Streptococcus* sp., has a high affinity towards various different IgG subclasses from different species, determined<sup>[14]</sup> in the case of rat IgG to be  $\approx 1$  nM. These two proteins are commonly used for antibody purification<sup>[15]</sup> and have previously been applied in immunogold staining for electron microscopy,<sup>[16]</sup> as well as for the attachment of antibodies to DNA nanostructures.<sup>[17]</sup> Thus, their small sizes and high affinities make them ideal tools for super-resolution microscopy and provide advantages over primary/secondary antibody staining.

Different methods have been introduced to conjugate DNA docking strands to protein-based affinity reagents. Typically, a bifunctional chemical crosslinker harboring a reactive moiety (which can subsequently react with a modified DNA oligonucleotide) was used to react with amino groups or reduced thiols.<sup>[3c,8,18]</sup> To produce DNA-modified secondary labeling reagents, protein A from *Staphylococcus aureus* and protein G from *Streptococcus* sp. were conjugated to DNA-PAINT docking strands in a two-step reaction sequence. First, proteins were allowed to react with a *trans*-cyclooctene *N*-hydroxysuccinimidyl ester (TCO-NHS) crosslinker and subsequently with commer-

cially available tetrazine-labeled DNA (Tz-DNA; see the Experimental Section for details). Additionally, protein A and protein G were labeled with NHS-Ester Alexa Fluor 647 for diffraction-limited imaging. To assess the general feasibility of our labeling approach, we first acquired confocal images of rat anti- $\alpha$ -tubulin stained with protein G (labeled with an Alexa Fluor 647 fluorophore) and rabbit anti-TOM20 protein A conjugates (also labeled with an Alexa Fluor 647 fluorophore) in A549 cells (Figure S1 in the Supporting Information). These immunofluorescence images clearly show specific microtubule and mitochondrial staining, indicating that protein A and protein G can bind stably and specifically to primary rabbit and rat antibodies, respectively. These results made us confident that fluorescently labeled protein A and protein G could be used as a replacement system for secondary antibodies for immunostaining and fluorescence imaging.

We then turned our attention to the DNA-conjugated secondary binders as candidates for DNA-PAINT super-resolution microscopy. As an initial proof-of-concept demonstration for DNA-PAINT imaging with these small bacterially derived binders, microtubules and TOM20 were chosen for proteins G and A, respectively. Both targets (Figure 2) could be resolved with DNA-PAINT, and the resulting images show features well below the diffraction limit (see arrows in Figure 2B, C). These datasets are qualitatively similar in performance to typical secondary-antibody-based DNA-PAINT data.<sup>[3c,5c,19]</sup>

Our first results confirmed that proteins G and A can be used as secondary antibody substitutes: protein G for rat or rabbit primary antibody targets and protein A for rabbit (Figure S2). We furthermore assayed binding of proteins A and G to primary mouse antibodies and succeeded with specific labeling of epidermal growth factor receptor (EGFR) proteins (Figure S3). A detailed overview of the possible binding partners of proteins A and G that we have assayed in this study can be found in Table S1. We also checked for potential non-specific binding of proteins A and G to cellular targets without primary antibody staining and did not find increased background signals (Figure S4).

Because we expected to observe measurable decreases in the observed sizes of targets labeled with these proteins, relative to targets labeled with primary and secondary antibodies (Figure 1A), we next designed experiments to test this hypothesis with DNA-PAINT imaging of EGF surface receptors. The fact that these surface receptors are homogeneously distributed on cell surfaces makes them excellent test candidates for super-resolution imaging. Recently, EGFRs were imaged by immunostaining with single-stranded DNA-based aptamers (SOMAmers) together with DNA-PAINT super-resolution microscopy to reveal their nanoscale distribution on the cell surface.<sup>[10a]</sup> To image EGFRs by using our newly identified small proteins and to compare this with primary and secondary antibody imaging, A549 cells were fixed and immunostained by using a monoclonal rabbit antibody against EGFRs. As expected, DNA-PAINT super-resolution images of both staining procedures (secondary antibodies and protein A binders) showed homogeneously distributed receptors on the cell surfaces (Figure 3A–C and H–J). Two nanoclusters that were spaced  $\approx 80$  nm apart

Ralf Jungmann received his Ph.D. in physics from the Technical University Munich in 2010. From 2011 to 2014, he was a postdoctoral fellow at the Wyss Institute at Harvard University. Since 2015, he has headed an independent research group at the MPI of Biochemistry and the LMU Munich supported by the Emmy Noether Program of the DFG. In 2016, he was appointed as an associate professor at the LMU. In 2017, he was named Allen Distinguished Investigator, and in 2018 HFSP Young Investigator. His research focuses on the development of DNA-based super-resolution techniques and their application in cell biology.



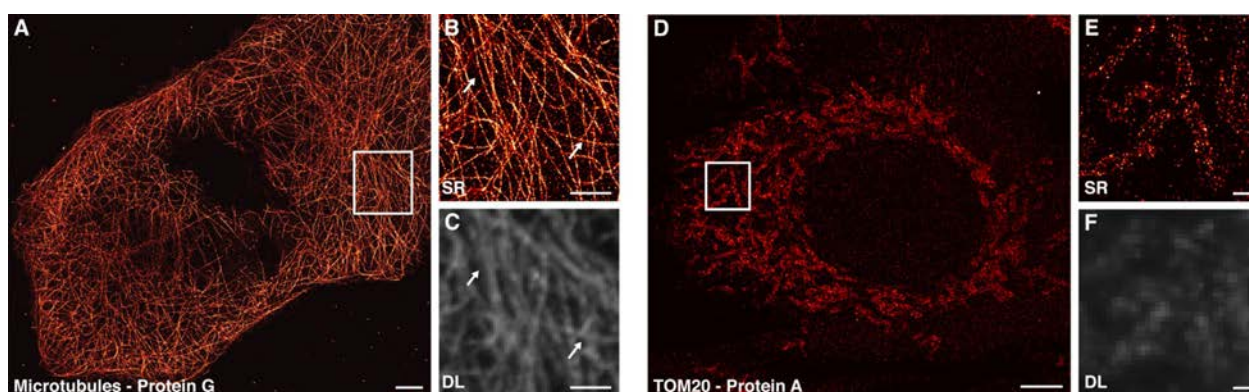


**Figure 2.** DNA-PAINT imaging with bacterially derived protein adapters. A) Microtubule overview super-resolution image in an A549 cell stained with protein G as secondary binder for the rat anti- $\alpha$ -tubulin antibody. B), C) Zoom-ins on the dense microtubule network, in which individual microtubule tracks can be resolved in B) the DNA-PAINT image, but not in C) the diffraction-limited image (white arrows). D) Mitochondrion network stained with protein A as secondary binder for rabbit anti-TOM20 antibody. Zoom-ins reveal E) mitochondrial cavities that could not be observed with F) diffraction-limited imaging. Scale bars: A), D) 5  $\mu$ m, B), C) 2  $\mu$ m, E), F) 500 nm.

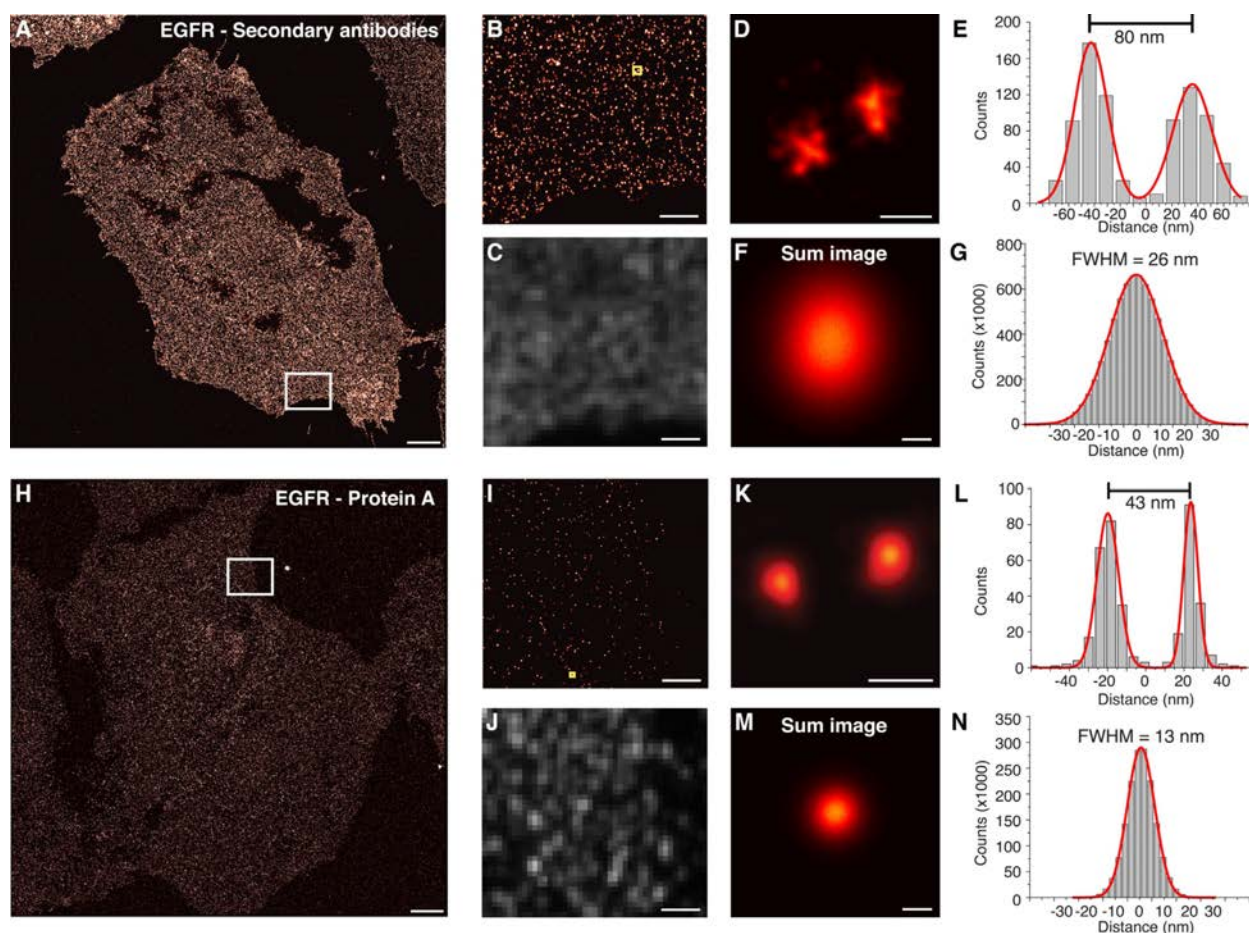


**Figure 3.** EGFR nanocluster imaging reveals a decrease in size with small bacterially derived protein adapters. A) Overview image of EGF receptors in A549 cells labeled with primary/secondary antibodies for DNA-PAINT. B), C) Zoom-ins on marked area in (A) show B) distribution of EGFR nanoclusters that are not visible in C) diffraction-limited imaging. D), E) Zoom-ins on two nanoclusters  $\approx$  80 nm apart. Left nanocluster shows a full-width half-maximum (FWHM) of 30 nm, right nanocluster a FWHM of 36 nm. F), G) Center-of-mass-aligned nanoclusters stained with primary/secondary antibodies from  $n = 25\,788$  EGFR nanoclusters show a FWHM of 26 nm. H) Overview image of EGF receptors in A549 cells labeled with protein A against the primary rabbit anti-EGF receptor antibody. I), J) Zoom-ins on marked area in (H) reveal I) single spots that are not visible in J) the diffraction-limited imaging. K), L) Two nanoclusters are 43 nm apart; the left nanocluster reveals a FWHM of 13 nm, the right nanocluster a FWHM of 8.8 nm. M), N) Center-of-mass aligned image of EGF receptor nanoclusters stained with the small bacterially derived secondary adapter protein A from  $n = 6567$  spots shows a FWHM of 13 nm. Scale bars: A), H) 5  $\mu$ m, B), C), I), J) 1  $\mu$ m, D) 50 nm, F) 10 nm, K) 25 nm, M) 10 nm.

could be resolved (Figure 3D, E), whereas, in comparison, two nanoclusters only 43 nm apart could be visualized in the case of the protein A staining (Figure 3K, L). To quantify the size distributions of individual EGFR nanoclusters labeled with primary and secondary antibodies, in relation to those labeled with primary antibodies and protein A as secondary adapters, we aligned thousands of molecules to their center of mass and measured the FWHM of the resulting distributions. The primary-/secondary-antibody-staining approach yielded a considerably larger size distribution (FWHM = 26 nm) than the protein A labeled primary antibody approach (FWHM = 13 nm, Figure 3F, G, M, N; see also Figure S5). These results demonstrate that labeling based on protein A is superior to antibody-based labeling in terms of reducing the linkage error in DNA-PAINT imaging.

After the quantification of this reduction of artefacts from secondary antibody-based labeling probes in comparison with protein A labeling as secondary adapter, we investigated the achieved reduction in linkage error further in a more challenging 3D imaging application. For this, microtubule structures with—according to electron microscopy studies<sup>[20]</sup>—a diameter of  $\approx 25$  nm were chosen. A recent DNA-PAINT study demonstrated that the coronas of labeling probes around microtubule filaments can be resolved with super-resolution fluorescence microscopy as hollow 3D cylinders.<sup>[21]</sup> By employing this biological system for 3D evaluation of our labeling approach, the potential decrease in the surrounding labeling coronas around single microtubule filaments as a function of the size of the labeling probe was investigated (Figure 4). Both approaches (secondary antibodies and protein G) revealed the expected coronas around the microtubules, but their diameters were, as expected, different. For primary/secondary antibody staining, we obtained a diameter of 57 nm (Figure 4D, E), whereas the staining approach based on protein G resulted in a considerably smaller diameter of 48 nm observed with 3D DNA-PAINT microscopy (Figure 4I, J). These results confirmed that using staining based on protein G or protein A as secondary labeling probes yields a smaller linkage error to the true target position than secondary-antibody staining.

Additionally, we assayed the applicability of using proteins A and G in a multiplexed DNA-PAINT imaging experiment. For this, we preincubated DNA-coupled protein A with a primary TOM20 rabbit antibody and DNA-coupled protein G with a primary microtubule rat antibody and removed excess protein A and G binders from the coupled reagents. We then performed simultaneous labeling of TOM20 and microtubules followed by a two-round Exchange-PAINT<sup>[5b]</sup> experiment using two orthogonal Cy3b imager strands (Figure S6) and thus verified that multiplexed imaging is indeed possible.

In conclusion, we have extended the use of bacterially derived binders for immunoglobulins—namely proteins A and G—as secondary binders for DNA-PAINT microscopy. The key advantage of this approach is that proteins A and G are cost-effective and commercially available in much larger quantities than secondary antibodies or nanobodies. Additionally, their small sizes allow for reduction of the linkage error to the true target position as shown with EGF receptor and microtubule

imaging. In the future, these small secondary binders can be evaluated for more species and IgG subclasses, as well as engineered for higher affinity.<sup>[13b,22]</sup> In addition, engineering of these proteins to carry unique chemical groups such as cysteine or unnatural amino acid residues could be employed for quantitative 1:1 labeling of protein to docking strands, which would enable applications in the direction of quantitative imaging such as quantitative points accumulation in nanoscale topography (qPAINT).<sup>[23]</sup>

## Experimental Section

**Buffer reagents:** Buffer C consisted of phosphate-buffered saline (PBS; Thermo Fisher Scientific, cat. no. 20012-019, 1 $\times$ ) mixed with sodium chloride (500 mM) at pH 7.2. Oxygen scavenger system: protocatechuate 3,4-dioxygenase (PCD)/protocatechuic acid (PCA)/( $\pm$ )-6-hydroxy-2,5,7,8-tetramethylchromane-2-carboxylic acid (Trolox). PCD (Sigma-Aldrich, cat. no. P8279-25UN, 100 $\times$ ) included PCD (9.3 mg) dissolved in buffer [13.3 mL, glycerol stock (50%) in KCl (50 mM), EDTA (1 mM), Tris-HCl (100 mM), pH 8.0]. It was usually stored as aliquots (20  $\mu$ L) at  $-20^\circ\text{C}$ . PCA (Sigma-Aldrich, cat. no. 37580-25G-F, 40 $\times$ ) solution included PCA (154 mg) in  $\text{H}_2\text{O}$  (10 mL) and was adjusted to pH 9.0 with NaOH. It was stored as aliquots (20  $\mu$ L) at  $-20^\circ\text{C}$ . Trolox (Sigma-Aldrich, cat. no. 238813-1G, 100 $\times$ ) solution included Trolox (100 mg), methanol (430  $\mu$ L), and NaOH (1 M, 345  $\mu$ L) in  $\text{H}_2\text{O}$  (3.2 mL) and was aliquoted in 20  $\mu$ L batches and stored at  $-20^\circ\text{C}$ .

**Protein A/G labeling through TCO-Tz conjugation:** Protein A (Thermo Fisher Scientific, cat. no. 21181) and protein G (Thermo Fisher Scientific, cat. no. 21193) were aliquoted at 2.5  $\text{mg mL}^{-1}$  in 1 $\times$  PBS and stored at  $-20^\circ\text{C}$ . Conjugation of single-stranded DNA to protein A or protein G was performed as described previously for nanobodies.<sup>[18]</sup> In brief, DNA and proteins were cross-linked by use of coupling between a *trans*-cyclooctene (TCO) and a methyl-tetrazine (Tz). The Tz variant we used was a tetrazine-PEG5 (methyltetrazine). The TCO variant we used was a TCO-NHS ester ((*E*)-cyclooct-4-enyl-2,5-dioxo-1-pyrrolidinyl carbonate). TCO-NHS ester crosslinker (Jena Bioscience, cat. no. CLK-1016-25) was added at 10 $\times$  molar excess in 5  $\mu$ L to the protein, and incubation was carried out for 2 h at  $4^\circ\text{C}$  on a shaker. Crosslinker aliquots were stored at 10  $\text{mg mL}^{-1}$  in DMF (Thermo Fisher Scientific, cat. no. 20673). Subsequently, Zeba spin desalting columns (Thermo Fisher Scientific, cat. no. 89882) were used to remove unreacted crosslinker, and Tz-DNA was added at fivefold molar excess for 1 h at  $20^\circ\text{C}$ . The final product was buffer-exchanged with 10 kDa Amicon spin filters (Merck, cat. no. UFC501096) and used for immunostaining at a concentration of 10  $\mu\text{g mL}^{-1}$ .

**Protein A/G conjugation with Alexa Fluor 647 NHS ester:** Protein A/G was conjugated with Alexa Fluor 647 NHS ester (Thermo Fisher Scientific, cat. no. A20006) in tenfold molar excess for 2 h at  $4^\circ\text{C}$  on a shaker. Conjugated construct was purified from the free fluorophore with 10 kDa Amicon spin filters (Merck, cat. no. UFC501096).

**Antibody-DNA conjugation:** DNA-labeled antibodies were prepared as previously reported.<sup>[3c]</sup> Secondary donkey anti-rat antibody (cat. no. 711-005-152, Jackson ImmunoResearch, 1  $\text{mg mL}^{-1}$ , 300  $\mu$ L) was concentrated with 100 kDa Amicon spin filters (cat. no. UFC500396, Merck/EMD Millipore), and the volume was adjusted to 100  $\mu$ L in PBS (1 $\times$ ). A tenfold molar excess over antibody of maleimide-PEG2-succinimidyl ester crosslinker (Sigma-Aldrich, cat. no. 746223) in DMF (5  $\mu$ L) was added to the antibody (100  $\mu$ L), and the

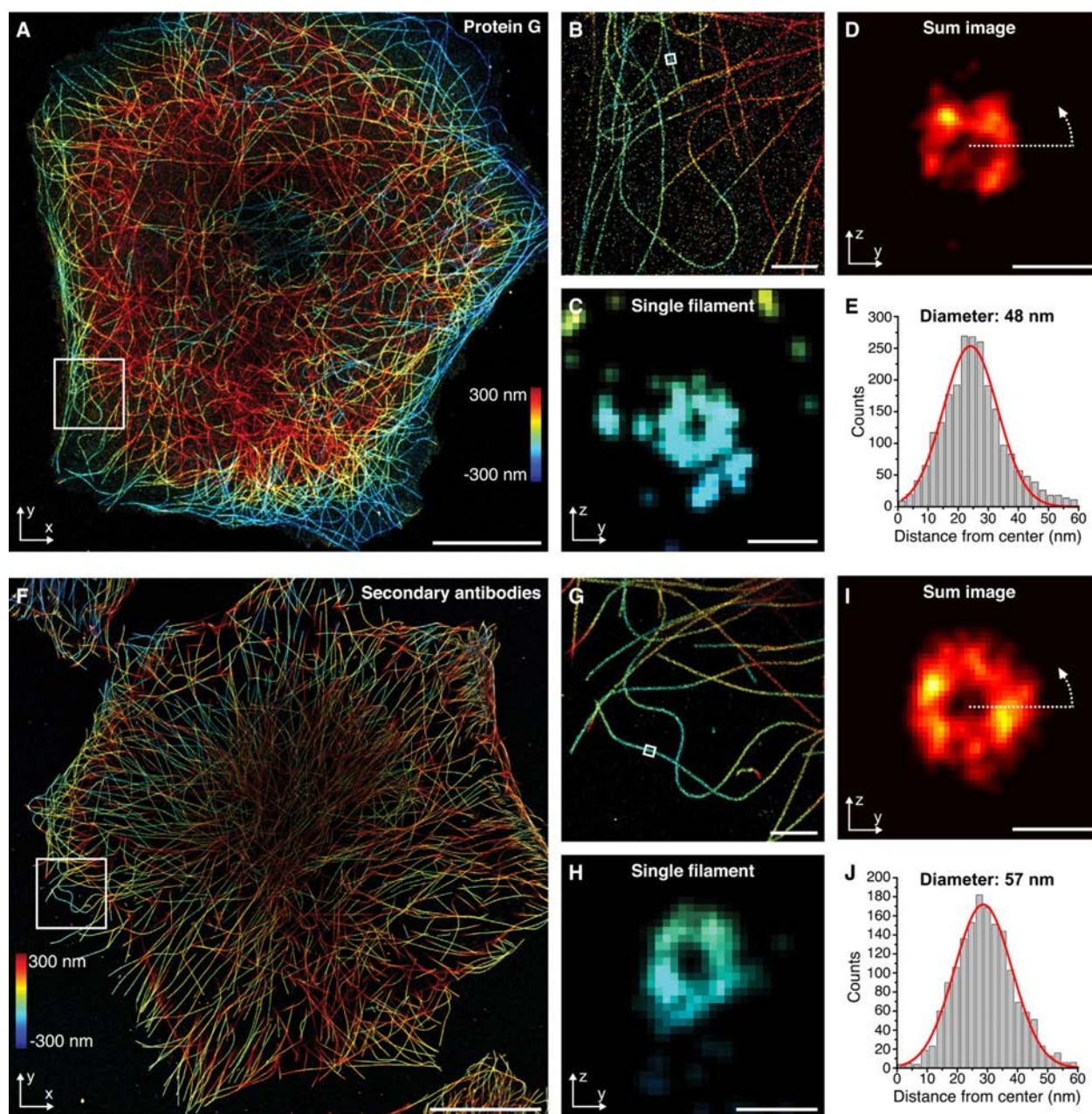


**Figure 4.** 3D imaging of microtubules reveals a decrease in diameter with small secondary labeling adapters. A) Overview image of stained rat anti-microtubule labeled with protein G. Color encodes for the Z-height. B) Zoom-in on area highlighted in (A) shows a closer view of the microtubule organization. C) Cross-sectional view through a microtubule stretch highlighted in (B). D) Cross-sectional view of an average of five microtubules. E) A ring-fit of the average microtubule cylinder shows a diameter of 48 nm (radius 24 nm). F) Overview image of primary-/secondary-antibody-labeled microtubules. G) Zoom-in on area highlighted in (F) shows a closer view of the microtubule architecture. H) Microtubule cross-section of highlighted area in (G). I) Cross-sectional view of average of five microtubules. J) An analysis of the diameter of the primary-/secondary-antibody-stained microtubules shows an increased diameter of 57 nm (radius 28.5) in comparison with the small bacterially derived secondary labeling probe. Scale bars: A), F) 10  $\mu\text{m}$ , B), G) 1  $\mu\text{m}$ , C), D), H), I) 50 nm.

reaction was allowed to proceed for 90 min at 4 °C on a shaker in the dark. Afterwards excess crosslinker was removed with zeba desalting spin columns (cat. no. 89882, Thermo Fisher Scientific). Meanwhile, thiol-DNA (1 mM dissolved in H<sub>2</sub>O, 30  $\mu\text{L}$ ) was added to dithiothreitol (DTT; cat. no. 20291, Thermo Fisher Scientific, 250 mM, 70  $\mu\text{L}$ ) and reduced for 2 h at room temperature on a shaker in the dark. A Nap5 column (cat. no. 17-0853-02, GE Health-

care) was used to remove DTT from reduced DNA, and peak fractions were pooled and concentrated with Amicon spin filters (cat. no. UFC500396, Merck/EMD Millipore, 3 kDa). DNA (10 $\times$  molar excess) was added to the antibody-crosslinker construct, and incubation was carried out overnight at 4 °C on a shaker in the dark. Amicon spin filters (100 kDa) were used to remove excess DNA, and the antibody was adjusted to 100  $\mu\text{L}$  in PBS (1 $\times$ ) and stored

for further use at 4 °C. Final usage concentration was 10  $\mu\text{g mL}^{-1}$ . Secondary anti-rat antibody was conjugated to the P1 handle. DNA handle and imager sequences can be found in Tables S2 and S3, respectively.

**Cell culture:** A549 cells (ATCC, cat. no. CRL-1651) or HeLa cells (Leibniz Institute DSMZ, Catalogue of Human and Animal Cell Lines (<http://www.dsmz.de>), cat. no. ACC-57) were passaged every other day and used between passage number 5 and 20. The cells were maintained in Dulbecco's modified Eagle's medium (DMEM; Thermo Fisher Scientific, cat. no. 10566016) supplemented with fetal bovine serum (Thermo Fisher Scientific, cat. no. 10500-064, 10%) and penicillin/streptomycin (Thermo Fisher Scientific, cat. no. 15140-122, 1%). Passaging was performed with PBS (1 $\times$ ) and trypsin-EDTA (Thermo Fisher Scientific, cat. no. 25300-054, 0.05%). Cells were seeded 24 h before immunostaining on ibidi eight-well glass coverslips (ibidi, cat. no. 80827) at 30 000 cells/well. For optimized microtubule imaging, prefixation was performed with prewarmed glutaraldehyde (SERVA, cat. no. 23115.01, 0.4%) and Triton X-100 (Carl Roth, cat. no. 6683.1, 0.25%) for 90 s. Main fixation was performed with use of glutaraldehyde (3%) for 15 min. For imaging of mitochondria, cell-surface receptors, and microtubule networks, paraformaldehyde (PFA, 3%) and glutaraldehyde (0.1%) fixation as main fixation without prefixation was performed for 15 min. Afterwards, reduction was carried out with sodium borohydride (Carl Roth, cat. no. 4051.1, 1  $\text{mg mL}^{-1}$ ) in PBS (1 $\times$ ) followed by one brief PBS (1 $\times$ ) rinse and 3 $\times$  5 min washing with PBS (1 $\times$ ). Blocking and permeabilization were done for 90 min with sterile filtered bovine serum albumin (BSA Sigma-Aldrich, cat. no. A4503-10g, 3%, w/v) and Triton X-100 (0.25%, v/v) in PBS (1 $\times$ ) at room temperature. Cells were stained with primary antibodies against tubulin (Thermo Fisher Scientific, cat. no. MA1-80017) or EGFR (Cell Signaling, cat. no. 4267S or Thermo Fisher Scientific, cat. no. MA5-13319) together with protein A or protein G overnight on the sample in sterile filtered BSA (3%, w/v) in PBS (1 $\times$ ) on a shaker at 4 °C. Cells were washed 3 $\times$  for 5 min in PBS (1 $\times$ ). For secondary antibody staining, cells were additionally incubated with DNA-labeled anti-rat or anti-rabbit for 1 h at room temperature and afterwards washed for 3 $\times$  5 min in PBS (1 $\times$ ). For drift correction purposes, cells were incubated with gold particles (cytodiagnosics, cat. no. G-90-100, 1:10 dilution of 90 nm) in PBS (1 $\times$ ), washed 3 $\times$  quickly, and immediately imaged.

**Super-resolution microscopy setup:** DNA-PAINT was carried out with an inverted Nikon Eclipse Ti microscope (Nikon Instruments) and the Perfect Focus System, by applying an objective-type total internal reflection fluorescence (TIRF) configuration with an oil-immersion objective (Apo SR TIRF 100 $\times$ , NA 1.49, oil). Two lasers were used for excitation: 561 nm (200 mW, Coherent Sapphire) or 488 nm (200 mW, Toptica iBeam smart). The laser beam was passed through a cleanup filter (ZET488/10 $\times$  or ZET561/10 $\times$ , Chroma Technology) and coupled into the microscope objective with use of a beam splitter (ZT488rdc or ZT561rdc, Chroma Technology). Fluorescence light was spectrally filtered with two emission filters (ET525/50m and ET500lp for 488 nm excitation and ET600/50 and ET575lp for 561 nm excitation, Chroma Technology) and imaged with a sCMOS camera (Andor Zyla 4.2) without further magnification, resulting in an effective pixel size of 130 nm after 2 $\times$  2 binning. Astigmatism for 3D imaging was introduced with the commercially available N-STORM adapter (Nikon Instruments). A second setup was interchangeably used for DNA-PAINT imaging consisting of an inverted Nikon Eclipse Ti 2 microscope (Nikon Instruments) with the Perfect Focus System, by applying an objective-type TIRF configuration with an oil-immersion objective (Apo

SR TIRF 100 $\times$ , NA 1.49, oil). For excitation, a 560 nm laser (2 W, MPB Communication, Inc.) was coupled into a single-mode fiber. The beam was coupled into the microscope body by use of a commercial TIRF Illuminator (Nikon Instruments). The laser beam was passed through a cleanup filter (ZET561/10 $\times$ , Chroma Technology). The beam splitter (ZT561rdc, Chroma Technology) was used. Fluorescence light was spectrally filtered with two emission filters (ET600/50 and ET575lp for 561 nm excitation, Chroma Technology) and imaged with a sCMOS camera (Andor Zyla 4.2) without further magnification, resulting in an effective pixel size of 130 nm after 2 $\times$  2 binning. Astigmatism for 3D imaging was introduced with an N-STORM Adapter (Nikon Instruments). Imaging parameters can be found in Table S4.

**Confocal setup:** The confocal imaging was performed at the Imaging Facility of the Max Planck Institute of Biochemistry, Martinsried, with a ZEISS (Jena, Germany) LSM780 confocal laser scanning microscope equipped with a ZEISS Plan-APO 63 $\times$ /NA 1.46 oil immersion objective.

**DNA-PAINT super-resolution microscopy:** Cells were imaged with use of  $\approx 3 \text{ kW cm}^{-2}$  561 nm laser excitation. Imager strand concentration varied depending on the measurement from 200 pM to 800 pM Cy3B-P1 and was adjusted to minimize double-binding events. Imaging was performed in PCA (Sigma-Aldrich, cat. no. 37580-25G-F, 1 $\times$ )/PCD (Sigma-Aldrich, cat. no. P8279-25UN, 1 $\times$ )/Trolox (Sigma-Aldrich, cat. no. 238813-1G, 1 $\times$ ) in buffer C [PBS (1 $\times$ ) + NaCl (500 mM)] with imaging for 10 000–50 000 frames at 100–250 ms exposure time (see also Table S3). 3D imaging was performed by using an astigmatism lens in the detection path.

**Multiplexed imaging with exchange-PAINT:** P5-conjugated protein G was incubated overnight with primary microtubule rat antibody, whereas P1-conjugated protein A was incubated (separately) overnight with primary TOM20 rabbit antibody. Unbound protein A or protein G from the coupled reagents was removed by centrifugal filtration with MWCO spin filters (Merck, cat. no. UFC500396, 100 kDa). The coupled reagents were then incubated together with fixed A549 cells for one hour for immunostaining of microtubules and TOM20. The cells were then washed thoroughly with PBS to remove excess protein A/G and antibody reagents and post-fixed with PFA (3%). The cells were imaged by DNA-PAINT super-resolution microscopy in two rounds with a buffer wash in-between. In round 1 we imaged microtubules by using Cy3B-P5 (1.5 nm). After washing off free Cy3B-P5, we then introduced Cy3B-P1 (2 nm) to image TOM20.

**Image data analysis:** Images were reconstructed with the Picasso and SMAP Software Suite. Drift correction was performed with a redundant cross-correlation and/or gold particles as fiducials. Localization precision was determined through a NeNA analysis.<sup>[24]</sup>

## Acknowledgements

*This work was supported by the DFG through the Emmy Noether Program (DFG JU 2957/1-1), the SFB 1032 (Nanoagents for spatiotemporal control of molecular and cellular reactions, Project A11), the ERC through an ERC Starting Grant (MolMap, grant agreement no. 680241), the Max Planck Society, the Max Planck Foundation, and the Center for Nanoscience (CeNS) to R.J. M.G. acknowledges funding from the European Union's Horizon 2020 research and innovation programme under the Marie Skłodowska-Curie grant agreement no. 796606. T.S., O.K.W. and A.A. ac-*

knowledge support from the DFG through the Graduate School of Quantitative Biosciences Munich (QBM). We thank Sebastian Strauss, Maximilian Strauss, Florian Schueder, Alexandra Sophia Eklund, and the whole Jungmann lab for fruitful discussion. We also thank Iris Stockmar for initial experiments with the NHS-TCO crosslinking strategy. We also acknowledge the support of the imaging facility at the MPI of Biochemistry.

### Conflict of Interest

The authors declare no conflict of interest.

**Keywords:** DNA-PAINT · nanotechnology · protein binders · single-molecule studies · super-resolution microscopy

- [1] S. J. Sahl, S. W. Hell, S. Jakobs, *Nat. Rev. Mol. Cell Biol.* **2017**, *18*, 685–701.
- [2] a) K. Xu, G. Zhong, X. Zhuang, *Science* **2013**, *339*, 452–456; b) J. Nixon-Abell, C. J. Obara, A. V. Weigel, D. Li, W. R. Legant, C. S. Xu, H. A. Pasolli, K. Harvey, H. F. Hess, E. Betzig, C. Blackstone, J. Lippincott-Schwartz, *Science* **2016**, *354*, aaf3928; c) I. Jayasinghe, A. H. Clowsley, R. Lin, T. Lutz, C. Harrison, E. Green, D. Baddeley, L. Di Michele, C. Soeller, *Cell Rep.* **2018**, *22*, 557–567.
- [3] a) M. Dai, R. Jungmann, P. Yin, *Nat. Nanotechnol.* **2016**, *11*, 798–807; b) F. Balzarotti, Y. Eilers, K. C. Gwosch, A. H. Gynna, V. Westphal, F. D. Stefani, J. Elf, S. W. Hell, *Science* **2017**, *355*, 606–612; c) J. Schnitzbauer, M. T. Strauss, T. Schlichthaerle, F. Schueder, R. Jungmann, *Nat. Protoc.* **2017**, *12*, 1198–1228.
- [4] M. Sauer, M. Heilemann, *Chem. Rev.* **2017**, *117*, 7478–7509.
- [5] a) R. Jungmann, C. Steinhauer, M. Scheible, A. Kuzyk, P. Tinnefeld, F. C. Simmel, *Nano Lett.* **2010**, *10*, 4756–4761; b) R. Jungmann, M. S. Avendaño, J. B. Woehrstein, M. Dai, W. M. Shih, P. Yin, *Nat. Methods* **2014**, *11*, 313–318; c) A. Auer, T. Schlichthaerle, J. B. Woehrstein, F. Schueder, M. T. Strauss, H. Grabmayr, R. Jungmann, *ChemPhysChem* **2018**, *19*, 3024–3034.
- [6] E. Betzig, G. H. Patterson, R. Sougrat, O. W. Lindwasser, S. Olenych, J. S. Bonifacino, M. W. Davidson, J. Lippincott-Schwartz, H. F. Hess, *Science* **2006**, *313*, 1642–1645.
- [7] M. J. Rust, M. Bates, X. Zhuang, *Nat. Methods* **2006**, *3*, 793–795.
- [8] T. Schlichthaerle, A. S. Eklund, F. Schueder, M. T. Strauss, C. Tiede, A. Curd, J. Ries, M. Peckham, D. C. Tomlinson, R. Jungmann, *Angew. Chem. Int. Ed.* **2018**, *57*, 11060–11063; *Angew. Chem.* **2018**, *130*, 11226–11230.
- [9] a) J. Ries, C. Kaplan, E. Platonova, H. Eghlidi, H. Ewers, *Nat. Methods* **2012**, *9*, 582–584; b) M. Mikhaylova, B. M. Cloin, K. Finan, R. van den Berg, J. Teeuw, M. M. Kijanka, M. Sokolowski, E. A. Katrukha, M. Maidorn, F. Opazo, S. Moutel, M. Vantard, F. Perez, P. M. van Bergen en Henegouwen, C. C. Hoogenraad, H. Ewers, L. C. Kapitein, *Nat. Commun.* **2015**, *6*, 7933.
- [10] a) S. Strauss, P. C. Nickels, M. T. Strauss, V. Jimenez Sabinina, J. Ellenberg, J. D. Carter, S. Gupta, N. Janjic, R. Jungmann, *Nat. Methods* **2018**, *15*, 685–688; b) F. Opazo, M. Levy, M. Byrom, C. Schafer, C. Geisler, T. W. Groemer, A. D. Ellington, S. O. Rizzoli, *Nat. Methods* **2012**, *9*, 938–939.
- [11] C. Tiede, R. Bedford, S. J. Heseltine, G. Smith, I. Wijetunga, R. Ross, D. Al-Qallaf, A. P. Roberts, A. Balls, A. Curd, R. E. Hughes, H. Martin, S. R. Needham, L. C. Zanetti-Domingues, Y. Sadigh, T. P. Peacock, A. A. Tang, N. Gibson, H. Kyle, G. W. Platt, N. Ingram, T. Taylor, L. P. Coletta, I. Manfield, M. Knowles, S. Bell, F. Esteves, A. Maqbool, R. K. Prasad, M. Drinkhill, R. S. Bon, V. Patel, S. A. Goodchild, M. Martin-Fernandez, R. J. Owens, J. E. Nettleship, M. E. Webb, M. Harrison, J. D. Lippiat, S. Ponnambalam, M. Peckham, A. Smith, P. K. Ferrigno, M. Johnson, M. J. McPherson, D. C. Tomlinson, *Elife* **2017**, *6*, e24903.
- [12] T. Pleiner, M. Bates, D. Gorlich, *J. Cell. Biochem.* **2018**, *119*, 1143–1154.
- [13] a) T. Moks, L. Abrahmsen, B. Nilsson, U. Hellman, J. Sjoquist, M. Uhlen, *Eur. J. Biochem.* **1986**, *156*, 637–643; b) W. Choe, T. A. Durgannavar, S. J. Chung, *Materials (Basel)* **2016**, *9*, 994.
- [14] a) B. Åkerström, L. Björck, *J. Biol. Chem.* **1986**, *261*, 10240–10247; b) U. Sjöbring, L. Björck, W. Kastern, *J. Biol. Chem.* **1991**, *266*, 399–405.
- [15] a) P. L. Ey, S. J. Prowse, C. R. Jenkin, *Immunochemistry* **1978**, *15*, 429–436; b) S. Hober, K. Nord, M. Linhult, *J. Chromatogr. B* **2007**, *848*, 40–47; c) E. S. Bergmann-Leitner, R. M. Mease, E. H. Duncan, F. Khan, J. Waitumbi, E. Angov, *Malar. J.* **2008**, *7*, 129.
- [16] F. J. Iborra, A. Pombo, D. A. Jackson, P. R. Cook, *J. Cell Sci.* **1996**, *109*, 1427–1436.
- [17] B. J. H. M. Rosier, G. A. O. Cremers, W. Engelen, M. Merx, L. Brunsveld, T. F. A. de Greef, *Chem. Commun.* **2017**, *53*, 7393–7396.
- [18] S. S. Agasti, Y. Wang, F. Schueder, A. Sukumar, R. Jungmann, P. Yin, *Chem. Sci.* **2017**, *8*, 3080–3091.
- [19] F. Schueder, J. Lara-Gutierrez, B. J. Beliveau, S. K. Saka, H. M. Sasaki, J. B. Woehrstein, M. T. Strauss, H. Grabmayr, P. Yin, R. Jungmann, *Nat. Commun.* **2017**, *8*, 2090.
- [20] E. Nogales, *Protein Sci.* **2015**, *24*, 1912–1919.
- [21] Y. Li, M. Mund, P. Hoess, J. Deschamps, U. Matti, B. Nijmeijer, V. J. Sabinina, J. Ellenberg, I. Schoen, J. Ries, *Nat. Methods* **2018**, *15*, 367–369.
- [22] R. K. Jha, T. Gaiotto, A. R. Bradbury, C. E. Strauss, *Protein Eng. Des. Sel.* **2014**, *27*, 127–134.
- [23] R. Jungmann, M. S. Avendaño, M. Dai, J. B. Woehrstein, S. S. Agasti, Z. Feiger, A. Rodal, P. Yin, *Nat. Methods* **2016**, *13*, 439.
- [24] U. Endesfelder, S. Malkusch, F. Fricke, M. Heilemann, *Histochem. Cell Biol.* **2014**, *141*, 629–638.

Manuscript received: November 30, 2018

Accepted manuscript online: December 27, 2018

Version of record online: March 19, 2019

CHEMBIOCHEM

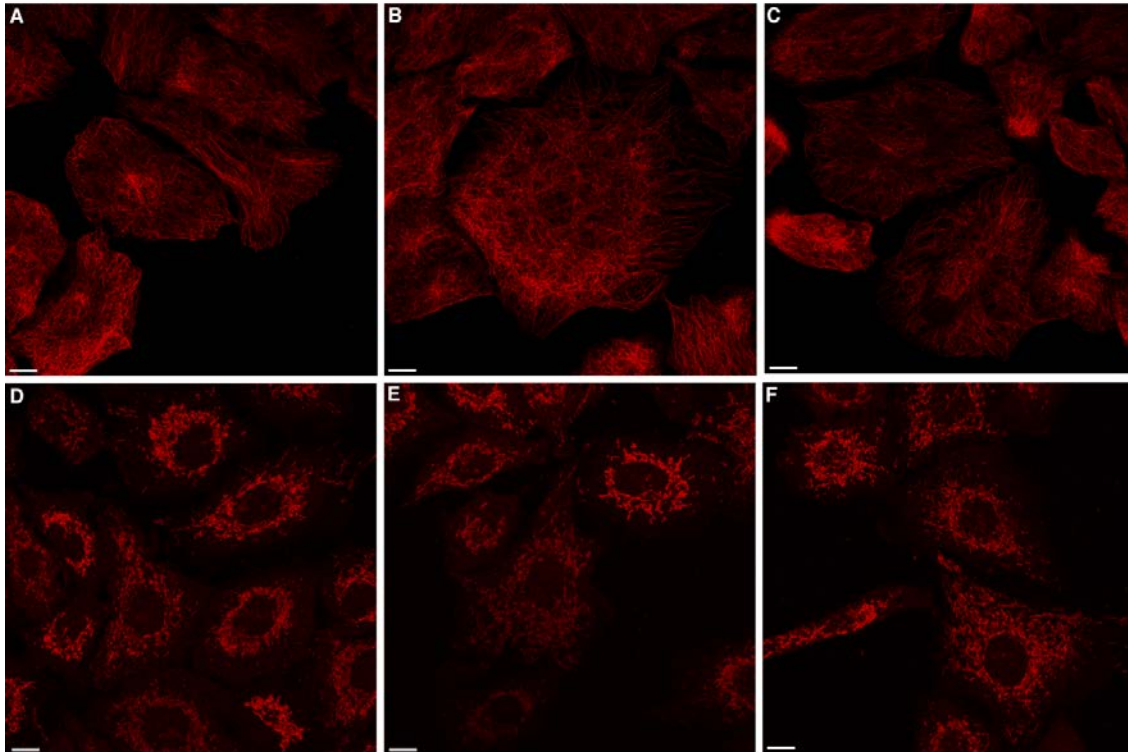
## Supporting Information

### **Bacterially Derived Antibody Binders as Small Adapters for DNA-PAINT Microscopy**

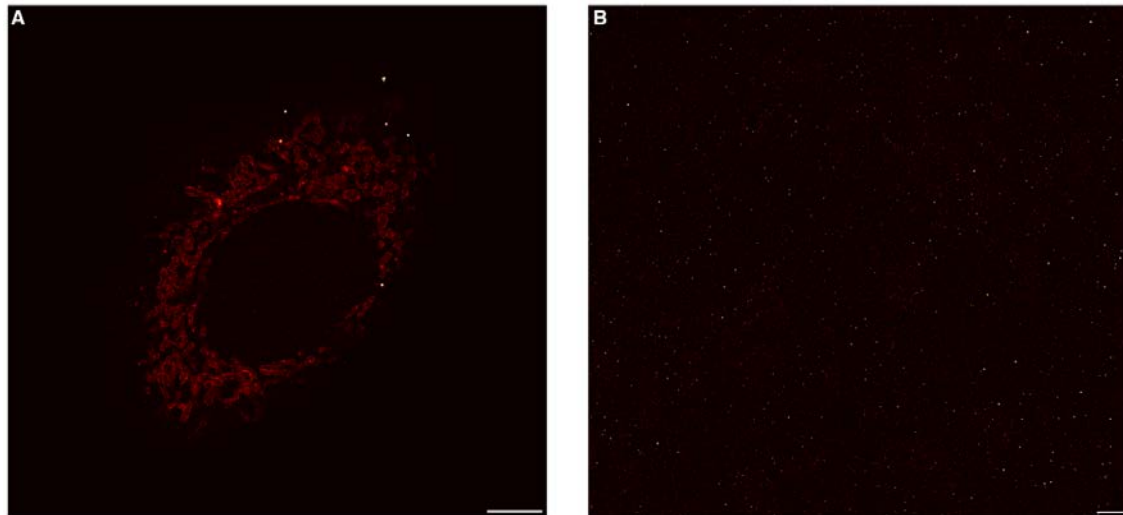
Thomas Schlichthaerle<sup>+, [a, b]</sup> Mahipal Ganji<sup>+, [a, b]</sup> Alexander Auer<sup>+, [a, b]</sup> Orsolya Kimbu Wade<sup>+, [a, b]</sup>  
and Ralf Jungmann<sup>\*, [a, b]</sup>

cbic\_201800743\_sm\_miscellaneous\_information.pdf

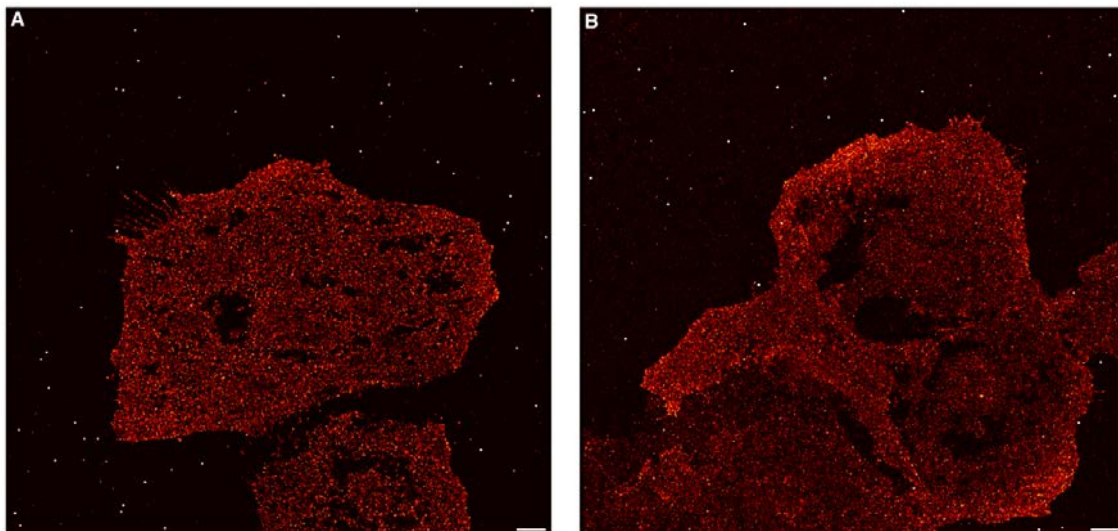
<b>Supplementary Figure 1</b>	Confocal imaging of bacterial-derived secondary adapters
<b>Supplementary Figure 2</b>	Imaging rabbit anti-TOM20 with protein G and rat anti-alpha tubulin with protein A
<b>Supplementary Figure 3</b>	Mouse anti-EGFR receptor imaging with protein A/G in A549 cells
<b>Supplementary Figure 4</b>	Control experiments without any primary antibodies in A549 cells
<b>Supplementary Figure 5</b>	EGF receptor nanoclusters imaged with different binders
<b>Supplementary Figure 6</b>	Exchange-PAINT imaging in A549 cells
<b>Supplementary Table 1</b>	Binding of Protein A/G to Antibody Species
<b>Supplementary Table 2</b>	Docking sequences
<b>Supplementary Table 3</b>	Imager sequences
<b>Supplementary Table 4</b>	Imaging parameters



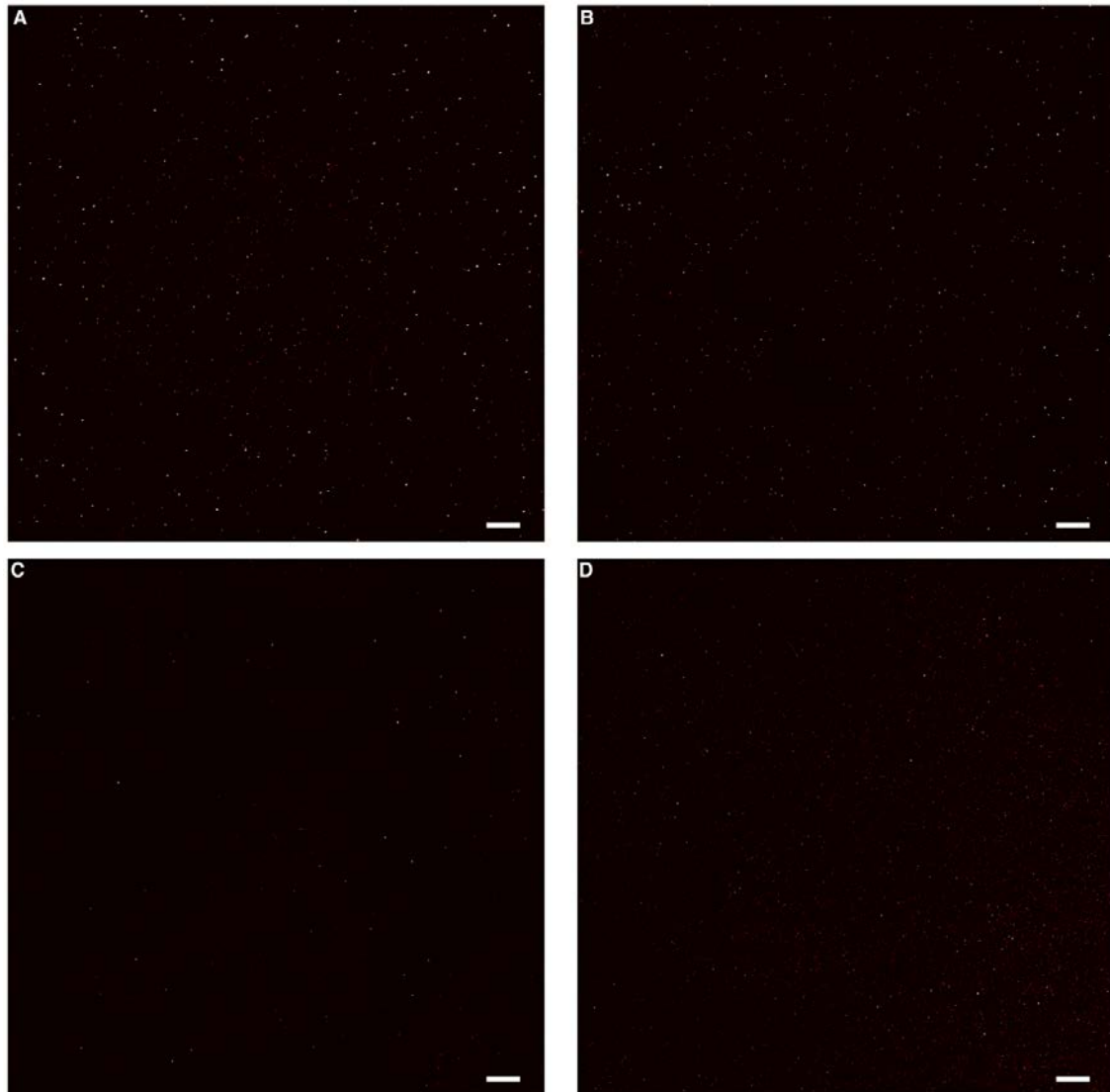
**Supplementary Figure 1 | Confocal imaging of bacterial-derived secondary antibody adapters.** a-c) Microtubule network stained with AF647-labeled protein G against primary rat anti- $\alpha$ -tubulin antibody. d-f) Mitochondrial network stained with AF647-labeled protein A against primary rabbit anti-Tom20 antibody. Scale bars, 10  $\mu$ m.



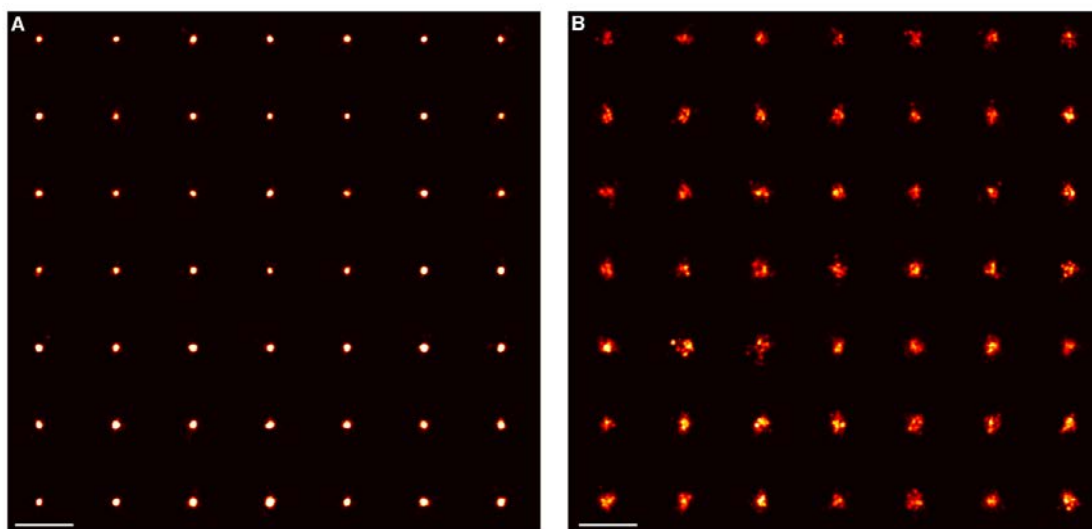
**Supplementary Figure 2 | Imaging rabbit anti-TOM20 with protein G and rat anti-alpha tubulin with protein A.** a) DNA-conjugated protein G imaging as secondary probe for rabbit anti-TOM20 reveals mitochondrial structure. This data shows that protein G can be used as a secondary binder against primary rabbit antibody. b) DNA-conjugated protein A imaging as secondary probe for rat anti-microtubule does not exhibit any specific staining pattern. Protein A cannot be used as secondary binders for rat IgG2a antibodies. Scale bars, 5  $\mu\text{m}$ .



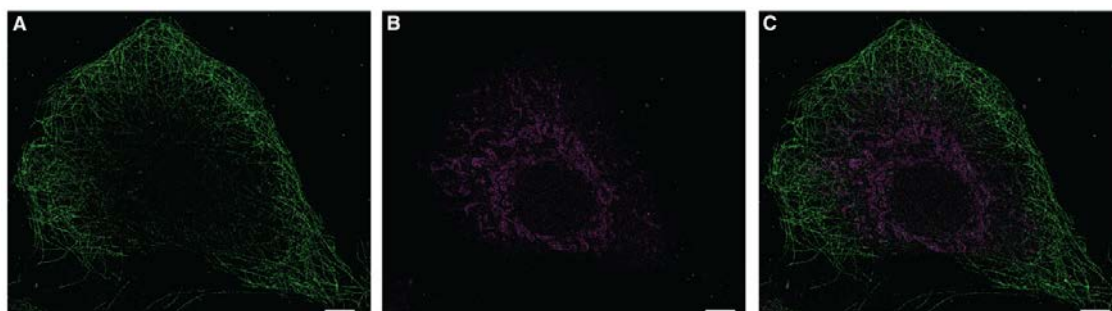
**Supplementary Figure 3 | Mouse anti-EGFR receptor imaging with protein A/G in A549 cells.** a) Imaging with DNA-conjugated protein A as secondary binder. b) Imaging with DNA-conjugated protein G as secondary binder. Protein A/G can be used as a secondary binder against mouse primary IgG2a antibodies. Scale bars, 5  $\mu\text{m}$ .



**Supplementary Figure 4 | Control experiments without any primary antibodies in A549 cells.** a) P1 imager strand only added to cells. b) P3 imager only added to cells. c) DNA-labeled (P1 docking strand) protein G staining only imaged with P1 imager strand. d) DNA-labeled (P1 docking strand) protein A staining only imaged with P1 imager strand. We do not see any non-specific labeling of cellular structures with protein A/G or the DNA imager strands in the absence of primary antibodies. Scale bars, 5  $\mu\text{m}$ .



**Supplementary Figure 5 | EGF receptor nanoclusters imaged with different binders.** a) Individual EGF receptor nanoclusters stained with protein A against rabbit anti-EGFR antibody. b) Individual EGF receptor nanoclusters stained with primary-secondary antibody sandwich. Individual nanoclusters selected from data from Figure 3. Scale bars, 200 nm.



**Supplementary Figure 6 | Exchange-PAINT imaging in A549 cells.** a) Microtubule imaging with DNA-labeled protein G against primary rat anti-microtubule reveals the filamentous structure. b) TOM20 imaging with DNA-labeled protein A against primary rabbit anti-TOM20 reveals the mitochondrial network. c) Overlay of microtubule imaging and TOM20. Scale bars, 5  $\mu\text{m}$ .

**Supplementary Table 1 | Binding of Protein A/G to Antibody Species**

Primary Antibody Species (subclass)	Protein A	Protein G
Rabbit (n.a.)	+	+
Rat (IgG2a)	-	+
Mouse (IgG2a)	+	+

**Supplementary Table 2 | Docking sequences**

Sequence name	Sequence	5'-mod	3'-mod	Vendor
P1	TTATACATCTA	TZ	None	Biomers.net
P3	TTTCTTCATTA	TZ	None	Biomers.net
P5	TTTCAATGTAT	TZ	None	Biomers.net

**Supplementary Table 3 | Imager sequences**

Sequence name	Sequence	5'-mod	3'-mod	Vendor
P1*	CTAGATGTAT	None	Cy3b	Eurofins Genomics
P3*	GTAATGAAGA	None	Cy3b	Eurofins Genomics
P5*	CATACATTGA	None	Cy3b	Eurofins Genomics

Supplementary Table 4 | Imaging parameters

Dataset	Parameters	Laser power @561 nm	Localization precision (NeNA)	Microscope
Figure 2a	100 ms, 2D, 50k Frames, 1.5 nM, P3*	2 kW/cm <sup>2</sup>	4.6 nm	Setup 1
Figure 2d	100 ms, 2D, 40k Frames, 2 nM, P1*	1.5 kW/cm <sup>2</sup>	5.6 nm	Setup 1
Figure 3a	100 ms, 2D, 30k Frames, 0.5 nM, P3*	1.5 kW/cm <sup>2</sup>	4.5 nm	Setup 2
Figure 3h	100 ms, 2D, 30k Frames, 0.5 nM, P3*	1.5 kW/cm <sup>2</sup>	4.7 nm	Setup 2
Figure 4a	250 ms, 3D, 60k Frames, 1 nM, P5*	3.3 kW/cm <sup>2</sup>	3.4 nm	Setup 1
Figure 4f	250 ms, 3D, 20k Frames, 200 pM, P1*	3.3 kW/cm <sup>2</sup>	2.6 nm	Setup 1
Supplementary Figure 2a	100 ms, 2D, 40k, 5 nM, P1*	1.5 kW/cm <sup>2</sup>	7.9 nm	Setup 1
Supplementary Figure 2b	100 ms, 2D, 2.5k, 5 nM, P3*	1.5 kW/cm <sup>2</sup>	n.a.	Setup 1
Supplementary Figure 3a	100 ms, 2D, 50k, 5 nM, P5*	1.5 kW/cm <sup>2</sup>	6 nm	Setup 1
Supplementary Figure 3b	100 ms, 2D, 40k, 5 nM, P1*	1.5 kW/cm <sup>2</sup>	5.4 nm	Setup 1
Supplementary Figure 4	100 ms, 2D, 2.5k, 5 nM, P1*/P3*	1.5 kW/cm <sup>2</sup>	n.a.	Setup 1
Supplementary Figure 6a	100 ms, 2D, 50k, 1.5 nM, P5*	1.5 kW/cm <sup>2</sup>	7.1 nm	Setup 1
Supplementary Figure 6b	100 ms, 2D, 30k, 2 nM, P1*	1.5 kW/cm <sup>2</sup>	5.5 nm	Setup 1

# Direct visualization of single nuclear pore complex proteins using genetically-encoded probes

**T. Schlichthaerle\***, **M.T. Strauss\***, **F. Schueder\***, A. Auer, B. Nijmeijer, M. Kueblbeck, V.J. Sabinina, J.V. Thevathasan, J. Ries, J. Ellenberg, R. Jungmann

*\*authors contributed equally*

published in

*Angewandte Chemie (2019)*

Reprinted from [144]  
CC BY 4.0

**Super-resolution Microscopy**

International Edition: DOI: 10.1002/anie.201905685

German Edition: DOI: 10.1002/ange.201905685

## Direct Visualization of Single Nuclear Pore Complex Proteins Using Genetically-Encoded Probes for DNA-PAINT

Thomas Schlichthaerle<sup>+</sup>, Maximilian T. Strauss<sup>+</sup>, Florian Schueder<sup>+</sup>, Alexander Auer, Bianca Nijmeijer, Moritz Kueblbeck, Vilma Jimenez Sabinina, Jervis V. Thevathasan, Jonas Ries, Jan Ellenberg, and Ralf Jungmann\*

**Abstract:** The nuclear pore complex (NPC) is one of the largest and most complex protein assemblies in the cell and, among other functions, serves as the gatekeeper of nucleocytoplasmic transport. Unraveling its molecular architecture and functioning has been an active research topic for decades with recent cryogenic electron microscopy and super-resolution studies advancing our understanding of the architecture of the NPC complex. However, the specific and direct visualization of single copies of NPC proteins is thus far elusive. Herein, we combine genetically-encoded self-labeling enzymes such as SNAP-tag and HaloTag with DNA-PAINT microscopy. We resolve single copies of nucleoporins in the human Y-complex in three dimensions with a precision of circa 3 nm, enabling studies of multicomponent complexes on the level of single proteins in cells using optical fluorescence microscopy.

Super-resolution techniques allow diffraction-unlimited fluorescence imaging<sup>[1]</sup> and with recent advancements, true biomolecular resolution is well within reach.<sup>[2]</sup> One implementation of single-molecule localization microscopy (SMLM) is called DNA points accumulation in nanoscale topography<sup>[2b]</sup> (DNA-PAINT), where dye-labeled DNA strands (called “imager” strands) transiently bind to their complements (called “docking” strands) on a target of interest, thus creating the typical “blinking” used in SMLM to achieve super-resolution. While localization precisions down to approximately one nanometer (basically the size of

a single dye molecule) are now routinely achievable from a technology perspective, this respectable spatial resolution has yet to be translated to cell biological research. Currently, this is mainly hampered by the lack of small and efficient protein labels. Recent developments of nanobody- or aptamer-based tagging approaches<sup>[3]</sup> are providing an attractive route ahead, however both approaches are not yet deploying their full potential either due to limited binder availability (in the case of nanobodies) or lack of large-scale analysis of suitable super-resolution probes (in the aptamer case).

While we are convinced that some of these issues might be resolved in the future, we introduce herein the combination of widely-used, genetically-encoded self-labeling enzymes such as SNAP-tag<sup>[4]</sup> and HaloTag<sup>[5]</sup> with DNA-PAINT to enable 1:1 labeling of single proteins in the nuclear pore complex (NPC) using ligand-conjugated DNA-PAINT docking strands. The NPC is responsible for the control of nucleocytoplasmic transport and a highly complex and sophisticated protein assembly. NPCs contain multiple copies of approximately 30 different nuclear pore proteins called nucleoporins (NUPs) and have an estimated total molecular mass of about 120 MDa, placing NPCs among the largest cellular protein complexes.<sup>[6]</sup> Owing to their diverse function in controlling molecular transport between the nucleus and the cytoplasm, NPCs are a major target for structural biology research with characterization by for example, cryogenic electron microscopy<sup>[6]</sup> (cryo-EM) or optical super-resolution techniques.<sup>[7]</sup> State-of-the-art cryo-EM studies,<sup>[8]</sup> reaching impressive pseudo-atomic resolution, have advanced our structural understanding in recent years. It is now possible to not only elucidate how NUPs in NPCs are arranged, but also to shed light on how structural changes of NPCs are connected to their dysfunction.<sup>[9]</sup> However, even with recent advancements in cryo-EM instrumentation, molecular specificity necessary to resolve single NUPs in NPCs proves still elusive, mainly due to the lack of high protein-specific contrast. Fluorescence-based techniques on the other hand offer exquisite molecular contrast and specificity owing to the use of dye-labeled affinity reagents targeting single protein copies in cells. However, until recently, the necessary resolution to spatially resolve single small proteins in a larger complex has not been achieved because of limitations in labeling (small and efficient probes) and imaging technology (providing sub-10-nm spatial resolution). In order to spatially resolve sub-10-nm distances using SMLM, one needs to obtain a localization precision of circa 4 nm. This is readily achievable with DNA-PAINT, as a comparably large number of photons is available for localization per single binding—that is, blinking—event.

[\*] T. Schlichthaerle,<sup>[4]</sup> Dr. M. T. Strauss,<sup>[4]</sup> F. Schueder,<sup>[4]</sup> A. Auer, Prof. Dr. R. Jungmann  
Faculty of Physics and Center for Nanoscience, LMU Munich  
Geschwister-Scholl-Platz 1, 80539 Munich (Germany),  
and

Max Planck Institute of Biochemistry  
Am Klopferspitz 18, 82152 Martinsried (Germany)  
E-mail: jungmann@biochem.mpg.de

B. Nijmeijer, M. Kueblbeck, Dr. V. Jimenez Sabinina,  
Dr. J. V. Thevathasan, Dr. J. Ries, Dr. J. Ellenberg  
Cell Biology and Biophysics Unit, European Molecular Biology  
Laboratory (EMBL)  
Meyerhofstraße 1, 69117 Heidelberg (Germany)

[†] These authors contributed equally.

Supporting information and the ORCID identification number(s) for the author(s) of this article can be found under:  
 <https://doi.org/10.1002/anie.201905685>.

© 2019 The Authors. Published by Wiley-VCH Verlag GmbH & Co. KGaA. This is an open access article under the terms of the Creative Commons Attribution License, which permits use, distribution and reproduction in any medium, provided the original work is properly cited.

While one can easily reach tens of thousands of photons per blinking event with DNA-PAINT, this is hard to achieve using STORM. Furthermore, the intrinsic resistance of DNA-PAINT to photobleaching enables repetitive localizations with high precision, while in the STORM case, the available photon budget is limited by a few fixed, target-bound fluorophores. Herein, we thus combine DNA-PAINT microscopy with small, genetically-encoded self-labeling enzymes such as SNAP- and HaloTag to overcome limitations in optical super-resolution microscopy.

We present a straightforward protocol to target these tags in a variety of engineered cell lines using the DNA-conjugated ligands benzylguanine (BG) and chloroalkane against SNAP-tag<sup>[4]</sup> and HaloTag<sup>[5]</sup> respectively (Figure 1 a and b). We investigate the achievable labeling precision and reduction of linkage error of SNAP-tag and HaloTag, examine their performance in contrast to DNA-conjugated nanobodies against GFP-tagged proteins in single NPCs and further compare them to primary and secondary antibody labeling. Finally, we resolve, for the first time, single copies of NUP96 proteins in the Y-complex of the NPC, spaced only circa 12 nm apart.

To implement genetically-encoded self-labeling tags for DNA-PAINT, we first assayed our ability to use BG-modified docking strands to target SNAP-tags C-terminally fused to NUP96 proteins in U2OS cell lines created by CRISPR/Cas9

engineering.<sup>[10]</sup> Labeling was performed post-fixation and -permeabilization using standard labeling protocols<sup>[7b]</sup> adapted for DNA-PAINT (see Online Methods). The resulting 2D DNA-PAINT image is shown in Figure 1 c. A zoom-in reveals the expected 8-fold symmetry of NUP96 proteins in the super-resolution micrograph (Figure 1 d). We then performed labeling of NUP107-GFP fusion proteins using a DNA-conjugated anti-GFP nanobody<sup>[11]</sup> and obtained qualitatively similar results (Figure 1 e–f, see also Supplementary Figure 1 in the Supporting Information for zoom-outs and comparison to diffraction-limited data).

To evaluate labeling quality and precision in a quantitative manner, we next compared results of more traditional labeling of NUP107-GFP using primary-secondary antibodies to those of NUP96-SNAP, NUP96-Halo, NUP107-SNAP, and NUP107-GFP cell lines targeted with their respective small ligands. The NPC architecture presents a well-suited model to benchmark novel labeling approaches with regards to overall labeling efficiency and limits of spatial resolution, in a sense similar to an *in vitro* DNA origami calibration standard,<sup>[12]</sup> but inside a cell. Previous EM studies revealed that NUP96 and NUP107 proteins are present in the Y-complex, which forms the cytoplasmic as well as nuclear NPC double ring arrangement in an 8-fold symmetry. The two double rings are spaced approximately 50 nm apart with each side containing 16 protein copies.<sup>[8a,13]</sup> The two copies of the proteins in each

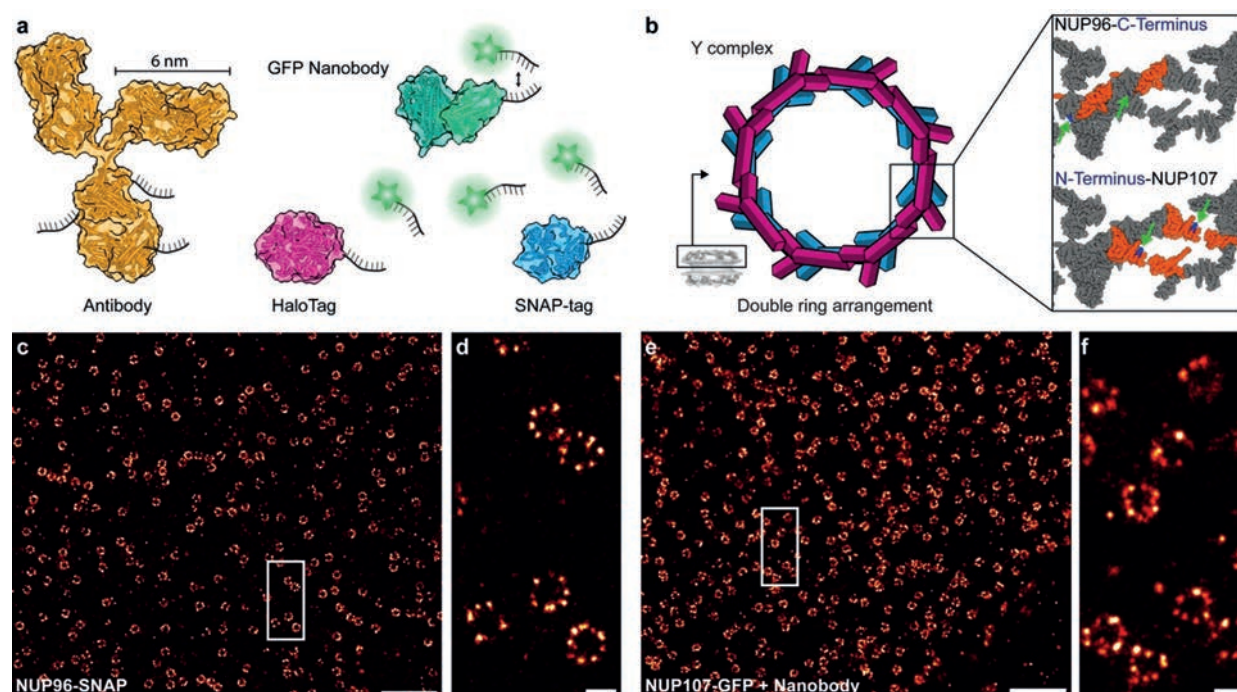


**Figure 1.** a) Comparison of different labeling probes (secondary antibody: yellow, GFP nanobody: green, HaloTag: magenta, SNAP-tag: blue) conjugated with DNA strands for DNA-PAINT imaging (cartoons are based on protein database (PDB) entries: Secondary antibody (1IGT), GFP nanobody (3K1K), HaloTag (4KAF), SNAP-tag (3KZZ)). Proteins are to scale. b) NPCs contain 16 copies of NUP96 and NUP107 in the cytoplasmic as well as the nuclear ring. Top right: C-terminally-labeled (blue, highlighted by green arrows) NUP96 structure (orange) highlighted in the zoom-in of a symmetry center on the ring (ca. 12 nm apart). Bottom right: N-terminally-labeled (blue, highlighted by green arrows), NUP107 structure (orange) in the zoom-in of a symmetry center on the ring (ca. 12 nm apart). Distances and cartoons derived from PDB entry: Nup(5A9Q). c) DNA-PAINT overview image of NUP96-SNAP in U2OS cells. d) Zoom-in of highlighted area reveals the arrangement of NUP96 in NPCs. e) DNA-PAINT overview image of NUP107-GFP in HeLa cells. f) Zoom-in of highlighted area. Scale bars: 5  $\mu\text{m}$  (c, e), 100 nm (d, f).

symmetry center are arranged in Y-complexes spaced circa 12 nm apart (Figure 1b). In order to quantitatively compare different labeling approaches, we first acquired 2D DNA-PAINT data using identical image acquisition parameters (see Supplementary Tables 1–3 in the Supporting Information for details). Next, we selected single NPC structures in the reconstructed super-resolution image, aligned them on top of each other (that is, the center of the NPC rings, thus creating a sum image) and performed a radial distance measurement over all localizations. This analysis yields two observables for comparison; first, the median fitted ring radius and second, the width of this distribution. Dissimilar fitted radii for the same protein labeled using different tags are a measure for potential systematic biases introduced by a preferential orientation of the labeling probes. The width of the distribution on the other hand is a proxy for label-size-induced linkage error, that is, broader distributions originate from “larger” labeling probes. Our data in Figure 2 provides a quantitative comparison of NUP107-SNAP, NUP107-GFP, NUP96-SNAP, and NUP96-Halo cell lines targeted with their respective DNA-conjugated labeling probes (see also Supplementary Figures 2–6 in the Supporting Information). Furthermore, we compare our results with NUP107-GFP labeled using primary and DNA-conjugated secondary antibodies. We obtained radii of  $53.7 \pm 13.1$  nm for NUP107-SNAP (Figure 2a and Supplementary Figure 2 in the Sup-

porting Information) and  $54.6 \pm 11.9$  nm for NUP107-GFP (nanobody staining) (Figure 2b and Supplementary Figure 3 in the Supporting Information), as well as  $55.9 \pm 12.6$  nm for NUP96-SNAP (Figure 2c and Supplementary Figure 4 in the Supporting Information) and  $56.2 \pm 10.2$  nm for NUP96-Halo (Figure 2d and Supplementary Figure 5 in the Supporting Information), in close overall agreement to earlier EM- and fluorescence-based studies.<sup>[7b,8a]</sup> For the antibody-stained sample against NUP107-GFP (Figure 2e and Supplementary Figure 6 in the Supporting Information), we obtained a considerably larger radius of 65.9 nm. This could be explained by primary and DNA-conjugated secondary antibodies potentially binding preferentially towards the outside of the NPCs. However, not only did the antibody-stained samples yield a larger apparent NPC radius, also the measured width of the distribution (18 nm) was larger compared to the genetically-encoded tags due to the increased size of the antibodies. In the case of genetically-encoded tags, the width of the distributions is considerably smaller (see also Supplementary Table 4 in the Supporting Information) due to the reduced linkage error to the actual protein location.<sup>[3c,e,14]</sup>

Next, we sought out to further optimize image acquisition conditions with respect to overall localization precision, sampling of single protein sites, and three-dimensional image acquisition (Supporting Information, Supplementary Figure 7). This allowed us to visualize single copies of NUP96

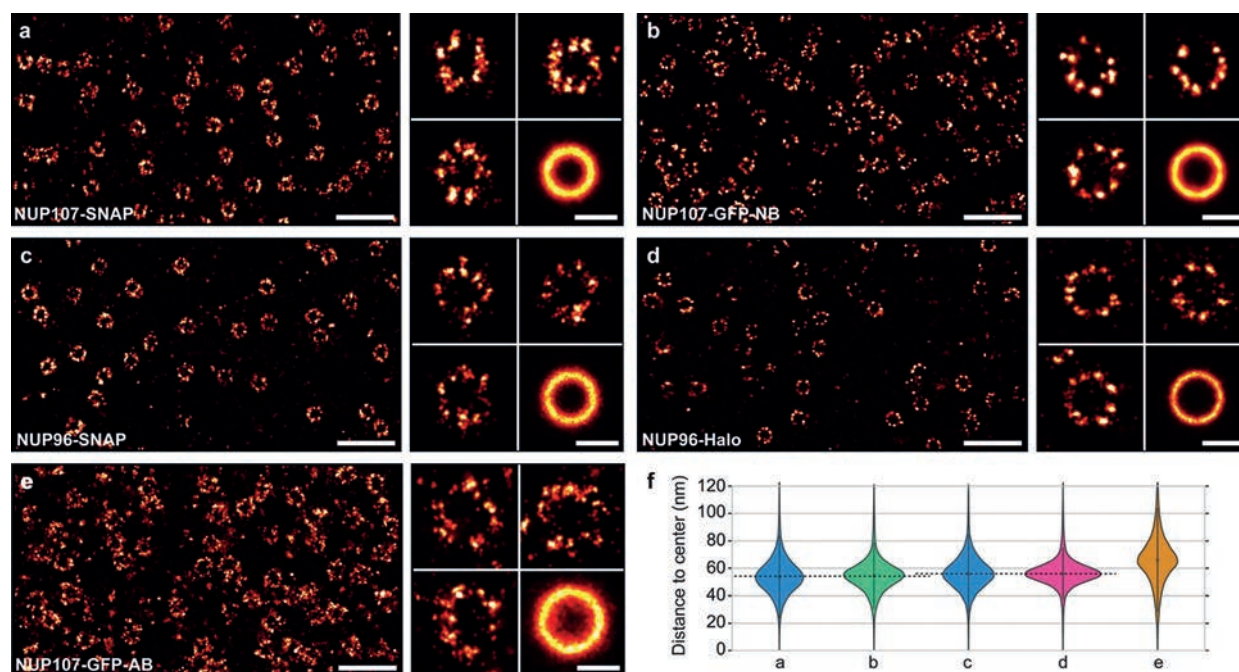


**Figure 2.** a) NUP107-SNAP overview image (left). Zoom-in to individual NPCs and sum image ( $n = 398$ ) (right). b) NUP107-GFP nanobody overview image (left). Zoom-in to individual NPCs and sum image ( $n = 486$ ) (right). c) NUP96-SNAP overview image (left). Zoom-in to individual NPCs and sum image ( $n = 288$ ) (right). d) NUP96-Halo overview image (left). Zoom-in to individual NPCs and sum image ( $n = 191$ ) (right). e) NUP107-GFP-Antibody overview image (left). Zoom-in to individual NPCs and sum image ( $n = 185$ ) (right). f) Violin plots of the distances between ring center and localizations. Median radii and standard deviation were obtained for each label: NUP107-SNAP (from a, 127 773 fitted localizations,  $53.7 \pm 13.1$  nm radius), NUP107-GFP (from b, 219 398 fitted localizations,  $54.6 \pm 11.9$  nm radius), NUP96-SNAP (from c, 57 297 fitted localizations,  $55.9 \pm 12.6$  nm), NUP96-Halo (from d, 45 143 fitted localizations,  $56.2 \pm 10.2$  nm radius), NUP107-GFP-Antibody (from e, 69 834 fitted localizations,  $65.9 \pm 17.5$  nm). See also Supplementary Table 2 in the Supporting Information. Scale bars: 500 nm (overviews), 100 nm (individual NPCs and sum image).

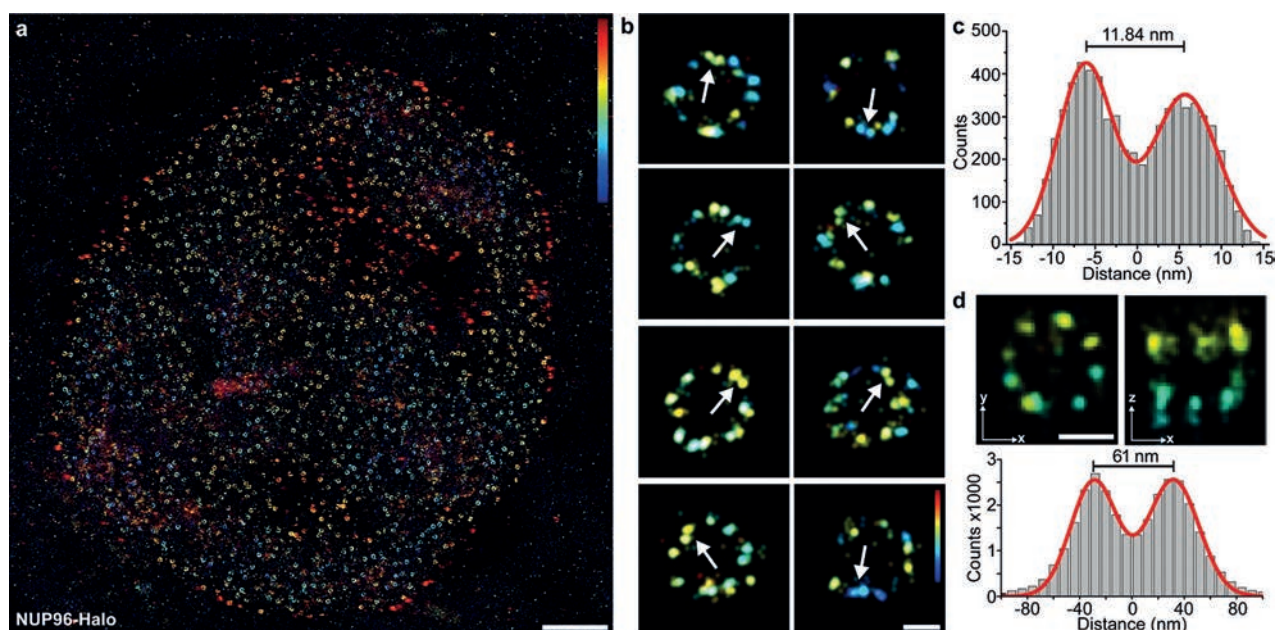


**Figure 3.** a) Overview image of NUP96-Halo imaged using 3D DNA-PAINT (color indicates height, range:  $-200$  (blue) to  $200$  nm (red)). b) Selection of single NPCs. Arrows are highlighting two copies of NUP96 proteins in the same symmetry center of the same ring (that is at the same height) spaced ca.  $12$  nm apart from each other (color indicates height, range:  $-100$  (blue) to  $100$  nm (red)). c) Cross-sectional histogram of 3D-summed pairs ( $n=45$ ) of NUP96 proteins in single symmetry centers as highlighted by arrows in b yields ca.  $12$  nm distance between single proteins. d) NUP96-Halo-labeled NPCs show the typical eightfold symmetry ( $xy$ -projection, left) and the organization in nuclear and cytoplasmic rings ( $xz$ -projection, right). Micrographs represent sum data from aligned NPCs ( $n=31$ ). Bottom: Cross-sectional histogram of localizations in the  $xz$ -projection yields ca.  $61$  nm separation between cytoplasmic and nuclear rings. Scale bars:  $2 \mu\text{m}$  (a),  $50$  nm (b, d).

proteins (Figure 3) using the NUP96-Halo cell line, which we chose based on its superior performance in the 2D study presented above (smallest distribution width). An overview of a typical 3D DNA-PAINT dataset is shown in Figure 3a. Zooming in to some of the NPCs (Figure 3b) reveals distinctive pairs of close-by “localization clouds” (arrows in Figure 3b), which we attribute to single NUP96 proteins. To quantitatively assess the Euclidian distance of the two copies of NUP96 on the two cytoplasmic or nuclear rings of the NPC, we selected about 50 pairs in NPCs, aligned them on top of each other and subsequently carried out particle averaging with Picasso.<sup>[2b,15]</sup> We then performed a cross-sectional histogram analysis of the resulting sum image and fitted the distribution with two Gaussian functions (Figure 3c). The fit yields a peak-to-peak distance of about  $12$  nm, well in agreement with the expected distance of NUP96 proteins on adjacent Y-complexes as derived from EM models.<sup>[8a]</sup> Furthermore, each peak fit exhibits a standard deviation of only circa  $3$  nm, highlighting the high localization precision and accuracy achievable with the combination of genetically-encoded tags with DNA-PAINT. Additionally, we measured the separation between the cytoplasmic and the nuclear rings for NUP96-Halo, yielding a distance of about  $61$  nm (Figure 3d), which we could clearly resolve. The capability to separate the nuclear from the cytoplasmic side of the NPC is a necessity to convince us, that the NUP pairs in each symmetry center (Figure 3b and c) are indeed part of either the nuclear or cytoplasmic rings of the NPC. Furthermore, we obtained qualitatively and quantitatively similar results for

the NUP96-SNAP cell line (Supporting Information, Supplementary Figure 8).

In conclusion, we present an approach to combine DNA-PAINT with genetically-encoded self-labeling tags. This provides a tool to investigate single proteins in higher order protein complexes in cells. However, we could only achieve a relatively modest labeling efficiency of approximately  $30\%$  (Supporting Information, Supplementary Table 5). Thus, one of the main challenges in the field remains, which is a route to highly efficient labeling probes ( $> 90\%$  labeling efficiency) without requiring genetic engineering. Besides the availability of peptide tags combined with nanobodies<sup>[16]</sup> and small scaffolds like nanobodies,<sup>[3a]</sup> affimers,<sup>[17]</sup> darpins,<sup>[18]</sup> or SOMAmers<sup>[19]</sup> novel approaches are necessary to tackle this challenge. Probes could include optimized host-guest systems,<sup>[20]</sup> direct transient binders,<sup>[21]</sup> or rationally-designed small proteins.<sup>[22]</sup> However, even with our current labeling efficiency, studies of single proteins in multicomponent complexes are within reach.

### Acknowledgements

We thank Bianca Sperl for experimental support. We thank Sandra Correia for assistance with generating the cell lines. This work has been supported in part by the German Research Foundation through the Emmy Noether Program (DFG JU 2957/1-1 to R.J.), the SFB1032 (project A11 to R.J.), the European Research Council through an ERC Starting

Grant (MolMap; grant agreement number 680241 to R.J.) and an ERC Consolidator Grant (ERC CoG-724489 to J.R.), the Allen Distinguished Investigator Program through The Paul G. Allen Frontiers Group (to J.E. and R.J.), the National Institutes of Health Common Fund 4D Nucleome Program (Grant U01 EB021223/ U01 DA047728 to J.E. and J.R.), the European Molecular Biology Laboratory (EMBL; B.N., M.K., V.J.S., J.V.T., J.R., and J.E.), the Max Planck Foundation (to R.J.) and the Max Planck Society (to R.J.). T.S. and A.A. acknowledge support by the QBM graduate school. M.T.S. acknowledges support from the International Max Planck Research School for Molecular and Cellular Life Sciences (IMPRS-LS). V.S.J. acknowledges support by the Boehringer Ingelheim Fonds. The cell lines are available via Cell Line Services (CLS, clsgmbh.de).

### Conflict of interest

The authors declare no conflict of interest.

**Keywords:** DNA-PAINT · genetically encoded tags · nuclear pore complex · single-molecule imaging · super-resolution microscopy

**How to cite:** *Angew. Chem. Int. Ed.* **2019**, *58*, 13004–13008  
*Angew. Chem.* **2019**, *131*, 13138–13142

- [1] a) S. J. Sahl, S. W. Hell, S. Jakobs, *Nat. Rev. Mol. Cell Biol.* **2017**, *18*, 685–701; b) M. Sauer, M. Heilemann, *Chem. Rev.* **2017**, *117*, 7478–7509.
- [2] a) M. Dai, R. Jungmann, P. Yin, *Nat. Nanotechnol.* **2016**, *11*, 798–807; b) J. Schnitzbauer, M. T. Strauss, T. Schlichthaerle, F. Schueder, R. Jungmann, *Nat. Protoc.* **2017**, *12*, 1198–1228; c) F. Balzarotti, Y. Eilers, K. C. Gwosch, A. H. Gynna, V. Westphal, F. D. Stefani, J. Elf, S. W. Hell, *Science* **2017**, *355*, 606–612.
- [3] a) J. Ries, C. Kaplan, E. Platonova, H. Eghlidi, H. Ewers, *Nat. Methods* **2012**, *9*, 582–584; b) S. Sograte-Idrissi, N. Oleksiievets, S. Isbaner, M. Eggert-Martinez, J. Enderlein, R. Tsukanov, F. Opazo, *Cells* **2019**, *8*, 48; c) F. Opazo, M. Levy, M. Byrom, C. Schafer, C. Geisler, T. W. Groemer, A. D. Ellington, S. O. Rizzoli, *Nat. Methods* **2012**, *9*, 938–939; d) V. Fabricius, J. Lefebvre, H. Geertsema, S. F. Marino, H. Ewers, *J. Phys. D* **2018**, *51*, 474005; e) S. Strauss, P. C. Nickels, M. T. Strauss, V. Jimenez Sabinina, J. Ellenberg, J. D. Carter, S. Gupta, N. Janjic, R. Jungmann, *Nat. Methods* **2018**, *15*, 685–688.
- [4] A. Keppler, S. Gendreizig, T. Gronemeyer, H. Pick, H. Vogel, K. Johnsson, *Nat. Biotechnol.* **2003**, *21*, 86–89.
- [5] G. V. Los, L. P. Encell, M. G. McDougall, D. D. Hartzell, N. Karassina, C. Zimprich, M. G. Wood, R. Learish, R. F. Ohana, M. Uhr, D. Simpson, J. Mendez, K. Zimmerman, P. Otto, G. Vidugiris, J. Zhu, A. Darzins, D. H. Klauert, R. F. Balleit, K. V. Wood, *ACS Chem. Biol.* **2008**, *3*, 373–382.
- [6] M. Beck, E. Hurt, *Nat. Rev. Mol. Cell Biol.* **2017**, *18*, 73–89.
- [7] a) A. Loschberger, S. van de Linde, M. C. Dabauvalle, B. Rieger, M. Heilemann, G. Krohne, M. Sauer, *J. Cell Sci.* **2012**, *125*, 570–575; b) A. Szymborska, A. de Marco, N. Daigle, V. C. Cordes, J. A. Briggs, J. Ellenberg, *Science* **2013**, *341*, 655–658.
- [8] a) A. von Appen, J. Kosinski, L. Sparks, A. Ori, A. L. DiGiulio, B. Vollmer, M. T. Mackmull, N. Banterle, L. Parca, P. Kastrius, K. Buczak, S. Mosalaganti, W. Hagen, A. Andres-Pons, E. A. Lemke, P. Bork, W. Antonin, J. S. Glavy, K. H. Bui, M. Beck, *Nature* **2015**, *526*, 140–143; b) D. H. Lin, T. Stuwe, S. Schilbach, E. J. Rundlet, T. Perriches, G. Mobbs, Y. Fan, K. Thierbach, F. M. Huber, L. N. Collins, A. M. Davenport, Y. E. Jeon, A. Hoelz, *Science* **2016**, *352*, aaf1015; c) S. J. Kim, J. Fernandez-Martinez, I. Nudelman, Y. Shi, W. Zhang, B. Raveh, T. Herricks, B. D. Slaughter, J. A. Hogan, P. Upla, I. E. Chemmama, R. Pellarin, I. Echeverria, M. Shivaraju, A. S. Chaudhury, J. Wang, R. Williams, J. R. Unruh, C. H. Greenberg, E. Y. Jacobs, Z. Yu, M. J. de la Cruz, R. Mironska, D. L. Stokes, J. D. Aitchison, M. F. Jarrold, J. L. Gerton, S. J. Ludtke, C. W. Akey, B. T. Chait, A. Sali, M. P. Rout, *Nature* **2018**, *555*, 475–482.
- [9] M. Eibauer, M. Pellanda, Y. Turgay, A. Dubrovsky, A. Wild, O. Medalia, *Nat. Commun.* **2015**, *6*, 7532.
- [10] a) B. Koch, B. Nijmeijer, M. Kueblbeck, Y. Cai, N. Walther, J. Ellenberg, *Nat. Protoc.* **2018**, *13*, 1465–1487; b) J. V. Thevathasan, M. Kahnwald, K. Cieśliński, P. Hoess, S. K. Peneti, M. Reitberger, D. Heid, K. C. Kasuba, S. J. Hoerner, Y. Li, Y.-L. Wu, M. Mund, U. Matti, P. M. Pereira, R. Henriques, B. Nijmeijer, M. Kueblbeck, V. J. Sabinina, J. Ellenberg, J. Ries, *bioRxiv* **2019**, <https://doi.org/10.1101/582668>.
- [11] S. S. Agasti, Y. Wang, F. Schueder, A. Sukumar, R. Jungmann, P. Yin, *Chem. Sci.* **2017**, *8*, 3080–3091.
- [12] C. Steinhauer, R. Jungmann, T. L. Sobey, F. C. Simmel, P. Tinnefeld, *Angew. Chem. Int. Ed.* **2009**, *48*, 8870–8873; *Angew. Chem.* **2009**, *121*, 9030–9034.
- [13] K. Kelley, K. E. Knockenhauer, G. Kabachinski, T. U. Schwartz, *Nat. Struct. Mol. Biol.* **2015**, *22*, 425–431.
- [14] T. Schlichthaerle, M. Ganji, A. Auer, O. K. Wade, R. Jungmann, *ChemBioChem* **2019**, *20*, 1032–1038.
- [15] F. Schueder, J. Lara-Gutierrez, B. J. Beliveau, S. K. Saka, H. M. Sasaki, J. B. Woehrstein, M. T. Strauss, H. Grabmayr, P. Yin, R. Jungmann, *Nat. Commun.* **2017**, *8*, 2090.
- [16] D. Virant, B. Traenkle, J. Maier, P. D. Kaiser, M. Bodenhofer, C. Schmees, I. Vojnovic, B. Pisak-Lukats, U. Endesfelder, U. Rothbauer, *Nat. Commun.* **2018**, *9*, 930.
- [17] C. Tiede, A. A. Tang, S. E. Deacon, U. Mandal, J. E. Nettleship, R. L. Owen, S. E. George, D. J. Harrison, R. J. Owens, D. C. Tomlinson, M. J. McPherson, *Protein Eng. Des. Sel.* **2014**, *27*, 145–155.
- [18] P. Forrer, H. K. Binz, M. T. Stumpp, A. Pluckthun, *ChemBioChem* **2004**, *5*, 183–189.
- [19] J. C. Rohloff, A. D. Gelinias, T. C. Jarvis, U. A. Ochsner, D. J. Schneider, L. Gold, N. Janjic, *Mol. Ther. Nucleic Acids* **2014**, *3*, e201.
- [20] K. J. Kossmann, C. Ziegler, A. Angelin, R. Meyer, M. Skoupi, K. S. Rabe, C. M. Niemeyer, *ChemBioChem* **2016**, *17*, 1102–1106.
- [21] T. Kiuchi, M. Higuchi, A. Takamura, M. Maruoka, N. Watanabe, *Nat. Methods* **2015**, *12*, 743–746.
- [22] A. Chevalier, D. A. Silva, G. J. Rocklin, D. R. Hicks, R. Vergara, P. Murapa, S. M. Bernard, L. Zhang, K. H. Lam, G. Yao, C. D. Bahl, S. I. Miyashita, I. Goresnik, J. T. Fuller, M. T. Koday, C. M. Jenkins, T. Colvin, L. Carter, A. Bohn, C. M. Bryan, D. A. Fernandez-Velasco, L. Stewart, M. Dong, X. Huang, R. Jin, I. A. Wilson, D. H. Fuller, D. Baker, *Nature* **2017**, *550*, 74–79.

Manuscript received: May 7, 2019

Revised manuscript received: June 26, 2019

Accepted manuscript online: July 17, 2019

Version of record online: August 21, 2019



## Supporting Information

### **Direct Visualization of Single Nuclear Pore Complex Proteins Using Genetically-Encoded Probes for DNA-PAINT**

*Thomas Schlichthaerle<sup>+</sup>, Maximilian T. Strauss<sup>+</sup>, Florian Schueder<sup>+</sup>, Alexander Auer, Bianca Nijmeijer, Moritz Kueblbeck, Vilma Jimenez Sabinina, Jervis V. Thevathasan, Jonas Ries, Jan Ellenberg, and Ralf Jungmann\**

anie\_201905685\_sm\_miscellaneous\_information.pdf

## Supplementary Information

Direct visualization of single nuclear pore complex proteins using genetically-encoded probes for DNA-PAINT

<b>Materials and Methods</b>	
Supplementary Figure 1	Diffraction-limited and super-resolution imaging comparison
Supplementary Figure 2	Overview of NUP107-SNAP, n=398
Supplementary Figure 3	Overview of NUP107-GFP-NB, n=486
Supplementary Figure 4	Overview of NUP96-SNAP, n=288
Supplementary Figure 5	Overview of NUP96-Halo, n=191
Supplementary Figure 6	Overview of NUP107-GFP-AB, n=200
Supplementary Figure 7	3D parameter optimization
Supplementary Figure 8	NUP96-SNAP 3D DNA-PAINT
Supplementary Table 1	Imaging Parameters
Supplementary Table 2	Imager Sequences
Supplementary Table 3	Handle Sequences
Supplementary Table 4	NPC radius quantification
Supplementary Table 5	NPC labeling efficiency
Supplementary References	

## Materials and Methods

**Tissue culture.** McCoy's 5A Medium modified (cat: 26600-023) was ordered from Gibco. Fetal Bovine Serum (FBS) (cat: 10500-064), 1× Phosphate Buffered Saline (PBS) pH 7.2 (cat: 20012-019), 0.05% Trypsin–EDTA (cat: 25300-054) and Penicillin–Streptomycin (cat: 15140-122) were purchased from Thermo Fisher Scientific. HeLa cells were purchased from the Leibniz Institute DSMZ (cat: ACC-57). U2OS cells were purchased from ATCC (cat: ATCC HTB-96). Glass-bottomed 8-well  $\mu$ -slides (cat: 80827) and sticky slide VI (cat: 80608) were obtained from ibidi. Falcon tissue culture flasks (cat: 734-0965) were ordered from VWR.

**Cell Fixation and immunostaining.** 16% (w/v) Paraformaldehyde (cat: 28906) and DTT (cat: 20291) were purchased from Thermo Fisher Scientific. Triton X-100 (cat: 6683.1) and Ammonium chloride (cat: K298.1) was purchased from Roth. Bovine Serum Albumin (cat: A4503-10G) was ordered from Sigma-Aldrich. Halo- and SNAP-ligand-modified oligos were custom-ordered from Biomers.net (see **Supplementary Table 3**). GFP Nanobody was ordered from NanoTag Biotechnologies (cat: N0301-1mg, Clone 1H1), Secondary polyclonal antibodies (cat: 711-005-152, 115-005-003) were purchased from Jackson ImmunoResearch. Primary rabbit polyclonal anti-GFP antibody was purchased from MBL (cat: 598).

**Cell imaging.** EDTA 0.5 M pH 8.0 (cat: AM9261), Sodium Chloride 5 M (cat: AM9759) and Tris 1 M (cat: AM9856) were ordered from Ambion. Ultrapure water (cat: 10977-035) was purchased from Thermo Fisher Scientific. Potassium chloride (cat: 6781.1) was ordered from Roth. Sodium hydroxide (cat: 31627.290) was purchased from VWR. Glycerol (cat: G5516-500ML), Methanol (cat: 32213-2.5L), Protocatechuate 3,4-Dioxygenase Pseudomonas (PCD) (cat: P8279), 3,4-Dihydroxybenzoic acid (PCA) (cat: 37580-25G-F) and (+)-6-Hydroxy-2,5,7,8-tetra-methylchromane-2-carboxylic acid (Trolox) (cat: 238813-5G) were purchased from Sigma-Aldrich. Dye modified DNA oligos were custom-ordered from MWG (see **Supplementary Table 4**). 90-nm-diameter Gold Nanoparticles (cat: G-90-100) were ordered from cytodiagnosics.

**Cell line generation.** The generation of cell lines was according to published procedures, where homozygosity of the cell lines has been verified by sequencing, Southern and Western blots. After FACS sorting and clonal expansion for all cell lines, several clones with homozygous gene replacement could be isolated after one round of CRISPR facilitated recombination. The NUP96 cell line was furthermore described elsewhere<sup>[1]</sup>.

**Buffers.** The imaging buffer was supplemented with: 100× Trolox: 100 mg Trolox, 430  $\mu$ l 100 % Methanol, 345  $\mu$ l 1M NaOH in 3.2 ml H<sub>2</sub>O. 40× PCA: 154 mg PCA, 10 ml water and NaOH were mixed and pH was adjusted 9.0. 100× PCD: 9.3 mg PCD, 13.3 ml of buffer (100 mM Tris-HCl pH 8, 50 mM KCl, 1 mM EDTA, 50 % Glycerol). Cell-imaging-buffer (buffer C): 1× PBS pH 7.2, 500 mM NaCl, 1× PCA, 1× PCD, 1× Trolox.

**PEG surface.** PEG surfaces were prepared as previously reported<sup>[2]</sup>. In brief, the coverslips (no. 1.5 high precision, 60x18 mm<sup>2</sup>) were rinsed twice and bath-sonicated in a Teflon-based custom-made slide holder in Milli-Q water for 10 min. Rinsing and bath-sonication was repeated with methanol and acetone. To activate the surface, the coverslips were bath-sonicated in 1 M KOH for 20 min and rinsed with Milli-Q water afterwards. After blow drying the coverslips with nitrogen, they were incubated with 95 ml methanol mixed with 5 ml acetic acid and 1 ml aminosilane for 20 min in the dark. Afterwards they were washed with methanol and water for 2 min and blow dried with nitrogen. The aminosilanized coverslips were stored under Argon atmosphere for <2 weeks until they were used. 24 h before use, the imaging chambers were assembled with double sided sticky tape. 16 mg of mPEG (Rapp Polymere, cat. no.: 125000-35) was dissolved in 70  $\mu$ l of freshly prepared sodium bicarbonate buffer (10 mM sodium bicarbonate, pH 8.5) and mixed 20:1 with biotin-PEG (Rapp Polymere, cat. no.: 135000-25-35). To remove air bubbles, the mix was briefly spun down for 30 s and added to the assembled chamber. The chamber was sealed with silicon (picodent) and stored at room temperature overnight in the dark. Before use, the chamber was washed with 1 ml Milli-Q water.

**Cysteine-based GFP-Nanobody labeling and purification.** GFP nanobodies were DNA-labeled as previously reported<sup>[3]</sup>. Nanobodies were concentrated via Amicon 10 kDa spin filters and buffer exchanged into 5 mM TCEP in 1× PBS + 3 mM EDTA at pH 7.5. 5 mM TCEP in 1× PBS + 3 mM EDTA was then added to the GFP Nanobody and was incubated for 2 h at 4 °C on a shaker. Subsequently, Amicon 10 kDa Spin Filters were prewashed with 1× PBS, and Nanobody was buffer-exchanged into 1× PBS for 5× 5 min at 14 000×g and the volume was adjusted to 100  $\mu$ l. DBCO-Maleimide Crosslinker was added in 20 molar excess in 5  $\mu$ l to the GFP Nanobody and incubated overnight at 4 °C on a shaker. Crosslinker aliquots were stored at 40 mg/ml concentration in DMF. DBCO crosslinker was removed via 10 kDa Amicon Spin Filters for 5× 5min at 14 000× g. Azide-DNA was added to the GFP Nanobody crosslinker at 10× excess for 1 h at 20 °C. The final product was buffer exchanged into Anion exchange binding buffer (1× PBS, pH 7.2) via Amicon 10 kDa Spin Filters. Purification from free DNA was performed using a GE Aekta purifier system and a RESOURCE Q 1 ml column via a 30 min gradient purification scheme from 1× PBS to 1× PBS + 1 M NaCl. Peak fractions were afterwards concentrated and buffer-exchanged via Amicon 10 kDa spin filters into 1× PBS.

**Antibody conjugation.** Antibodies were conjugated to DNA-PAINT docking sites via maleimide-PEG2-succinimidyl ester chemistry as previously reported<sup>[4]</sup> (see **Supplementary Table 3** for handle sequences). In short, secondary antibodies were concentrated via 100 kDa amicon spin filters to a final concentration of 1-3 mg/ml. 100  $\mu$ l of antibody was labelled with the maleimide-Peg2-succinimidyl ester for 90 min at 10x molar excess at 4 °C on a shaker. Crosslinker stocks of 10 mg/ml in DMF were diluted in 1x PBS to reach 10x molar excess in 5  $\mu$ l, which were subsequently added to the antibody. After the reaction had been done, unreacted crosslinker was removed via a zeba spin column. Thiolated DNA was reduced using DTT for 2 h at room temperature. DTT was purified from the reduced DNA via a Nap5 column and fractions containing DNA were concentrated via 3 kDa amicon spin filters. The reduced DNA was then added to the antibody bearing a functional maleimide group in 10x molar excess and incubated over night at 4 °C on a shaker in the dark. Antibody-DNA constructs were finally purified via 100 kDa amicon.

**Cell culture.** HeLa cells and U2OS cells were passaged every other day and used between passage number 5 and 20. The cells were maintained in DMEM supplemented with 10 % Fetal Bovine Serum and 1 % Penicillin/Streptomycin. Passaging was performed using 1× PBS and Trypsin-EDTA 0.05 %. 24 h before immunostaining, cells were seeded on ibidi 8-well glass coverslips at 30,000 cells/well.

**Cell fixation.** Prefixation was performed with prewarmed 2.4 % Paraformaldehyde for 20 seconds followed by the permeabilization at 0.4 % Triton-X 100 for 10 seconds. Next, cells were fixed (main fixation) with 2.4 % for 30 min. After 3× rinsing with 1× PBS the cells were quenched with 50 mM Ammoniumchloride (in 1× PBS) for 4 minutes. Then, cells were washed 3× with 1×PBS followed by incubation in 1× PBS for 5 minutes twice. Next, cells were stained with the corresponding ligand (see below). Finally, cells were washed 3× for 5 min in 1× PBS, incubated with 1:1 dilution of 90 nm gold particles in 1× PBS as drift markers, washed 3× 5 min and immediately imaged.

**Staining with SNAP.** For SNAP-labeling, cells were incubated with 1 μM of SNAP-ligand-modified DNA oligomer in 0.5 % BSA and 1 mM DTT for 2 hours.

**Staining with Halo.** For Halo-labeling, cells were incubated with 1 μM Halo-ligand-modified DNA oligomer in 3 % (w/v) BSA in 1× PBS for overnight at 4°C on a shaker.

**Staining with GFP.** GFP-Nanobody staining was done in 3% BSA in 1xPBS at 4°C overnight on a shaker.

**Staining with antibodies.** Antibody staining was done in two steps. First, cells were incubated with primary antibody anti-GFP (1:100) in 3% BSA at 4°C PBS overnight. After three washes for 5 min with 1× PBS, the sample was incubated with the secondary antibody (dilution 1:100) at RT for 1 hours.

**Super-resolution microscope setup.** Fluorescence imaging was carried out on an inverted Nikon Eclipse Ti microscope (Nikon Instruments) with the Perfect Focus System, applying an objective-type TIRF configuration with an oil-immersion objective (Apo SR TIRF 100×, NA 1.49, Oil). TIRF/Hilo angle was adjusted for highest signal to noise ratio when imaging. A 561 nm (200 mW, Coherent Sapphire) laser was used for excitation. The laser beam was passed through cleanup filters (ZET561/10, Chroma Technology) and coupled into the microscope objective using a beam splitter (ZT561rdc, Chroma Technology). Fluorescence light was spectrally filtered with an emission filter (ET600/50m and ET575lp, Chroma Technology) and imaged on a sCMOS camera (Andor Zyla 4.2) without further magnification, resulting in an effective pixel size of 130 nm (sCMOS after 2×2 binning).

#### Imaging conditions

**Figure 1c-e.** Imaging was carried out using an imager strand concentration of 300 pM (P3-Cy3B) in cell imaging buffer. 15,000 frames were acquired at 200 ms integration time. The readout bandwidth was set to 200 MHz. Laser power (@561 nm) was set to 30 mW (measured before the back focal plane (BFP) of the objective), corresponding to 0.7 kW/cm<sup>2</sup> at the sample plane.

**Figure 1f-h.** Images were acquired with an imager strand concentration of 2 nM (P3-Cy3B imager) in cell imaging buffer. 40,000 frames were acquired at 200 ms integration time. The readout bandwidth was set to 200 MHz. Laser power (@561 nm) was set to 80 mW (measured at the back focal plane (BFP) of the objective), corresponding to 1.8 kW/cm<sup>2</sup> at the sample plane.

**Figure 2a.** Images were acquired with an imager strand concentration of 2 nM of P3-Cy3B in cell imaging buffer. 30,000 frames were acquired at 200 ms integration time and a readout bandwidth of 200 MHz. Laser power (@560 nm) was set to 50 mW (measured before the back focal plane (BFP) of the objective), corresponding to 1.1 kW/cm<sup>2</sup> at the sample plane.

**Figure 2b.** Imaging was carried out using an imager strand concentration of 2 nM (P3-Cy3B) in cell imaging buffer. 30,000 frames were acquired at 200 ms integration time. The readout bandwidth was set to 200 MHz. Laser power (@561 nm) was set to 50 mW (measured before the back focal plane (BFP) of the objective), corresponding to 1.1 kW/cm<sup>2</sup> at the sample plane.

**Figure 2c.** Images were acquired with an imager strand concentration of 2 nM (P3-Cy3B imager) in cell imaging buffer. 30,000 frames were acquired at 200 ms integration time. The readout bandwidth was set to 200 MHz. Laser power (@561 nm) was set to 50 mW (measured at the back focal plane (BFP) of the objective), corresponding to 1.1 kW/cm<sup>2</sup> at the sample plane.

**Figure 2d.** Images were acquired with an imager strand concentration of 2 nM of P3-Cy3B in cell imaging buffer. 30,000 frames were acquired at 200 ms integration time. The readout bandwidth was set to 200 MHz. Laser power (@561 nm) was set to 50 mW (measured at the back focal plane (BFP) of the objective), corresponding to 1.1 kW/cm<sup>2</sup> at the sample plane.

**Figure 2e.** Imaging was carried out using an imager strand concentration of 300 pM (P3-Cy3B) in cell imaging buffer. 30,000 frames were acquired at 200 ms integration time. The readout bandwidth was set to 200 MHz. Laser power (@561 nm) was set to 50 mW (measured before the back focal plane (BFP) of the objective), corresponding to 1.1 kW/cm<sup>2</sup> at the sample plane.

**Figure 3a, b.** Images were acquired with an imager strand concentration of 2 nM (P3-Cy3B imager) in cell imaging buffer. 100,000 frames were acquired at 200 ms integration time. The readout bandwidth was set to 200 MHz. Laser power (@561 nm) was set to 40 mW (measured at the back focal plane (BFP) of the objective), corresponding to 1.0 kW/cm<sup>2</sup> at the sample plane.

For all imager strand sequences see **Supplementary Table 4**.

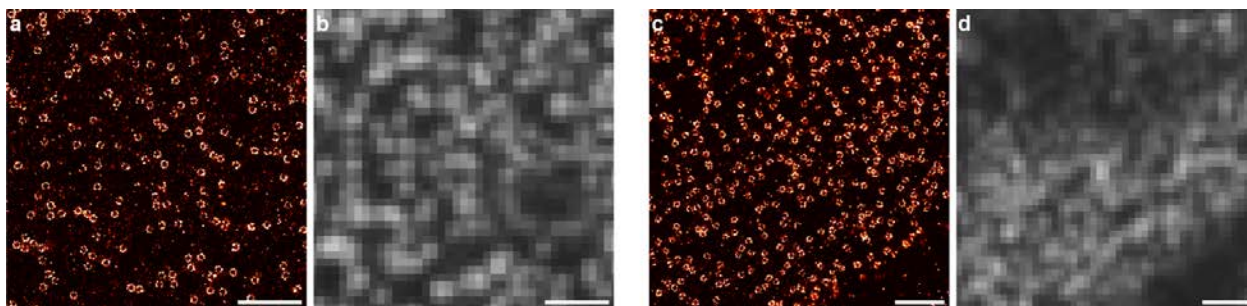
**3D DNA-PAINT calibration using latex microspheres.** The 3D look-up table was measured as previously reported<sup>[5]</sup>. In short, first an ibidi sticky slide VI was assembled with the pegylated coverslip. Then, 50  $\mu$ l of 1:10 avidin coated microspheres diluted in 1 $\times$  PBS were flown into the ibidi sticky slide chamber with the prepared PEG-Biotin surface and incubated for 10 min. Then the chamber was washed using 180  $\mu$ l of 1 $\times$  PBS. Second, 500 nM biotinylated oligonucleotides (10 nt, P1 docking site sequence, **Supplementary Table 4**) was then flown into the chamber and incubated for 10 min. Next, the chamber was washed with 180  $\mu$ l of 1 $\times$  PBS. Next, the chamber was incubated with 1:10 dilution of 90 nm gold particles in 1 $\times$  PBS as drift markers for 5 min and subsequently washed with 80  $\mu$ l 1 $\times$  PBS. Finally, 180  $\mu$ l imaging buffer with dye-labeled imager strands was flown into the chamber. 500 pM Cy3B labeled imager with sequence P1 and 1 $\times$  PCA, 1 $\times$  PCD, 1 $\times$  Trolox in buffer C was used. Latex microspheres attached to the PEG surface were identified using bright-field illumination and the radius was measured. The recoded latex microsphere data using DNA-PAINT was reconstructed using two-dimensional gaussian fitting. Lateral drift correction was performed using the gold nanoparticle. Gaussian width (sigma x and sigma y) were averaged in radial sections and linked to the corresponding z height to gather the calibration data<sup>[6]</sup>. Finally, the calibration data was fitted using sixth degree polynomial fit to generate the look-up table.

**Image analysis.** Raw fluorescence data was subjected to spot-finding and subsequent super-resolution reconstruction using the 'Picasso' software package<sup>[4b]</sup>. x, y drift correction was performed via a redundant cross-correlation and gold particles as fiducial markers. Drift correction in z was performed via 90 nm gold particles.

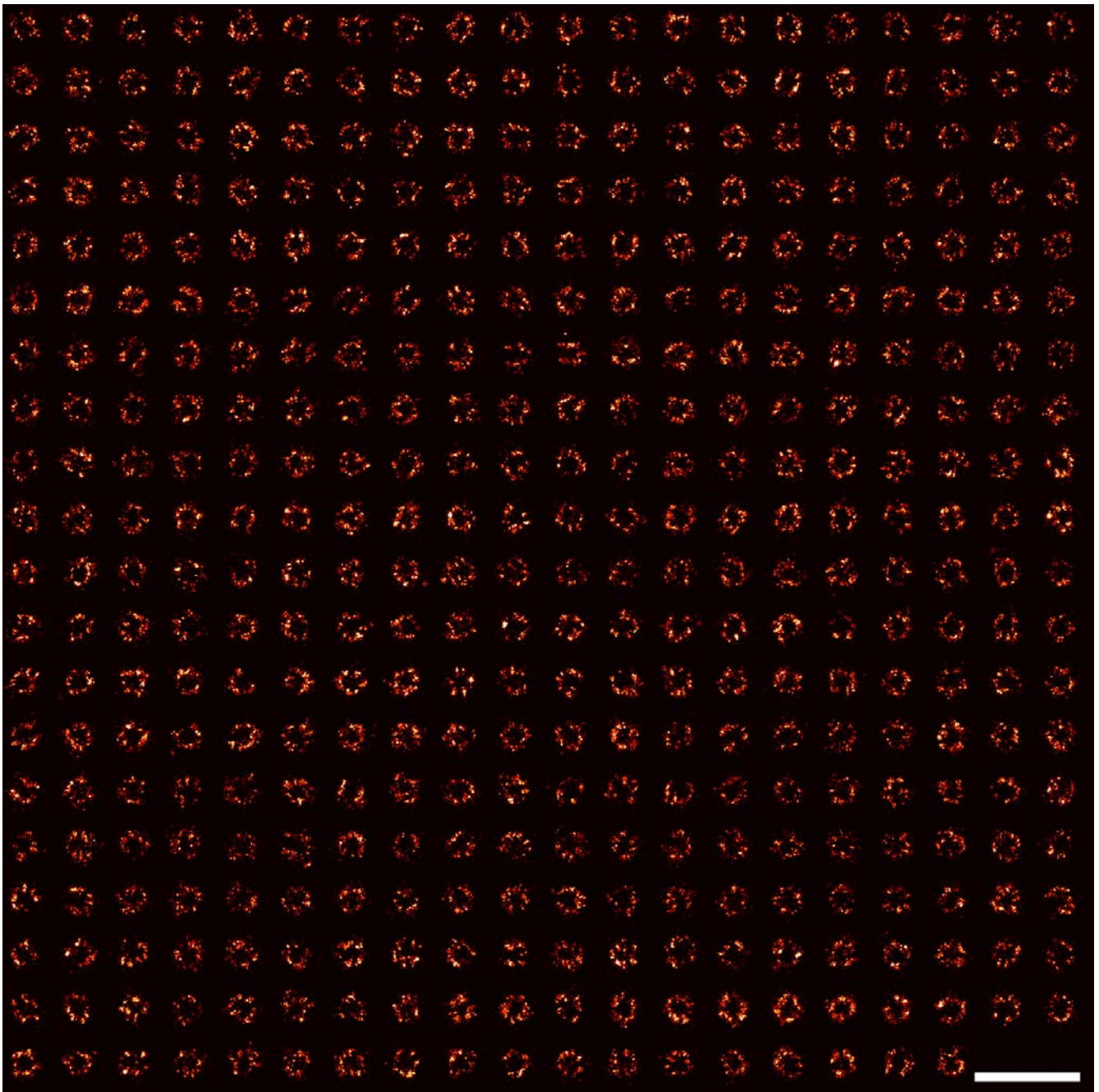
**Radius analysis.** To determine the radius of NPCs, picked NPCs were averaged using the 'Picasso:average3' module as previously described<sup>[4b]</sup>. In brief, localizations of particles are aligned on top of each other by rendering them and using cross-correlation to determine displacement. To account for ring-like structures, a 100 $\times$  symmetry was set. Each dataset was averaged with the following oversampling settings: 3 $\times$  15, 1 $\times$  20, 1 $\times$  40. Based on the resulting "superparticle", the center of mass was determined. The localizations were subsequently transformed into polar coordinates with the center of mass as the center point. The radius was calculated by taking the median of the polar coordinate distances.

**Labeling efficiency calculation.** To analyse the labelling efficiency for the different labelling methods (NUP96-Halo, NUP96-SNAP, NUP107-SNAP, NUP107-GFP). 100 nuclear pores were picked for each 3D dataset, and the apparent clusters were counted and compared to the expected 32 copies of the proteins.

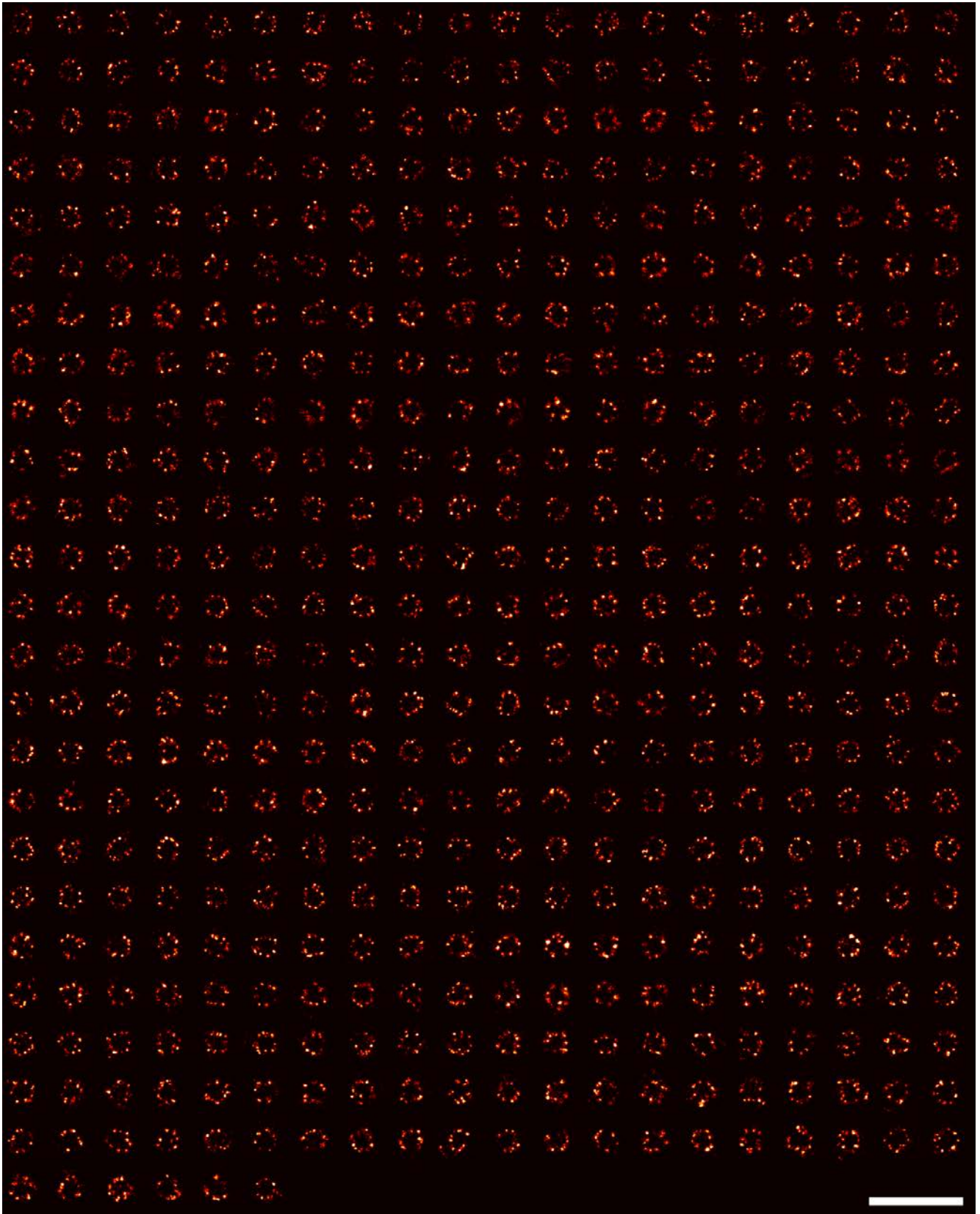
**Parameter optimization for 3D imaging.** For parameter optimization two main aspects for DNA-PAINT imaging should be considered: Resolution (x, y, z) and repetitive sampling. To estimate the resolution capabilities, 125 single clusters in nuclear pores were picked and center-of-mass-aligned with the Picasso average3 module. Localization distributions of aligned clusters were fitted with a Gaussian fit. For the analysis of repetitive sampling, the picked single 125 clusters were linked (max. distance: 26 nm, max. transient dark frames: 5) and DBSCANned (minimum local event density: 5, Radius: 26 nm) using the Picasso software to obtain the events per site as well as mean frame of the visits.



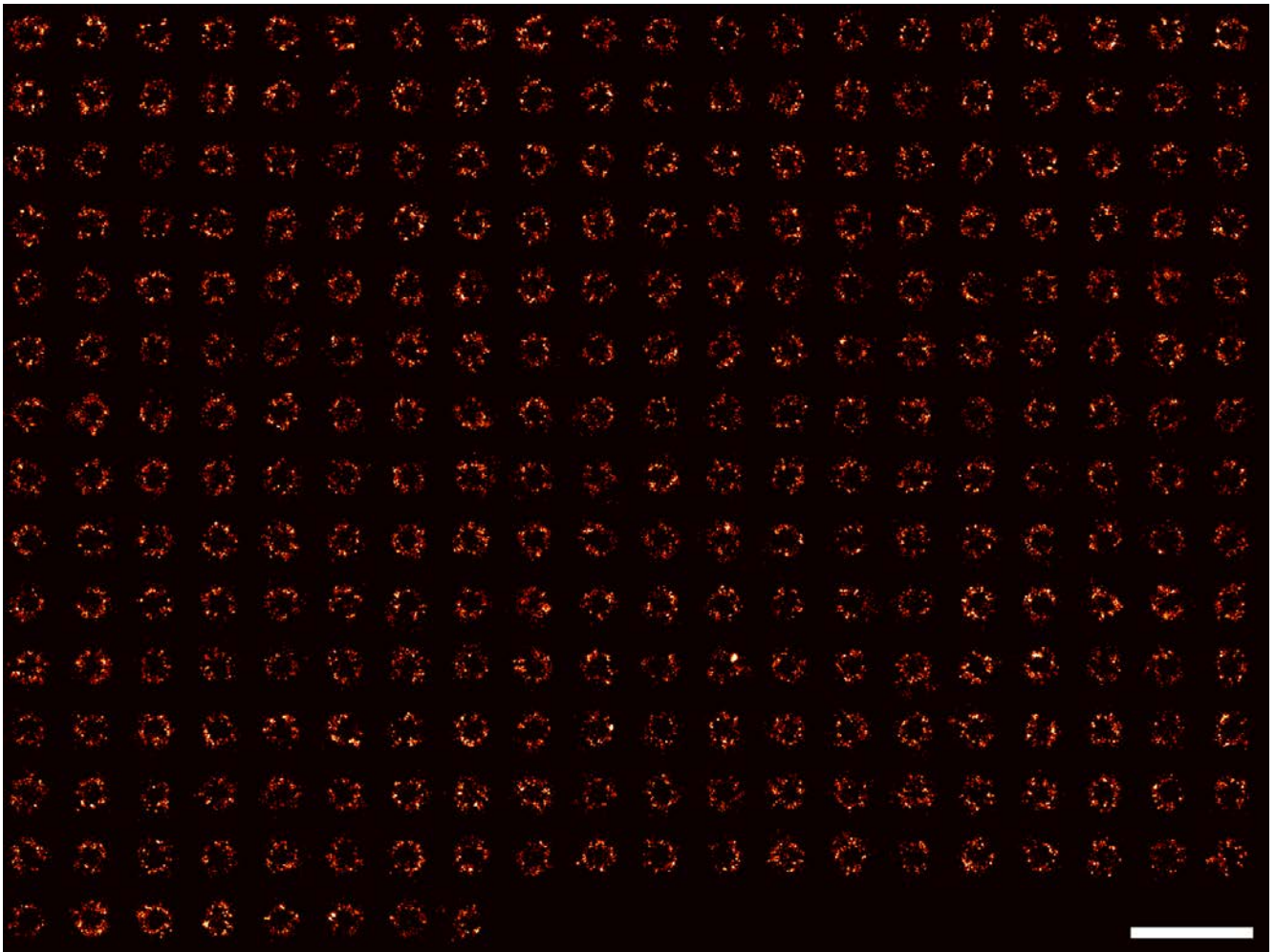
**Supplementary Figure 1 | Diffraction-limited and super-resolution imaging comparison.** (a) NUP96-SNAP super-resolved image. (b) Diffraction-limited image of the same area. (c) NUP107-GFP-NB super-resolved image. (d) Diffraction-limited image of the same area. Scale bars: 1  $\mu\text{m}$ .



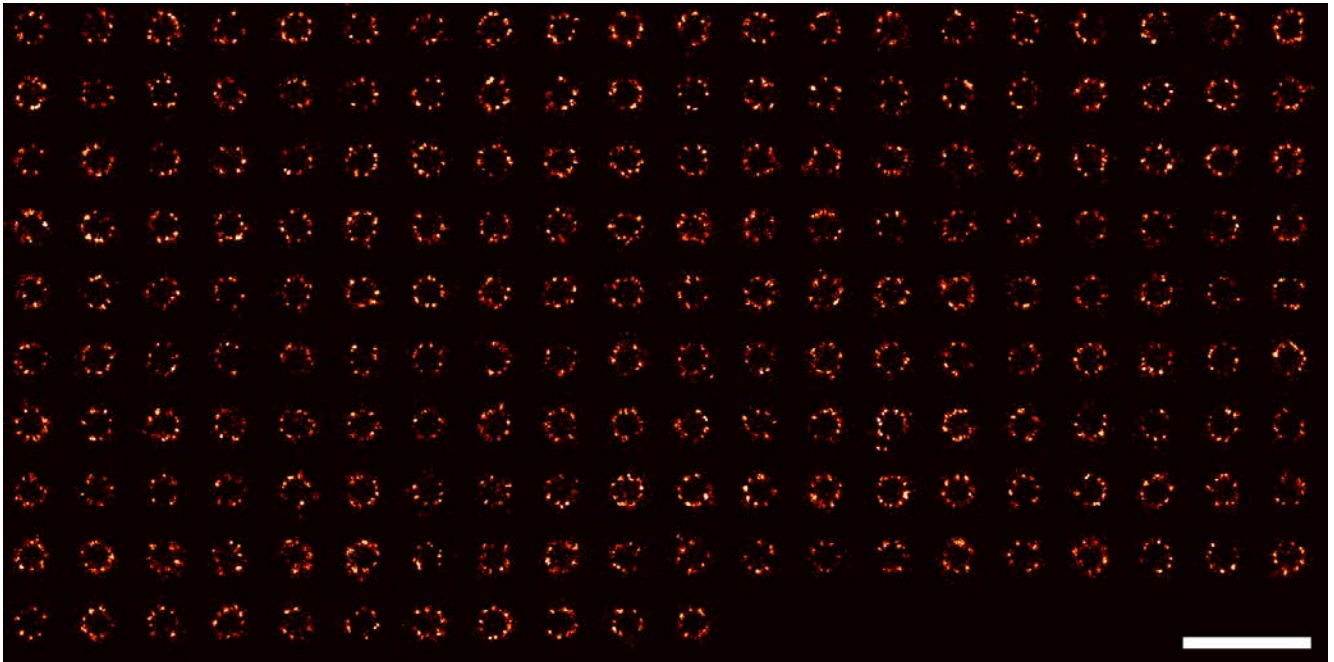
Supplementary Figure 2 | Overview of NUP107-SNAP, n=398. Scale bar: 500 nm.



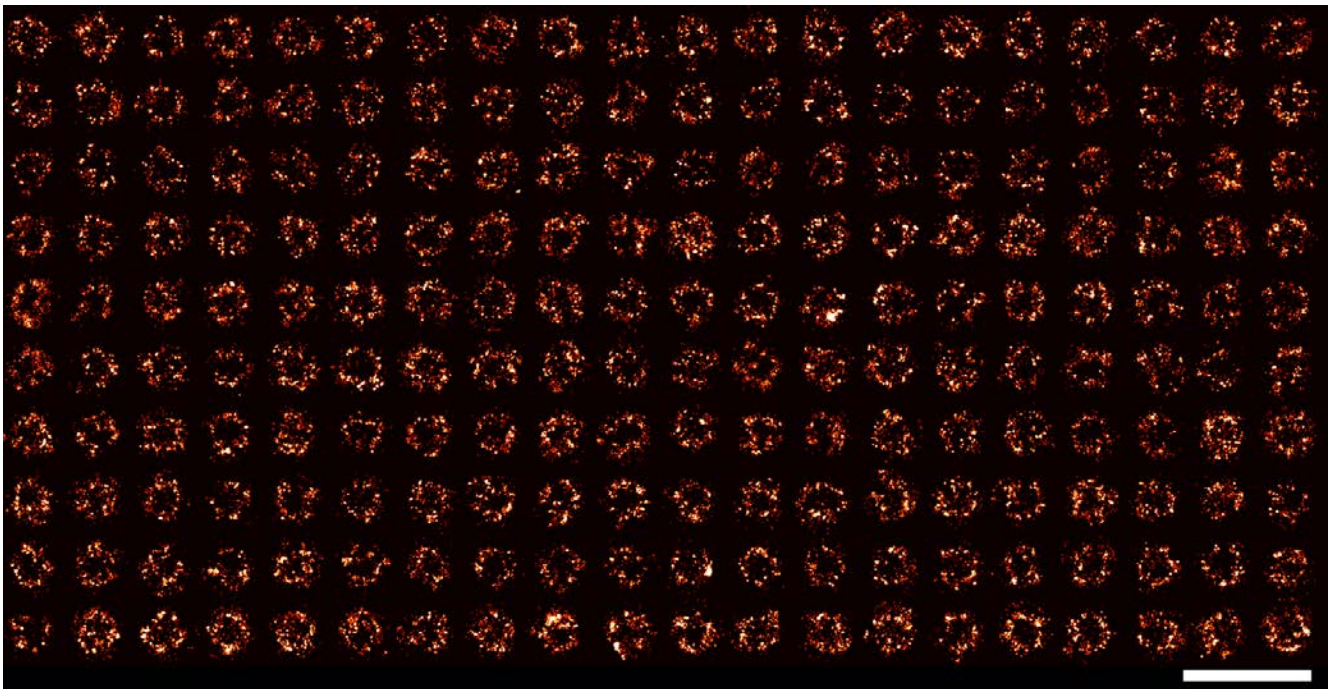
Supplementary Figure 3 | Overview of NUP107-GFP-NB, n=486. Scale bar: 500 nm.



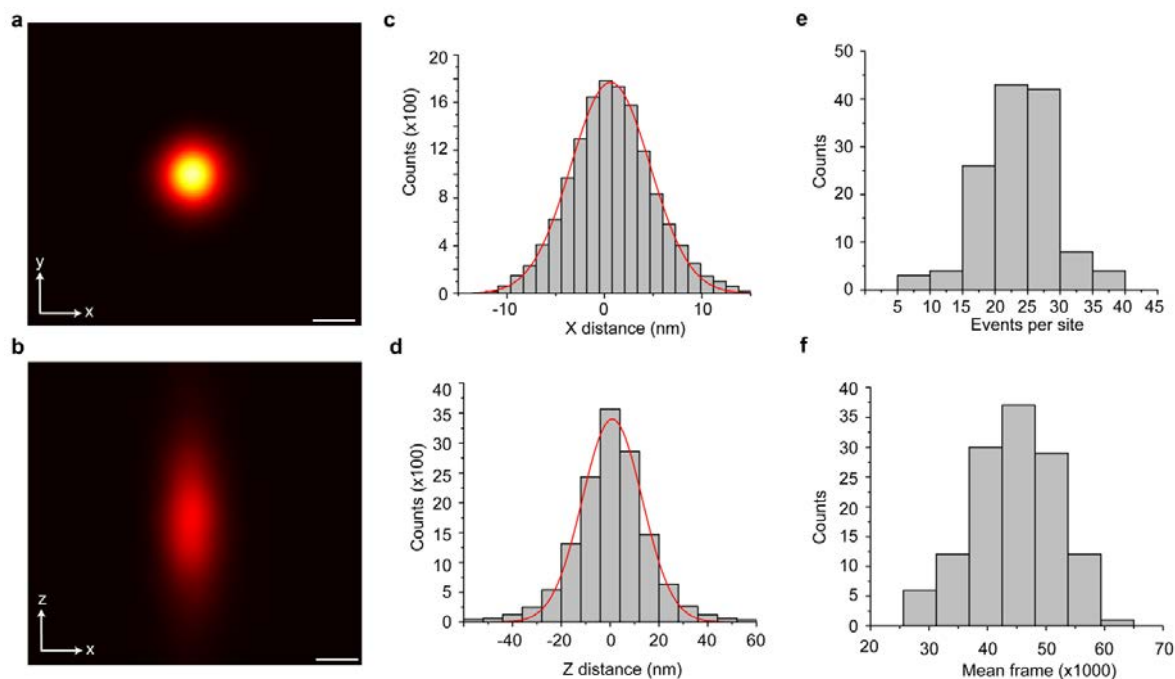
Supplementary Figure 4 | Overview of NUP96-SNAP, n=288. Scale bar: 500 nm.



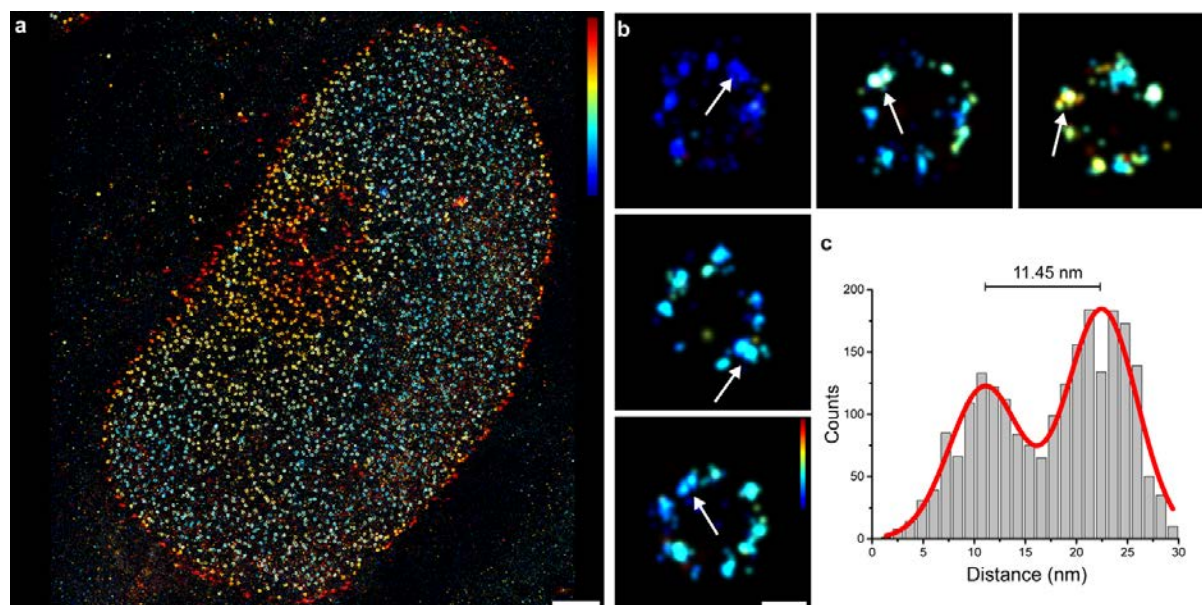
Supplementary Figure 5 | Overview of NUP96-Halo, n=191. Scale bar: 500 nm.



Supplementary Figure 6 | Overview of NUP107-GFP-AB, n=200. Scale bar: 500 nm.



**Supplementary Figure 7 | 3D parameter optimization.** For optimization of imaging parameters to resolve the two copies of NUP96 proteins spaced  $\sim 12$  nm apart, certain criteria need to be fulfilled, which are high spatial resolution as well as sufficient repetitive sampling of binding sites. **(a)** Center of mass alignment of 125 single protein clusters (x-y projection). **(b)** Center-of-mass alignment of the single protein clusters (x-z projection). **(c)** Histogram analysis of the x-y projection yields  $\sim 4$  nm localization precision. **(d)** Histogram analysis of the x-z projection yields  $\sim 12$  nm localization precision. **(e)** Histogram of events per cluster yields a mean of 23.0 (STD: 5.7) visits of imager strands per site. **(f)** Histogram analysis of the mean frame per cluster yields a mean value of 44008 (STD: 8627), highlighting that the clusters were repetitively visited over the whole course of image acquisition (100k frames). Analysis based on Figure 3 dataset. Scale bars: 10 nm **(a, b)**.



**Supplementary Figure 8 | NUP96-SNAP 3D DNA-PAINT.** (a) 3D DNA-PAINT overview image of NPCs labeled via Nup96-SNAP (color indicates height, range: -200 (blue) to 200 nm (red)). (b) Selection of single NPCs. Arrows are highlighting two copies of NUP96 proteins in the same symmetry center of the same ring (i.e. at the same height) spaced ~12 nm apart from each other (color indicates height, range: -100 (blue) to 100 nm (red)). (c) Cross sectional histogram of 3D-averaged pairs (N = 27) of NUP96-SNAP proteins in single symmetry centers as highlighted in (b). Scale bars: 2  $\mu\text{m}$  (a), 50 nm (b).

Imaging was carried out using an imager strand concentration of 2 nM (P3-Cy3B). 50k frames were acquired at 200 ms integration time. The readout bandwidth was set to 200 MHz. Laser power (@561 nm) was set to 40 mW (measured before the back focal plane (BFP) of the objective). This corresponds to 1  $\text{kW}/\text{cm}^2$  at the sample plane.

**Supplementary Table 1 | Imaging parameters**

Dataset	Parameters	Power @561 nm	NeNA precision
Figure 1c,d and SI Figure 1a,b	300ms, 2D, 15k Frames, 5nM, P3*	0.7 kW/cm <sup>2</sup>	6.3 nm
Figure 1e,f and SI Figure 1c,d	200ms, 2D, 30k Frames, 2nM, P3*	1.8 kW/cm <sup>2</sup>	6.9 nm
Figure 2a and SI Figure 2	200 ms, 2D, 30k Frames, 1 nM, P3*	1.1 kW/cm <sup>2</sup>	3.6 nm
Figure 2b and SI Figure 3	200 ms, 2D, 30k Frames, 2nM, P3*	0.6 kW/cm <sup>2</sup>	6.0 nm
Figure 2c SI Figure 4	200 ms, 2D, 30k Frames, 1 nM, P3*	1.1 kW/cm <sup>2</sup>	2.9 nm
Figure 2d and SI Figure 5	200 ms, 2D, 30k Frames, 1 nM, P3*	1.1 kW/cm <sup>2</sup>	4.5 nm
Figure 2e and SI Figure 6	200ms, 2D, 30k Frames, 300 pM, P3*	0.6 kW/cm <sup>2</sup>	4.5 nm
Figure 3 and SI Figure 7	200ms, 3D, 100k Frames, 2nM, P3*	1 kW/cm <sup>2</sup>	6.0 nm
SI Figure 6a	200 ms, 2D, 30k Frames, 300 pM, P3*	1.1 kW/cm <sup>2</sup>	2.2 nm
SI Figure 6b	200 ms, 2D, 30k Frames, 1 nM, P3*	1.1 kW/cm <sup>2</sup>	6.0 nm
SI Figure 8	200 ms, 3D, 50k Frames, 2 nM, P3*	1 kW/cm <sup>2</sup>	5.1 nm

**Supplementary Table 2 | Imager sequences**

Imager name	Sequence	5'-mod	3'-mod	Vendor
P1*	CTAGATGTAT	None	Cy3b	Eurofins Genomics
P3*	GTAATGAAGA	None	Cy3b	Eurofins Genomics

**Supplementary Table 3 | Handle sequences**

Handle Name	Sequence	5'-mod	3'-mod	Vendor
P1	TTATACATCTA	BG (Snap Ligand)	None	Biomers.net
P3	TTTCTTCATTA	BG (Snap Ligand)	None	Biomers.net
P1	TTATACATCTA	Halo Ligand (O2)	None	Biomers.net
P3	TTTCTTCATTA	Halo Ligand (O2)	None	Biomers.net
P1	TTATACATCTA	Thiol (for AB conjugation)	None	Eurofins Genomics
P3	TTTCTTCATTA	Thiol (for AB conjugation)	None	Eurofins Genomics
P1	TTATACATCTA	Biotin	None	Eurofins Genomics

**Supplementary Table 4 | NPC radius quantification, SE = standard error**

Dataset	Median (nm)	Mean (nm)	Std (nm)	SE of Median (nm)	SE of Mean (nm)	# Pores	# Locs
NUP107-SNAP	53.7	54.2	13.1	0.8	0.7	398	127773
NUP107-GFP-NB	54.6	54.8	11.9	0.7	0.5	486	219398
NUP96-SNAP	55.9	56.5	12.6	0.9	0.7	288	57297
NUP96-Halo	56.2	56.6	10.2	0.9	0.7	191	45143
NUP107-GFP-AB	65.9	66.1	17.5	1.5	1.2	200	69834

Supplementary Table 5 | NPC labeling efficiency (LE) estimation

Dataset	Mean LE (%)	Median LE (%)	Std (%)	# Pores
NUP107-SNAP	28.1	28.1	4.9	100
NUP107-GFP-NB	27.5	28.1	4.4	100
NUP96-SNAP	28.2	28.1	4.1	100
NUP96-Halo	29.7	31.3	5.4	100

## Supplementary References

- [1] J. V. Thevathasan, M. Kahnwald, K. Cieřliński, P. Hoess, S. K. Peneti, M. Reitberger, D. Heid, K. C. Kasuba, S. J. Hoerner, Y. Li, Y.-L. Wu, M. Mund, U. Matti, P. M. Pereira, R. Henriques, B. Nijmeijer, M. Kueblbeck, V. J. Sabinina, J. Ellenberg, J. Ries, *bioRxiv* **2019**, 582668.
- [2] A. Jain, R. Liu, Y. K. Xiang, T. Ha, *Nat Protoc* **2012**, *7*, 445-452.
- [3] T. Schlichthaerle, A. S. Eklund, F. Schueder, M. T. Strauss, C. Tiede, A. Curd, J. Ries, M. Peckham, D. C. Tomlinson, R. Jungmann, *Angew Chem Int Ed Engl* **2018**, *57*, 11060-11063.
- [4] aS. S. Agasti, Y. Wang, F. Schueder, A. Sukumar, R. Jungmann, P. Yin, *Chem Sci* **2017**, *8*, 3080-3091; bJ. Schnitzbauer, M. T. Strauss, T. Schlichthaerle, F. Schueder, R. Jungmann, *Nat Protoc* **2017**, *12*, 1198-1228.
- [5] A. Auer, T. Schlichthaerle, J. B. Woehrstein, F. Schueder, M. T. Strauss, H. Grabmayr, R. Jungmann, *Chemphyschem* **2018**, *19*, 3024-3034.
- [6] C. Cabriel, N. Bourg, G. Dupuis, S. Leveque-Fort, *Opt Lett* **2018**, *43*, 174-177.

## **Spatial association of integrin-talin-kindlin during cell matrix adhesions**

**L. Fischer\***, **C. Klingner\***, **T. Schlichthaerle\***, M.T. Strauss, R. Böttcher,  
C. Schreiber, J.O. Rädler, R. Fässler, C. Grashoff°, R. Jungmann°  
*\*authors contributed equally, °co-corresponding authors*

to be submitted

## Spatial association of integrin-talin-kindlin during cell-matrix adhesion

Lisa Fischer<sup>1,\*</sup>, Christoph Klingner<sup>1,\*</sup>, Thomas Schlichthaerle<sup>2,3,\*</sup>, Maximilian T. Strauss<sup>2,3</sup>, Ralph Böttcher<sup>4</sup>, Christoph Schreiber<sup>2</sup>, Joachim O. Rädler<sup>2</sup>, Reinhard Fässler<sup>4</sup>, Carsten Grashoff<sup>1,°</sup> and Ralf Jungmann<sup>2,3,°</sup>

<sup>1</sup>Department of Quantitative Cell Biology, Institute of Molecular Cell Biology, University of Münster, Münster D-48149, Germany

<sup>2</sup>Faculty of Physics and Center for Nanoscience, LMU Munich, Munich D-80539, Germany

<sup>3</sup>Research Group Molecular Imaging and Bionanotechnology, Max Planck Institute of Biochemistry, Martinsried D-82152, Germany

<sup>4</sup>Department of Molecular Medicine, Max Planck Institute of Biochemistry, Martinsried D-82152, Germany

\*These authors contributed equally.

°Correspondence should be addressed to R.J and C.G.

**Focal adhesions (FAs) are integrin-based structures that mediate the attachment of cells to the extracellular matrix (ECM) and govern mechano-chemical signaling cascades upon cell adhesion<sup>1,2</sup>. Even though FAs have a crucial function for a wide range of cell biological processes, it is still unknown how their resident proteins assemble on molecular scales. In particular, it remains unclear how the two integrin activators talin and kindlin assemble at the plasma membrane to facilitate receptor activation<sup>3-5</sup>. Here, we use DNA-PAINT super-resolution microscopy<sup>6,7</sup> to visualize and quantify the localization of  $\beta$ 1 integrin, talin-1 and kindlin-2 with molecular resolution in cells. Our experiments and simulations indicate that talin distributes across the plasma membrane at molecular distances of 40-50 nm at initial stages of cell adhesion. Dual target Exchange-PAINT experiments demonstrate that a significant portion of talin-1 and kindlin-2 molecules co-localize on molecular scales specifically in the adhesion area, and triple-target super-resolution imaging reveals their specific association with active  $\beta$ 1 integrin receptors. Together, the data provide the first molecularly resolved view of FA's lateral organization and provide evidence for an integrin-talin-kindlin complex underlying cell-ECM adhesion.**

The adhesion of cells to the extracellular matrix (ECM) is essential for the development and survival of metazoans and key to the function and repair of virtually all mammalian tissues<sup>1</sup>. Cell-ECM adhesions form after the activation of integrin receptors by two intracellular proteins, talin and kindlin, leading to integrin clustering and the recruitment of additional cytoplasmic proteins that condense in macromolecular complexes called focal adhesions (FAs)<sup>3,8</sup>. Previous super-resolution microscopy approaches revealed that FAs are characterized by a horizontal layering that compartmentalizes chemical and mechanical activities<sup>9,10</sup>, but owing to the inability to resolve FA proteins on truly molecular scales, a detailed understanding of FAs' lateral organization is thus far elusive. It is still unclear, for instance, how integrin

clustering occurs at the nanoscale, even though avidity regulation is an established concept of integrin-mediated cell adhesion<sup>5,11</sup>. Debated models range from the formation of integrin clusters through homomerization<sup>12</sup>, the assembly of heterogeneous substructures<sup>13</sup>, to specific nano-clusters into which active and inactive integrin receptors segregate<sup>14</sup>. In addition, it is unknown how the integrin-binding proteins talin and kindlin, which govern the first steps of integrin activation and FA formation<sup>11,15</sup>, assemble in cell adhesion sites, and it is controversially discussed whether both proteins can approach the relatively short cytoplasmic domain of  $\beta$  integrin receptors simultaneously. We therefore sought to establish a quantitative technique to visualize these proteins with molecular-scale resolution in cells.

To resolve individual molecules, we used DNA-PAINT, which allows quantitative and multiplexed super-resolution imaging with sub-10-nm spatial resolution<sup>6,7,16</sup> and combined it with genetically-encoded labeling tags<sup>17</sup>. DNA-PAINT uses the sequence-specific, transient binding of dye-labeled DNA oligonucleotides to their target-bound complements to create the blinking events necessary in single-molecule-based super-resolution approaches. To analyze the molecular organization of talin, we genetically inserted a HaloTag into a previously validated talin-1 insertion site<sup>18,19</sup> after the integrin-binding FERM domain at amino acid (aa) 447 and stably expressed the construct in cells genetically depleted of talin-1 and talin-2 (talin-Halo447)<sup>20</sup> (Supplementary Figure 1). We then seeded these cells onto fibronectin (FN)-coated glass slides and targeted the HaloTag in talin using a chloroalkane-modified DNA-PAINT 'docking' strand. Subsequent addition of the complementary Cy3b-labeled imager strand, DNA-PAINT image acquisition using TIRF microscopy, and data postprocessing<sup>21</sup> revealed distinct talin-1 localization clouds in FAs as well as the plasma membrane (MEM, Figure 1a-c) with a localization precision of about 5 nm (Figure 1d-f, Supplementary Figure 2). To quantify how many talin-1 molecules reside within a given localization cloud, we performed quantitative-PAINT (qPAINT) analyses<sup>16</sup> by placing DNA origami structures with a defined number of single binding sites next to talin-Halo447 expressing cells, and then analyzed the signals associated with DNA origamis and cells (Figure 1g, Supplementary Figure 3). To obtain molecularly precise quantification, qPAINT relies on the fact that the observed target binding frequency scales linearly with the imager strand concentration and the number of binding sites. The individual binding sites on DNA origami nanostructures served as calibration sites for comparison with the talin-1 localization clouds within the cell. We observed highly similar values for both localization clouds (DNA origami:  $0.96 \pm 0.3$  units; talin-1:  $0.97 \pm 0.378$  units) and confirmed with control experiments analyzing two and three docking sites the expected correlation between binding frequency and binding site number in our experiments (Figure 1e-f, Supplementary Figure 4). Thus, the observed localization clouds represent individual talin-1 molecules.

Next, we developed an analysis pipeline that distinguishes specific from non-specific signals and calculates the distance from one protein to its nearest neighbor to analyze the data in an automated fashion (Supplementary Figure 5) at a resolution of 25 nm (Supplementary Figure 6). We used the 'Nearest Neighbor Distance' (NND) value to systematically evaluate how labeled talin-1 molecules assemble during cell adhesion formation and FA maturation (Figure 2a, b). At the initial phase of cell adhesion, in the absence of identifiable adhesion complexes, single talin-1 molecules seemed randomly spaced at the plasma membrane with an NND of about 125 nm. After 15-25 min, when talin-1 started to aggregate in small FAs, these distances reduced to about 55 nm and then compacted with the onset of anisotropic cell spreading to a 45 nm spacing. This NND value then remained constant even in fully spread cells with large FAs (16 h). A fraction of talin-1 was consistently found outside of FAs in the MEM at distances >100 nm, and this value seemed largely insensitive to the cell adhesion state (Figure 2b). Consistent with our experiments above, qPAINT measurements indicated individual talin-1 molecules in the observed localization clouds at all analyzed time points (Supplementary Figure 7).

Since talin's primary binding partners in FAs are integrin receptors, we inserted a SNAP-tag into the extracellular domain of  $\beta 1$  integrin (before aa 108) and stably expressed the construct in integrin-deficient fibroblasts<sup>22</sup>. The reconstituted  $\beta 1$  integrin-SNAP cells, targeted with benzylguanine-modified DNA-PAINT docking strands, displayed restored cell morphology, and DNA-PAINT imaging revealed the expected localization of  $\beta 1$  integrin to FAs and the MEM. After 16 h of spreading,  $\beta 1$  integrin molecules assembled with molecular distances of about 50 nm in FAs and >100 nm in the MEM, reminiscent of the talin-1 distribution (Figure 2c). To test whether talin follows integrin receptor localization, we seeded talin-Halo447 cells onto micropatterned surfaces upon which FN-coated stripes were interspaced with passivated areas that cannot be engaged by integrin receptors. As expected, talin-1 was assembling at short molecular distances in FAs on FN-stripes and large separation distances in passivated areas (Figure 2d). Thus, the molecular assembly of talin-1 depends on integrin-ECM engagement.

To investigate talin's molecular organization in more detail, we next examined different theoretical models to describe the observed talin-1 NND distribution. Intriguingly, the data were best described by a homogenous Poisson function indicating – at least down to our detection limit – a random organization of molecules (Figure 2e). Since talin was implicated as an adaptor protein that governs the horizontal layering of FAs<sup>9,10</sup>, we tested our lateral talin-1 distribution for the presence of overlying patterns or clusters by evaluating distances to the third and fifth talin-1 molecule, covering a spacing of about 40-120 nm. However, also these data sets were consistent with a random organization of molecules indicating that talin-1 does not assemble in lateral FA substructures on these length scales. Finally, we estimated the

absolute molecular density of talin-1 in FAs, by assuming a 100 % labeling and detection efficiency and a random organization of talin-1 molecules. These simulations predicted an average talin-to-talin distance of 40-50 nm at early time points of spreading (5 min) and 20-25 nm in mature FAs (16 h) with a molecular density of about 600 talin-1 molecules/ $\mu\text{m}^2$  (Figure 2e). Together, these data suggest that the organization of FA molecules at the plasma membrane during receptor clustering is not set by a previously hypothesized function of talin as a molecular ruler<sup>23,24</sup>.

Cell adhesion requires the engagement of integrin receptors with talin but also kindlin. It has been shown that the FERM domains of talin and kindlin bind the cytoplasmic tail of  $\beta$ -integrins at two adjacent but distinct motifs<sup>25,26</sup>, yet it is unclear whether both proteins can co-assemble with integrin receptors in cells<sup>3,15</sup>. We therefore generated an N-terminal SNAP-tagged kindlin-2 construct (SNAP-Kindlin), co-expressed it with talin-Halo447 in kindlin-1/2 and talin-1/2-deficient fibroblasts<sup>27</sup> (Supplementary Figure 8), and performed dual target super-resolution microscopy using Exchange-PAINT<sup>6</sup> (Supplementary Figure 9). As expected, kindlin-2 was observed at high densities in FAs with intermolecular distances of 55 nm, while talin-1 assembled with a NND of about 40 nm in these cells (Figure 3a-c). Intriguingly, individual talin-1 and kindlin-2 molecules were frequently observed in close proximity with an average 'kindlin-to-talin' (K2T) distance of about 27 nm (Figure 3c).

To explore this in more detail, we first simulated two random distributions with the experimentally observed molecular densities of talin-Halo447 and SNAP-Kindlin. The results indicated that about 30 % of talin-1 and kindlin-2 molecules are expected to non-specifically localize within a distance of 25 nm, merely due to the high protein density in FAs. Next, we experimentally examined a positive control, in which a Halo-SNAP cassette was inserted into talin-1; Halo- and SNAP-tag are only separated by seven aa in this construct (talin-F7), which thus mimics co-localization. These experiments demonstrated that perfect co-localization is indicated by about 60 % of all kindlin and talin molecules assembling within 25 nm, which was again consistent with theoretical simulations considering the labeling efficiencies of both tags (Supplementary Figure 9). Remarkably, 45 % of talin-1 and kindlin-2 signals were co-localized in talin-Halo447 and SNAP-Kindlin reconstituted cells indicating the specific, spatial association of both integrin activators (Figure 3d). To validate this observation, we co-expressed a talin-1 construct, in which the HaloTag was located at talin's C-terminus, with SNAP-Kindlin. As expected, this C-terminally tagged talin-1 displayed a significantly reduced overlap with kindlin-2 signals (Figure 3d, Supplementary Figure 10, 11). Together, these data show that the FERM domains of talin-1 and kindlin-2 spatially associate at the plasma membrane of FAs. Since we did not detect significant molecular co-localization of talin-1 and kindlin-2 outside FAs (Figure 3d), the complex formation appears to occur specifically within the adhesion area.

In view of the proposed models of integrin activation<sup>3,15</sup>, the results above imply that talin-1 and kindlin-2 indeed associate in FAs to induce or maintain the active state of integrin receptors. To test this directly, we established three-target Exchange-PAINT experiments to visualize talin-1 and kindlin-2 molecules together with single integrin receptors. To detect active integrins, we utilized the 9EG7 antibody which binds to an extended conformation of the  $\beta 1$  subunit<sup>28</sup>. Talin-1 and kindlin-2 distributions were again characterized by an average molecular distance of about 45-55 nm, whereas active  $\beta 1$  integrin receptors were spaced at larger distances, presumably because the 9EG7 antibody detects only the activated fraction of all  $\beta 1$  integrin molecules, and because the here used cells express additional integrin receptors such as  $\alpha \beta 3$ . Nonetheless, we frequently observed  $\beta 1$  integrin localizations in vicinity of talin-kindlin clusters with average integrin-to-kindlin (I2K) and integrin-to-talin (I2T) distances of about 35 nm (Figure 4a-c). To again test the specificity of this observation, we analyzed our experimental data by localizing an active integrin receptor and then calculating its related next-kindlin and next-talin signal (I2KT). We compared these I2KT tuples with simulated data in which  $\beta 1$  integrin, kindlin-2 and talin-1 were randomly distributed at the experimentally observed molecular densities. Generating a 2D heat map of both data sets revealed a significant enrichment of short I2KT tuples in the experimental data set (Figure 4d), and bootstrap analysis confirmed that these differences are indeed highly significant (Figure 4e and Supplementary Figure 12). Thus, integrin  $\beta 1$ , talin-1 and kindlin-2 undergo a specific, spatial association during cell-ECM adhesion.

Altogether, our results reveal the lateral organization of FAs' three indispensable core proteins on the molecular scale. We find that talin concentrates upon receptor clustering to molecular densities in the order of 600 molecules/ $\mu\text{m}^2$ . This value is lower than a previously published estimate of integrin receptor density<sup>29</sup> but sufficiently high to facilitate frequent inter-molecular associations. In addition, talin-1 and kindlin-2 undergo spatial association specifically in the cell adhesion area, where they frequently assemble with  $\beta 1$  integrins in the extended state. This suggests that either activating integrin receptors or maintaining their active conformation is a process that involves the spatial association of all three proteins.

## References

- 1 Geiger, B., Spatz, J. P. & Bershadsky, A. D. Environmental sensing through focal adhesions. *Nat Rev Mol Cell Bio* **10**, 21-33, doi:10.1038/nrm2593 (2009).
- 2 Hoffman, B. D., Grashoff, C. & Schwartz, M. A. Dynamic molecular processes mediate cellular mechanotransduction. *Nature* **475**, 316-323, doi:10.1038/nature10316 (2011).
- 3 Moser, M., Legate, K. R., Zent, R. & Fassler, R. The Tail of Integrins, Talin, and Kindlins. *Science* **324**, 895-899, doi:10.1126/science.1163865 (2009).
- 4 Ye, F., Snider, A. K. & Ginsberg, M. H. Talin and kindlin: the one-two punch in integrin activation. *Front Med* **8**, 6-16, doi:10.1007/s11684-014-0317-3 (2014).

- 5 Iwamoto, D. V. & Calderwood, D. A. Regulation of integrin-mediated adhesions. *Curr Opin Cell Biol* **36**, 41-47, doi:10.1016/j.ceb.2015.06.009 (2015).
- 6 Jungmann, R. *et al.* Multiplexed 3D cellular super-resolution imaging with DNA-PAINT and Exchange-PAINT. *Nat Methods* **11**, 313-318, doi:10.1038/nmeth.2835 (2014).
- 7 Jungmann, R. *et al.* Single-molecule kinetics and super-resolution microscopy by fluorescence imaging of transient binding on DNA origami. *Nano Lett* **10**, 4756-4761, doi:10.1021/nl103427w (2010).
- 8 Hynes, R. O. Integrins: bidirectional, allosteric signaling machines. *Cell* **110**, 673-687 (2002).
- 9 Kanchanawong, P. *et al.* Nanoscale architecture of integrin-based cell adhesions. *Nature* **468**, 580-584, doi:10.1038/nature09621 (2010).
- 10 Liu, J. *et al.* Talin determines the nanoscale architecture of focal adhesions. *Proc Natl Acad Sci U S A* **112**, E4864-4873, doi:10.1073/pnas.1512025112 (2015).
- 11 Sun, Z., Costell, M. & Fassler, R. Integrin activation by talin, kindlin and mechanical forces. *Nat Cell Biol* **21**, 25-31, doi:10.1038/s41556-018-0234-9 (2019).
- 12 Li, R. H. *et al.* Activation of integrin alpha IIb beta 3 by modulation of transmembrane helix associations. *Science* **300**, 795-798, doi:DOI 10.1126/science.1079441 (2003).
- 13 Deschout, H. *et al.* Investigating Focal Adhesion Substructures by Localization Microscopy. *Biophys J* **113**, 2508-2518, doi:10.1016/j.bpj.2017.09.032 (2017).
- 14 Spiess, M. *et al.* Active and inactive beta 1 integrins segregate into distinct nanoclusters in focal adhesions. *J Cell Biol* **217**, 1929-1940, doi:10.1083/jcb.201707075 (2018).
- 15 Calderwood, D. A., Campbell, I. D. & Critchley, D. R. Talins and kindlins: partners in integrin-mediated adhesion. *Nat Rev Mol Cell Biol* **14**, 503-517, doi:10.1038/nrm3624 (2013).
- 16 Jungmann, R. *et al.* Quantitative super-resolution imaging with qPAINT. *Nat Methods* **13**, 439-442, doi:10.1038/nmeth.3804 (2016).
- 17 Schlichthaerle, T. *et al.* Direct Visualization of Single Nuclear Pore Complex Proteins Using Genetically-Encoded Probes for DNA-PAINT. *Angew Chem Int Ed Engl* **58**, 13004-13008, doi:10.1002/anie.201905685 (2019).
- 18 Austen, K. *et al.* Extracellular rigidity sensing by talin isoform-specific mechanical linkages. *Nat Cell Biol* **17**, 1597-1606, doi:10.1038/ncb3268 (2015).
- 19 Ringer, P. *et al.* Multiplexing molecular tension sensors reveals piconewton force gradient across talin-1. *Nature Methods* **14**, 1090-+, doi:10.1038/Nmeth.4431 (2017).
- 20 Theodosiou, M. *et al.* Kindlin-2 cooperates with talin to activate integrins and induces cell spreading by directly binding paxillin. *Elife* **5**, doi:ARTN e10130 10.7554/eLife.10130 (2016).
- 21 Schnitzbauer, J., Strauss, M. T., Schlichthaerle, T., Schueder, F. & Jungmann, R. Super-resolution microscopy with DNA-PAINT. *Nat Protoc* **12**, 1198-1228, doi:10.1038/nprot.2017.024 (2017).
- 22 Schiller, H. B. *et al.* beta(1)- and alpha(v)-class integrins cooperate to regulate myosin II during rigidity sensing of fibronectin-based microenvironments. *Nature Cell Biology* **15**, 625-+, doi:10.1038/ncb2747 (2013).

- 
- 23 Selhuber-Unkel, C., Lopez-Garcia, M., Kessler, H. & Spatz, J. P. Cooperativity in Adhesion Cluster Formation during Initial Cell Adhesion. *Biophys J* **95**, 5424-5431, doi:10.1529/biophysj.108.139584 (2008).
- 24 Klapholz, B. & Brown, N. H. Talin - the master of integrin adhesions. *J Cell Sci* **130**, 2435-2446, doi:10.1242/jcs.190991 (2017).
- 25 Moser, M., Nieswandt, B., Ussar, S., Pozgajova, M. & Fassler, R. Kindlin-3 is essential for integrin activation and platelet aggregation. *Nat Med* **14**, 325-330, doi:10.1038/nm1722 (2008).
- 26 Harburger, D. S., Bouaouina, M. & Calderwood, D. A. Kindlin-1 and -2 directly bind the C-terminal region of beta integrin cytoplasmic tails and exert integrin-specific activation effects. *J Biol Chem* **284**, 11485-11497, doi:10.1074/jbc.M809233200 (2009).
- 27 Bottcher, R. T. *et al.* Kindlin-2 recruits paxillin and Arp2/3 to promote membrane protrusions during initial cell spreading. *J Cell Biol* **216**, 3785-3798, doi:10.1083/jcb.201701176 (2017).
- 28 Su, Y. *et al.* Relating conformation to function in integrin alpha5beta1. *Proc Natl Acad Sci U S A* **113**, E3872-3881, doi:10.1073/pnas.1605074113 (2016).
- 29 Changede, R., Xu, X. C., Margadant, F. & Sheetz, M. P. Nascent Integrin Adhesions Form on All Matrix Rigidities after Integrin Activation. *Dev Cell* **35**, doi:10.1016/j.devcel.2015.11.001 (2015).

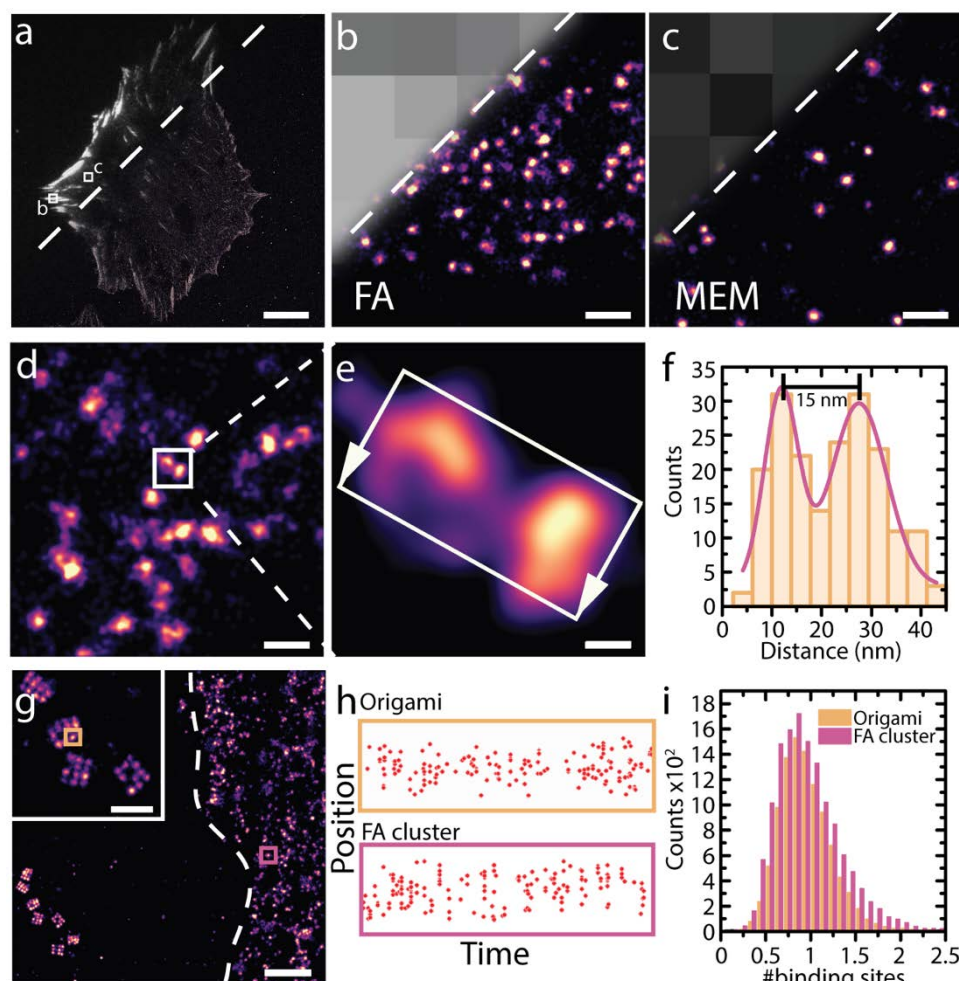


**Figure 1: Molecular Nanoscale Analysis using DNA-PAINT.** **a.** Overlay of diffraction-limited and super-resolved DNA-PAINT images of talin-Halo447 expressing cells. **b.** Zoom into FAs talin localization clouds. **c.** Zoom into the MEM reveals the presence of talin at the free plasma membrane. **d-f.** DNA-PAINT imaging allows to resolve FA proteins, here talin-1, with unprecedented resolution. **f.** Histogram analysis of (**e**) shows that signals with a separation distance of 15 nm can be resolved ( $\sigma_{\text{Peak1}}=3.5$  nm,  $\sigma_{\text{Peak2}}=5.6$  nm). **g.** DNA origami structures carrying individual binding sites were placed next to talin-Halo447 cells to calibrate the influx rate and estimate the number of molecules per localization cloud. Inset: Close-ups of DNA origami structures. **h.** Repetitive binding events of imager strands to DNA origami and Talin-Halo447 clouds indicate similar binding kinetics. **i.** Histogram showing the number of binding sites on DNA origamis and talin localization clouds. Scale bars: 15  $\mu\text{m}$  (**a**), 370 nm (**g**), 110 nm (**g** inset), 100 nm (**b**, **c**), 30 nm (**d**), 7 nm (**e**).

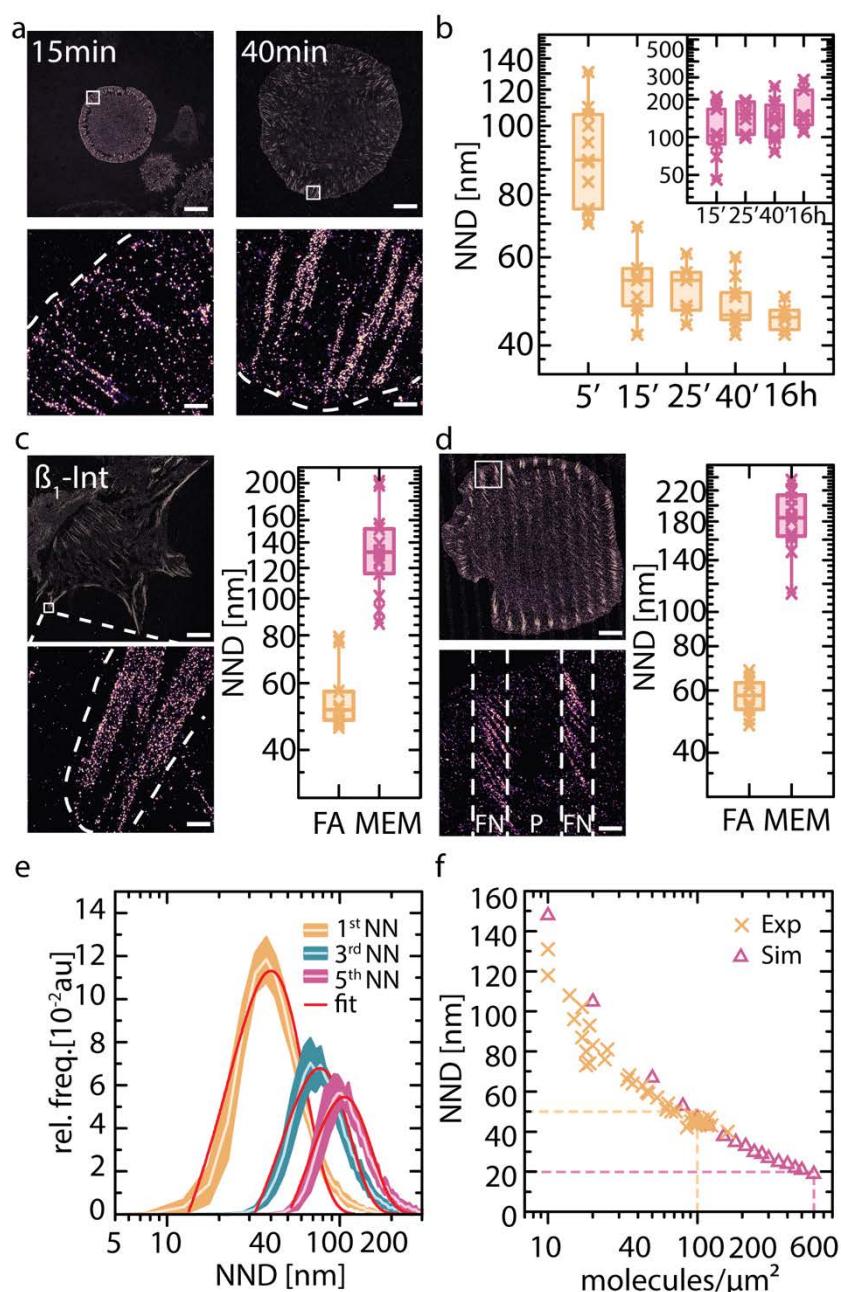


**Figure 2: Molecular assembly of talin-1 upon cell adhesion.** **a.** Talin-1 localization clouds in talin-Halo447 expressing cells 15 min and 16 h after initiation of cell-matrix adhesion. **b.** NND analysis reveals compaction of talin-1 molecules in FAs upon receptor clustering and FA maturation (yellow); the talin-1 spacing in MEM is unaffected by the cell adhesion state (magenta). **c.** Localization clouds in integrin deficient cells reconstituted with  $\beta_1$ -integrin-SNAP108. NND analysis demonstrates distances between individual  $\beta_1$  integrin molecules of about 50 nm in FAs and >100 nm in MEM similar to talin-1 (**b**). **d.** Talin-Halo447 expressing cells on micropatterned 1  $\mu$ -thick fibronectin stripes (FN) - separated by passivated 2  $\mu$  stripes (P) - demonstrates that talin's localization is governed by integrin mediated ECM engagement. **e.** Talin distribution of the 1<sup>st</sup>, 3<sup>rd</sup> and 5<sup>th</sup> nearest neighbor in FAs. Distributions were fitted with 2D Poisson density function (red line) indicating a random organization of talin-1 molecules on length scales between 40–120 nm. **f.** Random distribution simulations were used to estimate the absolute molecular density of talin-1 in FAs. Scale bars: 10  $\mu$ m (**a**, **c**), 5  $\mu$ m (**d**), 1  $\mu$ m (**d** inset), 500 nm (**a**, **c** inset).

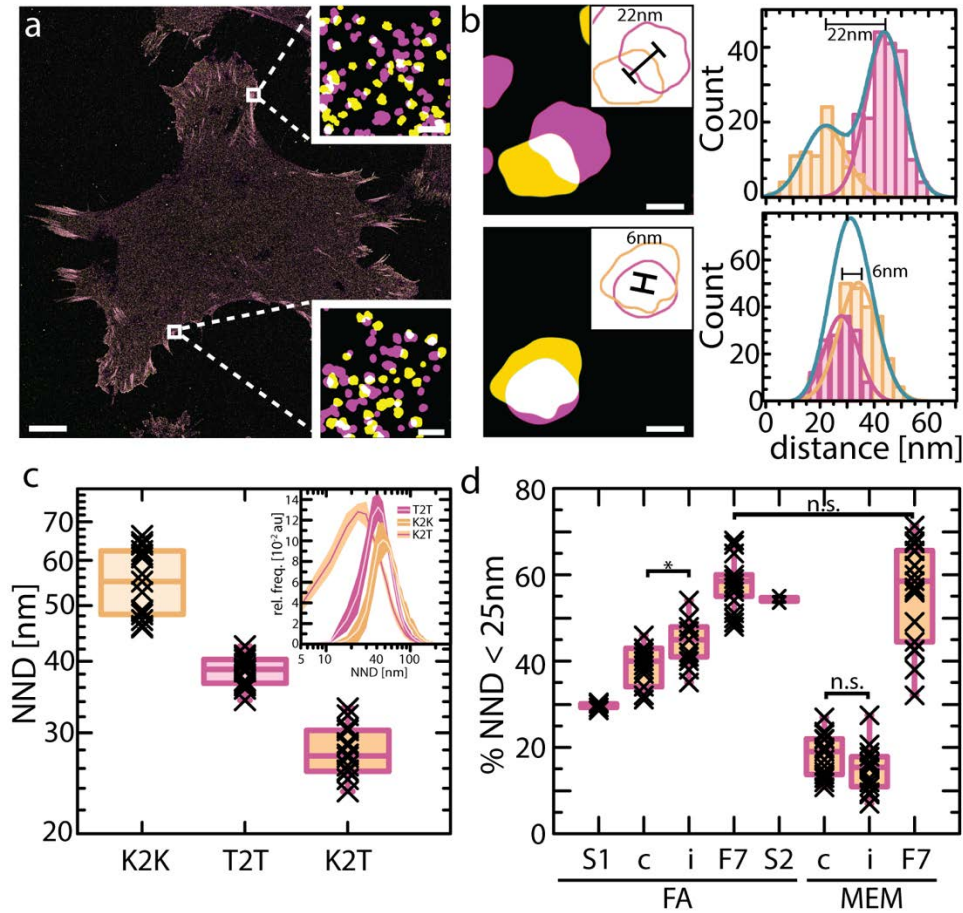


**Figure 3: Spatial association of talin-1 and kindlin-2 in FAs.** **a.** Talin-1/2 and kindlin-1/2 deficient cells were reconstituted with Talin-Halo447 and SNAP-Kindlin. Zoom into FAs reveals adjacent talin-1 and kindlin-2 localization clouds. **b.** Neighboring talin-1 (magenta) and kindlin-2 (yellow) localization clouds are frequently closer than 25 nm. **c.** NND analyses show the expected similar distributions and spacing between kindlin-2 (K2K) and talin-1 molecules (T2T). The average kindlin-to-talin distances (K2T) are significantly lower at around 26 nm. **d.** Theoretical simulations indicate 30 % of unspecific density-dependent co-localization of talin-1 and kindlin-2 in FAs at the observed molecular densities (S1). 45 % of labelled kindlin-2 molecules are within 25 nm of the next talin-1 molecule in Talin-Halo447 expressing cells (i). Co-localization is significantly reduced to 40 % in cells expressing C-terminally tagged talin-1 (c). Talin-F7 (F7) was used as a positive control to mimic perfect co-localization. Note that the obtained values are consistent with the theoretical simulations (S2) considering a 30% labeling efficiency of both tags. The observed effects are specific to FAs and not observed in MEM region. Scale bars: 6  $\mu$ m (a), 100 nm (a insets), 20 nm (b).

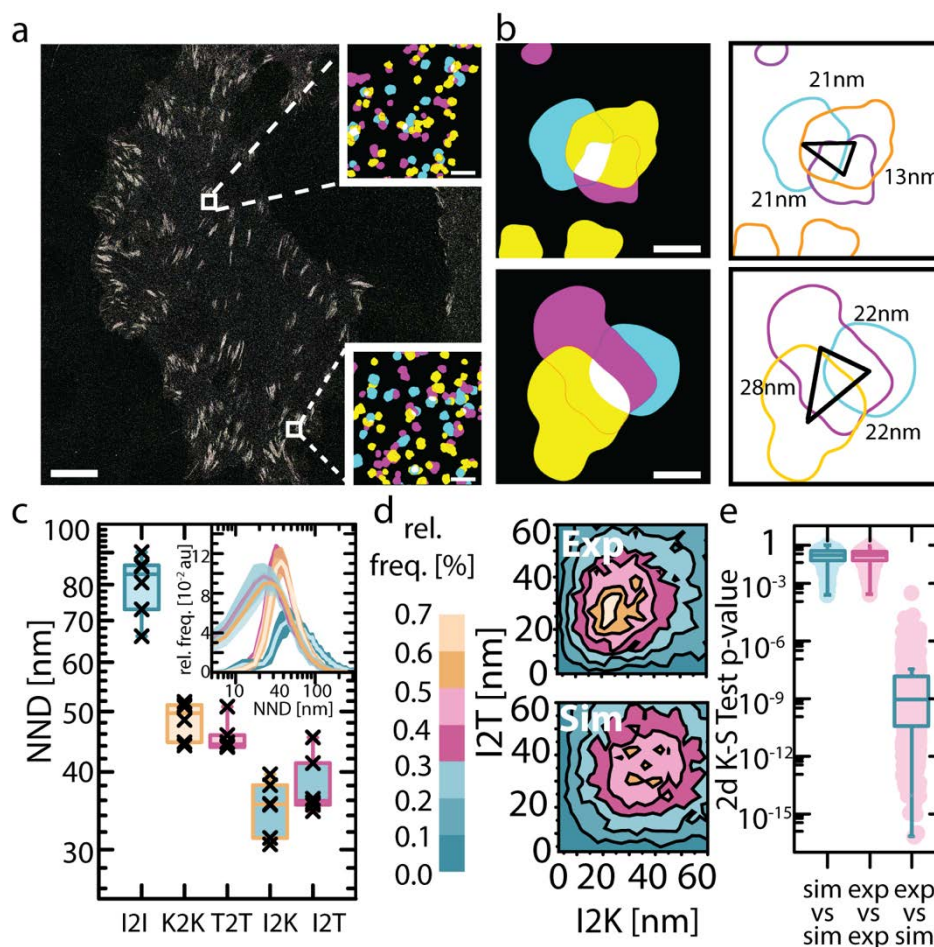


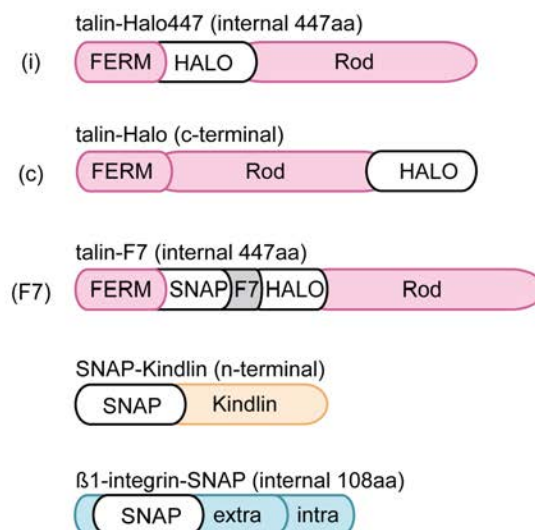
**Figure 4: Three-target DNA-PAINT imaging reveals spatial association of integrin-talin-kindlin in FAs.** **a.** Talin-1/2 and kindlin-1/2 deficient cells reconstituted with Talin-Halo447 and SNAP-Kindlin were labelled with a DNA conjugated antibody (9EG7) recognizing the extended  $\beta 1$  integrin conformation. **b.** Zoom into FAs reveals close proximity of talin-1 (magenta), kindlin-2 (yellow) and extended  $\beta 1$  integrin (cyan). **c.** NND analyses confirms the expected distribution of talin-1 (T2T) and kindlin-2 (K2K) at around 40 nm; labeled  $\beta 1$  is observed at larger distances of about 85 nm (I2I); average integrin-to-kindlin (I2K) and integrin-to-talin (I2T) distances were observed at 35 nm. **d.** Randomly simulated distributions, accounting for the observed talin-1, kindlin-2 and  $\beta 1$  integrin molecular densities, were compared to experimental data by plotting I2K and corresponding I2T tuples for each detected integrin. **e.** Statistical evaluation of bootstrapped data (sample size=1000 data points, test runs=1000) revealed high p-values for intrinsic data bootstrapping ('sim vs sim' and 'exp vs exp') but low p-values when comparing experimental with simulated data sets ('exp vs sim') suggesting non-random, spatial association of integrin-talin-kindlin during cell-ECM adhesions. Scale bars: 8  $\mu\text{m}$  (a), 100 nm (a insets), 20nm (b).

## Supplementary Information

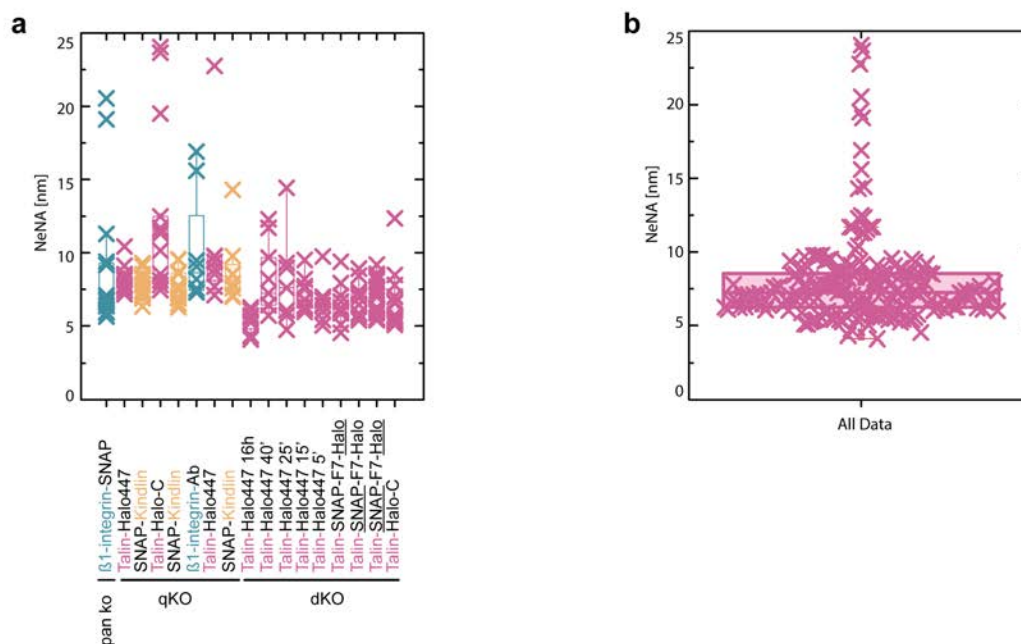
### Spatial association of integrin-talin-kindlin during cell-matrix adhesion

Supplementary Figure 1	List of constructs
Supplementary Figure 2	Average nearest neighbor analysis (NeNa)
Supplementary Figure 3	qPAINT analysis
Supplementary Figure 4	Control experiments for qPAINT analysis
Supplementary Figure 5	Workflow for data acquisition and processing
Supplementary Figure 6	DBSCAN resolution limit analysis
Supplementary Figure 7	Time resolved talin qPAINT analysis
Supplementary Figure 8	Westernblot analysis of talin protein expression levels
Supplementary Figure 9	Comparison of imager strands and labeling probes
Supplementary Figure 10	Simulations for Exchange Colocalization Experiments
Supplementary Figure 11	Nearest neighbor distance comparison
Supplementary Figure 12	Explanation of Bootstrap method
Materials and Methods	
Supplementary Table 1	Ligands with conjugated DNA-PAINT handles
Supplementary Table 2	DNA-PAINT sequences
Supplementary Table 3	Folding Protocol
Supplementary Table 4	Core staples and extension for DNA origami assembly
Supplementary Table 5	Biotinylated staples
Supplementary Table 6	Parameters for DNA-PAINT simulations
Supplementary References	

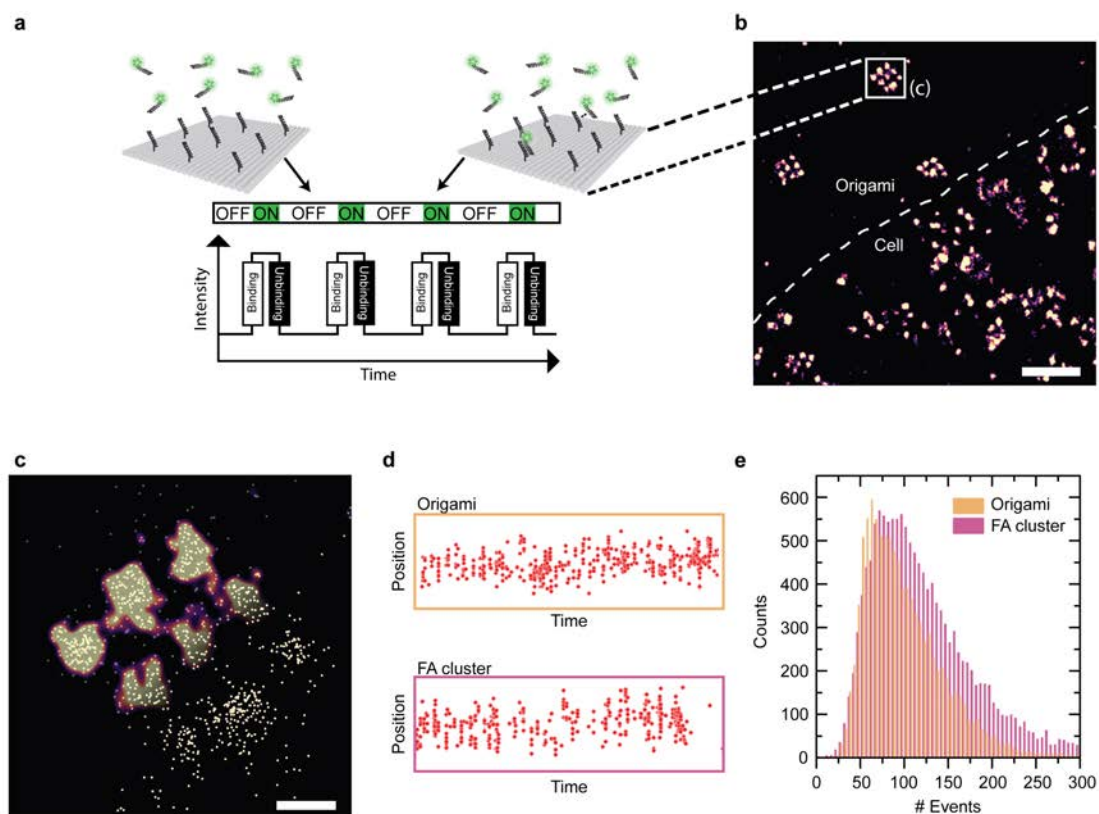
## Supplementary Figures



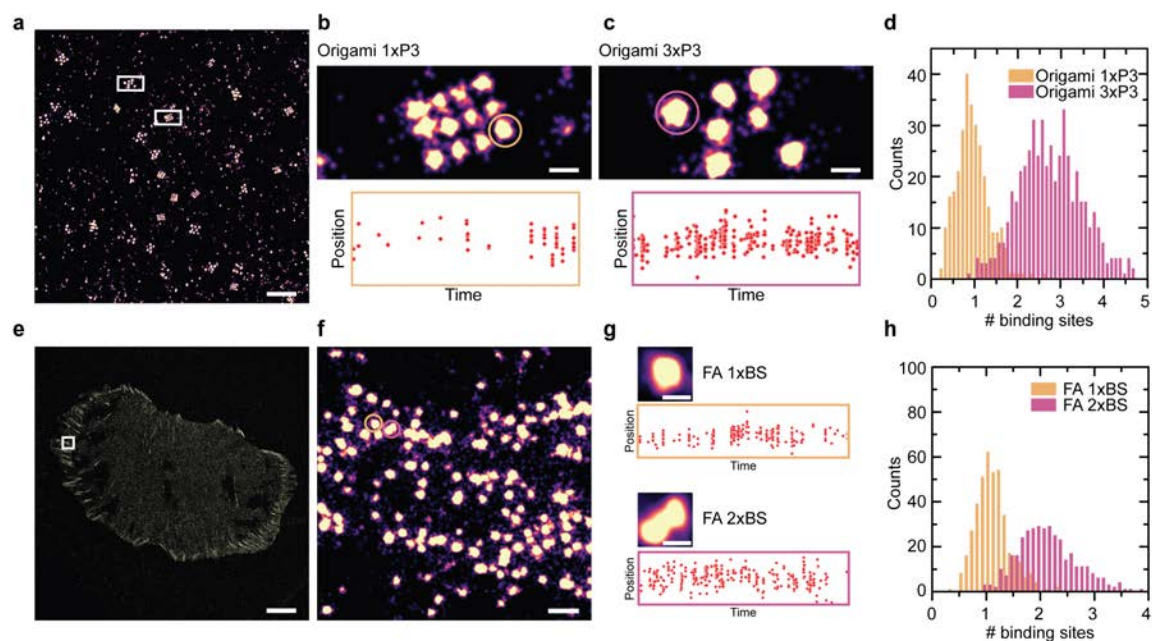
Supplementary Figure 1: List of constructs.



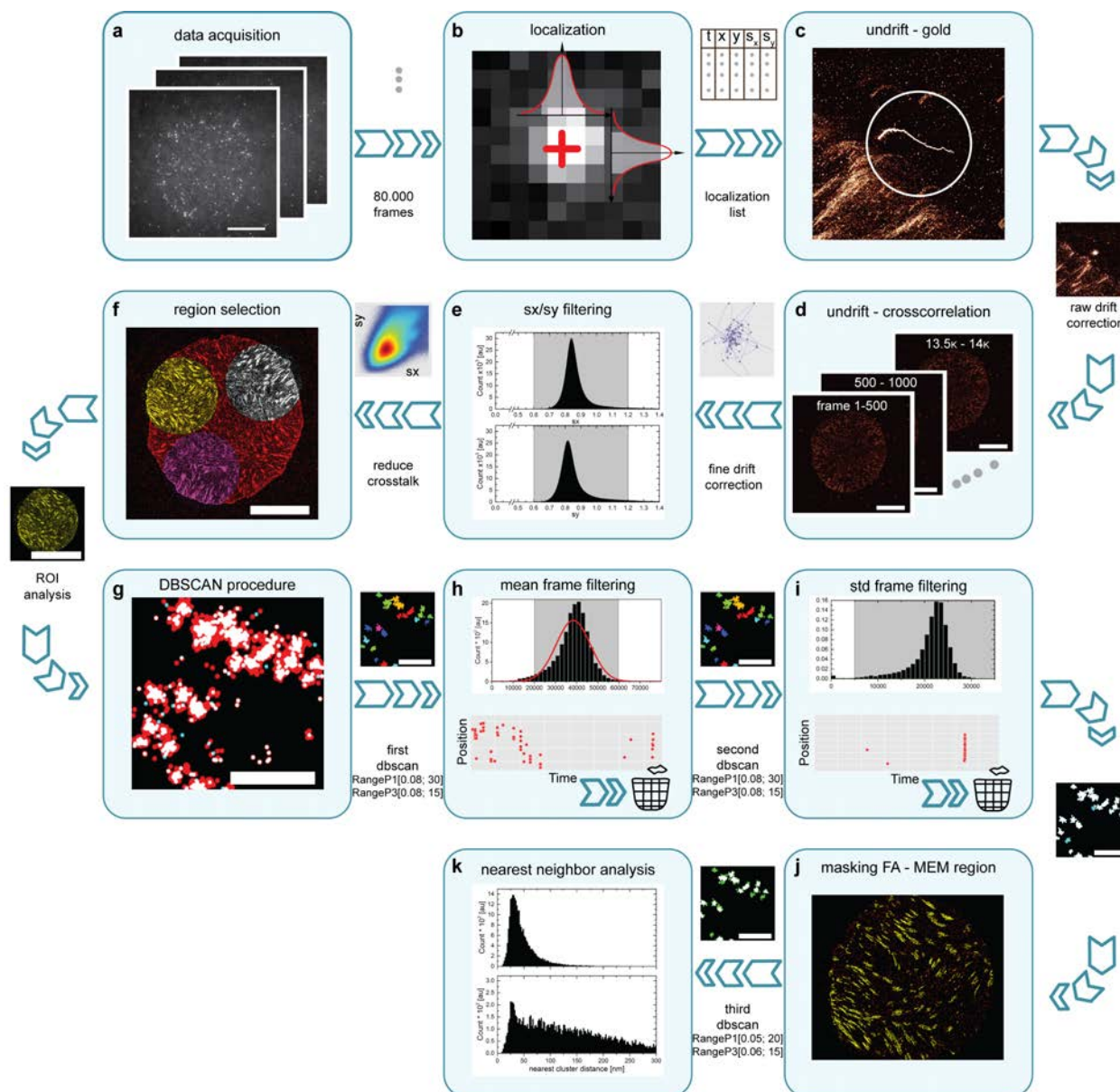
**Supplementary Figure 2: Average nearest neighbor analysis (NeNa).** **a.** Median localization precision of less than 10 nm for most experiments performed throughout two years of experimental work depicts robustness of setup leading to highly reproducible and comparable results. **b.** The overall achieved median localization precision of 7.2 nm, derived from NeNa calculations, ultimately results in about 17 nm resolution for single protein localization analysis.



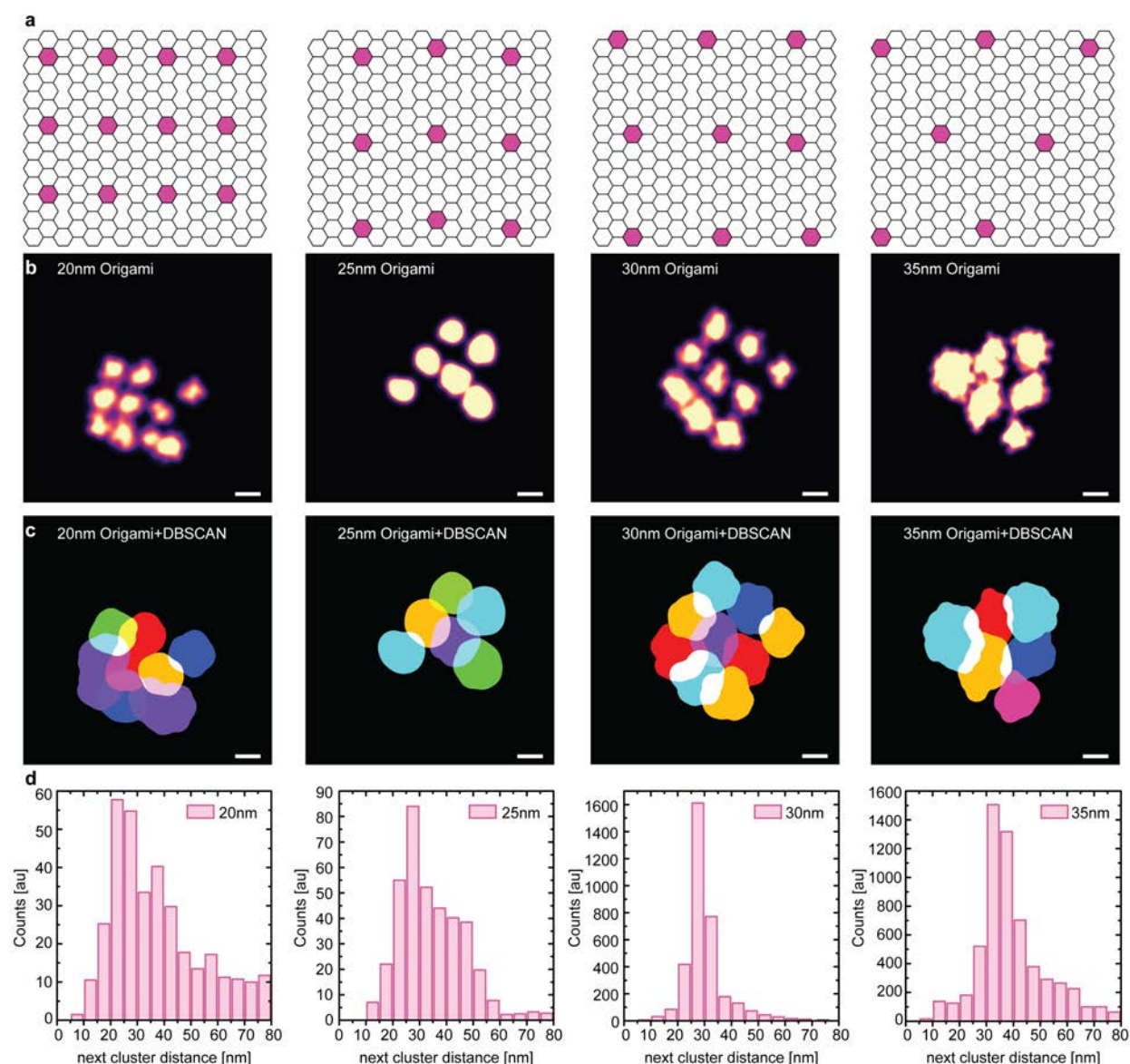
**Supplementary Figure 3: qPAINT analysis.** **a.** DNA origami scheme illustrating transient binding events of dye-labeled imager strands. For qPAINT analysis DNA origami structures were measured alongside the cells to determine and calibrate the binding events on single docking sites. **b.** Visualization of DNA origamis seeded next to the cell. **c.** Close-up of one DNA origami structure (indicated in b) with overlay of individual localization map. **d.** Comparison of binding events over time of one single site on the DNA origami and one localization cluster within the FA. **e.** Statistical analysis of large numbers of single docking sites on origami structures allows for calibration of mean number of events per site. Subsequent comparison to the events per localization cloud within the FA area reveals single molecules per localization cloud. Scale bars: 200nm (**b**), 25nm (**c**).



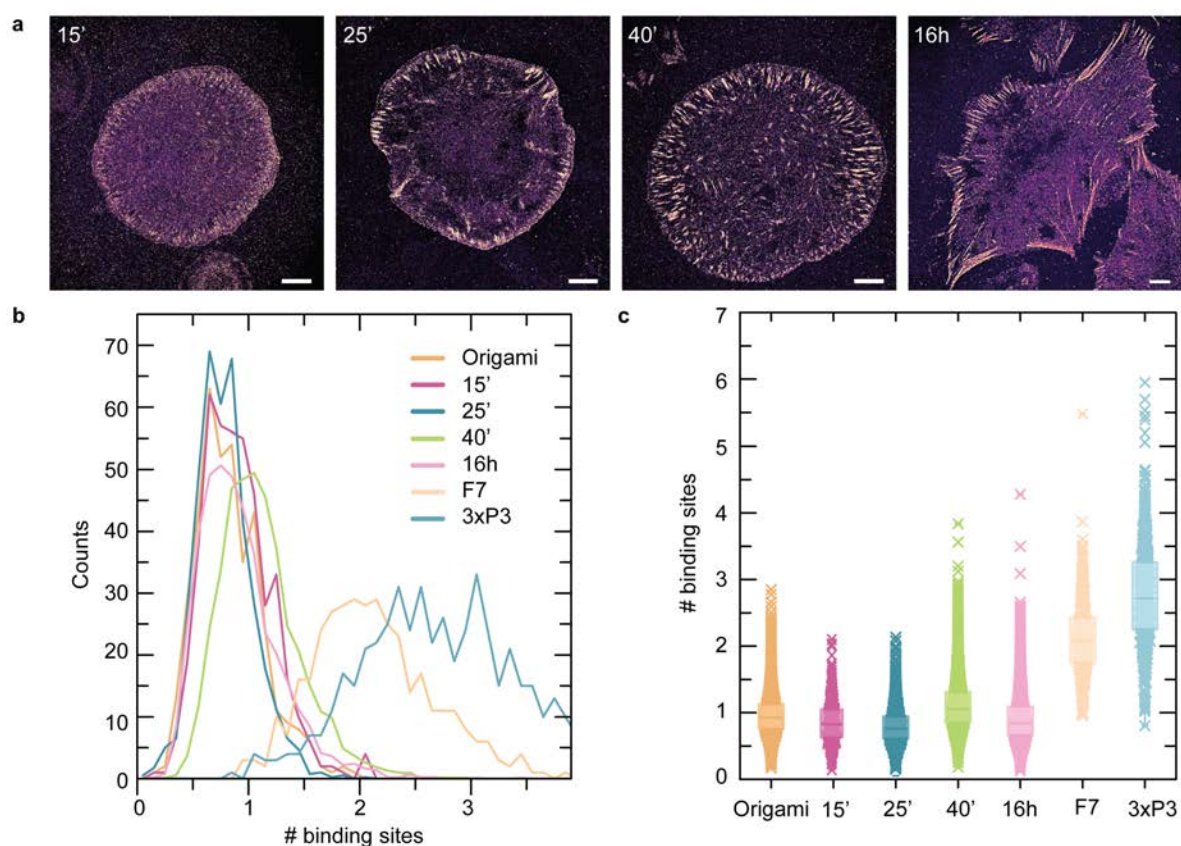
**Supplementary Figure 4: Control experiments for qPAINT analysis.** **a.** Super-resolved DNA-PAINT image of DNA origami structures with either one or three consecutive binding sites per spot. **b.** Close-up of DNA origami structure with single binding sequence and corresponding trace displays the binding frequency of a single binding site. **c.** Close-up of DNA origami structure with three consecutive binding sequences (3xP3) and corresponding trace displays the higher binding frequency at respective label site. **d.** Number of binding sites per label site could not be discriminated visually, but qPAINT analysis reveals either one or three binding sites per localization cloud. **e.** Super-resolved DNA-PAINT image of talin-F7 expressing cell mimicking either one or two binding sites per localization cloud by labeling SNAP and Halo pockets with P3 docking strands. **f.** Zoom in FA area reveals single distinct localization clouds (yellow circle) and localization clouds in very close proximity (magenta circle). **g.** Trace of localizations for single and two proximal localization clouds **h.** qPAINT analysis depicts different number of binding sites per localization cloud corresponding to one or two binding sites per molecule. Scale bars: 7  $\mu\text{m}$  (e), 300 nm (a), 100 nm (f), 25 nm (b,c), 20 nm (g)



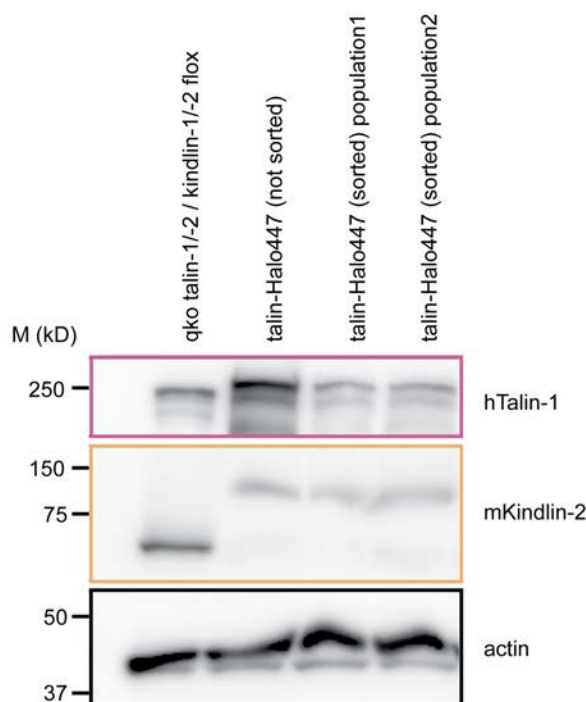
**Supplementary Figure 5: Workflow of data acquisition and subsequent data processing using Picasso Software.** **a.** Data was acquired using a Cy3b imager sequences, sCMOS camera and inverted TIRF microscope. In general, 80.000 frames with an integration time of 100 ms and 20 mW laser exposure at the sample were used (power density: 0.8 kW/cm<sup>2</sup>). **b.** Images were reconstructed by identification and fitting of single-molecule spots in each frame. **c.** First, images were drift corrected using 5-10 gold particles as fiducial markers. **d.** Subsequently, images were drift corrected using image substack redundant cross-correlation (RCC). **e.** In an additional post-processing step, the sigma value (sx/sy) derived from the gaussian localization fit in b, was filtered to eliminate double binding and spurious binding events. **f.** Next, regions of interest were picked and used for further NND analysis. **g.** DBSCAN analysis was used to detect distinct localization clouds in ROIs. **h.** Further, mean frame filtering was used to remove DBSCAN detected clouds, which are not continuously visited by an imager strand over the whole course of imaging. **i.** Filtering of the standard deviation frame removes long binding events (imager sticking). **j.** Gaussian blur-based masking was performed to discriminate between FA and MEM regions. **k.** Final DBSCAN procedure with adjusted parameter sets dependent on the used imager sequences and individual localization cloud data is generated. The center of mass for each individual localization cloud was calculated to allow for nearest neighbor distance analysis using a kd-tree algorithm.



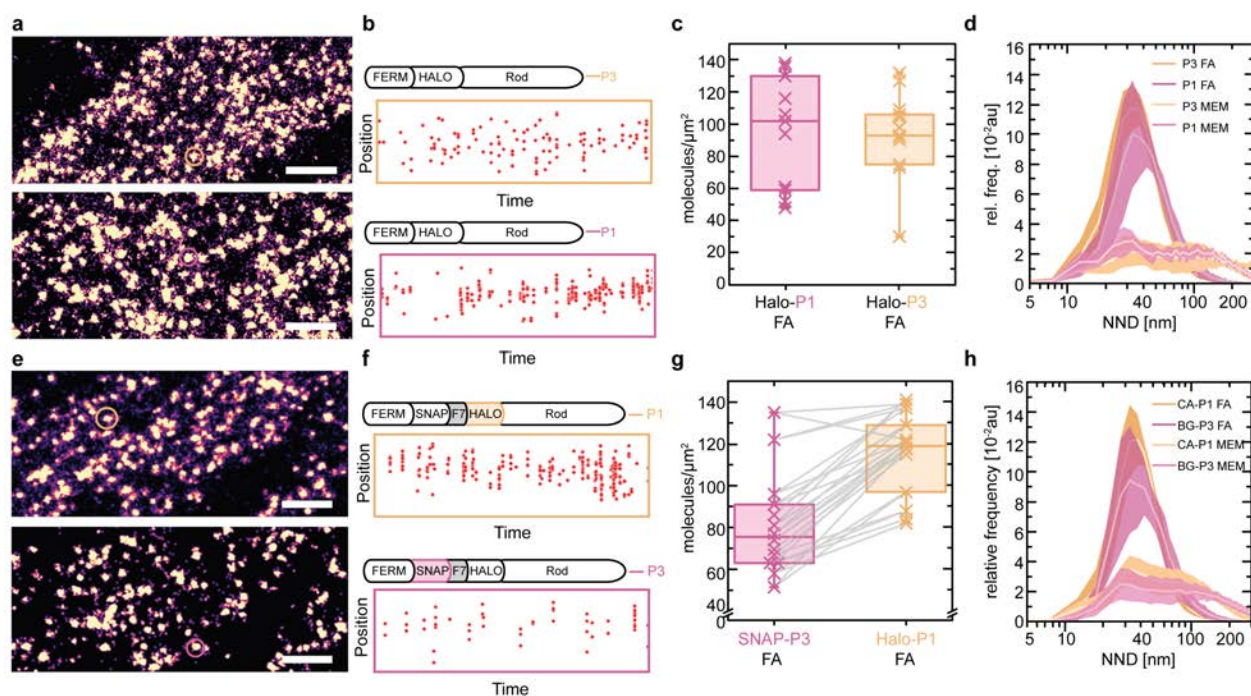
**Supplementary Figure 6: DBSCAN resolution limit analysis.** **a.** Design schematics for four different DNA origami structures with 12 binding sites spaced 20 nm, 9 binding sites at 25 nm or 30 nm and 7 binding sites spaced 35 nm apart (from left to the right). **b.** Super-resolved DNA-PAINT images of all DNA origami structures visually reveal distinct binding sites. **c.** Images of DBSCAN analysis with parameter sets used for FA analysis on DNA origami structures show proper separation of localization clouds down to 25 nm and merging of clouds at 20 nm distances due to increased crosstalk between individual localization clouds. **d.** Nearest neighbor distance (NND) histograms depict the proper localization cloud detection by fully automatized DBSCAN based analysis at least down to 25 nm. Scale bar: 20 nm (b,c)



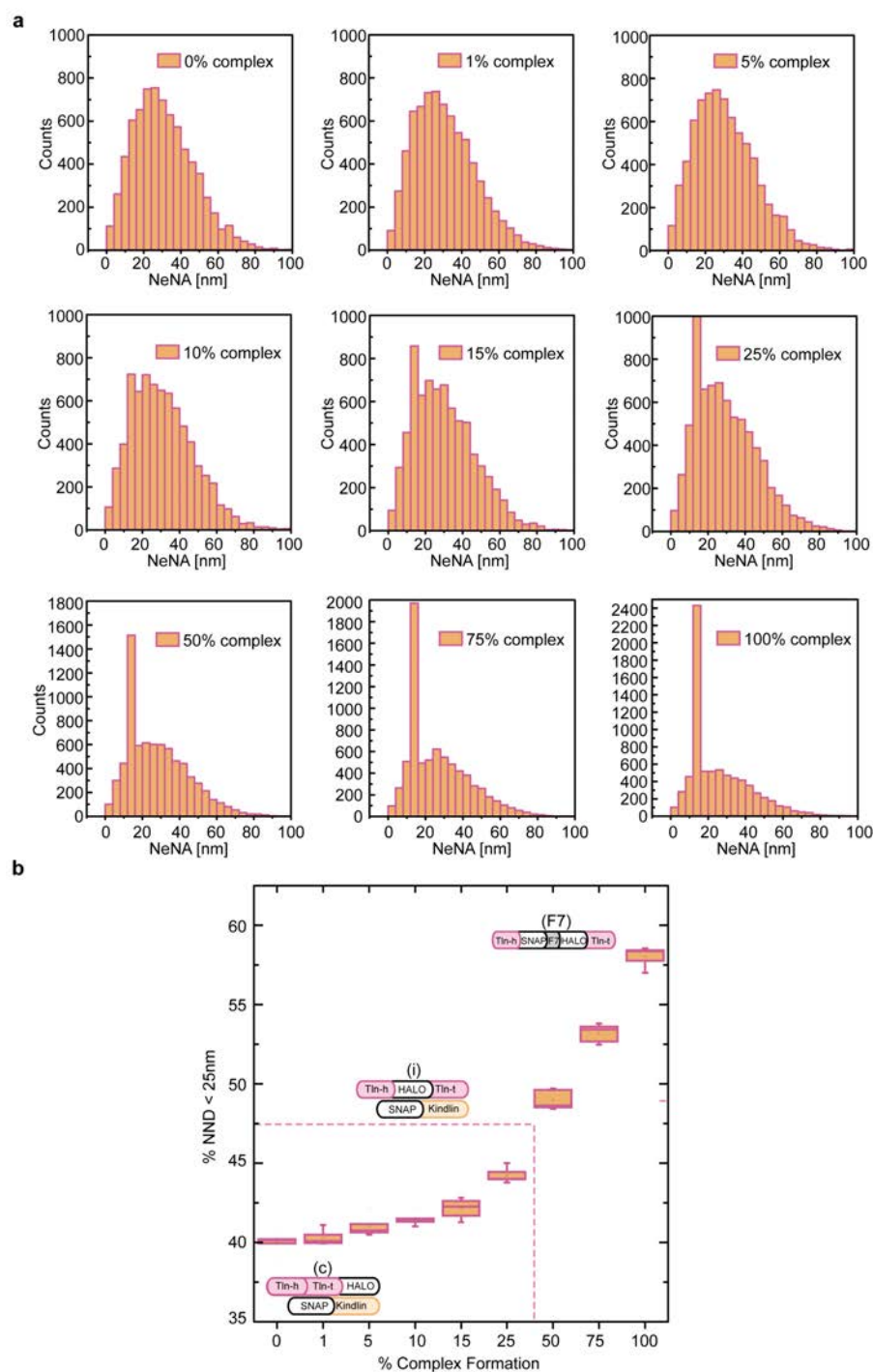
**Supplementary Figure 7: Time resolved talin qPAINT analysis.** **a.** DNA origami structures were seeded next to cells and analysed alongside at defined time points as qPAINT calibration. **b.** qPAINT analysis reveals single binding sites per talin localization cloud at each FA maturation time point, whereas double labeling of F7 construct and 3xP3 show a clear shift towards two binding sites and three binding sites per localization cloud, respectively. **c.** Boxplots of qPAINT analysis reveal medians around one binding site for time course data, two and three binding sites for F7 and triple P3 origami data. Scale bar: 10  $\mu\text{m}$  (at 15'), 5  $\mu\text{m}$  (at 25', 40', 16h).



**Supplementary Figure 8: Western blot analysis of talin protein expression levels.** From left to right. qko talin-1/-2 / kindlin-1/-2 flox: Expression level of talin and kindlin-2 in wildtype floxed cell line. Talin-Halo447 (not sorted): Overexpression of talin in talin-1/-2 / kindlin-1/-2 deficient fibroblasts (qko) reconstituted with SNAP-Kindlin and talin-Halo447. Talin-Halo447 (sorted) population 1/2: Sorting for lower 20 % talin expression level in two different populations, talin bands appear similar as wildtype talin-1/-2 and kindlin-1/-2 floxed cell line. Similarly, SNAP-kindlin bands of talin-Halo447 FACS sorted qko cells depict band intensities comparable to wildtype mKindlin2 expression.

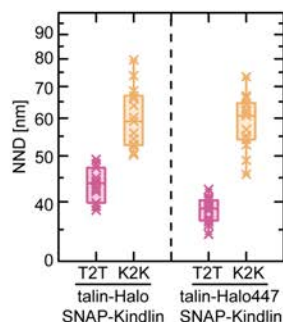


**Supplementary Figure 9: Comparison of Imager Strands and Labeling Probes.** **a.** DNA-PAINT images of FAs using P3 or P1 imager strand. **b.** Comparison of P1 and P3 traces reveal different binding kinetics. P3 imager binds shorter than P1. **c.** After adjusting the parameter in the analysis pipeline, the same molecular densities are detected with P1 and P3. **d.** Distribution curves of the NND in FAs and membrane region using P1 and P3 show no apparent differences. **e.** DNA-PAINT images of the same FA area labeled with SNAP or HaloTag using talin-F7 construct. **f.** Traces of Halo labeled with P1 and SNAP labeled with P3. **g.** Analysis of the molecular density in FAs, labeled with SNAP (BG) or HaloTag (CA), show approximately 30% less SNAP labeling compared to Halo. **h.** Nearest neighbor distance distribution curve of SNAP (BG) and Halo (CA) in FAs and in the membrane region reveal a lower frequency count for SNAP and thus display a decreased number of detected localization clouds. Scale bars: 200 nm (a,e).

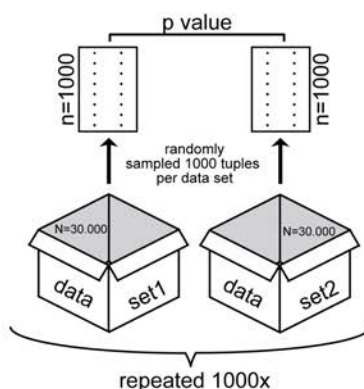


**Supplementary Figure 10: Simulations for Exchange Colocalization Experiments. a.** Histograms of simulated colocalization data assuming a labeling efficiency of 30%, randomly organized localization clouds and the molecular density for kindlin and talin from the experiments. In addition, the simulations assume a certain percentage of complex formation at 12-16 nm (from 0% up to 100% complex formation) and were analyzed using the simulated x- and y-coordinates without subjecting the spots to an additional simulated DNA-PAINT process and the established cluster detection pipeline. The histograms reveal that colocalization of two populations under 15% is not detectable due to the inherent statistical variability. **b.** The percentage of complex formation was plotted against the percentage of localization clouds closer than 25 nm. This simulation nicely reproduces the kindlin-talin exchange colocalization data, where 100% complex formation shows around 60% colocalization (talin-F7= 58% colocalization) whereas 0% complex formation has still 40%

colocalization (Talin-Halo + SNAP-mKindlin (c) = 40% colocalization). This high percentage is presumably due to the high molecular densities in focal adhesions. Almost no difference can be detected up to 15% complex formation. The talin-Halo447 and SNAP-mKindlin2 cell line (i) experiment reveal a colocalization of 45%, which is in good accordance to a 40-50% simulated complex formation.



**Supplementary Figure 11: Nearest neighbor distance comparison of talin-Halo (c-term) and talin-Halo447 qko cell line.** Talin-Halo (c-term) or talin-Halo447 stably transfected in kindlin-1/2 and talin-1/2- deficient fibroblasts together with SNAP-Kindlin exhibit expected comparable NNDs in FAs (magenta) of about 45 nm (left) and 40 nm (right) distances. Moreover, SNAP-Kindlin NNDs are equivalent in both cell lines.



**Supplementary Figure 12: Comparison of Integrin-Talin-Kindlin Experimental Data with Simulations using Bootstrap Method.** To determine the goodness of fit and significance level between experimental data and simulated data a 2d Kolmogorov-Smirnov (K-S) test was established. Bootstrap method was utilized to calculate the level of differences by repeatedly calculating p-values. In detail, 1000 data points (tuples) were randomly sampled out of each data set consisting of 30.000 tuples and the maximum difference (p value) obtained by performing 2d K-S test. The above described process is repeated for 1000 times to obtain a series of maximum differences between two data sets leading to the mean differences.

## Supplementary Materials & Methods

**Labeling probes and reagents.** Chloroalkane (CA; HaloTag ligand) or benzylguanine (BG; SNAP-tag ligand)-modified docking strands carrying an Atto488 dye at the 3'-end were custom-ordered from Biomers.net. Imager strands with a Cy3b modification at the 3'-end were purchased from Eurofins; for oligonucleotide sequences see Supplementary Table 1 and 2. For imaging, the following antioxidant stock solutions were used: 40x PCA solution (154 mg PCA diluted in 10 ml ddH<sub>2</sub>O, pH 9.0); 100x Trolox (100 mg of Trolox in 430  $\mu$ l Methanol, 345  $\mu$ l NaOH (1M) and 3.2ml ddH<sub>2</sub>O); 100x PCD solution (9.3 mg of PCD diluted in 13.3 ml of 50 % glycerol with 50 mM KCl, 1 mM EDTA and 100 mM Tris-HCl, pH 8.0). PCD, PCA and Trolox stocks were stored at -20 °C. In addition, the following antibodies and reagents were used:  $\alpha$ -integrin 9EG7 (BD Biosciences, 553715),  $\alpha$ -Talin (Sigma, T3287),  $\alpha$ -Kindlin-2 (Sigma, K3269), paraformaldehyde (Roth, 4980.1), Triton X-100 (Roth, 3051.4), bovine serum albumin (Serva, 11930.03) and dimethylformamid (Thermo Fisher, 20673).

**Plasmid construction.** Talin-1 expression constructs are based on human talin-1 cDNA (NM\_006289). For internal tagging, a linker encoding for 5'Sall/3'NotI restriction sites was generated after the base pair encoding for aa 447, and HaloTag (Promega), SNAP-tag (New England Biolabs) or the F7 cassette were inserted by Gibson Cloning. The C-terminal fusion construct (htln1-Halo-Cterm) was generated using EcoRI/BamHI restriction sites. The assembled cDNAs were then transferred into pLPCXmod that drives expression through a CMV promoter and the correct sequence of all constructs was confirmed by DNA sequencing (Eurofins Genomics). Kindlin expression constructs are based on mouse Kindlin-2 (Gene ID: 218952), which was tagged N-terminally with SNAP-tag via Gibson cloning using HindIII/NotI restriction sites. The construct was cloned into pLPCXmod with a crippled CMV promoter to avoid overexpression. The human SNAP-tagged  $\beta$ 1 integrin was cloned by exchanging the GFP cDNA from the extracellularly tagged  $\beta$ 1A integrin (NM\_002211, GeneID:3688) described before<sup>1</sup> with SNAP cDNA in a loop in the hybrid domain (before aa 108) using AgeI and XhoI.

**Cell Culture.** Cells were maintained in high glucose DMEM (ThermoFisher, 31966047) supplemented with 10 % Fetal Bovine Serum (ThermoFisher, 10270106) and 1 % Penicillin/Streptomycin (Sigma, P4333). The talin constructs were stably expressed in double knockout fibroblasts deficient for talin-1 and talin-2 (Tln1<sup>-/-</sup>Tln2<sup>-/-</sup>; dKO)<sup>2</sup> as previously described<sup>3</sup>, or co-expressed with kindlin-2 in quadruple knockout fibroblasts deficient for talin-

1, talin-2, kindlin-1 and kindlin-2 (Tln1<sup>-/-</sup>Tln2<sup>-/-</sup> K1<sup>-/-</sup>K2<sup>-/-</sup>; qKO)<sup>4</sup>. To control expression artefacts this qko cell line, expressing talin-halo447 and SNAP-kindlin, was FACS sorted for lower 20 % talin expression level using HaloTag® TMR ligand (Promega G825A) labeling as sorting marker. The integrin-SNAP construct was analyzed in integrin pan knockout cells ( $\alpha v^{-/-}\beta 1^{-/-}\beta 3^{-/-}\beta 7^{-/-}$ )<sup>5</sup>. For imaging, 40,000 cells were seeded on ibidi  $\mu$ -Dishes (Ibidi, 81158,) with or without coating of 10  $\mu$ g/ml fibronectin (Calbiochem, 341631).

**Cell fixation and labeling of Halo- or SNAP-tag.** Cells were fixed with pre-warmed 4 % PFA solution for 10 min, washed 3 $\times$  with phosphate buffered solution (PBS), and stained with 1  $\mu$ M of either chloroalkane (HaloTag) or benzylguanine (SNAP-tag)-linked docking strands, as summarized in Supplementary Table 1. Staining was performed in PBS containing 0.2 % Triton X-100 overnight. Cells were then washed 3 $\times$  for 5 min in 1 $\times$  PBS, incubated with a 1:3 dilution of 90 nm gold particles (Cytodiagnosics, G-90-100) as drift markers in 1 $\times$  PBS for 5 min, washed again 3 $\times$  5 min in PBS, and immediately imaged.

**Stamp production for micropatterning.** To produce polydimethylsiloxane (PDMS) stamps for microcontact printing, we use photolithography to create micro-structured silicon wafers as a master. The silicon wafers (MicroChemicals) were dipped into 1% hydrofluoric acid (MicroChemicals) to make the surface hydrophobic and promote the adhesion of the resist. The wafer was then coated with AZ40XT D11 (MicroChemicals, Merck) photo-resist and soft baked ramped to 125°C. Desired areas are exposed to UV light using laser direct imaging (Protolaser LDI, LPKF). The exposed wafer was then post baked at 110°C before development (AZ 726 MIF, MicroChemicals) and silanization (Trichloro(1H,1H,2H,2H-perfluoro-octyl)silane, Sigma-Aldrich). Next, PDMS monomer and cross linker (DC 184 elastomer kit, Dow Corning) was mixed in a 10:1 ratio and poured onto the master. After degassing in a desiccator, the PDMS stamp was cured overnight at 50°C.

**Microcontact printing.** PDMS stamps were treated with UV light (PSD-UV, novascan) for 5 min and inked with 50  $\mu$ g/ml FN (Yo proteins) solution (80% unlabelled FN, 20% labelled with Alexa Fluor 647 NHS ester (Thermo Fisher Scientific)) for 45 min. Subsequently, a petri dish ( $\mu$ -Dish, Ibidi) was treated with UV light for 15 min, stamps were washed with deionized water, dried and placed on the petri dish. A droplet of a solution containing 2 mg/ml poly-L-lysine-grafted polyethylene glycol (PLL-PEG, 2 kDa PEG chains, SuSoS), 10 mM HEPES, and 150 mM NaCl was placed at the side of the stamp to allow flowing into the free space under the stamp. After 30 min stamps were removed and another drop of PLL-PEG solution was added.

Next, the surface was covered with a glass slide for 30 min to ensure coverage with PLL-PEG. The glass slide was then removed and the patterned surface was washed 3× 5 min in PBS and stored in PBS.

**Super-resolution microscopy.** Fluorescence imaging was carried out on an inverted Nikon Eclipse Ti microscope (Nikon Instruments) equipped with the Perfect Focus System, applying an objective-type TIRF configuration with an oil-immersion objective (Apo SR TIRF 100×, NA 1.49, Oil). TIRF angle was adjusted for highest signal to noise ratio prior to imaging. For excitation of Atto488 and Cy3b, a 488 nm laser (Toptica iBeam smart, 200 mW) or a 561 nm (Coherent Sapphire, 200 mW) laser were used. The lasers were fiber coupled and, after entering the microscope, the laser beam was passed through cleanup filters (ZET488/10x or ZET561/10, Chroma Technology) and coupled into the microscope objective using a beam splitter (ZT488rdc or ZT561rdc, Chroma Technology). Fluorescence light was spectrally filtered with two emission filters (ET525/50m and ET500lp for 488 nm excitation and ET600/50m and ET575lp for 561 nm laser excitation, Chroma Technology) and imaged on a sCMOS camera (Andor Zyla 4.2) without further magnification resulting - after 2x2 binning - in an effective pixel size of 130 nm per pixel.

**DNA-PAINT imaging in cells.** FAs of cells were focused by using 488 nm excitation, which excited the fixed Atto488 fluorophore on the DNA docking site. For DNA-PAINT imaging, samples were imaged using 561 nm excitation wavelength and a laser power of 20 mW at the sample (power density: 0.8 kW/cm<sup>2</sup>); qPAINT measurements were performed with reduced laser power of 10 mW at the sample (power density: 0.4 kW/cm<sup>2</sup>). Depending on the docking site sequence, the imager strand concentration was set between 250 pM–2.5 nM and imaging was performed in the presence of antioxidants using a solution of 1x PCA (Stock 40x PCA solution; Sigma, 37580), 1x PCD (Stock 100x PCD solution; Sigma, P8279) and 1x Trolox (Stock 100x Trolox solution; Sigma, 238813) in 1× PBS + 500 mM NaCl. To experimentally mimic different molecular densities, chloroalkane (CA)-P1 and chloroalkane (CA)-P3 docking strands were mixed in different ratios (1:2 – 1:10) to ensure only partial P1 imager binding, and subsequently added to fixed cells as described above. Typically, 80.000 frames at 100 ms exposure time were acquired for NND imaging, and 160.000 frames and 100 ms for qPAINT measurements.

**Multiplexed imaging with Exchange-PAINT.** Chloroalkane (CA)-P1 and benzylguanine (BG)-P3 (in case of three-target Exchange PAINT also P5-conjugated 9EG7 antibody) were diluted in 1× PBS containing 0.02 % Triton X-100 and added to PFA-fixed qKO cells expressing SNAP-Kindlin-2 and talin-Halo447. The cells were then washed thoroughly with

1× PBS and imaged in two (or three) subsequent steps by DNA-PAINT super-resolution microscopy. In the first step, SNAP-Kindlin-2 was imaged using 2.5 nM Cy3b-P3 imager strand concentration (250 pM Cy3b-R2 for triple color experiments). After washing, 2.5 nM Cy3b-P1 (or 250 pM Cy3b-R1 for triple color experiments) was added to image talin-Halo447. For triple color experiments, an additional round of exchange was performed with Cy3b-P3 (1nM) to label 9EG7 bound  $\beta$ 1 integrin. To confirm that results are unaffected by the employed docking strand sequence, experiments were repeated using CA-P3 and BG-P1 docking strands in combination with the respective imager strands.

**Exchange-PAINT experiments for docking strand damage and label efficiency.** To test for docking stand breaks due to laser light and the influence of buffer exchange, talin-Halo447, expressed in double knockout fibroblasts deficient for talin-1 and talin-2 (Tln1<sup>-/-</sup>Tln2<sup>-/-</sup>; dKO), was labeled with Chloroalkane (CA)-P3 as described above, measured a first round ( 80.000 frames, 100 ms exposure), washed thoroughly with 1xPBS and imaged a second round (80.000 frames , 100 ms exposure) analogously. Docking strand sequence label influence (P1 vs. P3) was determined by labeling talin-Halo447 expressing cells with either CA-P1 or CA-P3 docking strands accordingly and performing sequential imaging of cells prior to analysis. To determine influence of Halo and SNAP label efficiency, talin-F7 construct was stably expressed in double knockout fibroblasts deficient for talin-1 and talin-2 (Tln1<sup>-/-</sup>Tln2<sup>-/-</sup>; dKO) and labeled with CA-P1 and benzylguanine (BG)-P3 respectively. Sequential imaging was performed, starting with SNAP measurement (P3 imager sequence) followed by thorough washing steps using 1xPBS and a second measurement round of Halo (P1 sequence).

**DNA Origami self-assembly.** DNA origami structures were designed using the Picasso software<sup>6</sup>. The DNA origami self-assembly was performed in a reaction mix (Supplementary Table 3) containing 10 nM p7249 scaffold strand M13mp18 (tilibit nanosystems), 100 nM folding staples (Eurofins, Supplementary Table 4), 10 nM biotinylated staples (Eurofins, Supplementary Table 5) and 1  $\mu$ M P3-docking strand in 5 mM Tris and 1 mM EDTA buffer containing 12.5 mM MgCl<sub>2</sub>. Subsequently, the DNA origami self-assembled in a thermocycler running the following cycling protocol: Step 1: 80°C for 5 min; step 2: immediate cool down to 60°C; step 3: further cool down from 60°C to 4°C in steps of 1°C per 3.21 min.

**PEG precipitation for DNA origami.** Polyethylenglycol (PEG) was used to decrease the solubility of origami in solution and induce origami precipitation<sup>7</sup>. Origami solution in 1× TE buffer with 12.5 mM MgCl<sub>2</sub> was mixed 1:1 with 15 % PEG-buffer (7.5g PEG-8000, 1× TAE, 12.5 mM MgCl<sub>2</sub>, 500 mM NaCl) and centrifuged at 20.000 ×g at 4°C for 30 min. The

supernatant was removed and origamis were resuspended in folding buffer (12.5 mM MgCl<sub>2</sub>, 5 mM Tris, 1 mM EDTA at pH 8.0). Centrifugation and supernatant removal was repeated three additional times. Origamis were then stored at -20°C.

**Cell experiments with DNA origami.** Cells were seeded, fixed and labelled as described above. To perform qPAINT experiments, labeling solution was removed and cells were washed 3× times with 1× PBS. Next, 200 µl BSA-Biotin solution (1 mg/ml BSA in buffer A+ (10 mM Tris-HCL, 100 mM NaCl and 0.05% Tween 20, pH 8.0)) was added and incubated for 10 min. The dish was then carefully washed with buffer A+, 200 µl streptavidin solution (0.5 mg/ml in buffer A+) was added and incubated for another 10 min. Afterwards, the dish was washed with buffer A+ and subsequently with buffer C (1× PBS + 500 mM NaCl). Then, 200 µl of biotin labeled DNA origami solution was added (200 pM in buffer C) and incubated for 60 min. Finally, the dish was carefully washed with buffer C and imaging buffer was added.

**Antibody conjugation with DNA-PAINT docking strands.** Integrin β1 9EG7 antibody was conjugated to DNA-PAINT docking strands via available amine groups using a bifunctional NHS-ester crosslinker harboring an additional trans-cyclooctene moiety (TCO; TCO-NHS ester ((E)cyclooct-4-enyl-2,5-dioxo-1-pyrrolidinyl carbonate), Jena Bioscience, CLK-1016-25), which was later reacted with a methyltetrazine-PEG5 modified DNA strand to yield the final antibody-DNA conjugate<sup>8</sup>. In brief, the antibody storage buffer was exchanged via dialysis to 1× PBS overnight at 4°C under constant stirring. The antibody was then concentrated with 100 kDa Amicon spin filters (Merck/EMD Millipore, UFC500396), TCO-NHS ester crosslinker was added at 10× molar excess and incubated for 2 h at 4°C on a shaker. Afterwards, 7k zeba spin desalting columns (ThermoFisher, 89882) were used to remove unreacted crosslinker. Tz-DNA was added to the purified antibody-crosslinker solution at 5x molar excess and incubated for 1 h at room temperature. Subsequently, amicon spin filters were used to remove free Tz-DNA and the antibody conjugate was stored at 4°C.

**Image reconstruction.** Images were reconstructed with the Picasso Software. Drift correction was performed stepwise starting with the gold nanoparticles for global drift correction followed by image sub-stack cross-correlation analysis. Localization precision was determined by nearest neighbor based analysis (NeNA)<sup>9</sup>.

**qPAINT analysis.** First, images were localized and drift corrected as described previously<sup>6</sup>. Then, single binding sites on DNA origami structures were picked using the 'Picasso-Render-picking-tool' (about 200-500 single origami binding sites/image). Afterwards, the picked single

binding sites were calibrated to one unit per pick and the influx rate was estimated from the binding kinetics of the picked single binding sites on DNA origamis<sup>6,10</sup>. The binding kinetics depend on the imager strand length, GC content, buffer salt concentration and imager concentration. Subsequently, talin localization clouds were picked (about 1000-1500 picks/image) and the mean number of binding sites in FAs were calculated from the calibrated influx rate.

**Data processing and analysis.** For further analysis, we used DBSCAN (density based clustering of application with noise) as a data clustering algorithm<sup>6,11</sup>. This DBSCAN clustering algorithm detects localization clouds by looking for minimal numbers of localizations within a circle with radius,  $\epsilon$ . Moreover, the algorithm utilizes a minimum number of points (MinPts) within an area of the circle as a second parameter. For  $\epsilon$ , we used *the localization precision in pixels of our images (NeNA)* and MinPts were chosen according to the binding frequency of the imager strand (Extended Data 4). Furthermore, we used a mean frame filter and a standard deviation filter to remove unspecific signals of the imager strands.

For NND calculations, we used custom written python scripts based on kd-tree analysis<sup>12</sup> to calculate the nearest neighbor within a localization cloud dataset. For co-localization analysis, the nearest neighbor distance for each localization cloud of one dataset with respect to the reference dataset was calculated (kindlin-to-talin, integrin-to-talin, and integrin-to-kindlin). Molecular densities were calculated by dividing the determined number of localization clouds within the FA mask by the respective FA mask area.

**Statistical analysis.** Determining if two data sets were equal, two-sample t-tests were applied with a p-value threshold of less than 0.05 defining statistical significance (Fig. 3d, Extended Data 9). To determine the goodness of fit between experimental data and simulated data in Fig. 4d, a 2D Kolmogorov-Smirnov (K-S) test was used<sup>13</sup>. Bootstrapping was performed to calculate the mean differences and standard deviation. In brief, 1000 data points (tuples) were randomly sampled out of each data set consisting of approximately 30.000 tuples. This procedure was applied on both data sets and the maximum difference obtained by performing a K-S test. This process was repeated 1000 times to obtain a series of maximum differences between the two data sets leading to the mean differences and stdv (Extended Data 16). Simulated vs simulated data and experimental vs experimental data were compared as a control, resulting in high p-values for intrinsic data. Then, experimental data (integrin-kindlin-talin distances; I2KT) vs randomly simulated data were compared, leading to high differences and thus low p-values (ns  $P > 0.05$ ; \*  $P \leq 0.05$ ; \*\*  $P \leq 0.01$ ; \*\*\*  $P \leq 0.001$ ).

**Fitting of NND distributions.** Plotting the NND over a logarithmic distance scale results in symmetric, Gaussian-shaped distributions pointing towards a structural order parameter. The simplest assumption of order is a random point localization, which - in two dimensions- is mathematically described by the 2D Poisson point process and its respective homogeneous Poisson density probability function ( $\rho$  being the density):

$$P(r) = 2\pi r \rho e^{-\pi \rho r^2}$$

NND data was fitted in Origin9.1 using this custom built fitting function (Fig. 3e).

**Simulation parameters.** Simulations of random particle distributions were performed with custom python scripts. In brief, for random distributions, random x- and y-coordinates were generated using the molecular particle densities extracted from the measured DNA-PAINT data. In agreement with previously published data and our own talin-F7 experiments<sup>14,15</sup> (Extended Data 10), we assumed labeling efficiencies of 30 % (Halo-tag) and 20 % (SNAP-tag). DNA-PAINT simulations were performed with the previously reported Picasso software<sup>6</sup> using parameters that were extracted from our experimental data to mimic raw data for image reconstruction and post processing filter steps (shown in Supplementary Table 6). To estimate the absolute molecular density and the corresponding NND, we set the CA labeling efficiency to 30 %. To determine the localization cloud detection efficiency of the DBSCAN analysis, we compared hand-picked data with automatically analyzed data, which revealed a detection efficiency of about 50-60 % (Fig. 2f). For simulations of complex formation, clusters were simulated to be within 12-16 nm, which corresponds to the measured distances in the F7 control construct (Fig. 3d, Extended Data 13). To calculate the degree of co-localization within three random distributions, clusters were simulated with the measured molecular density of the respective experiment (Fig. 4d). All simulation scripts are available upon request.

**Supplementary Table 1: Ligands with conjugated DNA-PAINT handles**

Docking strand	Sequence	5'-mod	3'-mod	Company
CA-P1	TTA TAC ATC TAT T	Chloroalkane	Atto488	Biomers
CA-P3	TTT CTT CAT TAT T	Chloroalkane	Atto488	Biomers

Spatial association of integrin-talin-kindlin during cell matrix adhesions

CA-R1	TTT CCT CCT CCT CCT CCT CCT	Chloroalkane	None	Biomers
SNAP-R2	AAA CCA CCA CCA CCA CCA CCA AA	Benzylguanine	Atto488	Biomers
BG-P1	TTA TAC ATC TAT T	Benzylguanine	Atto488	Biomers
BG-P3	TTT CTT CAT TAT T	Benzylguanine	Atto488	Biomers
BG-P5	TTT CAA TGT AT	Benzylguanine	Atto488	Biomers
TZ-P3	TTT CTT CAT TA	Tetrazine (Methyltetrazin- PEG5)	None	Biomers

**Supplementary Table 2: DNA-PAINT sequences**

Imager strand	Sequence	5'-mod	3'-mod	Company
P1	AGA TGT AT	None	Cy3b	Eurofins
P3	AAT GAA GA	None	Cy3b	Eurofins
P5	TAC ATT GA	None	Cy3b	Eurofins
R1	AGGAGGA	None	Cy3b	Metabion
R2	TGGTGGT	None	Cy3b	Metabion

**Supplementary Table 3: Folding Protocol**

Component	Initial conc. [μM]	Parts	Pool conc. [nM]	Target conc. [nM]	Vol. [ul]	Excess
Scaffold	0.1	1	100	10	4	1
Core Mix	100	164	609.76	100	6.56	10
P3 Mix	100	12	8333.3	1000	4.8	100
Biotin 1:10	100	80	1250	10	0.32	1
H2O					20.32	
10x Folding Buffer					4	
Total Vol.					40	

**Supplementary Table 4: Core staples and extension for DNA origami assembly.**

Color coded staples were extended in the respective structures at the 3'-end with a P3 DNA-PAINT docking site: 5'- staple – TTTCTTCATTA -3'; red: 35 nm origami; orange: 30 nm origami; light green: 25 nm origami; dark green: 20 nm origami

Plate	Plate position	Oligo name	Sequence
1	A1	21[32]23[31]BLK	TTTTCACTCAAAGGGCGAAAAACCATCACC
1	A2	19[32]21[31]BLK	GTCTACTTCGGCCAACGCGCGGGGTTTTTC
1	A3	17[32]19[31]BLK	TGCATCTTTCCCAGTCACGACGGCCTGCAG
1	A4	15[32]17[31]BLK	TAATCAGCGGATTGACCGTAATCGTAACCG
1	A5	13[32]15[31]BLK	AACGCAAAATCGATGAACGGTACCGGTTGA
1	A6	11[32]13[31]BLK	AACAGTTTTGTACCAAAAACATTTTATTTTC
1	A7	9[32]11[31]BLK	TTTACCCCAACATGTTTTAAATTTCCATAT
1	A8	7[32]9[31]BLK	TTTAGGACAAATGCTTTAAACAATCAGGTC
1	A9	5[32]7[31]BLK	CATCAAGTAAAACGAACTAACGAGTTGAGA
1	A10	3[32]5[31]BLK	AATACGTTTGAAAGAGGACAGACTGACCTT
1	A11	1[32]3[31]BLK	AGGCTCCAGAGGCTTTGAGGACACGGGTAA
1	A12	0[47]1[31]BLK	AGAAAGGAACAATAAAGGAATTCAAAAAAA
1	B1	23[32]22[48]BLK	CAAATCAAGTTTTTTGGGGTTCGAAACGTG GA

Spatial association of integrin-talin-kindlin during cell matrix adhesions

1	B2	22[47]20[48]BLK	CTCCAACGCAGTGAGACGGGCAACCAG CTGCA
1	B3	20[47]18[48]P3	TTAATGAACTAGAGGATCCCCGGGGGGT AACG TTTCTTCATTA
1	B4	18[47]16[48]BLK	CCAGGGTTGCCAGTTTGAGGGGACCCGT GGGA
1	B5	16[47]14[48]BLK	ACAAACGGAAAAGCCCCAAAAACACTGG AGCA
1	B6	14[47]12[48]BLK	AACAAGAGGGATAAAAAATTTTAGCATAA AGC
1	B7	12[47]10[48]P3	TAAATCGGGATTCCAATTCTGCGATATA ATG TTTCTTCATTA
1	B8	10[47]8[48]BLK	CTGTAGCTTGACTATTATAGTCAGTTCAT TGA
1	B9	8[47]6[48]BLK	ATCCCCCTATACCACATTCAACTAGAAAA ATC
1	B10	6[47]4[48]BLK	TACGTTAAAGTAATCTTGACAAGAACCGA ACT
1	B11	4[47]2[48]P3	GACCAACTAATGCCACTACGAAGGGGGT AGCA TTTCTTCATTA
1	B12	2[47]0[48]BLK	ACGGCTACAAAAGGAGCCTTTAATGTGAGAAT
1	C1	21[56]23[63]BLK	AGCTGATTGCCCTTCAGAGTCCACTATTAAG GGTGCCGT
1	C2	BIOTIN PLACEHOLDER	see Supplementary Table 5
1	C3	BIOTIN PLACEHOLDER	see Supplementary Table 5
1	C4	15[64]18[64]BLK	GTATAAGCCAACCCGTCGGATTCTGACGACAG TATCGGCCGCAAGGCG
1	C5	13[64]15[63]BLK	TATATTTTGTTCATTGCCTGAGAGTGGAAGATT
1	C6	11[64]13[63]BLK	GATTTAGTCAATAAAGCCTCAGAGAACCC TCA
1	C7	9[64]11[63]BLK	CGGATTGCAGAGCTTAATTGCTGAAACGAGTA
1	C8	7[56]9[63]BLK	ATGCAGATACATAACGGGAATCGTCATAAATAA AGCAAAG

1	C9	BIOTIN PLACEHOLDER	see Supplementary Table 5
1	C10	BIOTIN PLACEHOLDER	see Supplementary Table 5
1	C11	1[64]4[64]BLK	TTTATCAGGACAGCATCGGAACGACACCAACC TAAACGAGGTCAATC
1	C12	0[79]1[63]BLK	ACAAC TTTCAACAGTTTCAGCGGATGTATCGG
1	D1	23[64]22[80]BLK	AAAGCACTAAATCGGAACCCTAATCCAGTT
1	D2	22[79]20[80]BLK	TGGAACAACCGCCTGGCCCTGAGGCCCGCT
1	D3	20[79]18[80]BLK	TTCCAGTCGTAATCATGGTCATAAAAGGGG
1	D4	18[79]16[80]BLK	GATGTGCTTCAGGAAGATCGCACAATGTGA
1	D5	16[79]14[80]BLK	GCGAGTAAAAATATTTAAATTGTTACAAAG
1	D6	14[79]12[80]BLK	GCTATCAGAAATGCAATGCCTGAATTAGCA
1	D7	12[79]10[80]BLK	AAATTAAGTTGACCATTAGATACTTTTGCG
1	D8	10[79]8[80]BLK	GATGGCTTATCAAAAAGATTAAGAGCGTCC
1	D9	8[79]6[80]BLK	AATACTGCCCAAAGGAATTACGTGGCTCA
1	D10	6[79]4[80]BLK	TTATACCACCAAATCAACGTAACGAACGAG
1	D11	4[79]2[80]BLK	GCGCAGACAAGAGGCCAAAAGAATCCCTCAG
1	D12	2[79]0[80]BLK	CAGCGAACTTGCTTTTCGAGGTGTTGCTAA
1	E1	21[96]23[95]BLK	AGCAAGCGTAGGGTTGAGTGTGTAGGGAGCC
1	E2	19[96]21[95]BLK	CTGTGTGATTGCGTTGCGCTCACTAGAGTTGC
1	E3	17[96]19[95]BLK	GCTTTCCGATTACGCCAGCTGGCGGCTGTTTC
1	E4	15[96]17[95]BLK	ATATTTTGGCTTTTCATCAACATTATCCAGCCA
1	E5	13[96]15[95]BLK	TAGGTAACTATTTTTGAGAGATCAAACGTTA
1	E6	11[96]13[95]BLK	AATGGTCAACAGGCAAGGCAAAGAGTAATGTG
1	E7	9[96]11[95]BLK	CGAAAGACTTTGATAAGAGGTCATATTTGCA
1	E8	7[96]9[95]BLK	TAAGAGCAAATGTTTAGACTGGATAGGAAGCC
1	E9	5[96]7[95]BLK	TCATTCAGATGCGATTTTAAGAACAGGCATAG
1	E10	3[96]5[95]BLK	ACACTCATCCATGTTACTTAGCCGAAAGCTGC
1	E11	1[96]3[95]BLK	AAACAGCTTTTTGCGGGATCGTCAACACTAAA
1	E12	0[111]1[95]BLK	TAAATGAATTTTCTGTATGGGATTAATTTCTT
1	F1	23[96]22[112]BLK	CCCGATTTAGAGCTTGACGGGAAAAAGAATA
1	F2	22[111]20[112]BLK	GCCCGAGAGTCCACGCTGGTTTGCAGCTAACT
1	F3	20[111]18[112]P3	CACATTAATTTGTTATCCGCTCATGCGGGCC TTTCTTCATTA

Spatial association of integrin-talin-kindlin during cell matrix adhesions

1	F4	18[111]16[112]BLK	TCTTCGCTGCACCGCTTCTGGTGCGGCCTTCC
1	F5	16[111]14[112]BLK	TGTAGCCATTAAAATTCGCATTAATGCCGGA
1	F6	14[111]12[112]BLK	GAGGGTAGGATTCAAAGGGTGAGACATCCAA
1	F7	12[111]10[112]P3	TAAATCATATAACCTGTTTAGCTAACCTTTAA TTTCTTCATTA
1	F8	10[111]8[112]BLK	TTGCTCCTTTCAAATATCGCGTTTGAGGGGGT
1	F9	8[111]6[112]BLK	AATAGTAAACACTATCATAACCCTCATTGTGA
1	F10	6[111]4[112]BLK	ATTACCTTTGAATAAGGCTTGCCCAAATCCGC
1	F11	4[111]2[112]P3	GACCTGCTCTTTGACCCCCAGCGAGGGAGTTA TTTCTTCATTA
1	F12	2[111]0[112]BLK	AAGGCCGCTGATACCGATAGTTGCGACGTTAG
1	G1	21[120]23[127]BLK	CCCAGCAGGCGAAAAATCCCTTATAAATCAAGCC GGCG
1	G2	BIOTIN PLACEHOLDER	see Supplementary Table 5
1	G3	BIOTIN PLACEHOLDER	see Supplementary Table 5
1	G4	15[128]18[128]BLK	TAAATCAAATAATTCGCGTCTCGGAAACCAGGC AAAGGGAAGG
1	G5	13[128]15[127]BLK	GAGACAGCTAGCTGATAAATTAATTTTTGT
1	G6	11[128]13[127]BLK	TTTGGGGATAGTAGTAGCATTAAAGGCCG
1	G7	9[128]11[127]BLK	GCTTCAATCAGGATTAGAGAGTTATTTTCA
1	G8	7[120]9[127]BLK	CGTTTACCAGACGACAAAGAAGTTTTGCCATAAT TCGA
1	G9	BIOTIN PLACEHOLDER	see Supplementary Table 5
1	G10	BIOTIN PLACEHOLDER	see Supplementary Table 5
1	G11	1[128]4[128]BLK	TGACAACCTCGCTGAGGCTTGCATTATACCAAGC GCGATGATAAA
1	G12	0[143]1[127]BLK	TCTAAAGTTTTGTCGTCTTCCAGCCGACAA
1	H1	21[160]22[144]BLK	TCAATATCGAACCTCAAATATCAATTCCGAAA
1	H2	19[160]20[144]BLK	GCAATTCACATATTCCTGATTATCAAAGTGTA
1	H3	17[160]18[144]BLK	AGAAAACAAAGAAGATGATGAAACAGGCTGCG
1	H4	15[160]16[144]BLK	ATCGCAAGTATGTAAATGCTGATGATAGGAAC

1	H5	13[160]14[144]BLK	GTAATAAGTTAGGCAGAGGCATTTATGATATT
1	H6	11[160]12[144]BLK	CCAATAGCTCATCGTAGGAATCATGGCATCAA
1	H7	9[160]10[144]BLK	AGAGAGAAAAAATGAAAATAGCAAGCAAAC
1	H8	7[160]8[144]BLK	TTATTACGAAGAACTGGCATGATTGCGAGAGG
1	H9	5[160]6[144]BLK	GCAAGGCCTCACCAGTAGCACCATGGGCTTGA
1	H10	3[160]4[144]BLK	TTGACAGGCCACCACCAGAGCCGCGATTTGTA
1	H11	1[160]2[144]BLK	TTAGGATTGGCTGAGACTCCTCAATAACCGAT
1	H12	0[175]0[144]BLK	TCCACAGACAGCCCTCATAGTTAGCGTAACGA
2	A1	23[128]23[159]BLK	AACGTGGCGAGAAAGGAAGGGAAACCAGTAA
2	A2	22[143]21[159]BLK	TCGGCAAATCCTGTTTTGATGGTGGACCCTCAA
2	A3	20[143]19[159]BLK	AAGCCTGGTACGAGCCGGAAGCATAGATGATG
2	A4	18[143]17[159]BLK	CAACTGTTGCGCCATTCGCCATTCAAACATCA
2	A5	16[143]15[159]BLK	GCCATCAAGCTCATTTTTTAACCACAAATCCA
2	A6	14[143]13[159]BLK	CAACCGTTTTCAAATCACCATCAATTCGAGCCA
2	A7	12[143]11[159]BLK	TTCTACTACGCGAGCTGAAAAGGTTACCGCGC
2	A8	10[143]9[159]BLK	CCAACAGGAGCGAACCAGACCGGAGCCTTTAC
2	A9	8[143]7[159]BLK	CTTTTGCAGATAAAAACCAAATAAAGACTCC
2	A10	6[143]5[159]BLK	GATGGTTTGAACGAGTAGTAAATTTACCATTA
2	A11	4[143]3[159]BLK	TCATCGCCAACAAAGTACAACGGACGCCAGCA
2	A12	2[143]1[159]BLK	ATATTCGGAACCATCGCCCACGCAGAGAAGGA
2	B1	23[160]22[176]BLK	TAAAAGGGACATTCTGGCCAACAAAGCATC
2	B2	22[175]20[176]BLK	ACCTTGCTTGGTCAGTTGGCAAAGAGCGGA
2	B3	20[175]18[176]P3	ATTATCATTCAATATAATCCTGACAATTAC TTTCTTCATTA
2	B4	18[175]16[176]BLK	CTGAGCAAAAATTAATTACATTTTGGGTTA
2	B5	16[175]14[176]BLK	TATAACTAACAAAGAACGCGAGAACGCCAA
2	B6	14[175]12[176]BLK	CATGTAATAGAATATAAAGTACCAAGCCGT
2	B7	12[175]10[176]P3	TTTTATTTAAGCAAATCAGATATTTTTTGT TTTCTTCATTA
2	B8	10[175]8[176]BLK	TTAACGTCTAACATAAAAACAGGTAACGGA
2	B9	8[175]6[176]BLK	ATACCCAACAGTATGTTAGCAAATTAGAGC
2	B10	6[175]4[176]BLK	CAGCAAAGGAAACGTCACCAATGAGCCGC
2	B11	4[175]2[176]P3	CACCAGAAAGGTTGAGGCAGGTCATGAAAG TTTCTTCATTA
2	B12	2[175]0[176]BLK	TATTAAGAAGCGGGGTTTTGCTCGTAGCAT

Spatial association of integrin-talin-kindlin during cell matrix adhesions

2	C1	21[184]23[191]BLK	TCAACAGTTGAAAGGAGCAAATGAAAAATCTAG AGATAGA
2	C2	BIOTIN PLACEHOLDER	see Supplementary Table 5
2	C3	BIOTIN PLACEHOLDER	see Supplementary Table 5
2	C4	15[192]18[192]BLK	TCAAATATAACCTCCGGCTTAGGTAACAATTTCA TTTGAAGGCGAATT
2	C5	13[192]15[191]BLK	GTAAAGTAATCGCCATATTTAACAAAACCTTTT
2	C6	11[192]13[191]BLK	TATCCGGTCTCATCGAGAACAAGCGACAAAAG
2	C7	9[192]11[191]BLK	TTAGACGGCCAAATAAGAAACGATAGAAGGCT
2	C8	7[184]9[191]BLK	CGTAGAAAATACATACCGAGGAAACGCAATAAG AAGCGCA
2	C9	BIOTIN PLACEHOLDER	see Supplementary Table 5
2	C10	BIOTIN PLACEHOLDER	see Supplementary Table 5
2	C11	1[192]4[192]BLK	GCGGATAACCTATTATTCTGAAACAGACGATTG GCCTTGAAGAGCCAC
2	C12	0[207]1[191]BLK	TCACCAGTACAACTACAACGCCTAGTACCAG
2	D1	23[192]22[208]BLK	ACCCTTCTGACCTGAAAGCGTAAGACGCTGAG
2	D2	22[207]20[208]BLK	AGCCAGCAATTGAGGAAGTTATCATCATTTT
2	D3	20[207]18[208]BLK	GCGGAACATCTGAATAATGGAAGGTACAAAAT
2	D4	18[207]16[208]BLK	CGCGCAGATTACCTTTTTTAATGGGAGAGACT
2	D5	16[207]14[208]BLK	ACCTTTTTATTTTAGTTAATTTTCATAGGGCTT
2	D6	14[207]12[208]BLK	AATTGAGAATTCTGTCCAGACGACTAAACCAA
2	D7	12[207]10[208]BLK	GTACCGCAATTCTAAGAACGCGAGTATTATTT
2	D8	10[207]8[208]BLK	ATCCCAATGAGAATTAACCTGAACAGTTACCAG
2	D9	8[207]6[208]BLK	AAGGAAACATAAAGGTGGCAACATTATCACCG
2	D10	6[207]4[208]BLK	TCACCGACGCACCGTAATCAGTAGCAGAACCG
2	D11	4[207]2[208]BLK	CCACCCTCTATTCACAAACAAATACCTGCCTA
2	D12	2[207]0[208]BLK	TTTCGGAAGTGCCGTCGAGAGGGTGAGTTTCG
2	E1	21[224]23[223]BLK	CTTTAGGGCCTGCAACAGTGCCAATACGTG
2	E2	19[224]21[223]BLK	CTACCATAGTTTGAGTAACATTTAAAATAT
2	E3	17[224]19[223]BLK	CATAAATCTTTGAATACCAAGTGTTAGAAC

2	E4	15[224]17[223]BLK	CCTAAATCAAATCATAGGTCTAAACAGTA
2	E5	13[224]15[223]BLK	ACAACATGCCAACGCTCAACAGTCTTCTGA
2	E6	11[224]13[223]BLK	GCGAACCTCCAAGAACGGGTATGACAATAA
2	E7	9[224]11[223]BLK	AAAGTCACAAAATAAACAGCCAGCGTTTTA
2	E8	7[224]9[223]BLK	AACGCAAAGATAGCCGAACAAACCCTGAAC
2	E9	5[224]7[223]BLK	TCAAGTTTCATTAAAGGTGAATATAAAAGA
2	E10	3[224]5[223]BLK	TTAAAGCCAGAGCCGCCACCCTCGACAGAA
2	E11	1[224]3[223]BLK	GTATAGCAAACAGTTAATGCCCAATCCTCA
2	E12	0[239]1[223]BLK	AGGAACCCATGTACCGTAACACTTGATATAA
2	F1	23[224]22[240]BLK	GCACAGACAATATTTTTGAATGGGGTCAGTA
2	F2	22[239]20[240]BLK	TTAACACCAGCACTAACAATAATCGTTATTA
2	F3	20[239]18[240]P3	ATTTTAAAATCAAATTATTTGCACGGATTCC TTTCTTCATTA
2	F4	18[239]16[240]BLK	CCTGATTGCAATATATGTGAGTGATCAATAGT
2	F5	16[239]14[240]BLK	GAATTTATTTAATGGTTTGAAATATTCTTACC
2	F6	14[239]12[240]BLK	AGTATAAAGTTCAGCTAATGCAGATGTCTTTC
2	F7	12[239]10[240]P3	CTTATCATTCCCGACTTGCGGGAGCCTAATTT TTTCTTCATTA
2	F8	10[239]8[240]BLK	GCCAGTTAGAGGGTAATTGAGCGCTTTAAGAA
2	F9	8[239]6[240]BLK	AAGTAAGCAGACACCACGGAATAATATTGACG
2	F10	6[239]4[240]BLK	GAAATTATTGCCTTTAGCGTCAGACCGGAACC
2	F11	4[239]2[240]P3	GCCTCCCTCAGAATGGAAAGCGCAGTAACAGT TTTCTTCATTA
2	F12	2[239]0[240]BLK	GCCCGTATCCGGAATAGGTGTATCAGCCCAAT
2	G1	21[248]23[255]BLK	AGATTAGAGCCGTCAAAAAACAGAGGTGAGGC CTATTAGT
2	G2	BIOTIN PLACEHOLDER	see Supplementary Table 5
2	G3	BIOTIN PLACEHOLDER	see Supplementary Table 5
2	G4	15[256]18[256]BLK	GTGATAAAAAGACGCTGAGAAGAGATAACCTTG CTTCTGTTCGGGAGA
2	G5	13[256]15[255]BLK	GTTTATCAATATGCGTTATACAAACCGACCGT
2	G6	11[256]13[255]BLK	GCCTTAAACCAATCAATAATCGGCACGCGCCT
2	G7	9[256]11[255]BLK	GAGAGATAGAGCGTCTTTCCAGAGGTTTTGAA

Spatial association of integrin-talin-kindlin during cell matrix adhesions

2	G8	7[248]9[255]BLK	GTTTATTTTGT CACAATCTTACCGAAGCCCTTA ATATCA
2	G9	BIOTIN PLACEHOLDER	see Supplementary Table 5
2	G10	BIOTIN PLACEHOLDER	see Supplementary Table 5
2	G11	1[256]4[256]BLK	CAGGAGGTGGGGTCAGTGCCTTGAGTCTCTGA ATTTACCGGGAACCAG
2	G12	0[271]1[255]BLK	CCACCCTCATTTTCAGGGATAGCAACCGTACT
2	H1	23[256]22[272]BLK	CTTTAATGCGCGAACTGATAGCCCCACCAG
2	H2	22[271]20[272]BLK	CAGAAGATTAGATAATACATTTGTGCGACAA
2	H3	20[271]18[272]BLK	CTCGTATTAGAAATTGCGTAGATACAGTAC
2	H4	18[271]16[272]BLK	CTTTTACAAAATCGTCGCTATTAGCGATAG
2	H5	16[271]14[272]BLK	CTTAGATTTAAGGCGTTAAATAAAGCCTGT
2	H6	14[271]12[272]BLK	TTAGTATCACAATAGATAAGTCCACGAGCA
2	H7	12[271]10[272]BLK	TGTAGAAATCAAGATTAGTTGCTCTTACCA
2	H8	10[271]8[272]BLK	ACGCTAACACCCACAAGAATTGAAAATAGC
2	H9	8[271]6[272]BLK	AATAGCTATCAATAGAAAATTCAACATTCA
2	H10	6[271]4[272]BLK	ACCGATTGTCGGCATTTCGGTCATAATCA
2	H11	4[271]2[272]BLK	AAATCACCTTCCAGTAAGCGTCAGTAATAA
2	H12	2[271]0[272]BLK	GTTTTAACTTAGTACCGCCACCCAGAGCCA

**Supplementary Table 5: Biotinylated staples**

No	Pos.	Name	Sequence	Mod.
1	C02	18[63]20[56]BIOTIN	ATTAAGTTTACCGAGCTCGAATTC GGGAAACCTGTGCTGC	5'-BT
2	C09	4[63]6[56]BIOTIN	ATAAGGGAACCGGATATTCATTAC GTCAGGACGTTGGGAA	5'-BT
3	G02	18[127]20[120]BIOTIN	GCGATCGGCAATTCCACACAACA GGTGCCTAATGAGTG	5'-BT
4	G09	4[127]6[120]BIOTIN	TTGTGTCGTGACGAGAAACACCAA ATTTCAACTTTAAT	5'-BT
5	K02	18[191]20[184]BIOTIN	ATTCATTTTTGTTTGGATTATACTA AGAAACCACCAGAAG	5'-BT

6	K09	4[191]6[184]BIOTIN	CACCCTCAGAAACCATCGATAGCA TTGAGCCATTTGGGAA	5'-BT
7	O02	18[255]20[248]BIOTIN	AACAATAACGTAAAACAGAAATAA AAATCCTTTGCCCGAA	5'-BT
8	O09	4[255]6[248]BIOTIN	AGCCACCACTGTAGCGCGTTTTCA AGGGAGGGAAGGTAAA	5'-BT

**Supplementary Table 6: Parameter for DNA-PAINT simulations**

Parameter	Value
$k_{on}$	1715000 M <sup>-1</sup> s <sup>-1</sup>
Imager concentration	2.5 nM
Bright time	400 ms
Incorporation	100 %
Power density	1.24 kW cm <sup>-2</sup>
Photon detection rate	30 Photons ms <sup>-1</sup> kW <sup>-1</sup> cm <sup>2</sup>
Integration time	100 ms
Frames	80000
Pixelsize	130 nm

**Supplementary References**

- 1 Soto-Ribeiro, M. *et al.*  $\beta$ 1D integrin splice variant stabilizes integrin dynamics and reduces integrin signaling by limiting paxillin recruitment. **132**, jcs224493, doi:10.1242/jcs.224493 %J Journal of Cell Science (2019).
- 2 Theodosiou, M. *et al.* Kindlin-2 cooperates with talin to activate integrins and induces cell spreading by directly binding paxillin. *Elife* **5**, doi:ARTN e10130 10.7554/eLife.10130 (2016).
- 3 Austen, K., Kluger, C., Freikamp, A., Chrostek-Grashoff, A. & Grashoff, C. Generation and analysis of biosensors to measure mechanical forces within cells. *Methods Mol Biol* **1066**, 169-184, doi:10.1007/978-1-62703-604-7\_15 (2013).
- 4 Bottcher, R. T. *et al.* Kindlin-2 recruits paxillin and Arp2/3 to promote membrane protrusions during initial cell spreading. *J Cell Biol* **216**, 3785-3798, doi:10.1083/jcb.201701176 (2017).
- 5 Schiller, H. B. *et al.* beta(1)- and alpha(v)-class integrins cooperate to regulate myosin II during rigidity sensing of fibronectin-based microenvironments. *Nature Cell Biology* **15**, 625-+, doi:10.1038/ncb2747 (2013).
- 6 Schnitzbauer, J., Strauss, M. T., Schlichthaerle, T., Schueder, F. & Jungmann, R. Super-resolution microscopy with DNA-PAINT. *Nat Protoc* **12**, 1198-1228, doi:10.1038/nprot.2017.024 (2017).
- 7 Wagenbauer, K. F. *et al.* How We Make DNA Origami. *Chembiochem* **18**, 1873-1885, doi:10.1002/cbic.201700377 (2017).
- 8 Schlichthaerle, T., Ganji, M., Auer, A., Kimbu Wade, O. & Jungmann, R. Bacterially Derived Antibody Binders as Small Adapters for DNA-PAINT Microscopy. *Chembiochem* **20**, 1032-1038, doi:10.1002/cbic.201800743 (2019).
- 9 Endesfelder, U., Malkusch, S., Fricke, F. & Heilemann, M. A simple method to estimate the average localization precision of a single-molecule localization microscopy experiment. *Histochem Cell Biol* **141**, 629-638, doi:10.1007/s00418-014-1192-3 (2014).

- 
- 10 Jungmann, R. *et al.* Quantitative super-resolution imaging with qPAINT. *Nat Methods* **13**, 439-442, doi:10.1038/nmeth.3804 (2016).
  - 11 Ester, M., Kriegel, H.-P., Sander, J. & Xu, X. (KDD).
  - 12 Pedregosa, F. *et al.* Scikit-learn: Machine Learning in Python. **12**, 2825–2830 (2011).
  - 13 Peacock, J. A. Two-Dimensional Goodness-of-Fit Testing in Astronomy. *Mon Not R Astron Soc* **202**, 615-627, doi:DOI 10.1093/mnras/202.3.615 (1983).
  - 14 Thevathasan, J. V. *et al.* Nuclear pores as versatile reference standards for quantitative superresolution microscopy. *Nat Methods* **16**, 1045-1053, doi:10.1038/s41592-019-0574-9 (2019).
  - 15 Schlichthaerle, T. *et al.* Direct Visualization of Single Nuclear Pore Complex Proteins Using Genetically-Encoded Probes for DNA-PAINT. *Angew Chem Int Ed Engl* **58**, 13004-13008, doi:10.1002/anie.201905685 (2019).